Report MCR-72-91

SYSTEMS-LEVEL STUDY OF A NONSURVIVABLE JUPITER TURBOPAUSE PROBE

Volume II - Supporting Technical Studies

R. S. Wiltshire, Program Manager
Martin Marietta Corporation
Denver Division
Post Office Box 179
Denver, Colorado 80201

June 1972

Final Report

Prepared for

GODDARD SPACE FLIGHT CENTER

Greenbelt, Maryland 20771

STANDARD TITLE PAGE

1. Report No. MCR-72-91	2. Government Accession No.	3. Recipient's Catalog No.
4. Title and Subtitle Systems-Level Study of a Non-survivable Jupiter Turbopause Probe. Vol I Summary, Vol II Supporting Technical Studies, Vol III Appendixes		5. Report Date June 1972 6. Performing Organization Code
7. Author(s) R. S. Wiltshire, Program Manager		8. Performing Organization Report No. MCR-72-91
9. Performing Organization Name and Address Martin Marietta Corporation Denver Division P.O. Box 179 Denver, Colorado 80201		10. Work Unit No. 11. Contract or Grant No. NAS5-11445 13. Type of Report and Period Covered Study Report June 4, 1971 thru March 4, 1972
12. Sponsoring Agency Name and Address National Aeronautics and Space Administration Goddard Space Flight Center Greenbelt Road Greenbelt, Maryland 20771		14. Sponsoring Agency Code
15. Supplementary Notes		

16. Abstract

This nine-month study of a probe to explore the Jovian atmosphere and environment included five major tasks: definition of science requirements, mission evaluation, definition of the probe system, definition of spacecraft support requirements, and nonequilibrium flow-field analysis for communications blackout evaluation.

This report emphasizes the overall mission and system design and describes the integration of the various technology efforts into complete mission designs. Included are the study constraints, science and mission objectives, mission selection rationale, and design summaries describing required engineering implementation. Critical technical problems and major trade study results are discussed.

Results showed that a nonsurvivable turbopause probe mission to Jupiter, with adequate data return to meet the science objectives, is feasible and practical within the 1975 state of the art. Many probe mission options are practical using the Pioneer or MOPS spacecraft with the 5-segment solids Titan IIID/Centaur/Burner II launch vehicle.

17. Key Words (Selected by Author(s))	18. Distribution Statement
1. Nonsurvivable Turbopause Probe 2. Jupiter Atmosphere 3. Mission and System Design 4. Outer-Planet Missions	

19. Security Classif. (of this report)	20. Security Classif. (of this page)	21. No. of Pages	22. Price
UNCLASSIFIED	UNCLASSIFIED		29.00

FOREWORD

This final report has been prepared in accordance with requirements of Contract NAS5-11445 to present data and conclusions from a nine-month study for Goddard Space Flight Center by the Martin Marietta Corporation, Denver Division. The work was done under the management of the NASA Project Manager, Mr. George M. Levin, Advanced Plans Staff, NASA-Goddard Space Flight Center. The report is divided into the following volumes:

I - SUMMARY

II - SUPPORTING TECHNICAL STUDIES

III - APPENDIXES

ACKNOWLEDGEMENTS

The following Martin Marietta Corporation, Denver Division, personnel participated in this study, and their efforts are greatly appreciated:

R. S. Wiltshire	Study Leader, Program Manager
Leonard R. Anderson	Mission Analysis
Eugene A. Berkery	Telecommunications, Data Handling, Power, and ACS, Lead
Leo R. Bonorden	Mechanical Design
Ronald D. Bryant	Nonequilibrium Flow-Field Analysis, Lead
Jack O. Bunting	Science Instruments
Dennis V. Byrnes	Navigation
Patrick C. Carroll	Systems, Lead
Revis E. Compton, Jr.	Telecommunications
Robert G. Cook	Mechanical Design
C. Thomas Edquist	Aerophysics
Robert B. Fischer	Mission Analysis
John W. Hungate	Systems
Carl L. Jensen	Thermal Analysis
Melvin W. Kuethe	Mechanical/Structural/Probe Integration, Lead
Kenneth W. Ledbetter	Science, Lead
James M. Lefferdo	Aerophysics, Lead
Wayne D. Meitzler	Mission Analysis
Jack D. Pettus	Data Link Analysis
Robert J. Richardson	Receiver Systems
Arlen I. Reichert	Propulsion
Peter C. Steel	Aeroheating
John G. Vega	Data Handling
E. Doyle Vogt	Mission Analysis, Lead
Donald E. Wainwright	Systems
Clifford M. Webb	Thermal Analysis
Charles E. Wilkerson	Data Handling

CONTENTS

Figure

Table

I. INTRODUCTION

This volume contains discussions of the technical studies and detailed descriptions of the missions studied. The report is arranged to present the environments, science studies, and mission analysis and design studies first because these efforts establish the science and mission constraints that lead to system design criteria. Sample mission descriptions illustrate required hardware implementation for various mission options and provide a basis for comparing options. Supporting hardware studies follow--telecommunications, data handling, power, probe mechanical/structural, probe attitude control, and spacecraft modification. These hardware-description chapters present basic parametric and trade-study results for the various subsystems. The trade studies necessarily interrelate two or more technical areas and considerable cross-referencing is required.

To highlight their importance, two additional study tasks are included in this volume as separate chapters. Chapter X presents the aerophysics work, with particular emphasis on the prediction of electron density in the wake, using a detailed thermochemical nonequilibrium analysis of the complete hypersonic flow field surrounding the entry probe. These data provided input to Chapter VI, in which the telecommunications analysis predicted RF-data blackout as a function of both probe depth of penetration into the atmosphere and RF frequency.

Chapter XI presents the general problem of radiation and its effects on subsystem design. The latest model of the estimated Jupiter radiation-belt intensities for the upper-limit case has a significant effect on both probe and spacecraft design. Until additional information is obtained from the Pioneer-Jupiter flyby missions, it will be necessary to design for this environment and accept the resulting system penalties. Within the scope of this study, only a brief evaluation of the effects of the Jupiter radiation belt on probe design was possible. However, preliminary results indicate that acceptable design penalties are possible through appropriate choice of subsystem components.

II. ENVIRONMENTAL MODELS

This chapter presents the environmental models used in the study for the Jupiter atmosphere, ionosphere, radiation belt, meteoroid and magnetic field. These data establish the basic environmental design criteria from which science measurements and engineering design requirements are developed. The atmosphere model was specified by GSFC in the statement of work, while the remaining models were assumed by Martin Marietta and based on NASA reports for the meteoroids and magnetic fields, a JPL working group report for the radiation belts, and Martin Marietta analyses for the ionosphere done under separate contract to GSFC.

A. ATMOSPHERIC MODEL

The atmospheric models used in this study were furnished by GSFC as Attachment II to the statement of work. They are primarily based on the work of Dr. D. M. Hunten at Kitt Peak National Observatory, and in particular, Ref II-1. Appendix F to this report includes the curves for the model. Figure II-1 shows a condensed version of the number densities in the vicinity of the turbopause. The curve for methane came from Ref II-2 and is not shown on any of the curves in the appendix.

There are two lines shown in Fig. II-1. The dashed line represents a H/He ratio of 1.0 while the solid line represents a H/He ratio of about 8.0. These are considered to be the limiting bounds for this study. As can be seen, the differences are generally not large. The largest separation at the turopause is with helium and methane. With helium, the variation is slightly more than one order of magnitude in number density, which is a good representation of the uncertainty of this model. For methane, the difference is larger--about 1.5 orders of magnitude--but, in general, not enough is known about the minor constituents to accurately establish their profiles. It is generally accepted, however, that methane disappears very rapidly above the turbopause. This means that detection of carbon by the instruments indicates that the probe has reached the turbopause.

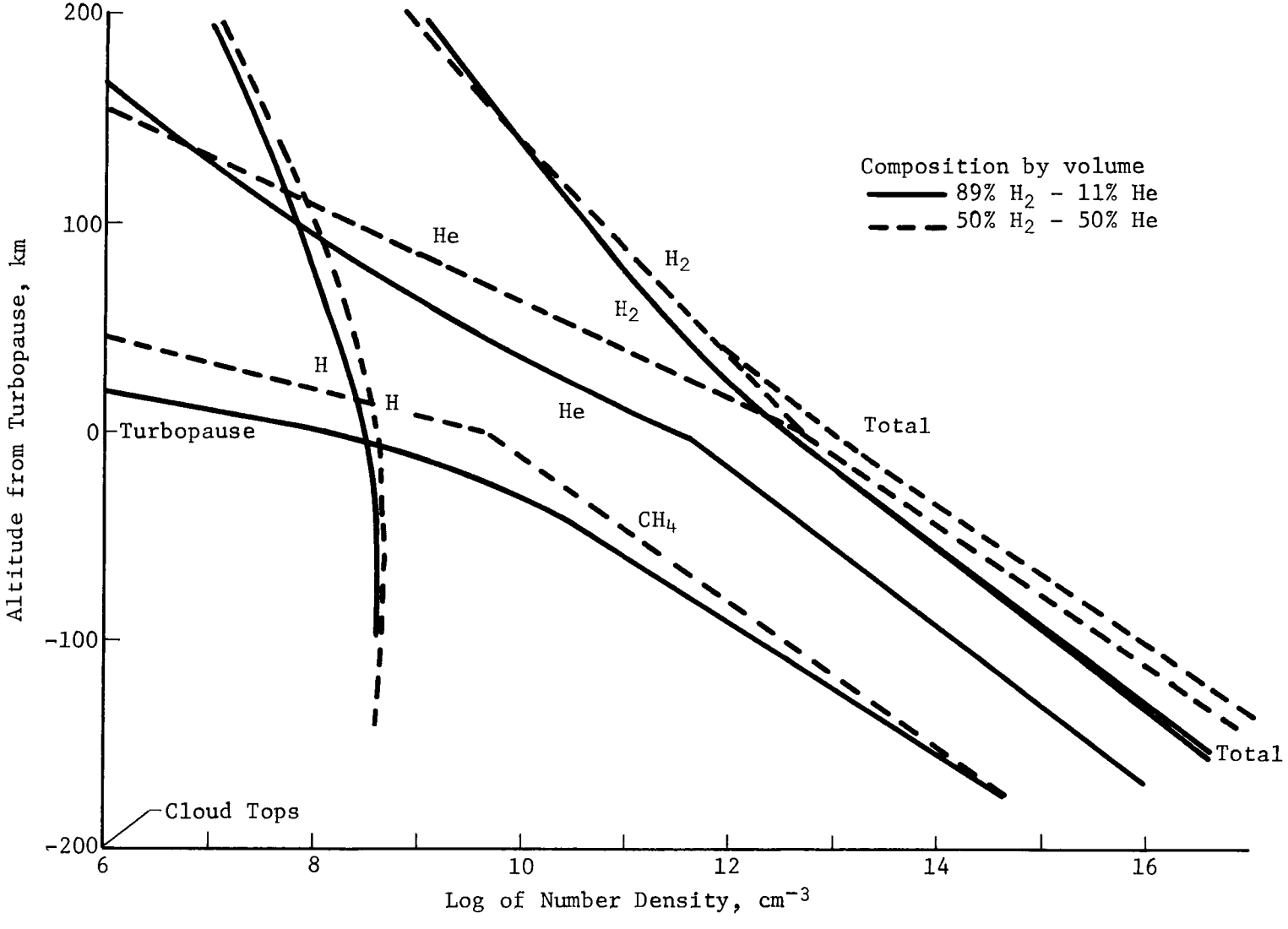

Fig. II-1 Number Densities of the Jovian Atmosphere

Table II-1 gives the abundance and number density in the vicinity of the turbopause for the 11 most abundant isotopes for the 89% H_2 - 11% He atmosphere. H^1 and He^4 are the primary constituents, with C^{12} the next most abundant.

Table II-1 Isotope Abundance at Turbopause

Isotope	Abundance	Density, particles/cm^3
H^1	3.44×10^{10}	4.91×10^{12}
D^2	5.2×10^{6}	7.42×10^{8}
He^3	7.6×10^{5}	1.08×10^{8}
He^4	2.53×10^{9}	3.61×10^{11}
C^{12}	1.20×10^{7}	1.71×10^{9}
C^{13}	1.35×10^{5}	1.93×10^{7}
N^{14}	2.94×10^{6}	4.19×10^{8}
Ne^{20}	1.85×10^{6}	2.64×10^{8}
Ne^{22}	1.80×10^{5}	2.57×10^{7}
A^{36}	8.4×10^{4}	1.20×10^{7}
A^{38}	1.6×10^{4}	2.28×10^{6}

The density scale height of a particular constituent is the distance (altitude) it requires for the number density to change by one exponential decay factor. Theoretically, for an isothermal atmosphere, density is given by the following (Ref II-3):

$$\rho = \rho_0 \, e^{-gz/RT}$$

where:

R = Specific gas constant

T = Temperature

z = Altitude

g = Acceleration of gravity

where the scale height is defined as

$$H = \frac{RT}{g}$$

so the density becomes

$$\rho = \rho_0 \, e^{-z/H}.$$

On a plot of altitude (z) versus the natural logarithm of the density, the scale height for any atmosphere is the slope of the curve, that is:

$$H = - \frac{dz}{d\ln\rho}$$

Given the equations for the number densities, the scale heights can be found by numerical differentiation. This has been done for H, H_2, and He. The equations and scale heights used in this study are shown in Table II-2.

Table II-2 Neutral Number Densities and Scale Heights

	Equation	Scale Height, km, at z = 200 km
H	$\log_{10} n = -0.0079z + 10.075$	55.0
H_2	$\log_{10} n = \begin{cases} -0.0267z + 17.82 & (z < 29 \text{ km}) \\ -0.0158z + 15.275 & (z > 29 \text{ km}) \end{cases}$	27.5
He	$\log_{10} n = -0.0315z + 17.50$	13.8

B. IONOSPHERIC MODEL

The model ionosphere used in this study is shown in Fig. II-2. It was extrapolated from D. M. Hunten's work by the Flow Technology group at Martin Marietta. The details of this effort are described in Ref II-4. Dr. Hunten has agreed with the approach used, and that the results are adequate for planning purposes (Ref II-5).

All the curves, except for H_2^+, are relatively straight with a a sharp knee. The knee for H_1^+ occurs just above the turbopause, H_3^+ at 129 km, and He^+ and HeH^+ ions at about 95 km. This gives all but the H_2^+ ion a relatively constant scale height above the knee. Equations for the number density production rates are given in Table II-3 and associated scale heights for two altitudes in Table II-4.

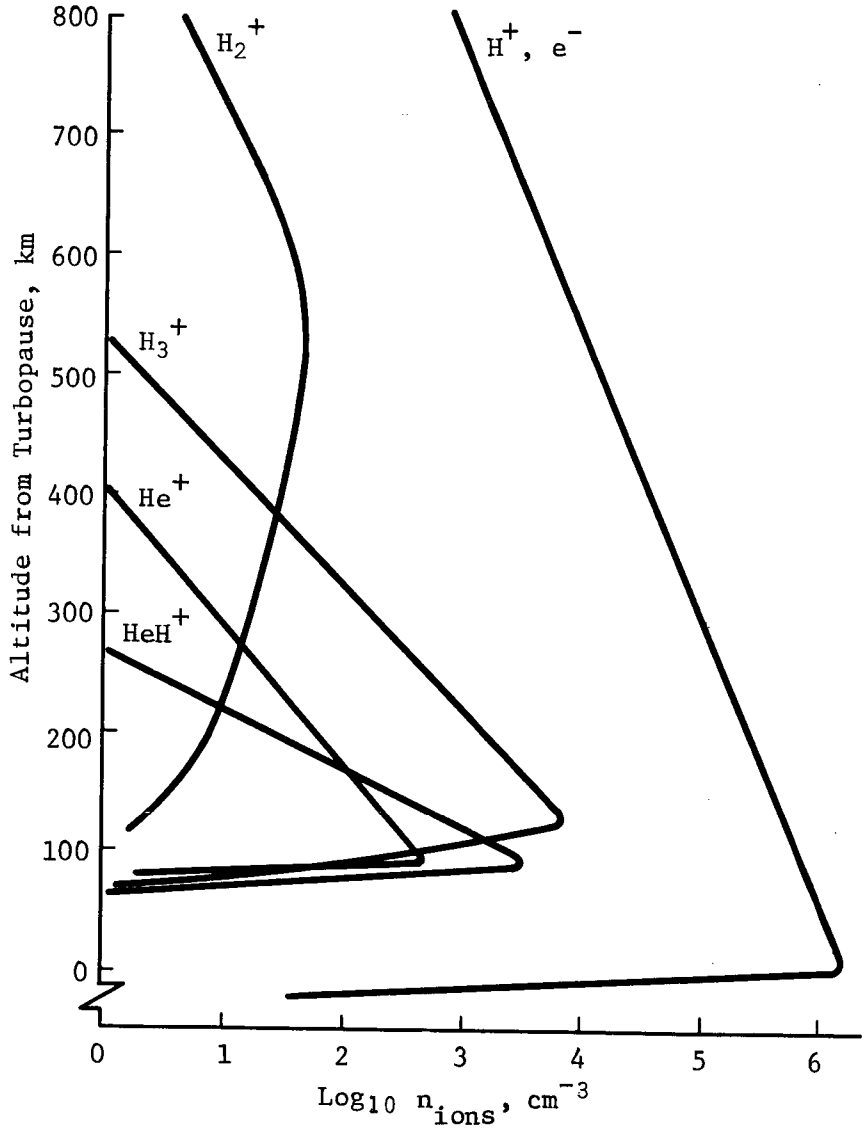

Fig. II-2 Ion Number Density

Table II-3 Ion Number Density Equations

$$(1)\quad \dot{n}(He^+) = Q_e(He) - \alpha_{11}\, n_e\, n(He^+) - \alpha_4\, n(He^+)\, n(H_2) - \alpha_5\, n(He^+)\, n(H_2)$$

$$(2)\quad \dot{n}(H_2^+) = Q_e(H_2) - \alpha_9\, n_e\, n(H_2^+) - \alpha_8\, n(He)\, n(H_2^+) - \alpha_6\, n(H_2)\, n(H_2^+) - \alpha_7\, n(H)\, n(H_2^+) + \alpha_4\, \dot{n}(H)\, n(He^+)$$

$$(3)\quad \dot{n}(HeH^+) = \alpha_5\, n(H_2)\, n(He^+) + \alpha_8\, n(He)\, n(H_2^+) - \alpha_{10}\, n_e\, n(HeH^+)$$

$$(4)\quad \dot{n}(H_3^+) = \alpha_6\, n(H_2)\, n(H_2^+) - \alpha_{12}\, n_e\, n(H_3^+)$$

$$(5)\quad \dot{n}(H^+) = Q_e(H) + \alpha_7\, n(H_2^+)\, n(H) - \alpha_{13}\, n_e\, n(H^+)$$

$$(6)\quad \dot{n}_e = Q_e(H_2) + Q_e(He) + Q_e(H) - \alpha_9\, n_e\, n(H_2^+) - \alpha_{10}\, n_e\, n(HeH^+) - \alpha_{11}\, n_e\, n(He^+) - \alpha_{12}\, n_e\, n(H_3^+) - \alpha_{13}\, n_e\, n(H^+)$$

Table II-4 Ion Scale Heights

Particle	Altitude = 200 km	Altitude = 800 km
H_1^+	-108.4	-99.5
H_2^+	+151.3	-86.9
H_3^+	-48.8	-26.4
He^+	-50.5	-50.5
HeH^+	-21.3	-21.7

C. RADIATION BELT MODEL

Jupiter proton and electron natural radiation environment models were generated by the Jupiter Radiation Belt workshop in mid-summer 1971. Data for equatorial flyby trajectories include nominal and upper-limit models and show the protection afforded by shielding up to 16 grams/cm^2. Data shown in Fig. II-3 and II-4 were used in determining the radiation environments for the probe and spacecraft. At 1 R_J in Fig. II-3, it can be seen that shielding is ineffective for both the nominal and upper-limit models. Probe environment was taken at 1 R_J with only half the fluence values because the probe sees only half the flyby exposure. Table II-5 shows the data translated into upper-limit radiation environments (without any shielding) for fluence, radiation dosage, and equivalent neutrons, because many of the subsystem damage thresholds are expressed in these units.

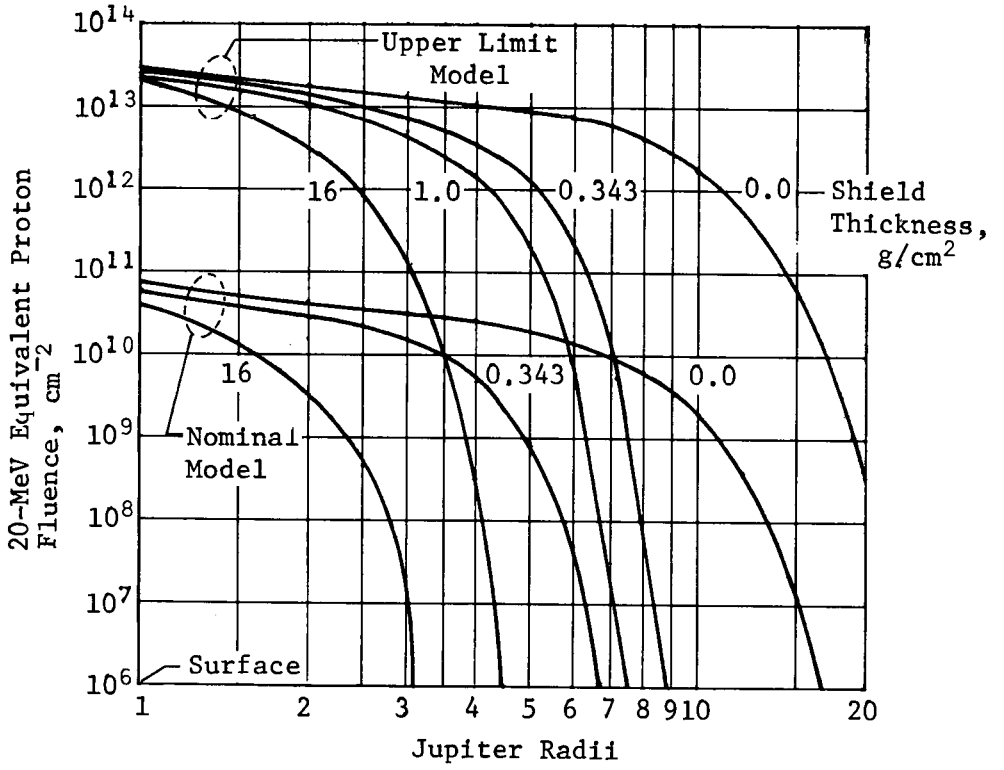

Fig. II-3 Equatorial Flyby Trajectories Workshop Nominal and Upper-Limit Proton Models

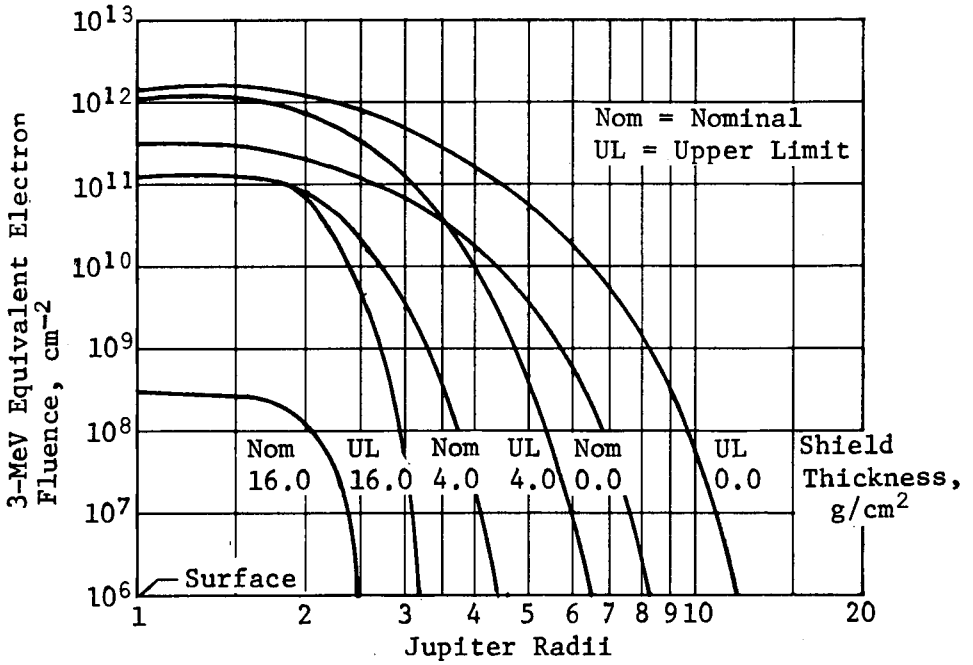

Fig. II-4 Equatorial Flyby Trajectories Workshop Nominal and Upper-Limit Electron Models

Table II-5 Jupiter Turbopause Probe Radiation Environment - Unprotected

Environment	Fluence, particles/cm^2)		Dose, rad		Equivalent Neutrons	
	Nominal	Upper Limit	Nominal	Upper Limit	Nominal	Upper Limit
20-Mev Protons	3.6×10^{10}	1.43×10^{13}	1,200	477,000	7.2×10^{10}	2.9×10^{13}
3-MEV Electrons	1.6×10^{11}	8.0×10^{12}	5,300	27,000	5.3×10^{7}	2.7×10^{8}
Totals			6,500	504,000	7.2×10^{10}	2.9×10^{13}
Conversion Factors Used:	3×10^7 protons/rad 3×10^7 electrons/rad		1 neutron = 0.5 protons 1 neutron = 3000 electrons			

The spacecraft (S/C) and probe itself provide artifical radiation fields as a result of the radioisotope thermoelectric generators (RTGs), which are power sources on the S/C, and radioisotope heater units on the probe. Throughout the mission these articicial devices emit gamma rays and energetic neutrons. The RTGs and the heaters on the probe impose artificial environments on the probe, as shown in Table II-6.

Table II-6 Artificial Radiation Probe Environment

Radiation Source	Dose Rates		Dose for JS-77 Mission	
	Gamma, rad/hr	Neutrons, $n/cm^2/sec$	Gamma, rad	Neutrons, n/cm^2
Pioneer RTGs	1×10^{-2}	3.6×10^{2}	N/A	N/A
TOPS RTGs	5.6×10^{-2}	2×10^{3}	N/A	N/A
MOPS RTGs	4.9×10^{-2}	1.7×10^{3}	6550	8.3×10^{8}
Probe Heaters	--	1.2×10^{3} at surface		5.3×10^{8}
S/C data calculated using North American Rockwell Report SD 71-770, November 1971.				

D. METEOROID MODEL

The meteoroid model used to evaluate the Jupiter Turbopause probe is defined by NASA SP-8038, NASA Space Vehicle Design Criteria (Environment), Meteoroid Environment Model - 1970 (Interplanetary and Planetary), dated October 1970. Figure II-5 shows the cometary meteroid spatial density from 1 to 5.3 AU from the Sun (Jupiter encounter distance for JS-77 mission). Cometary meteroid distributions are shown for three different meteoroid mass values: 10^{-12}, 10^{-6}, and 10^{2} grams, all for ecliptic missions. In addition, the figure shows a ratio of asteroid spatial density from 1 to 4.66 AU from the Sun. From the above reference, it can be seen that the meteroid and asteroid flux is directly proportional to the respective spatial density and weighted average particle velocity. Other factors, such as asymmetry of the asteroid belt with the heliocentric longitude and latitudinal distribution of asteroidal particles, are of secondary importance.

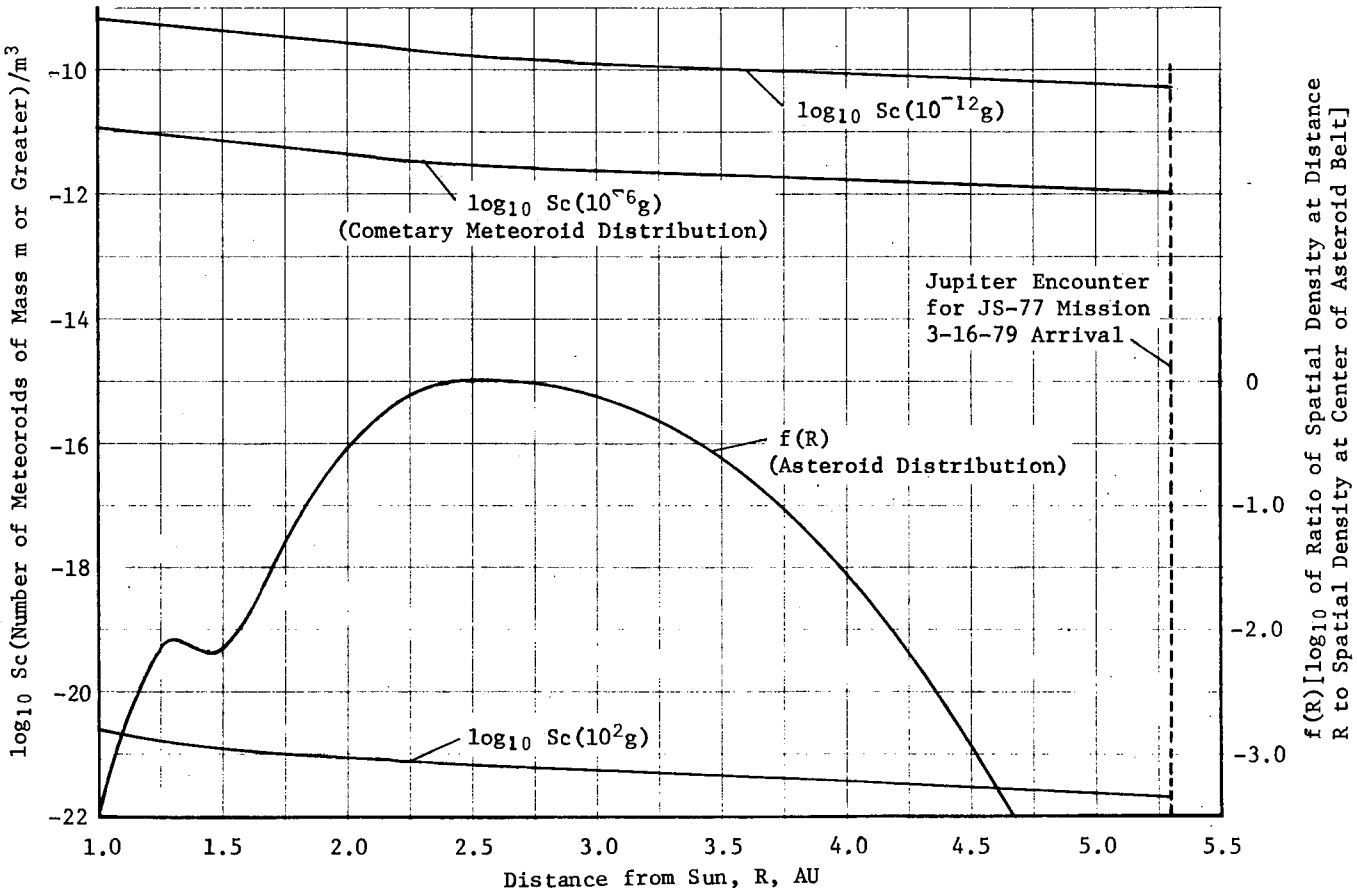

Fig. II-5 Cometary Meteoroid and Asteroid Radial Distribution

E. MAGNETIC FIELD MODEL

The magnetic field model used for this study was taken from NASA SP-8069, Ref II-6. The given dipole moment is between 3×10^{30} and 4×10^{30} gauss-cm^3. The equation for field strength for any latitude (ϕ) and radius (R) is

$$B = \frac{M}{R^3} [1 + 3 \sin^2 \phi]^{\frac{1}{2}}$$

where M is the dipole moment. Reference II-6 states: "The consequent range of field strengths in the atmosphere is from 6 gauss at the equator to 48 gauss at the poles if the dipole is centered on Jupiter." In the vicinity where the Langmuir probes are measuring, a conservative value for the strength is 12 gauss.

F. REFERENCES

II-1. D. M. Hunten: "The Upper Atmosphere of Jupiter," *Journal of the Atmospheric Sciences*, Vol. 26, No. 5, Part 1, Sept 1969.

II-2. R. M. Goody and G. M. Levin: *The Jovian Turbopause Probe*, Parts I and II, GSFC Report No. X-110-70-442, Dec 1970.

II-3. Seymour L. Hess: *Introduction to Theoretical Meteorology*, Holt, Rinehart and Winston, New York, 1959.

II-4. S. G. Chapin, Program Manager: *Jupiter Turbopause Probe Gas Physics Environment and Instrument Response Study*, Final Report, Martin Marietta Corporation Report MCR-71-142.

II-5. D. M. Hunten: Letter to J. Bunting and W. Rumpel concerning model ionosphere, May 13, 1971.

II-6. "The Planet Jupiter (1970)," *NASA Space Vehicle Design Criteria*, NASA SP-8069. Aug 1971.

III. SCIENCE INVESTIGATIONS

In this section, the overall science rationale will be discussed. The science requirements, objectives, and constraints were provided by GSFC at the beginning of the study. They are summarized here for completeness. The set of measurements needed to satisfy the objectives are listed and discussed. In addition, performance criteria are presented for the measurements, and entry site targeting constraints are analyzed. This is followed by a description of the GSFC supplied instruments to be used and their measurement techniques, including operational descriptions. The final section is science mission analysis with a detailed investigation of mission parameters related to science performance, and a discussion of how best to fly the mission for optimum science return. This last section is the study's major contribution to the science area.

A. OBJECTIVES

The science objectives of a Jovian turbopause probe mission resulting from prior studies (Ref III-1 and III-2) are to:

1) directly determine bulk composition of the mixed atmosphere;

2) investigate properties of the upper atmosphere and ionosphere

As defined here, upper atmosphere is the region of diffusive gravitational separation of light and heavy gases with its base at the turbopause. Below the turbopause, constituents become mixed so that composition is roughly constant and appreciably heavier gases are present. An important requirement imposed by the first objective is that the probe must penetrate deep enough below the turbopause to determine bulk composition. This requires a time long enough to sweep from 1 to 38 amu with a mass spectrometer. An investigation of the upper atmosphere and ionosphere (specifically, their structure, composition, ionization, and photochemistry) is equally important. Measurements in these regions should determine temperature, composition, particle separation, positive ion density, and electron density, permitting a thorough understanding of both regions. Further details on objectives are given in *The Jovian Turbopause Probe* by G. M. Levin and R. M. Goody, GSFC Report X-110-70-442, Part I, Ref III-1.

B. RELEVANT MEASUREMENTS AND PERFORMANCE CRITERIA

1. Measurements and Criteria

To satisfy the requirements and objectives, a list of necessary measurements related to objectives is shown in Table III-1 with corresponding performance criteria. The most important measurements to be made are those necessary to determine the neutral hydrogen/helium ratio in the mixed atmosphere. Thus, penetration below the turbopause for a time necessary to make H and He abundance measurements is essential. The performance requirement for sampling, given in the table, is a minimum of two measurements below the turbopause.

The second measurement is the relative abundance for a set of 11 isotopes ranging from masses of 1 to 38 amu. The heavier isotopes are not expected to appear until near the turbopause (<20 km altitude). The criterion here is also a minimum of two full abundance measurements below the level where heavier isotopes may become measurable, which is from 20 km above the turbopause to 60 km below. However, because the first measurement (H/He ratio) is actually measured with the second [i.e., $(H^1 + H^2)/(He^3 + He^4)$], the mass spectrometer will measure both, and there will also always be two full sweeps of the isotopes below the turbopause.

The third measurement is to establish, as well as possible, relative abundances of such minor atmospheric constituents as Ch_4, Ch_3, and NH_3 in the vicinity of the turbopause. Again, the requirement is to get at least two full measurements below the turbopause. This measurement requires information from both the mass spectrometer and a neutral retarding potential analyzer.

The fourth and fifth establish number density concentration profiles for neutral particles in the upper atmosphere and ions that constitute the ionosphere. The ionosphere may begin at a very high altitude. Thus, to account for uncertainties, the search for positive ions begins at about 50,000 km. To account for the five ions--H_1^+, H_2^+, H_3^+, He^+ and HeH^+--the range of the instrument should be from 1 to 5 amu.

There will not be a measurable number of neutral particles above 1000 km altitude; thus, measurements beginning here should collect all available information. However, this measurement is specified to begin at 5000 km to provide the same conservatism used for ionic

Table III-1 Measurements and Performance Requirements

Measurement to Determine	Performance Requirements		
	Altitude Coverage	Sampling	Targeting
1. H/He ratio at several levels below turbopause	0 (turbopause) to -60 km	Min of 2 below 0 km	Equatorial between ± 1° latitude or in one of two belts at 9 to 11° equatorial latitude
2. Relative abundances of isotopes H^1, D^2 He^3, He^4, C^{12}, C^{13}, N^{14}, Ne^{20}, Ne^{22}, A^{36}, A^{38}, at several levels near turbopause	100 to -60 km	Min of 2 below +20 km	
3. Relative abundances of minor atmospheric constituents like CH_4, CH_3, CH_2, NH_3, at several levels near turbopause			
4. Neutral particle concentration profiles through upper atmosphere (H, H_2, He)	1000 km to turbopause	Min of 1 per scale height for each constituent	Above constraint plus restrict to lightside entry within 70° of subsolar
5. Ion concentration profiles through upper atmosphere & ionosphere	50,000 km to turbopause		
6. Electron density & temperature through upper atmosphere & ionosphere			
7. Neutral particle temperature profiles through upper atmosphere	1000 km to turbopause		
8. Ion temperature profiles through upper atmosphere	50,000 km to turbopause		
9. Lyman α dayglow profiles of H(1216 Å) & He (584 Å) through upper atmosphere	1000 to 20 km		

measurements. The primary neutrals detected will undoubtedly be H, H_2, and He, but as the probe nears the turbopause it may also pick up significant CH_4, NH_3, and others if their abundance is within the dynamic range of the instrument. The performance requirement is one measurement per scale height for both neutrals and ions to adequately establish a number density concentration profile. Because scale heights vary for each constituent as a function of mass, the heaviest particles will govern measurement time.

The electron number density concentration profiles are to be established from where the instrument first picks them up, probably less than 50,000 km, but slightly higher than protons $\left(H_1^+\right)$ down to the turbopause. In addition, the rate of change of electron current caused by varying the voltage should be read accurately enough to yield an onboard calculated electron temperature profile as the probe descends. The criterion here is also one measurement per scale height, and, because scale heights of electrons and protons are modeled the same, performances on any given mission will be identical.

The seventh and eighth measurements are similar for ions and neutrals in that the desire is for ion temperatures and neutral particle temperatures. This also requires the use of onboard data processing to reduce the amount of necessary data.

The purpose of the last measurement is to establish dayglow profiles, as the probe descends into the atmosphere, of two particular wavelengths of H and He ultraviolet reemitted radiation. In particular, H is the Lyman-α line at 1216 Å and He is the 584 Å line. In addition to information about resonance light scattering, this measurement would also give a redundant, independent check of the H/He ratio. These measurements would begin as soon as the photometric instruments were pointed toward Jupiter. The criterion here is not rigid because this is primarily a backup measurement, but it would be desirable to obtain one complete measurement within a distance equal to the scale height of neutral hydrogen.

2. Targeting Constraints

There are two targeting constraints listed in the table under Performance Requirements. To permit extrapolation of the measurements over the rest of the planet from first-generation probe missions, the entry site should be selected so that it is both relevant to desired

objectives and typical of the planet as a whole. The planet is covered with latitudinal belts and zones, any one being no more typical than another. However, because the goal of a turbopause probe requires getting below the turbopause, selection of a site, where the planet's turbopause lies at the highest possible altitude is desirable. There is an indication that an entry site at the center of a belt or zone would accomplish this, but this targeting constraint is taken as soft until better data are available.

The second targeting requirement is specified for upper atmospheric and ionospheric measurements, and is restricted to a lightside entry within 70° of subsolar. This is a requirement for both measurements of ions and measurements of dayglow, for different reasons. The ion production rate, and therefore the number density of ions at any given position, is largely a function of photoionization by the Sun. On the dark side, the ionospheric structure is conceivably very different because photoionization has ceased and recombination has begun. Also, because we do not accurately know the properties of the ionosphere or upper atmosphere, equations of recombination on the dark side can only be approximated. Knowing properties of the Sun's radiative field and photometric measurements of Jupiter's Sun side, gives us some knowledge, of the photoionization processes on the day side. Thus, probe ionospheric measurements on the Sun side would be more meaningful.

In addition, the photometric dayglow instrument must enter on the light side in order to measure the reemission of sunlight from H and He in the appropriate ultraviolet wavelengths.

C. INSTRUMENTS AND MEASUREMENT TECHNIQUES

The baseline instruments proposed for a turbopause probe mission and their detailed characteristics were supplied by GSFC. During the course of the study, the best approach to using these instruments in a Jupiter probe was discussed with the following instrument Principal Investigators at GSFC under the direction of Drs N. Spencer and S. Bauer.

Neutral Mass Spectrometer	Dr. H. Niemann Dr. D. Harpold
Langmuir Probes	Dr. L. Brace

Neutral Retarding Potential Analyzer	Dr. H. Niemann
Ion Retarding Potential Analyzer	Dr. E. Maier B. Troy
Dayglow Photometers/Spectrometer	Dr. D. Heath

These five instruments are adequate for meeting the science objectives given in Section A and are described in detail in the following subsections.

1. Positive Ion Retarding Potential Analyzer (IRPA)

The IRPA establishes the positive ion number density concentration profiles through the ionosphere as the probe descends. A secondary purpose is to establish ion temperatures in conjunction with the concentrations. The instrument has a range of 1 to 5 amu to include H_1^+, H_2^+, H_3^+, He^+, and HeH^+. It will begin operation at about 50,000 km and take data for several minutes before the grid wires burn up near the turbopause. The sampling time for one complete measurement has been set at 0.5 sec which results in a nominal bit rate of 192 bps. The characteristics of the instrument are shown in Table III-2.

The configuration and location of the instrument are shown in Fig. III-1. It is circular with a conical entrance cone that forms a 30° angle with the horizontal (cone angle at vertex = 120°) and has side vents to allow particles to flow through. For ideal instrument operations, the plate containing the inlet should be flat and infinitely thin, giving a cosine distribution of particles inside the aperture that would allow for simpler analysis of the data, but interference from reflected particles requires an angle. This problem was analyzed completely in the previous study final report (Ref III-2) and the results showed that the 30° angle is the minimum to prevent significant interference. To minimize particle reflection from one instrument to another, the IRPA is located on a short strut off the nose of the vehicle so that the aperture is on the side and forward in line with the stagnation point.

The circular aperture area is about 5 cm^2. Below the aperture is a grid of 1-mil wire grounded to probe surface potential. Ions enter and are retarded by a second set of grids successively varied from -3 to 63V in 5.5 V steps. The ion then passes through

Table III-2 IRPA Characteristics (Ref. III-5)

Weight - sensor = 0.23kg (0.5 lb), electronics = 1.36 kg (3 lb), total = 1.58 kg (3.5 lb)

Size - sensor = 10x10x4 cm,

Volume - sensor = 400 cm^3,

Shape - sensor is rectangular or circular, electronics packed around or separate

Power Required = 3 W (nominal upper limit)

Warm-Up Times = 15-30 sec

Sampling Interval* - min = 0.12 sec, nominal = 0.5 sec

Data Bits per Sample - 96

Data Bit Rate - max = 800 bps, nominal = 192 bps

Temperature Limits - min = -30°C, max 1000°C

Heat Dissipated - 3 W

Material Composition - stainless steel

Onboard Processing Required** - nominally, no; yes for ion temperatures

Angle of Attack Limits - $\pm 10°$

Operational Altitudes - 50,000 to 0 km above turbopause

Sensitivity - 10 ion/cm^3 → 5 ion/cm^3 by 1975

External Location -

Desired Position: On side of probe forward to be in line with stagnation point

Alternate: On side of probe at shoulder

Orientation & Pointing -

1. Aperture normal to incoming flux, thus perpendicular to flight velocity vector.
2. Instrument will need a conical entrance cone and vented side plates

*12 sample points required based on a 5.5-V step size (1 to 5 amu range).

**For a mission that includes onboard ion temperature processor, add 0.5 lb to electronics weight. The data bit rate will not be larger than the nominal value given here.

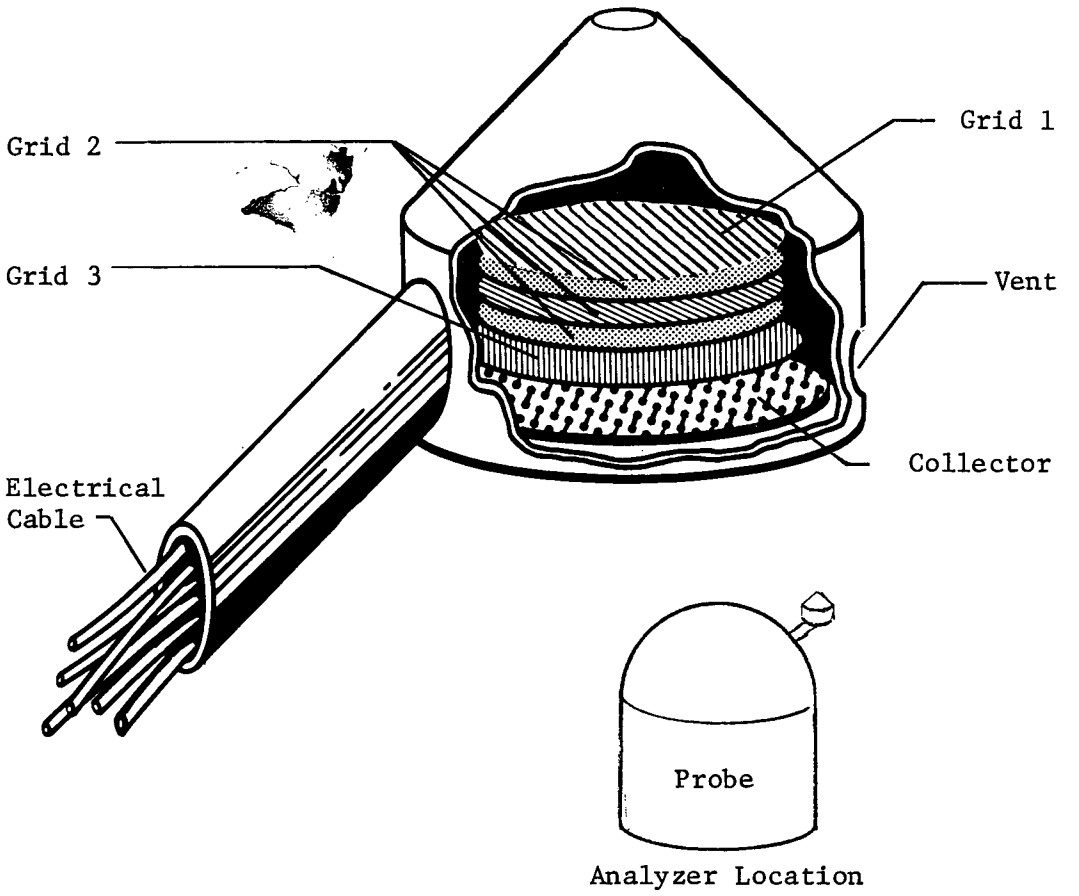

RPA Element	Potential Relative to Probe Ground
Grid 1	0 V
Grid 2	Variable retarding voltage (-3 to 63 V in 5.5-V steps)
Grid 3	-20 V to exclude electron collection & suppress emission of secondary electrons from collector
Collector	- 5 V

Fig. III-1 Ion Retarding Potential Analyzer

a third grid biased at about -20 V and collected on a plate at about -5 V. The purpose of the last grid is to suppress emission of secondary electrons from the collector. As voltages are varied, corresponding current values resulting from collection of various positive ions are measured and telemetered back to be coupled with the preset voltage values to establish a current-voltage (I-V) curve from which density, temperature, composition, and potential can be derived. A typical curve for a representative velocity of 50 km/sec is shown in Fig. III-2.

To obtain ion denisty and composition, only one current value per mass number is necessary. However, there is a danger of missing a step if voltage step size equals voltage per mass number, which is about 12 V/amu. Also, two measurements per step can better determine step level and length. Thus, for the 1 to 5-amu range, voltage step size has been set at the 5.5-V value for the 66 V sweep. This gives twelve current values to be sent back, and, assuming an 8-bit word at the half-second sampling time, gives 192 bps.

If ion temperature is to be determined, the I-V curve reconstruction must be detailed enough to accurately define the sharp drop corresponding to a given ion mass number. For ion temperatures expected, the number of data points needed to define the curve will be excessively large for telemetry. Therefore, onboard data processing will be necessary. The overall bit rate could be less because the output to be telemetered is now processed, therefore condensed.

This instrument is state-of-the-art flight hardware, and except perhaps for some development for the onboard temperature processor, will require no major development.

2. Neutral Particle Retarding Potential Analyzer (NRPA)

The NRPA establishes neutral-particle number density concentration profiles through the upper atmosphere as the probe flow field goes from free molecular into the transitional region. It also can establish neutral-particle temperatures in conjunction with concentrations. The instrument has a dual range covering 1 to 20 amu. It will begin operation nominally at about 5000 km above the turbopause and take data for about two minutes before the grid wires burn up. The sampling time for one complete measurement has been set at 0.5 sec.

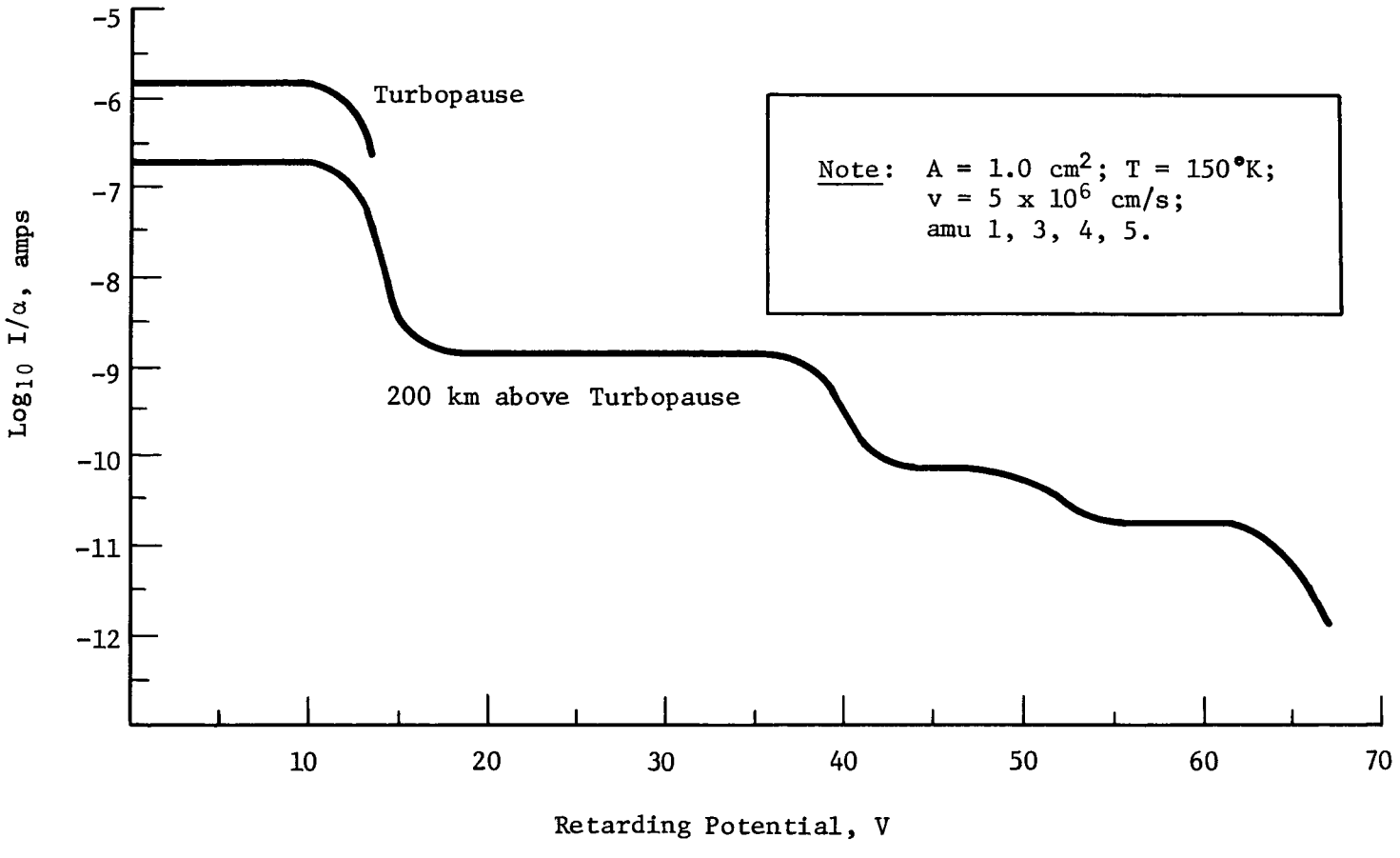

Fig. III-2 Ion RPA Response

Instrument characteristics are shown in Table III-3. Power required is larger than the IRPA, primarily because an ionizing beam is required. Bit rate is larger because of the extended sweep range.

The configuration and location of the instrument are shown in Fig. III-3. The conical entrance is limited to the same minimum 30° from horizontal as the IRPA, but is designed at 45° to lessen interference with heavier neutral particles and because the distribution inside the instrument is not as critical. Because it operates generally in a denser portion of the atmosphere, this instrument is vented at the back to allow greater flow. The position of the NRPA is symmetrical to that of the IRPA on the opposite side of the probe centerline with its aperture even with the stagnation point.

The rectangular entrance aperture area is about 5 cm^2, with the long axis parallel to the direction of an ionizing beam inside the sensor. Below the inlet is a ground grid of 1-mil wire at zero relative potential to the probe surface. Inside are grids charged at +300 and -300 V to prevent all charged particles from getting inside the instrument, allowing only neutral particles in. The electron beam gun ionizes the neutrals, which are subsequently retarded and collected as in the IRPA.

The first part of the dual sweep range is from 1 to 4 amu to account for H, H_2, and He, and the second from 14 to 20 amu, including CH_2, CH_3, CH_4, NH_3, H_2O, and Ne. The corresponding retarding sweep voltage ranges would be approximately 0 to 60 V and from 180 to 280 V. The steps on the resulting I-V curve will be a little greater than 13 V/amu. Because of the greater amount of data and the limitations on bit rate, only one current value per mass number is allowed. However, there is a danger of missing a step (mass number) if the voltage step size equals 13 V/amu. Thus, for this study, 11 V was chosen for the step size. One sample or sweep then consists of 14 words (for approximately 160 V). With an 8-bit word and a half-second sampling time, the nominal bit rate for the NRPA is 224 bps.

If the neutral-particle temperature is to be determined, the I-V curve must be detailed enough to accurately define the sharp drop corresponding to a given mass number. For particle temperatures expected, the number of data points needed to define the curve will exceed the data handling capability. Therefore, onboard data processing will be necessary. The overall bit rate could be less because the output is now processed, therefore condensed.

Table III-3 NRPA Characteristics (Ref III-6)

Weight - sensor = 0.45 kg (1 lb), electronics = 1.82 kg (4 lb), total = 2.27 kg (5 lb)(2.5 kg with temperature processor)
Size - sensor = 10x10x4cm, electronics + sensor = 25x10x10 cm
Volume - sensor = 400 cm^3, total package = 2500 cm^3
Shape - sensor is rectangular or circular, electronics packed around or separate
Power Required - 5 W
Warm-Up Times - ~30 sec
Sampling Interval* - min = 0.3 sec, nominal = 0.5 sec
Data Bits per Sample - 112
Data Bit Rate - max = 800 bps, nominal = 224 bps
Temperature Limits - min = -30°C, max = 1000°C
Heat Dissipated - 5 W
Material Composition - stainless steel
Onboard Processing Required** - nominally, no; yes for neutral-particle temperatures
Angle of Attack Limits - $\pm$10°
Operational Altitudes - 0 to 1000 km above turbopause
Sensitivity: 10^5 particles/cm^3 → 10^4 particles/cm^3 by 1975
External Location - Same as IRPA
Protection Required - For protection against contaminants, entrance & exit vents are covered and vacuum sealed until after probe separation.
Orientation & Pointing -
1. Aperture normal to incoming flux, thus perpendicular to flight velocity vector.
2. Instrument will need conical entrance cone and vent in bottom.

*14 sample points based on a bias voltage step size of 11 V (1 to 20 amu range).

**For a mission that includes onboard neutral-particle temperature processor, add 0.5 lb to electronics weight. Data bit rate will not be greater than nominal value given here.

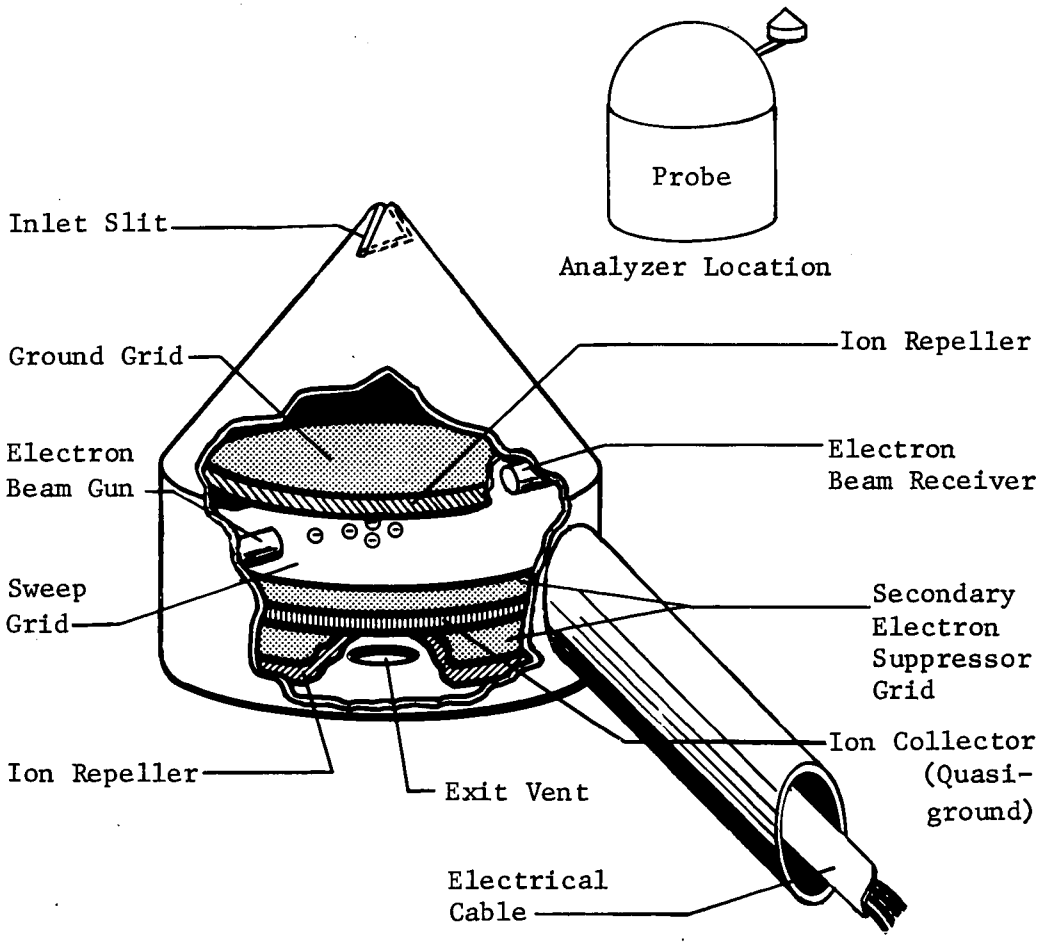

RPA Element	Potential Relative to Ground
Ion repeller	+300 V
Beam receiver anode	0 V
Sweep grid	0 to 280 V
Secondary electron suppressor grid	-300V

Fig. III-3 Neutral Particle Retarding Potential Analyzer

This instrument is not state-of-the-art flight hardware, and will require considerable development, although the technology gained from the operational IRPA is applicable.

3. Langmuir Probe (Electron Temperature Probe) (ETP)

The ETP establishes the electron number density concentration profiles and electron temperature profiles as the vehicle descends through the ionosphere in free molecular flow. It will begin searching for electrons at 50,000 km, but probably will not obtain readings until later (See Section D. 4.). It will take data down to near the turbopause. Sampling time for one complete measurement, including onboard processing, has been set at 0.5 sec. Characteristics of the instruments are shown in Table III-4. Only one set of electronics is required for both Langmuir probes.

The configuration and location of the two instruments are shown in Fig. III-4. The guards protrude from the nose of the vehicle, about 90° from the RPA strut locations. The sensor is a 7.6-cm (3-in.) long hollow tube, 0.158 cm (1/16 in.) OD. Electrical heaters are included in the hollow ETP and heated to 500°C for 10 min before use. The purpose of heating the probe is to remove all contaminant particles that have been collected on the sensor from launch operations, outgassing during cruise, or fuel deposits from engine firings. The probe needs a 2-min warmup time and a 2-min cooling time before making measurements. It does not have to reach ambient temperature before use. The suggested best time for performing this operation is after separation and a few hours before entry, but it could be done before separation from spacecraft power if the separation is clean.

One ETP is perpendicular to the flight velocity vector, has a constant voltage applied and measures the electron current as it varies with the descent altitude. These measurements are processed on board to yield the electron number density. The other ETP is fixed so that the sensor is parallel to the flight velocity vector and has variable voltage applied. When this variable voltage is high and negative, the ETP measures the ion current, which is processed on board to give ion number density. As the voltage is swept from negative to positive, current readings are taken to obtain the shape of the I-V curve. After further onboard processing, the electron temperature is obtained.

The primary reasons for aligning the variable-voltage sensor parallel to the velocity vector are to substantially reduce extraneous voltage induced by the large magnetic field of Jupiter

Table III-4 Electron Temperature Probe (ETP) Characteristics (Ref III-7)

Weight - sensor = negligible, electronics = 3 lb

Size - sensor = 7.6 cm long (3 in), 0.16 cm (0.0625 in.) dia.
electronics = 5x15x15 cm (2x6x6 in.)

Volume - ~1200 cm^3

Shape - sensor = hollow tube

Power Required - 3 W (2 W by 1975)
heater power = 5 W for 12 min before entry

Sampling Interval* - min = 0.1 sec, nominal = 0.5 sec

Data Bits per Sample* - 24 to 32

Data Bit Rate - max = 320 bps, nominal - 48 to 64 bps

Sensor Temperature Limits - min = -100°C, max = 700°C

Heat Dissipated - 3 W

Material Composition - nickel, plated with rhodium

Onboard Processing Required - yes*

Angle of Attack Limits - $\pm 5°$

Operational Altitude - 50,000 to 0 km above turbopause

Sensitivity - 10^1 to 10^7 cm^{-3}, 200 to 20,000° K

Orientation & Pointing -

One sensor normal to and one parallel to flight velocity vector

*About 30 current measurements are obtained from one voltage sweep. After onboard processing, the nominal three words of information telemetered back are the electron number density, ion number density, and electron temperature. However, as an option, the entire 30 current measurements could be sent back from every 30th voltage sweep by adding a fourth word of prestored current data to be telemetered every sample.

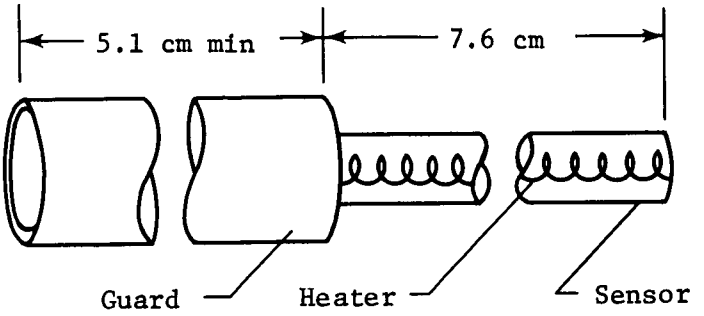

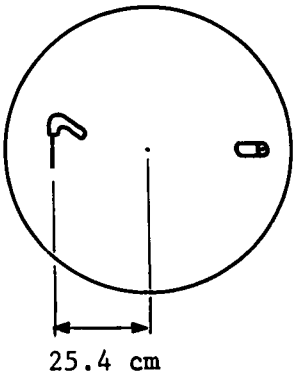

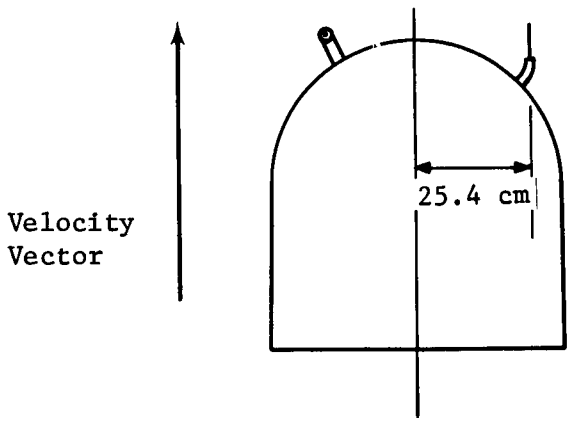

One sensor parallel with flight velocity vector & other perpendicular to it.

Fig. III-4 Langmuir Probe

as the probe moves through it; to keep variations in distribution of potential along the sensor length small, and to prevent translational energy of the probe from interfering with particle thermal energy measurement. This orientation is more sensitive to angle of attack--the limit being about ±5°.

The nominal data telemetered consists of three 8-bit words, all processed on board--electron number density, ion number density, and electron temperature. However, to verify accuracy of the data, one complete set of current readings (30) along a voltage sweep should be sent back somewhere between every tenth and every thirtieth sample. If four 8-bit words are used, the last being a current reading at one voltage, 29 currents and one voltage sweep rate could be sent back every thirtieth sample at the expense of increasing the bit rate from 48 to 64 bps at a 0,5-sec sampling time. This will later be referred to as added return for a "science enhanced" mission.

The effect of the sinusoidal voltage induced on the Langmuir probes by the planet's magnetic field was analyzed to determine the impact upon the total design. The result was that both the distance of the sensor from the vehicle centerline (ℓ) and the spin rate should be minimized.

Table III-5 lists some data points from a parametric study to select a spin rate. The minimum distance for ℓ is about 10 in. This is to prevent significant interference, both particle reflection and mounting constraints, with the mass spectrometer and RPAs. The spin rate is varied from 37.5 rpm, which is the required spin rate to obtain one probe revolution within one scale height of neutral H, and which is used for several of the design missions. The last column shows the V/sec change as the sinusoidal induced voltage goes from maximum positive to maximum negative in a half period. To reduce this slope to below 20 V/sec requires the spin rate to be less than 20,2 rpm if $\ell \geq$ 25,4 cm (10 in,). The last line in the table will be used as the design value for missions with the Langmuir probes on the vehicle nose. Spin rate is 20 rpm and the entire probe instrument must be within 25.4 cm of the centerline. This can be accomplished easily by turning the probe instrument that is perpendicuular to the flight velocity vector so that it is also perpendicular to a radius vector from the centerline.

The Langmuir probe and all its electronic equipment have been flown on Earth-orbital missions, and as such, are all state of the art.

Table III-5 Induced Voltages

ℓ		Voltage Amplitude, V	Spin Rate, rpm	Half Period Time, sec	V/sec
in.	cm				
30.8	78.0	45.4	37.5	0.80	112.0
15.0	38.1	22.2	37.5	0.80	55.4
15.0	38.1	22.2	20.0	1.50	29.5
15.0	38.1	22.2	13.5	2.22	20.0
12.0	30.5	17.7	37.5	0.80	44.3
12.0	30.5	17.7	20.0	1.50	23.6
12.0	30.5	17.7	16.9	1.77	20.0
10.0	25.4	14.8	37.5	0.80	36.9
10.0	25.4	14.8	25.0	1.20	24.6
10.0	25.4	14.8	20.2	1.48	20.0
10.0	25.4	14.8	20.0	1.50	19.7

4. Neutral Mass Spectrometer (NMS)

The NMS measures isotopic-relative abundances enabling determination of the important hydrogen/helium ratio, It has a nominal range of 1 to 38 amu and operates near and below the turbopause until communications blackout, The time for a complete sweep has been selected as 0.4 sec, with data telemetered in real time.

As a recommendation of the previous study (Ref III-2), the instrument is of the molecular beam sampler-type to better reproduce the undisturbed ambient conditions from a sample of reactive species. It is placed inside the probe body with the aperture at the stagnation point. The characteristics are given in Table III-6 and configuration and location are shown in Fig. III-5. The instrument consists of an ionizer region, a quadrupole analyzer section, and a secondary electron multiplier. The stability of the trajectory through the analyzer of a given ionized particle is a function of

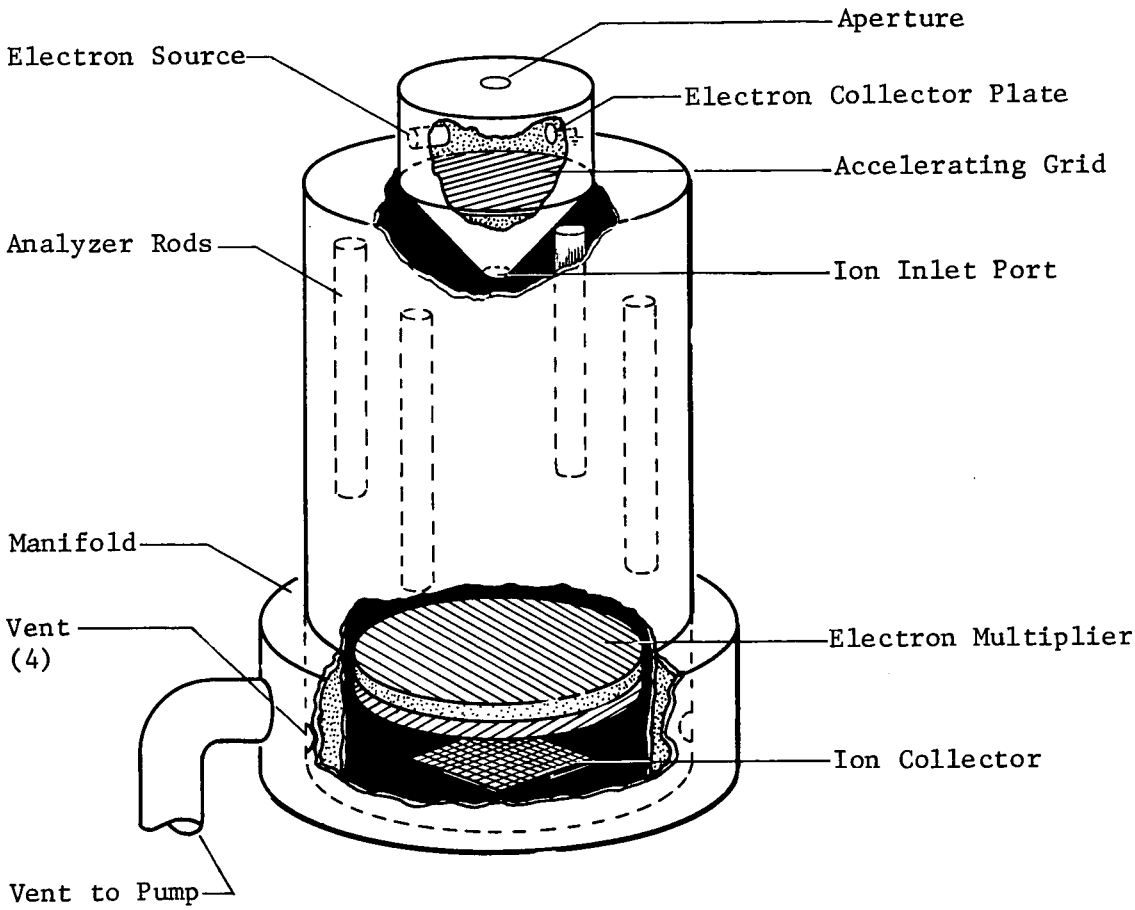

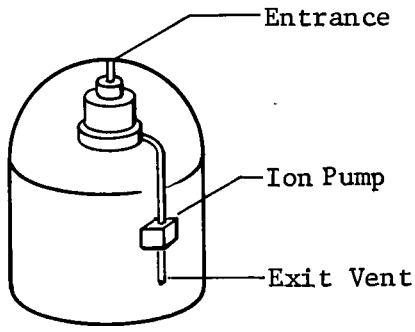

Spectrometer Location

Fig. III-5 Neutral Mass Spectrometer

Table III-6 Mass Spectrometer Characteristics (Ref III-8)

Weight - sensor = 5.9kg (13 lb), pump = 0.45kg (1 lb), total = 6.4kg (14 lb)

Size - sensor = 5-cm dia tube (1.97-in.) 20-cm long (7.9-in.), total = 12x20x33 cm (4.7x7.9x13.0 in.), pump = 44.2 (27 in.^{3})

Volume - $\sim$7920 cm^3 (483 in.^{3}) total

Shape - sensor = tube given above
electronics packaged around it

Power Required - 15 W

Warm-Up Times - 3 to 5 min

Sampling Interval* - min = 0.22 sec, nominal = 0.4 sec

Data Bits per Sample - 176

Data Bit Rate - max = 800 bps, nominal = 440 bps

Temperature Limits - < 200°C

Heat Dissipated - 15 W max

Material Composition - stainless steel

Onboard Processing Required - Nominally, no.

Angle of Attack Limits - $\pm$10°

Operational Altitudes - < 100 km above turbopause to 60 km below turbopause

Sensitivity - 1 to 38 amu, dynamic range = 10^6

External Location/Operation - Stagnation-point molecular beam sampler system, thus NMS must be located inside vehicle shell behind stagnation point

Protection Required - Entrance and exit apertures covered and vacuum sealed until after probe separation. Instrument to be opened several days before entry to allow contaminants to disperse

Orientation & Pointing -

Aperture at stagnation point

*11-isotope sampling required.

its charge to mass ratio and the field of the analyzer. By successively readjusting the field for each of the 11 isotopes under consideration, only the particles with the appropriate mass/charge will have a stable trajectory and be collected.

A selective scanning technique is proposed for the 11 isotopes with an initial dwell of 2 msec. If a threshold current from a specific isotope is detected the field remains set for an additional 18 msec. If all isotopes existed in sufficient quantities to be measured, the total time for a complete sweep would be 0.22 sec, which is less than the allotted 0.4 sec. A small percentage of the difference is used to digitize, format and telemeter the data. For 11 settings, there is a voltage or RF field word to identify the isotope, and a resulting current word to give the concentration, constituting 22 eight-bit words. At the nominal sample time the bit rate is 440 bps.

Figure III-6a and III-6b are two different designs of a molecular beam inlet system which were used to calculate the concentrations given in Table III-7. This table lists the 11 isotopes and the projected concentrations that constitute the molecular beam in the ionizer as a function of altitude below the turbopause. The particular inlet design shown, tapered at 45° on both sides of the entrance, appears to be the best compromise in order to prevent thin or sharp beryllium sections from becoming too hot and yet retain a molecular beam of sufficient intensity. The flow enters a small chamber through the first aperture at the rate given below for two altitudes.

	Mass flow rate (particles/sec)	
Configuration 1	1st aperture	2nd aperture
Turbopause (0 km)	3.0×10^{17}	3.0×10^{15}
Blackout (-60 km)	1.1×10^{19}	1.1×10^{17}
Configuration 2	1st aperture	2nd aperture
Turbopause (0 km)	7.4×10^{16}	1.9×10^{14}
Blackout (-60 km)	2.7×10^{18}	6.7×10^{15}

A portion of the flow enters the mass spectrometer analyzer, as indicated by the flow rates for the second aperture, and the remainder is vented in a manifold around the instrument. The total flow passes through an ion pump that has a pumping capability governed by the flow rate through the first aperture. From the pump, the flow is vented to the base of the vehicle through a 2.5 cm diameter line.

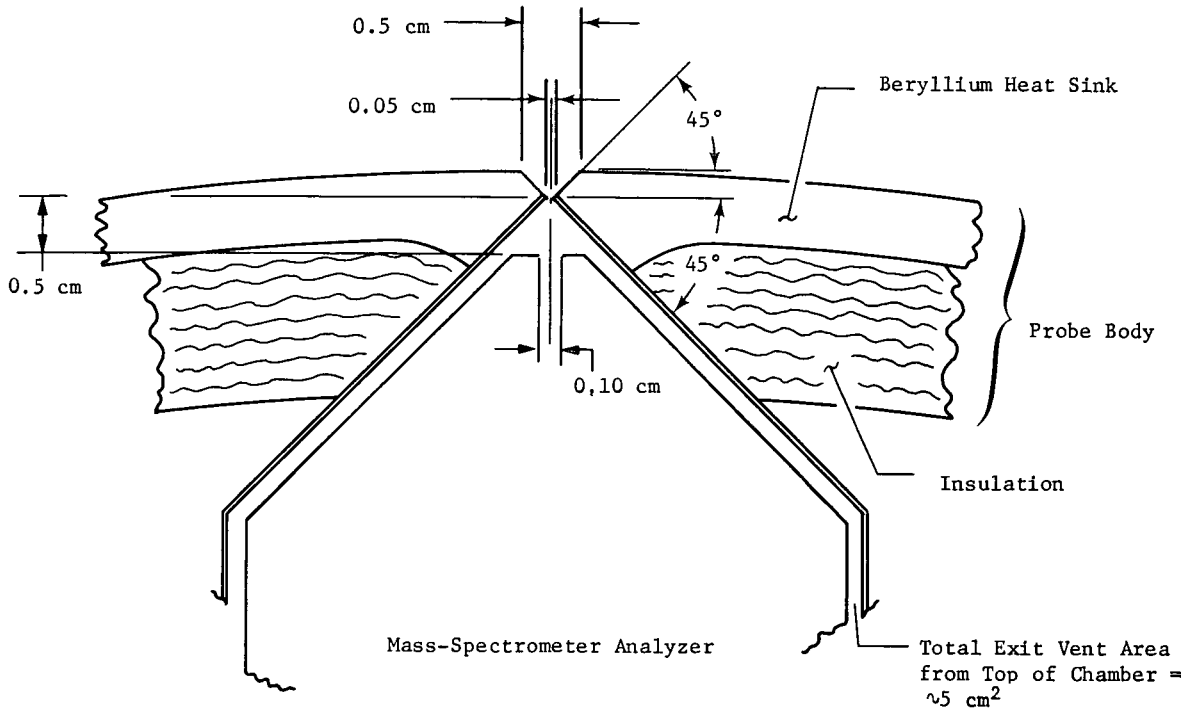

Fig. III-6a Mass-Spectrometer Inlet Specifications (Configuration 1)

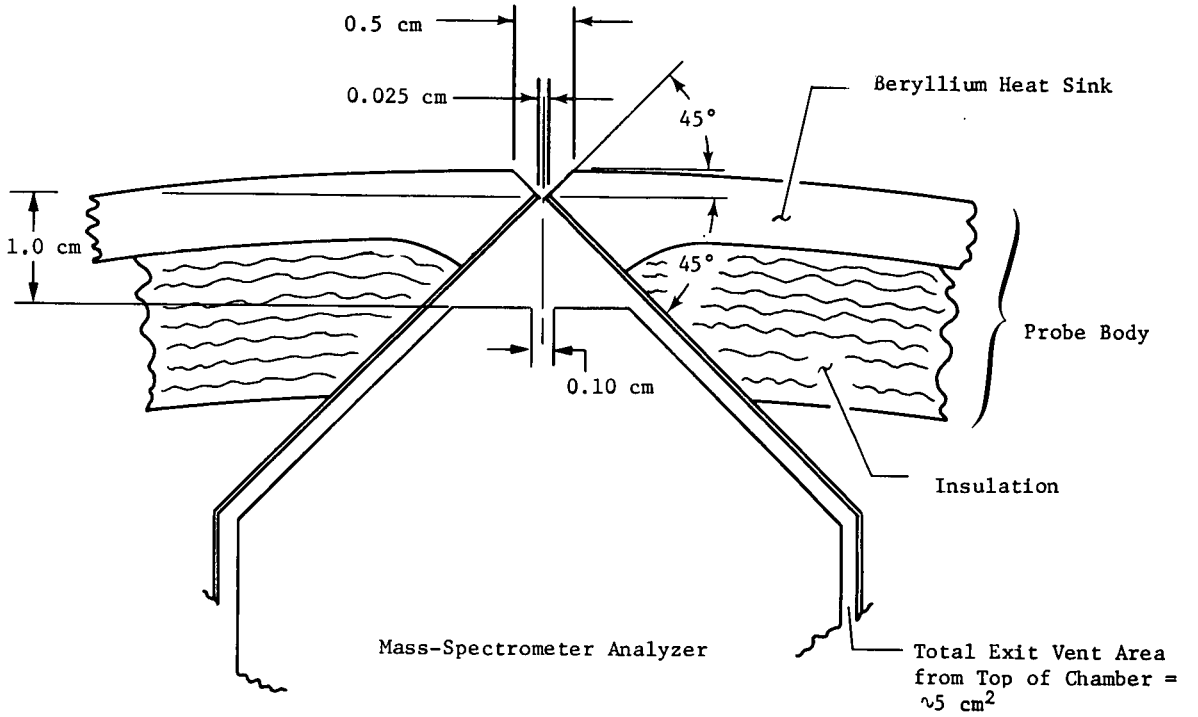

Fig. III-6b Mass-Spectrometer Inlet Specifications (Configuration 2)

Table III-7 Isotope Concentrations in Molecular Beam in Particles/cm^3

Isotope	Concentrations for Configuration 1			Concentrations for Concentration 2			
	Altitude (km)			Altitude (km)			
	-80	-60	-40	-80	-60	-40	-20
$H^1 \times 10^{12}$	11,9	8.29	2,47	1,70	0,52	0,16	0,048
$D^2 \times 10^8$	18,0	12.5	3,70	2,58	0,78	0,23	0,073
$He^3 \times 10^8$	2,63	1,83	0,55	0,38	0,11	0,034	0,011
$He^4 \times 10^{11}$	8,76	6,09	1,82	1,25	0,38	0,11	0,036
$C^{12} \times 10^9$	4,15	2,89	0,86	0,59	0,18	0,054	0,017
$C^{13} \times 10^7$	4,67	3,25	0,99	0,67	0,20	0,061	0,019
$N^{14} \times 10^8$	10.2	7,08	2,11	1,45	0,44	0,13	0,041
$Ne^{20} \times 10^8$	6,41	4,46	1,33	0,92	0,28	0,083	0,026
$Ne^{22} \times 10^7$	6,23	4,33	1,29	0,89	0,27	0,081	0,025
$A^{36} \times 10^7$	2,90	2,02	0,60	0,42	0,13	0,038	0,012
$A^{38} \times 10^6$	5,54	3,85	1,15	0,79	0,24	0,072	0,023

Several manufacturers were contacted for information on current and advanced ion pumps. Current state-of-the-art pumping speed is about 1.5×10^{16} particles/sec (4 liter/sec at 10^{-4} torr). It is generally believed that with considerable development, the maximum pumping speed that could be obtained by 1976 is approximately 10^{18} particles/sec (10 liters/sec at 5×10^{-3} torr).

An evaluation was made to determine if the wake region of the flow could be used for pumping the mass spectrometer system. Wind tunnel tests showed that the base pressure is approximately 18 times free stream pressure. The tabulation shows the pressure relationships for two different altitudes:

	Turbopause (0 km)	Blackout (-60 km)
Free stream pressure	$P_f = 6 \times 10^{-8}$ atm	$P_f = 2 \times 10^{-6}$ atm
Stagnation pressure	$P_s = 3 \times 10^{-4}$ atm	$P_s = 1.1 \times 10^{-2}$ atm
Base pressure	$P_b = 1.1 \times 10^{-6}$ atm	$P_b = 3.6 \times 10^{-5}$ atm
Maximum pressure in NMS analyzer region	$P_a = 6.6 \times 10^{-8}$ atm	$P_a = 6.6 \times 10^{-8}$ atm
Ratio of pressure in analyzer to base	$P_a/P_b = 0.06$	$P_a/P_b = 0.002$

The pressure ratio is adverse to base pumping since P_a must always be greater than P_b in order for the wake to serve as a pump.

In conjunction with the configurations in Fig. III-6 and concentrations in Table III-7, the altitude at which the concentration of each isotope falls within the dynamic range of the instrument was calculated.

	Altitude of First Measurement	
Isotope	Configuration 1	Configuration 2
H^1	> +20	> +20
D^2	> 0	> 0
He^3	> 0	-19
He^4	> +20	> +20
C^{12}	> +20	> +20
C^{13}	-2	-48
N^{14}	> 0	> 0
Ne^{20}	> 0	-4
Ne^{22}	∿ 0	-44
A^{36}	-12	-56
A^{38}	-37	-84

These two configurations represent bounds on an actual design. Configuration 1 can measure all the isotopes before blackout but requires a pumping speed beyond the capability of a feasible ion pump. Configuration 2 has a feasible pumping speed but loses the A^{38} measurement completely.

The mass spectrometer system will require significant experimental test and development before actual flight, particularly in the inlet sampling and pumping mechanism designs. The pressure and temperature behind the normal shock needs to be simulated; separately, simulation of the stagnation enthalpy and verification of the small orifice inlet operation is required.

5. Ultraviolet Dayglow (Photometers or Spectrometer)

The function of the ultraviolet dayglow instrument is to measure the intensity of the H Lyman-α dayglow at 1216 Å and the He resonance scattering dayglow at 584 Å. The H dayglow primarily comes from resonance scattering of atomic hydrogen, but a small amount may be from dissociative fluorescence of diatomic H_2. Because these are the dominant particles in the upper atmosphere, the results will bear directly on the structure of the region.

Figure III-7 shows the dayglow strengths predicted by Dr. D. M. Hunten from his model upper atmosphere (Ref III-4). The detector should be sensitive enough to detect down to at least 5 Rayleighs and, if possible, to 1 Rayleigh. At 1 Rayleigh, the H resonance will begin to be detected at about 1000 km, but because of uncertainty, the instruments will be turned on at 10,000 km.

The instruments considered are listed below.

Ultraviolet photomultiplier photometer

Two separate instruments and detectors. Original proposal instrument. Operation similar to Mariner 5 (Venus 1967) instruments.

Reflection grating spectrometer

One instrument with three fixed channeltron (spiraltron) detectors. Proposed by Dr. D. M. Hunten of Kitt Peak Observatory Operation similar to Mariner Venus-Mercury 1973 proposed instruments.

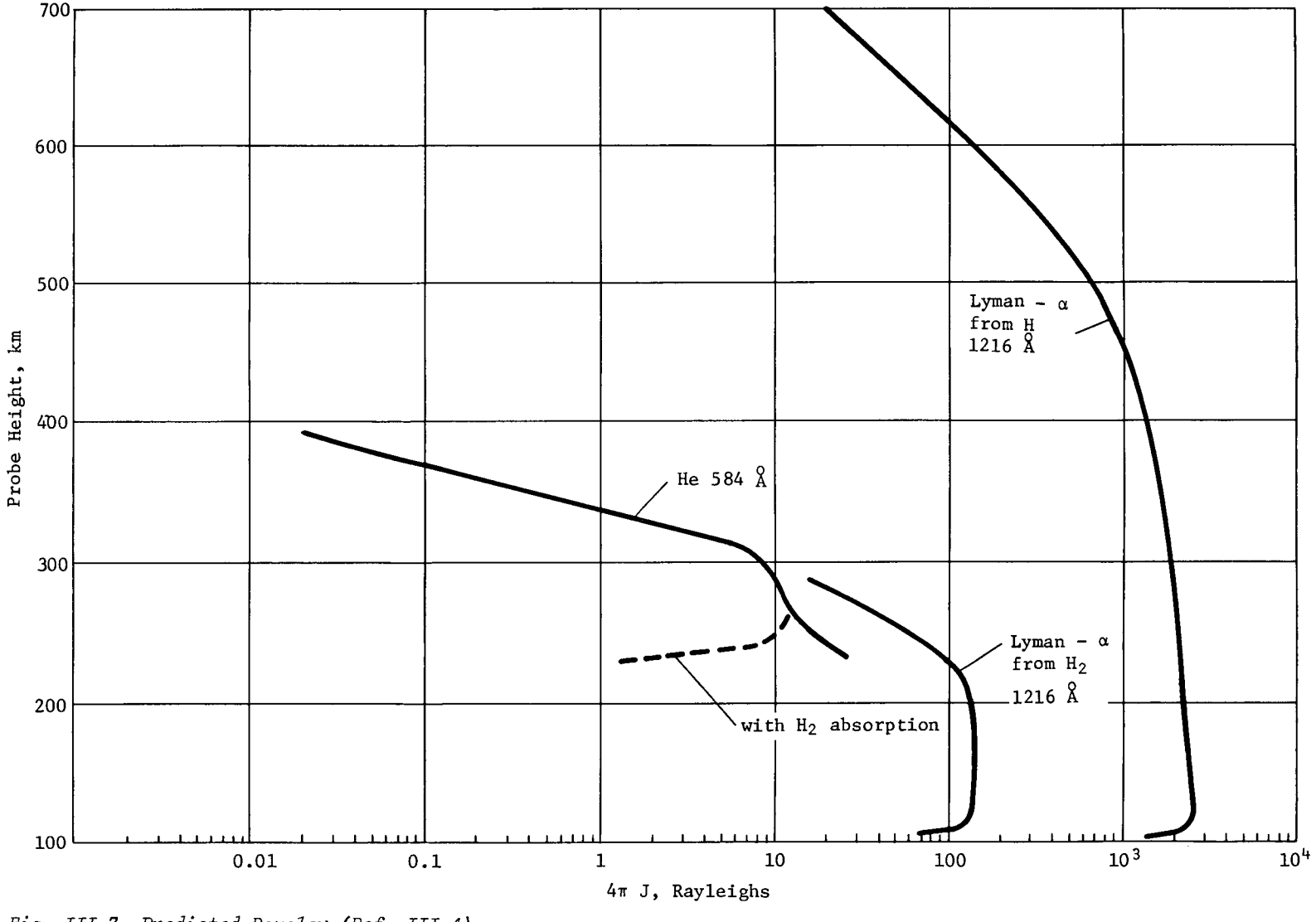

Fig. III-7 Predicted Dayglow (Ref. III-4)

Thin-filter channeltron photometer

Separate instruments and detectors. Proposed by Dr. D. Heath of GSFC. Independently proposed through discussion with J. Pranke, Research Assistant to Dr. C. Barth, LASP, University of Colorado.

The ultraviolet photomultiplier photometer is satisfactory only for the H measurement. The photometer optics (window and filter) have a lower cutoff point at about 900 Å minimum and will not transmit the He dayglow at 584 Å. It is a two-detector photomultiplier photometer. Each detector has a UV filter, in one case composed of magnesium fluoride and the other of calcium fluoride. The output current reading is proportional to the intensity of the light. Characteristics of the instrument are given in Table III-8 and the detector configuration is shown in Fig. III-8.

The reflection grating spectrometer is satisfactory for both H and He dayglow measurements. It is a body fixed objective grating spectrometer with no moving parts. A mechanical collimator defines the field of view and a fixed concave grating disperses and images the spectrum. Fixed slits and channel multiplier detectors are placed at the wavelengths of interest in the image plane. Photon counting techniques are used, and random pulses are counted. The detectors used would be channeltrons placed at 1216 Å, 584 Å, and at a background wavelength. Thus, this one instrument would make all necessary dayglow measurements. The field of view is rectangular, on the order of 2 x 20°. Its characteristics are given in Table III-9 and its configuration shown in Fig. III-9. The original instrument was developed by Dr. L. Broadfoot at Kitt Peak National Observatory.

The thin-filter channeltron photometer is sufficient for both H and He dayglow, but is not the most efficient for H at these particular wavelengths. To collect the light from the 584 Å He dayglow, a channeltron detector is required because the light at this wavelength cannot pass through any glass optics. The light passes through a very thin (1690 Å) Sn metal filter supported by wire mesh, and strikes the side of the tube that is coated with a photosensitive semiconductor. A high voltage is applied along the tube and a gradient is thus established. The incidence of photons on this surface causes a current to flow that is proportional to intensity. The characteristics of this instrument are given in Table III-10 and the configuration in Fig. III-10.

Table III-8 Hydrogen Photomultiplier Photometer Characteristics

Weight - 2.05 kg total (4.5 lb)
Size - 10x12.5x12.5 cm (4x5x5 in.)
Volume - $\sim$1600 cm^3 (100 $in.^3$)
Shape - sensor = tube approx 2.54 cm in dia (1 in.)
Power Required - 3 W
Warm-Up Time - 5 sec
Sampling Interval* - 0.09 to 1.6 sec
Data Bits per Sample - 8
Data Bit Rate* - 5 to 90 bps
Temperature Limits - -30 to 50°C
Heat Dissipated - 3 W
Onboard Processing Required - possible
Angle of Attack Limits - none
Operational Altitudes - 0 to 5000 km
Sensitivity - 10^4 photons/measurement
Location/Operation - Looking out side of vehicle and rotating with it. Possibly pointing slightly forward.
Protection Required -
Cover over aperture during launch and coast

*Sample time varies from one measurement every 20° of rotation to one measurement every revolution (360°) based on a rotation rate of 37.5 rpm.

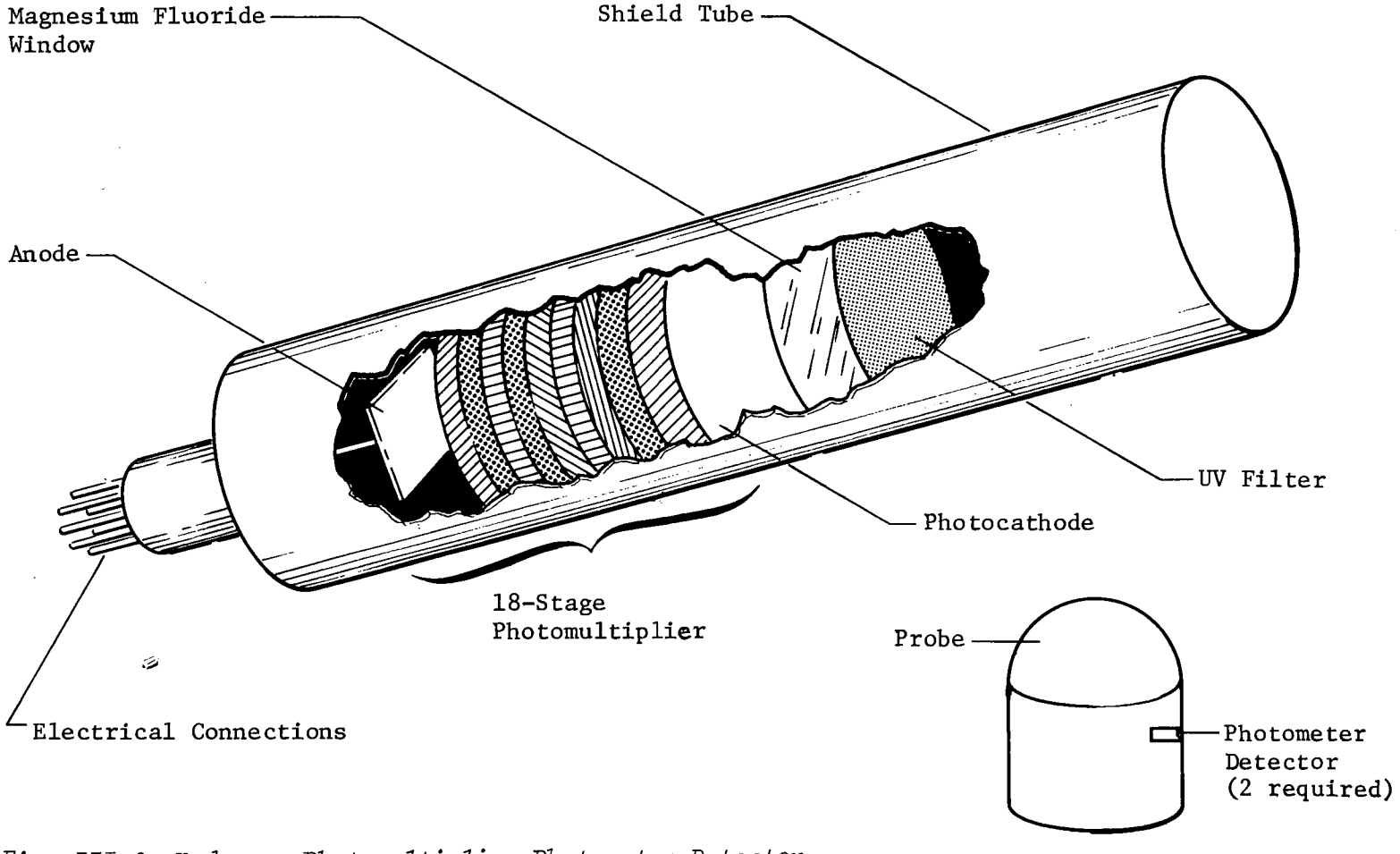

Fig. III-8 Hydrogen Photomultiplier Photometer Detector

Table III-9 Ultraviolet Reflection Grating Spectrometer Characteristics

Weight - 2.3 kg (5 lb) total

Size - 10x10.8x34 cm (4x4.25x13.5 in.)

Volume - ∿3400 cm^3 (200 $in.^3$)

Shape - sensor = intersecting tubes, electronics packaged around it

Power Required - <5 W

Warm-Up Time - 5 sec

Sampling Interval* - 0.09 to 1.6 sec

Data Bits/Sample - 24

Data Bit Rate* - 15 to 270 bps

Temperature Limits - operating = 0 to 40°C, nonoperating = -20°C to 75°C

Heat Dissipated - <5 W

Onboard Processing Required - yes, for lower data rates

Angle of Attack Limits - none

Operational Altitudes - 0 to 5000 km

Sensitivity - 2 photons/sec/Rayleigh

Location/Operation -

Looking out side of vehicle and rotating with it. Possibly pointing slightly forward.

Protection Required -

Cover over aperture during launch and coast

*Sample time varies from one measurement every 20° of rotation to one measurement every revolution (360°) based on a rotation rate of 37.5 rpm.

C.2

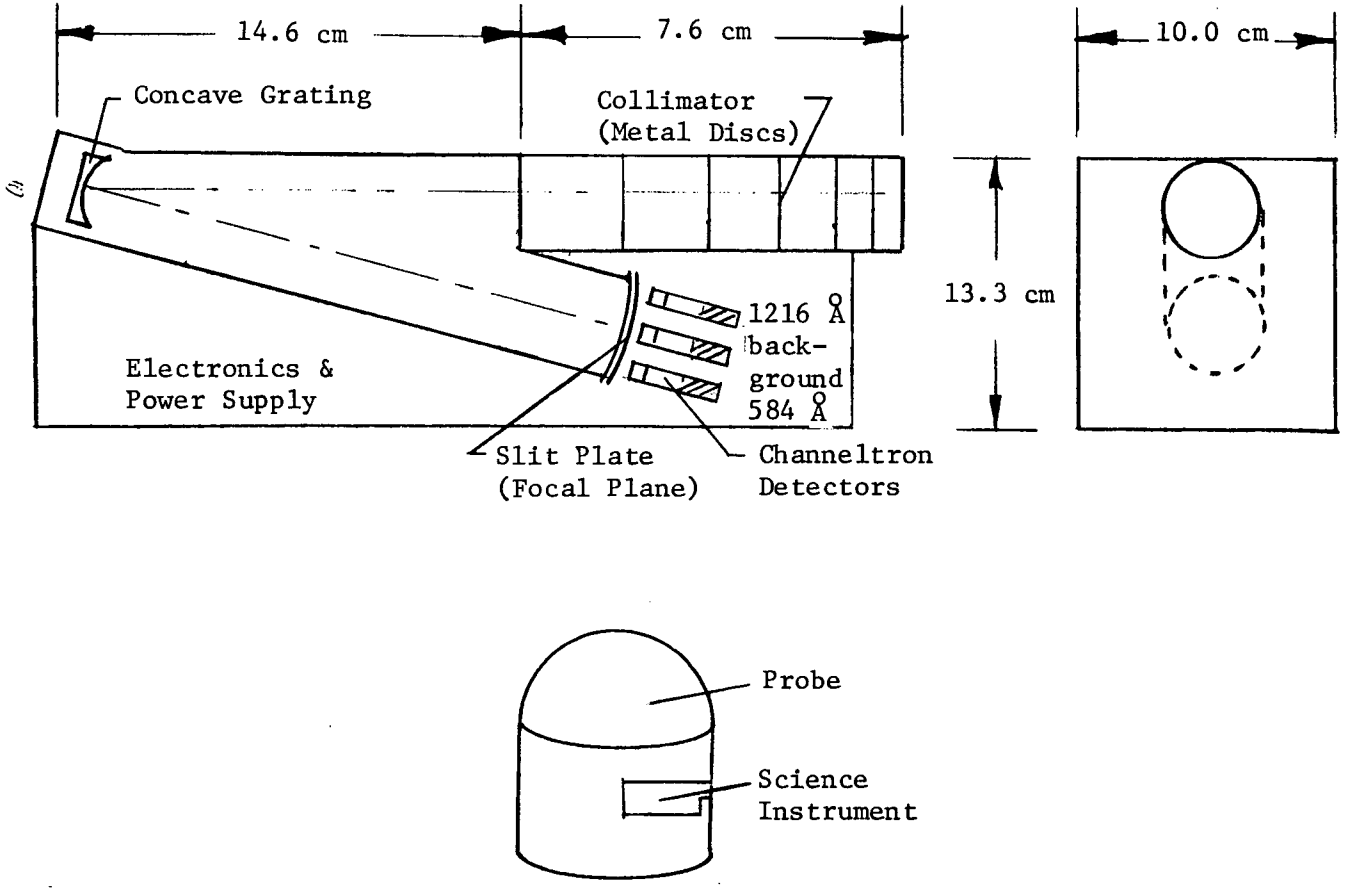

Fig. III-9 Ultraviolet Reflection Grating Spectrometer

Table III-10 Helium Channeltron Photometer Characteristics

Weight - 0.9 kg (2 lb) total

Size - 10.2x10.2x12.7 cm (4x4x5 in.)

Volume - 1311 cm^3 (80 $in.^3$)

Shape - sensor = tube 1.2 cm (<1/2 in.) dia.

Power Required - 2 W

Warm-Up Time - none

Sampling Interval* - 0.09 to 1.6 sec

Data Bits per Sample - 8

Data Bit Rate* - 5 to 90 bps

Temperature Limits - -30 to 50°C

Heat Dissipated - 2 W

Onboard Processing Required - possible

Angle of Attack Limits - none

Operational Altitudes - 0 to 5000 km

Sensitivity - 10^4 photons/measurement

Location/Operation -

Looking outside of vehicle and rotating with it. Possibly pointing slightly forward.

Protection Required -

Cover over aperture during launch and coast

*Sample time varies from one measurement every 20° of rotation to one measurement every revolution (360°) based on a rotation rate of 37.5 rpm.

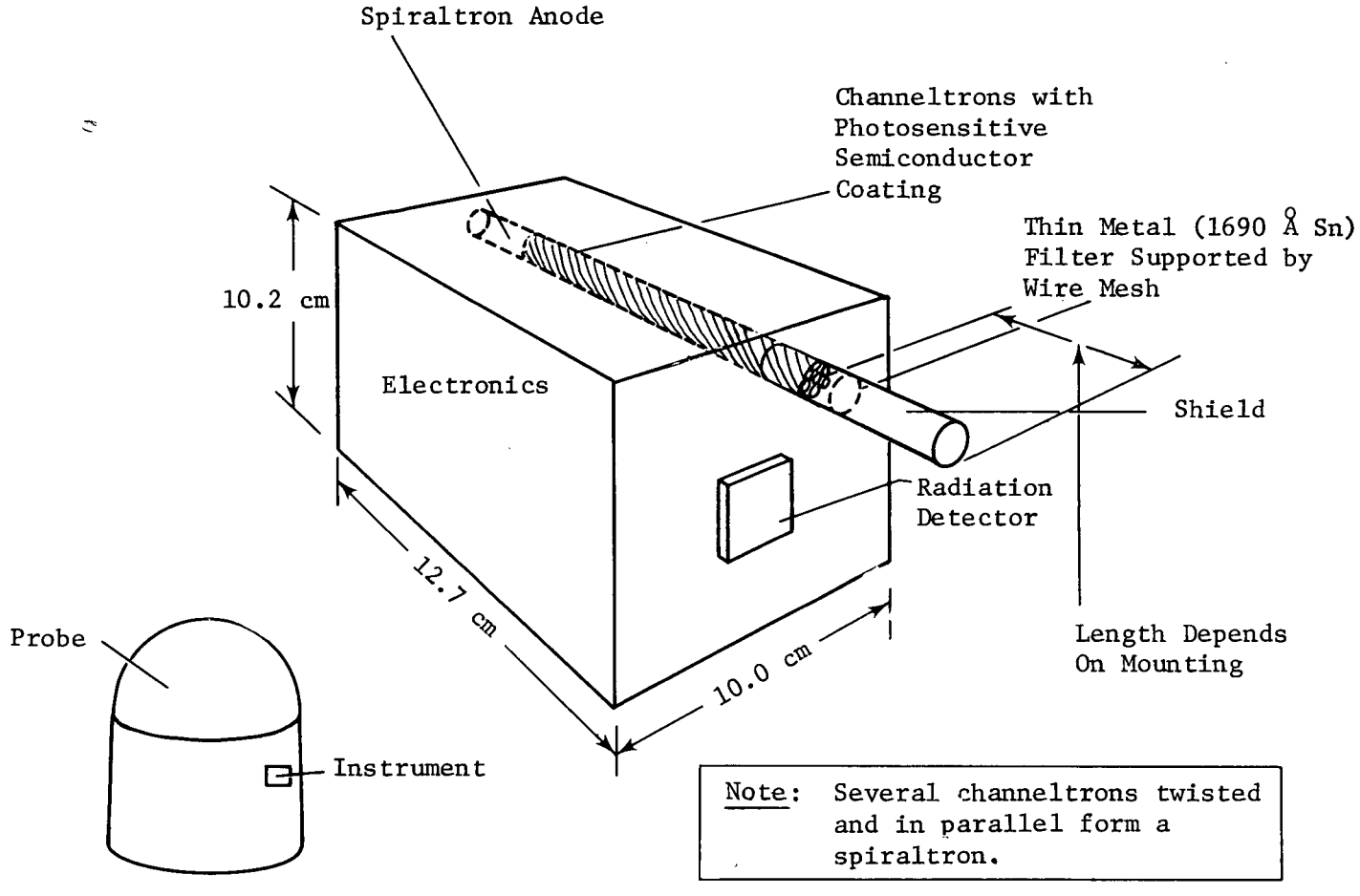

Fig. III-10 Helium Channeltron Photometer

Either photometers or a spectrometer will adequately measure the dayglow. Photometers generally collect more solid angle of light of a particular wavelength and have a higher signal/noise ratio. A spectrometer is used when a narrower specific selection of wavelength is desired. Both H and He photometers or the spectrometer can be packaged in a volume of about 13 x 13 x 20 cm with a weight of 2.3 kg and power requirement of 5 W. The final designs in this report have been based on these assumptions.

All three dayglow instruments will suffer some measurement interference from the radiation field, but the channeltron-type instruments are the most susceptible. To measure He dayglow on the entry probe, some form of channeltron detector must be used as a component in either the spectrometer or photometer. The effects of radiation depend on the number of counts the detector has to make. A high radiation field causes the channeltron to have too fast a counting rate. This will cause excessive current to be drawn and break down the voltage gradient along the wall.

With the high voltage supply on and operating, the channel multiplier will begin to suffer light to moderate damage at a radiation field strength of 10^{10} particles/cm^2. However, if the high voltage supply is left off and the instrument is not in the operating mode, it does not begin to suffer light to moderate damage until a field strength of 10^{14} particles/cm^2 is reached. The radiation-model upper limit is about 10^{13} particles/cm^2. Thus, if the instrument was not turned on until after it had passed through Jupiter's radiation belts, it would have survived to measure the dayglow. This is acceptable because the strength of the signal caused by the radiation field would completely swamp any signal due to the dayglow.

To sequence the photometer (or spectrometer) requires the use of some type of radiation detector (e.g., scintillator or semiconductor) to continuously monitor the strength of the radiation field and turn on the optical instrument when the strength drops below some minimum value for a certain length of time. This solution offers, in effect, another instrument of negligible size, weight, and power, operating within the data bit rates allowed for the optical instrument, yielding a radiation strength profile as the probe descends, only at the expense of adding a sequencing mechanism.

The dayglow instrument will be mounted inside the probe body with the aperture looking out the side of the vehicle, so that the field of view rotates with the probe. Both dayglow instruments

should look in the same direction and make measurements simultaneously. Because the instrument must rotate with the probe, the measurement time will be a direct function of the spin rate. It is desirable, but not necessary, to obtain profiles over 360° of probe rotation as the probe descends. There will be a variation in dayglow intensity with one rotation, thus a modulation in signal caused partially by interference from the Sun, even though the line to the Sun will always be 60° or more from the look direction of the instrument.

Two modes of operation of the dayglow instrument are possible. Both require that measurements be made every 20 to 30° of probe rotation. In the nominal case, these readings are processed onboard to yield the maximum and minimum intensity valves each revolution. In an expanded return case, every value is telemetered resulting in a full dayglow profile over each probe rotation. In the first case, the data consists of 2 words/revolution and in the second, 12 to 18 words/revolution for each hydrogen, helium, and background measurement. Thus, depending upon the mode of operation and the probe spin rate, the data rate can vary from 10 to 270 bps for the dayglow. A silicon diode sun sensor could be used to detect the exact rotation rate by observing sun crossings.

D. SCIENCE MISSION ANALYSIS

This section describes the relationship between the mission analysis parameters and the science instrument performance. The measurement performance of each instrument is evaluated as a function of altitude and entry flight path angle, and the effect of atmospheric model uncertainties on science instrument performance and mission time is discussed.

1. Measurement Performance along Entry Trajectory

The criterion for judging the measurement performance of the upper atmospheric instruments has been given as one measurement per scale height for each particle. The scale heights are tabulated in Chapter II. The first mission studied under the contract was the reference mission that had an entry flight path angle of -35°. Using this mission entry trajectory, the number of measurements per scale height for the primary constituents are given in Table III-11 as a function of altitude above turbopause. As can be seen, the number of measurements per scale height for the majority of the particles does not change as a function of altitude.

Table III-11 Reference Mission Measurement Performance

Particle	Measurements/Scale Height at Given Altitude				
	800 km	600 km	400 km	200 km	100 km
H	3.2	3.2	3.2	3.2	3.2
H_2	1.6	1.6	1.6	1.6	1.6
He			0.8	0.8	0.6
H_1^+ & e^-	6.0	6.0	6.0	6.0	6.0
H_2^+	5.5	7.3	8.6	5.0	2.0
H_3^+			2.7	2.7	
He^+			3.0	3.0	3.0
HeH^+			1.3	1.3	1.3

The blank spaces in the table reflect where the specific particle does not exist in sufficient quantity to be measurable, according to the models. Note that the smaller the atomic mass, the higher the number of measurements per scale height, for both the neutrals and the ions. The only performance numbers below one, are those for neutral He, heaviest of the listed neutrals.

The change in performance for the H_2^+ ion is directly attributable to its constantly varying concentration profile in the model. (See Chapter II.) The reduction in the numbers for both the neutral He and the H_3^+ ion result from the sudden rapid drop in their number densities starting at about 129 km.

For the mass spectrometer, the criterion is to make two full sweeps of all 11 mass numbers below the turbopause. This particular mission obtained 4.4 sweeps from 0 to -60 km, therefore satisfying the requirements. An additional 1.1 sweep is obtainable from 30 km above the turbopause, and will yield additional data if there is a sufficient abundance for measurement.

2. Science Mission Analysis Parameters

Figure III-11 shows four graphs of the primary measurement portion of the entry trajectory from 8000 km (∿250 sec) through the turbopause and the variations of the science mission analysis parameters. The first graph shows how the three velocities vary along the entry profile. The inertial velocity is that relative to the center of the planet and, as can be seen, its variations are small. The next line down shows the velocity relative to the planet's atmosphere, assuming that the atmosphere rotates exactly with the planet. It stays roughly parallel to the inertial, increasing slightly as the probe nears the turbopause. The radial velocity is shown on the bottom line, and is the one that establishes the science instrument measurement time and number of measurements that can be obtained within a certain distance. Its variations are the smallest of the three, but it is significant that it decreases, and that at entry it is a full 15 km/sec slower than the relative velocity.

The figure on the lower left shows the change in flight path angles along the entry trajectory. Note that while the inertial flight path angle at entry is the referenced -35°, the relative flight path angle is about 8° greater. The radial velocity is a direct function of the sine of the inertial flight path angle. The graph on the lower right shows that the change in angle of attack from 8000 km is only 1.2° and, during the portion of the entry where the primary science measurements are being taken, it changes only a fraction of a degree. This is well within the limits of the instruments, which are about ±5°. The 3σ dispersions around the flight path angles are about 1.2°, while those around the angle of attack are about 3°. The latter means that the change in angle of attack is less than the uncertainty in its value.

3. Performance versus Entry Flight Path Angle

Figure III-12 shows the parametric variations of velocity and measurement time as a function of inertial flight path angle at entry. The graph on the left shows that while the inertial velocity is almost independent, the relative velocity increases significantly with increasing flight path angle, and the radial velocity increases drastically. It is interesting that up until about 50°, the rate of increase of radial velocity is 1.0 km/sec/degree and that the magnitude of the entry angle approximately equals the magnitude of the radial velocity.

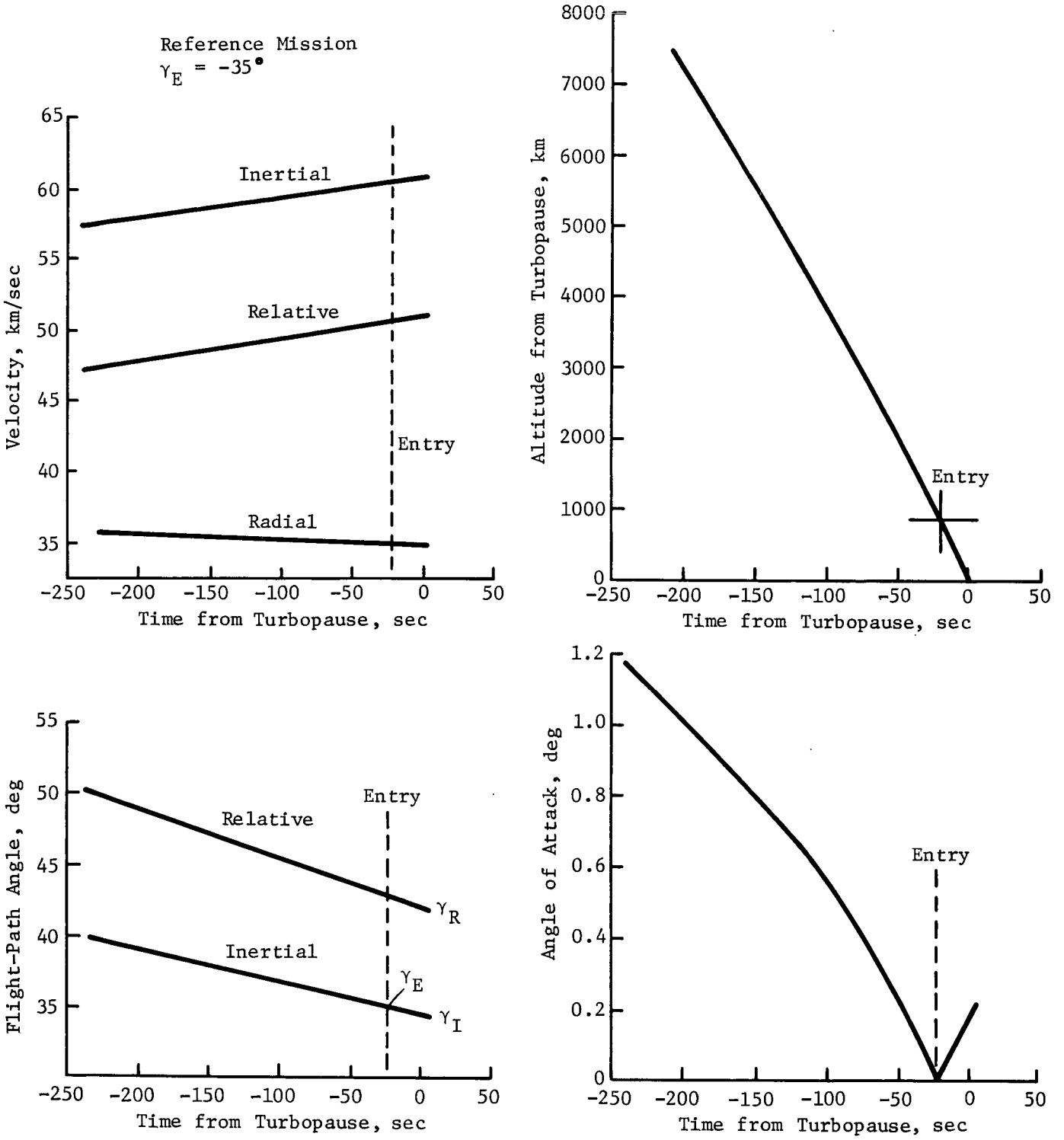

Fig. III-11 Mission Analysis Parameters Related to Science

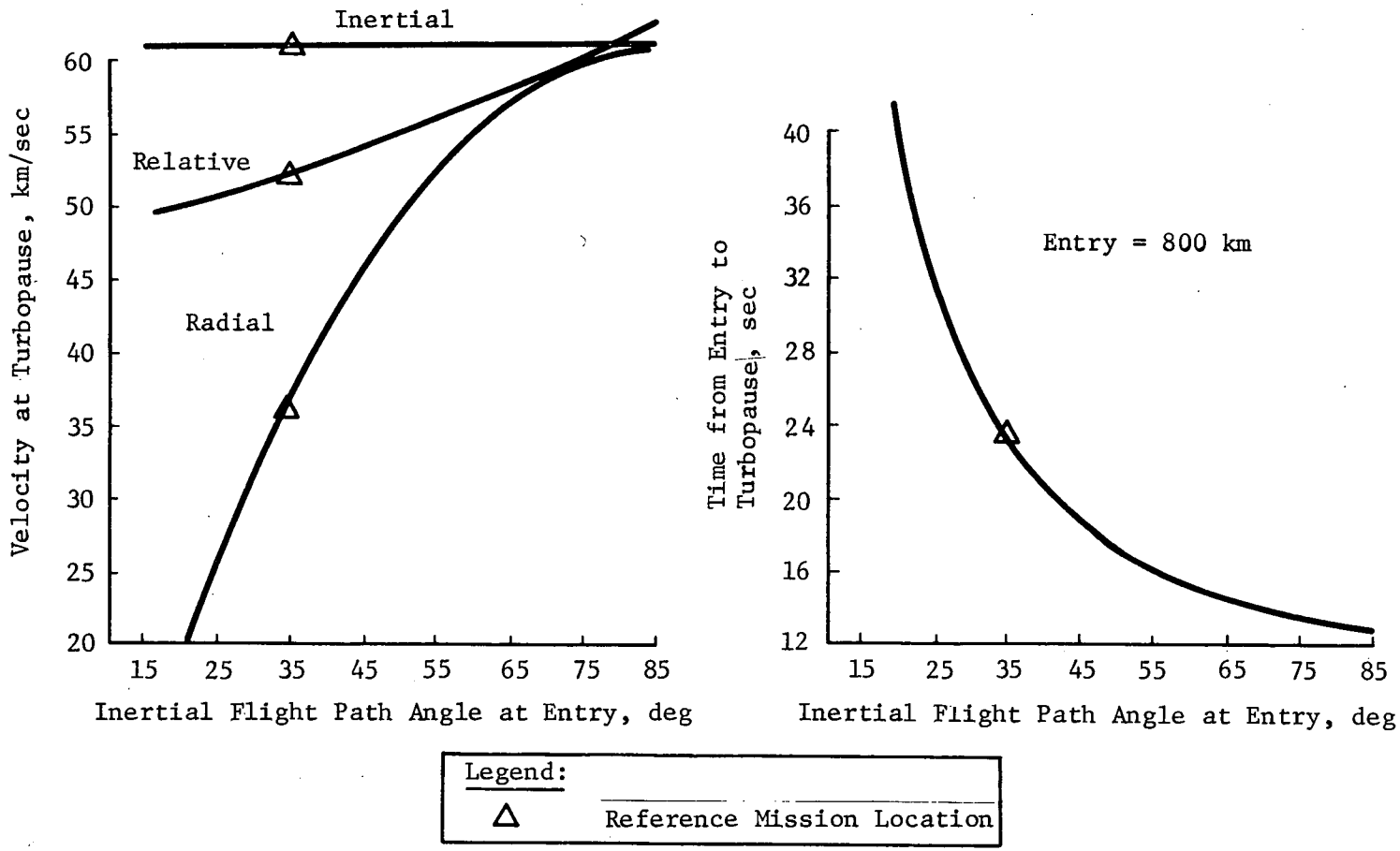

Fig. III-12 Velocity and Time vs Entry Flight Path Angle

This change in radial velocity directly affects the time between any two altitudes, as graphically shown by the curve on the right. It presents the time from entry to turbopause as a function of entry angle. By comparing the two graphs, it can be seen that, as the radial velocity goes up, the time to make measurements decreases rapidly. A curve representing the time below the turbopause down to blackout would look identical--the time at 15°, being 4.0 sec; at 35°, 1.7 sec; and at 85° only 1.0 sec. This strongly indicates that the lower flight path angles are much more desirable for making measurements.

Table III-12 shows the measurements per scale height for each of the ions and neutrals specified by the models as a function of entry flight path angle for an altitude of 200 km above the turbopause. This altitude is one where there are enough of all particles, according to the models, to be measured. Again, the evidence is strong that the lower the entry angle, the better the mission. An entry angle of about 26° is required to give 1.0 measurements per scale height for neutral He. Figure III-13 shows the individual measurements by the NRPA for an entry angle of 33° superimposed on the model concentration profile for neutral He. It represents 0.86 measurements per scale height. Unless the actual profile is extremely nonlinear, the number shown will be sufficient for determination of concentration profiles.

The top set of numbers in Table III-13 represents the mass spectrometer measurements for the reference location of the turbopause. The criterion of obtaining two measurements below the turbopause is satisfied for all flight path angles, but, as before, the performance increases with lower values. Because of the uncertainty of the models, and the variation in theories concerning the turbopause, it may be located as much as one order of magnitude in atmospheric density higher than the reference. This means a lowering in altitude of the turbopause of about 40 km. The second set of numbers in the table represents the measurements obtainable by the mass spectrometer below the turbopause if it is displaced 40 km down in the atmosphere. From this it can be seen that an entry angle of 25° or less is required to satisfy the criterion. Figure III-14 shows this difference graphically, the required two-measurement minimum designated with a dashed line.

4. Margins for Science Instrument Sequencing Times

A sufficient margin should be used in determining times for science instruments to begin monitoring data to ensure that they are operating early enough for any significant measurements. Margins used

Table III-12 Measurement Performance vs Entry Flight Path Angle

Particle	Scale Height at h = 200 km	Measurements/Scale Height							
		Entry Flight Path Angle, deg							
		-15	-25	-35	-45	-55	-65	-75	-85
H	55	7.4	4.3	3.2	2.5	2.1	2.0	1.8	1.8
H_2	28	3.6	2.1	1.6	1.2	1.1	1.0	0.9	0.9
He	14	1.8	1.0	0.8	0.6	0.5	0.5	0.4	0.4
H_1^+ & e^-	108	14.3	8.3	6.0	4.9	4.2	3.8	3.5	3.4
H_2^+	87	11.8	6.8	5.0	4.0	3.5	3.1	3.0	2.9
H_3^+	49	6.4	3.7	2.7	2.2	1.9	1.7	1.6	1.5
He^+	51	7.1	4.1	3.0	2.4	2.1	1.9	1.8	1.7
HeH^+	22	2.9	1.7	1.3	1.0	0.9	0.8	0.7	0.7

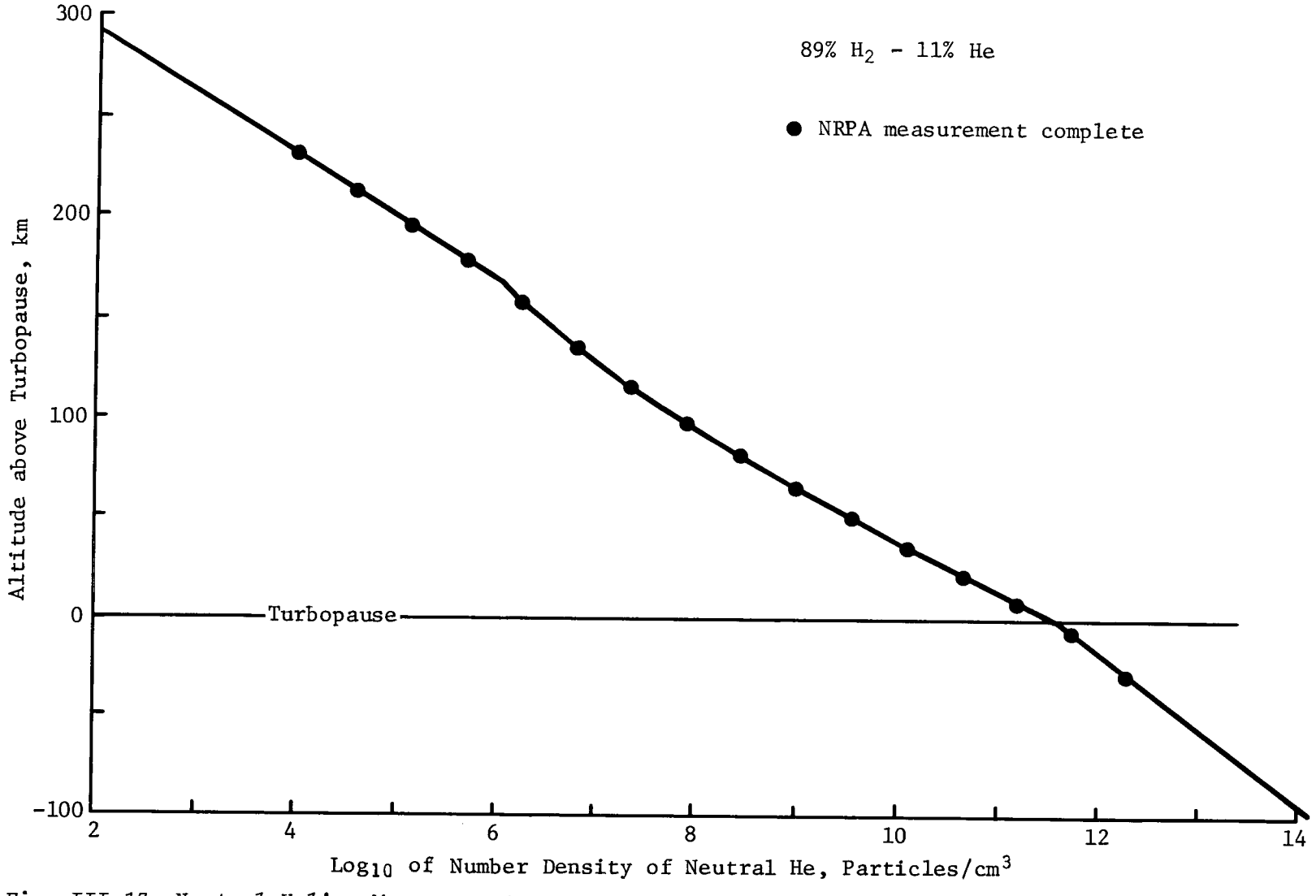

Fig. III-13 Neutral Helium Measurements

Table III-13 Mass Spectrometer Performance vs Entry Flight Path Angle

	Entry Flight Path Angle, deg							
Measurements:	-15	-25	-35	-45	-55	-65	-75	-85
Above turbopause	2.61	1.50	1.09	0.88	0.76	0.68	0.64	0.62
Below turbopause	10.48	6.02	4.37	3.50	3.02	2.73	2.56	2.48
Total	13.09	7.52	5.46	4.38	3.78	3.41	3.20	3.10
With Lower Turbopause*:								
Below turbopause	3.50	2.01	1.46	1.17	1.01	0.91	0.85	0.83
Total	6.11	3.51	2.55	2.05	1.77	1.59	1.49	1.45

*Measurements obtainable if turbopause is 40 km lower than model indicates, which is one order of magnitude increase in atmospheric density at that location.

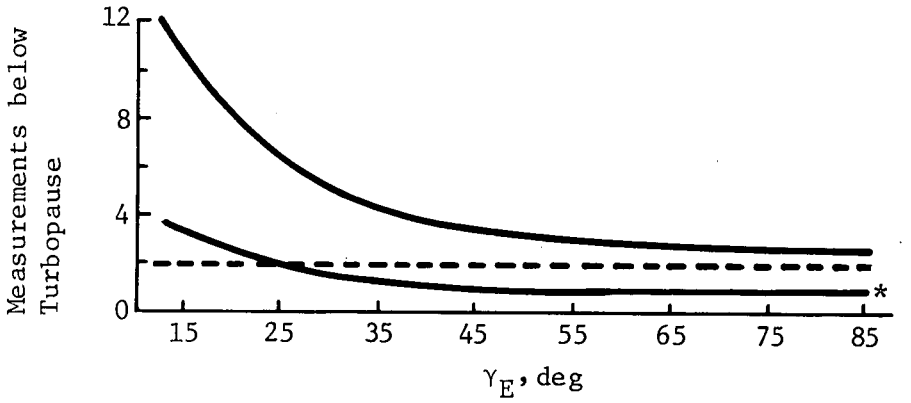

Fig. III-14 Mass Spectrometer Performance vs Entry Flight Path Angle with Turbopause Uncertainty

4. Margins for Science Instrument Sequencing Times

A sufficient margin should be used in determining times for science instruments to begin monitoring data to ensure that they are operating early enough for any significant measurements. Margins used so far have been computed on the basis of two considerations:

1) An altitude margin based on uncertainties in the nominal atmosphere model to account for the highest altitude at which particles might be detected;

2) A time margin based on the uncertainty in the time at which the probe would arrive at the desired instrument monitoring altitude. This uncertainty results from errors in the tracking, midcourse correction, and deflection maneuver processes.

Note also that the instruments are turned on 5 min earlier to allow them time to warm up to operating temperature.

The altitude margin is based on the upper atmospheric model and sensitivity of the instruments plus an allowance for model uncertainties. The most optimistic 1975 state-of-the-art sensitivity for the Langmuir probe is 10 particles/cm^3. The lightest particle that would exist highest in the atmosphere is the electron, and according to the model, the altitude above the turbopause at which the electron number density falls below 10 particles/cm^3 is 1240 km. However, because of possible large uncertainties in the model and possible interaction with the solar wind, the Langmuir probe is set to begin monitoring at an altitude of 50,000 km, which is approximately 23 min from turbopause.

For the IRPA, the best possible sensitivity is 5 particles/cm^3 by 1975. For monatomic H ions, the altitude at which this number density is reached, according to the model, is 1370 km and for diatomic H_2 ions, 820 km. For simplicity in sequencing mechanisms, the IRPA has been set to begin simultaneously with the Langmuir probe.

For the NRPA, the best possible sensitivity by 1975 is 10^4 particles/cm^3. For neutral monatomic H, the altitude at which this density is reached, according to the model, is 575 km and for neutral diatomic H_2 it is 515 km above the turbopause. For neutral He, it is only 225 km. The altitude to begin monitoring without trajectory uncertainties was set at 5000 km for all missions. For a detailed discussion of the time margin mentioned in 2) above, see Chapter IV, Section F.

For the nominal payload data rates, Figure III-15 shows the science instrument sequencing with altitude and time. The time-to-turbopause scale, although typical, is shown for a mission (Mission 7) with an entry angle of -33°. (See Chapter V for Mission descriptions.) Figure III-16 shows similar data for the expanded science payload of Mission 1A.

The instruments are sequenced in two steps, the ETP, IRPA, and photometers coming on first and then the remainder of the instruments at a lower altitude. The dashed line represents the altitudes which, according to the model atmosphere and ionosphere and the projected state-of-the-art 1975 instrument sensitivities, would be the points at which that instrument would begin taking relevant data. The solid line represents the altitudes at which the instruments will begin operation in the mission sequence. The difference between the lines is the margin allowed for variation in model atmosphere and ionosphere. Note that the altitude reference is "cloud tops" (71,550 km) rather than turbopause because of the log scale.

5. Longitude and Latitude Variations along Entry Trajectory

A study was conducted to investigate the amount of longitude and latitude traversed by the probe from the time instruments are turned on until communications blackout. The tabulation below presents those variations along with the time increment covered for two intervals over a range of entry flight path angles (γ_E).

	50,000 to Blackout*			1400 to Blackout*		
γ_E, deg	Δ Lat, deg	Δ Long., deg	Δt, min	Δ Lat, deg	Δ Long., deg	Δt, sec
45	1.4	23.6	20.7	0.10	1.2	34.3
35	1.9	32.1	22.6	0.10	1.7	42.3
25	2.3	42.1	26.3	0.11	2.6	57.5
15	2.6	55.2	31.3	0.13	4.4	94.9
Equatorial inclination for all missions = 3.50°.						
*Blackout is taken as -60 km altitude.						

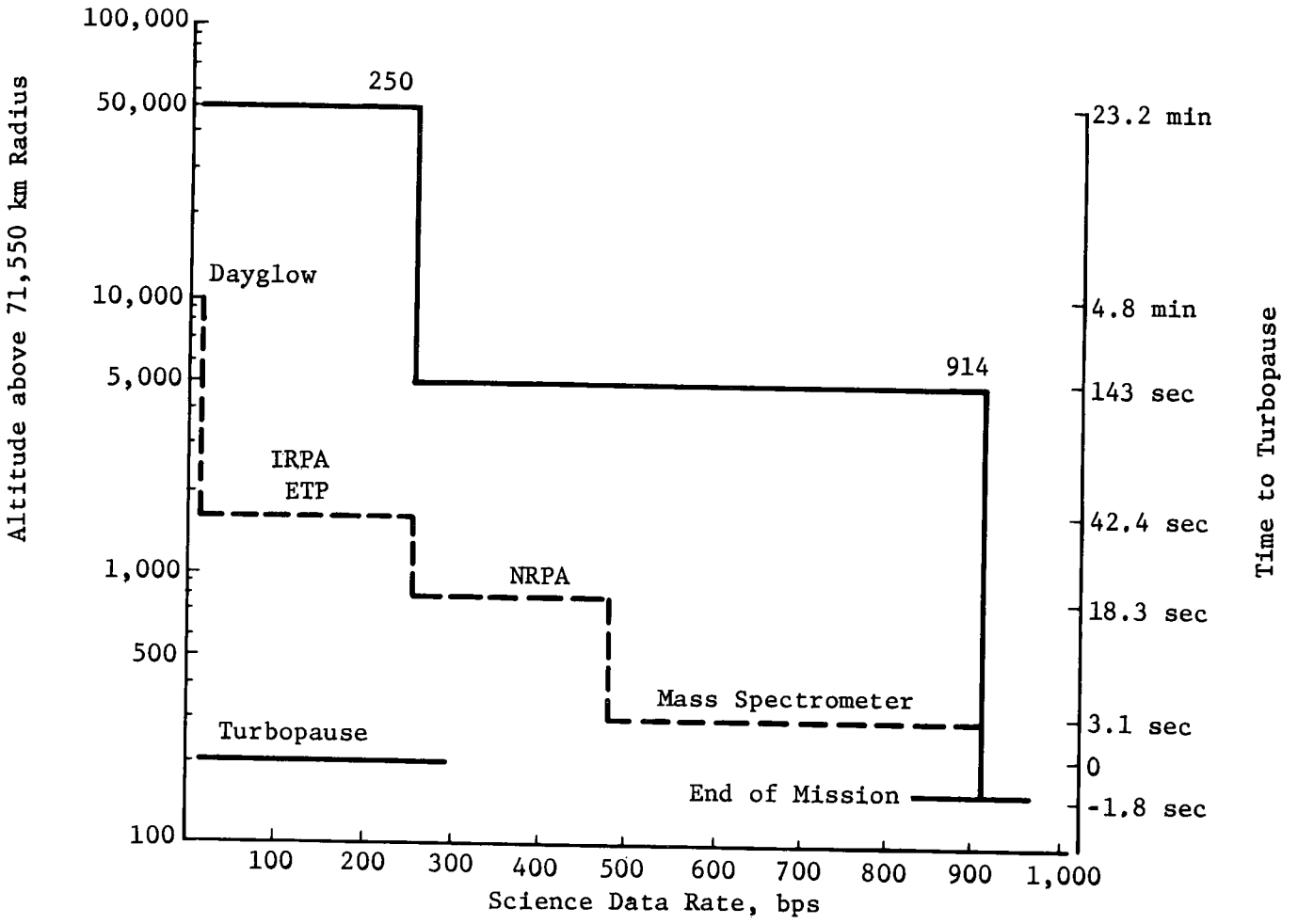

Fig. III-15 Nominal Payload Instruments Sequence and Data Rates

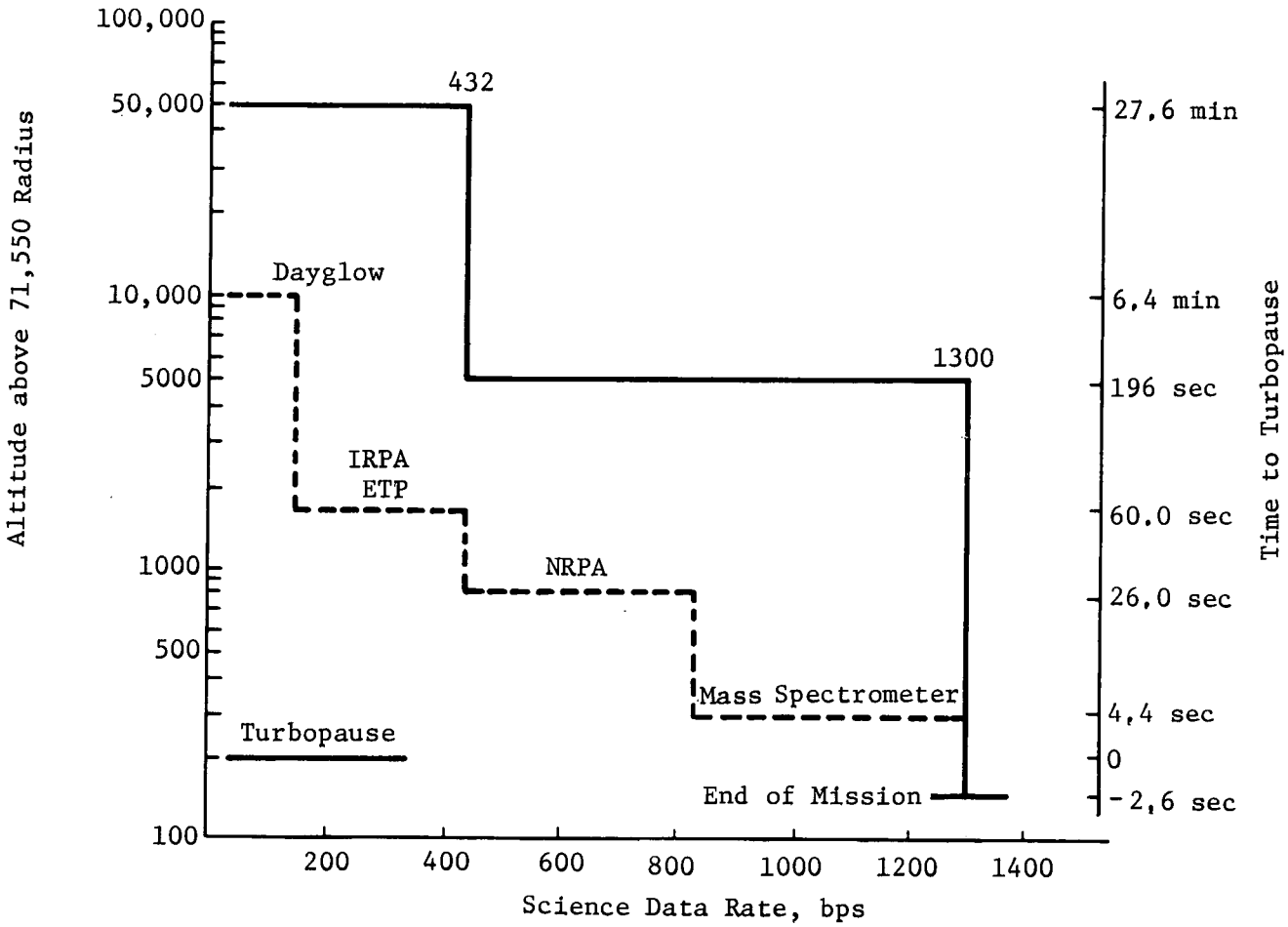

Fig. III-16 Enhanced Science Payload Instruments Sequence and Data Rates

The first interval is from 50,000 km altitude to blackout and begins where the Langmuir probe first begins to monitor for electrons. The second interval is from 1400 km to blackout and represents the approximate maximum region that the density of particles, according to the adopted models, is within the measurable range of the instruments.

The latitude and longitude variations for the range beginning at 1400 km are probably the most realistic from the standpoint of actual measurements made by the instruments, and these variations appear negligible. However, longitude variation for the total time the instruments are operating is significant, and if the data are nonzero in this higher range, it could become important. Trajectory uncertainties are unimportant here because a displacement in time does not affect the length of the operating range.

The above data were based on probe deflection at 10^6 km and a spacecraft periapsis of 1.1 R_J, but additional information has shown that the order of magnitude of the variations is the same for any reasonable deflection or periapsis radius.

REFERENCES

1. R. M. Goody, and G. M. Levin: *The Jovian Turbopause Probe*, Parts I and II, GSFC Report No. X-110-70-442, Dec 1970.

2. S. G. Chapin, Program Manager: *Jupiter Turbopause Probe Gas Physics Environment and Instrument Response Study*, Final Report, MMC Report No. MCR-71-142, Aug 1971.

3. "The Planet Jupiter (1970)," *NASA Space Vehicle Design Criteria*, NASA SP-8069, Aug 1971.

4. D. M. Hunten: Letter to G. M. Levin concerning Jupiter dayglow intensities, Aug 1969.

5. E. Maier: Telecon.

6. H. Niemann: Telecon.

7. L. H. Brace: Telecon.

8. H. Niemann and D. Harpold: Telecon.

IV. MISSION ANALYSIS AND DESIGN

Results of major parametric studies in mission analysis and design for the Jupiter turbopause mission are presented in this chapter, which comprises the following sections.

A. Science Requirements on Mission Design

B. Entry and Approach Trajectories

C. Interplanetary Trajectories

D. Deterministic Probe Mission Analysis

E. Navigation and Guidance

F. Dispersion Analysis

The titles of the first two sections are self-explanatory. The launch and arrival considerations involved in selecting the interplanetary trajectory are analyzed in Section C. Requirements for Jupiter swingbys to other planets and to the solar apex are provided in addition to Jupiter-only missions. The deterministic analysis of the deflection and postdeflection phases of the mission is described in Section D. An extensive discussion of the deflection is included here, with descriptions of the precession maneuver and communication link parameter. The dispersions of entry parameters and communication parameters resulting from deflection uncertainties and execution errors are analyzed in the final section.

Generally, the parametric data are based on the reference mission defined below. To demonstrate the effects of mission date, data are occasionally referenced to other missions. The dates defining these key missions are provided in Table IV-1.

Table IV-1 Kew Missions

Mission	Launch Date	Arrival Date	Flight Time, days	V_{HP}, cm/sec	Periapsis Radius, R_J	Deflection Radius, 10^6 km	Deflection ΔV, m/sec	Entry Angle, deg
Reference	10/10/78	3/27/80	534	11.9	Variable	Variable	Variable	Variable
1	10/21/78	12/26/80	797	6.8	1.1	30	16	-21
1A	10/21/78	11/19/80	760	6.8	1.1	10	55	-23
2,2A	10/13/78	7/29/80	655	8.6	4.0	50	101	-29
3	10/3/78	5/1/80	576	10.7	1.9	30	82	-33
4A	11/5/79	6/8/81	581	10.9	9.9	50	243	-33
4B	11/11/79	5/2/81	538	12.1	6.6	50	180	-34
5	10/9/78	4/1/80	540	11.7	1.8	30	75	-34
7B	9/5/77	3/16/79	557	10.6	4.9	50	130	-33
7C	9/5/77	3/1/79	542	11.1	4.5	50	122	-33

A. SCIENCE REQUIREMENTS ON MISSION DESIGN

Mission design is determined by the science objectives and performance requirements of the mission. These are discussed in detail in the previous chapter. A brief summary of requirements most important to mission design will be given in this section. The pertinent constraints are illustrated in Fig. IV-1.

Because of Jupiter's large size and rapid rotation rate of 36.6°/hr, its equatorial velocity is about 12.6 km/sec. Therefore, entry in the direction of Jupiter's rotation in the vicinity of the equatorial plane can reduce the relative entry speed with respect to the atmosphere from about 60 km/sec to 47 km/sec. Thus, posigrade approaches with low inclinations are desirable. If an entry at zero latitude is not possible, entries at latitudes of ±10° are desirable because of the turbulent region in those latitudes.

It is necessary that the probe enter on the sun side of the planet to obtain acceptable dayglow intensities and to enter in the predictable ionization region. Because the ionization drops off abruptly about 70° from the subsolar point (or 20° from the evening terminator), a constraint is imposed that entry must occur within 70° of the subsolar point. Science measurement performance is enhanced with low entry angles. The entry angle is reduced as the angle from the subsolar point to the entry site is increased. Therefore, there is a minimum entry angle consistent with the 20° mask angle constraint. The implication of these requirements on launch and arrival date selection will be discussed in more detail in Section C.

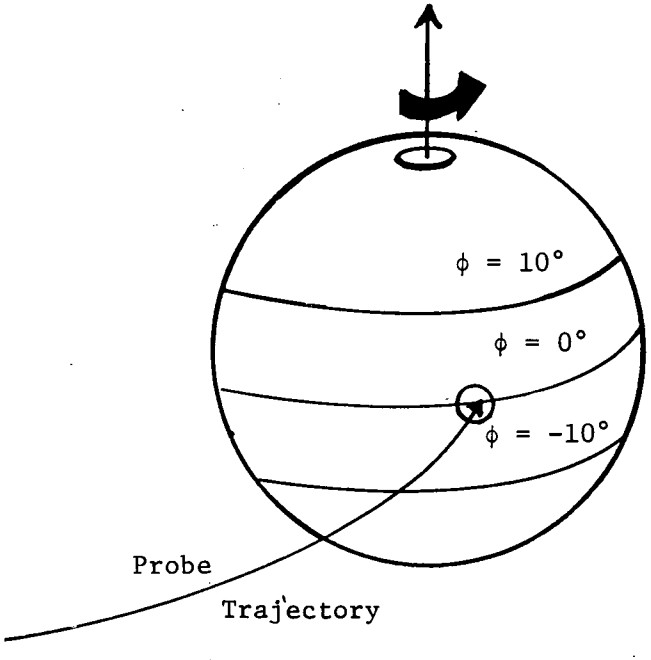

Entry Site Selection

- Prefer Posigrade Approach Near Equator to Reduce Relative Velocity
- Prefer Regions of Higher Turbulence (Latitudes 0°, ± 10°)

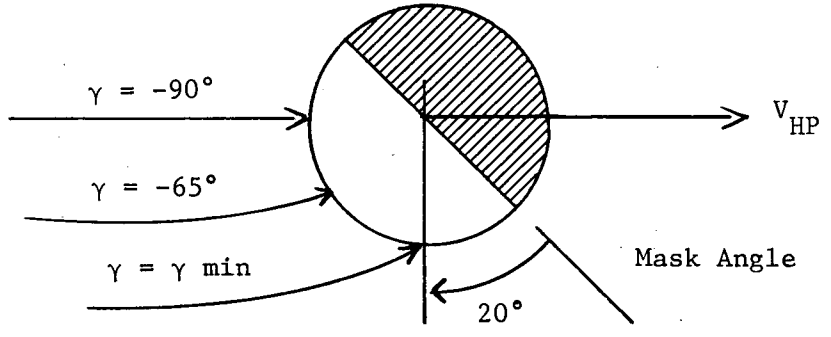

Approach Conditions

- Satisfy 20° Mask Angle Constraint
- Obtain Low Entry Angle

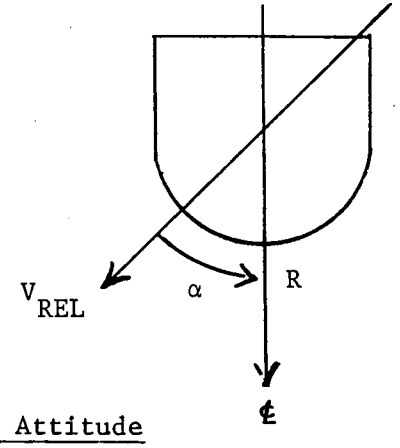

α = Relative Angle of Attack

Entry Attitude

- Obtain 0° Relative Angle of Attack

Fig. IV-1 Science/Mission Analysis Constraints

Science requirements also stipulate that the probe enter with a relative angle of attack of zero. Otherwise, the collection and interpretation of the science data would be impaired. A zero relative angle of attack also assures that aeroheating will be well defined and simplifies design of thermal control.

B. ENTRY AND APPROACH TRAJECTORIES

The critical phase of the turbopause mission is the period when science measurements are being taken and resulting data transmitted to the spacecraft and relayed to Earth. This phase includes the approach and entry trajectories of the probe and the approach trajectory of the spacecraft.

In this study, the entry radius is assumed to be at a Jovian radius of 72,550 km which is 800 km above the turbopause. This altitude corresponds to a pressure of 10^{-17} atm. The mission terminates at communication blackout approximately 60 km below the turbopause at a pressure of 10^{-5} atm. The postentry phase of the mission therefore occurs over an interval of 860 km in altitude and less than 50 sec in time. The entry angle and velocity stay approximately constant during this interval. Thus, the aerodynamic effects on the postentry trajectory can be ignored. The aerodynamic heating and communication blackout are, of course, of crucial importance, and are discussed in Chapter X of this volume.

The critical trajectory parameters at entry are the relative and inertial flight path angles, relative and inertial velocities and components, relative angle of attack, and lighting. The variation in lighting is a function of entry angle and arrival date. Discussion of these effects will be deferred to Section C.

The flight path angle at entry will be designated the entry angle. Figure IV-2 provides a comparison of relative and inertial entry angles. In this report, references will generally be based on inertial entry angle so that the term *entry angle* will imply inertial entry angle unless otherwise noted. The figure then provides a convenient conversion to the relative angles.

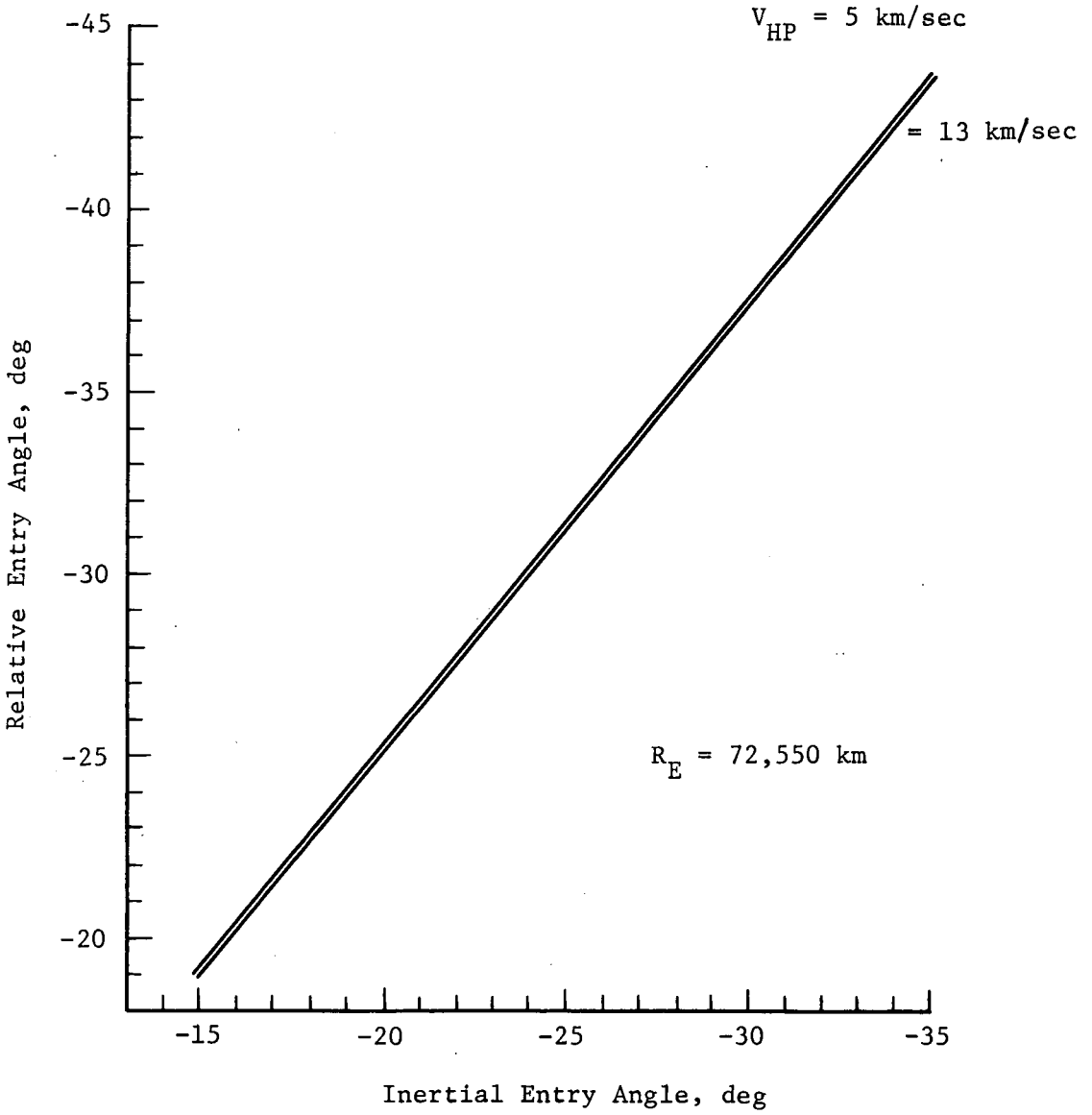

Fig. IV-2 Inertial and Relative Entry Angles

The relative velocity at entry is a function of the entry angle and latitude of entry. Figure IV-3 provides a quantitative measure of these effects. The relative velocity is least for small entry angles and entry latitudes and increases as either is increased. The entry velocity is relatively insensitive to variations in approach velocity, V_{HP}, (Fig. IV-4) so that entry velocity is not a function of arrival date at Jupiter.

The value of the entry angle also has a critical effect on the value of the radial velocity component, which translates into the time interval from entry to turbopause. These effects are illustrated in Fig. IV-5. For the missions identified in this study, the entry angles vary from $\gamma_E = -20°$ to $\gamma_E = -34°$. For this range, the critical time interval varies from about 36 to 24 sec.

The final probe trajectory profile for the reference mission is illustrated in Fig. IV-6. The time histories of velocity components, altitude, flight path angle, and relative angle of attack are provided in this figure.

The approach trajectory of the spacecraft is constrained because of the requirements for the probe trajectory. The requirement for posigrade trajectories for the probe to reduce its relative velocity constrains the spacecraft trajectory to the same type of approach because of relay link requirements. The deflection, ΔV, is generally reduced if an in-plane maneuver is used. Therefore, the desire for low-inclination probe trajectories translates into a preference for low-inclination spacecraft trajectories. Finally, the communication range is reduced as the spacecraft periapsis radius is reduced. Thus, low periapsis radii are also preferred. Quantitative evaluations of these variations are given in Section D of this chapter.

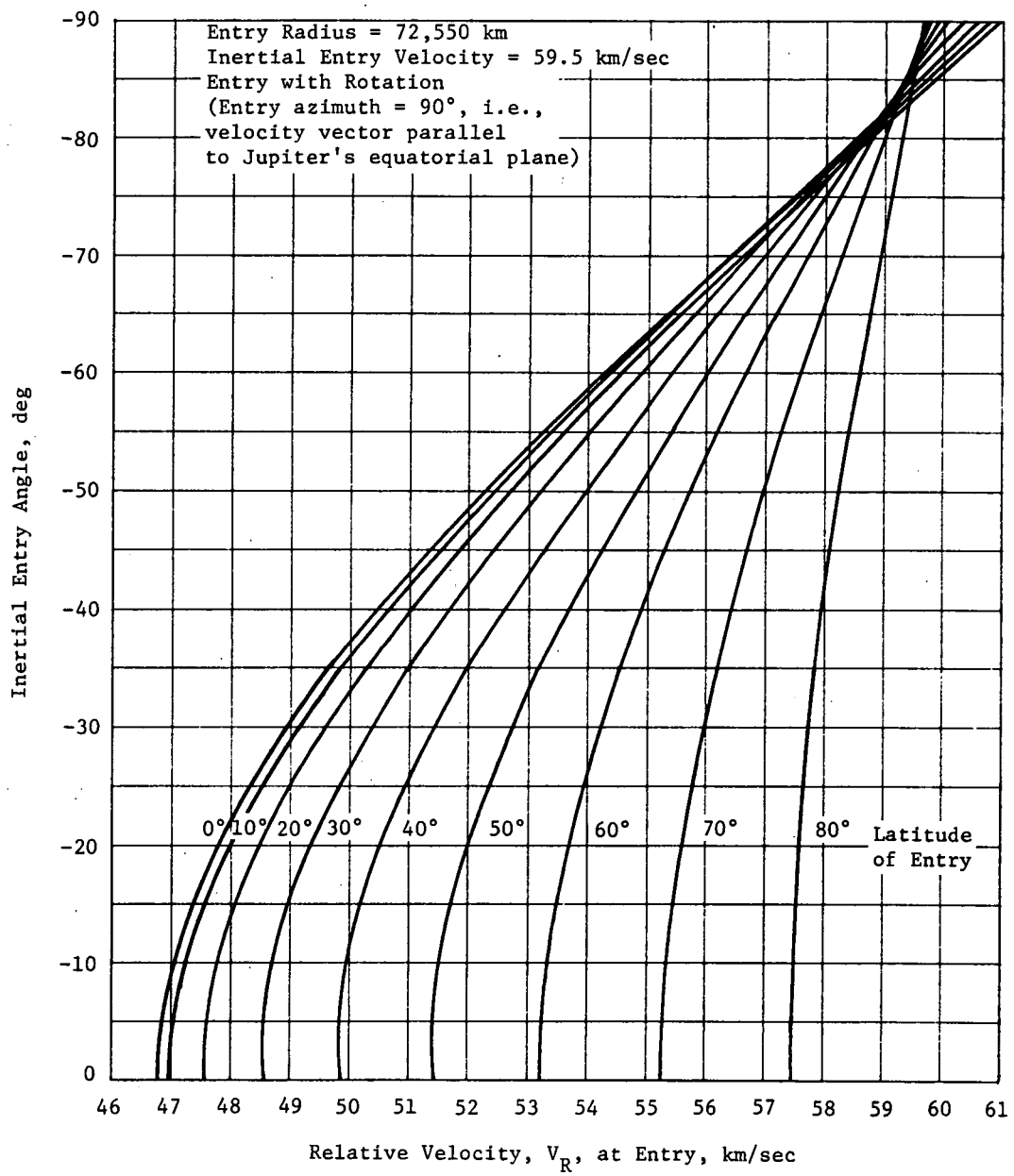

Fig. IV-3 Relative Velocity Variation with Entry Conditions

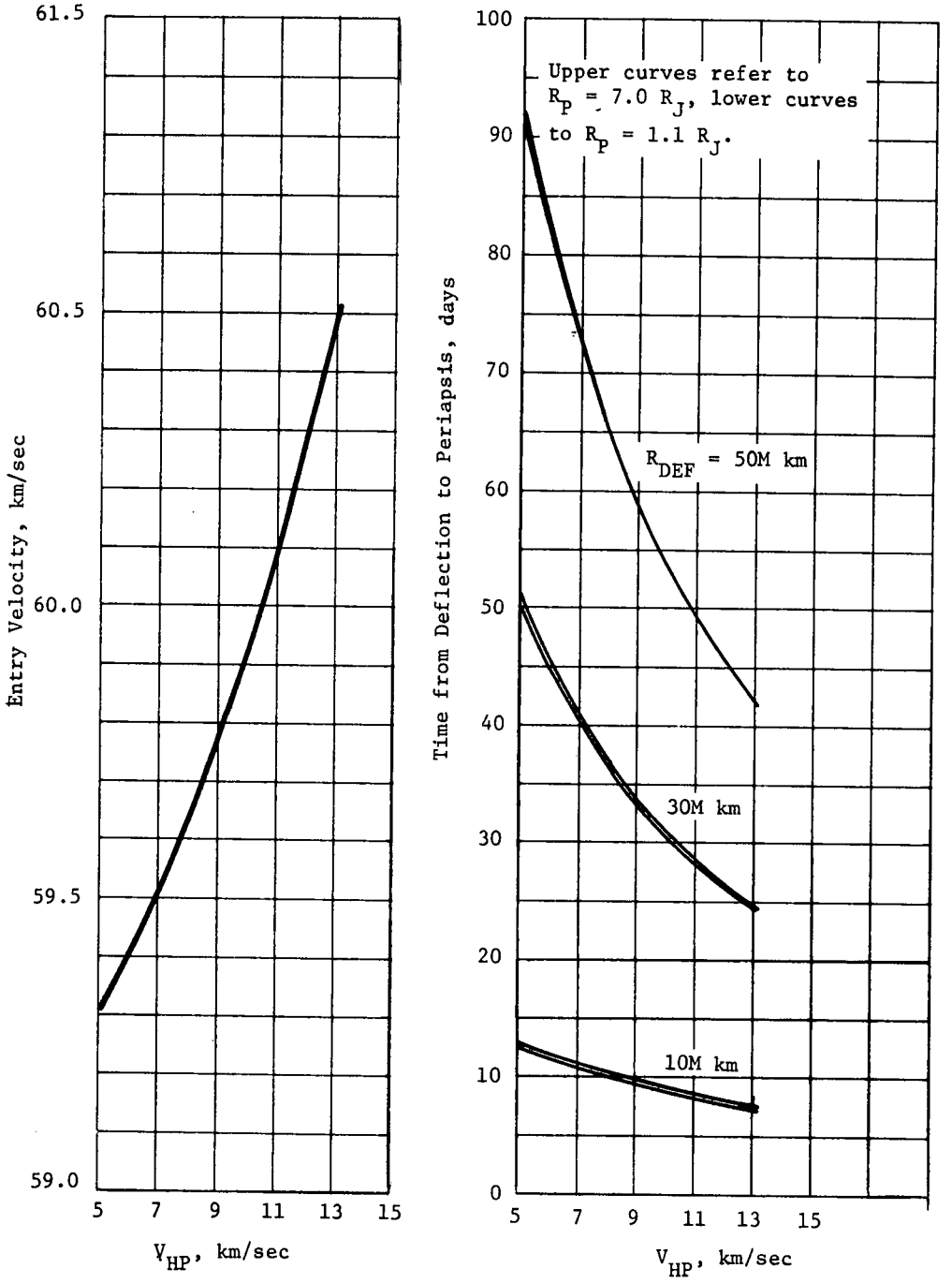

Fig. IV-4 V_{HP} Effects

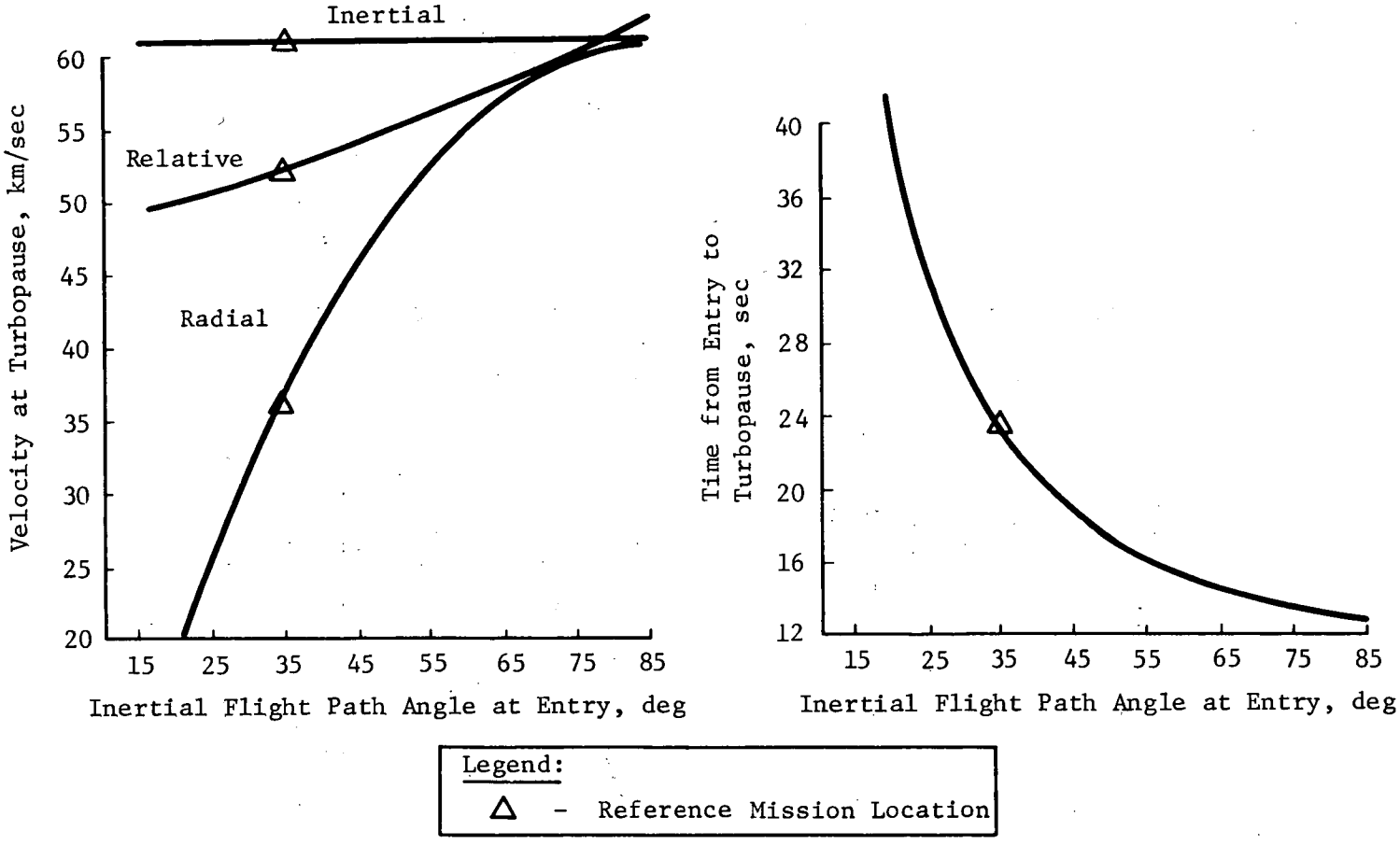

Fig. IV-5 Entry Angle Effects on Velocity and Mission Time

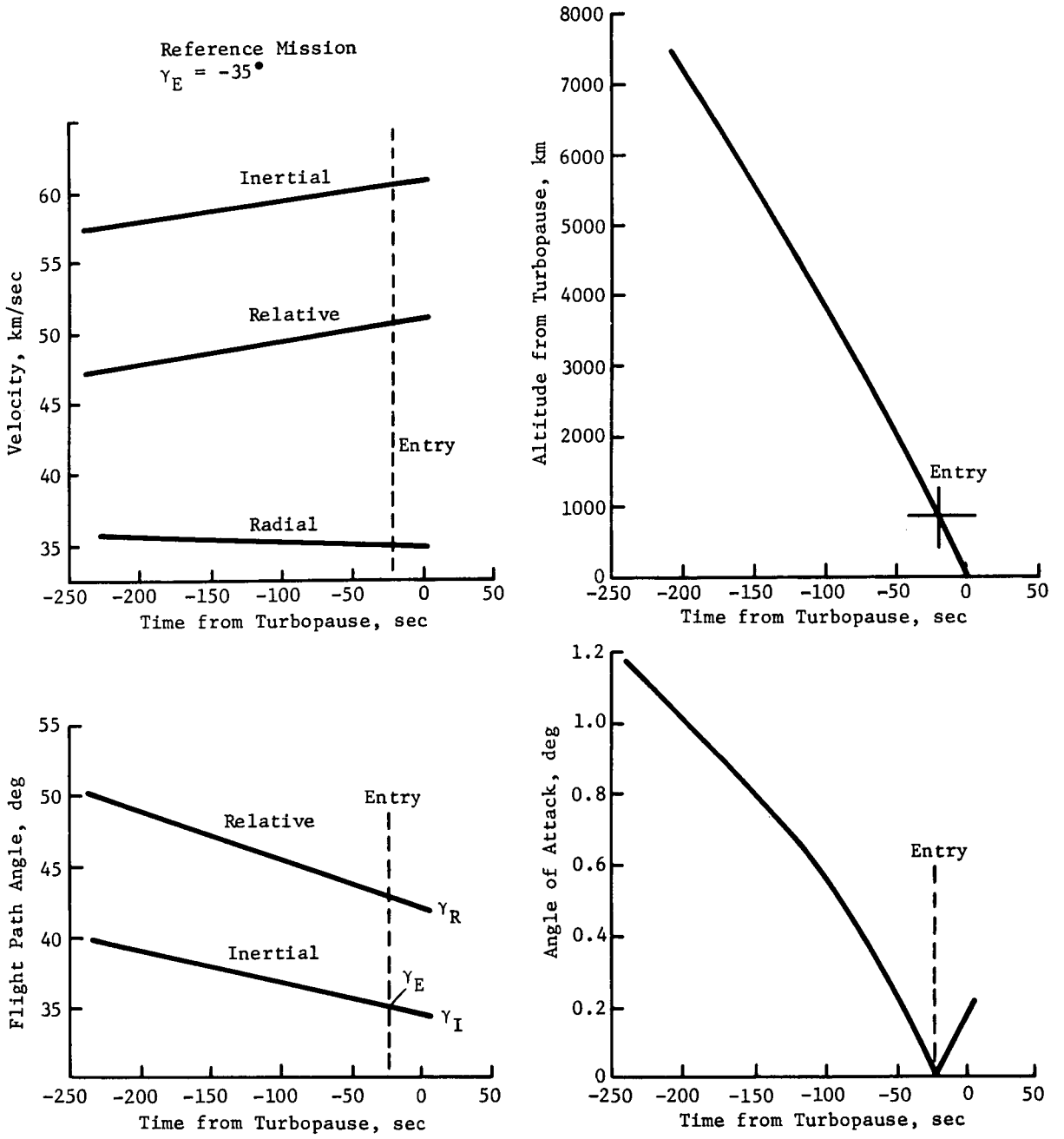

Fig. IV-6 Critical Phase of Probe Trajectory for Reference Mission

C. INTERPLANETARY TRAJECTORIES

Opportunities for Earth-Jupiter transfers occur approximately every 13 months when the Earth and Jupiter are in relative opposition to each other. If the two planets traveled in coplanar circular orbits, the minimum energy transfer would consist of an ellipse with periapsis at Earth launch position and apoapsis at the Jupiter arrival position (Hohmann transfer). Because of nonplanar effects (Jupiter's orbit is inclined 1.3° to that of the Earth.), a 180° transfer would require a transfer plane normal to the ecliptic plane, which would result in a prohibitive launch energy requirement. Therefore, physically realizable transfers are divided into two types: Type I with central angles of less than 180° and Type II with central angles greater than 180°.

1. Launch Energy

Fixing the launch and arrival dates essentially determines the Earth-Jupiter transfer. Given those dates, the heliocentric position vectors of Earth at launch and Jupiter at arrival are determined. By Lambert's theorem (Ref IV-1) those two vectors and the time interval required to traverse them determine the heliocentric conic that closely approximates the actual flight path on the mission. The geocentric hyperbola may then be computed so that, at departure from Earth, the velocity of the spacecraft relative to the Earth (called the hyperbolic excess velocity, $\vec{V}_{HE}$) plus the orbital velocity of the Earth, $\vec{V}_{EL}$, matches the velocity, $\vec{V}_L$, of the heliocentric conic at launch:

$$\vec{V}_{HE} = \vec{V}_L - \vec{V}_{EL} \qquad [IV-1]$$

The variable normally used to discuss launch energy is C_3, the *vis viva* energy, defined as the square of the magnitude of the hyperbolic excess velocity or

$$C_3 = V_{HE}^2 \qquad [IV-2]$$

which represents twice the energy per unit mass of the spacecraft. An alternate variable used to describe launch energies is the characteristic velocity, V_{CH}, which represents the velocity needed at the injection radius R_I to have the equivalent energy, or

$$V_{CH}^2 = V_{HE}^2 + \frac{2\mu}{R_I} \qquad [IV-3]$$

For a given launch vehicle, the amount of payload that can be injected into interplanetary trajectories is a function of the launch energy--the smaller the required energy, the larger the possible payload.

Figure IV-7 illustrates the payload capability for the launch vehicles considered in this study: the Reference Titan IIID five- and seven-segment vehicles, both with an without Burner II stages, and an updated Titan IIID five-segment vehicle being investigated for outer planet exploration missions. The data indicated are taken from Ref IV-2 and IV-3, respectively. The performances for standard Titan vehicles are based on a launch azimuth of 115°, while the updated Titan vehicle performance is evaluated at an azimuth of 90°. Performance data for all vehicles assume a 185-km parking orbit. The payload in all cases refers to probe, spacecraft, spacecraft modifications, and adapters. Generally, a Pioneer spacecraft weighing about 249 kg would be launched by a standard five-segment Titan/Centaur, while a MOPS (Modified Outer Planet Spacecraft) weighing about 589 kg would require either a seven-segment vehicle or the updated five-segment. Adding the weight of a turbopause probe and spacecraft modifications (91 kg) to these weights demonstrates that launch energies much greater than $C_3 = 130$ km^2/sec^2 are not realizable. certain combinations, the maximum C_3 obtainable is even less than this limit.

Figures IV-8 through IV-10 provide the C_3 contours for launch years 1978, 1979, and 1980, respectively. It can be seen that the launch energy requirements decrease progressively during those years. Using these figures, reasonable selections of launch date/arrival date (LD/AD) and, equivalently, the interplanetary trajectory can be made.

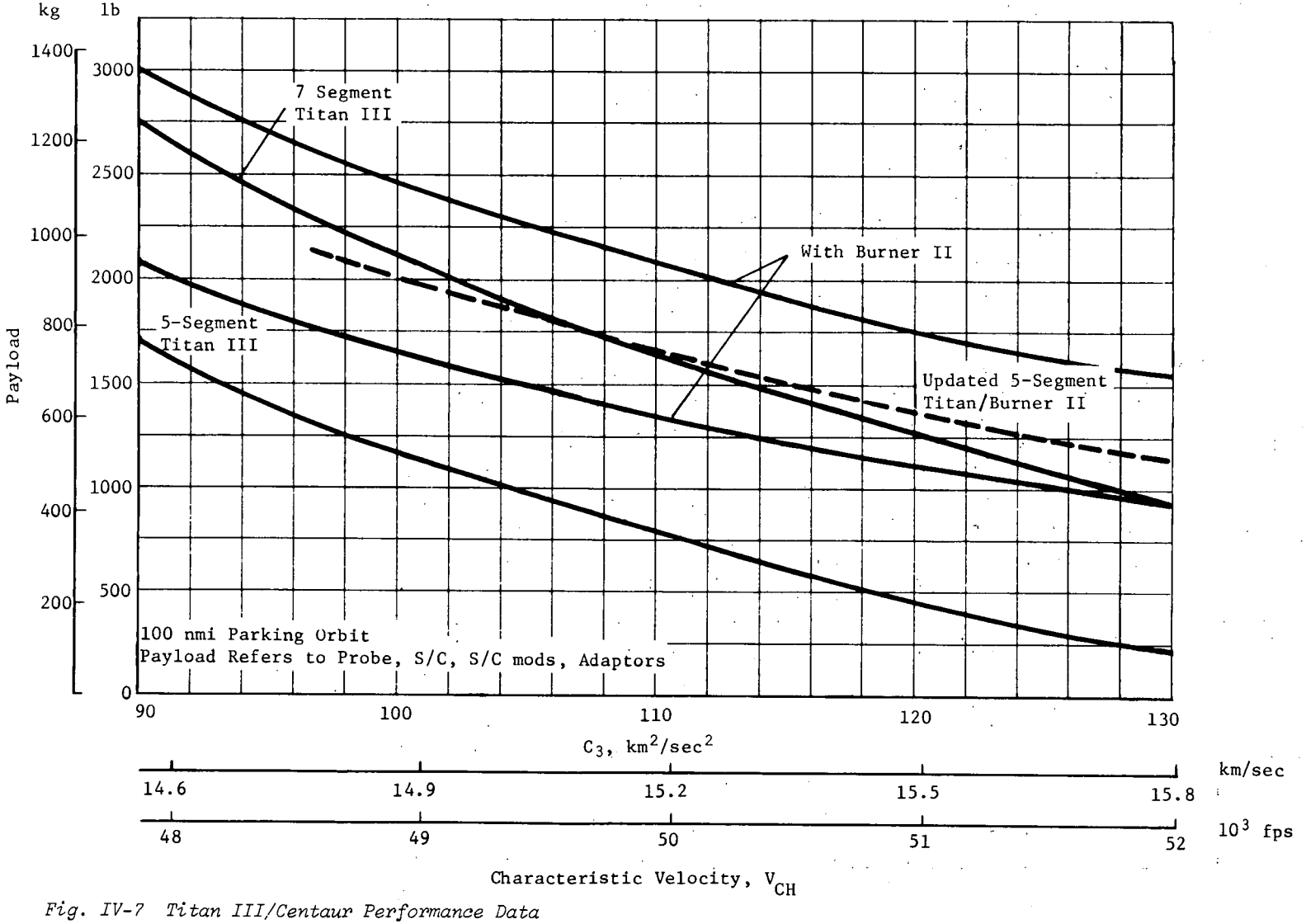

Fig. IV-7 Titan III/Centaur Performance Data

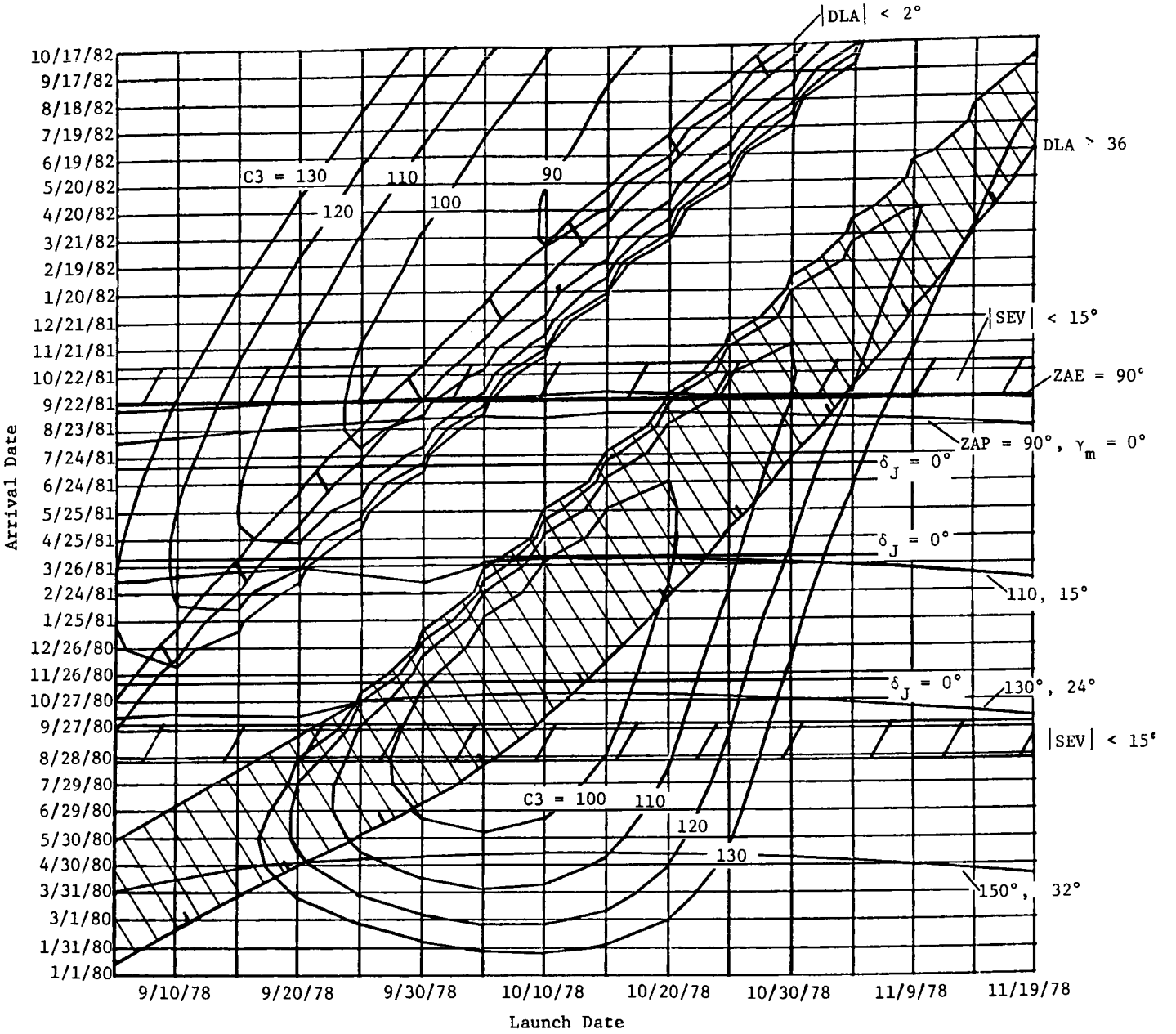

Jupiter Turbopause Probe Study
1978 Launch, Type I and II
(TF at $X_1Y = (0_1 0)$ is 483 Days)

Fig. IV-8 Launch Energy Requirements, 1978

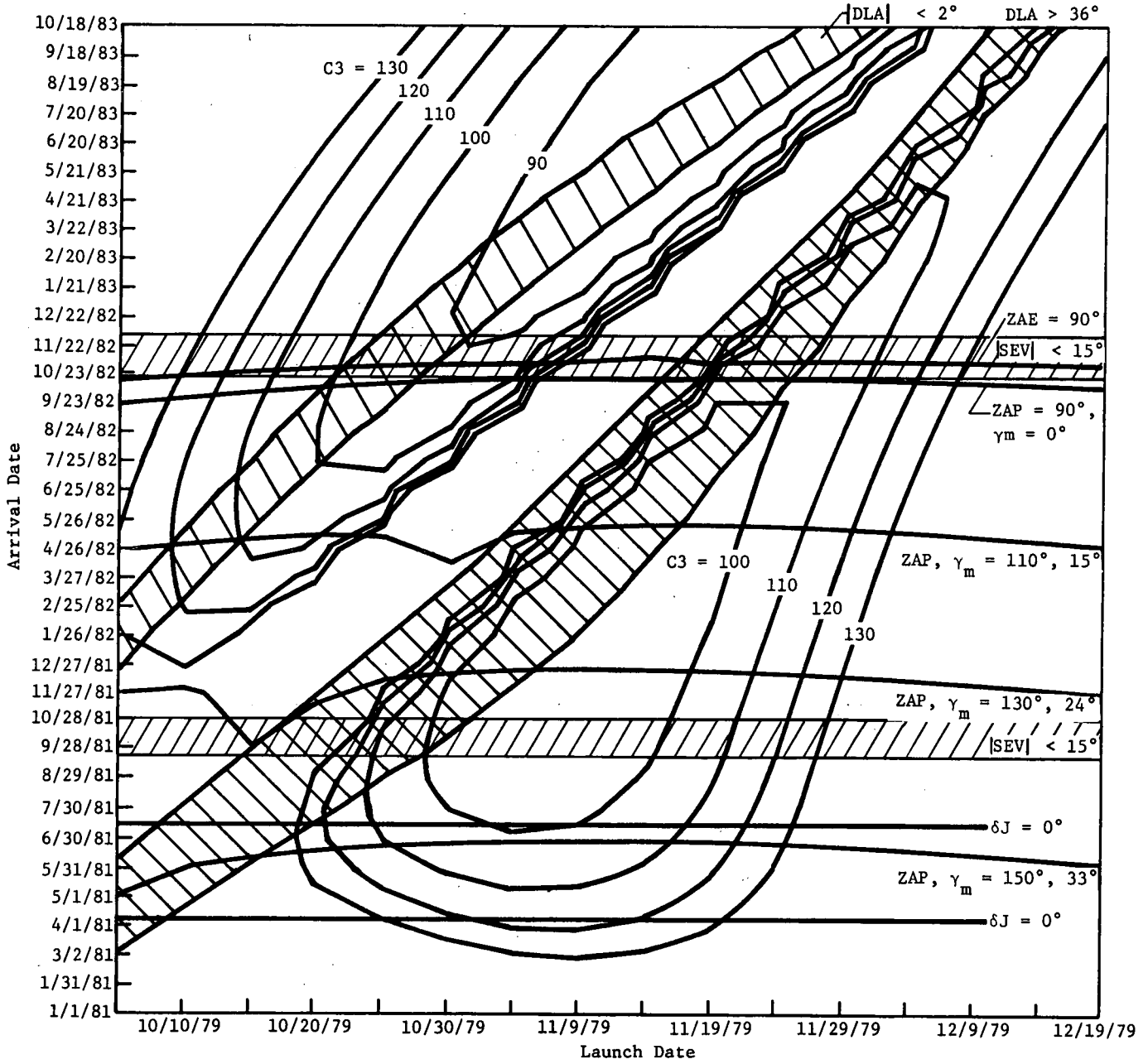

Jupiter Turbopause Probe Study
1979 Launch, Type I and II
(TF at X, Y = (0,0) is 454 Days)

Fig. IV-9 Launch Energy Requirements, 1979

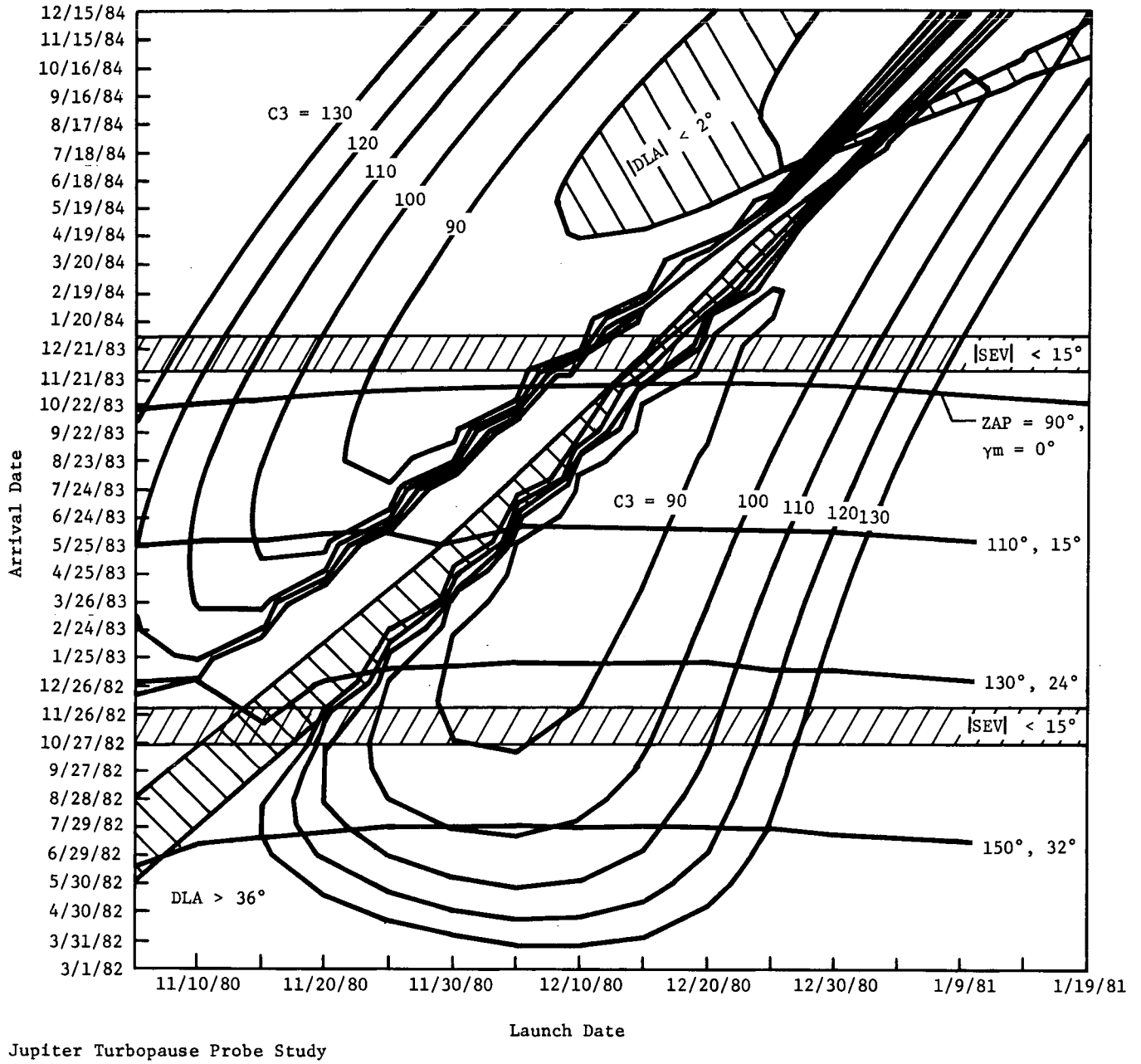

Jupiter Turbopause Probe Study
1980 Launch, Type I and II
(TF at X, Y = (0,0) is 481 Days)

Fig. IV-10 Launch Energy Requirements, 1980

2. Launch Constraints

LD/AD selection must consider other requirements in addition to launch energy. A primary restriction involves the range safety constraint. Given a launch site, the launch azimuth essentially determines the ground trace of the trajectory. The standard launch profile includes azimuths from $\Sigma_L = 90°$ to $\Sigma_L = 115°$. Because Cape Kennedy is at 28.5° latitude, the maximum declination of the launch asympote, V_{HE}, would be DLA = 28.5° for $\Sigma_L = 90°$, and DLA = 36° for $\Sigma_L = 115°$. The range safety constraint can therefore be translated into the requirement that the DLA must be less than 36° in absolute value. The contours of DLA = 36° are indicated in Fig. IV-8 through IV-10. The constraint is most restrictive for 1978 Type I launches, eliminating nearly half the available period. By 1980, it is of little consequence.

A second launch constraint is frequently imposed on the DLA to avoid possible problems in navigation for the first midcourse maneuver. The uncertainty in the declination of the spacecraft is given by

$$\Delta\delta = \frac{\Delta r_s / r_s}{\tan \delta} \qquad \text{[IV-4]}$$

where δ is the geocentric declination of the spacecraft, and Δr_s and r_s are the uncertainty and mean value of the spin axis radius of the station taking the measurement (Ref IV-4). Thus, the navigation process is degraded when the spacecraft trajectory is near zero declination. The spacecraft will be on the launch asymptote two to three days after launch and will therefore have the declination of the asymptote at that time. If the declination is near zero, the critical tracking for the first midcourse would then be impaired. Therefore, the navigation constraint

$$|\text{DLA}| > 2° \qquad \text{[IV-5]}$$

is noted on Fig. IV-8 through IV-10 but is considered somewhat soft. Two relatively minor constraints are applied to parking orbit coast time and daily launch windows. Generally, parking orbit time, Δt_p, (at 185-km orbit) must be less than 1 hr and hopefully under 0.5 hr.

$$\Delta t_p \leq 1 \text{ hr} \qquad \text{[IV-6]}$$

The daily launch window defined by launches over the range of azimuths $\Sigma_L = 90 - 115°$ must be at least 1 hr.

$$\Delta t_w \geq 1 \text{ hr} \qquad \text{[IV-7]}$$

These constraints are checked to ensure that they are not violated.

3. Arrival Constraints

Arrival constraints are placed on missions to avoid possibly poor geometries at that critical time. Because the launch period for Jupiter missions is generally a month or two and the trip time to Jupiter is greater than 1½ years, the arrival constraints can usually be written as a function of arrival date only, with the launch date assumed to be in the middle of the allowable launch period.

The most critical arrival constraint is an observability limitation. At the time of arrival at Jupiter, the spacecraft must be visible from Earth. If the Sun is between Earth and Jupiter at this time, the critical tracking and communication tasks could not be performed. Therefore, the SEV angle (angle from the Sun to Earth to Vehicle or Jupiter) at arrival must be bounded away from zero. The recommended constraint is

$$|\text{SEV}| > 15°. \qquad \text{[IV-8]}$$

A second constraint is imposed to avoid poor navigation at approach to the planet. Because of relation [IV-4], the navigation process is degraded if the spacecraft is arriving at Jupiter when the geocentric declination of Jupiter is near zero. Therefore, the constraint is applied

$$\delta_J \neq 0° \qquad \text{[IV-9]}$$

However, a new navigation technique known as Quasi-Very Long Baseline Interferometry has recently been discovered that permits effective tracking of the spacecraft even when this constraint is violated (Ref IV-5). Thus, the constraint can be deemphasized if this technique can be used. Arrival dates resulting in poor navigation, $\delta_J = 0$, are also noted in Fig. IV-8 through IV-10.

A key parameter defining the arrival geometry is the hyperbolic excess velocity at the planet, V_{HP}, defined by

$$\vec{V}_{HP} = \vec{V}_A - \vec{V}_{PA} \qquad \text{[IV-10]}$$

where $\vec{V}_A$ is the velocity on the interplanetary transfer conic at arrival, and $\vec{V}_{PA}$ is the orbital velocity of the planet at arrival.

For Jupiter missions, the magnitude of this vector varies between approximately 5 and 13 km/sec, as indicated in Fig. IV-11a. The major impact of V_{HP} magnitude is on coast time from deflection to periapsis. V_{HP} affects entry velocity only very slightly. The results of both these variations are indicated in Fig. IV-4.

Of more importance is the direction of the $\vec{V}_{HP}$ vector relative to the Sun and Earth. Let $\vec{V}_{JS}$ and $\vec{V}_{JE}$ represent the vectors from Jupiter to the Sun and Earth respectively at the arrival time.

The ZAE angle is defined as the angle between the $\vec{V}_{HP}$ and $\vec{V}_{JE}$ vectors, as indicated in Fig. IV-11b. The ZAE value fixes the geometry of the approach relative to Earth. Therefore, for example, it contributes to the efficacy of approach orbit determination. Values of ZAE near 90° generally lead to a degradation of the tracking process as the accelerative effects of the target planet are in the plane normal to the earth-spacecraft line and the effects on the tracking are reduced. However, with a planet as large as Jupiter, accelerative effects are large enough to reduce the effect of this condition. Values of ZAE as functions of the arrival date are given in Fig. IV-11b. For reference purposes, the C_3 contours indicate the dates where the following constraint is violated.

$$|\text{ZAE} - 90°| > 5° \qquad \text{[IV-11]}$$

The ZAP angle is defined as the angle between the $\vec{V}_{HP}$ and the $\vec{V}_{JS}$ vectors, as indicated in Fig. IV-11c. This parameter determines the lighting conditions of the approach trajectory. Figure IV-12 demonstrates the relation between ZAP, entry angle, γ_E, and the entry site location relative to the Sun.

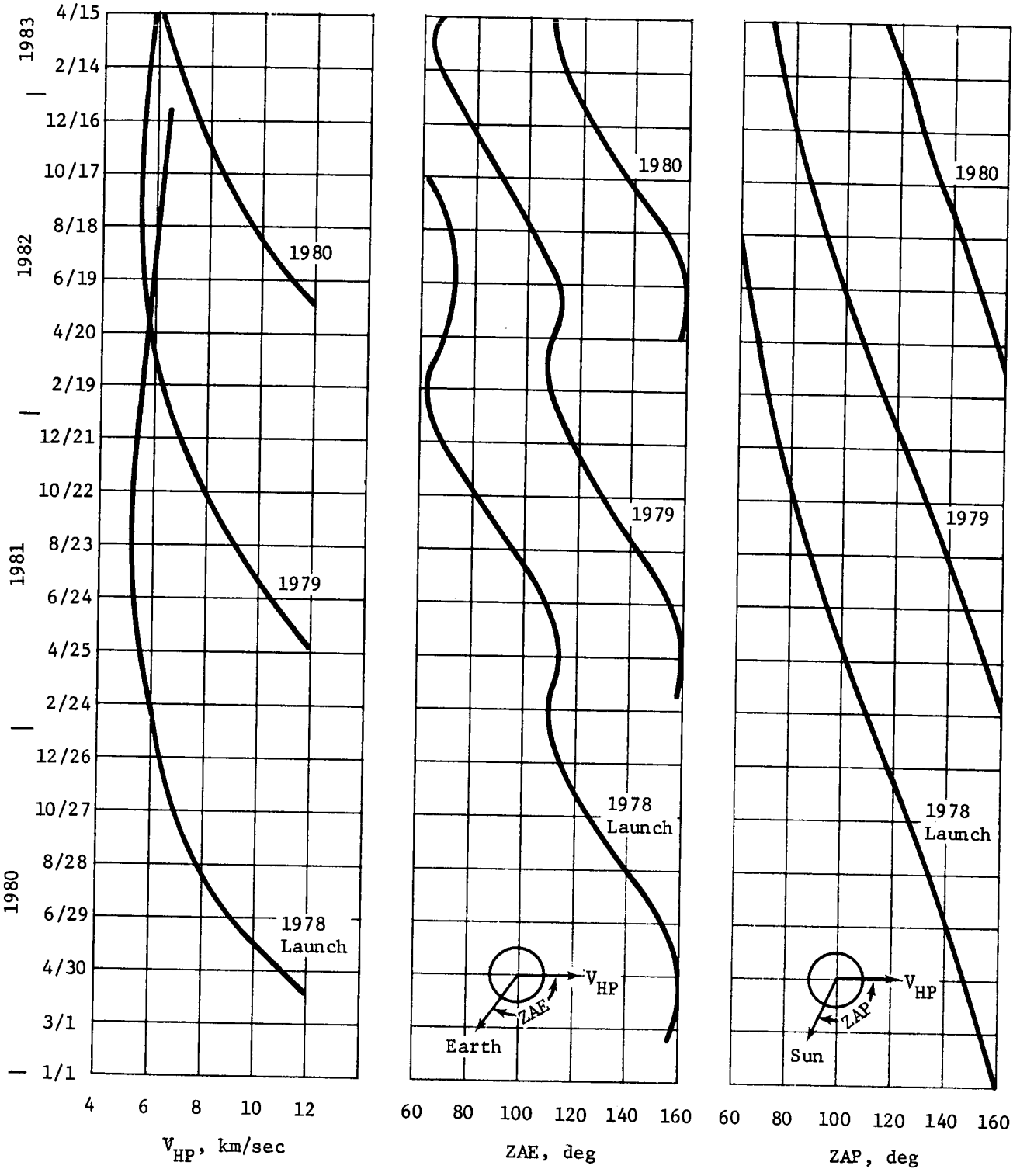

Fig. IV-11 V_{HP} Variations with Arrival Date

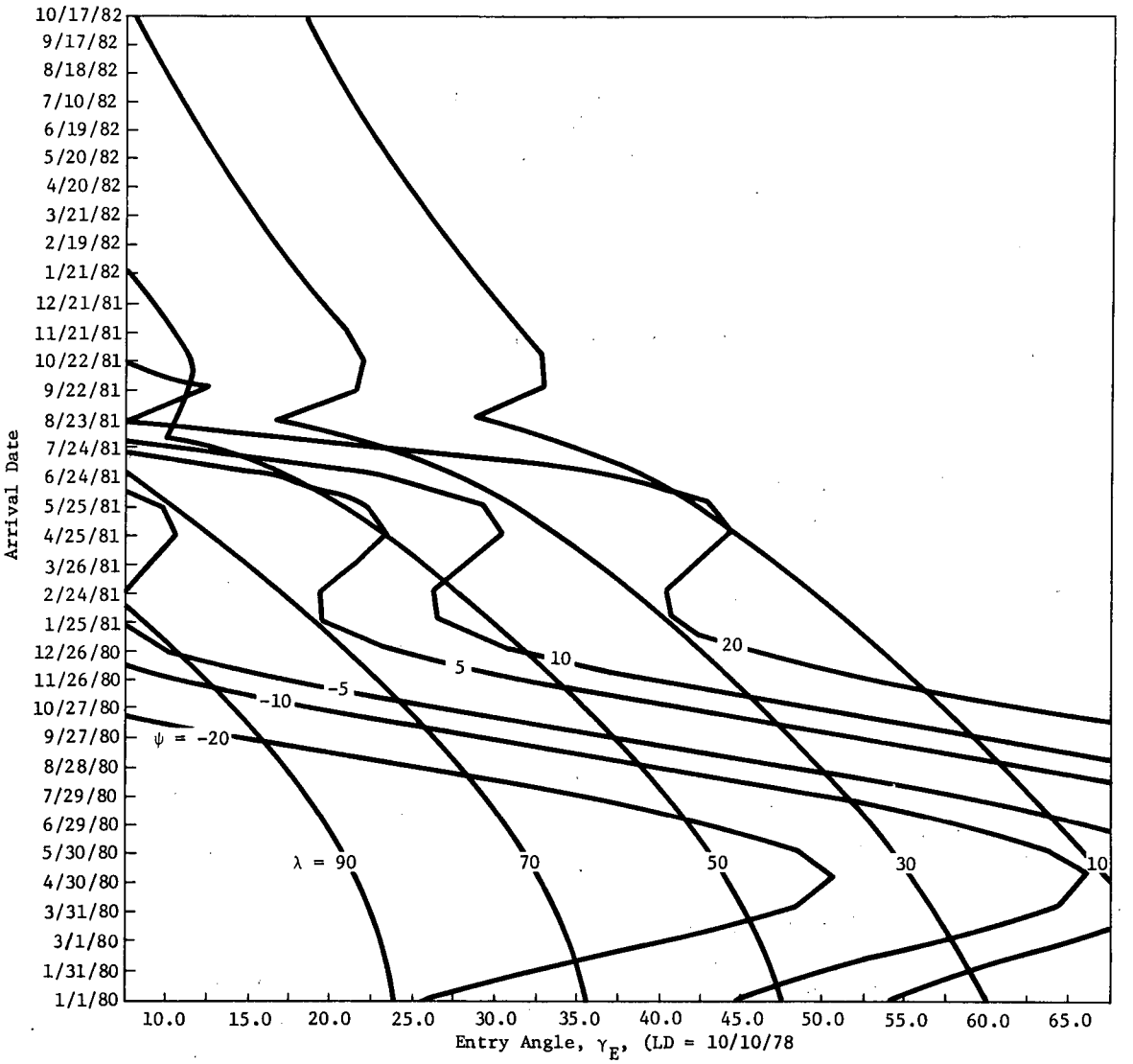

a. Jupiter Turbopause Probe Study
1978 Launch, Type I and II
(TF at X, Y = (0.0) is 483 days)

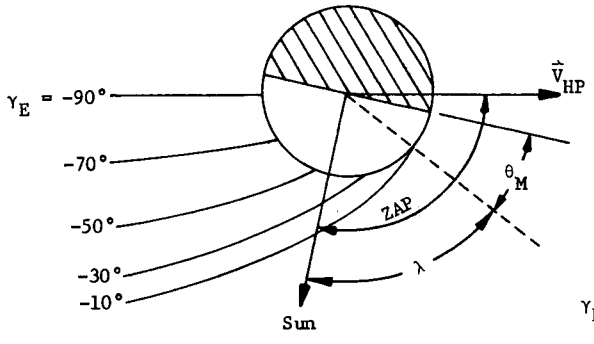

b. Mask Angle and Subsolar Longitude

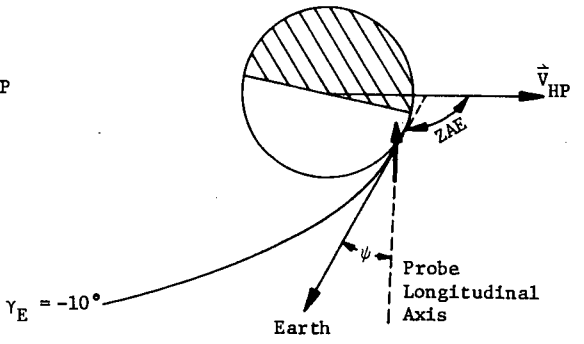

c. Probe to Earth Look Angle

Fig. IV-12 Probe Entry Considerations

Figure IV-12 contains the key data for selecting optimal arrival dates for probe missions. The science requirements state that the probe should enter at least 20° from the evening terminator. This is called the mask angle constraint

$$\theta_M \geq 20° \qquad \text{[IV-12]}$$

This is equivalent to requiring that the subsolar longitude of the probe satisfy

$$\lambda \leq 70° \qquad \text{[IV-13]}$$

A second science requirement is to obtain as low an entry angle, γ_E, as possible, consistent with the above constraint. Figure IV-12a illustrates the results of these requirements for the 1978 Jupiter opportunity. Allowable entry angles are those to the right of the $\lambda = 70°$ contour. Thus, for an arrival on 8/28/1980, the minimum entry angle consistent with the mask constraint is $\gamma_M = 30°$.

An attractive scheme for designing probe missions is to have the probe axis collinear with the spacecraft axis and direction to Earth. The effect of this requirement on arrival-date selection is illustrated in Fig. IV-12c. At entry, the probe is aligned for zero relative angle of attack, that is, the probe longitudinal axis is in the direction of the probe velocity relative to Jupiter. The angle between this direction and the direction to Earth is called the probe-to-Earth look angle, ψ_E. Values of $\psi_E = 0$ then define opportunities for the linear arrangement described above or for direct link communication from probe to Earth. Contours of constant ψ_E are superimposed on Fig. IV-12a. Note that an arrival near 11/26/1980 allows a low entry angle, $\gamma_E = 22.5$, while satisfying $\theta_M \geq 20°$ and $\psi_E = 0°$.

Figure IV-12a can also be used to approximate conditions for the 1979 and 1980 Jupiter opportunities by adding 13 or 26 months to the dates on the ordinate. The exact contours for these launch years are included in Appendix K (Vol III).

A general summary of the Type I missions for launch years 1978, 1979, and 1980 is provided in Fig. IV-13. The cyclical nature of the contours with a period of approximately 13 months should be noted. Contours for launch energies of C_3 = 100 and 130 km^2/sec^2 are shown. The restricted areas that violate the range safety constraint, $|DLA| < 36°$, are marked. The 1978 opportunity is most affected by this constraint. For reference, the location of the DLA = 36° contour for the 1977 opportunity is approximately the same as it is in 1979. Thus, 1978 appears to be the worst year in the late 1970s for Jupiter missions. The minimum entry angles, γ_M, consistent with the 20° mask angle constraint are also noted. Finally, several of the design missions are indicated in the figure. Because of the periodicity of the characteristics of the trajectories, alternative dates for missions 1 and 2 are indicated in 1979 and 1980.

4. Jupiter Swingby Missions to Outer Planets

Because of the extreme mass of Jupiter, trajectories passing close to the planet will experience a significant energy transfer. For a posigrade trajectory with a low inclination at Jupiter, this energy transfer results in an increase in the energy of the spacecraft trajectory so that the post-Jupiter heliocentric trajectory is hyperbolic. For certain arrival dates and periapsis radius, this post-Jupiter trajectory will intersect one or several of the other outer planets. Favorable alignments for Jupiter-Saturn, Jupiter-Uranus, Jupiter-Neptune, and Jupiter-Pluto missions occur every 20, 14, 13, and 12½ years, respectively. Opportunities for multiple-planet swingbys using gravity assists at other planets occur with less frequency. Using this assist, missions to outer planets can be flown that normally would be impossible because of excessive launch-energy or flight-time requirements. There is a possibility of including a turbopause probe on the spacecraft on such flyby missions and deflect it into Jupiter as it passes that planet.

Given the launch and arrival dates at Earth and Jupiter, respectively, the data presented in the previous three sections can, of course, be applied. However, to arrive at the next planet as desired, the flyby radius at Jupiter must be properly selected. Thus, for probe missions from Jupiter swingby trajectories, an added constraint must be applied: the periapsis radius is no longer free to vary but is a unique function of the launch and arrival dates.

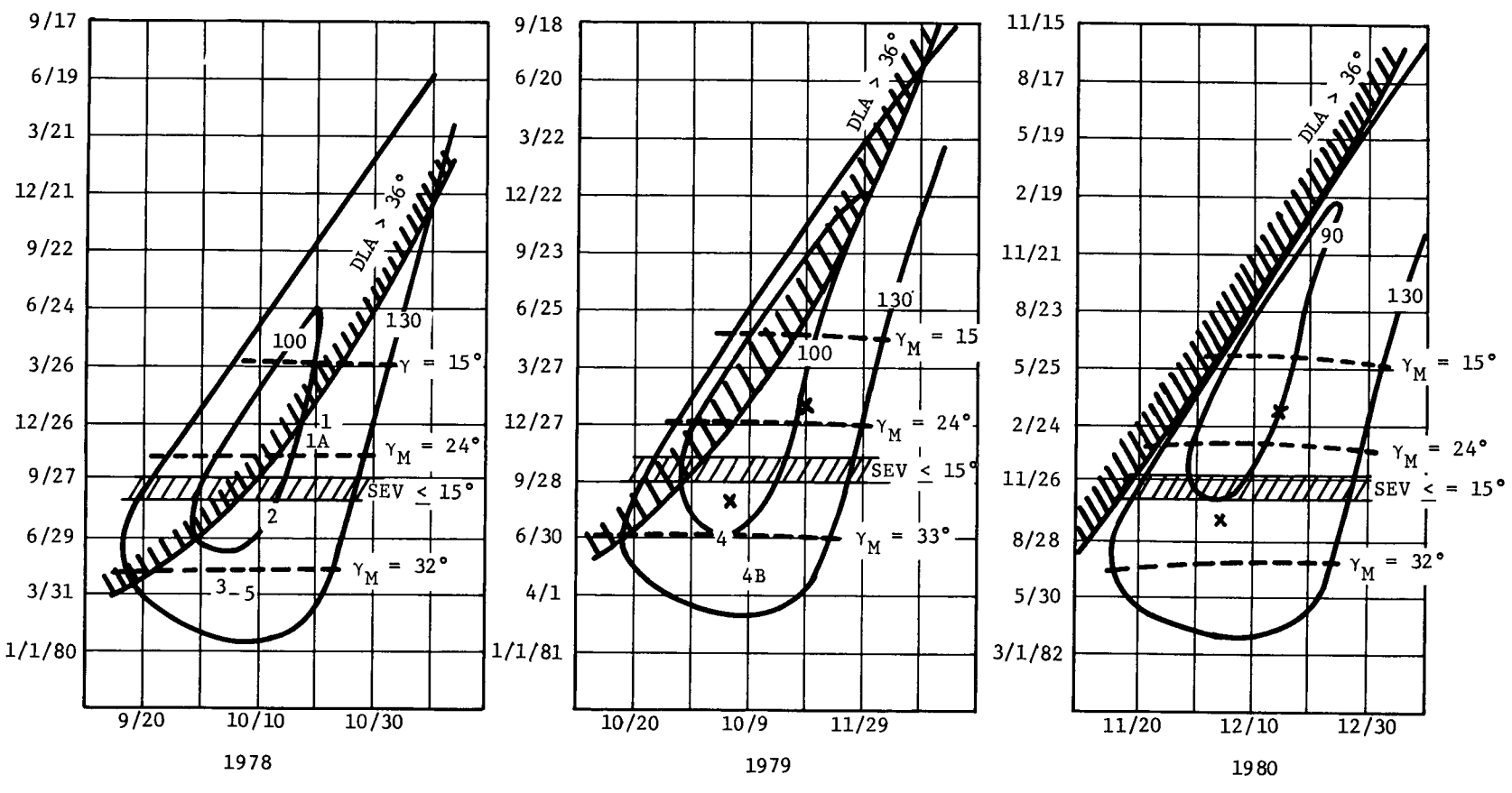

Fig. IV-13 Comparison of Launch Opportunities, 1978 thru 1980

Figures IV-14 and IV-15 illustrate the required Jupiter periapsis radius as a function of launch and arrival dates for the JUN 78, 79, and JU 80 and the JS 77 and 78 opportunities. Periapsis radii are given in terms of Jupiter radii, R_J. It can be seen that the JU 80 and JS 78 missions have extremely large periapsis radii $\left(R_P > 15\ R_J\right)$ for realistic launch energies. The other missions have much more reasonable periapsis radii $\left(R_P < 6\ R_J\right)$ and offer opportunities for turbopause probe missions.

The actual trajectories for selected missions for these opportunities are illustrated in Chapter V.

5. Solar Apex Missions

The solar system is moving toward a point in galactic space called the solar apex. For field and particle measurements of the interstellar medium and its interaction with the solar system bow shock, it would be useful to send a spacecraft toward that point (Ref IV-6). The interstellar medium may be encountered at a heliocentric distance of 30 to 50 AU. Because of the length of time needed to reach such a distance and the distance (50°) out of the ecliptic plane that is required, a Jupiter swingby is advisable.

Opportunities for Solar Apex missions were analyzed in Ref IV-7. The results of that study will be summarized here. Three requirements for solar apex missions were identified.

1) Jupiter must be in a favorable location in its 12-year heliocentric orbit to deflect the spacecraft toward the solar apex. The 1978 opportunity offers the best conditions for this.

2) Escape from the solar system must be accomplished quickly because of spacecraft component life restrictions. This implies short Earth-to-Jupiter transfer times and relatively close approaches to Jupiter $\left(R_P < 2\ R_J\right)$.

3) Because the solar apex is 50° out of the ecliptic, high spacecraft post-Jupiter heliocentric inclinations are required, again implying short Earth-to-Jupiter transfer times.

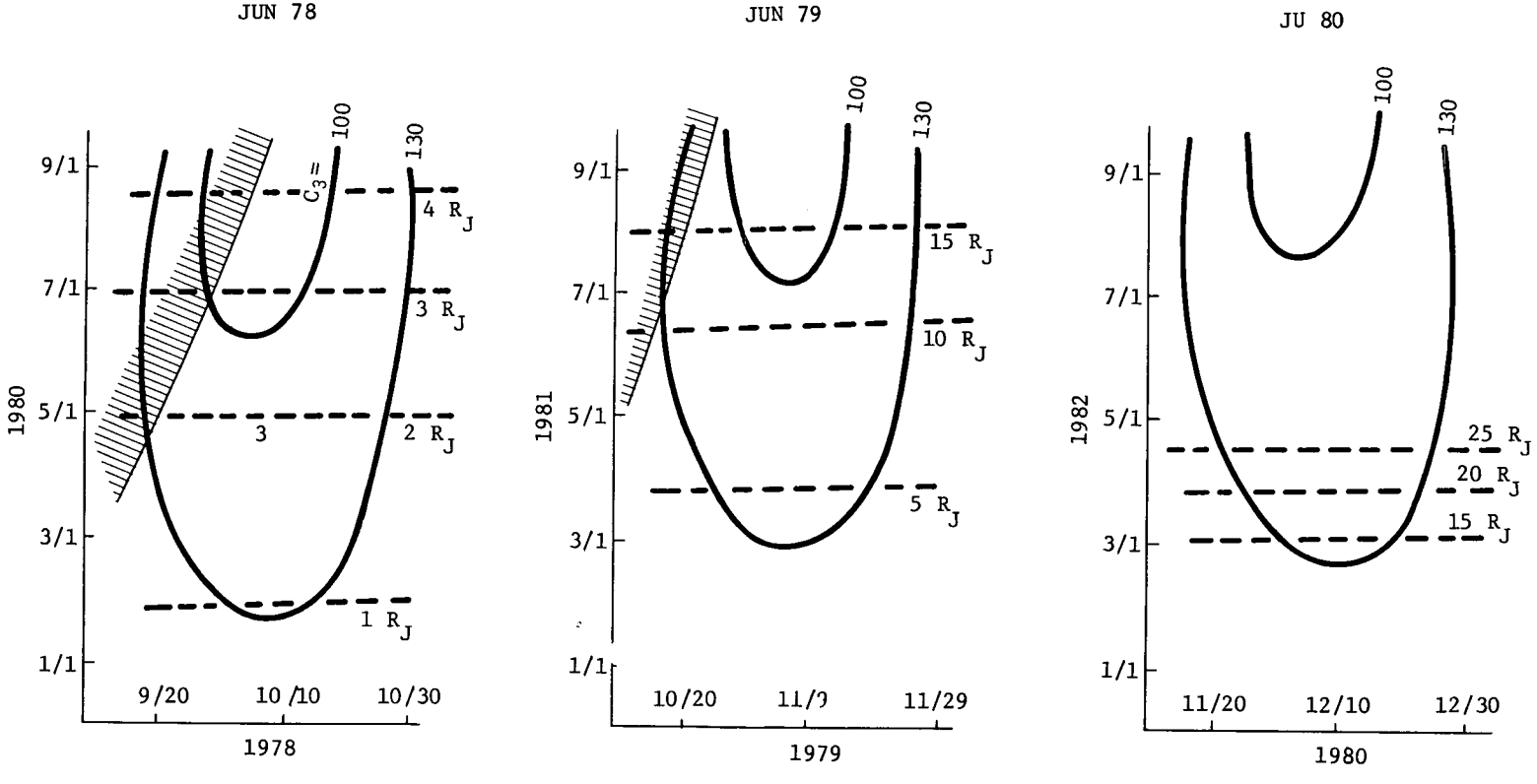

Fig. IV-14 Comparison of JUN Opportunities 1978, 1979, and JU 1980

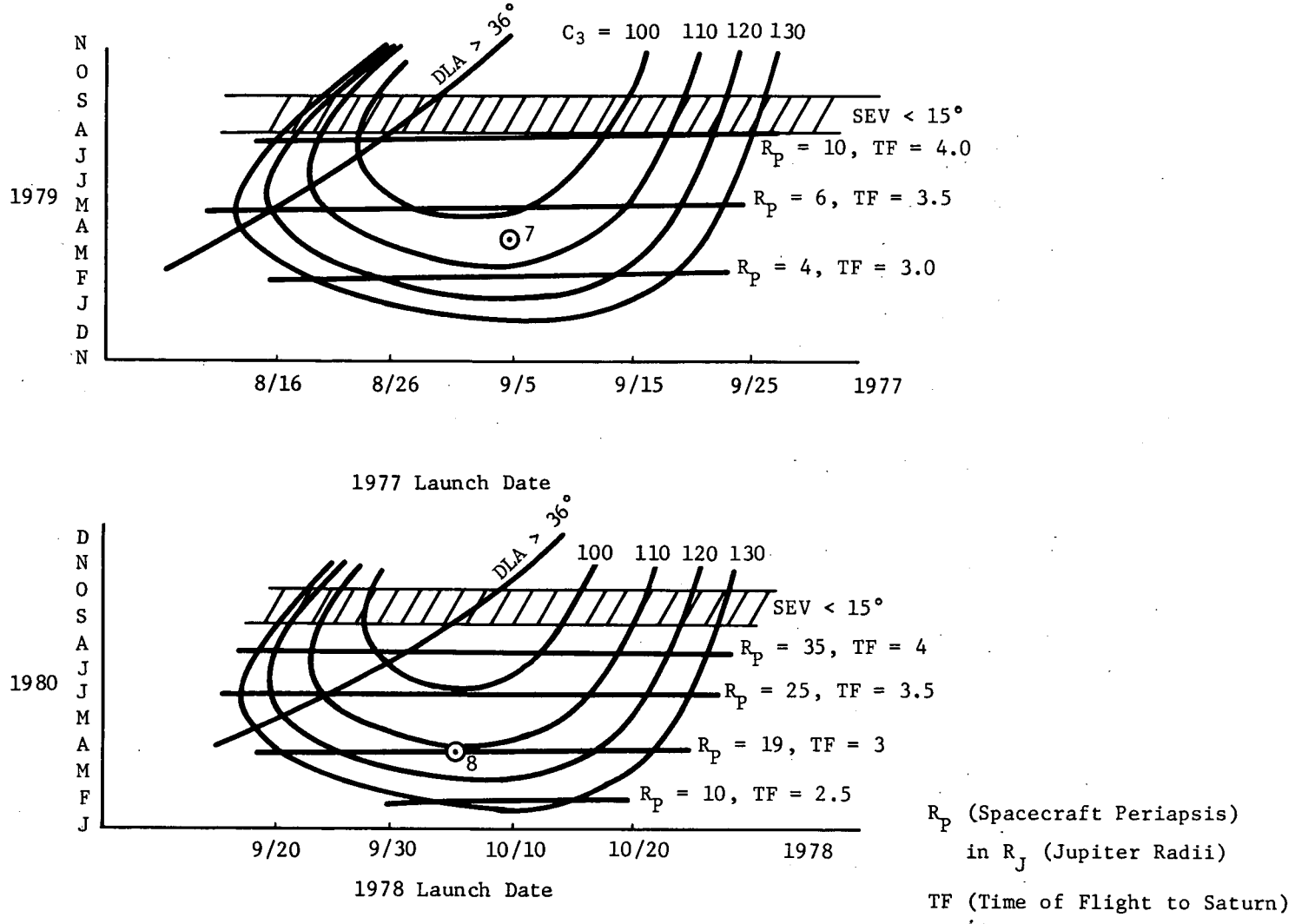

Fig. IV-15 Comparison of JS Opportunities, 1977 and 1978

For the 1978 opportunity, Fig. IV-16 illustrates the effects of transfer time and spacecraft aim point at Jupiter[1] on the hyperbolic escape velocity from the solar system. In general, the hyperbolic escape velocity decreases as θ, B, and transfer time increase. However, the launch energy associated with a transfer time of 460 days is excessive ($C_3 \geq 140$ km^2/sec^2 for 15-day launch period). Therefore, attention is focused on the 540-day transfer-time trajectory. Figure IV-17 shows the escape asymptote variation with aim point for this mission. For small θ and B, the distance from the solar apex decreases as θ and B increase. Thus, large hyperbolic escape velocity and small distance between escape asymptote and solar apex present conflicting requirements on aim-point location. The selected aim point of $\theta = 30°$ and B = 500,000 km results in an escape asymptote 45° from the solar apex and an escape velocity of 15 km/sec. The distance of 50 AU from the Sun is reached in 13.7 years for the trajectory selected.

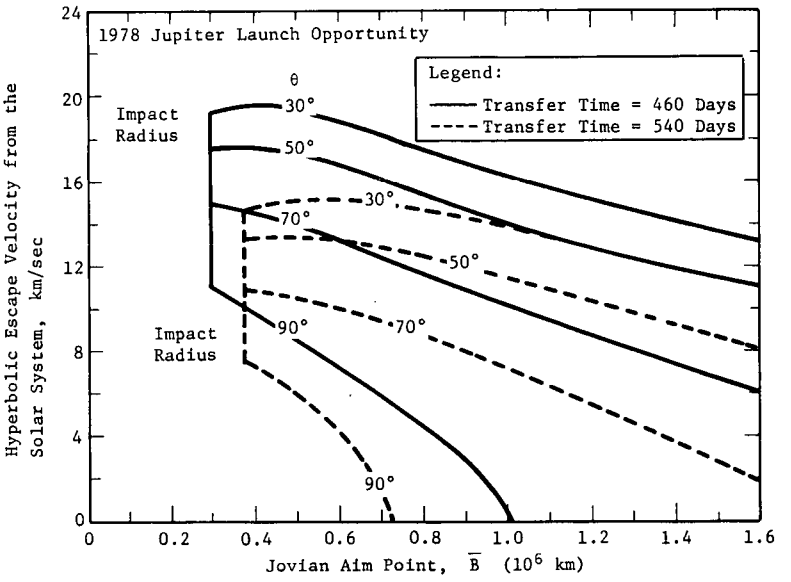

Fig. IV-16 Variation in Solar System Hyperbolic Escape Velocity

---

[1]The spacecraft aim point is defined in terms of the standard impact plane parameters. Let $\hat{S}$ be in the direction of the approach asymptote. Let $\hat{K}$ be the normal to the ecliptic plane. Then $\hat{T}$ = unit ($\hat{S} \times \hat{K}$) and $\hat{R} = \hat{S} \times \hat{T}$. The impact parameter, $\vec{B}$, is the vector in the R-T plane for the center of the planet to the asymptote pierce point. θ is measured from the T axis to $\vec{B}$, clockwise. (See Fig. IV-18.)

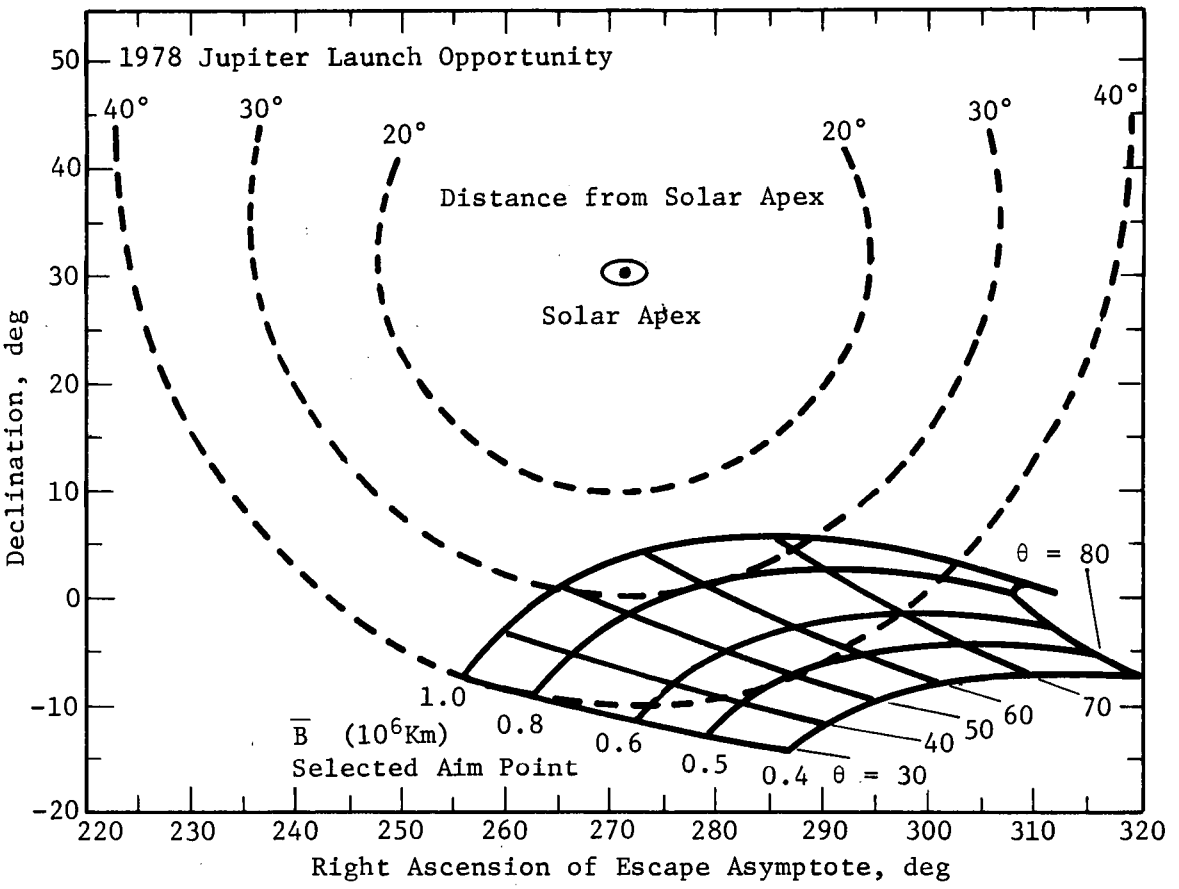

Fig. IV-17 Variation in Location of Escape Asymptote for a Solar Apex Mission, TF = 540 Days

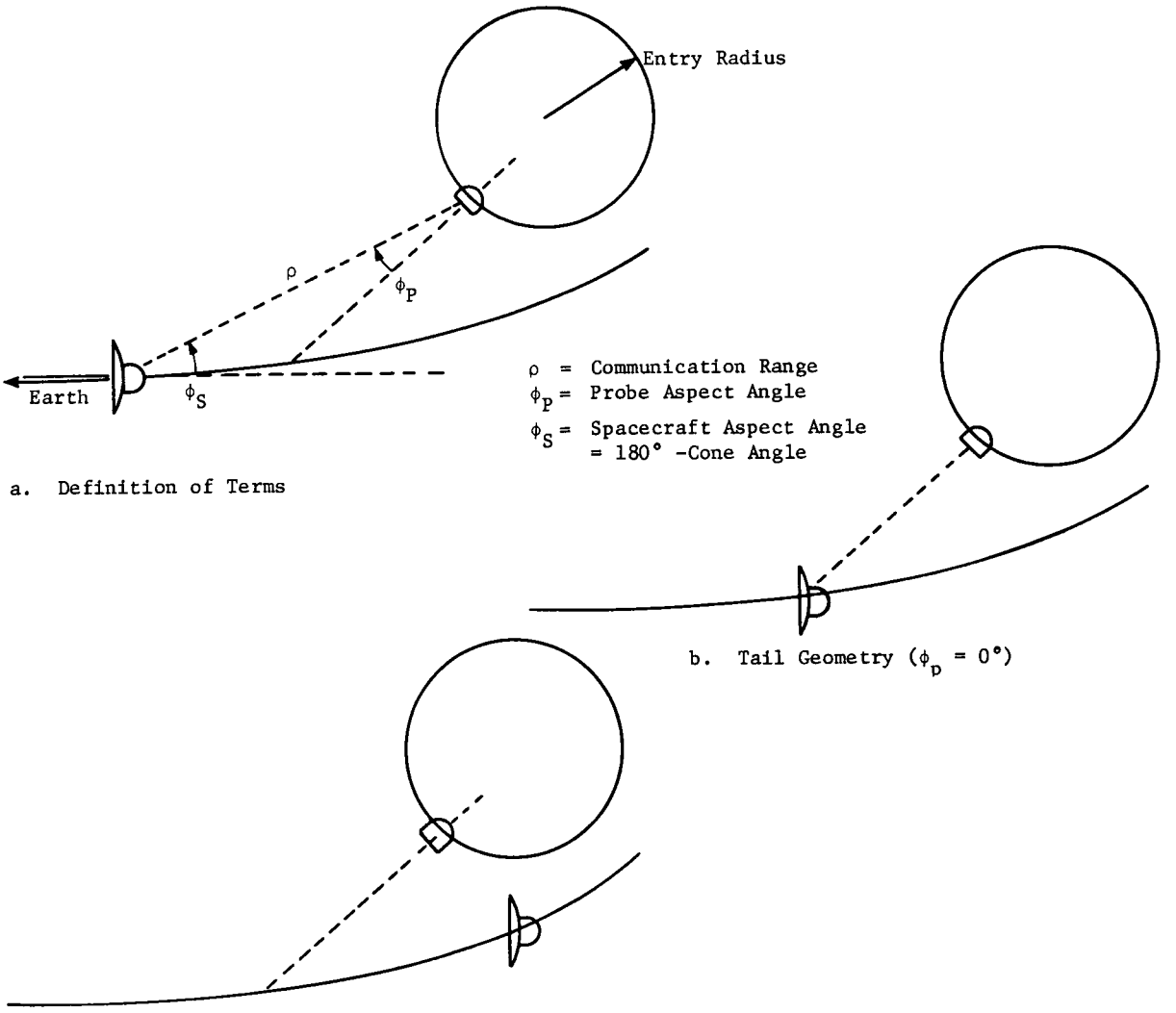

a. Definition of Terms

b. Tail Geometry (ϕ_p = 0°)

c. Side Geometry (ρ = Minimum)

Fig. IV-18 Communication Parameters and Geometry

D. DETERMINISTIC PROBE MISSION ANALYSIS

1. Deflection Maneuver Description

a. Definition - The critical maneuver in a probe mission is the deflection maneuver in which the probe is separated from the spacecraft or bus and sent on a trajectory impacting the target planet. The deflection maneuver is the sequence of events required of the probe and spacecraft to accomplish three purposes:

1) Place the probe on a trajectory intersecting the desired entry site;

2) Orient the probe for its required attitude at entry;

3) Establish the relative geometry between the probe and spacecraft for an effective communication link.

The desired entry conditions, including both the entry site selection and the probe attitude at entry (zero angle of attack), were discussed in Section A.

b. Communication Geometry - Two types of spacecraft-probe relative geometry have been analyzed in this study. In the tail geometry, timing between the probe and spacecraft is such that, at entry, the spacecraft is in line with the probe longitudinal axis (assuming the probe is aligned for zero angle of attack). In side geometry, timing is such that the spacecraft is at the point on its trajectory nearest the probe at probe entry. Figure IV-18 shows tail and side geometries with definitions of important communication parameters.

c. Deflection Modes - Three modes for implementing the deflection maneuver have been identified for analysis. Each can be used to acquire a given entry site and a desired communication geometry. The resulting trajectories for both the probe and spacecraft are almost identical for the three modes. The only difference is in the deflection ΔV, rotations required, and the procedure used to effect the maneuver.

The first mode is the probe deflection mode. Here, the spacecraft is targeted to fly by the planet at the desired periapsis and inclination. At the deflection point, the ΔV magnitude and direction are determined so as to deflect the probe to the entry

site and establish the desired communication geometry between the probe and spacecraft. The probe must be aligned independently for the required attitude for zero angle of attack. The ΔV and rotation generated can be executed in two distinct sequences depending on the type of thrusters used by the probe.

1) Axial Thrusters - The spacecraft is first rotated off Earth lock to orient, spin up, and release the probe so its axis is in the direction of deflection ΔV. Deflection velocity is fired by the probe. The probe is then precessed [using an attitude control system (ACS)] to obtain the attitude required for entry. The spacecraft reacquires Earth lock after probe release.

2) Nonaxial Thrusters - The spacecraft rotates off Earth lock, spins up, and releases the probe for zero angle of attack. A single thruster aligned in the required ΔV direction (or a combination of thrusters whose net effect is in the same direction) then fires the deflection ΔV to accomplish the maneuver. This thrust must not destroy the attitude of the probe. The difficulty in implementing this scheme makes it inferior to the first scheme.

The first mode therefore requires that the probe either have a ΔV capability, precession, and ACS or a very complicated ΔV capability.

The second mode is the shared deflection. The spacecraft is again targeted to flyby conditions. In this mode, the probe ΔV is constrained to the direction required for zero angle of attack. The magnitude is chosen so that the probe trajectory intersects the desired entry site. The spacecraft must then be accelerated to establish the required communications geometry. This correction is applied in the direction of spacecraft velocity to minimize perturbations to the spacecraft trajectory. The implemention sequence for this mode is as follows:

1) The spacecraft rotates off Earth lock, spins up, and releases the probe for the zero angle of attack.

2) The probe then fires its axial thruster for its deflection ΔV.

3) The spacecraft is then rotated to align it in the direction of its velocity.

4) After applying the correction velocity, the spacecraft is reoriented toward Earth.

Thus, the probe is only required to generate the axial thrust; the spacecraft handles the other maneuvers. Because of this possibility of using the shared deflection mode on a mission involving post-Jupiter encounter objectives, perturbations on the spacecraft trajectory caused by the spacecraft correction maneuver are included in Table IV-2.

The third mode of deflection, spacecraft deflection, has the simplest probe requirements of the candidate modes. The spacecraft trajectory is initially targeted to impact the entry site. The probe is spun up and released for zero angle of attack. The spacecraft is then deflected away from the planet to establish communication geometry and required flyby radius. Thus, the spacecraft performs all the maneuvers, and the probe is kept as simple as possible.

The deflection sequence for the three modes, when applied to the reference mission, is compared in Fig. IV-19.

2. Deflection Parametrics

The ΔV magnitude and attitude requirements for deflection maneuvers are functions of a wide range of parameters. In this section, the effect on the deflection maneuver of varying deflection mode, communication geometry, deflection radius, periapsis radius, approach velocity, and entry angle will be discussed.

a. Deflection Mode - The deflection requirements of the three deflection modes for the reference mission are compared in Fig. IV-19. Essentially, the ΔV requirements are identical for Modes 1 and 3, the probe and spacecraft deflections. For a Mode 2 deflection, the ΔV required for the probe is significantly higher because of the requirement to deflect in the direction of zero angle of attack. This direction is 42° ahead of the normal to the trajectory. Using Mode 1 or 3, the probe or spacecraft ΔV direction is only 9° ahead of the normal for the tail geometry. (The angle would be -22° for the side geometry.) The ΔV magnitude would be minimized with a deflection normal to the trajectory. Therefore, the significant increase in probe ΔV requirements for a Mode 2 deflection is readily explained. As expected, the spacecraft correction ΔV of 78 m/sec for the shared deflection is lower than the spacecraft deflection of Mode 3. But again, because probe deflection velocity was directed so far forward, a significant correction is required to allow the spacecraft to catch up with the probe at entry.

Table IV-2 Perturbation of Spacecraft Trajectory in Shared Deflection

R_P	R_{EJ}, 10^6 km	Tail Geometry				Side Geometry			
		R_P, km	V_{HP} km/sec	θ_T^* deg	i, deg	R_P, km	V_{HP}, km/sec	θ_T^*	i, deg
1.1 Original Trajectory		79,200	11.86	133.61	1.34782	79,200	11.86	133.61	1.34782
S/C Corrected at	10	80,076	11.94	133.07	1.34782	80,751	12.01	132.64	1.34782
S/C Corrected at	30	79,533	11.89	133.42	1.34782	79,700	11.90	133.32	1.34782
S/C Corrected at	50	79,405	11.88	133.50	1.34782	79,405	11.88	133.50	1.34782
2.0 Original Trajectory		143,000	11.86	119.31	1.34782	143,000	11.86	119.31	1.34782
S/C Corrected at	10	146,742	12.07	117.64	1.34782	150,450	12.29	115.99	1.34782
S/C Corrected at	30	144,409	11.93	118.72	1.34782	145,416	11.98	118.30	1.34782
S/C Corrected at	50	143,857	11.90	118.96	1.34782	144,428	11.93	118.72	1.34782
4.0 Original Trajectory		285,760	11.86	98.78	1.34782	285,760	11.86	98.78	1.34782
S/C Corrected at	10	297,194	12.24	95.45	1.34782	313,942	12.81	90.63	1.34782
S/C Corrected at	30	290,396	12.00	97.53	1.34782	295,080	12.13	96.26	1.34782
S/C Corrected at	50	288,615	11.94	98.02	1.34782	291,321	12.02	97.30	1.34782
6.8 Original Trajectory		483,969	11.86	81.16	1.34782	483,969	11.86	81.16	1.34782
S/C Corrected at	10	505,567	12.37	76.75	1.34782	545,853	13.39	68.71	1.34782
S/C Corrected at	30	493,338	12.05	79.40	1.34782	505,910	12.31	77.06	1.34782
S/C Corrected at	50	489,935	11.98	80.06	1.34782	497,065	12.12	78.75	1.34782

*θ_T is the turn angle of the spacecraft hyperbola; that is, the angle measured from the incoming asymptote to the outgoing asymptote.

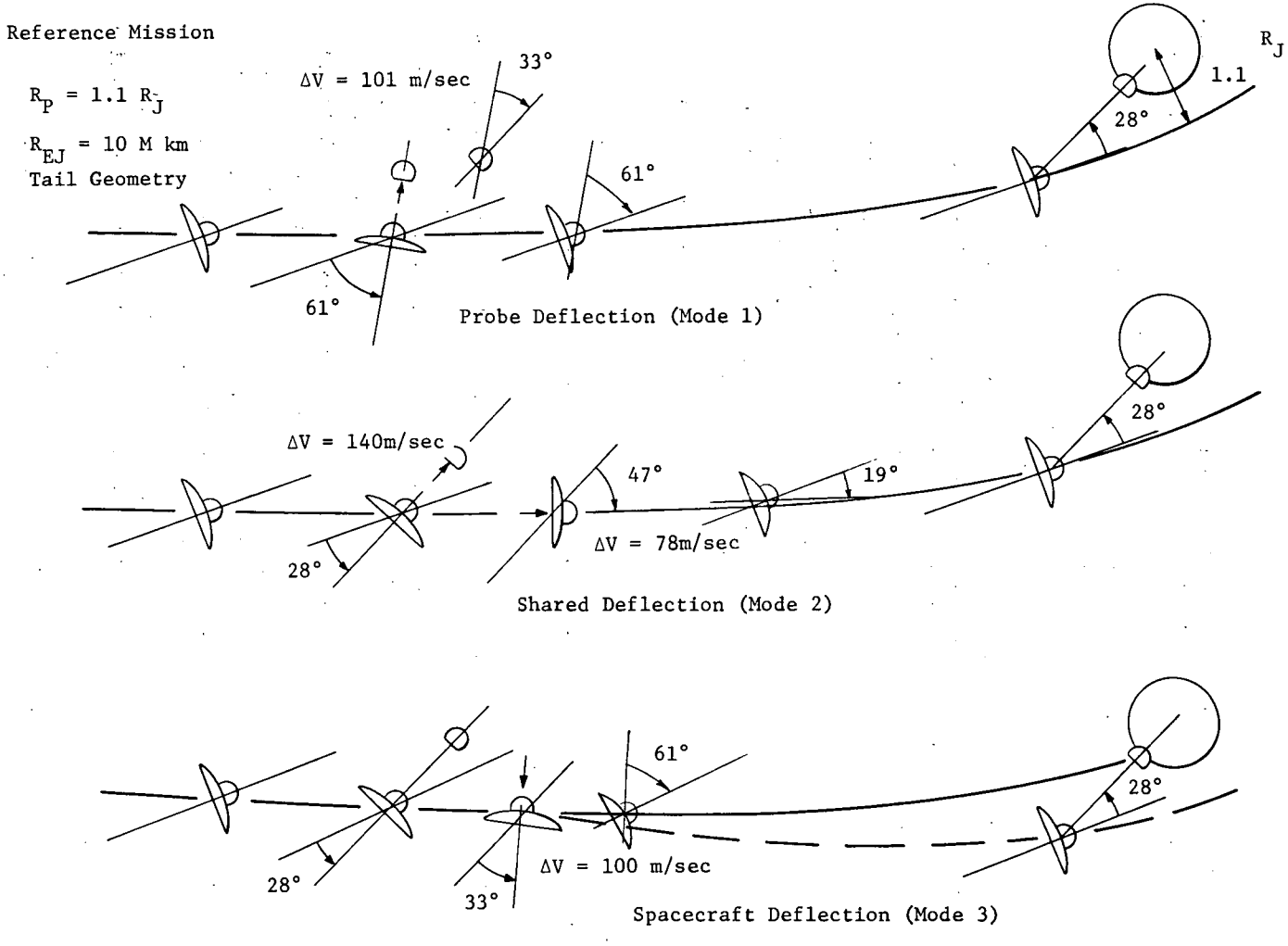

Fig. IV-19 Comparison of Deflection Modes for Reference Mission

In Fig. IV-20, the deflection requirements for three widely differing missions are compared. In general, the same comments made for the reference mission hold for the three missions depicted here. The probe and spacecraft ΔVs are identical for Modes 1 and 3. The probe ΔV for Mode 2 is greater than this value, while the spacecraft correction ΔV is slightly lower. The net ΔV penalty is greater for Mode 2 than for the other modes, and the propellant weight for Mode 2 is slightly higher than Mode 3, in general. The rotation requirements for the three modes and three missions are also indicated. The precession angle for Mode 1 deflection is between 30 and 35° for all missions. The angles that the spacecraft must move off Earth lock are critical parameters because the Pioneer pointing errors are proportional to these values; specifically, the pointing error (3σ) is 4% of the angle off Earth lock. The close relation between the three modes should be noted. The angle required for deflection direction for the probe in Mode 1 is identical to that of the spacecraft in Mode 3. The angle at which the probe is released is identical for Modes 2 and 3. Only the sequence of events is changed.

The actual ΔV requirements for Modes 1/3 and Mode 2 are provided in Fig. IV-21 and IV-22, respectively, in which values for a wide range of parametrics are given.

b. Communication Geometry - The effects of communication geometry on ΔV requirements are illustrated in Fig. IV-21 through IV-23. The ΔV requirements are always higher (for comparable cases) for side geometry than for tail geometry. This can be explained by the fact that side geometry requires a deflection of about 20° backward from the optimal direction (normal to spacecraft flight), while tail geometry requires a deflection of about 10° forward of optimal direction for Mode 1 and 3 deflections. After the probe has been deflected in a Mode 2 deflection, the spacecraft must be accelerated more to arrive at the minimum-range location than if it only had to be at the tail geometry location at probe entry. Thus, the penalty for side geometry is more pronounced for Mode 2 deflection. It also becomes more important as the periapsis radius is increased.

c. Deflection Radius - The distance from the planet at which the deflection maneuver is performed is the deflection radius. Deflection radii have been analyzed from 10 million km to 50 million km. Deflection ΔVs become excessively high for deflection radii lower than 10 million km, even for spacecraft flyby radii, R_p, of 1.1 Jovian radii, R_J. The upper limit of 50 million km was used because this is approximately the radius of the Jovian sphere of influence.

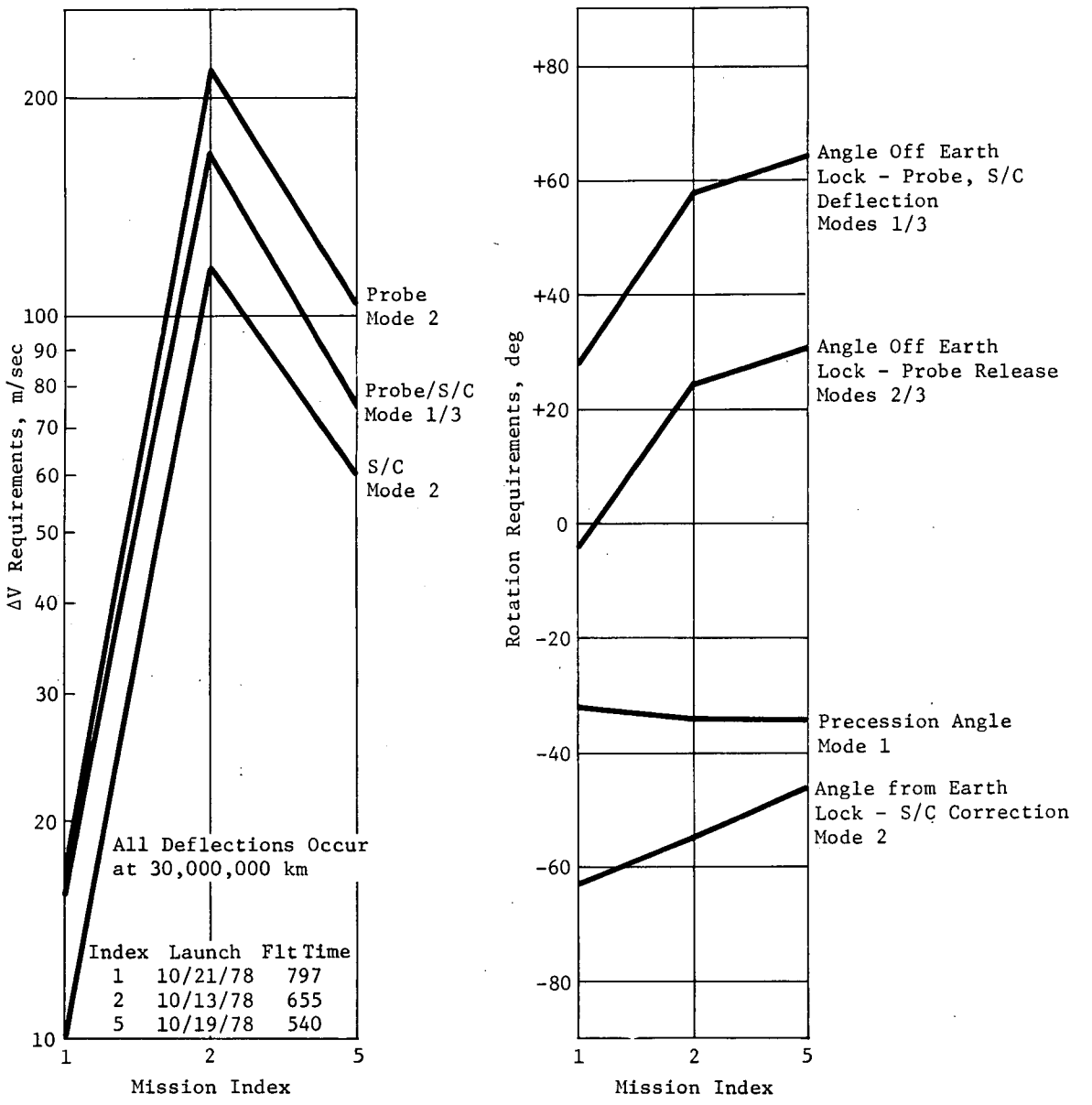

Fig. IV-20 Variation of Deflection Mode Requirements with Missions

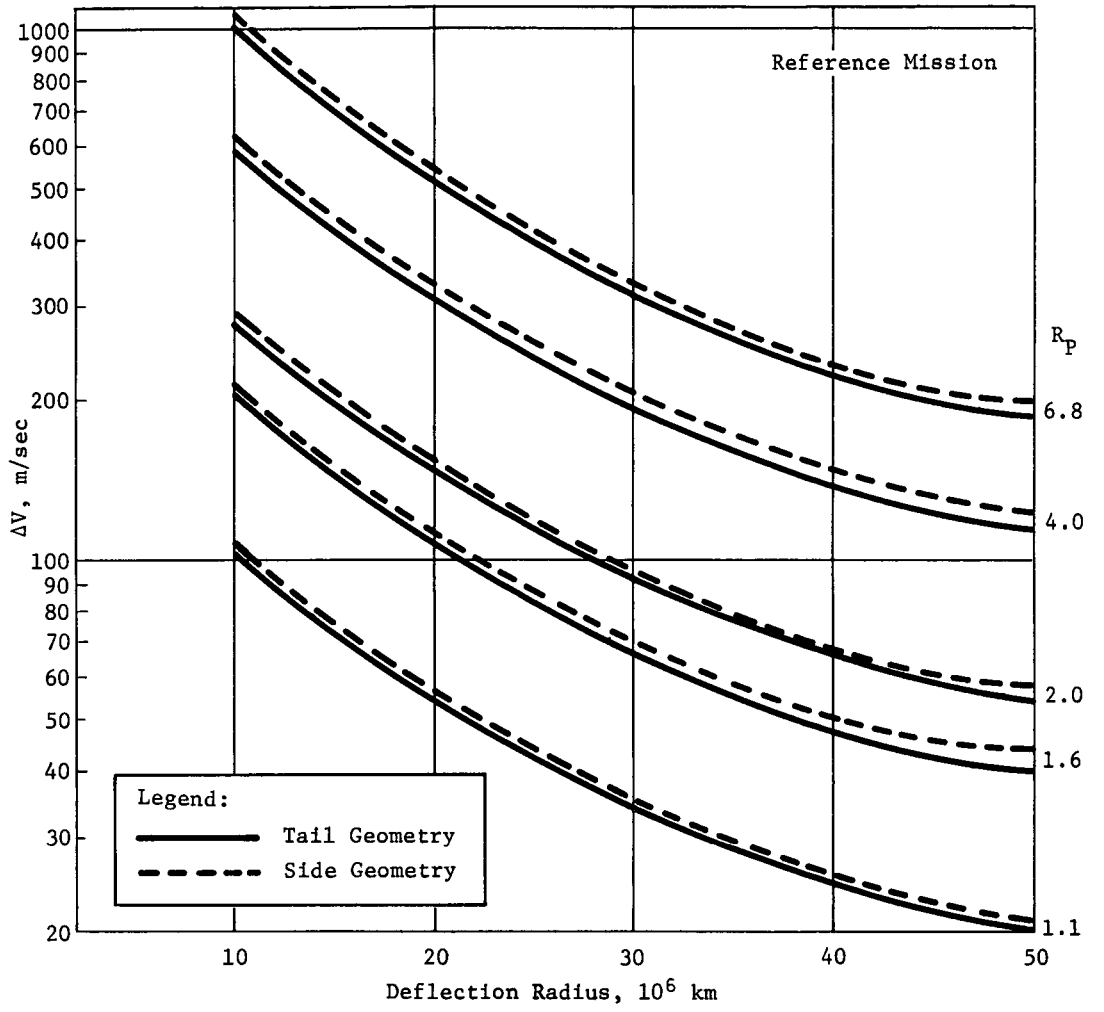

Fig. IV-21 ΔV Requirements for Modes 1 and 3

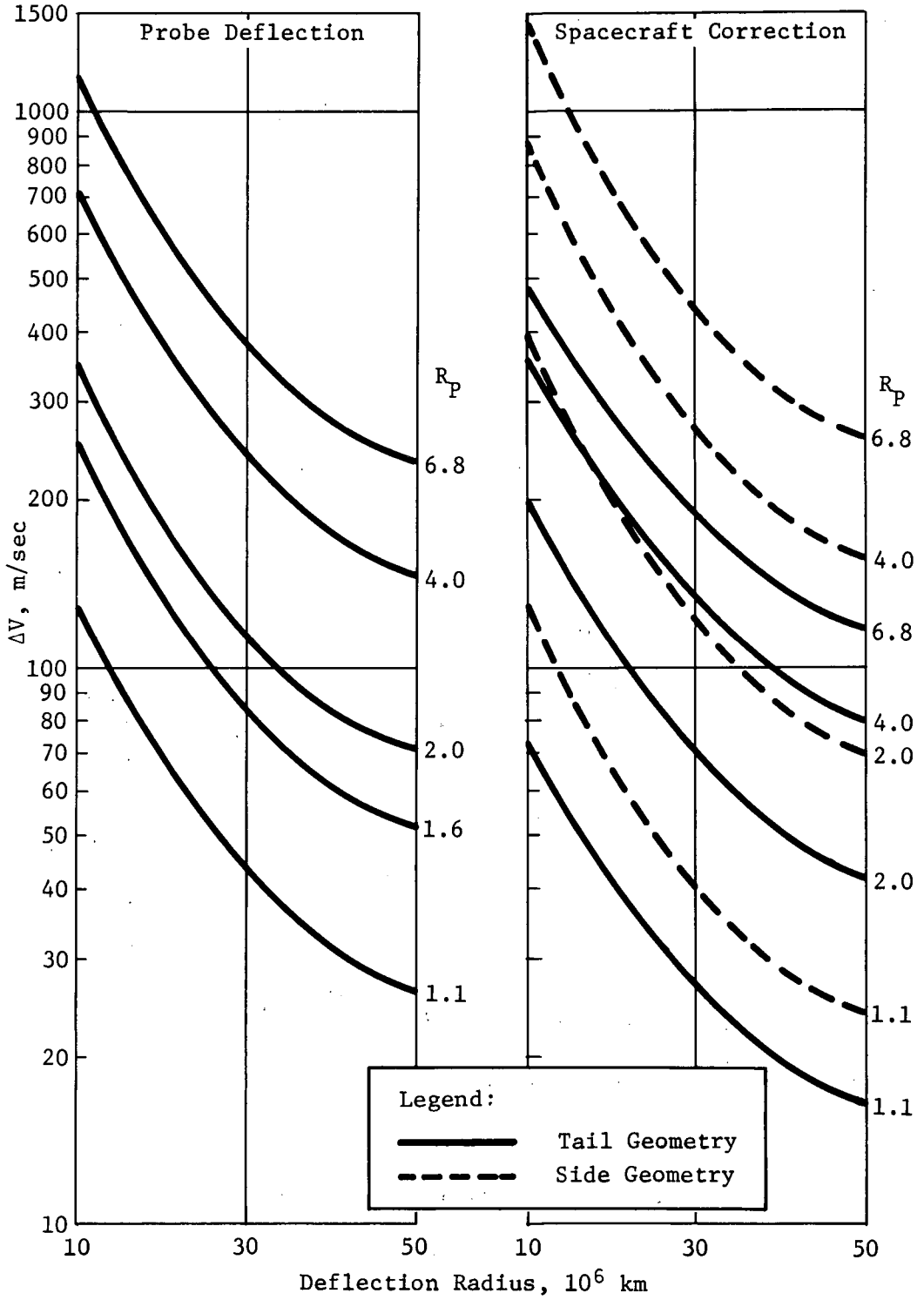

Fig. IV-22 ΔV Requirements for Mode 2

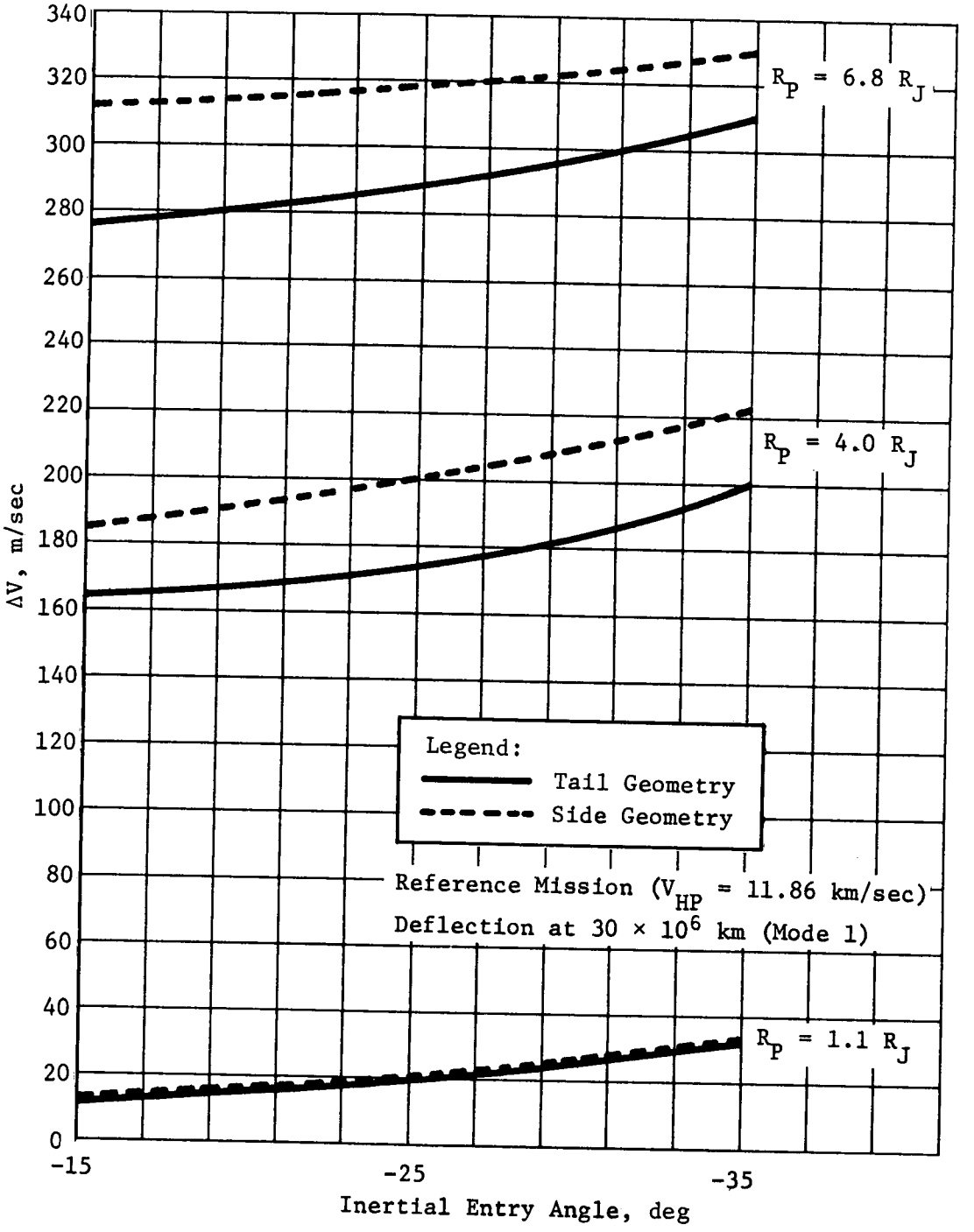

Fig. IV-23 Entry Angle Effects on ΔV Requirements

Deflection radius has an extremely strong effect on deflection ΔV requirements, as can be seen by studying Fig. IV-21, IV-22, and IV-24. The logarithmic scale of these figures should be noted. Thus, for a Mode 1 deflection on a trajectory with an R_P of 1.6 R_J, the deflection velocity is reduced from 200 to 67 to 40 m/sec as deflection radius is increased from 10 to 30 to 50 million km. Thus, most of the advantage is achieved in going from 10 to 30 million km.

d. Periapsis Radius - The effects of varying the periapsis radius, R_P, of the spacecraft flyby trajectory are illustrated in Fig. IV-21 through IV-24. The ΔV requirements are approximately linearly related to periapsis radius; thus, ΔV requirements are reduced from 115 to 54 to 20 m/sec ad periapsis radius is decreased from 4.0 to 2.0 to 1.1 Jupiter radii for a Mode 1 deflection at 50 million km.

e. Approach Velocity - Variations in selection of launch and arrival dates influence the deflection maneuver requirements primarily through the intermediate variable of approach velocity or hyperbolic excess velocity at Jupiter, V_{HP}. Dependence of V_{HP} on arrival date is illustrated in Fig. IV-22. Figure IV-24 provides the relation between approach velocity and deflection ΔV. Briefly, the V_{HP} magnitude has a minor effect on deflection on small periapsis trajectories $\left(\sim 1.1\ R_J\right)$, increasing the ΔV by 5% as V_{HP} varies from 5 to 12 km/sec. The effect becomes more pronounced as periapsis radius increases so that on trajectories with a spacecraft periapsis of 6.8 R_J, the deflection ΔV increases about 15% as approach velocity increases from minimum to maximum value.

f. Entry Angle - Variation of deflection velocity with inertial entry angle is illustrated in Fig. IV-23. The ΔV requirements increase as the magnitude of the entry angle increases. For low periapsis trajectories, the proportional increase is large (100%) as entry angle varies from -15° to -35°. For large periapsis trajectories $\left(R_P > 4\ R_J\right)$, ΔVs increase by 10 to 20 m/sec as entry angle varies from -15° to -35°.

Q.5

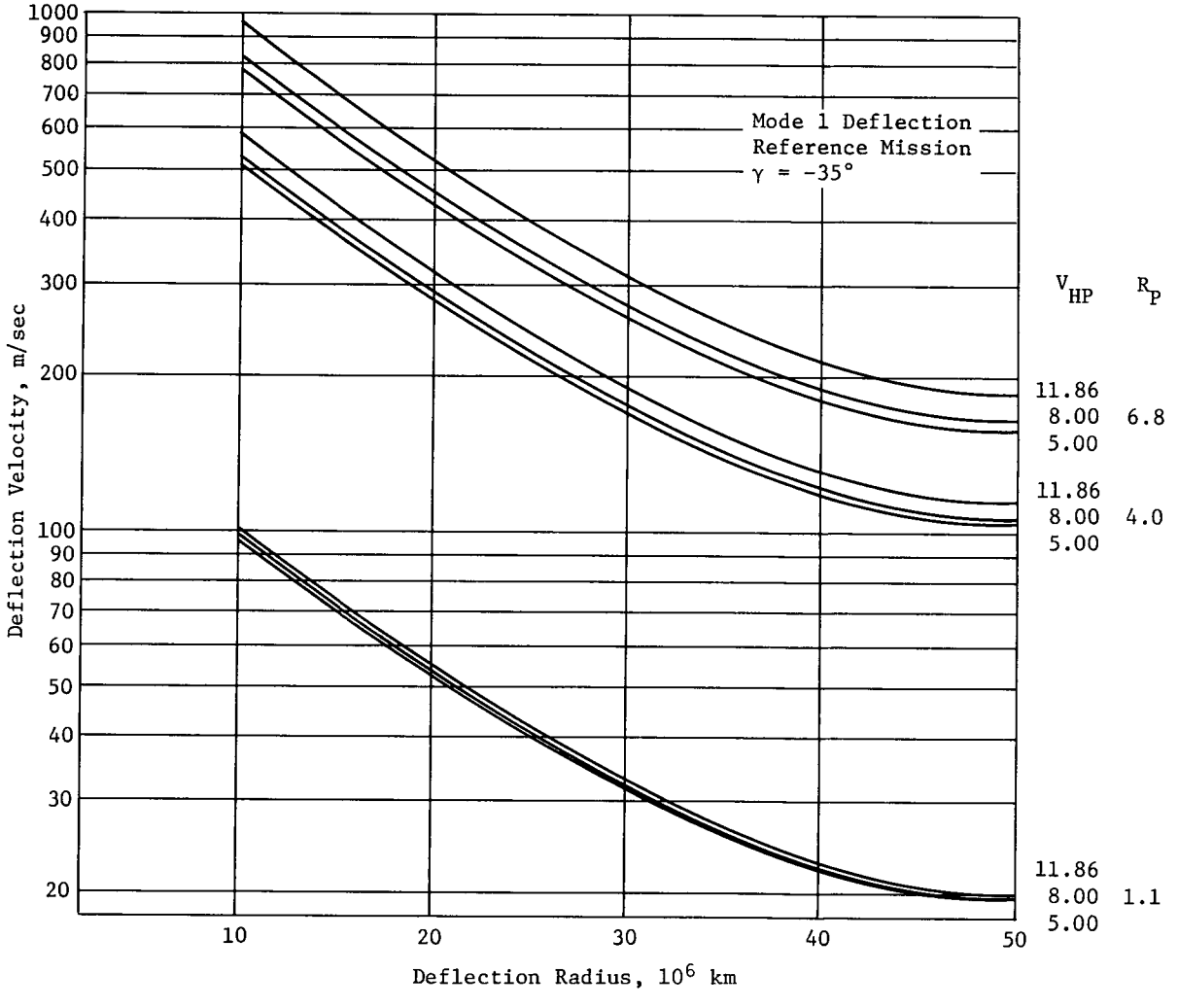

Fig. IV-24 Approach Velocity Effects on ΔV Requirements

3. Precession and ACS Requirements

In the Mode 1 deflection (probe deflection), a precession maneuver and an active ACS system are required for the probe. A brief study has been made of the feasibility of an approach to this problem.

The nominal maneuver sequence is defined in Fig. IV-25a. The first maneuver is a precession approximately in the plane determined by the Sun-probe direction and initial probe orientation (deflection velocity direction) through the angle θ_1 to achieve the desired solar aspect angle $\left(\psi_S = 180° - \angle \text{SOC}\right)$. A second precession is now performed, holding the solar aspect angle constant (moving on the surface of the cone OBC) to obtain the desired probe orientation for zero angle of attack at entry by rotating through the predetermined angle θ_2.

The terminal phase of the maneuver involves an ACS that can refine the attitude to obtain desired probe orientation. Sensors required for this system are illustrated in Fig. IV-25b. A sun sensor on the base of the probe can measure the solar aspect angle ψ_S as well as monitor Sun crossings. A Jupiter sensor, only required to monitor Jupiter crossings, is on the side of the probe. The accuracy with which the final probe direction is on the proper cone is determined by measurement of the angle ψ_S. The proper direction on that cone is determined by checking angle β against a predetermined value. This measurement can be translated into a measurement of the timing between Jupiter and Sun crossings.

The feasibility of precession and ACS systems rests on certain characteristics of the probe trajectory and probe, Jupiter, and Sun geometries. The solar and Jupiter aspect angles ψ_S and ψ_J must be checked to ensure that the sensors can identify crossings $\left(\text{i.e., } \psi_S = 0 \text{ or } \psi_S \geq 90° \text{ must be avoided as well as } \psi_J = 0\right)$. The sensitivity of the measured quantities, ψ_S and β, to small changes in the final probe orientation must also be assessed.

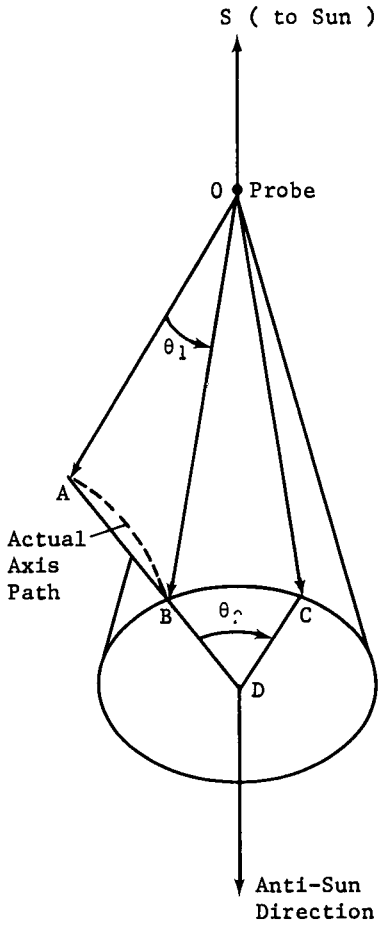

a. Precession Angles for Probe Orientation Maneuver

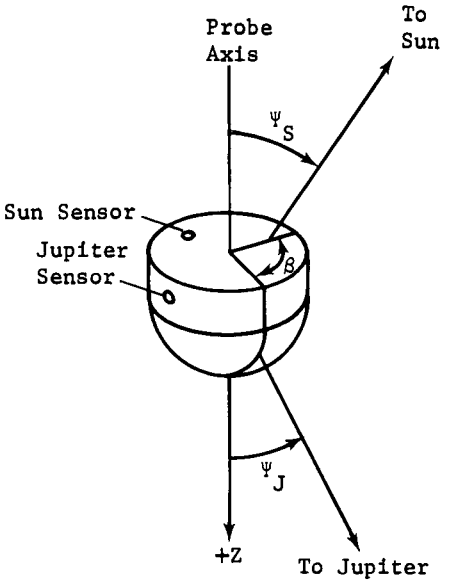

b. Sensor Angles for ACS System

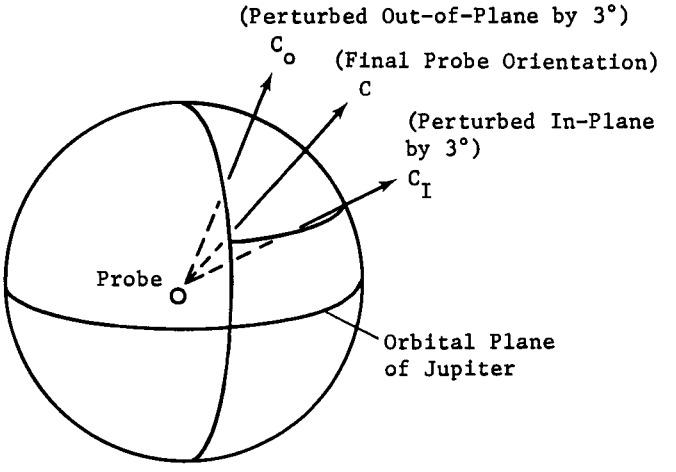

c. Definition of Sensitivity Analysis

Legend:	
OA	Initial Probe Orientation (ΔV Direction)
OB	Intermediate Orientation
OC	Final Probe Orientation (α = 0 Direction)

Fig. IV-25 Precession and ACS Parameter Definitions

Table IV-3 provides data necessary to assess the feasibility of the systems described above. A wide range of missions was analyzed to determine effects of differing geometries. Missions 1, 2, and 5 arrive in the late, middle, and early periods of the 1978 launch opportunity, respectively. Mode 1 deflections were run for these missions, even though the nominal deflection mode is Mode 3. Missions 4A and 7B are the two most probable Jupiter swingby trajectories anticipated in the near future. Mode 1 deflections would be required on these missions. All missions have low-inclination trajectories except Mission 5, which has a 30° inclination.

The nominal precession and sensor angles refer to the nominal sequence required to effect the maneuver and sensor measurements expected at the desired orientation. Thus, in Mission 1, the probe first rotates 31.9° (θ_1) to obtain the proper solar aspect angle and then rotates 13.0° (θ_2) on the final precession cone to obtain the desired orientation. At that point, sensors should record a 6.9° solar aspect angle $\left(\psi_S\right)$ and an angular separation between Jupiter and Sun crossings of 165.3° (β). The in-plane and out-of-plane precession angles indicate how errors in precession maneuvers affect final probe orientation. For example, an error of 3° in θ_1 and 4° in θ_2 results in an in-plane error of 3° in final probe orientation for Mission 1. The in-plane and out-of-plane sensor angles indicate how errors in final orientation affect angles measured by the sensor; thus an in-plane error of 3° in final probe orientation corresponds to errors of 3° in ψ_S and 4° in β.

4. Communications Link Parametrics

The key communications link parameters were defined in Fig. IV-18. Variation of these parameters as functions of trajectories and deflection maneuvers are discussed in the following sections.

a. Trajectory Variations - Variations in communication range and probe and spacecraft aspect angles are indicated as functions of spacecraft periapsis radius, communications geometry, and entry angle in Fig. IV-26. Communication range is nearly a linear function of spacecraft periapsis radius. Communication range is about twice as great for tail geometry as it is for side geometry. Range is independent of entry angle for side geometry, but greatly influenced by entry angle for tail geometry.

Table IV-3 Comparison of Precession and ACS Requirements for Selected Missions

Mission Index	1	2	4A	5	7B
Mission Title	Probe Opt 78	Rad Comp 78	Jun 79	Solar Apex 78	JS 77
Flight Time (Days)	797	655	581	540	557
Arrival Date	12/26/80	7/29/80	6/8/81	4/1/80	3/16/79
Initial Attitude					
ψ_S	38.8	52.1	48.3	59.1	52.8
ψ_J	94.4	89.0	74.8	80.4	80.7
β	182.4	180.5	180.8	165.6	178.4
Precession Angles					
Nominal Θ_1/Θ_2	-31.9/-13.0	-34.6/-1.5	-26.0/- .6	-32.7/19.7	-31.6/-4.4
In-Plane* Θ_1/Θ_2	-29.0/- 9.2	-31.6/-1.6	-23.0/- .7	-30.9/14.9	-28.6/-3.8
Out-of-Plane* Θ_1/Θ_2	-31.9/ 12.2	-34.3/ 8.3	-25.8/ 7.3	-30.4/23.1	-31.6/4.0
Final Sensor Angles					
Nominal ψ_S/β	6.9/165.3	17.4/181.7	22.3/181.4	26.4/150.7	21.2/175.2
In-Plane ψ_S/β	9.9/169.0	20.4/181.8	51.8/181.4	28.2/153.9	24.2/175.8
Out-of-Plane ψ_S/β	6.9/171.3	17.8/174.5	22.5/176.8	28.7/150.1	21.2/179.6

*In-plane and out-of-plane refer to perturbations of final probe orientation by 3° in and out of the Ionian Orbital Plane as defined by Fig. IV-25.

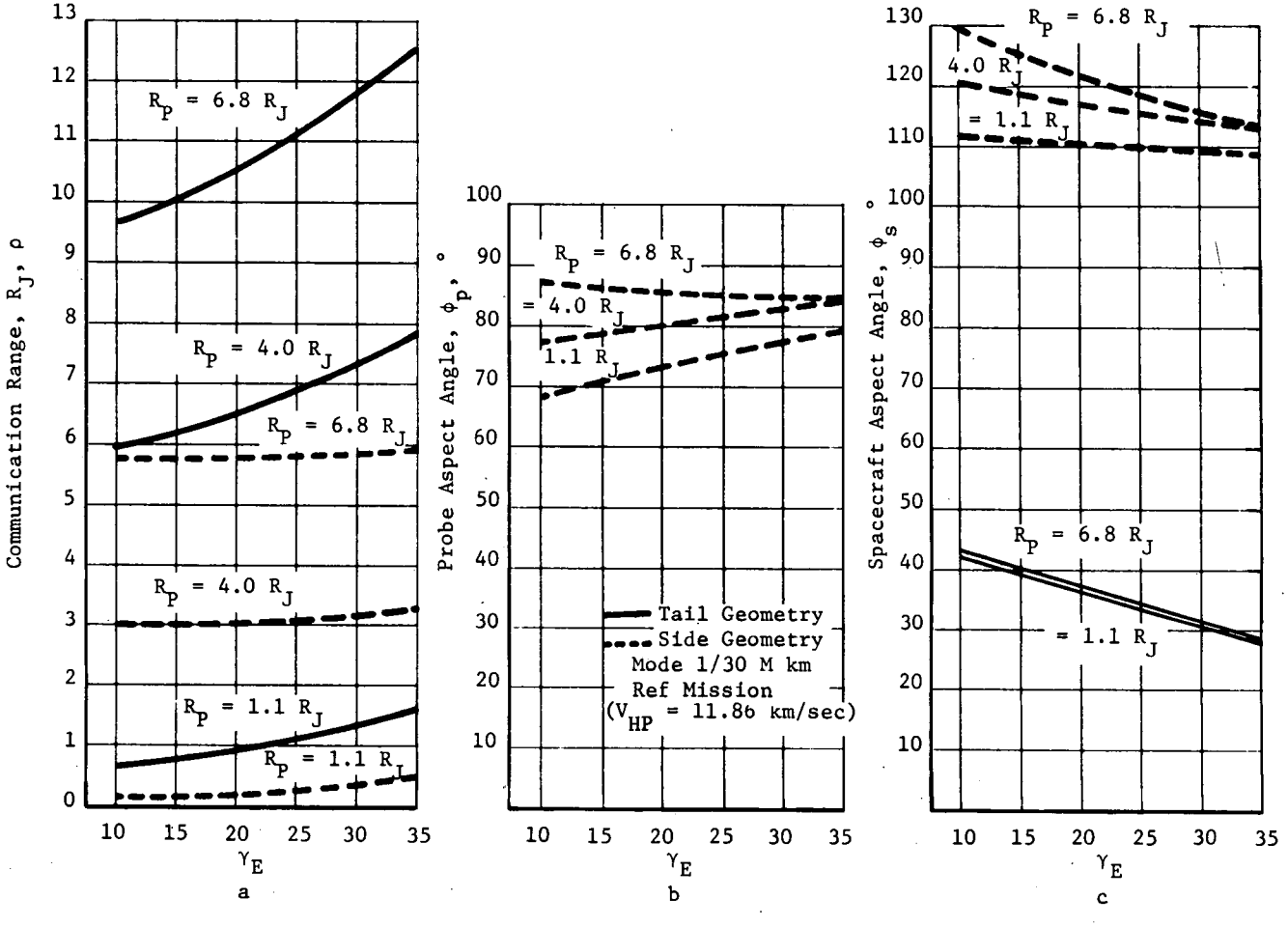

Fig. IV-26 Communication Parameter Variation with Entry Angle

Probe aspect angle is always approximately zero for tail geometry. In side geometry, probe aspect angle for minimum range is indicated in Fig. IV-26b. The angles range between 68° and 87° for entry angles between -10° and -35° and spacecraft periapsis radii of 1.1 to 6.8 Jupiter radii.

For tail geometry, spacecraft aspect angle is strongly dependent on entry angle and nearly independent of spacecraft periapsis. For side geometry, both entry angle and spacecraft periapsis radius affect spacecraft aspect angle. Magnitudes of these variations are shown in Fig. IV-26c.

b. Deflection Maneuver - A very convenient characteristic of probe missions is that communication geometry at entry is not a function of the deflection maneuver; neither deflection mode nor deflection radius affect communication parameters. Justification for this statement is provided in Fig. IV-27. For tail geometry, communication range is plotted for the three modes and three values of deflection radius. For spacecraft radii from 1.1 to 6.8 Jupiter radii, range is demonstrated to be nearly constant.

For side geometry, the probe angle corresponding to minimum range direction at entry is plotted for periapsis radii from 1.1 to 6.8 Jupiter radii and deflection radii from 10 to 30 million km. Probe aspect angles remain nearly constant, varying less than 5° in all cases.

E. NAVIGATION AND GUIDANCE

The purpose of the navigation and guidance analysis is to determine the knowledge and control uncertainties at the deflection point. Results of the midcourse sizing analysis affect the weight that must be allowed for midcourse correction propellant. Knowledge and control uncertainties partially determine dispersions that must be accounted for in the mission. (See Section F.)

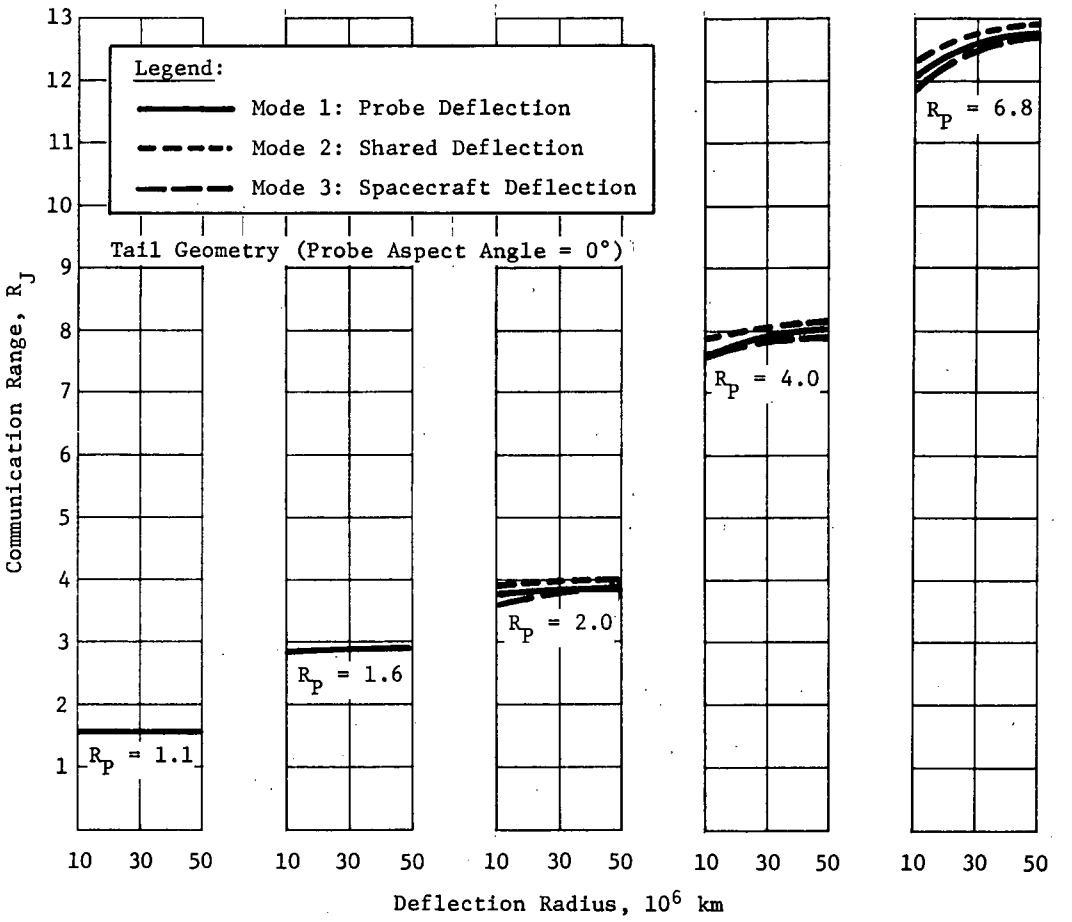

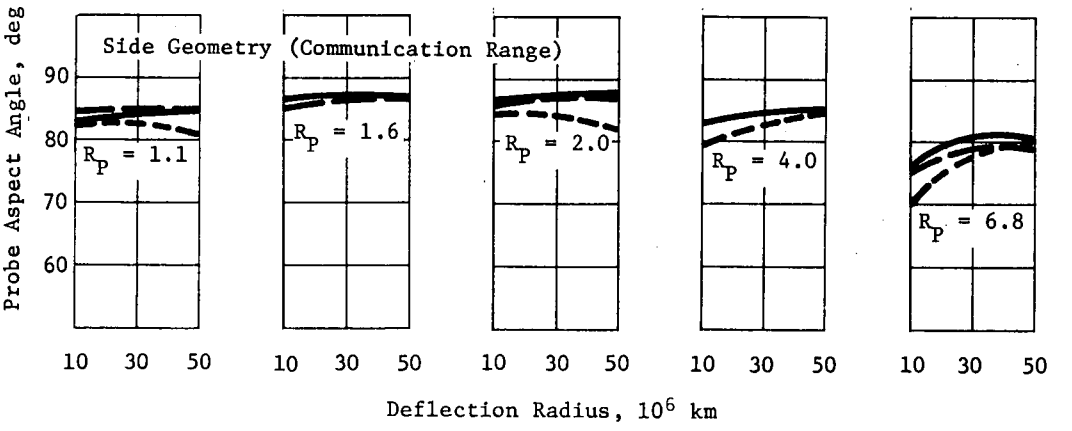

Fig. IV-27 Variation of Communication Parameters with Deflection

1. Procedure and Ground Rules

The navigation and guidance sequence assumed for the missions can be summarized as follows. The spacecraft is launched from Cape Kennedy. The first midcourse maneuver employing a fixed-time-of-arrival guidance policy is performed ten days after injection. Tracking for this maneuver begins one day after injection and continues until half a day before midcourse maneuver. The second midcourse maneuver is performed 13 days before the deflection maneuver. This maneuver uses a variable-time-of-arrival guidance policy. Tracking for this maneuver is initiated at 40 or 80 days before the probe deflection maneuver and continues until half a day before the midcourse maneuver. Tracking for the deflection maneuver continues until half a day before the deflection point. In all cases, tracking is performed by the Deep Space Network (DSN).

The mathematical model used to simulate the navigation and guidance sequence is discussed in detail in Ref 8. Briefly, at any point along the spacecraft trajectory, probabilistic dispersions are described by control and knowledge covariances. The control covariance, P_c, defines uncertainties between the nominal (or desired) trajectory and possible actual trajectories. The knowledge covariance, P_k, defines uncertainties between the actual trajectory and possible estimates of that trajectory. The control covariance is propagated along the trajectory by standard linear formulas until a guidance maneuver. The control covariance following a guidance maneuver is the sum of the knowledge covariance at that maneuver and the execution error covariance. The knowledge covariance is linearly propagated between measurements. At measurements, the knowledge covariance is reduced by the new information content of that measurement. At guidance events, the knowledge covariance is increased by adding to it the execution error covariance. Initially, knowledge and control uncertainties are set equal to the injection covariance.

It is inconvenient to describe the trajectory uncertainties by giving the 6x6 covariances in terms of Cartesian coordinates. Usually these uncertainties are translated into the more intuitive quanties of impact plane and time-of-flight uncertainties. The impact plane is defined as the plane centered at the target body

normal to the approach atmosphere, $\hat{S}$. (See Fig. IV-28). The impact parameter, $\hat{B}$, is the vector from the center of the planet to the point at which the asymptote pierces the impact plane. The T axis in the plane is defined by

$$T = \frac{\hat{S} \times \hat{K}}{|\hat{S} \times \hat{K}|} \qquad [IV-14]$$

where $\hat{K}$ is the normal to the ecliptic plane. The $\hat{R}$ axis completes the RST right-hand system

$$\hat{R} = \hat{S} \times \hat{T}. \qquad [IV-15]$$

The distribution of dispersed trajectories can be described by an ellipse centered about the nominal impact point (Fig. IV-28b). Ellipse size is specified by the semimajor (SMAA) and semiminor (SMIA) axes. The orientation is given by the angle β. Time-of-flight uncertainty is then the uncertainty in the time at which the impact plane is pierced.

The principal variables affecting the navigation and guidance analysis are injection covariance, tracking-station location uncertainties, tracking-station measurement noise, Jupiter mass and ephermeris uncertainties, and midcourse execution errors. The injection covariance consistent with the Titan III/Centaur/Burner II launch vehicle (Ref IV-9) is in Table IV-4. Standard deviations of position (km) and velocity (m/sec) are given on the diagonal with correlation coefficients supplied below. The coordinate system ecliptic equinox.

The DSN tracking data used in the study are in Table IV-5. Equivalent station location errors are three times larger than the most optimistic predictions for the late 1970s (Ref IV-10), but are realistic in light of recent estimates for Viking '75. Doppler data noise is taken from Ref IV-11, supplied by the contractor. The measurement noise of 0.3 mm/sec for a 1-min count is simulated by taking ten measurements per day and using a doppler uncertainty of 0.025 mm/sec (1σ).

The Jupiter ephemeris and mass uncertainties are based on Ref IV-12 and IV-13. The values are given in Table IV-6.

Midcourse execution errors have been analyzed for Pioneer and MOPS spacecraft. Data used are summarized in Table IV-7. The data for Pioneer is taken from Ref IV-14. The MOPS model is assumed to be identical to the TOPS model given in Ref IV-15.

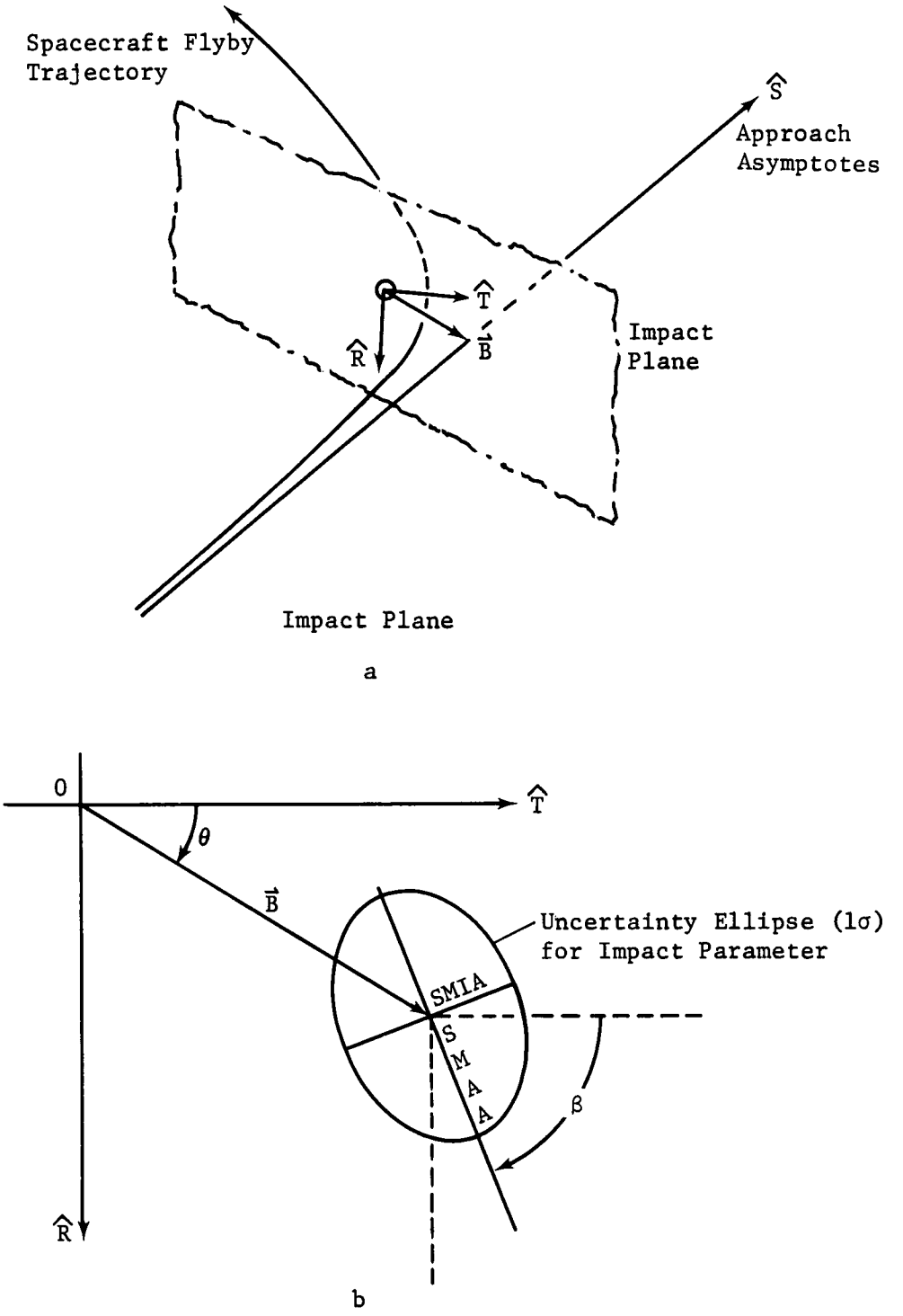

Fig. IV-28 Impact Plane and Uncertainty Ellipse

Table IV-4 Titan III/Centaur/Burner II Injection Covariance

	X	Y	Z	$\dot{X}$	$\dot{Y}$	$\dot{Z}$
X	3.412					
Y	-0.946	2.068				
Z	-0.877	0.685	1.625			
$\dot{X}$	0.752	-0.625	-0.688	5.000		
$\dot{Y}$	0.715	-0.628	-0.653	0.886	5.123	
$\dot{Z}$	-0.298	0.202	0.357	0.120	0.273	6.857

Table IV-5 DSN Tracking Data Summary

Tracking Stations	Equivalent Station Location Errors (1σ)	
Madrid Canberra Goldstone	Distance from Earth spin axis Longitudinal distance Distance parallel to spin axis Station longitude correlation	1.5 m 3.0 m 2.0 m 0.97
Doppler noise: 0.5 m, 5×10^4-sec count = 0.3 mm/sec for 1-min count		

Table IV-6 Jupiter Ephemeris and Mass Uncertainties (1σ)

In-orbit track	500 km
Radial	300 km
Out of plane	100 km
Mass	1.4×10^{-5} μ_J

Table IV-7 Pioneer and MOPS Executiuon Errors (3σ)

	Pioneer	MOPS
Proportionality Error, %	4.8	0.6
Resolution Error, m/sec	0.036	0.018
Pointing Error, deg	3.6*	0.39
*Assumes 90° rotation from Earth lock		

2. First Midcourse Maneuver

The first midcourse maneuver has been analyzed for four different missions to determine its dependency on launch date/arrival date selection. The results of this study are summarized in Table IV-8. A fixed-time-of-arrival guidance policy was used in all cases. The injection covariance used is that given in Table IV-4.

Table IV-8 Analysis of First Midcourse Maneuver

	Mission 1	Mission 2	Mission 5	Mission 7
Mean ΔV, m/sec	14.3	14.8	13.9	18.3
Standard deviation, σ, m/sec	10.4	10.7	9.9	10.9
Loading ($\Delta V + 3\sigma$), m/sec	45.5	46.9	43.7	51.0
Premidcourse dispersions[1]	281 × 70 × 3.4	675 × 50 × 2.14	805 × 54 × 1.11	937 × 75 × 1.50
Postmidcourse dispersions (Pioneer)[2]	17.4 × 4.9 × 123	11.0 × 4.7 × 70	13.2 × 4.1 × 34	--
Postmidcourse dispersions (MOPS)[2]	1.93 × 0.58 × 14.4	--	--	203 × 0.52 × 5.2

1 Premidcourse Dispersions are given in SMAA (10^3 km) × SMIA (10^3 km) × TOF (days)

2 Postmidcourse Dispersions are given in SMAA (10^3 km) × SMIA (10^3 km) × TOF (min)

The loading (mean plus 3σ) requirements for the first midcourse maneuver are essentially independent of mission, varying from 45.5 to 51 m/sec. The premidcourse dispersions (given in the parameters SMAA × SMIA × TOF defined in Subsection 1) show the effects of propagating injection convariance along different trajectories to Jupiter. The postmidcourse dispersions are dominated by execution errors, thus, the large difference between the dispersions for the Pioneer and MOPS spacecraft.

3. Second Midcourse Maneuver

The size of the second midcourse maneuver is a function of--

1) execution errors at the first midcourse maneuver (spacecraft-dependent),

2) propagation of the control covariance (trajectory- and dynamic-model dependent),

3) distance from Jupiter at the second midcourse maneuver (related to deflection radius),

4) guidance policy used.

The dependency on the trajectory and deflection radius is summarized in Table IV-9. Results are for a Pioneer spacecraft and a variable time-of-arrival guidance policy. The table indicates that midcourse requirements increase as deflection radius decreases. This is explained by the fact that to move the final impact parameter on a trajectory when close to the planet is more expensive than when further from the planet. Dependence on trajectory is evident from comparing the loading requirements for Missions 1 and 2 at a deflection radius of 50 million km.

Table IV-9 Variation of ΔV Requirements with Mission and Radius

	Mission 1			Mission 2	
Deflection radius, 10^6 km	50	30	10	50	10
Mean ΔV, m/sec	2.0	2.8	5.7	1.4	4.0
Standard deviation, σ, m/sec	1.4	2.0	4.0	0.8	2.4
Loading - ΔV + 3σ. m/se)	6.2	8.7	17.7	3.8	11.2

The dependence of ΔV magnitude on guidance policy used (on Mission 1) is indicated in Table IV-10. Two guidance policies were considered: a fixed time-of-arrival (FTA) policy and a variable time-of-arrival policy (VTA). In the FTA policy, the midcourse correction is chosen to null errors in both postion (B·T, B·R) and arrival time. In the VTA policy, only position errors are nulled so midcourse correction magnitude can be minimized.

Detailed descriptions of these policies can be found in Ref IV-8. Because the turbopause probe is not sensitive to variations of several hours in arrival time (as long as that arrival time can be estimated) the VTA policy is preferable. The table indicates the substantial savings in ΔV that can be obtained by using the VTA policy. The progressive nature of the advantage as deflection radius decreases should also be noted.

Table IV-10 Variation of Midcourse Requirements with Guidance Policy and Radius

	Deflection radius (10^6 km)					
	50		30		10	
Guidance policy	FTA	VTA	FTA	VTA	FTA	VTA
Mean ΔV, m/sec	6.7	2.0	13.3	2.8	41.4	5.7
Standard deviation, σ, m/sec	5.1	1.4	9.	2.0	30.4	4.0
Loading - $\Delta V + 3\sigma$, m/sec	21.9	6.2	42.5	8.7	132.5	17.7
Note: Data based on Mission 1 using Pioneer spacecraft						

Data in Table IV-9 and IV-10 are based on the Pioneer spacecraft. For MOPS spacecraft, the errors are typically one-fifth to one-tenth as large.

4. Approach Orbit Determination

In contrast to the first midcourse maneuver, the postmaneuver dispersions for the second are dominated by the knowledge covariance of the spacecraft state at maneuver time and are quite insensitive to maneuver execution errors. Control covariance at deflection can therefore be approximated by tracking from 40 (or 80) days before deflection to the midcourse maneuver (13 days before deflection) and then propagating the result to deflection. The knowledge covariance is generated by continuing the tracking for the 13 days from the midcouse maneuver to deflection. This tracking comprises the approach-orbit determination phase of the mission. Control and knowledge covariances at deflection are functions of approach trajectory, length of the tracking arc, and radius of deflection.

a. Approach Trajectory - The two most important characteristics of approach trajectory for navigation analysis are the geocentric declination at approach and approach velocity. Geocentric declination is important because doppler tracking degenerates for small values of this parameter according to formula

$$\Delta\delta = \frac{\Delta r_s / r_s}{\tan \delta}$$

where δ is the declination, r_s is the distance of the tracking station from the spin axis of the Earth, and $\Delta\delta$ and Δr_s are the respective uncertainties in those parameters. Approach velocity would appear to be a factor because the slower the approach, the less the geometric change in the trajectory over a fixed time interval.

Figure IV-29 illustrates the variation of the geocentric declination of Jupiter over an interval of about six years and of the spacecraft over an 80-day tracking arc for four typical missions. The geocentric declination of the missions and the approach velocities cover a wide range of values. Resulting control and knowledge uncertainties are summarized in Table IV-11. The first two missions have about the same flight time and approach velocity, but the declination of Mission 5 is about half that of Mission 7. Knowledge and control uncertainties of Mission 5 are about twice those of Mission 7. Missions 5 and 2 have about the same geocentric declination, but the approach velocity of Mission 5 is significantly higher than that of Mission 2. The resulting knowledge and control for the two missions are about equal. Mission 1, with the geocentric declination of zero in the middle of the tracking arc and slowest approach velocity of any of the missions, has significantly worse knowledge and control than the other missions.

A technique known as Quasi Very Long Baseline Interferometry has been recently introduced to combat the low-declination problem (Ref IV-5). Using this technique, errors of Mission 1 could possibly be reduced to the order of the other missions.

Thus, dependence of knowledge and control on geocentric declination is empirically verified. Effects of approach velocity on tracking appear to be much weaker. So many geometrical factors influence the navigation process that it is extremely difficult to quantify critical characteristics of tracking.

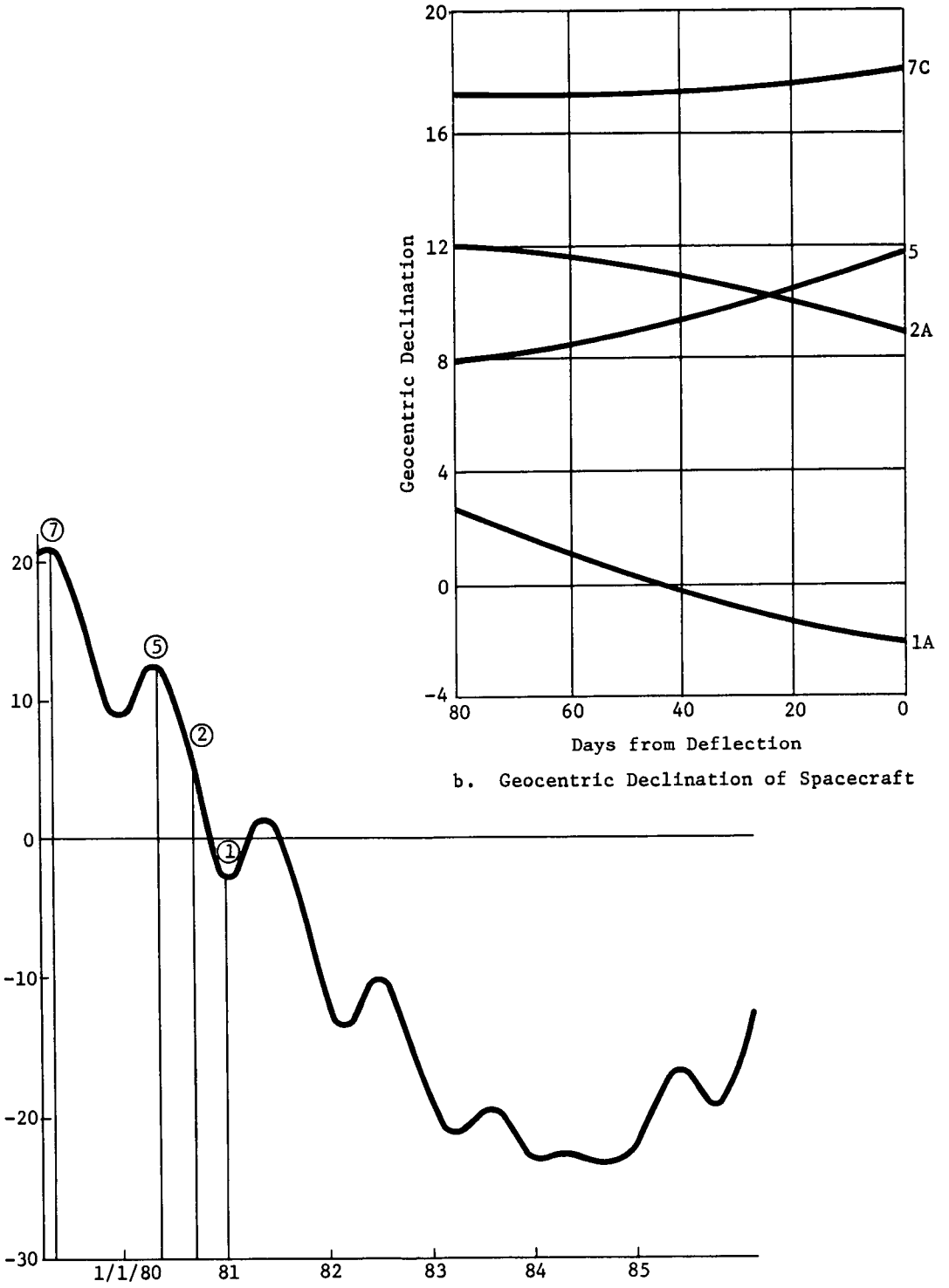

Fig. IV-29 Geocentric Declination of Jupiter and Spacecraft

Table IV-11 Variation of Knowledge and Control with Approach Trajectory

Mission Index	Flt Time, days	Approach Vel, V_{HP}, km/sec	Geocentric Declination, deg	Deflection Radius, 10^6 km	Control Uncertainty SMAA × SMIA × TOF km km sec	Knowledge Uncertainty SMAA × SMIA × TOF km km sec
7	542	11.1	18	50	347 × 188 × 24	313 × 180 × 23
5	540	11.7	10	10	507 × 399 × 51	504 × 328 × 47
2	655	8.6	10	10	861 × 208 × 54	857 × 114 × 44
1	797	6.8	0	10	1404 × 1087 × 113	1396 × 899 × 89
Note: Knowledge and control based on 80-day tracking						

b. Tracking Arc Length - A study determined the effect of length of the tracking arc on resulting knowledge and control. Typical results are summarized in Table IV-12. Mission 5, which has a geocentric delination of about 10°, illustrates the general trend. Increasing the tracking arc from 40 to 80 days results in only a minor decrease in knowledge and control. Thus, tracking uncertainties have been reduced to as low a level as possible during the 40-day arc.

Table IV-12 Variation of Knowledge and Control with Tracking-Arc Length

Mission Index	Deflection Radius, 10^6 km	Arc Length, days	Control Uncertainty SMAA × SMIA × TOF km km sec	Knowledge Uncertainty SMAA × SMIA × TOF km km sec
5	10	40	586 × 348 × 49	550 × 267 × 45
	10	80	507 × 399 × 51	504 × 328 × 47
1	10	40	2714 × 1106 × 225	2480 × 973 × 186
	10	80	1404 × 1087 × 113	1396 × 899 × 89
1	30	40	5344 × 1596 × 453	1735 × 1126 × 125
	30	80	4616 × 1138 × 374	3935 × 1047 × 331

For Mission 1, which has a near-zero geocentric declination, the situation is somewhat different. For the 10-million-km deflection radius, doubling the length of the tracking arc decreases knowledge and control uncertainties by half. Referring to Fig. IV-29b, the last 40 days of tracking for Mission 1 include several days of near-zero declination that contribute little to the tracking process. Thus, tracking uncertainties have not yet leveled off. By increasing the tracking arc to 80 days, some days of stronger tracking early in the arc are added that permit uncertainties to be decreased by additional tracking.

The situation is even more complex for a deflection at 30 million km for Mission 1. For this deflection, the last midcourse maneuver occurs right at the point at which geocentric declination is zero. Thus, the last 13 days of tracking that are critical to deflection knowledge uncertainty have extremely small geocentric declinations. Thus, slight variations in orientation of knowledge covariance at the beginning of that final tracking can significantly affect the final knowledge uncertainty. This may cause the observed result that, for this case, increasing the tracking arc from 40 to 80 days decreases the control covariance slightly but increases the knowledge covariance. Thus, the effect of length of tracking arc on control and knowledge covariance is an extremely complex problem. Generally, covariances are reduced as the tracking arc is lengthened. In general, 40 days represents an arc long enough to reduce uncertainties to the plateau values. However, for certain cases such as encountered in Mission 1, the 40-day arc is not enough. Each mission should be analyzed individually to determine the navigational aspects of the final approach.

c. Deflection Radius - Variation of knowledge and control uncertainties with deflection radius is summarized in Table IV-13. In the cases analyzed, increasing deflection radius generally increased tracking uncertainties. This is to be expected because being nearer to the target planet leads to greater accelerations on the trajectory, which can be picked up by the navigation algorithm. It might be noticed that the only unusual increase in uncertainties in going from one deflection radius to a larger one is on Mission 1 where the geocentric declination is near zero.

Table IV-13 Variation of Knowledge and Control with Deflection Radius

Mission Index	Deflection Radius, 10^6 km	Control Uncertainty SMAA × SMIA × TOF km km sec	Knowledge Uncertainty SMAA × SMIA × TOF km km sec
5	10	507 × 399 × 51	504 × 328 × 47
	30	511 × 406 × 58	483 × 336 × 51
	50	807 × 642 × 131	542 × 392 × 57
2	10	861 × 208 × 54	857 × 114 × 44
	50	646 × 224 × 103	644 × 184 × 101
1	10	1404 × 1087 × 113	1396 × 899 × 89
	30	4616 × 1138 × 374	3935 × 1047 × 331
Note: 80-day tracking used for all cases.			

F. DISPERSION ANALYSIS

Errors and uncertainties are inherent in any mission. Unavoidable errors in navigation and guidance processes lead to uncertainties in spacecraft state at the deflection point. Execution errors in the deflection maneuver itself cannot be escaped. These errors and their resulting dispersions must be considered in mission design.

Parameters whose dispersions are most critical fall naturally into two classes--entry parameters and communication parameters. Entry parameters are variables associated with probe entry, such as entry site, flight path angle, angle of attack, or time of entry. Dispersions in these parameters could affect the science return of the mission. The most important science dispersion constraint is that the angle of attack 3σ dispersions be less than $5°$. Communication parameters are quantities describing the communication link between probe and spacecraft. (See Section D, Subsection 1b.) Dispersions in communication parameters must be accounted for in the design of the link to ensure that science data can be returned to Earth.

1. Monte Carlo Procedure

A Monte Carlo analysis is used to translate errors at deflection into critical mission dispersions. Details of the Monte Carlo program used are given in the Appendix D (Vol III). A brief summary of the technique will be given here. For definiteness, assume that a Mode 1 deflection is being considered. The generalization to the other modes is straightforward. Nominal deflection state of the spacecraft X_{NOM}, control and knowledge covariances at deflection P_C and P_K (See Section E, Subsection 4), and deflection execution errors are first computed for the required mission. The control covariance is sampled to obtain an actual spacecraft state deviation, ΔX_{ACT}. The actual state of the spacecraft is then

$$X_{ACT} = X_{NOM} + \Delta X_{ACT} \qquad \text{[IV-16]}$$

for this sample. The knowledge covariance is sampled to generate the error in the estimated state, ΔX_{EST}. Estimated spacecraft state is then

$$X_{EST} = X_{ACT} + \Delta X_{EST}. \qquad \text{[IV-17]}$$

The estimated state is used to determine the commanded direction of the probe deflection, ΔV. (Magnitude of ΔV is set at the nominal value as the probe deflection engine is built specifically for nominal ΔV.) The execution error model is sampled to generate an execution error, $\delta\Delta V$. Actual probe state at deflection is then computed as

$$Y_{act} = X_{ACT} + \begin{bmatrix} - - \underline{0} - - \\ \Delta V + \delta\Delta V \end{bmatrix}$$

Actual probe and spacecraft states are then propagated over certain time intervals from deflection, and resulting (off-nominal) communication parameter values are recorded. Conditions at actual probe entry (which occurs at different times from different samples) are also recorded. This process is repeated for a large number of cases. The resulting collection of dispersions is then statistically analyzed to determine variations in parameters that can be expected when the mission is actually flown.

Generation of knowledge and control covariances was discussed in Section E, Subsection 4. The execution error model will be described in the next subsection.

2. Execution Error Modeling

The Monte Carlo program used in this study requires execution errors to be defined in terms of six sources:

1) Proportional error in ΔV delivered $\left(\sigma_k\right)$;

2) Resolution error in ΔV delivered $\left(\sigma_s\right)$;

3) Directional error (in-plane component) of ΔV delivered $\left(\sigma_A\right)$;

4) Directional error (out-of-plane component) of ΔV delivered $\left(\sigma_B\right)$;

5) Directional error (in-plane componet) of final probe attitude $\left(\sigma_I\right)$;

6) Directional error (out-of-plane component) of final probe attitude $\left(\sigma_O\right)$;

The distinction between in-plane and out-of-plane directional errors is made because of the nonsphericity of pointing errors for the Pioneer spacecraft when rotating off Earth lock. The dominant pointing error is in the plane of the rotation, which is generally in the ecliptic plane.

Thus, physical implementation errors involved in the maneuver sequence must be translated into these six components. Table IV-14 provides the physical characteristics of the systems used in this study.

3. Communications Link Dispersions

a. Cone, Clock, and Cross-Cone Angles - The direction that the spacecraft must look to see the probe is generally described in terms of cone angle (CA) and clock angle (CLA) referenced to the Earth and Canopus. (See Fig. IV-30a.) Cone angle is the angle included by the Earth-to-spacecraft-to-probe alignment. Clock angle is the angle between the Canopus meridian and the cone meridan measured clockwise looking toward Earth. The Canopus meridan is the great circle defined by the Earth-spacecraft axis and the Canopus direction. The cone meridian is the great circle defined by the Earth-spacecraft axis and the spacecraft probe direction.

Table IV-14 Deflection Execution Errors (3σ)

	TOPS/ MOPS	Pioneer	Probe Solid Rocket	Probe Precession & ACS
ΔV Errors				
Proportionality, %	0.6	1.0/4.8[a]	1.0	--
Resolution, m/sec	0.018	0.036	0.0	--
Direction,[b] deg	0.0	0.0	0.5	--
Pointing in Earth Lock,[c] deg	0.15	0.25	--	--
Orientation Errors[d]				
In-plane, deg	1.0	4% of θ_E[e]	--	1.0/2.0[f]
Out-of-plane, deg	1.0	1% of θ_E	--	1.0/2.0
Probe Release[g]				
Spin-up, deg	--	1.0	--	--
Probe tip-off, deg	--	0.2	--	--
Probe tip-off & spin-up, deg	0.5	--	--	--

[a] First number refers to predicted error after inflight calibration, second number to no calibration.

[b] ΔV direction refers to error in direction of delivered ΔV caused by misalignment of engine, coning effects, etc.

[c] Pointing in Earth lock refers to angular error in locating Earth in cruise.

[d] Orientation errors refer to final errors in pointing after maneuver & possibly ACS to achieve commanded direction off Earth lock.

[e] θ_E is the rotation angle off Earth lock.

[f] Two levels of probe ACS have been considered in the study.

[g] Probe release pointing errors refer to errors introduced during mechanical separation of probe from spacecraft. Pioneer spins up (while off Earth lock), then tips off the probe. MOPS tips off the probe, the probe spins up, & probe ACS fine tunes it.

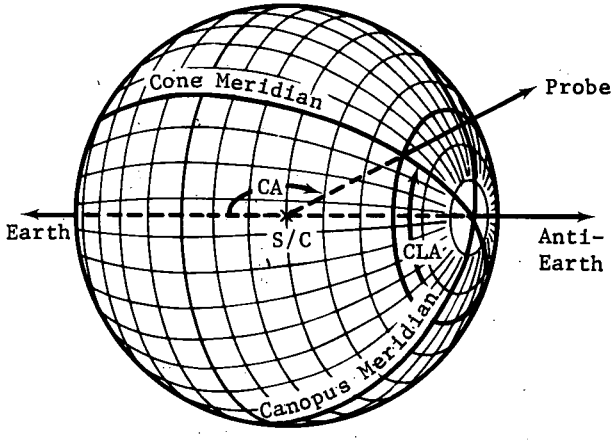

a. Definition of CA & CLA

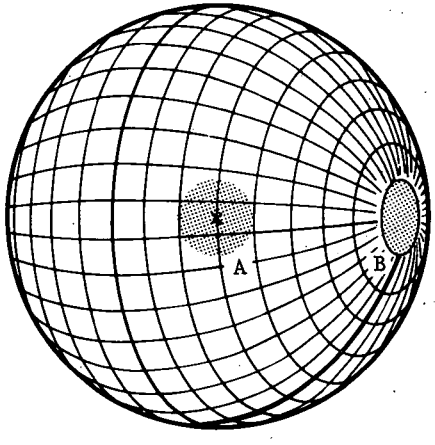

b. Dispersions in CA & CLA.

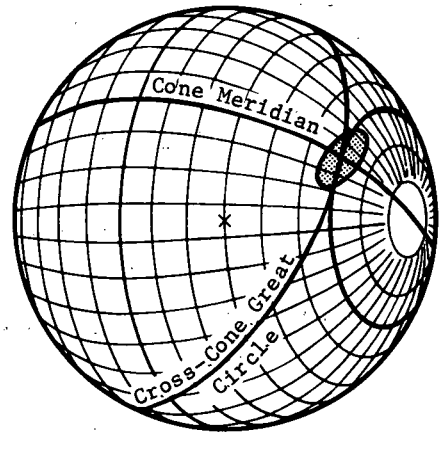

c. Definition of XCA

Fig. IV-30 Cone, Clock, and Cross-Cone Angles

It is inconvenient to describe dispersions in spacecraft-probe look direction in terms of cone and clock angles. Figure IV-30b illustrates the problem. Location A has a nominal look direction of CA = 120° and CLA = 75° with circular dispersions about that point of 10° radius. In terms of cone angle and clock angle, dispersions would be $\Delta CA = \pm 10°$ and $\Delta CLA = \pm 12°$, which adequately describe the area the spacecraft antenna must cover. However, suppose the same distribution is now moved to point B defined by a nominal cone angle of CA = 180°. Now, dispersions in cone angle and clock angle are given by $\Delta CA = \pm 10°$ and $\Delta CLA = \pm 180°$. Thus, the definition of dispersions in clock angle breaks down when the nominal cone angle is close to 180°.

This problem can be eliminated by describing dispersions in spacecraft-probe look directions in terms of cone angle and cross-cone angle (XCA). Given the nominal look direction, the cone meridian can be constructed as usual. The cross-cone circle is the great circle normal to the cone meridian at the nominal probe point. As seen from the spacecraft, the cone and cross-cone axes appear to be Cartesian coordinates. Cross-cone dispersions remain well defined for all values of nominal cone and clock angles. Cross-cone and clock-angle dispersions are approximately related by $\Delta XCA = \Delta CLA \sin CA$. Dispersions in terms of cone and clock angles and in terms of cone and cross-cone angles are given in Fig. IV-31 for Mission 7. The points 1 through 5 denote 57, 40, 20 and 0 min before nominal end of mission and the actual end of mission, respectively.

b. Timing Uncertainties - Science requirements stipulate that the probe begin taking measurements 50,000 km above the turbopause and continue until the end of the mission. The end of the mission occurs with communication blackout 60 km below the turbopause. This critical period is called the performance phase of the mission. Both the science instruments and the communication link must operate during this phase of the mission.

A key parameter influencing sequencing for the performance phase of the mission is the coast-time uncertainty, which is the 3σ uncertainty in the nominal time interval from probe deflection to mission end. It is due to uncertainties and execution errors at deflection. The performance phase is initiated by a timer set to activate the probe at a predetermined time after deflection. Sufficient margin must be allowed in this sequence so that science requirements are met, whether the actual probe arrives early or late.

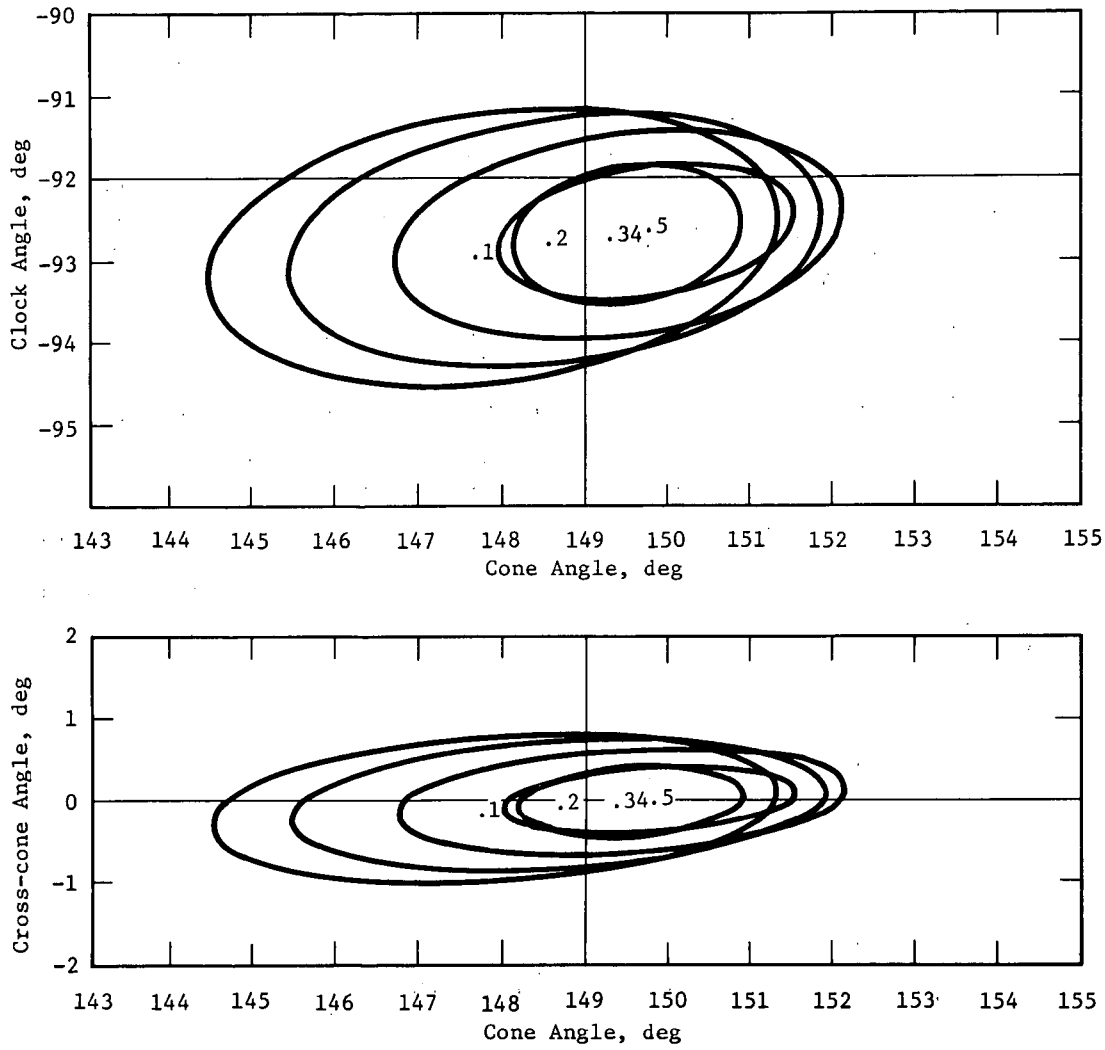

Fig. IV-31 Spacecraft Look-Direction Dispersions for Mission 7

A schematic of the problem is provided in Fig. IV-32. The performance phase of the nominal trajectory is indicated by the solid diagonal line. It is convenient to reference times in the performance phase of the mission to the nominal end of the mission (NE). The time from 50,000-km altitude to NE is the performance time, Δt_p. Nominal coast time, ΔT_c, defines the time on the nominal trajectory from deflection to NE. Thus, if there were no errors, acquisition could occur at NE - Δt_p. The communication link would be required only over the interval Δt_p. However, deflection uncertainties lead to a cost time error of Δt_u. If a probe were early by this amount (lower dashed line), acquisition at NE - Δt_p would not be early enough to make the measurements at 50,000 km. Thus, to satisfy that requirement, acquisition must take place at NE - Δt_p - Δt_u.

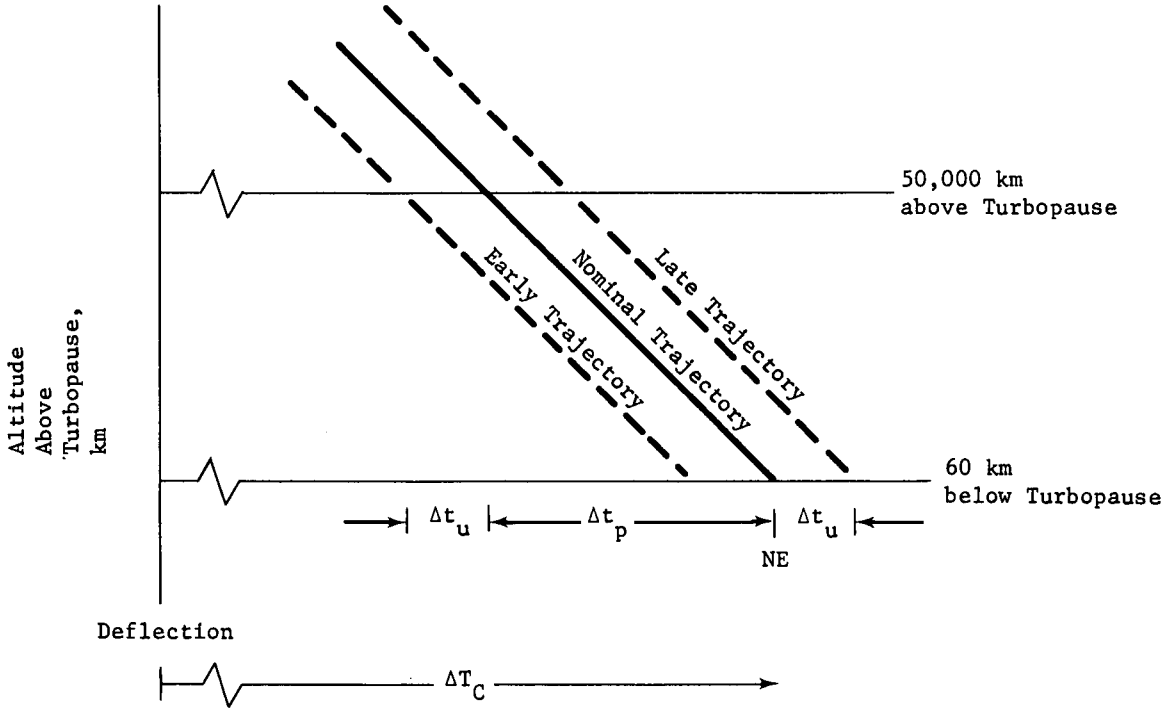

Fig. IV-32 Coast-Time Uncertainty and Mission Sequencing

If a probe were late by the coast-time error (upper dashed line), it would not reach the 60 km below turbopause until NE + Δt_u. To cover this possibility, the communication link must operate until this time.

Thus, for this simplified analysis, acquisition must occur by NE - Δt_p - Δt_u. The link must operate at least until NE + Δt_u. Science instruments and communication equipment must therefore operate during a time interval of Δt_p + 2 Δt_u units. For the exact mission sequences, acquisition occurs earlier than NE by the sum of the contributions listed in Table IV-15.

Table IV-15 Contributors to Acquisition Time Computation

Source	Δt allotment, min	Comment
Performance time	Variable	Depends on probe trajectory entry angle
Coast-time uncertainty (3σ)	Variable	Depends on deflection radius & mode, uncertainties, execution errors, trajectory
Acquisition time	1.0	Time required for acquisition search
Engineering data	2.0	Engineering data transmitted after acquisition, but before science data
Science instrument warmup	0.5	
Mechanical timer uncertainty	t_T	Δt_T (min) = 0.0107 ΔT_c (days) (Accutron timer)
Margin	Variable	5% of total of other contributors

c. Link Analysis - As discussed in the previous subsection (3b), the communication link must operate from NE - Δt_p - Δt_u until NE + Δt_u, where Δt_p is the nominal performance time and Δt_u is the 3σ coast-time uncertainty. An example of the possible spacecraft-look-directions required to see the probe at various times for Mission 7 is given in Fig. IV-33. Requirements for the time points from acquisition (NE - 57 min) until NE are straightforward. At any time, the spacecraft antenna must have a beamwidth and/or search pattern sufficient to cover the ellipse of possible look directions. Provisions must also be made to cover dispersions in other communication parameters such as probe aspect angle and range rate.

However, the situation becomes more complex after NE. For example, assume that, at NE + Δt_u, the spacecraft were still forced to cover all possible spacecraft-probe directions. The resulting dispersion ellipse would be unnecessarily large because 99.7% of the directions considered would be associated with probes that have already completed their mission and are in communication blackout at NE + Δt_u. Thus, although the link must be designed to operate from NE - Δt_p - Δt_u to NE + Δt_u, it need not be designed to cover all possible spacecraft-probe geometries possible during that interval. Spacecraft-probe geometries occurring after the probe has completed its mission need not be considered.

Thus, the communication link must be designed to last until NE + Δt_u only so that late arriving probes can be monitored. If the possible geometries of late-arriving probes at their actual end of mission were known, then the assumption could be made that, during the interval from NE until NE + Δt_u, possible geometries change smoothly from those at NE to those at actual end of mission. Therefore, the spacecraft-look-direction dispersion ellipse is computed at actual end of mission for all probes in the Monte Carlo sample. This ellipse must therefore include all possible look directions for late-arriving probes. The range of possible look directions that the link must be designed to cover is then the union of the NE and the actual end-of-mission ellipses. This, of course, is still conservative, but in all cases, the actual end-of-mission ellipse lies between the ellipses for NE and the point immediately before it (NE - 20 min in Fig. IV-33). Thus, the spacecraft antenna beamwidth/search pattern has not been penalized because of this conservatism. In designing the system, this same procedure is used with the other link parameters.

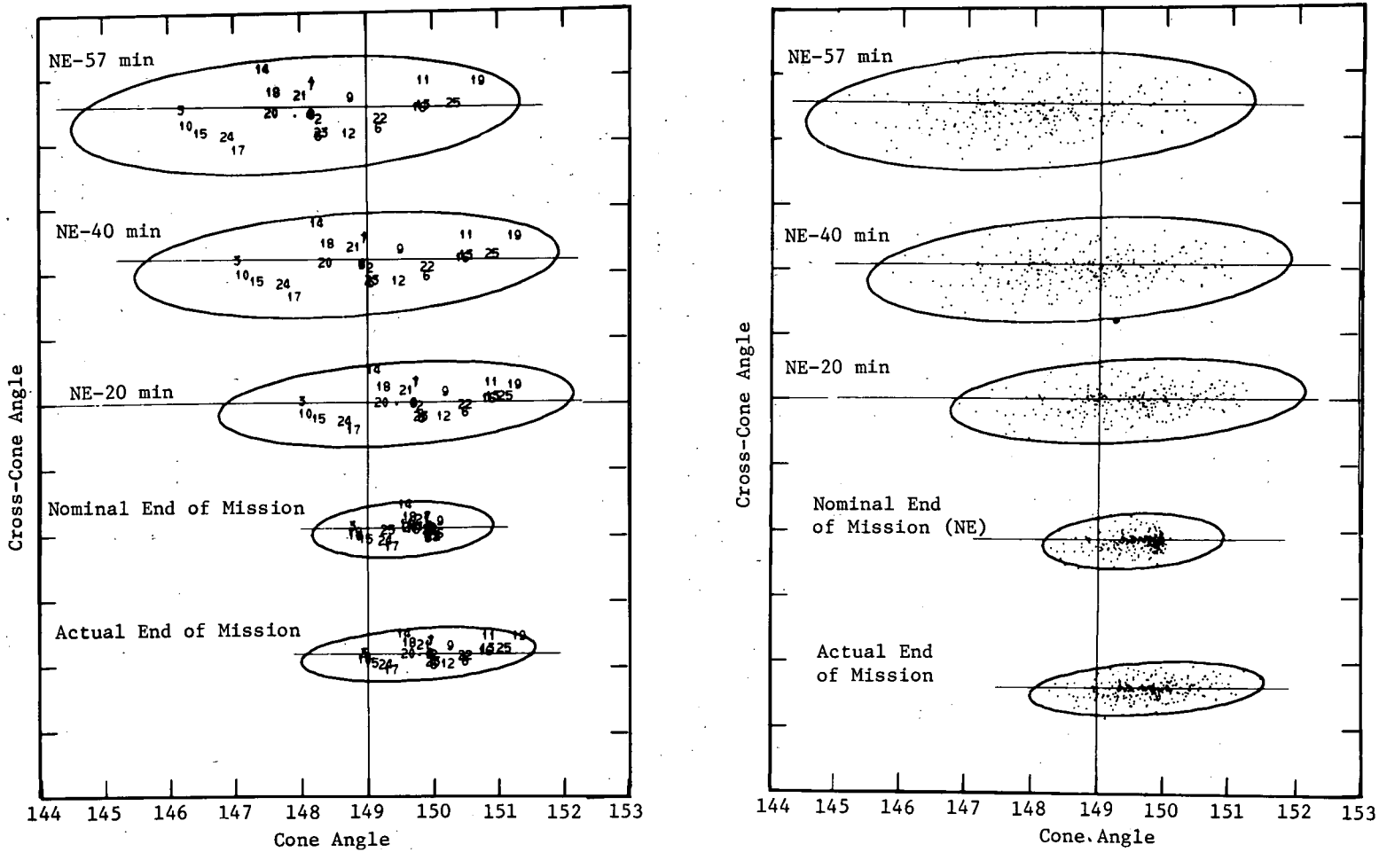

a. Time Histories

b. Construction of Statistics

Fig. IV-33 Cone and Cross-Cone Dispersion Analysis

Two general features of the tracking problem are illustrated in Fig. IV-33. The time-varying behavior of the spacecraft look direction is indicated in Fig. IV-33a. Here, cone and cross-cone dispersions of 25 individual trajectories of sampled cases are followed in time. Generally, points in the right section of the first ellipse stay to the right in succeeding ellipses. A similar relation holds for the left and center sections. Thus, for example, trajectories 3, 10, 14, and 11 hold their relative positions throughout. Trajectory 25 is an illustration of an early-arrival probe. Thus, in the actual time sequence of the points, the bottom two ellipses would be reversed. Then the probe stays to the right of the ellipses through the actual end of mission. At NE, it has been pulled to the left by its close approach to the planet.

The general statistical nature of the dispersions is illustrated in Fig. IV-33b. Here, the entire 250 samples of the Monte Carlo analysis are plotted against the uncertainty ellipses they produce. The ellipses generally describe the distributions of the individual points quite accurately. Thus, the assumed normal distribution of the points is verified. However, the ellipse at NE does not mirror the distribution of the points. This is because of nonlinear effects of gravitational attraction. Early-arriving probes are generally accelerated between the time of their actual end of mission and the NE time. Thus, they are pulled toward the planet, which is indicated by a shift to the left in the figure, corresponding to a smaller cone angle.

4. General Dispersion Trends

Entry and communication dispersions are functions of deflection mode, communication geometry, deflection radius, spacecraft periapsis radius, entry angle, and the level of errors at deflection. Qualitative assessments of these effects are discussed in this section.

a. Deflection Mode - Deflection mode effects on dispersions are illustrated in Fig. IV-34. The first three sets of figures give the entry-site footprints and spacecraft-look-direction dispersion ellipses for the three deflection modes as applied to the reference mission. The Mode 2 deflection has execution errors occurring both on the probe and on the spacecraft. Thus, it has the largest dispersions. The entry-site footprint is much smaller for Mode 3 than for Mode 1 because there is no deflection ΔV execution errors given the probe at release in Mode 3; the

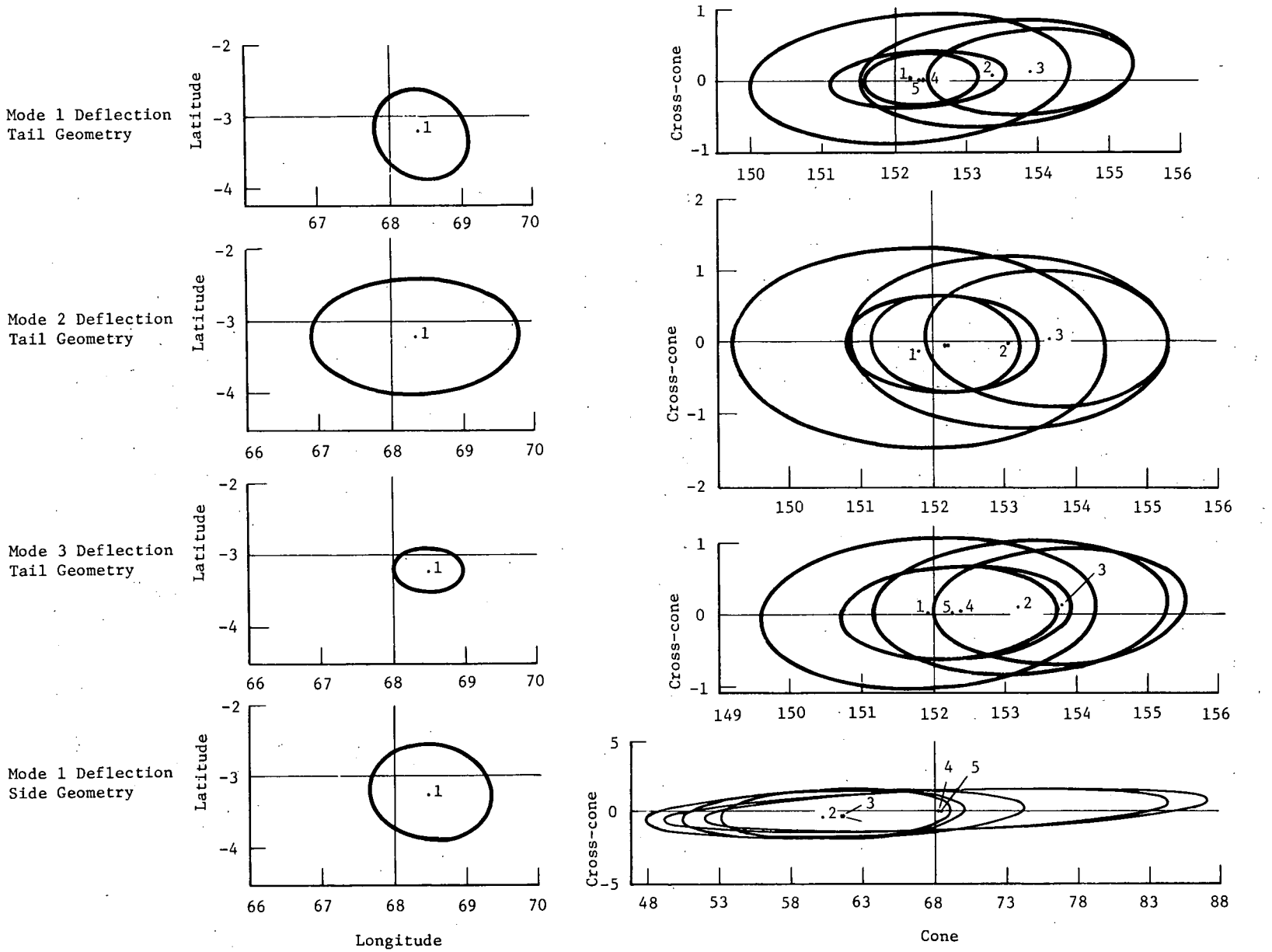

Fig. IV-34 Comparison of Dispersion for Deflection Mode and Communication Geometry

Mode 3 footprint is caused only by errors in knowledge and control. The spacecraft look direction dispersions are approximately the same for Mode 1 and Mode 3 because now execution errors are added in both modes--to the probe in Mode 1 and to the spacecraft in Mode 3.

b. Communication Geometry - A comparison of the dispersions resulting from the two candidate communication geometries is given by the first and last pairs in Fig. IV-34. Mode 1 deflection was used in both cases. The entry site dispersions are slightly larger for the side geometry because ΔV magnitude is slightly greater (106 vs 102 m/sec) and coast time is slightly longer (7.85 vs 7.82 days). The spacecraft look-direction dispersions are significantly larger for side geometry than for tail geometry. This is primarily caused by two effects. The spacecraft is nearer its periapsis and is therefore moving much faster during the mission performance phase in side geometry. Thus, timing uncertainties are more significant for this geometry. The second factor is the shorter range between the probe and spacecraft. This results in larger angular deviations for equivalent position deviations.

c. Periapsis Radius - Variation in dispersions caused by changing the periapsis radius is illustrated in Fig. IV-35. The dispersions are approximately linearly dependent on periapsis radius. This results from the larger required ΔV. Some relief is obtained by resorting to larger radii of deflection for the larger periapsis radii.

d. Entry Angle - Variation dispersions with entry angle is shown in Fig. IV-36. Trends here are mixed. Latitude and communication range dispersions increase with increasing entry angle. This is partly because of larger deflection ΔV required. Longitude and entry-angle dispersions increase with decreasing entry angle. This is due to the greater sensitivity of these parameters to lower entry angles. Angle of attack and probe aspect angle are insensitite to entry-angle variations.

e. Deflection Radius - Figure IV-37 shows the effects of deflection radius on dispersion. Here, the resulting dispersions form execution errors only, state uncertainties only, and the net effects of both are plotted individually. Dispersions resulting from uncertainties increase with increasing radius for all parameters. The effect of execution errors is variable. As radius increases, dispersions decrease for entry parameters and increase for communication parameters. This probably results from interaction between ΔV magnitude and coast time. The net effect generally increases with increasing deflection radius.

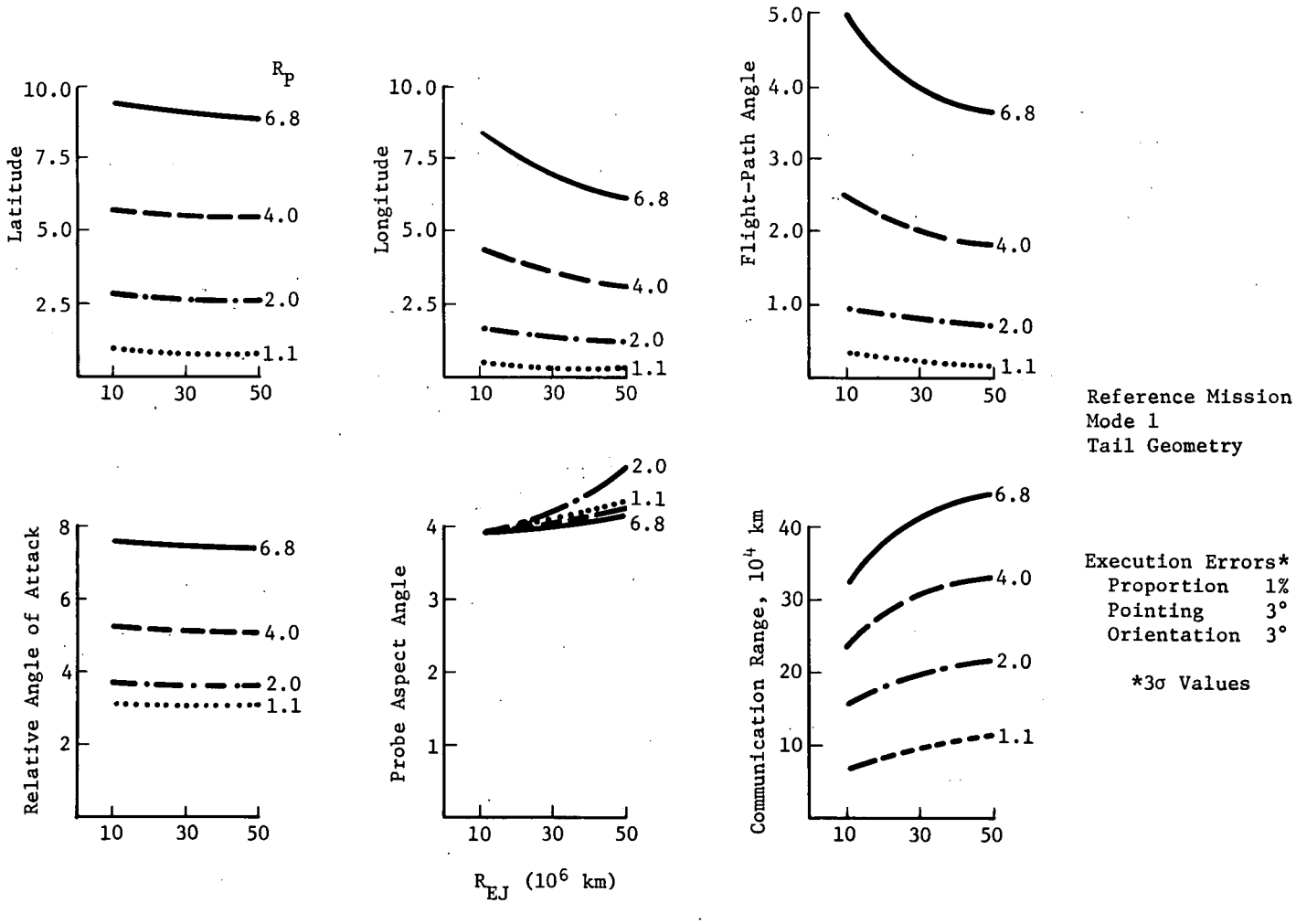

Fig. IV-35 Entry Dispersions in Periapsis Radius

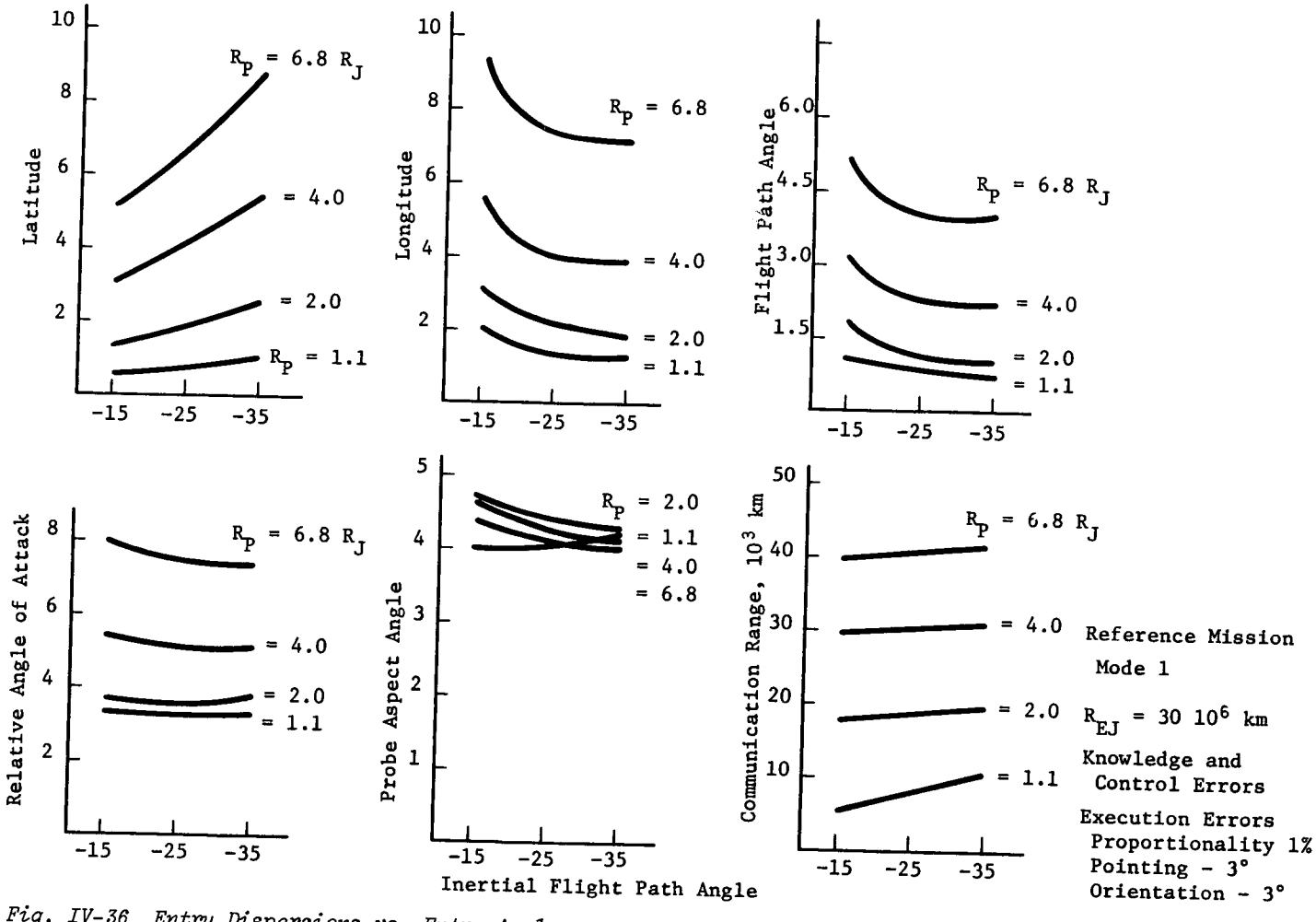

Fig. IV-36 Entry Dispersions vs. Entry Angle

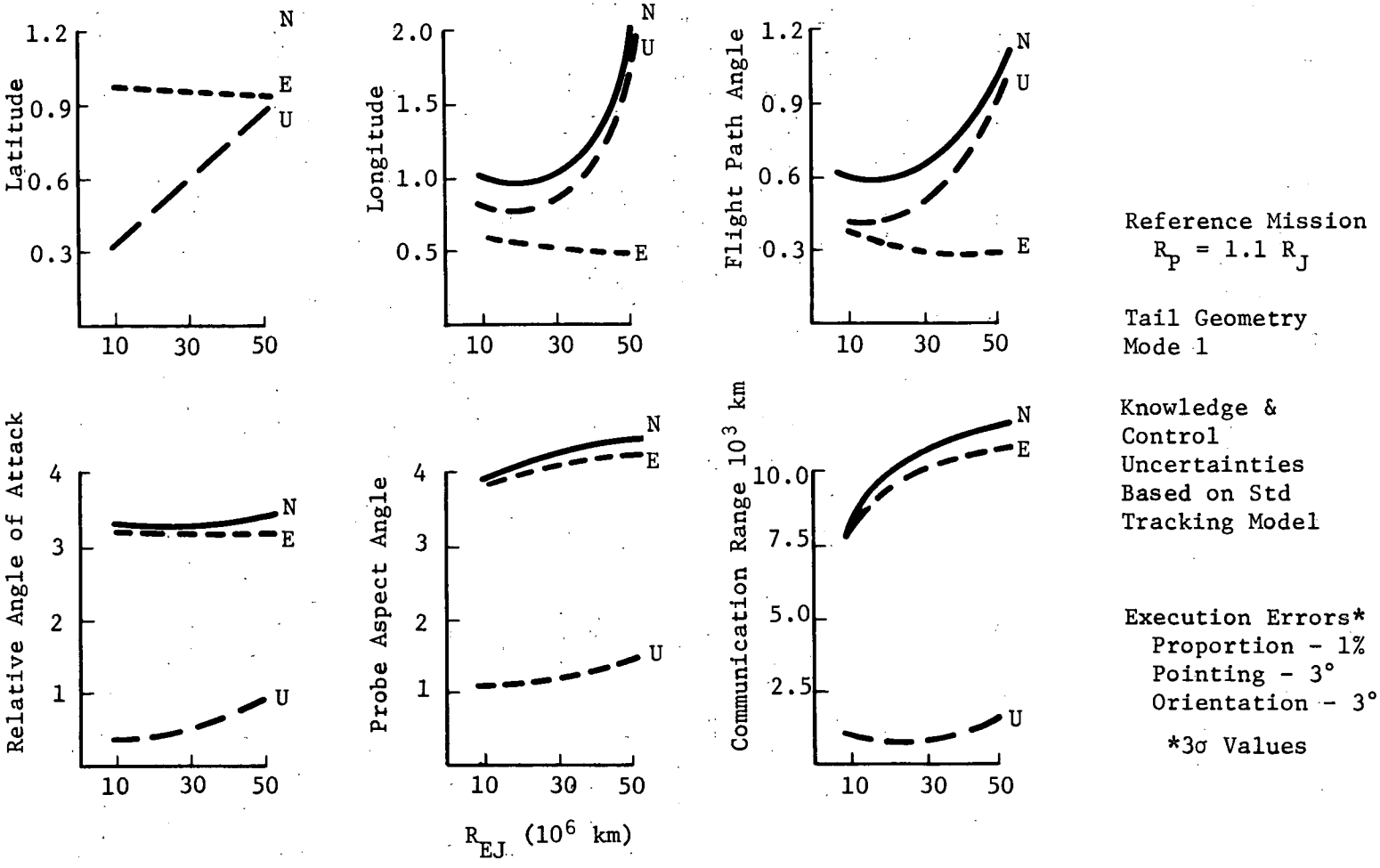

Reference Mission
$R_P = 1.1\ R_J$

Tail Geometry
Mode 1

Knowledge &
Control
Uncertainties
Based on Std
Tracking Model

Execution Errors*
Proportion - 1%
Pointing - 3°
Orientation - 3°

*3σ Values

E - Deflection Execution Errors Only
U - Knowledge & Control Only
N - Net Effect of Both

Fig. IV-37 Entry Dispersions vs. Deflection Radius

f. Execution Errors - Effects of execution error levels on dispersions are linear. Reducing the proportionality and pointing errors by half generally reduces dispersions by half. The orientation error of the probe essentially dominates the probe aspect angle and angle-of-attack dispersions.

G. REFERENCES

IV-1 R. H. Battin: *Astronautical Guidance*, McGraw Hill Book Co., New York, 1964.

IV-2 *Titan III/Centaur Family Launch Vehicle Definition for a Jupiter Entry Mission Study*, Jet Propulsion Laboratory, Jan 4, 1970.

IV-3 "Updated Performance for Centaur D-1T and GT Concepts," Enclosure E, *Minutes of Second Meeting OPGT Spacecraft - Launch Vehicle Interface Panel*, Jet Propulsion Laboratory, Dec 21, 1971.

IV-4 D. W. Curkendall and R. R. Stephenson: "Earthbased Tracking and Orbit Determination," *Astronautics and Aeronautics*, May 1970.

IV-5 D. W. Curkendall and J. P. McDanell: "An Investigation of the Effects of the Major Earth-Based Navigation Error Sources for and Outer Planet Mission," AAS Preprint 71-118, June 28, 1971.

IV-6 G. M. Levin and R. M. Goody: *The Jovian Turbopause Probe: Part I: The Scientific Requirements for the Jovian Turbopaus Probe*. Document GSFC X-110-70-442, December 1970.

IV-7 G. M. Levin and C. K. Wilkinson: *The Jovian Turbopause Probe - Part III - Mission Analysis*, GSFC X-110-71-218, May 1971.

IV-8 D. Vogt *et al.*: *Computer Program for Mission Analysis of Lunar and Interplanetary Missions*, NASA Contract NAS 5-11795, Goddard Space Flight Center, Greenbelt, Maryland, 1971.

IV-9 Personal Communication from Louis Friedman, JPL, to T. C. Hendricks, Martin Marietta Corporation, Jan 1971.

IV-10 D. W. Curkendall and R. R. Stephenson: "Earthbased Tracking and Orbit Determination," *Astronautics and Aeronautics*, May 1970.

IV-11 *Brief Summary of DSN Capabilities for Jupiter Atmospheric Probe Mission (1978 Launch Opportunity)*, Jet Propulsion Laboratory Document 131-11, 30 March 1970.

IV-12 W. G. Melbourne: "Planetary Ephemerides," *Astronautics and Aeronautics*, May 1970.

IV-13 Personal Communication from W. J. Klepczynski, Naval Observatory, to H. A. Garcia, Martin Marietta Corporation, June, 1971.

IV-14 V. N. Dvornychenko: *A Model for the Pioneer F & G Midcourse Execution Errors*, TRW Document 13432-6013-RO-00, Sept 22, 1970.

IV-15 "Functional Requirement: Corrective Velocity and Navigation Accuracy Requirement," *TOPS Spacecraft Design Book*, Jet Propulsion Laboratory Document TOPS-3-150, May 5, 1971.

V. SAMPLE MISSIONS/SYSTEMS DESCRIPTIONS

This chapter presents detailed descriptions of each of the sample mission designs. Emphasis is on describing the mission operation, configuration definition, and hardware implementation required to meet the objectives of each mission. Parametric and trade studies for these engineering designs are in the other chapters of this volume, along with the rationale for design and discussions of the advantages and disadvantages of various approaches in subsystem areas. Descriptions in this chapter represent typical integrated system designs that provide practical engineering solutions for missions of interest.

A. MISSION-SELECTION RATIONALE

One of the basic intents of this study was to investigate a broad range of mission options to demonstrate the effects of various constraints on system design. The study included probe-optimized missions as well as missions in which the probe is a passenger on a spacecraft with postencounter objectives. The Grand Tour and dual-planet missions such as Jupiter/Saturn 1977 (JS 77), as well as the solar apex mission in 1978 are examples of this type.

Early in the study, a reference mission was defined that helped identify general bounds of the problem and focused and guided parametric and tradeoff efforts within pertinent ranges of study. The reference mission also provided a focus for system-level integration problems. After the first three months of study, a set of missions was selected for more detailed system-level definition; these are listed in Table V-1, from 1 through 6. Missions 7 and 8 were added later in the study by GSFC because of increasing NASA interest in the Jupiter-Saturn flyby opportunities.

Missions 1A, 2A, and 7 have been refined to incorporate an updated model of the wake electron density. These missions were selected for refinement because they best represent a broad range of typical designs. Mission 1A represents the probe- and science-optimized design, which incorporates a simplified probe with neither an attitude-control system nor deflection propulsion. Mission 2A considers the radiation hazard to the spacecraft that restricts the spacecraft's nearest approach to 4 R_J. Mission 7 was chosen because of recent interest in this launch opportunity as a possible early mission.

Table V-1 Design Missions

Mission	Launch Vehicle	Spacecraft	Launch Date	Arrival Date	TOF, days	Deflection			R_P, R_J	Entry Angle, γ_E, deg	Science Data Rate, bps	Depth of Study	Remarks
						Mode	Radius, 10^6 km	Velocity, m/sec					
1 Probe Optimized	Titan IIID/ 5-seg/Centaur/ Burner II	Pioneer	10/21/78	12/26/80	797	S/C	30	16	1.1	-21	934	Complete system description	
1A Probe Optimized/ Science Optimized			10/21/78	11/19/80	760	S/C	10	54.6	1.1	-23.2	1300		Refinement of 1; reduced transmitter power rqmt used to increase data rate
2 Radiation-Compatible Spacecraft			10/13/78	7/29/80	655	S/C	50	101	4.0	-29.0	914		
2A Radiation-Compatible Spacecraft			10/13/78	7/29/80	655	S/C	50	101	4.0	-29.0	914		Refinement of 2; X-band transmitter reduces total power reqd
3 Grand Tour JUN 78	Titan IIID/ 7-seg/Centaur (w/wo Burner II)	TOPS	10/3/78	5/1/80	576	Probe	30	82	1.94	-33.0	958		
4 Grand Tour JUN 79			11/5/79	6/8/81	581	Probe	50	243	9.85	-33.0	958	Mission analysis & communications	Transmitter power rqmt high; large battery load; large ΔV required
			11/11/79	5/2/81	538	Probe	50	180	6.6	-34.0	958		
5 Solar Apex 78	Titan IIID/ 5-seg/Centaur (w/wo Burner II)	Pioneer	10/9/78	4/1/80	540	Probe	30	75	1.77	-34.0	958	Complete system description	
6 JU 80	--	TOPS	--	--	--	--	50	400	>15	--	--	Mission analysis	Transmitter power prohibitive; ΔV rqmt also prohibitive
7 JS 77	Titan IIID/ 5-seg/Centaur (w/wo Burner II)	MOPS	9/5/77	3/1/79	557	Probe	50	130.7	4.85	-33.3	914	Complete system description	
8 JS 80	--		10/5/78	7/31/80	543	Probe	50	402.1	15.7	-34.0	--	Mission analysis	Transmitter power prohibitive; ΔV rqmt also prohibitive

B. MISSION 1 - PROBE OPTIMIZED

The objective of this mission/system design was to minimize probe system complexity, maintaining capability to meet the required science return. This was accomplished by designing the mission for a minimum R_p, with the most favorable communications geometry at probe atmospheric entry. Additionally, the mission uses a spacecraft deflection mode, eliminating the requirement for a probe onboard deflection propulsion system and attitude-control system.

This system requires the Pioneer spacecraft to orient itself for probe ejection, which results in a zero angle of attack for the probe at entry; spinup and release the probe; despin, reorient itself, and apply the necessary deflection propulsion (ΔV); reorient itself to Earth lock; and, at the end of the coast period, acquire the probe RF transmission and relay the data received to Earth.

Functional requirements of probe systems are limited to activation and operation of science instruments and data processing and transmission requirements.

Figure V-1 is a functional block diagram typical of the Mission 1 probe system. Table V-2 shows the Mission 1 sequence of events.

1. Science Payload and Performance

Instrument characteristics and mission performance for Mission 1 are shown in Table V-3. The primary difference between this and other missions is the dayglow instrument, whose data rate depends on probe spin rate. For this mission, the spin rate is 37.5 rpm. For a description of the contents of data words, see Chapter III, Section C, in the subsection describing the particular instrument. On the left side of the lower part of the table are the upper atmospheric and ionospheric performance, the criterion being one measurement per scale height. The lowest values are the heaviest particles of both neutrals and ions. For a detailed discussion of these numbers, see Chapter III, Subsections D1 and D3.

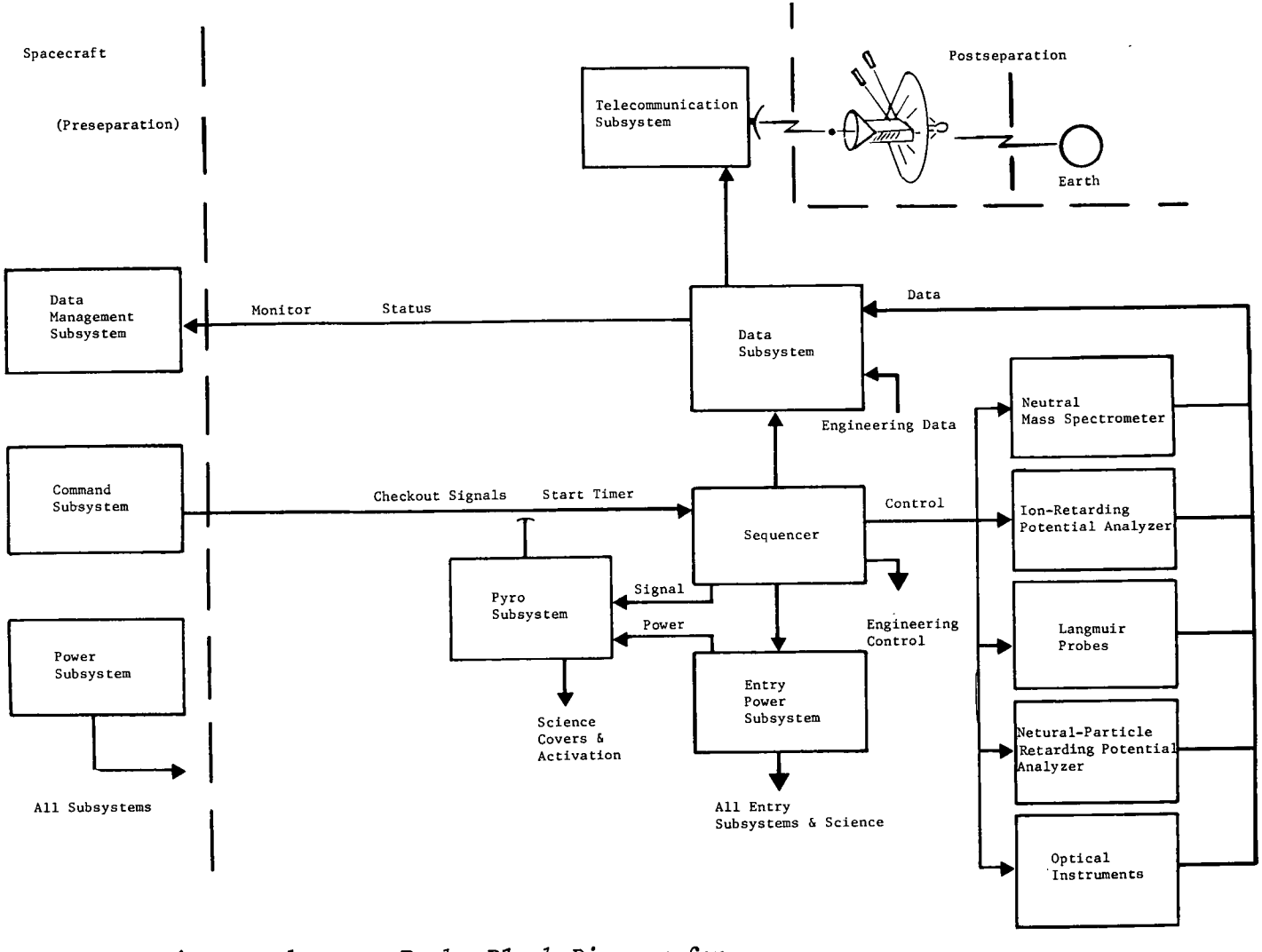

Figure V-1 Jupiter Turbopause Probe Block Diagram for Missions 1, 1A, 2, and 2A

Table V-2 Mission 1 Probe-Optimized Sequence of Events

Event	Time, hr:min:sec	Function
1	L	Launch October 21, 1978
2	L + 02:00:00	Separate S/C system from L/V; begin S/C cruise
3	S - 05:30:00	Separate environmental enclosure Supply S/C power to probe Begin probe checkout
4	S - 00:30:00	Complete probe checkout
5	S - 00:17:00	Orient S/C for probe release (-4°)
6	S - 00:15:20	Start S/C spin to 37.5 rpm
7	S - 00:12:00	Begin 12-min Langmuir probe decontamination
8	S - 00:00:20	Start probe timer; enable probe separation ordnance
9	S, L + 755 d	Separate probe
10	S + 00:01:40	Reduce S/C spin to 4.8 rpm (100-m separation)
11	S +	S/C reorientation (32°)
12	S +	S/C ΔV (16 m/sec)
13	S +	S/C reorientation (-28°) to Earth lock
14	T - 01:18:41	Enable battery activation
15	T - 00:58:41	Activate entry battery
16	T - 00:38:41	Energize probe bus
17	T - 00:38:31	Data system on
18	T - 00:38:16	Transmitter on
19	T - 00:37:56	Enable ordnance
20	T - 00:37:46	Fire pyros at 15-sec interval
21	T - 00:36:16	Start probe acquisition/disable ordnance
22	T - 00:35:16	Turn on instruments (ETP, IRPA, ORGS); complete probe acquisition
23	T - 00:34:46	Transmit instrument engineering data (ETP, IRPA, ORGS)
24	T - 00:32:46	Start data transmission (ETP, IRPA, ORGS)
25	T - 00:31:48	Start transmission of engineering data (including stored)
26	T - 00:13:08	Turn on instruments (MS, NRPA)
27	T - 00:11:08	Stop transmission of engineering (housekeeping) data
28	T - 00:09:08	Transmit MS & NRPA engineering data
29	T - 00:08:08	Start data transmission (MS, NRPA)
30	T	Turbopause
31	T + 2.9 sec	Blackout
32	L + 797 days	S/C periapsis; December 26, 1980

Includes 1.9-min trajectory uncertainty, 0.45-min timer uncertainty, and 5% of time from acquisition start to T = 0.

Table V-3 Mission 1 Science Instruments and Performance

Characteristics

Instruments	Weight, kg, lb		Power, W	Words/ Sample	Bits/ Sample	Sampling Time, sec	Science Bit Rate, bps
Langmuir Probes	1.36	3.0	3	3	24	0.5	48
IRPA	1.59	3.5	3	12	96	0.5	192
NRPA	2.27	5.0	5	14	112	0.5	224
Mass Spectrometer	5.90	13.0	15	22	176	0.4	440
Ultraviolet Spectrometer	1.59	3.5	5	3	24	0.8	30
Totals	12.71	28.0	31				934

Mission Performance

Particle	Measurement/ Scale Height
H	5.3
H_2	2.7
He	1.3
H_1^+ & e^-	10.4
H_2^+	8.3
H_3^+	4.7
He^+	4.9
HeH^+	2.0

Note: Entry Flight-Path Angle, $\gamma_E = -21°$

Mission Times from

50,000 km to turbopause (min) 28.7

1000 km to turbopause (sec) 47.5

Turbopause to blackout (sec) 2.9
(minimum time below turbopause)

Mass-Spectrometer Measurements
(0.4 sec each)

Above turbopause (+20 to 0 km) = 2.43

Below turbopause (0 to -60 km) = 7.30

Total (+20 to -60 km) = 9.73

2. Mission Description

The interplanetary trajectory for Mission 1 was selected to obtain an entry angle as low as possible $\left(\gamma_E = -21°\right)$ consistent with the 20° lighting mask and a reasonable launch period. The spacecraft flyby radius (following deflection) was selected to be as small as practical $\left(R_P = 1.1\ R_J\right)$ to enhance the communication link. Interplanetary and approach trajectories are shown in Fig. V-2.

To simplify mission implementation, the spacecraft deflection mode (Mode 3) was used. To reduce deflection ΔV, a 30×10^6km deflection radius was selected. Thus, the spacecraft trajectory is targeted to impact the entry site. At the deflection radius, the probe is released and the spacecraft deflected to fly by at $1.1\ R_J$. The operational sequence for the deflection maneuver is also shown in Fig. V-2.

The launch analysis is summarized in Table V-4. The resulting launch period for the Titan IIID-5-segment Centaur-Burner II launch vehicle is 15 days using standard data and 19 days using updated data.* The daily launch window (1.1 hr) just satisfies the 1.0-hr minimal value.

Navigation and guidance aspects of the mission are summarized in Table V-5. The spacecraft must have propellant for midcourse ΔV of 4.8 m/sec. The knowledge and control uncertainties mapped into impact plane coordinates (See Section IV E1.) are provided in the table. These uncertainties are optimistic because they are generated assuming a good spacecraft approach from a navigational standpoint. More realistic numbers were used in Mission 1A. (See Subsection IV E4a.)

Deflection execution errors and entry dispersions are summarized in Table V-6. The proportionality error of $3\sigma_K = 1\%$ requires an inflight calibration of the spacecraft (Pioneer) engines. Probe orientation and ΔV pointing errors are small because of small rotations off Earth-lock that are required (-4 and 28°, respectively). Dispersions are all within acceptable tolerances.

---

* See Section IV C1 for launch-vehicle description.

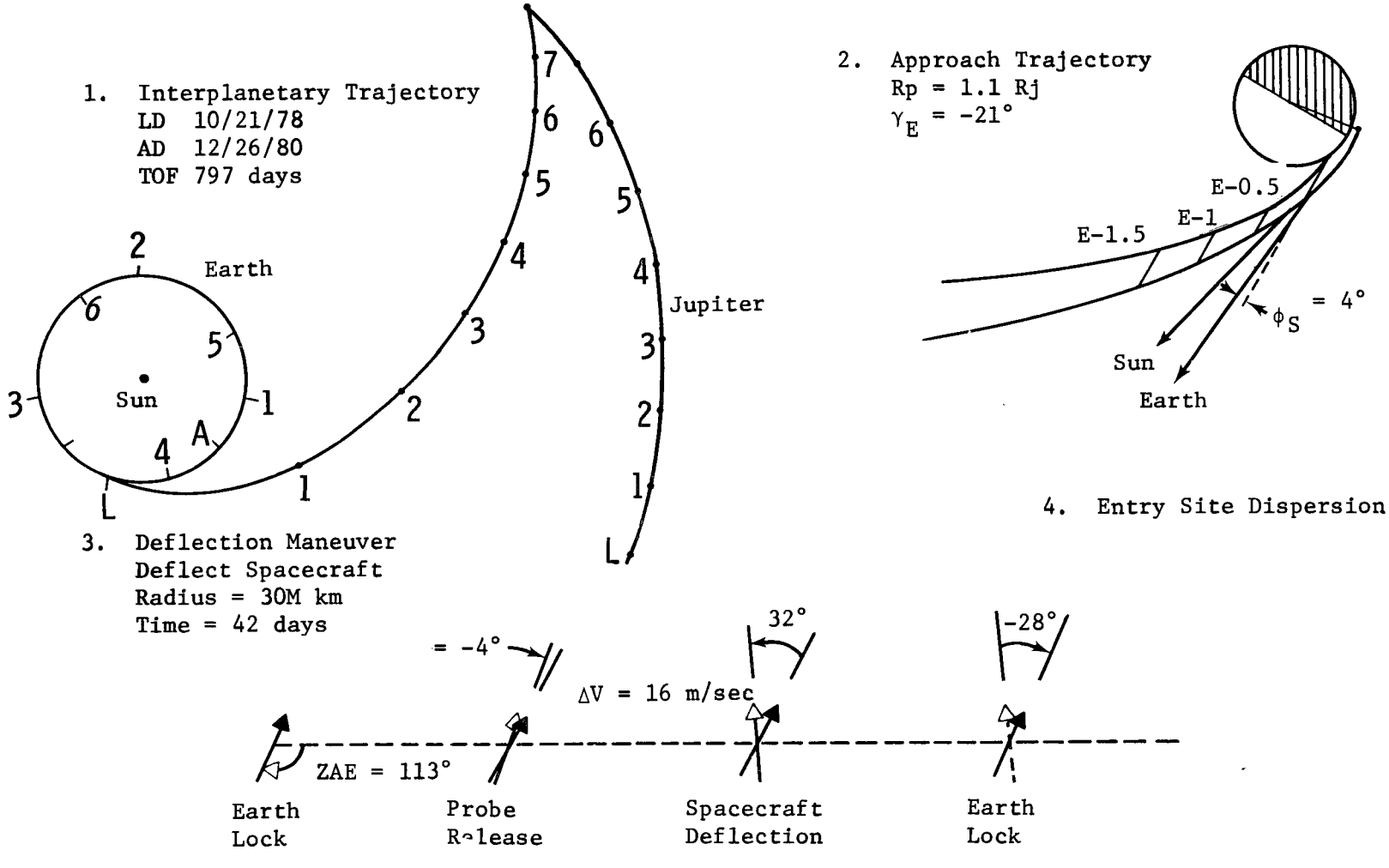

Figure V-2 Probe-Optimized Mission 1 Trajectories

Table V-4 Summary of Launch Requirements for Mission 1

Payload Summary	kg (lb)	Nominal Launch		Launch-Period Analysis			
Probe (15% margin)	61(135)	C_3, km^2/sec^2	104	Vehicle	Titan III/5-seg Centaur		
					Burner II	Burner II*
S/C Mods (15% margin)	41(91)	Park Orbit Time, hr	0.7	C_3, km^2/sec^2	108	135	148
Spacecraft (no margin)	248(547)	Launch Window, hr	1.1	Period, days	6	15	19
Adapter (15 % margin)	29(63)	DLA, deg	34				
Total	379(836)						

* Updated

Table V-5 Summary of Navigation and Guidance Analysis for Mission 1

Midcourse Requirements, m/sec				Navigation Uncertainties, 1σ			
	Mean ΔV	σ	ΔV + 3σ		SMAA, km	SMIA, km	TOF, sec
First Midcourse	14.3	10.4	45.5	Control	948	610	38
Second Midcourse	5.7	4.0	17.7	Knowledge	811	601	35
Total, RSS			48.8				

Table V-6 Summary of Execution Errors and Entry Dispersions for Mission 1

Deflection Execution Errors, 3σ			Entry Dispersions, 3σ			
	ΔV	Probe Attitude	Latitude, deg	0.3	Entry Angle, deg	0.9
Proportionality, %	1.0		Longitude, deg	0.6	Angle of Attack, deg	1.4
In-Plane Pointing, deg	1.0	1.0				
Out-Plane Pointing, deg	1.0	1.0	Coast Time, min	1.9		

3. Configuration

The configuration for Mission 1 is a simple probe with no ACS or deflection propulsion required and consists of a hemispherical forward section and cylindrical aft section. The basic probe is 0.71 m (28 in.) in diameter and 0.56 m (22 in.) long, as shown in Fig. V-3 and V-4.

Science experiments are integrated in the overall probe design, constrained by their functional requirements. The mass spectrometer, IRPA, NRPA, and Langmuir probes all require unobstructed access to atmospheric particles during entry. This requirement is met by placing the neutral mass spectrometer inlet directly at the nose-cap stagnation point and the RPAs at approximately one body radius from the Z axis at the same body station as the stagnation point of the probe nose cap. Reference V-1 includes studies of two other locations for RPAs (just off the dome/cylinder juncture and at the stagnation point) and the position shown has approximately half the reflected particle interference of other locations considered. The mass spectrometer is vented to the probe's wake through a 2.5-cm (0.98-in.) tube as shown in Fig. V-4. The Langmuir probes extend radially from the cylindrical section when deployed. They are not placed symetrically on the probe because of their required position relative to the optical spectrometer aperture cover, which is used to retain the probes in the stowed position. To meet the scientific requirements, the probe sensors are at the ends of 35.6-cm-long (14-in.) guards, with one sensor parallel and the other perpendicular to the probe Z axis. This probe has been modified in Mission 1A because of newer science requirements. The optical spectrometer viewing aperture is in the cylindrical portion of the probe body providing adequate viewing and placing the viewing port in an area of low entry heating. Location of the aperture in the aft bulkhead or nose cap is not desirable because of Sun aspect angles and entry heating problems.

Interrelation of components of various subsystems and the relationship of one subsystem to others are considered in the integration of internal equipment in the probe. For example, power system components like batteries, filters, distribution boxes, electronics, and cabling are grouped to improve the power-subsystem mass fraction.

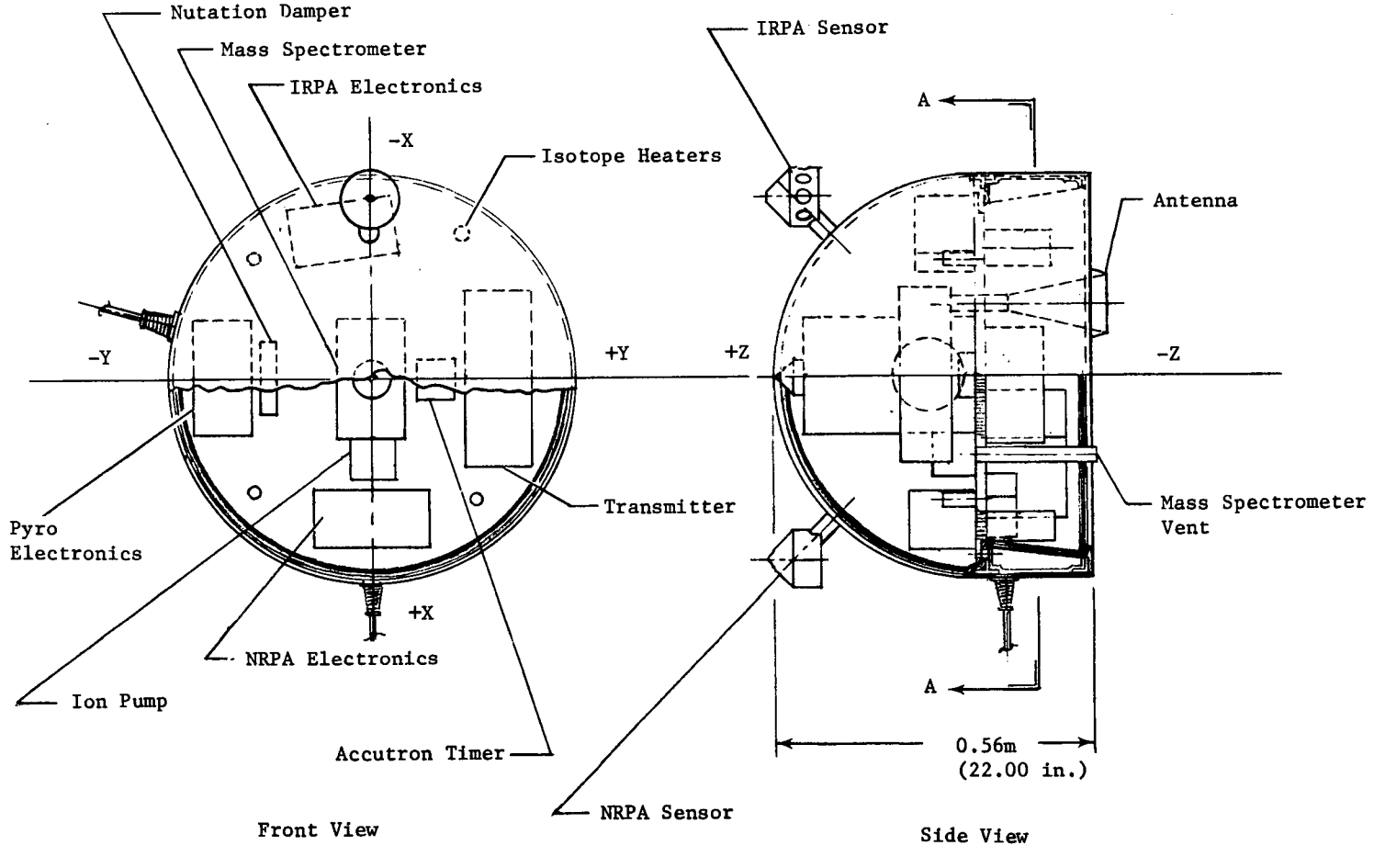

Figure V-3 Mission 1 Probe Configuration Front and Side

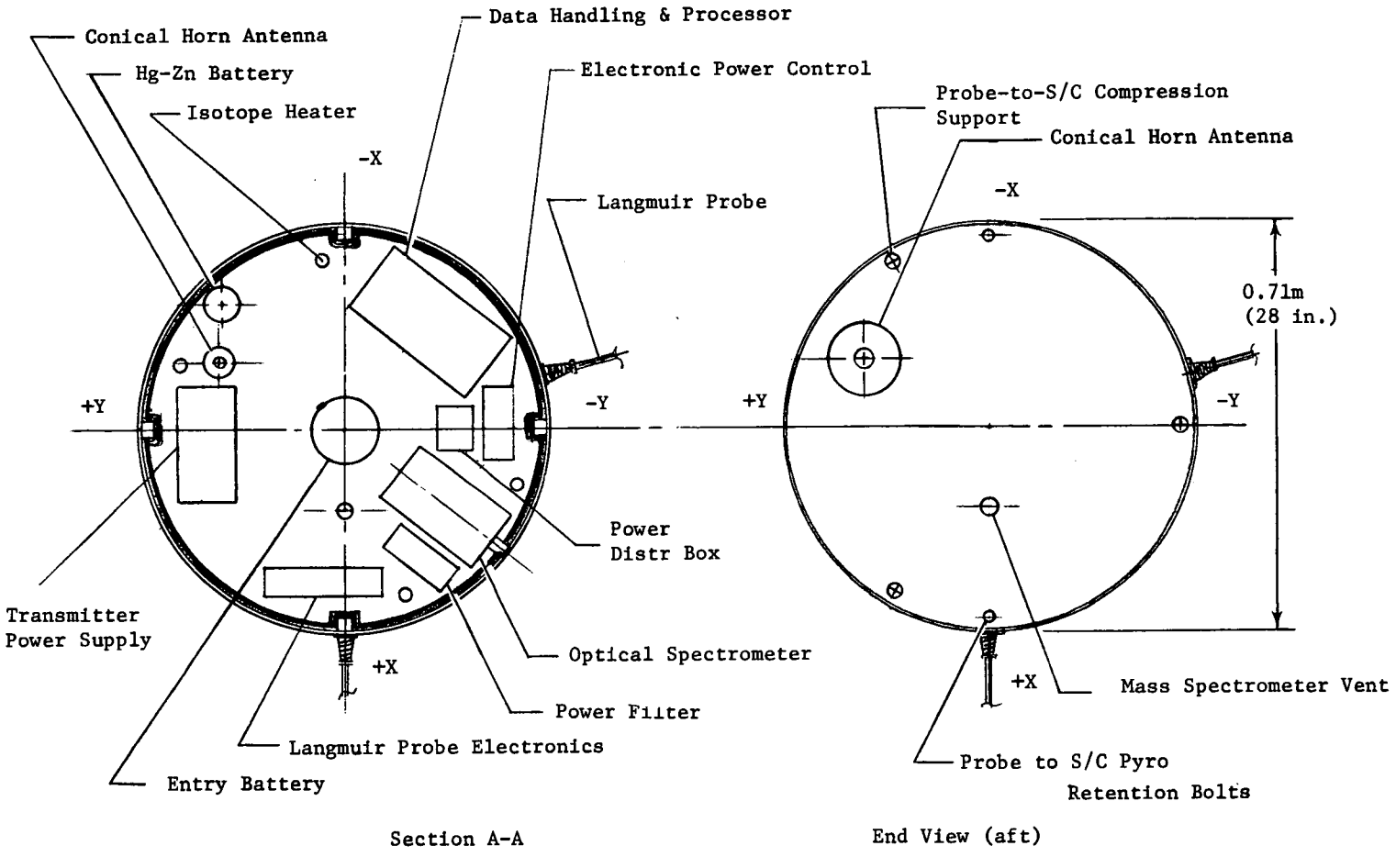

Figure V-4 Mission 1 Probe Configuration End and Section

The probe's transmitting conical-horn antenna is in the aft bulkhead and is aimed at the receiver on the trailing spacecraft to which it is transmitting. Location of the antenna relative to the transmitter is influenced by the desire for short direct waveguide coupling. The transmitter power supply is near the transmitter to reduce cabling and power losses.

The pyro system must operate or activate other subsystems throughout the probe. Therefore, its location is more flexible than those of other subsystems. Pyro system equipment includes electronics, capacitors, relays, and squibs.

A thermal blanket covers the entire inner surface of the probe structure except for the equipment deck, and ten 1-W radioisotope heaters are distributed inside the probe.

Spin stabilization of the probe requires that the mass moment of inertia about the Z-Z axis (spin axis) be greater than that about the transverse axes. It is desirable that the spin-axis mass moment of inertia be greater by 20% and that the mass moment of inertia about the X-X axis be equal to that about the Y-Y axis. A further requirement is that the principal mass moment of inertia coincide with the Z-Z axis of the probe. These requirements are met by properly locating components and by ballasting.

Probe support and retention locations are shown on the end view in Fig. V-4. Probe weight estimates are given in Table V-7.

a. Telecommunications - The RF link requires 12 W at K-band, with a 10° horn on the probe and an 8° dish on the spacecraft. Power requirements are moderate because of the low periapsis radius $\left(1.1\ R_J\right)$. Relative probe angular movement from nominal acquisition to entry is 5°. To cover both events with a 8° S/C antenna beam, the beam center is between the event, and entry is not centered near the maximum gain point, as seen in Fig. V-5. The spacecraft must have a despun platform with a single axis gimbal, which adds weight and complexity to the relay antenna subsystem.

Design details of the RF components that comprise the telecommunications subsystem are listed in Table V-8. Complete details are given in Chapter VI, Section A.

Table V-7 Mission 1 Weight Estimate

	kg	lb
Science	13.3	29.4
Structure & Heat Sink	12.6	27.8
Thermal Control	2.5	5.5
Guidance & Control (less propellant)	1.2	2.7
Deflection Propulsion (less propellant)	0.0	0.0
Communications	8.1	18.0
Data Handling	4.3	9.3
Electrical	6.8	14.9
Mechanisms	0.3	0.7
Pyro	2.5	5.6
Ballast	1.4	3.0
15% Design Margin	7.9	17.5
Total - Probe Coast	60.9	134.4
Solid Propellant +15%	0.0	0.0
Nitrogen Gas +15%	0.0	0.0
Covers	0.1	0.2
Total - Probe Ejected	61.0	134.6

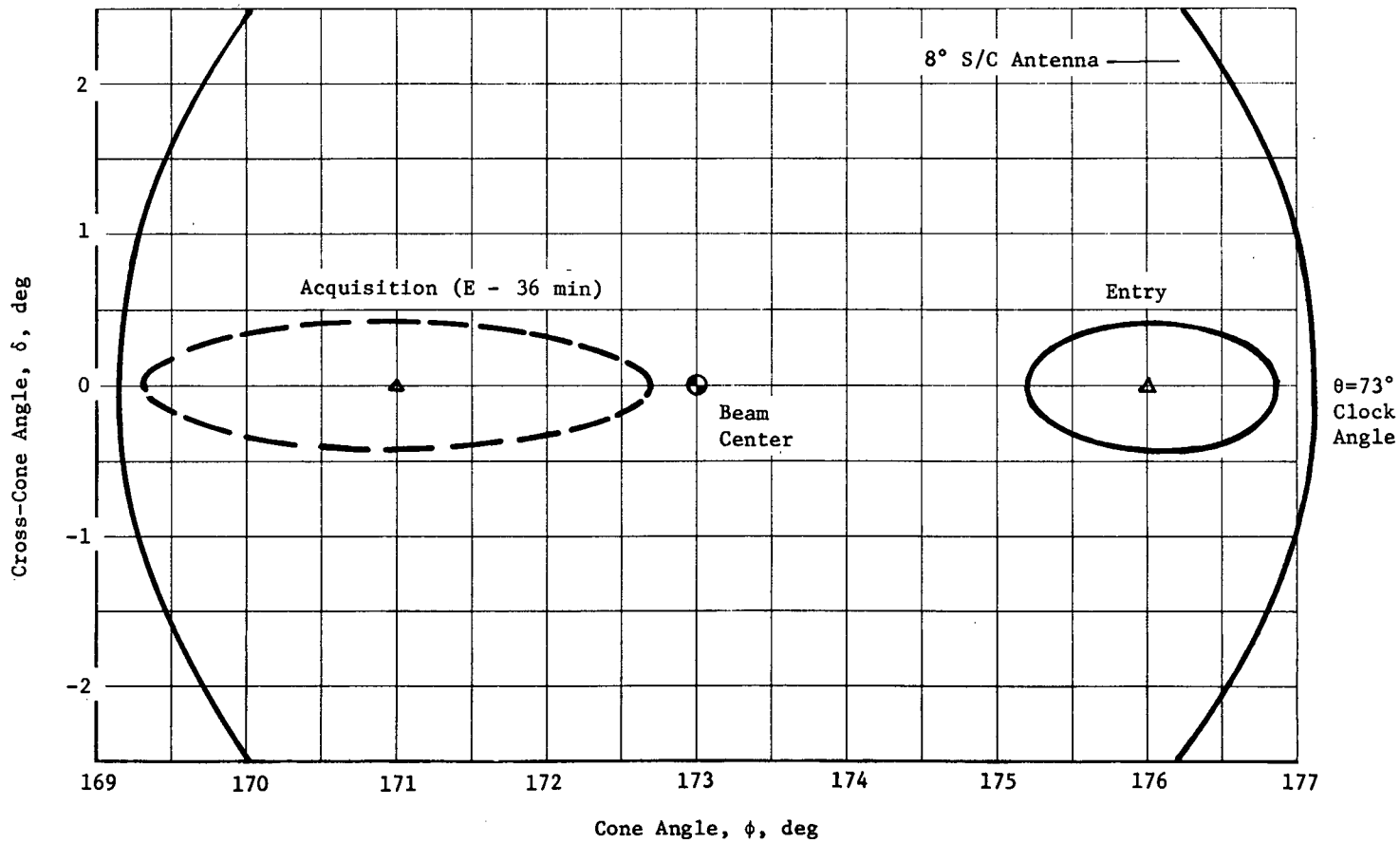

Figure V-5 Spacecraft-Antenna Requirements for Mission 1

Table V-8 Telecommunications RF Subsystem for Mission 1

Conditions:	S/C - Pioneer		Bit Rate - 1024 bps*	
			Value	
Component	Characteristic	Unit	K Band, 20 GHz	X Band, 10 GHz
Probe Conical-Horn Antenna	Electrical B/W	deg	10.0	10.0
	Max Gain	dB	23.4	23.4
	Dia	cm	9.8	19.6
		in.	3.8	7.6
	Total Length	cm	25.4	46.8
		in.	10.0	18.4
	Weight	kg	0.16	0.34
		lb	0.35	0.75
Transmitter & Power Supply	RF Power Out	W	8.0	3.0
	Overall Efficiency	%	24.0	24.0
	dc Power at 28 Vdc	W	33.4	12.5
	Total Weight	kg	7.7	7.7
		lb	17.0	17.0
S/C Dish Antenna	Electrical B/W	deg	8.0	8.0
	Max Gain	dB	26.3	26.3
	Dia	cm	13.3	26.6
		in.	5.25	10.5
	Weight	kg	9.07	.54
		lb	20.0	21.0
	Despin		yes	yes
	Position Search		no	no
	Freq Acquisition	sec	60.0	30.0
	Clock Angle, θ	deg	73.0	73.0
	Cone Angle, ϕ	deg	171-176	171-176
S/C Receiver	System Temperature	°K	400.0	315.0
	dc Power at 28 Vdc	W	10.0	10.0
	Weight	kg	5.9	5.9
		lb	13.0	13.0

*Science plus engineering

This mission was designed for K-band; however, subsequent analysis indicates a capability for an RF link requiring 3 W at X-band, with probe antenna requirements as shown in Table V-8.

b. Data Handling - Data handling for Mission 1 provides timing and sequencing, formating, A/D conversion, encoding, and limited memory capability where required. The configuration of the data handling subsystem is shown in Fig. V-6. Operation of the data handling system is initiated by the appearance of voltage on the power bus. A voltage sensor with a short time delay ensures that all semiconductor elements (timing function generator, sequence generator) are in the proper state. This is achieved by a single voltage discrete operating through diode logic. The system then sequences the vehicle engineering events like pyrotechnics, transmitter turn-on, and engineering measurements. Engineering data on these events and vehicle status will be stored for later transmission to the spacecraft because such information may provide additional insight for analysis of science data. There are two data modes used in this mission. The initial mode obtains data from the Langmuir probe, IRPA, and the photometers/spectrometer. During the final phase, the NMS and NRPA are activated. Before final high science-data rate, engineering measurements will be made by the science instruments.

Basically there are four types of memory functions required.

1) Nonvolatile memory that retains information for formating and sequencing - This may consist of hard wire, plated wire, or core memory functions. A design decision on the particular approach must be made on the basis of program schedule, function, and flexibility. The hard wire approach incurs the least development cost but entails expensive long turnaround periods with late modifications. Core memories have had successful space applications but nonvolatile readout may be a problem. Plated wire has significant implementation advantages, but some extensive development may be required for this program. Both of the latter alternatives allow valuable capability for reprogramming at any time before separation, but also increase cost, weight, and power;

2) Engineering data storage - This would be an electronic system with predominently hard-wired logic for storing temperature measurements and discrete events;

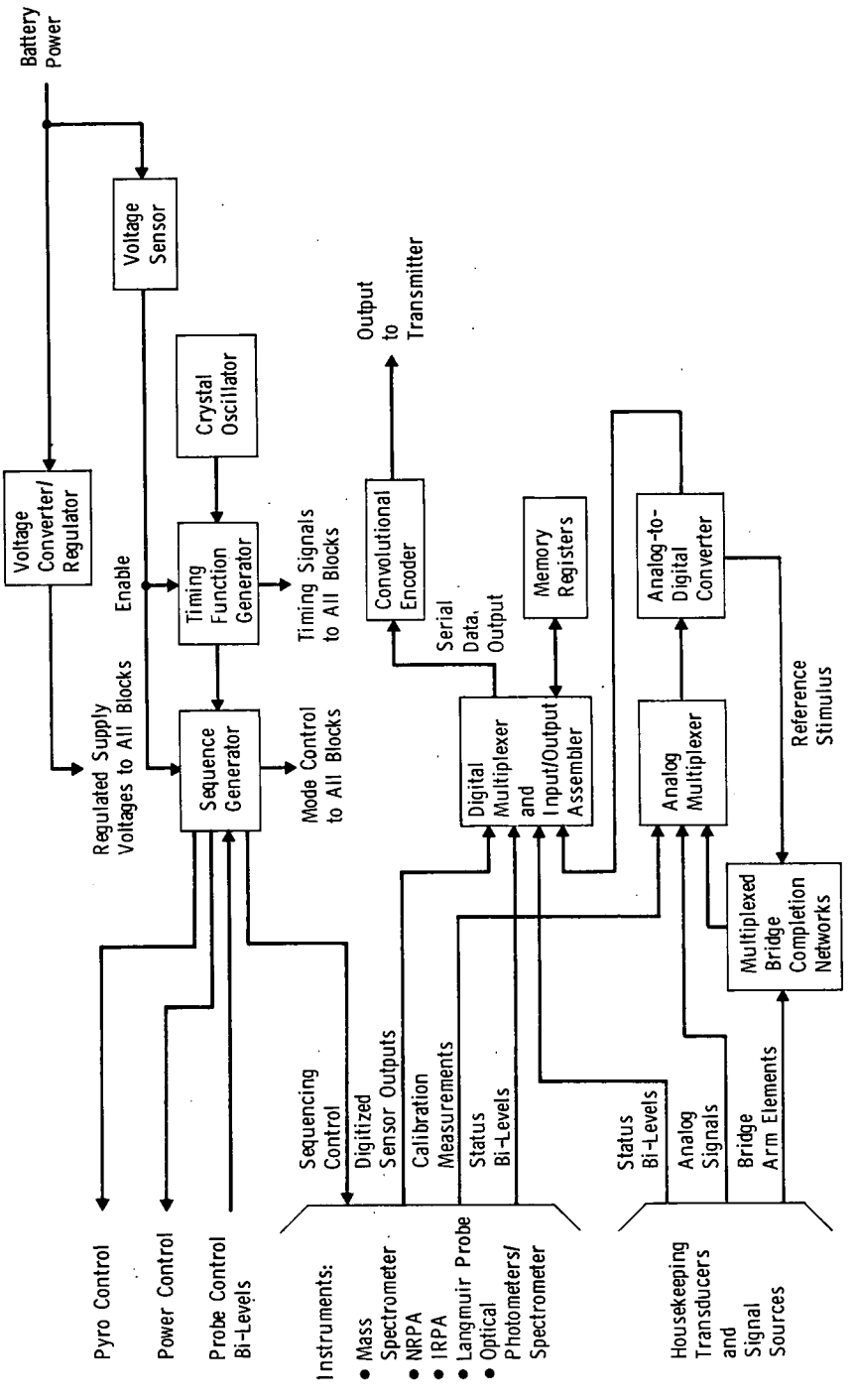

Figure V-6 Data-Management Unit

3) Langmuir probe data - The Langmuir probe sequence requires complete measurement of probe characteristic at discrete intervals. To prevent interruption of the continuous data stream, the characteristic data are stored and interleaved with the data stream;

4) Buffer memories are used for very short-term storage at the instrument science data interfaces because the instruments do not necessarily have coherent sampling rates. During the final high-data-rate period, formating will be optimized to reduce the delay of NMS data to a minimum. A model format has been generated that indicates that the maximum delay of NMS data can be held to 35 msec.

After formating and generation of the digital data stream, the binary information is convolutionally encoded. The principle reason for coding is reduction in transmitter power that can be obtained for systems that are not bandwidth limited. A secondary advantage is realized because increased bandwidth reduces the possibility of significant information power density in the spacecraft receiver phase-lock tracking loop and decreases the possibility of false lock. For these reasons, a convolutional code with a one-third rate and a constraint rate of four was selected. A further discussion of alternative approaches and format considerations for the data handling system is in Section B of Chapter VI.

c. Power Subsystem - The power subsystem consits of a primary battery power source, power-isolation filters, and a relay-controlled power distribution component. A functional block diagram of the subsystem is in Fig. V-7. Magnetic latching relays provide flexibility and reduced power during both preseparation checkout and the entry phase of the mission. A full range of battery types was considered and a duplex pile-construction remotely activated Ag-Zn battery selected. The remote activation mechanism employs a burst diaphragm to provide a path for the electrolyte to the cells, a flexible diaphragm for secondary driving pressure, and a pyrotechnically operated gas generator for primary driving pressure. This system has a weight advantage over the more common manifold system and results in a higher total system density. A more complete description of battery and power system tradeoffs is in Section C of Chapter VI.

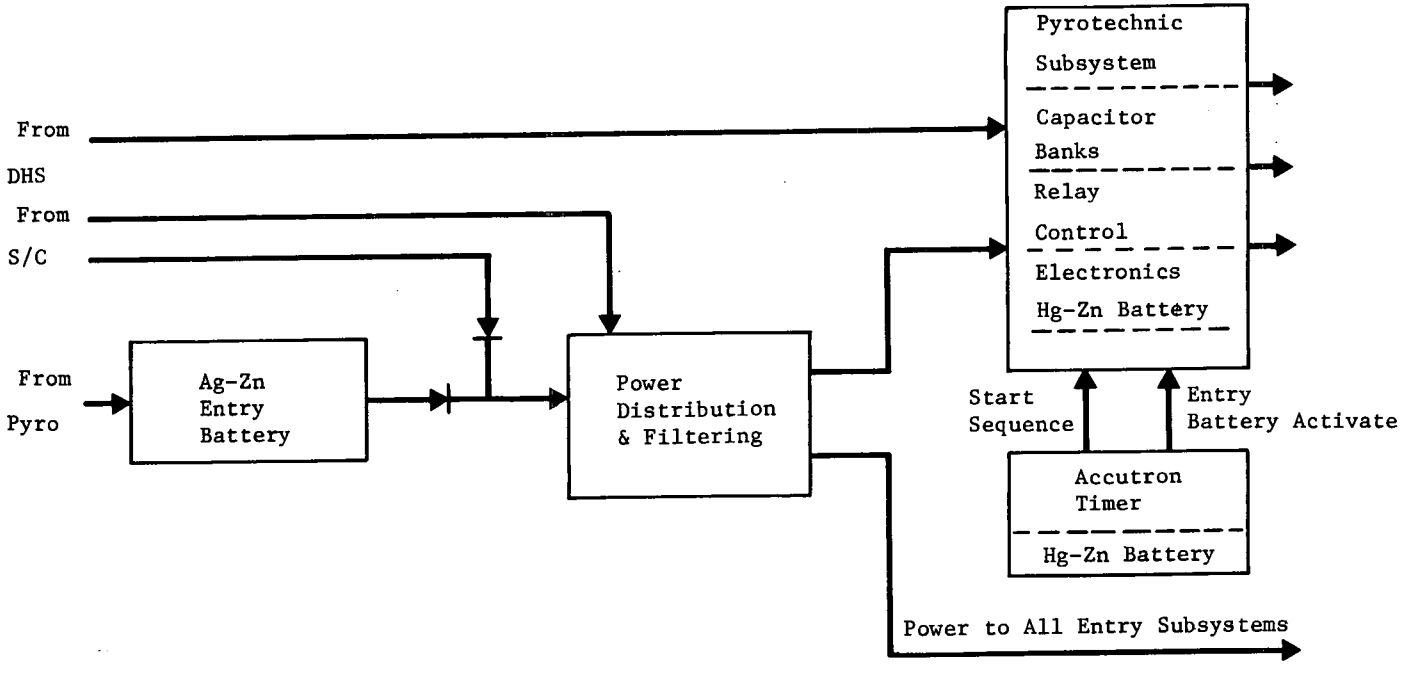

Figure V-7 Power and Pyrotechnic Subsystems

d. Pyrotechnic Subsystem - The pyrotechnic subsystem is similar to designs applied to several space vehicle configurations, such as Mariner and Viking. Specific constraints and devices considered were principally derived from Viking, which has severe restrictions on weight and radiation environment. The pyrotechnic subsystem consists of power-conditioning equipment, relay switching control, control logic, and capacitor banks for high-pulse discharge. (Fig. V-7.)

Pyrotechnic functions required for this mission are entry battery activation, mass spectrometer cover release, and photomter cover release. Physical parameters of the design are given in the table below.

	Electronics	Capacitor Banks	Relays
Weight, kg (lb)	0.91 (2.05)	0.36 (0.79)	0.59 (1.30)
Size, cm^3 ($in.^3$)	2100 (128.4)	655 (40.1)	230 (14.1)

Except for the entry battery pyro event, all power-conditioning required in the pyrotechnic control subsystem is generated by an internal power supply. Outputs are not regulated and have a tolerance of ±10%.

The supply has an output capability of approximately 50 W and a stand-by power dissipation of 450 mW. Because the supply is essentially on standby at all times, except for approximately 5 sec after each event, the assumed average power requirement is 0.5 W.

Except for the entry battery pyrotechnic event, all pyrotechnic event control is provided through the data management subsystem. The control signal is in the form of parallel digital-address, enable, fire, and safe commands. The pyrotechnic subsystem is enabled by applying power through a power-control relay in the power distribution control. For a more detailed discussion of the pyrotechnic subsystem refer to Chapter VI, Subsection C2.

e. Heat Sink and Structure - The heat sink consists of a 0.713-m-dia (28-in.) hemispherical beryllium nose cap and cylindrical skin on the skirt assembly weighing 6.6 kg (14.5 lb). The nose cap is plated with platinum or rhodium to preclude beryllium particle emission. It is 0.55 cm (0.216 in.) thick at the stagnation point and 1.4 mm (0.055 in.) thick at the trailing edge.

C.4

The structure consists of conventional aluminum machinings, bonded aluminum honeycomb, and bonded fiberglass/composite structures.

f. Thermal Control - The thermal control subsystem consists of an internally mounted multilayer insulation blanket surrounding the probe interior equipment, and an insulating cover for the optical spectrometer aperture (removable before entry), and radioisotope heaters placed where space is available between the internal equipment packages. The multilayer insulation blanket consists of 72 layers of 1/4 mil Kapton polyimide film aluminized on one side with beta glass cloth spacer material between layers. Total blanket thickness is 1.53 cm (0.6 in.) Ten 1-W radioisotope heaters are required (based on analysis), although it is expected that the actual requirement could be 8 to 12 W, depending on results of thermal testing of actual probe hardware.

g. Mechanical Subsystems - Mechanical subsystems consist of the optical spectrometer aperture cover and release and probe-to-spacecraft separation systems. Both are described in detail in Subsection A3 of Chapter VII. The Langmuir probes are retained in the stowed position by the photometer aperture cover.

h. Attitude Control - The attitude-control requirements for this mission are met by using spin stabilization and a passive damper. The probe is released from the spacecraft in the final entry attitude, spinning at approximately 3.93 rad/sec (37.5 rpm). Pointing errors are functions of spacecraft attitude accuracy, tip-off rates and spin rates. The present estimate of Pioneer attitude accuracy off Earth lock is 4% of the maneuver angle, which is 4° for this mission. High separation rates are not required and low tip-off rates (1°/sec) may be obtained. In practice, these errors are combined statistically as described in Chapter IV.

A passive damper is used to remove nutation. It is estimated that a damper 12 cm (3.6 in.) in diameter will provide a time constant of 20 hr for this probe. Because coast time will be about 40 days, completely adequate damping will be achieved. A more complete discussion of the damper is in Chapter VIII.

4. Spacecraft Interface Modification and Launch Vehicle

The Pioneer spacecraft with probe is launched on a Titan IIID-5-segment-Centaur-Burner II. The following components are either modified or added to the spacecraft for probe support or mission operation: probe support structure, environmental enclosure, electrical cabling and interface connector, receiver subsystem, despin and gimbal tracking antenna and platform, and data handling. Modification weight to the spacecraft is 41.4 kg (91.3 lb). The integration arrangement is shown in Fig. V-8.

C. MISSION 1A - PROBE AND SCIENCE OPTIMIZED

The objective of this mission/system design was to enhance science data return of the probe to the maximum within the capability of the system. Hence, the data return would not be limited to basic data necessary to answer science questions. Additionally, completion of the tasks of evaluating the electron density in the wake of the probed allowed refinement of the RF system (from K band to X band), requiring less probe power and increasing telecommunications reliability.

Operationally, the system performs the same as in Mission 1--a spacecraft deflection mode is used, eliminating the need for a probe onboard deflection propulsion system and attitude-control system.

The system requires the spacecraft to orient itself for probe ejection on a trajectory that results in a zero angle of attack for the probe at entry; spin up and release the probe; despin, reorient itself, and apply the necessary deflection propulsion (ΔV); reorient itself to Earth lock; and, at the end of the coast period, acquire the probe RF transmission and relay the data received to Earth.

Functional requirements of the probe systems are limited to activation and operation of the science instruments, data processing, and data transmission to the S/C. Figure V-1 shows the system functional block diagram and Table V-9 the sequence of events for the mission.

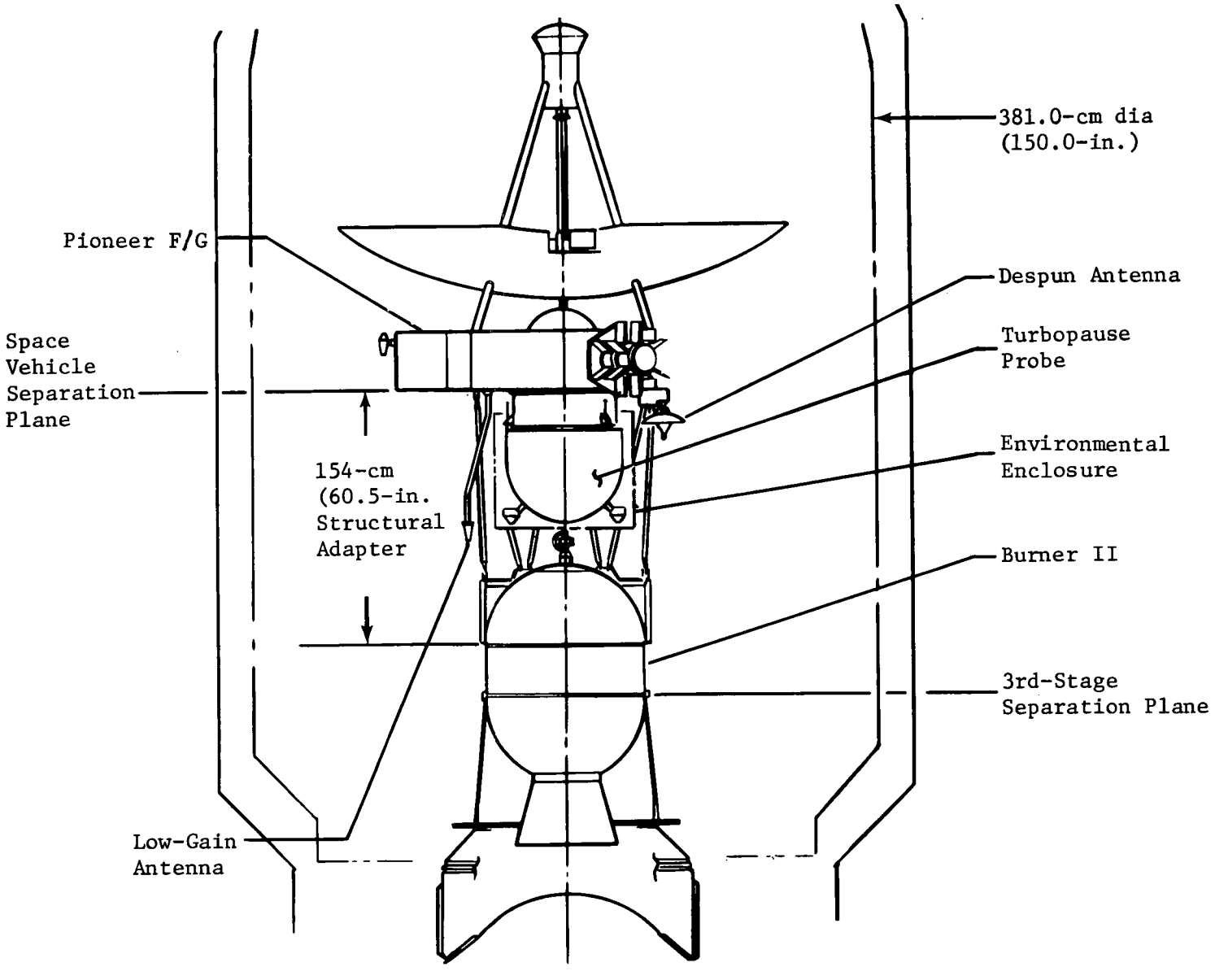

Fig. V-8 Probe-Spacecraft Interface for Mission 1

Table V-9 Mission 1A Probe-Optimized/Science-Optimized Sequence of Events

Event	Time, hr:min:sec	Function
1	L	Launch October 21, 1978
2	L + 02:00:00	Separate S/C system from L/V; begin S/C cruise
3	S - 05:30:00	Separate environmental enclosure Supply S/C power to probe Begin probe checkout
4	S - 00:30:00	Complete probe checkout
5	S - 00:17:00	Orient S/C for probe release (1°)
6	S - 00:15:20	Start S/C spin to 20 rpm
7	S - 00:12:00	Begin 12-min Langmuir probe decontamination
8	S - 00:00:20	Start probe timer; enable probe separation ordnance
9	S, L + 749 d	Separate probe
10	S + 00:01:40	Reduce S/C spin to 4.8 rpm (100-m separation)
11	S +	S/C reorientation (33.1°)
12	S +	S/C ΔV (54.6 m/sec)
13	S +	S/C reorientation (-34.1°) to Earth lock
14	T - 01:20:35	Enable battery activation
15	T - 01:00:35	Activate entry battery
16	T - 00:40:35	Energize probe bus
17	T - 00:40:25	Data system on
18	T - 00:40:10	Transmitter on
19	T - 00:39:50	Enable ordnance
20	T - 00:39:40	Fire pyros at 15-sec interval
21	T - 00:38:10	Start probe acquisition/disable ordnance
22	T - 00:37:10	Turn on instruments (ETP, IRPA, ORGS); complete probe acquisition
23	T - 00:36:40	Transmit instrument engineering data (ETP, IRPA, ORGS)
24	T - 00:34:40	Start data transmission (ETP, IRPA, ORGS)
25	T - 00:33:40	Start transmission of engineering data (including stored)
26	T - 00:12:09	Turn on instruments (MS, NRPA)
27	T - 00:10:09	Stop transmission of engineering housekeeping data
28	T - 00:08:09	Transmit MS & NRPA engineering data
29	T - 00:07:09	Start data transmission (MS, NRPA)
30	T	Turbopause
31	T + 2.6 sec	Blackout
32	L + 760 days	S/C periapsis; November 19, 1980

Includes 5.52-min trajectory uncertainty, 0.12-min timer uncertainty, and 5% of time from acquisition start to T = 0 .

1. Science Payload and Performance

The shorter communication distance from spacecraft to probe for Mission 1 means that transmitter power requirements on board the probe are less than their maximum limit. Consequently, the maximum bit rate allowed by transmitter sizing is larger than for other missions. Because science data return is generally restricted by bit rate, the broadening of this limit means that a science-enhanced version of Mission 1 with additional return can be considered. This mission has been studied and is called Mission 1A.

Instrument characteristics and mission performance for Mission 1A are listed in Table V-10. The probe is spinning at 20 rpm. Table V-11 compares science data returned from Mission 1 baseline and Mission 1A enchanced. As can be seen, the return from each instrument has been increased. A full discussion of the increased science-return mode for the Langmuir probes is in Chapter III, Subsection C3. For the IRPA, the addition was in voltage words to ensure accurate interpretation of data. These are in addition to any voltage monitoring performed by engineering bit rate. For the NRPA, the number of current readings was increased by both reducing the voltage step size from 11 V/amu to 10 V/amu and by increasing the sweep range by 30 V. Also, 25% of the data words were designated as voltage readings to check for possible drift, especially across the dual range. The range of the mass spectrometer was extended by one isotope. This extension could be used in other ways, as explained in Chapter III, Subsection C4. For the dayglow measurement, the gain was in continuous monitoring so that a full dayglow profile is obtained each revolution as the probe descends. A full discussion of this is in Chapter III, Subsection C5.

The left side of Table V-10 shows upper atmospheric and ionospheric performance, the criterion being one measurement per scale height. The lowest values are the heaviest particles of both neutrals and ions. For a detailed discussion of these numbers, see Chapter III, Subsections D1 and D3.

Table V-10 Mission 1A Science Instruments and Performance

Characteristics

Instruments	Weight, kg, lb		Power, W	Words/ Sample	Bits/ Sample	Sampling Time, sec	Science Bit Rate, bps
Langmuir Probes	1.36	3.0	3	4	32	0.5	64
IRPA	1.82	4.0	3	12I + 2V	112	0.5	224
NRPA	2.49	5.5	5	18I + 6V	194	0.5	388
Mass Spectrometer	5.90	13.0	15	24	192	0.4	480
Ultraviolet Spectrometer	2.27	5.0	5	3	24	0.167	144
Totals	13.84	30.5	31				1300

Mission Performance

Particle	Measurement/ Scale Height
H	4.8
H_2	2.4
He	1.2
H_1^+ & e^-	9.5
H_2^+	7.5
H_3^+	4.3
He^+	4.4
HeH^+	1.8

Note: Entry Flight-Path Angle, $\gamma_E = -23.2°$

Mission Times from

50,000 km to turbopause (min) 27.6

1000 km to turbopause (sec) 43.1

Turbopause to blackout (sec) 2.6
(minimum time below turbopause)

Mass-Spectrometer Measurements (0.4 sec each)

Above turbopause (+20 to 0 km) = 2.19

Below turbopause (0 to -60 km) = 6.57

Total (+20 to -60 km) = 8.76

Table V-11 Comparison of Baseline and Enhanced Science

Instrument	Number of Data Words		Additional Science Return
	Baseline	Enhanced	
Langmuir Probe	3 (processed)	4 (processed)	Full I-V curve every 30th sample
IRPA	12 current	12 current & 2 voltage	Accurate check on possible voltage drive
NRPA	14 current	18 current & 6 voltage	Additional current readings Check on voltage drift (Also smaller step size)
Mass Spectrometer	22 (2 each for 11 isotopes)	24 (2 each for 12 isotopes)	Added voltage step, thus extended measurements
Optical Spectrometer	6 intensities/ rev (2 measurements)	48 intensities/ rev (16 measurements)	Full dayglow profile each revolution as probe descends

2. Mission Description

The interplanetary trajectory for Mission 1A arrives about one month earlier than Mission 1 in order to obtain alignment of the probe axis with the spacecraft axis and the direction to Earth. This results in a slight increase in entry angle to $\gamma_E = -23.2°$. (See Fig. V-9.) The spacecraft periapsis radius remains at $R_P = 1.1\ R_J$. For this mission, the spacecraft (Pioneer) can use a fixed antenna for the communication link.

The spacecraft defleciton (Mode 3) is used to simplify the probe. Deflection radius was decreased to 10×10^6 km to decrease the coast time and solve a navigational problem. (See Chapter IV Subsection E4.) The trajectories and deflection sequence are illustrated in Fig. V-9.

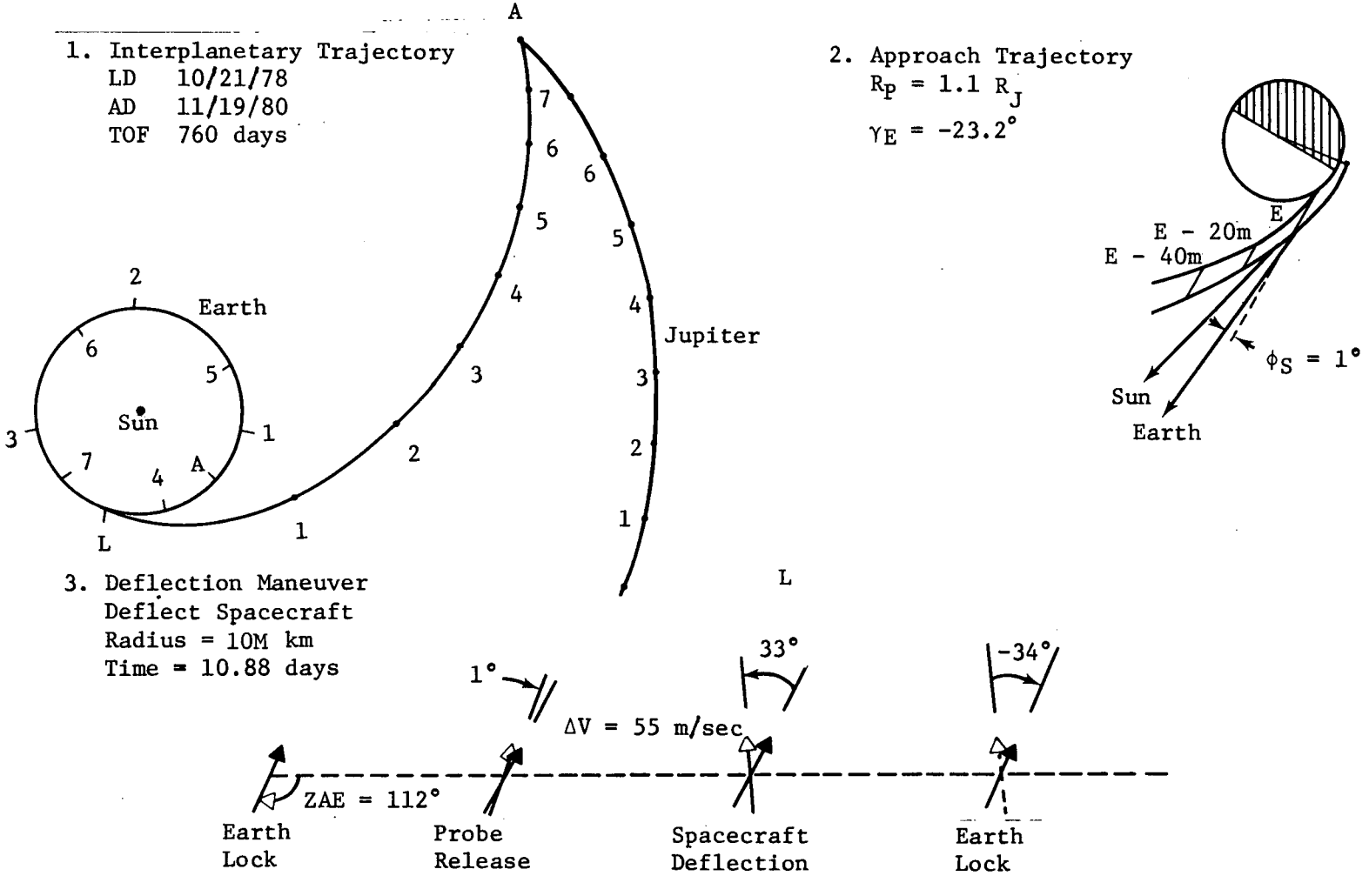

Fig. V-9 Mission 1A - Probe Optimized/Science Optimized Trajectories

The launch analysis (Table V-12) indicates a slight improvement in launch period over Mission 1. The launch periods are now 19 and 21 days for the standard and updated performances, respectively, for the Titan IIID-5-segment Centaur-Burner II launch vehicle.

The midcourse correction requirements shown in Table V-13 are the same as Mission 1. The navigational uncertainties indicated were developed for an actual Mission 1A approach trajectory instead of a typical approach. This resulted in larger uncertainties because of the zero geocentric declination encountered in that approach. (See Chapter IV, Subsection E4a.)

The deflection execution errors shown in Table V-14 are consistent with realistic Pioneer execution errors. (See Chapter IV, Subsection F2.) The entry dispersions remain within allowable tolerances.

3. Configuration

Configuration for Mission 1A is a simple probe with no ACS or deflection propulsion required and consists of a hemispherical forward section and cylindrical aft section. The basic probe is 0.71 m (28 in.) in diameter and 0.56 m (22.00 in.) long, as shown in Fig. V-10 and V-11.

Science experiments are integrated in the overall probe design, constrained by their functional requirements. The mass spectrometer, IRPA, NRPA, and Langmuir probes all require unobstructed access to atmospheric particles during entry. This requirement is met by placing the neutral mass spectrometer inlet directly at the nose-cap stagnation point and the RPAs at approximately 1 body radius from the Z axis at the same body station as the stagnation point of the probe nose cap. Reference V-1 includes studies of two other locations for RPAs (just off the dome/cylinder juncture and at the stagnation point) and the position shown in Fig. V-10 has approximately half the reflected particle interference of other locations considered. The mass spectrometer is vented to the probe's wake through a 2.5-cm (0.98-in.) dia tube as shown in Fig. V-11. An improved location for the Langmuir probes is 25 cm (9.8 in.) from the Z axis on the nose cap and a minimum of 6.5 cm (2.56 in.) between the sensor and the nose-cap surface. These probe sensors are 90° to the RPA with one sensor parallel and the other perpendicular to the probe Z axis, as shown in Fig. V-10. This arrangement reduces induced voltage transients caused by rotation within Jupiter's magnetic fields and eliminates the need for a deployment mechanism.

Table V-12 Summary of Launch Requirements for Mission 1A

Payload Summary	kg (lb)	Nominal Launch		Launch Period Analysis			
Probe (15% margin)	60(132)	C_3, km^2/sec^2	106	Vehicle	Titan III/ 5-seg/Cent	Titan III/5-seg/Centaur B II	Titan III/5-seg/Centaur B II*
S/C Mods (15% margin)	31(91)	Park Orbit Time, hr	0.7	C_3, km^2/sec^2	108	135	148
Spacecraft (no margin)	248(547)	Launch Window, hr	1.1	Period, days	9	19	21
Adapter (15 % margin)	29(63)	DLA, deg	33				
Total	368(811)						

* Updated

Table V-13 Summary of Navigation and Guidance Analysis for Mission 1A

Midcourse Requirements, m/sec				Navigation Uncertainties, 1σ			
	Mean ΔV	σ	ΔV + 3σ		SMAA, km	SMIA, km	TOF, sec
First Midcourse	14.3	10.4	45.5	Control	1404	1087	113
Second Midcourse	5.7	4.0	17.7	Knowledge	1396	899	89
Total, RSS			48.8				

Table V-14 Summary of Execution Errors and Entry Dispersions for Mission 1A

Deflection Execution Errors, 3σ			Entry Dispersions, 3σ			
	ΔV	Probe Attitude	Latitude, deg	.16	Entry Angle, deg	1.3
Proportionality, %	4.8		Longitude, deg	.62	Angle of Attack, deg	0.7
In-Plane Pointing, deg	1.47	.82				
Out-Plane Pointing, deg	.64	.82	Coast Time, min	5.4		

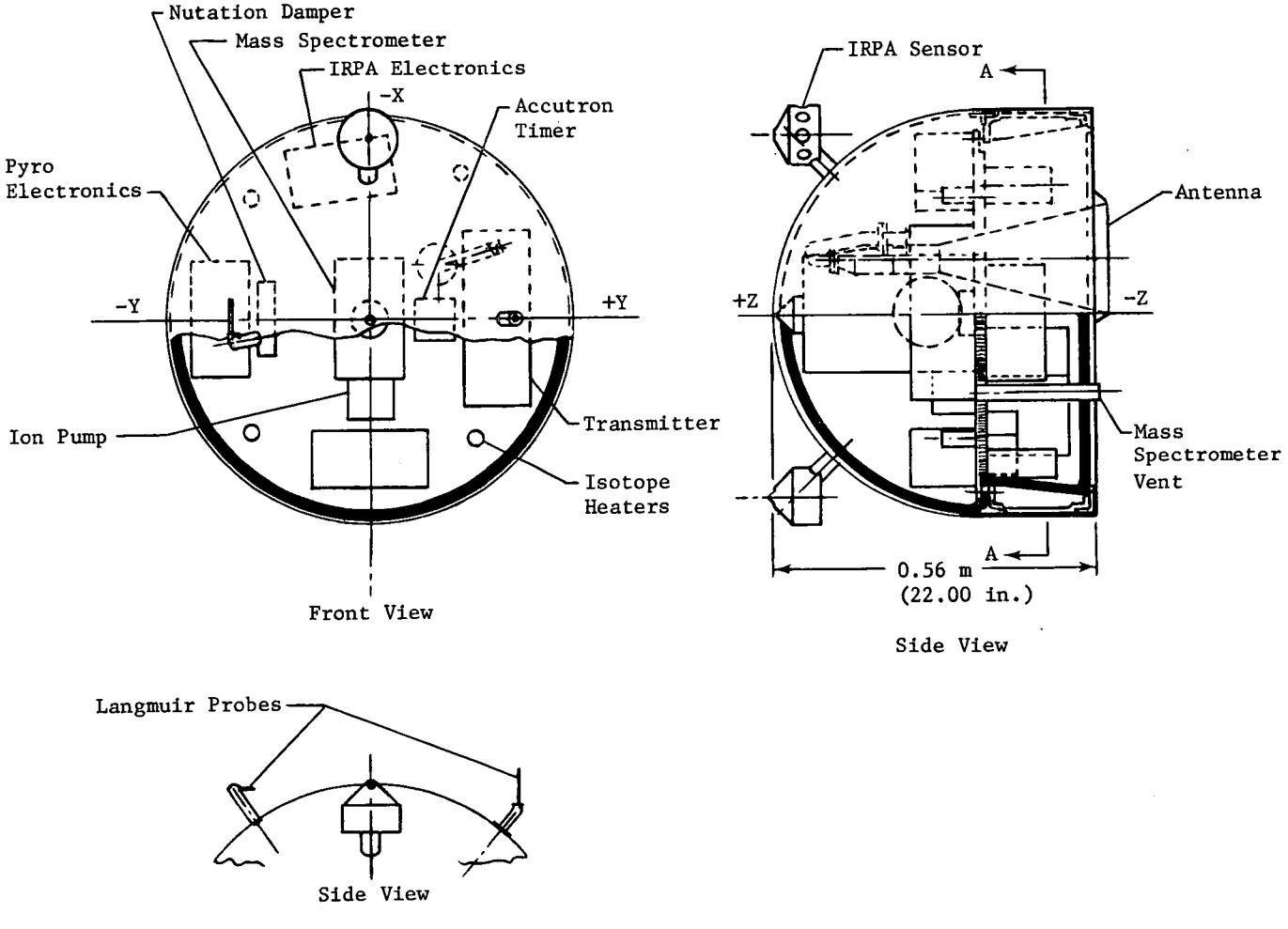

Fig. V-10 Mission 1A - Probe Configuration Front and Side

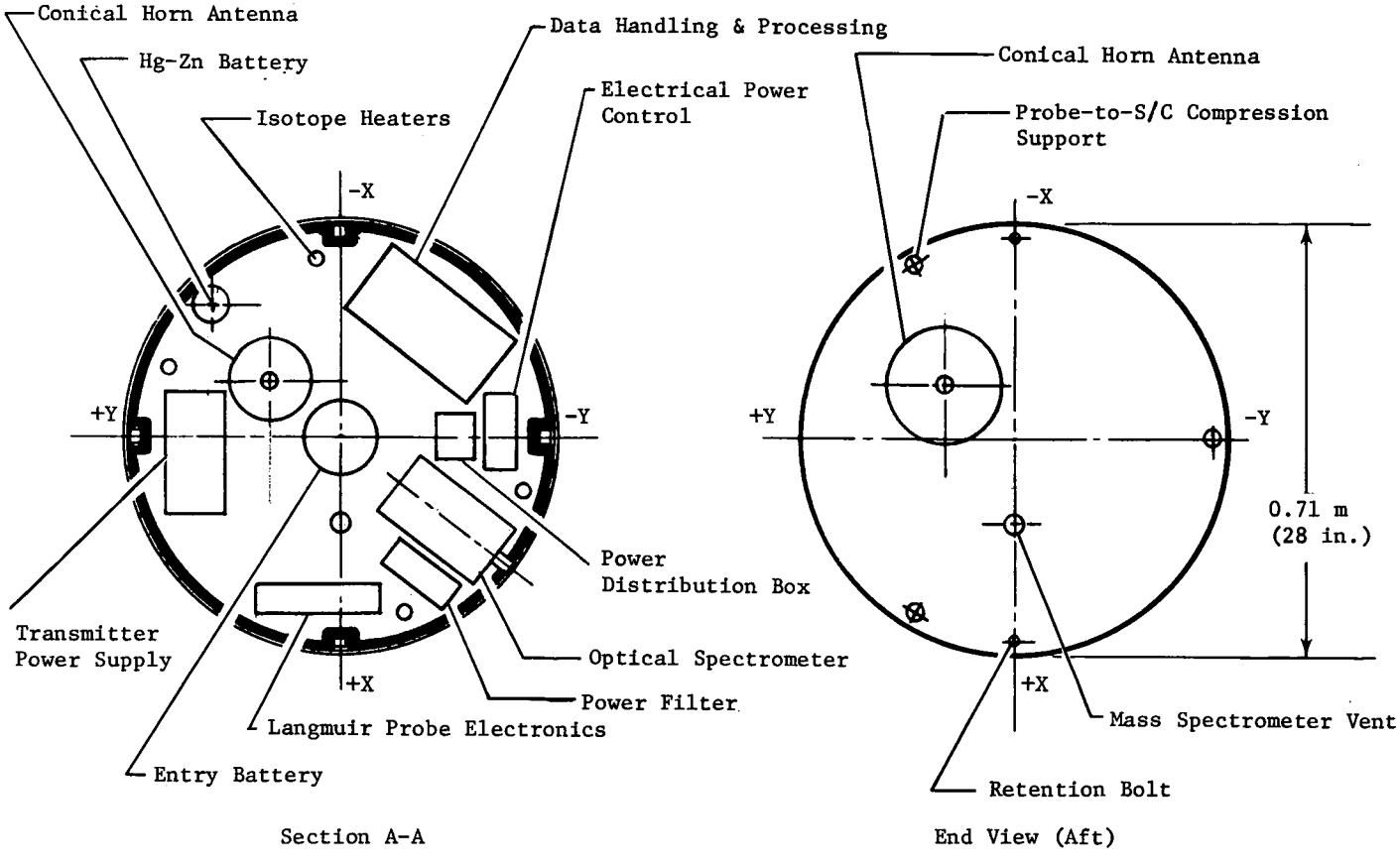

Fig. V-11 Mission 1A - Probe Configuration End and Section

Spectrometer/photometer viewing aperture is in the cylindrical portion of the probe body providing adequate viewing and placing the viewing port in an area of low entry heating. Location of the aperture in the aft bulkhead or nose cap is not desirable because of Sun aspect angles and entry heating problems.

The interrelation of components of various subsystems and the relationship of one subsystem to others are considered in the integration of internal equipment in the probe. For example, power system components like batteries, filters, distribution boxes, electronics, and cabling are grouped to improve the power-subsystem mass fraction. Location of the antenna relative to the transmitter is influenced by the desire for short direct waveguide coupling. The transmitter power supply is near the transmitter to reduce cabling and power losses.

The pyro system is required to operate or activate other subsystems throughout the probe. Therefore, its location is more flexible than those of other systems. Pyro system equipment includes electronics, capacitors, relays, and squibs.

A thermal blanket covers the entire inner surface of the probe structure, except for the equipment deck, and ten 1-W radioisotope heaters are evenly distributed inside the probe.

Spin stabilization of the probe requires that the mass moment of inertia about the Z-Z axis (spin axis) be greater than that about the transverse axes. It is desirable that the spin-axis mass moment of inertia be greater by 20% and that mass moments of inertia about the transverse axes be equal. A further requirement is that the principal mass moment of inertia coincide with the Z-Z axis of the probe. These requirements are met by properly locating components and by ballasting.

Probe support and retention locations are shown on the end view in Fig. V-9. Probe weight estimates are given in Table V-15.

a. Telecommunications - The trajectory of Mission 1A was adjusted in arrival date and deflection radius to optimize the probe and S/C trajectories so the probe, S/C, and Earth are in alignment. With the S/C high-gain antenna on Earth lock, the probe tracking antenna is aligned with the S/C spin axis and fixed at a cone angle of 180° so that no despin or position tracking is required. The resulting S/C antenna is a parabolic dish with a 16° beamwidth and a required probe X-band power of 20 W.

Table V-15 Mission 1A Weight Estimate

		kg	lb
Science		14.4	31.7
Structure and Heat Sink		12.2	26.9
Thermal Control		2.5	5.5
Guidance and Control		1.2	2.7
Deflection Propulsion		0.0	0.0
Communications		8.4	18.5
Data Handling		2.3	5.0
Electrical		7.0	15.4
Mechanisms		0.1	0.3
Pyro		2.5	5.6
Ballast		1.3	3.0
	15% Margin	7.8	17.3
	Ejected Weight	59.8	131.9
Cover Mechanisms		- 0.1	- 0.3
	Entry Weight	59.7	131.6

S/C antenna requirements are shown in Fig. V-12. The wake and and plasma-attenuation analyses (Chapter VI, Subsection A5) showed that X-band allowed probe penetration to 64 km below turbopause. Initially, the mission was designed for K-band, using smaller knowledge and control and proportionality errors, with timing based on nominal end-of-mission position. This resulted in a narrower-beamwidth (9°) S/C antenna, as seen in Table V-16. Using a 16° dish at K-band results in an RF requirement of 42 W. Therefore, it would be necessary to use a smaller beamwidth and despun dish with a single-axis gimbal to reduce K-band power to 25 W, which is an upper limit.

Design details of the RF components that comprise the telecommunications subsystem are listed in Table V-16. Complete details are given in Chapter VI, Section A for each component. This mission was redesigned for X-band with a larger S/C antenna beamwidth used to cover increased dispersions. The decrease in space loss at a lower frequency fell short of compensating for the increase in power required with a S/C antenna, with lower gain resulting in RF power increasing from 13 to 20 W, as seen in the table.

b. Data Handling - The data rate for this probe-optimized science-enhanced mission is increased to 1376 bps from the Mission 1 rate of 1024 bps. In all other respects, the data handling system is similar to Mission 1. Chapter VI, Section B provides a detailed discussion of alternative approaches and formating for this mission.

c. Electrical Power - The power system for Mission 1A is similar to that for Mission 1. A power profile is shown in Fig. V-13 and a detailed discussion of battery evaluation and selection is found in Chapter VI, Section C.

d. Pyrotechnic - The pyrotechnic subsystem is similar to Mission 1. A detailed discussion of pyrotechnic control is in Chapter VI, Section C.

e. Heat Sink and Structure - The heat sink consists of a 0.713-m (28-in.) dia beryllium hemispherical nose cap and cylindrical skin on the skirt assembly weighing 6.3 kg (13.8 lb). It is 0.52 cm (0.204 in.) thick at the stagnation point and 1.27 mm (0.050 in.) thick at the trailing edge.

The structure consists of conventional aluminum machinings, bonded aluminum honeycomb, and bonded fiberglass/composite structures.

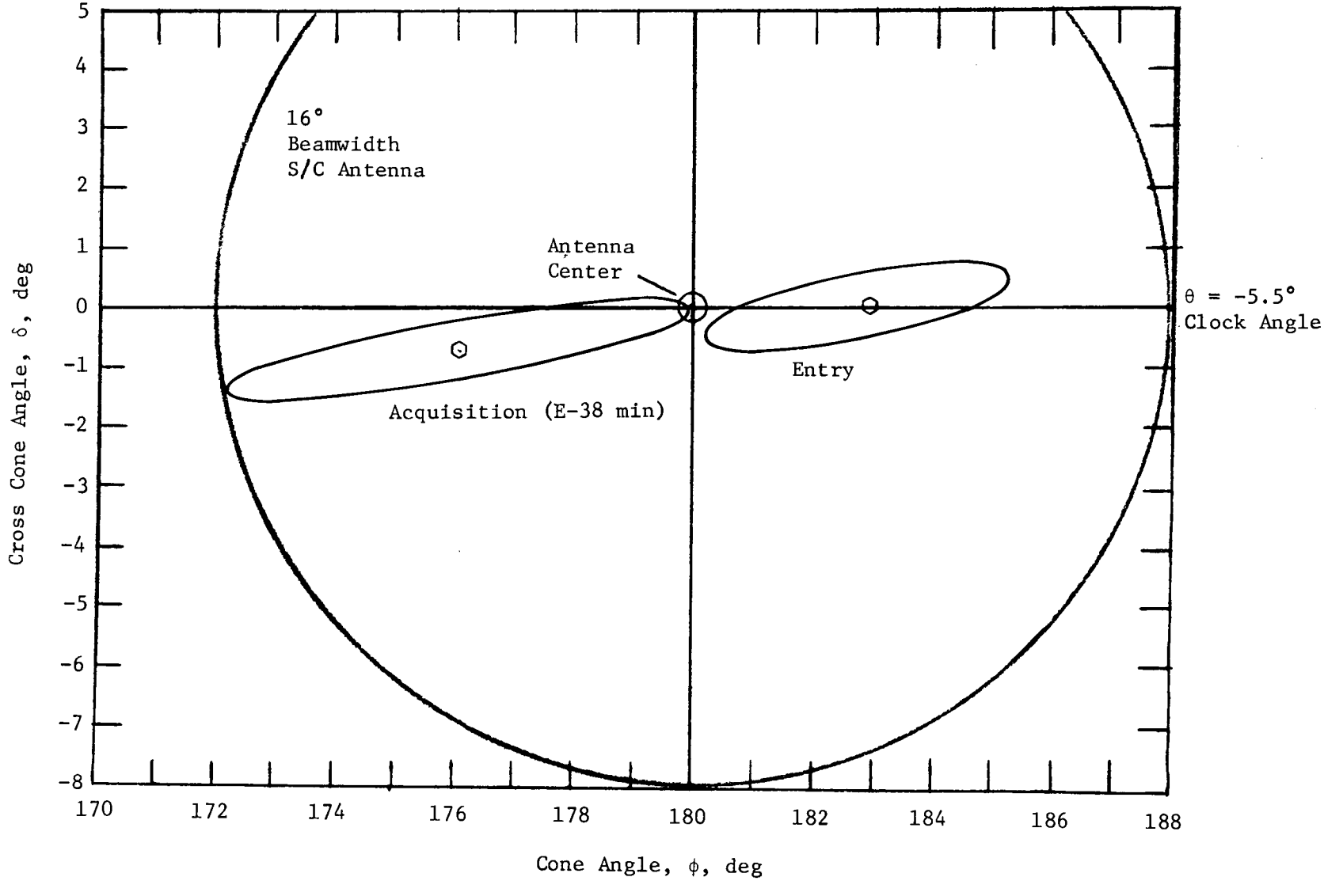

Fig. V-12 Spacecraft-Antenna Requirements for Mission 1A

Table V-16 Telecommunications RF Subsystem for Mission 1A

Conditions:	S/C - Pioneer		Bit Rate - 1376 bps**	
			Value	
Component	Characteristic	Unit	K Band, 20 GHz	X Band, 10 GHz
Probe Conical-Horn Antenna	Electrical B/W	deg	10.0	10.0
	Max Gain	dB	23.4	23.4
	Dia	cm	9.8	19.6
		in.	3.8	7.6
	Total Length	cm	25.4	46.8
		in.	10.0	18.4
	Weight	kg	0.16	0.34
		lb	0.35	0.75
Transmitter & Power Supply	RF Power Out	W	13*	20.0
	Overall Efficiency	%	24.0	24.0
	dc Power at 28 Vdc	W	48.2	83.2
	Total Weight	kg	7.7	7.7
		lb	17.0	17.0
S/C Dish Antenna	Electrical B/W	deg	9.0	16.0
	Max Gain	dB	25.25	20.25
	Dia	cm	11.8	13.2
		in.	4.63	5.2
	Weight	kg	0.91	0.91
		lb	2.0	2.0
	Despin		no	no
	Position Search		no	no
	Freq Acquisition	sec	54.0	27.0
	Clock Angle, θ	deg	-5.5	-5.5
	Cone Angle, ϕ	deg	180.0	180.0
S/C Receiver	System Temperature	°K	400.0	315.0
	dc Power at 28 Vdc	W	10.0	10.0
	Weight	kg	5.9	5.9
		lb	13.0	13.0

*Based on original knowledge and control, and proportionality errors and timing for nominal end of mission.

**Science plus engineering

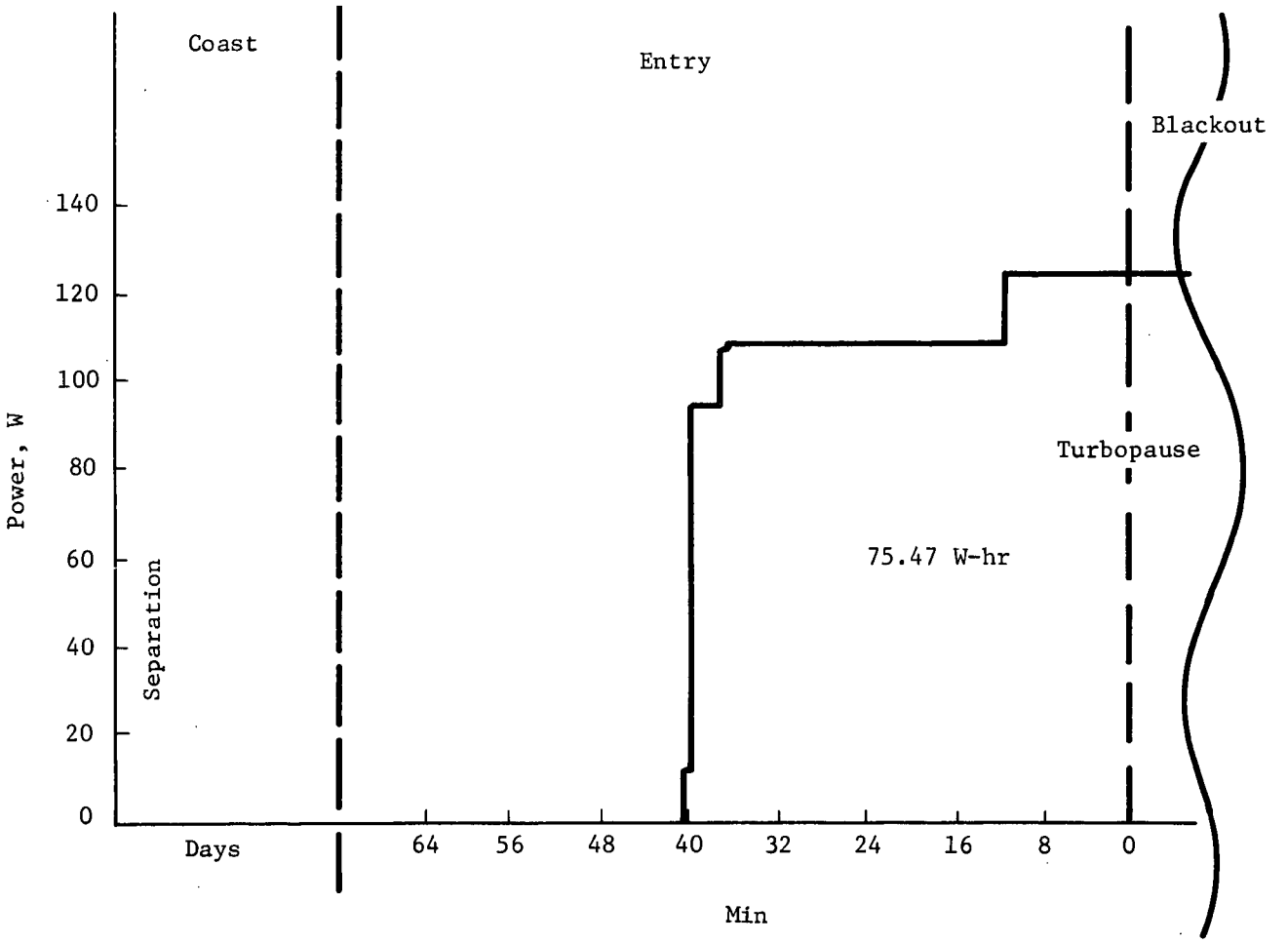

Fig. V-13 Mission 1A Probe Power Profile

f. Thermal Control - The thermal control subsystem consists of an internally mounted multilayer insulation blanket surrounding the probe interior equipment, an insulating cover for the photometer/optical spectrometer aperture (removable before entry), and radioisotope heaters placed where space is available between the internal equipment packages. The multilayer insulation blanket consists of 72 layers of 1/4 mil Kapton polyimide film aluminized on one side with beta glass cloth spacer material between layers.

Total blanket thickness is 1.53 cm (0.6 in.). Ten 1-W radioisotope heaters are required (based on analysis), although it is expected that the actual requirement could be 8 to 12 W, depending on results of thermal testing of actual probe hardware. For this mission, an RF-transparent radome covers the communications antenna. This reduces heat loss from the probe interior through the antenna coupling.

g. Mechanical Subsystems - Mechanical subsystems for Mission 1A consist of the spectrometer/photometer aperture cover and release and probe-to-spacecraft separation systems. Both are described in detail in Chapter VII, Subsection A3.

h. Attitude Control - The attitude-control analysis and performance is similar to Mission 1 (Subsection B3h of this chapter. Spin rate has decreased to 2.09 rad/sec (20 rpm) and the Pioneer maneuver from 4 to 1°. The lower maneuver requirement proportionately reduces the final attitude error.

The reduction in coast time has no significant effect on damper performance because the 10.9-day coast represents approximately 25 damper time constants at the 2.09 rad/sec (20 rpm) spin rate. For a general discussion of ACS performance, see Chapter VII.

4. Spacecraft Interface/Modification and Launch Vehicle

For Mission 1A, the Pioneer spacecraft with probe is launched on a Titan IIID-5-segment-D1 Centaur-Burner II. The following components are either modified or added to the spacecraft for the probe's support or mission operation: probe support structure, environmental enclosure, electrical cabling and interface, receiver subsystem, fixed tracking antenna and platform, and data handling. Modification weight to the spacecraft is 31.5 kg (69.4 lb). The integration arrangement is shown in Fig. V-14.

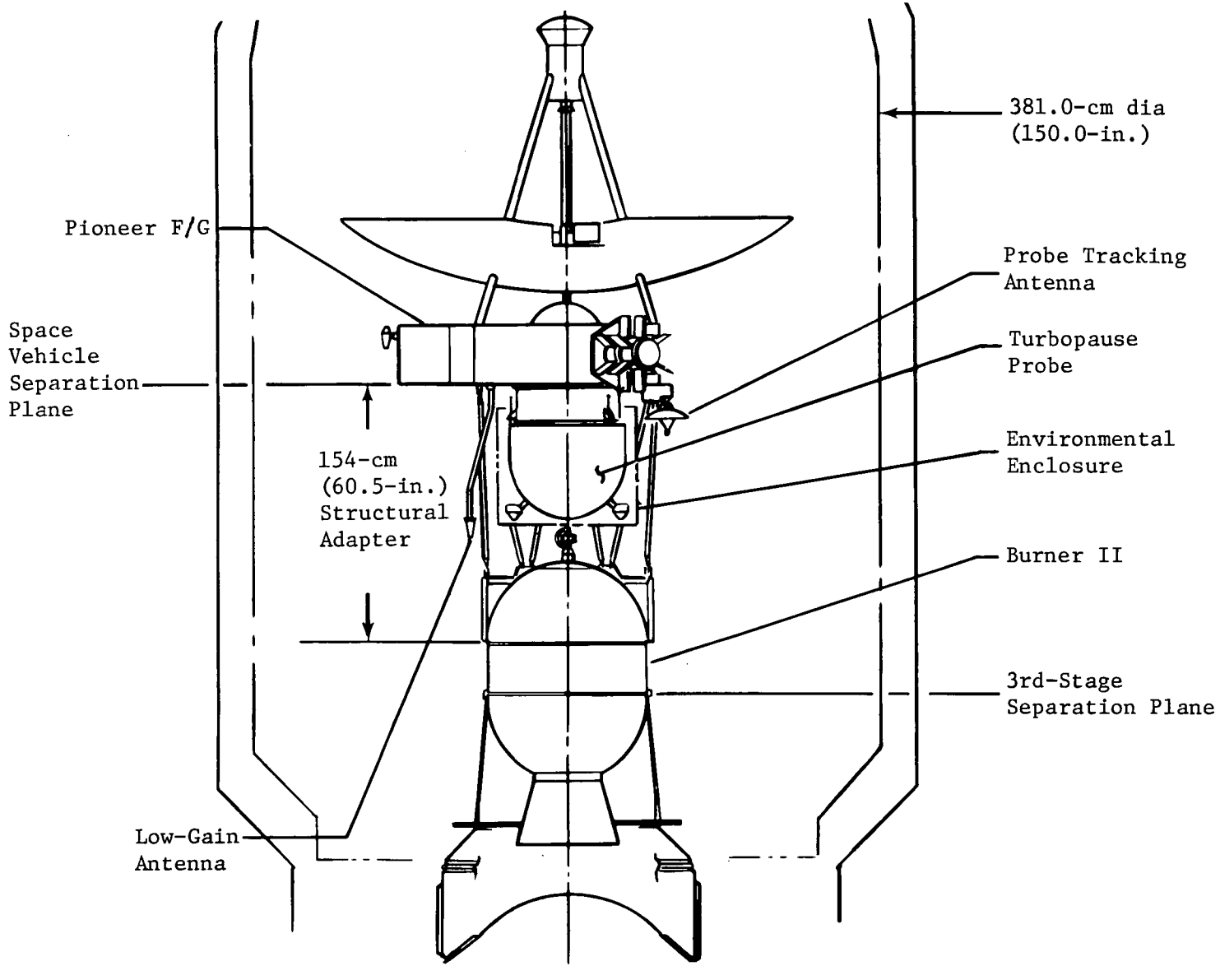

Fig. V-14 Probe-Spacecraft Interface for Mission 1A

D. MISSION 2 RADIATION-COMPATIBLE SPACECRAFT

The objective of this mission/system design was to constrain mission parameters enough to assure no degradation of the spacecraft systems by emissions from the Jupiter radiation belt while maintaining a simplified probe system and effective science data-acquisition and transmission. Spacecraft modification to decrease its susceptibility to radiation damage was not a consideration in this probe system defintion.

The major constraining parameter is an increased R_P $\left(\text{to } 4\ R_J\right)$ which in turn directly affects the communications geometry and RF link. The simplified probe system defined for Mission 1 has the capability for this mission. As with Mission 1, this probe system uses a spacecraft deflection mode in which the spacecraft spins up and orients the probe for release at the proper attitude (zero angle of attack) at entry; releases the probe and then despins and reorients itself for deflection propulsion; reorients itself to Earth lock; and, at the end of the coast period, acquires the probe RF transmission and relays the data received to Earth.

Functional requirements of the probe systems are limited to activation and operation of the science instruments, data processing, and data transmission to the spacecraft. Figure V-1 shows the system functional block diagram (similar to Mission 1 and 1A), and Table V-17 shows the mission sequence of events.

1. Science Payload and Performance

Instrument characteristics and mission performance for Mission 2 are shown in Table V-18. The primary difference between the science-instrument bit rate for this and other missions is the dayglow instrument, whose data rate depends on probe spin rate. For this mission, it is 3.93 rad/sec (37.5 rpm). A detailed breakdown of the data word collection that specifies a given bit rate is also presented. For a description of the contents of data words, see Chapter III Section C, under the subsection describing the particular instrument. On the left side of the lower part of the table are the upper atmospheric and ionospheric performance, the criteria being one measurement per scale height. The lowest values are the heaviest particles of both the neutrals and ions. For a detailed discussion of these numbers, see Chapter III, Subsections D1 and D3.

Table V-17 Mission 2 Radiation-Compatible Spacecraft Sequence of Events

Event	Time, hr:min:sec	Function
1	L	Launch October 13, 1978
2	L + 02:00:00	Separate S/C system from L/V; begin S/C cruise
3	S - 05:30:00	Separate environmental enclosure Supply S/C power to probe Begin probe checkout
4	S - 00:30:00	Complete probe checkout
5	S - 00:17:00	Orient S/C for probe release (23°)
6	S - 00:15:20	Start S/C spin to 37.5 rpm
7	S - 00:12:00	Begin 12-min Langmuir probe decontamination
8	S - 00:00:20	Start probe timer; enable probe separation ordnance
9	S, L + 595 d	Separate probe
10	S + 00:01:40	Reduce S/C spin to 4.8 rpm (100-m separation)
11	S +	S/C reorientation (35°)
12	S +	S/C ΔV (101.3 m/sec)
13	S +	S/C reorientation (-58°) to Earth lock
14	T - 01:29:11	Enable battery activation
15	T - 01:09:11	Activate entry battery
16	T - 00:49:11	Energize probe bus
17	T - 00:49:01	Data system on
18	T - 00:48:46	Transmitter on
19	T - 00:48:26	Enable ordnance
20	T - 00:48:16	Fire pyros at 15-sec interval
21	T - 00:46:46	Start probe acquisition/disable ordnance
22	T - 00:45:46	Turn on instruments (ETP, IRPA, ORGS); complete probe acquisition
23	T - 00:45:16	Transmit instrument engineering data (ETP, IRPA, ORGS)
24	T - 00:43:16	Start data transmission (ETP, IRPA, ORGS)
25	T - 00:41:24	Start transmission of engineering data (including stored)
26	T - 00:27:24	Turn on instruments (MS, NRPA)
27	T - 00:25:24	Stop transmission of engineering (housekeeping) data
28	T - 00:22:24	Transmit MS & NRPA engineering data
29	T - 00:21:24	Start data transmission (MS, NRPA)
30	T	Turbopause
31	T + 2.1 sec	Blackout
32	L + 655 days	S/C periapsis; July 29, 1980

Includes 15.4-min trajectory uncertainty, 0.65-min timer uncertainty, and 5% of time from acquisition start to T = 0.

Table V-18 Mission 2 Science Instruments and Performance

Characteristics

Instruments	Weight, kg	Weight, lb	Power, W	Words/ Sample	Bits/ Sample	Sampling Time, sec	Science Bit Rate, bps
Langmuir Probes	1.36	3.0	3	3	24	0.5	48
IRPA	1.59	3.5	3	12	96	0.5	192
NRPA	2.27	5.0	5	14	112	0.5	224
Mass Spectrometer	5.92	13.0	15	22	176	0.4	440
Ultraviolet Spectrometer	1.59	3.5	5	3	24	0.8	30
Totals	12.73	28.0	31				934

Mission Performance

Particle	Measurement/ Scale Height
H	3.8
H_2	1.9
He	1.0
H_1^+ & e^-	7.5
H_2^+	6.0
H_3^+	3.4
He^+	3.5
HeH^+	1.5

Note: Entry Flight-Path Angle, $\gamma_E = -29°$

Mission Times from

50,000 km to turbopause (min) 25.0

1000 km to turbopause (sec) 34.7

Turbopause to blackout (sec) 2.1
(minimum time below turbopause)

Mass-Spectrometer Measurements
(0.4 sec each)

Above turbopause (+20 to 0 km) = 1.75

Below turbopause (0 to -60 km) = 5.25

Total (+20 to -60 km) = 7.00

2. Mission Description

The mission description for Mission 2 is the same as for Mission 2A, Subsection E2.

3. Configuration

The Mission 2 configuration is the same as Mission 1 (Subsection B3) except for addition of a radiation detector and decrease in heat shield thickness and weight resulting from the increase in entry angle. The increase in the periapsis radius also increases the power requirements of the communications transmitter, increasing required battery size. These changes are included in the weight estimates shown in Table V-19.

a. Telecommunications - Increasing the deflection radius to 4 R_J for the spacecraft radiation-compatible mission required the use of probe and S/C antennas with higher gains (smaller beamwidths) in order not to exceed 20 to 25 W at K-band. Design details of the RF components that comprise the telecommunications subsystem are listed in Table V-20. See Chapter VI, Section A for complete design details on the components.

Probe dispersions at entry are less than 1° in both planes (cone and cross-cone angle), therefore a 2° S/C relay antenna with a single-axis gimbal on a despun platform was chosen. An 8° horn antenna on the probe provided enough gain in the RF link so that required power was 20 W. The S/C relay antenna with the 2° beam can cover the acquisition ellipse without position search, but it must be programmed in cone angle to traverse 1.5° in 45 min from acquisiton to the end of the mission.

b. Data Handling, Power, and Pyrotechnics - The design approach, performance, and requirements are similar to Mission 1 (Subsections B4b, c, d). Differences in transmitter power required and sequence of events produce small weight and size variations in the AG-Zn primary battery source. Pyrotechnic control is the same as for Mission 1. Radiation is the major consideration of this mission and is discussed in Chapter XI. The reduction of semiconductor life from radiation is the major hazard to electronics. The most susceptible components in these electronic subsystems are power transistors and battery separator material. Bipolar transistors or selected P-MOS are considered appropriate for this mission. The semiconductor radiation resistance is assisted somewhat by the power-off condition during coast, but the vehicle will be in heavy radiation belts when the system is energized.

Table V-19 Mission 2 Weight Estimate

	kg	lb
Science	13.3	29.4
Structure & Heat Sink	11.7	25.9
Thermal Control	2.5	5.5
Guidance & Control (less propellant)	1.2	2.7
Deflection Propulsion (less propellant)	0.0	0.0
Communications	8.8	19.4
Data Handling	4.2	9.3
Electrical	7.8	17.2
Mechanisms	0.3	0.7
Pyro	2.5	5.6
Ballast	1.4	3.0
15% Design Margin	8.1	17.8
Total - Probe Coast	61.8	136.5
Solid Propellant +15%	0.0	0.0
Nitrogen Gas +15%	0.0	0.0
Covers	0.1	0.2
Total - Probe Ejected	61.9	136.7

Table V-20 Telecommunications RF Subsystem for Mission 2

Conditions:	S/C - Pioneer,		Bit Rate - 1024 bps*
Component	Characteristic	Unit	Freq. - K-Band, 20 GHz Value
Probe Conical-Horn Antenna	Electrical B/W	deg	8.0
	Max Gain	dB	25.3
	Dia	cm	12.2
		in.	4.8
	Total Length	cm	36.0
		in.	14.2
	Weight	kg	0.3
		lb	0.6
Transmitter & Power Supply	RF Power Out	W	20.0
	Overall Efficiency	%	24.0
	dc Power at 28 Vdc	W	83.3
	Total Weight	kg	7.7
		lb	17.0
S/C Dish Antenna	Electrical B/W	deg	2.0
	Max Gain	dB	38.5
	Dia	cm	54.20
		in.	21.34
	Weight	kg	10.4
		lb	23.0
	Despin		yes
	Position Search		no
	Freq Acquisition	sec	78.0
	Clock Angle, θ	deg	106.3
	Cone Angle, ϕ	deg	155.5-157
S/C Receiver	System Temperature	°K	400.0
	dc Power at 28 Vdc	W	10.0
	Weight	kg	5.9
		lb	13.0

*Science plus engineering

Semiconductor radiation hardening can be improved by selection and allowing greater design margin for decreased output. The discrete design of the power subsystem is good design practice in a radiation environment. Dispersion of the regulation and control function decreases the volt-ampere requirements on the semiconductors and allows the selection of less sensitive devices. Studies of the effect of electron irradiation on separator material indicate that severe deterioration does take place. It appears that selection of substitute materials will provide enough radiation resistance. Separator materials will be modified and evaluated for the radiation and active life required for the turbopause mission.

c. Heat Sink and Structure - All items are the same as for Mission 2A (Subsection E3c).

d. Thermal - Thermal control system is the same as that for Mission 1 (Subsection B3f).

e. Attitude Control - Spin stabilization and passive damper design are similar to Missions 1 and 1A (Subsections B3h and C3h). A general discussion of attitude control is in Chapter VIII.

5. Spacecraft Interface/Modification and Launch Vehicles

The Pioneer spacecraft with probe is launched on a Titan IIID-5-segment-D1 Centaur-Burner II. The following components are either modified or added to the spacecraft for probe support or mission operations; probe support structure, environmental enclosure, electrical interface, receiver subsystem, despun and gimbal tracking antenna and platform, data handling, and propellant-tank (capacity increased). The modification weight to the spacecraft is 49.3 kg (109.8 lb) for Mission 2. The integration configuration is shown in Fig. V-15.

E. MISSION 2A RADIATION-COMPATIBLE SPACECRAFT

The objective for the mission/system design for this mission was to refine the Mission 2 probe by incorporating the improved RF system (K-band to X-band) used on Mission 1A.

As with Mission 2, this probe system uses a spacecraft deflection mode, eliminating the requirement for probe onboard deflection propulsion and attitude control systems.

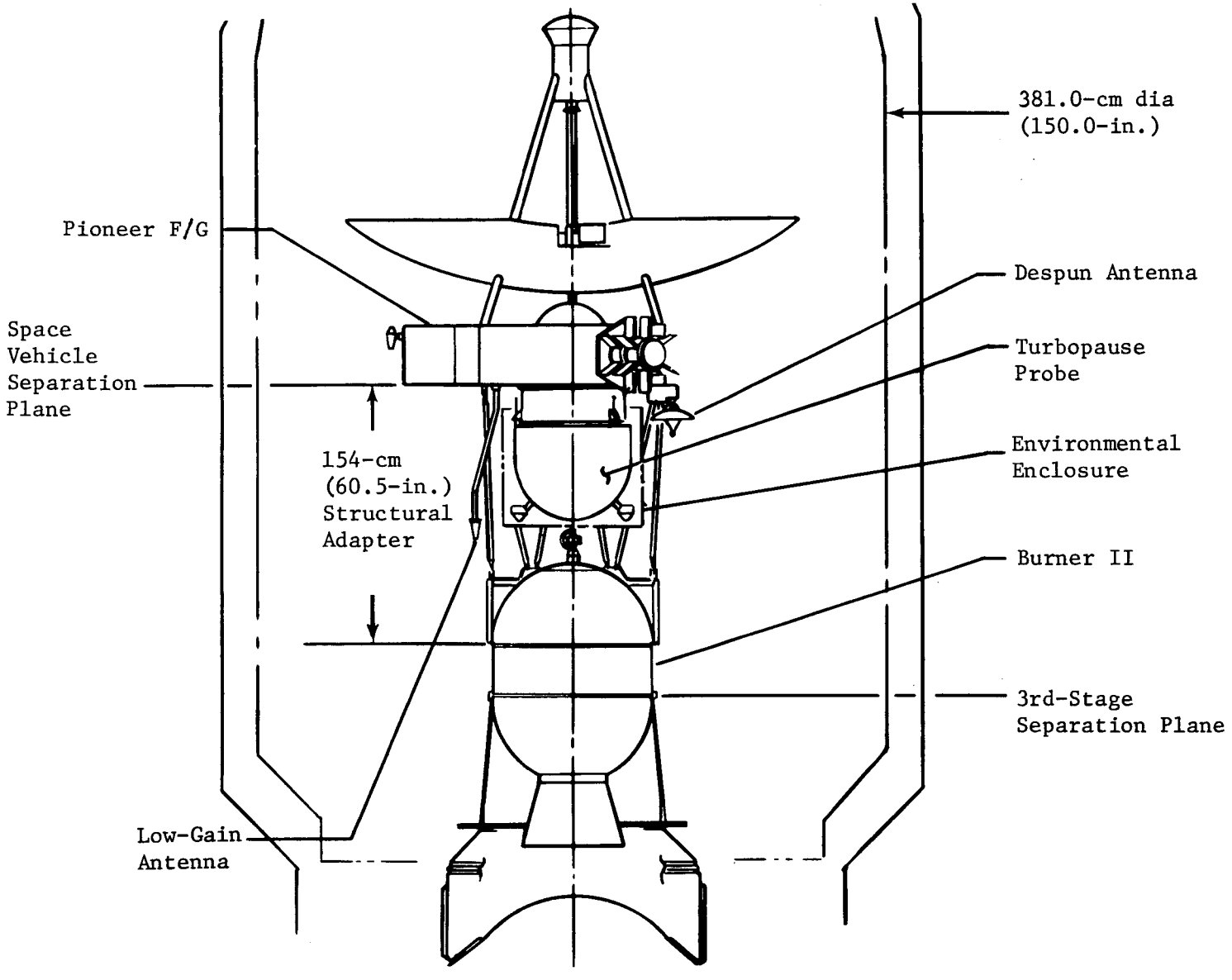

Fig. V-15 Probe-Spacecraft Interface for Mission 2

This system requires that the spacecraft orient itself for probe ejection on a trajectory that results in zero angle of attack for the probe at entry; spin-up and release the probe; despin, reorient itself and apply the necessary deflection propulsion (ΔV); reorient itself to Earth lock; and, at the end of the coast period, acquire the probe RF transmission and relay the data received to Earth.

Functional requirements of the probe systems are limited to activation and operation of the science instruments, data processing, and data transmission. Figure V-1 is the system functional block diagram (similar to Missions 1 and 1A), and the mission sequence of events is shown in Table V-21. The probe mission power profile is shown in Fig. V-16.

1. Science Payload and Performance

The instrument characteristics and mission performance for Mission 2A are shown in Table V-22. The primary difference between this and other missions is the dayglow instrument, whose data rate depends on probe spin rate. For this mission, the spin rate is 20 rpm. For a description of the contents of data words, see Chapter III, Section C under the subsection describing the particular instrument.

On the left side of the lower half of the table are the upper atmospheric and ionospheric performance, the criterion being one measurement per scale height. The lowest values are the heaviest particles of both neutrals and ions. For a detailed discussion of these numbers, see Chapter III, Subsections D1 and D3.

2. Mission Description

The interplanetary trajectory for Mission 2A was chosen to arrive approximately in the middle of the possible arrival dates. This results in a longer launch period than Missions 1 or 1A but requires a larger entry angle $\left(\gamma_E = -29°\right)$. The spacecraft flyby trajectory has a periapsis radius of $R_P = 4.0\ R_J$ to reduce possible radiation damage to the spacecraft. Interplanetary and approach trajectories are shown in Fig. V-17.

Table V-21 Mission 2A Radiation-Compatible Spacecraft Sequence of Events

Event	Time, hr:min:sec	Function
1	L	Launch October 13, 1978
2	L + 02:00:00	Separate S/C system from L/V; begin S/C cruise
3	S - 05:30:00	Separate environmental enclosure Supply S/C power to probe Begin probe checkout
4	S - 00:30:00	Complete probe checkout
5	S - 00:17:00	Orient S/C for probe release (23°)
6	S - 00:15:20	Start S/C spin to 20 rpm
7	S - 00:12:00	Begin 12-min Langmuir probe decontamination
8	S - 00:00:20	Start probe timer; enable probe separation ordnance
9	S, L + 595 d	Separate probe
10	S + 00:01:40	Reduce S/C spin to 4.8 rpm (100-m separation)
11	S +	S/C reorientation (34°)
12	S +	S/C ΔV (101.3 m/sec)
13	S +	S/C reorientation (-57°) to Earth lock
14	T - 01:18:27	Enable battery activation
15	T - 00:58:27	Activate entry battery
16	T - 00:38:27	Energize probe bus
17	T - 00:38:17	Data system on
18	T - 00:38:02	Transmitter on
19	T - 00:37:42	Enable ordnance
20	T - 00:37:32	Fire pyros at 15-sec interval
21	T - 00:36:02	Start probe acquisition/disable ordnance
22	T - 00:35:02	Turn on instruments (ETP, IRPA, ORGS); complete probe acquisition
23	T - 00:34:32	Transmit instrument engineering data (ETP, IRPA, ORGS)
24	T - 00:33:32	Start data transmission (ETP, IRPA, ORGS)
25	T - 00:31:32	Start transmission of engineering data (including stored)
26	T - 00:22:36	Turn on instruments (MS, NRPA)
27	T - 00:20:36	Stop transmission of engineering (housekeeping) data
28	T - 00:17:36	Transmit MS & NRPA engineering data
29	T - 00:16:36	Start data transmission (MS, NRPA)
30	T	Turbopause
31	T + 2.1 sec	Blackout
32	L + 655 days	S/C periapsis; July 29, 1980

Includes 5.13-min trajectory uncertainty, 0.65-min timer uncertainty, and 5% of time from acquisition start to T = 0.

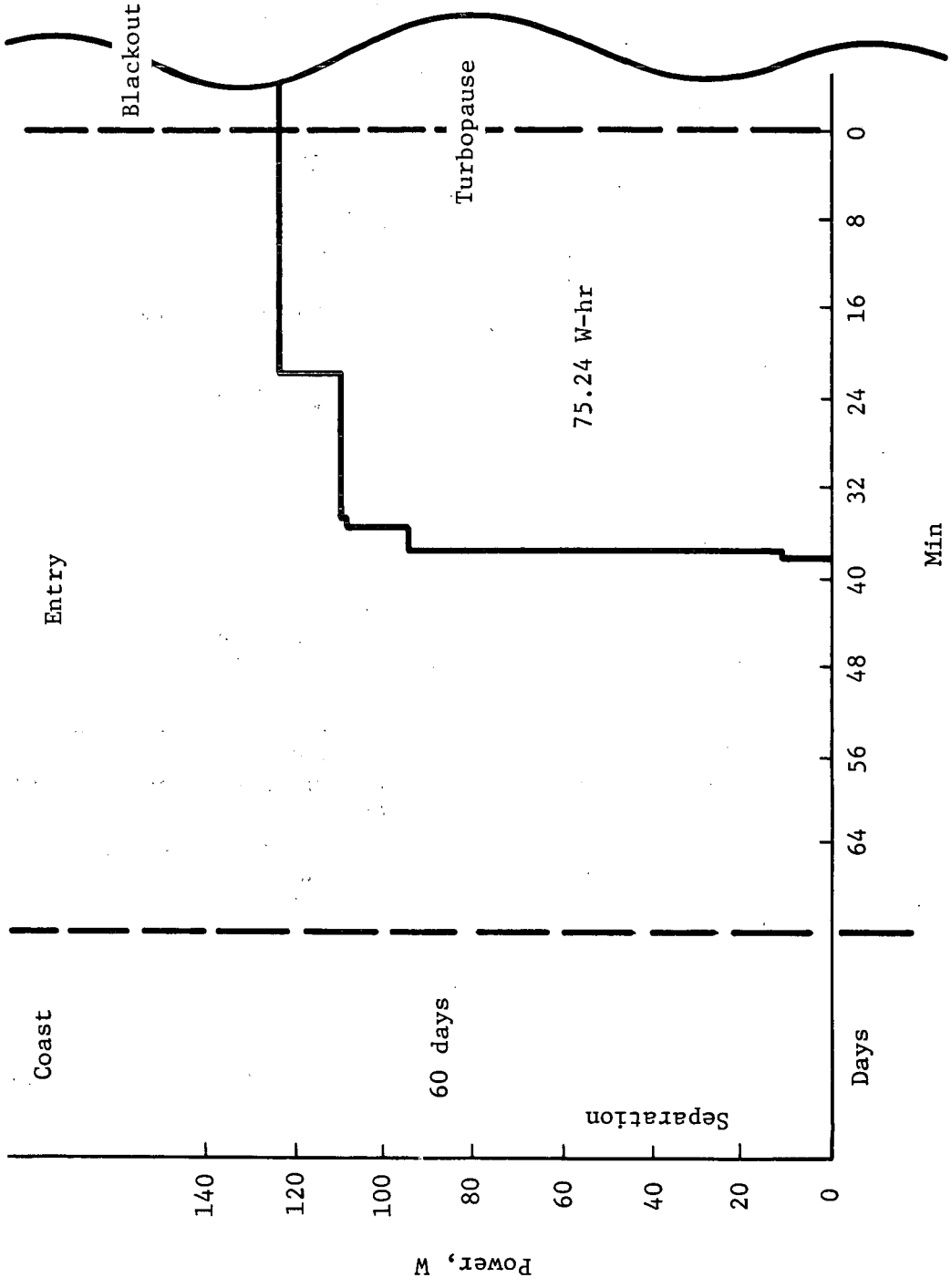

Fig. V-16 Mission 2A Probe Power Profile

Table V-22 Mission 2A Science Instruments and Performance

Characteristics

Instruments	Weight, kg	Weight, lb	Power, W	Words/ Sample	Bits/ Sample	Sampling Time, sec	Science Bit Rate, bps
Langmuir Probes	1.36	3.0	3	3	24	0.5	48
IRPA	1.81	4.0	3	12	96	0.5	192
NRPA	2.49	5.5	5	14	112	0.5	224
Mass Spectrometer	5.90	13.0	15	22	176	0.4	440
Photometers/Spectrometer	2.27	5.0	5	4	32	3.0	10
Totals	13.83	30.5	31				914

Mission Performance

Particle	Measurement/ Scale Height
H	3.8
H_2	1.9
He	1.0
H_1^+ & e^-	7.5
H_2^+	6.0
H_3^+	3.4
He^+	3.5
HeH^+	1.5

Note: Entry Flight-Path Angle, $\gamma_E = -29°$

Mission Times from

50,000 km to turbopause (min)	25.0
1000 km to turbopause (sec)	34.7
Turbopause to blackout (sec) (minimum time below turbopause)	2.1

Mass-Spectrometer Measurements (0.4 sec each)

Above turbopause (+20 to 0 km)	= 1.75
Below turbopause (0 to -60 km)	= 5.25
Total (+20 to -60 km)	= 7.00

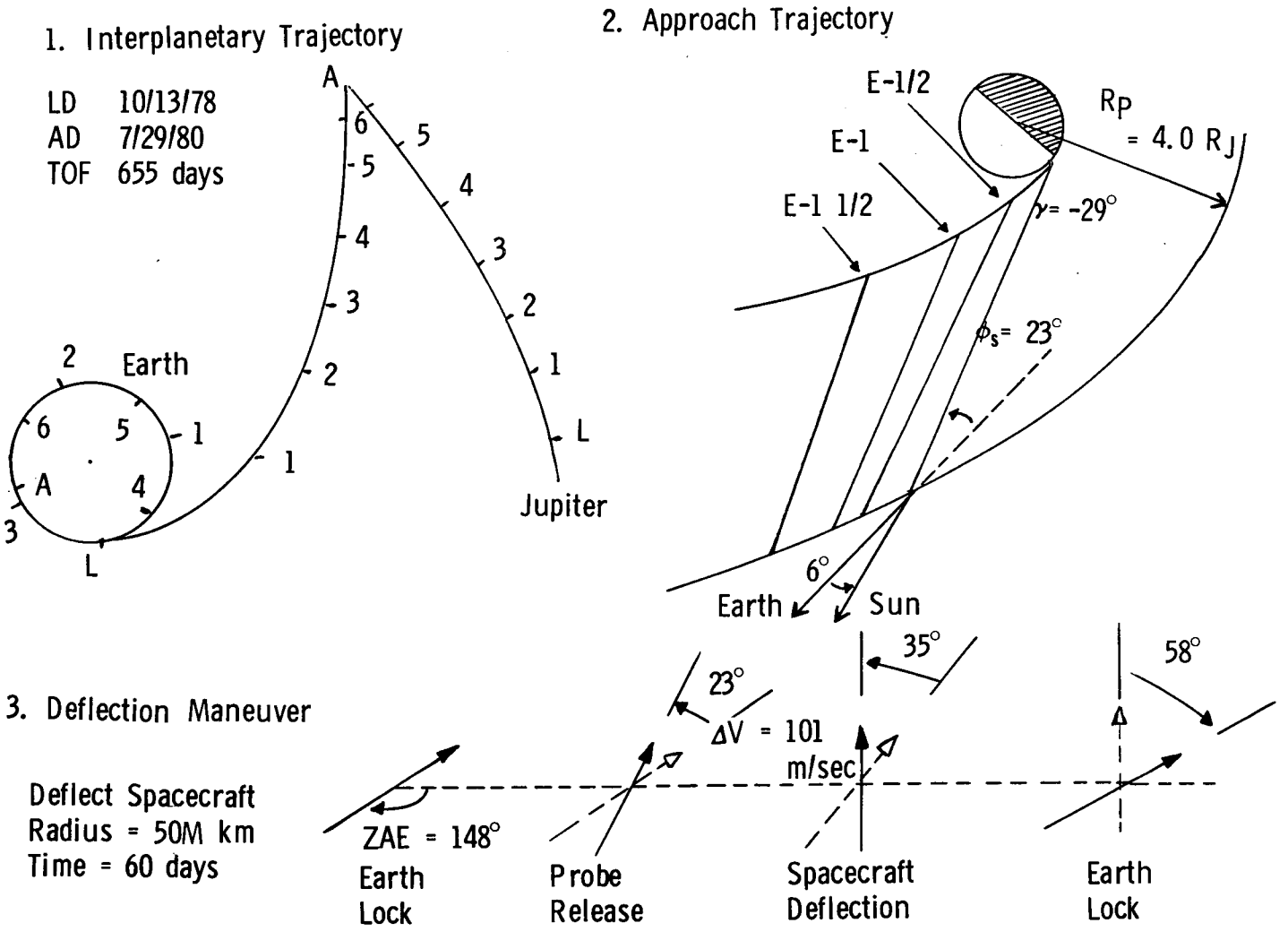

Fig. V-17 Radiation-Compatible Mission 2A Trajectories

Because there are no post-Jupiter objectives, spacecraft deflection mode (Mode 3) is again used. To keep deflection ΔV reasonable, a 50×10^6-km deflection radius was chosen. The deflection maneuver sequence is shown in Fig. V-17.

Launch requirements are summarized in Table V-23. Allowable launch periods are 25 and 27 days for the standard and updated performance, respectively for the Titan IIID-5-segment-Centaur-Burner II vehicle. The parking orbit coast time is just below its upper allowable limit of 1 hr.

As shown in Table V-24, requirements for the two midcourse deflection maneuvers for this mission result in a ΔV of 47.1 m/sec. Knowledge and control uncertainties listed in Table V-25 were developed for the specific approach geometry of Mission 2. Deflection execution errors are based on the operational sequence of the mission, using a realistic model for the Pioneer spacecraft. The dispersions are all within allowable tolerances.

3. Configuration

The Mission 2A configuration is the same as that for Mission 1A except for the radiation detector and a decrease in heat-shield weight and thickness resulting from an increase in entry angle. These changes are included in the weight estimates in Table V-26. The Mission 2A configuration is a simple probe with a hemispherical forward section and a cylindrical aft section. The basic probe is 0.71 m (28 in.) in diameter and 0.56 m (22.00 in.) long, as shown in Fig. V-18 and V-19.

Science experiments are integrated in the overall probe design, constrained by their functional requirements. The mass spectrometer, IRPA, NRPA, and Langmuir probes all require unobstructed access to atmospheric particles during entry. This requirement is met by placing the neutral mass spectrometer inlet directly at the nose cap stagnation point and the RPAs at approximately 1 body radius from the Z axis and at the same body station as the stagnation point of the nose cap. In Ref V-1, two other locations for RPAs were studied (just off the dome/cylinder juncture and at the stagnation point.), and the position shown in Fig. V-18 has approximately half the reflected particle interference of other locations considered. The mass spectrometer is vented through a 2.5-cm (0.98-in.) tube to the probe's wake, as shown in Fig. V-19.

Table V-23 Summary of Launch Requirements for Missions 2 and 2A

Payload Summary	kg (lb)	Nominal Launch		Launch-Period Analysis			
Probe (15% margin)	60(130)*	C_3, km^2/sec^2	99	Vehicle	Titan III/ 5-seg/Cent	Titan III/5-seg/Centaur B II	Titan III/5-seg/Centaur B II†
S/C Mods (15% margin)	51(112)*	Park Orbit Time, hr	1.0	C_3, km^2/sec^2	107	133	146
Spacecraft (no margin)	248(547)	Launch Window, hr	1.3	Period, days	15	25	27
Adapter (15 % margin)	29(63)	DLA, deg	32				
Total	388(852)*						

* Mission 2A only.
† Updated

Table V-24 Summary of Navigation and Guidance Analysis for Missions 2 and 2A

Midcourse Requirements, m/sec				Navigation Uncertainties, 1σ			
	Mean ΔV	σ	ΔV + 3σ		SMAA, km	SMIA, km	TOF, sec
First Midcourse	14.8	10.7	46.9	Control	646	224	103
Second Midcourse	1.4	0.8	3.8	Knowledge	644	184	101
Total, RSS			47.1				

Table V-25 Summary of Execution Errors and Entry Dispersions for Missions 2 and 2A

Deflection Execution Errors, 3σ			Entry Dispersions, 3σ			
	ΔV	Probe Attitude	Latitude, deg	0.1	Entry Angle, deg	0.2
Proportionality, %	4.8		Longitude, deg	0.2	Angle of Attack, deg	1.7
In-Plane Pointing, deg	2.3	1.4				
Out-Plane Pointing, deg	0.7	1.0	Coast Time, min	5.0		

Table V-26 Mission 2A Weight Estimate

		kg	lb
Science		14.4	31.7
Structure and Heat Sink		11.7	25.9
Thermal Control		2.5	5.5
Guidance and Control		1.2	2.7
Deflection Propulsion		0.0	0.0
Communications		8.4	18.5
Data Handling		2.3	5.0
Electrical		7.0	15.4
Mechanisms		.1	.30
Pyro		2.5	5.6
Ballast		1.3	3.0
	15% Margin	7.8	17.1
	Ejected Weight	59.4	130.7
Cover Mechanisms		- .1	- .3
	Entry Weight	59.3	130.4

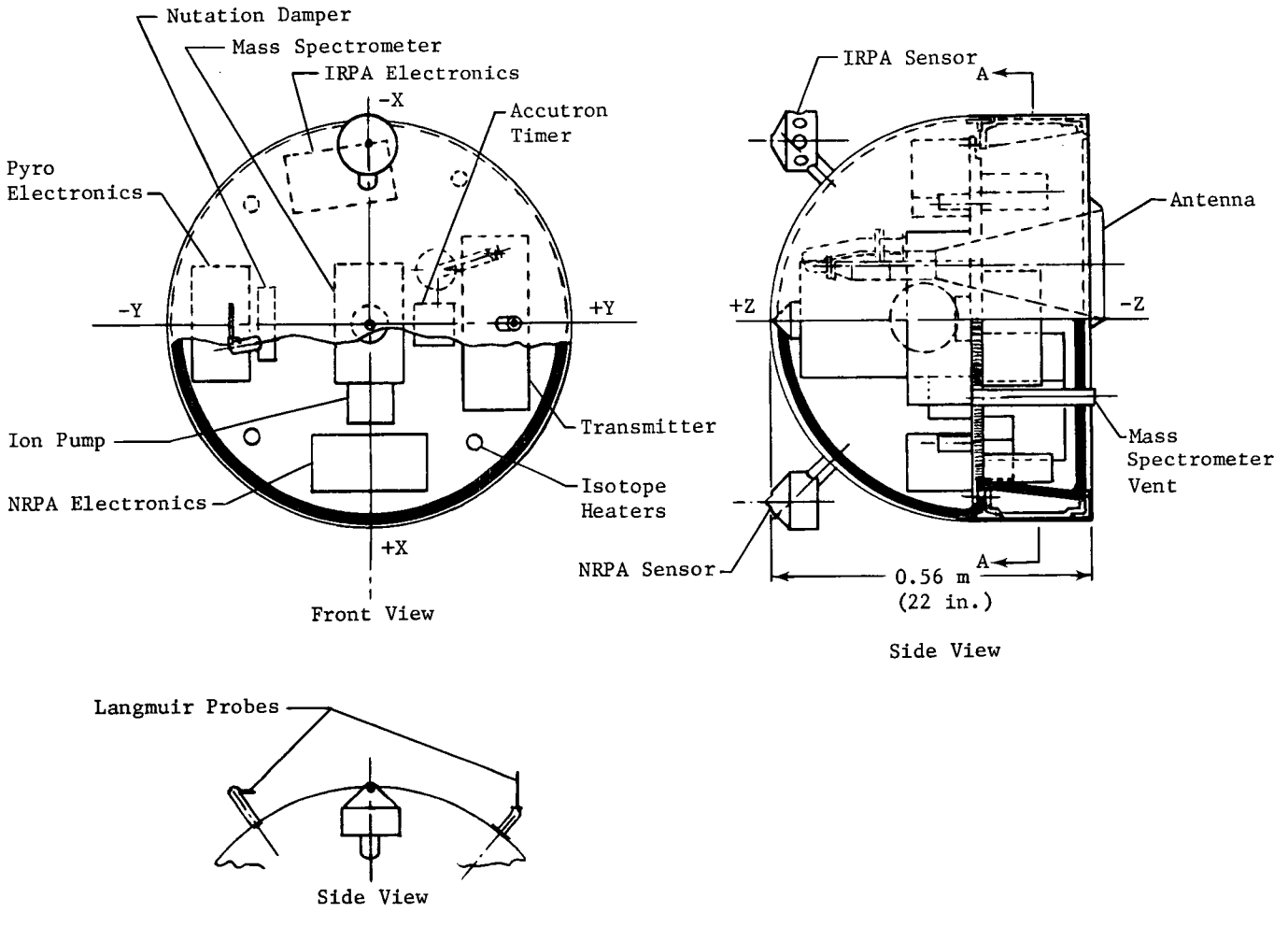

Fig. V-18 Mission 2A Probe Configuration Front and Side

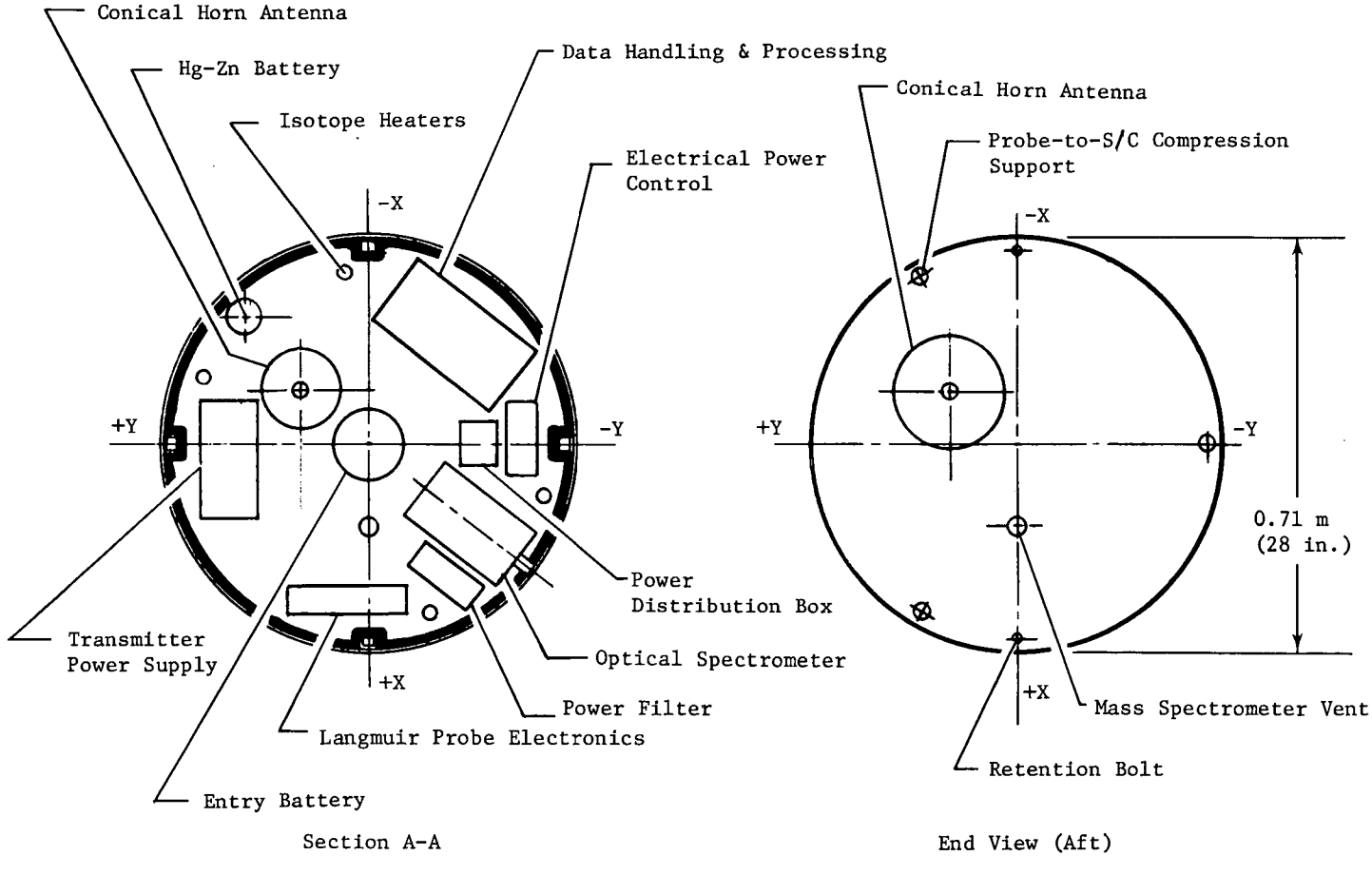

Fig. V-19 Mission 2A Probe Configuration

An improved location for the Langmuir probes is 25 cm (9.8 in.) from the Z axis on the nose cap and a minimum of 6.5 cm (2.56 in.) between the sensor and the surface of the nose cap. These probe sensors are 90° to the RPA, with one sensor parallel and the other perpendicular to the probe Z axis, as shown in Fig. V-18. This arrangement reduces the induced voltage transients from rotation in Jupiter's magnetic field and eliminates the need for a deployment mechanism.

The spectrometer/photometer viewing aperture is in the cylindrical portion of the probe body, providing adequate viewing and placing the viewing port in an area of low entry heating. Location of the aperture in the aft bulkhead or nose cap is not desirable because of Sun aspect angles and entry heating problems.

Interrelation of components of various subsystems and relationship of one subsystem to others are considered in the integration of internal equipment in the probe. For example, components of the power system, like batteries, filters, distribution boxes, electronics, and cabling are grouped to improve the power-subsystem mass fraction. Location of the antenna relative to the transmitter is influenced by the desire for short direct wave-guide coupling. The transmitter power supply is near the transmitter to reduce cabling and power losses.

The pyro system is required to operate or activate other subsystems throughout the probe. Therefore, its location is more flexible than those of other systems. The pyro system equipment includes electronics, capacitors, relays, and squibs.

A thermal blanket covers the entire inner surface of the probe structure except for the equipment deck, and ten 1-W radioisotope heaters are evenly distributed inside the probe, as shown in Fig. V-18 and V-19.

Spin stabilization of the probe requires that the mass moment of inertia about the Z-Z axis (spin axis) be greater than that about the transverse axes. It is desirable that the spin axis mass moment of inertia be greater by 20% or more, and that mass moments of inertia about the transverse axes be equal. A further requirement is that the principal mass moment of inertia coincide with the Z-Z axis of the probe. These requirements are met by properly locating components and by ballasting.

Probe support and retention locations are shown on the end view in Fig. V-19. Probe weight estimates are given in Table V-26.

a. Telecommunications - In the RF area, this mission differs from Mission 2 in the frequency of operation and use of nominal end-of-mission times. Spacecraft antenna acquisition requirements are shown in Fig. V-20. A five-position search during acquisition was selected with a 2.5° S/C antenna beamwidth, using the semiactive sector-scan technique discussed in Chapter VI, Subsection A4.

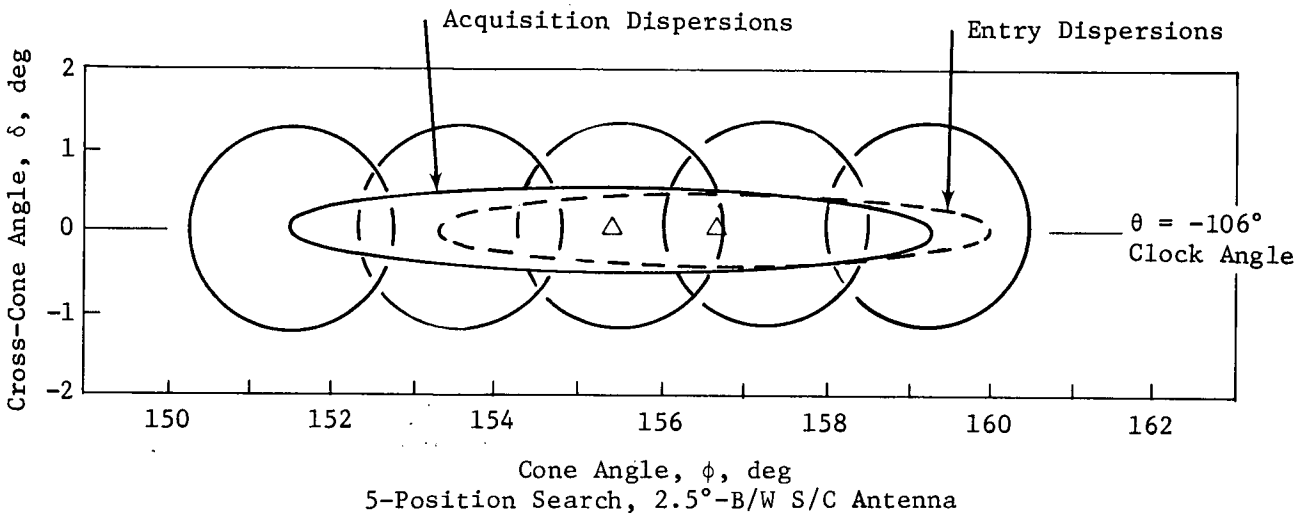

Fig. V-20 Spacecraft-Antenna Acquisition Requirements for Mission 2A

Design details of the RF components that comprise the telecommunications subsystem are listed in Table V-27. Complete details are given in Chapter VI, Section A for each component. This mission was redesigned for X-band, with larger S/C and probe antenna beamwidths used to cover increased dispersions in postition at acquisition and the end of the mission. Total RF power remains 20 W for either frequency because of compensating losses and gains in the RF link.

Table V-27 Telecommunications RF Subsystem for Mission 2A

Conditions:	S/C - Pioneer,	Bit Rate - 1024 bps*	
Component	Characteristic	Unit	Freq. - X-Band, 10 GHz Value
Probe Conical-Horn Antenna	Electrical B/W	deg	10.0
	Max Gain	dB	23.4
	Dia	cm	19.6
		in.	7.6
	Total Length	cm	46.8
		in.	18.4
	Weight	kg	0.34
		lb	0.75
Transmitter & Power Supply	RF Power Out	W	20.0
	Overall Efficiency	%	24.0
	dc Power at 28 Vdc	W	83.2
	Total Weight	kg	7.7
		lb	17.0
S/C Dish Antenna	Electrical B/W	deg	2.5
	Max Gain	dB	36.4
	Dia	cm	84.5
		in.	33.3
	Weight	kg	11.3
		lb	25.0
	Despin		yes
	Position Search		yes-5
	Freq Acquisition	sec	39.0
	Clock Angle, θ	deg	-106.0
	Cone Angle, ϕ	deg	151.5-159
S/C Receiver	System Temperature	°K	315.0
	dc Power at 28 Vdc	W	10.0
	Weight	kg	5.9
		lb	13.0

*Science plus engineering

b. Data Handling, Power, Pyrotechnics - The design approach of Mission 1 (Subsections B3b, c, d) and comments on Mission 2 (Subsection D3b) apply to the electronics of Mission 2A. For a general discussion of these electronic subsystems see Chapter VI, Sections B and C.

c. Heat Sink and Structure - The heat sink consists of 0.713-m (28-in.) dia beryllium hemispherical nose cap and the cylindrical skin on the skirt assembly weighing 5.8 kg (12.8 lb). It is 0.448 cm (0.176 in.) thick at the stagnation point and 1.27 mm (0.050 in.) thick at the trailing edge.

The structure is the same as that for Mission 1 (Subsection B3e).

d. Thermal Control - The thermal control subsystem consists of an internally mounted multilayer insulation blanket surrounding the probe equipment, insulating cover for the photometer aperture (removable before entry), and radioisotope heaters between the internal equipment packages. The multilayer insulation blanket consists of 72 layers of 1/4 mil Kapton polyamide film aluminized on one side, with beta glass cloth spacer material between layers. Total blanket thickness is 1.53 cm (0.6 in.). Ten 1-W radioisotope heaters are required (based on analysis), although it is expected that the actual requirement could be 8 to 12 W, depending on results of thermal testing of actual probe hardware. For this mission, an RF-transparent radome covers the communications antenna. This reduces heat loss from the probe interior through the antenna coupling.

e. Mechanical Subsystems - Mechanical subsystems consist of the spectrometer/photometer aperture cover and release system and probe-to-spacecraft separation system. Both are described in detail in Chapter VI, Subsection A3.

f. Attitude Control - Spin stabilization and passive damper design are similar to Missions 1 and 1A (Subsections B3h, and C3h). A general discussion of attitude control is in Chapter VIII.

4. Spacecraft, Interface/Modification, and Launch Vehicle

The Pioneer spacecraft with probe is launched on a Titan IIID-5-segment-D1 Centaur-Burner II. The following components are either modified or added to the spacecraft for the probe support or mission operation; probe support structure, environmental enclosure, electrical interface, receiver subsystem, despin and gimbal tracking antenna and platform, data handling, and propellant tank (capacity increased). Modification weight to the spacecraft is 50.2 kg (111.6 lb) for Mission 2A. The integration arrangement is shown in Fig. V-21.

F. MISSION 3 - GRAND TOUR JUN 78

The objective of this mission/system design was to incorporate a Jupiter probe as a passenger aboard a TOPS spacecraft to be launched in 1978 with postencounter objectives beyond a Jupiter flyby--Uranus and Neptune flybys.

To minimize perturbation of the spacecraft Grand Tour mission operations, probe deflection and attitude maneuvers were made a probe-system functional requirement. Consequently, mission design includes a probe deflection mode, and a propulsion and attitude-control system is incorporated in the probe.

The system requires the spacecraft to orient itself for probe ejection, thereby establishing probe attitude for deflection. After ejecting the probe, the spacecraft reorients to Earth lock and, at the end of the probe coast period, acquires the probe RF transmission, relays the data received, and continues toward its next objective (Uranus encounter).

Once ejected from the spacecraft, the probe, in turn, spins up, applies the required deflection ΔV, and then precesses to obtain a zero angle of attack at atmospheric entry.

The remaining probe systems are those necessary to satisfy the functional requirements of science data collection, data processing and transmission.

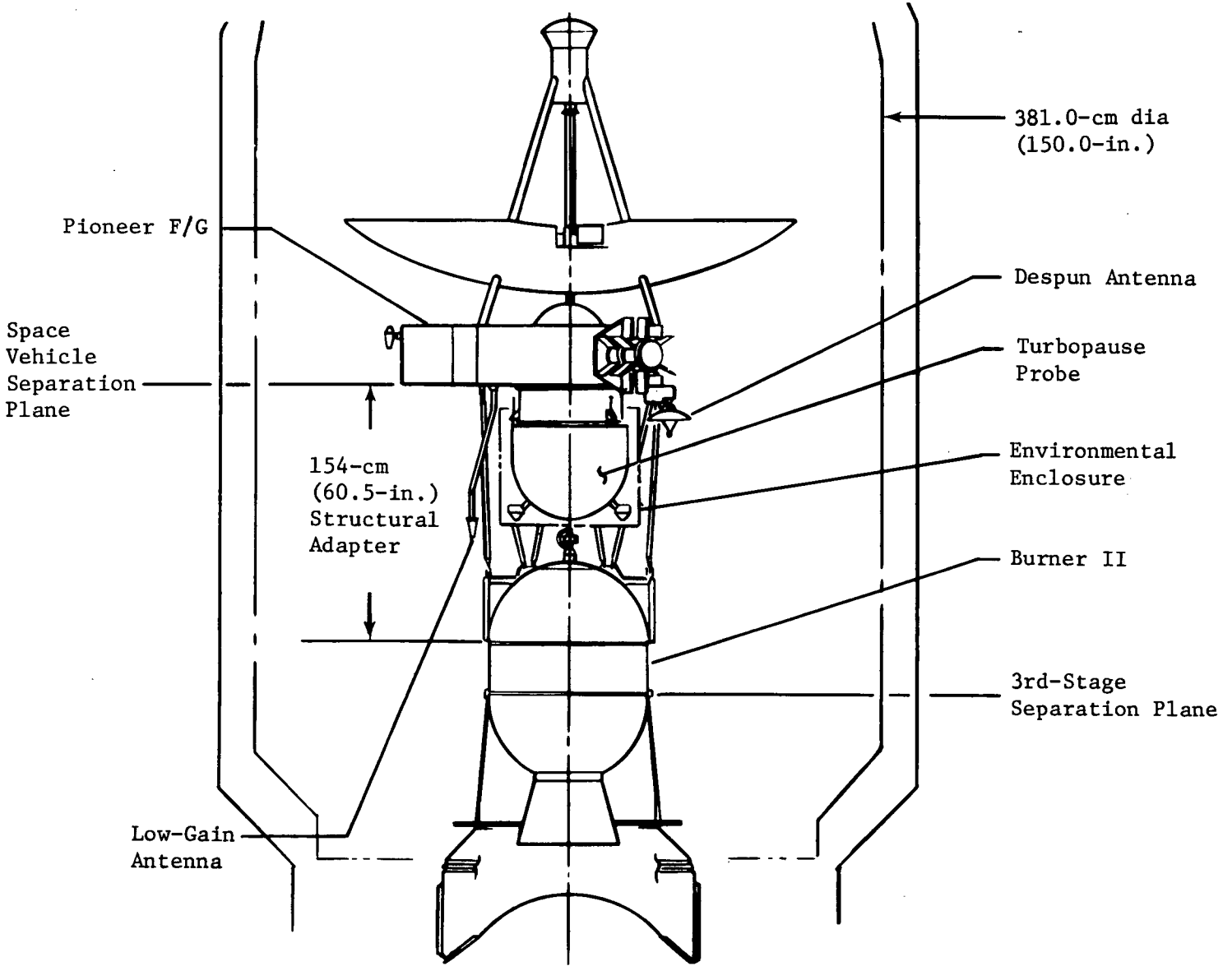

Fig. V-21 Probe-Spacecraft Interface for Mission 2A

Table V-28 lists the sequence of events, and Fig. V-22 shows the probe functional block diagram, which, in this case, includes the deflection-propulsion and attitude-control subsystems.

1. Science Payload and Performance

The instrument characteristics and mission performance for Mission 3 are shown in Table V-29. The primary difference between the science-instrument bit rate for this and other missions is the dayglow instrument, whose data rate depends on probe spin rate. For this mission, the spin rate is 100 rpm. A detailed breakdown of the data word collection that specifies a given bit rate is also presented. For a description of the contents of data words, see Chapter III, Section C, under the subsection concerning the particular instrument. On the left side of the lower part of the table are the upper atmospheric and ionospheric performance, the criterion being one measurement per scale height. The lowest values are the heaviest particles of both the neutrals and ions. For a detailed discussion of these numbers, see Chapter III, Subsections D1 and D3.

2. Mission Description

Interplanetary and approach trajectories for Mission 3 are constrained by the post-Jupiter encounter objectives of the JUN 78 mission. Launch and arrival dates were chosen to maximize the launch period. This results in a TOPS periapsis radius at Jupiter of 1.77 R_J. The lowest possible entry angle (consistent with the 20° lighting mask) is $\gamma_E = -33°$.

To affect the flyby trajectory as little as possible, a probe deflection (Mode 1) is used. Tradeoffs between ΔV requirements and entry dispersions resulted in selection of a 30×10^6-km deflection radius. Interplanetary and approach trajectories and the deflection maneuver are shown in Fig. V-23.

The launch analysis was initially performed with the Titan IIID-7-segment-Centaur with and without Burner II. The allowable launch periods for these vehicles are 28 and 13 days, respectively. The launch parameters are shown in Table V-30. Additionally, an analysis was performed using the MOPS configuration and the updated Titan IIID-5-segment-Centaur-Burner II model. The total weight for this spacecraft modification is approximately 33 kg (73 lb), the $C_3 = 108$, and the launch period is 14 days.

Table V-28 Mission 3 Grand Tour JUN 78 Sequence of Events

Event	Time, hr:min:sec	Function
1	L	Launch; October 3, 1978
2	L + 02:00:00	Separate S/C system from L/V; begin S/C cruise
3	S - 05:30:00	Separate probe protective enclosure S/C power on probe; start probe checkout
4	S - 00:30:00	Complete probe checkout
5	S - 00:20:10	Enable probe battery activation
6	S - 00:20:00	Activate probe separation battery
7	S - 00:17:00	Start S/C orientation for probe release
8	S - 00:02:00	Complete S/C orientation for probe release
9	S - 00:00:30	Activate probe separation battery
10	S - 00:00:20	Switch to probe internal power; energize probe power bus energize data system; start probe sequencer begin monitor of probe engineering data; enable probe separation ordnance
11	S L + 526 d	Separate probe (S/C power & signal)
12	S + 00:00:01	Initiate probe spin (0.91-m separation)
13	S + 00:00:17	Probe spin complete (100 rpm)
14	S + 00:10:00	Initiate probe ΔV (approx 549-m separation)
15	S + 00:10:06	Probe ΔV complete (82 m/sec)
16	S + 00:10:30	Begin probe precession (-36°); begin S/C reorientation
17	S + 00:23:00	Orient S/C (-67°) for Earth lock
18	S + 12:10:30	Probe precession complete
19	S + 12:10:40	Deactivate ACS; begin Langmuir probe decontamination
20	S + 12:22:40	Langmuir probe decontamination complete Deactivate probe power; deactivate data system
21	T - 01:17:26	Enable battery activation
22	T - 00:57:26	Activate entry battery
23	T - 00:37:26	Energize probe bus
24	T - 00:37:16	Data system on
25	T - 00:37:01	Transmitter on
26	T - 00:36:41	Enable ordnance/start probe acquisition
27	T - 00:36:31	Fire pyros at 15-sec interval
28	T - 00:35:01	Disable ordnance/start probe acquisition
29	T - 00:34:01	Complete probe acquisition/turn on instruments (ETP, IRPA, OPT)
30	T - 00:33:31	Transmit instrument engineering data (ETP, IRPA, OPT)
31	T - 00:31:31	Start data transmission (ETP, IRPA, OPT)
32	T - 00:30:32	Start transmission of engineering data (including stored)
33	T - 00:16:32	Turn on instruments (MS, NRPA)
34	T - 00:12:32	Stop transmission of engineering (housekeeping) data
35	T - 00:11:32	Transmit MS & NRPA engineering data
36	T - 00:10:32	Start data transmission (MS, NRPA)
37	T	Turbopause
38	T + 1.9 sec	Blackout
39	L + 576 days	S/C periapsis; May 1, 1980

Includes 5.15-min trajectory uncertainty, 0.3-min timer uncertainty, and 5% of time from acquisition start to T = 0.

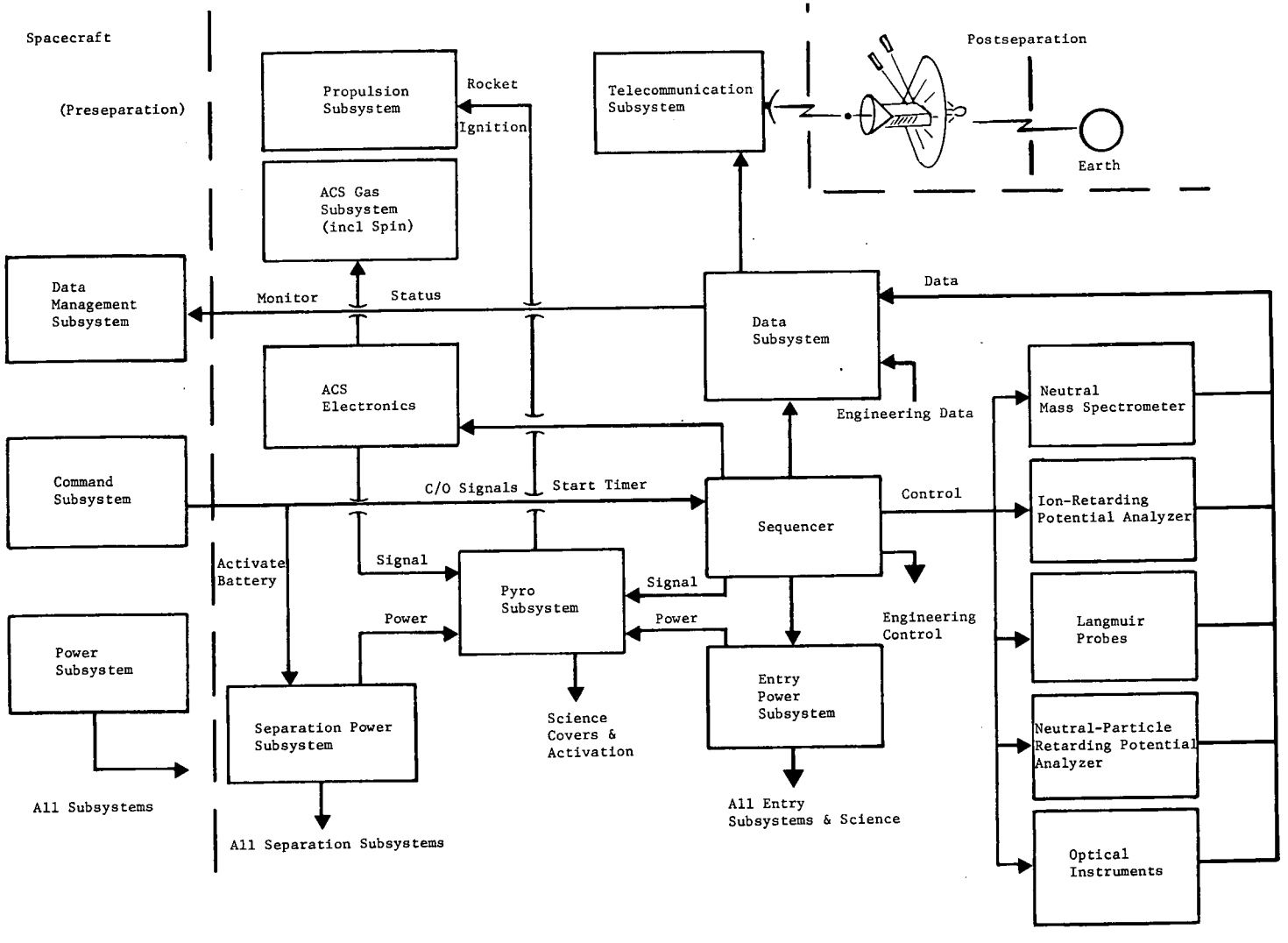

Figure V-22 Probe Block Diagram for Missions 3, 5, and 7

Table V-29 Missions 3 and 4 Science Instruments and Performance

Characteristics

Instruments	Weight, kg	Weight, lb	Power, W	Words/ Sample	Bits/ Sample	Sampling Time, sec	Science Bit Rate, bps
Langmuir Probes	1.36	3.0	3	3	24	0.5	48
IRPA	1.59	3.5	3	12	96	0.5	192
NRPA	2.27	5.0	5	14	112	0.5	224
Mass Spectrometer	5.91	13.0	15	22	176	0.4	440
Photometers	2.96	6.5	5	2	16	0.3	54
Totals	14.09	31.0	31				958

Mission Performance

Particle	Measurement/ Scale Height
H	3.4
H_2	1.7
He	0.9
H_1^+ & e^-	6.6
H_2^+	5.3
H_3^+	3.0
He^+	3.1
HeH^+	1.3

Note: Entry Flight-Path Angle, $\gamma_E = -33°$

Mission Times from

50,000 km to turbopause (min) 23.4

1000 km to turbopause (sec) 30.6

Turbopause to blackout (sec) 1.9
(minimum time below turbopause)

Mass-Spectrometer Measurements
(0.4 sec each)

Above turbopause (+20 to 0 km) = 1.54

Below turbopause (0 to -60 km) = 4.63

Total (+20 to -60 km) = 6.17

1. Interplanetary Trajectory

LD	10/3/78		
AD_J	5/1/80	TOF_J	576 days
AD_U	3/15/85	TOF_U	1780 days
AD_N	8/25/88	TOF_N	1255 days

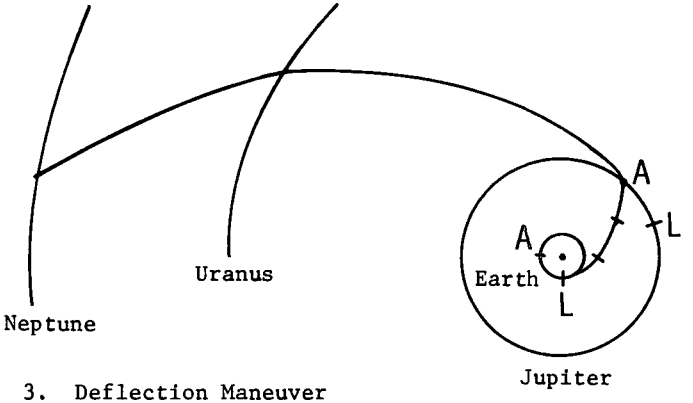

2. Approach Trajectory
   Rp = 1.94 Rj
   γ_E = -33°

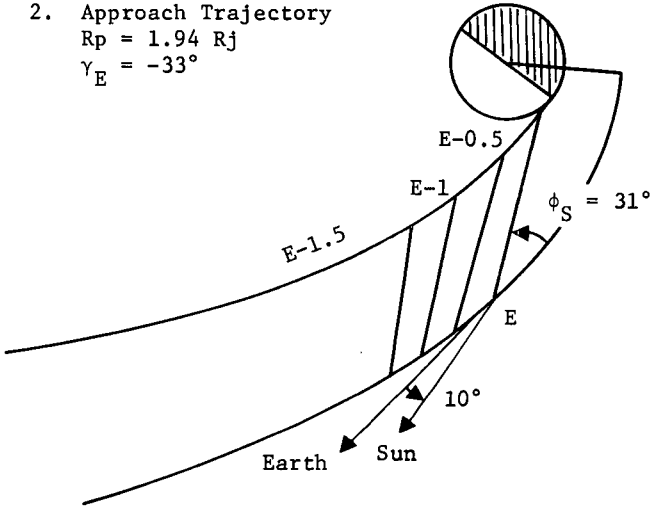

3. Deflection Maneuver
   Deflect Probe
   Radius = 30M km
   Time = 29 days

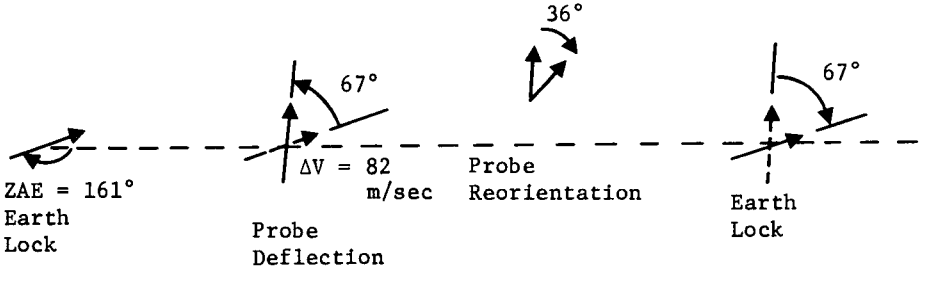

Figure V-23 Mission 3 June 78 Trajectories

Table V-30 Summary of Launch Requirements for Mission 3

Payload Summary	kg (lb)	Nominal Launch		Launch-Period Analysis		
Probe (15% margin)	87(194)	C_3, km^2/sec^2	105	Vehicle	Titan III/7-segment Centaur	Burner II
S/C Mods (15% margin)	34(74)	Park Orbit Time, hr	0.6	C_3, km^2/sec^2	107	120
Spacecraft (no margin)	658(1450)	Launch Window, hr	1.3	Period, days	13	28
Adapter (15 % margin)	16(35)	DLA, deg	31.8			
Total	795(1753)					

Table V-31 Summary of Navigation and Guidance Analysis for Mission 3

Midcourse Requirements, m/sec				Navigation Uncertainties, 1σ			
	Mean ΔV	σ	ΔV + 3σ		SMAA, km	SMIA, km	TOF, sec
First Midcourse	18.3	10.9	51.0	Control	948	610	55
Second Midcourse	.7	.5	2.2	Knowledge	811	601	49
Total, RSS			51.1				

Table V-32 Summary of Execution Errors and Entry Dispersion for Mission 3

Deflection Execution Errors, 3σ			Entry Dispersions, 3σ			
	ΔV	Probe Attitude	Latitude, deg	0.7	Entry Angle, deg	1.7
Proportionality, %	1.0		Longitude, deg	1.5	Angle of Attack, deg	3.2
In-Plane Pointing, deg	1.0	2.0				
Out-Plane Pointing, deg	1.0	2.0	Coast Time, min	5.2		

The midcourse requirements were assumed to be those of a typical fast-approach trajectory with a 30×10^6-km deflection radius. Execution errors used are a bit optimistic in view of data obtained later in the study. The resulting dispersions are all acceptable. The navigation parameters and execution errors are in Tables V-31 and V-32.

3. Configuration

The configuration for Mission 3 probe contains both ACS and deflection propulsion systems, with a hemispherical forward section and cylindrical aft section. The basic probe is 0.76 m (30 in.) in diameter and 0.61 m (24 in.) long, as shown in Fig. V-24 and V-25.

Science experiments are integrated in the overall probe design, constrained by their functional requirements. The mass spectrometer, IRPA, NRPA, and Langmuir probes all require unobstructed access to atmospheric particles during entry. This requirement is met by placing the neutral mass spectrometer inlet directly at the nose-cap stagnation point and the RPAs at approximately one body radius from the Z axis at the same body station as the stagnation point of the nose cap. In Ref V-1, two other locations for RPAs were studied (just off the dome/cylinder juncture and at the stagnation point) and the position shown in Fig. V-24 has approximately half the reflected particle interference of the dome/cylinder juncture location. The mass spectrometer is vented through a 2.5-cm (0.98-in.) tube to the probe's wake, as shown in Fig. V-25.

The Langmuir probes extend radially from the cylindrical section when deployed. They are located symetrically on the probe and are retained in the stowed position by the photometer aperture covers. The probes are deployed with the covers. To meet the scientific requirements, probe sensors are located 36 cm (14.2 in.) radially from the probe surface to reduce the effect of the body sensors. One sensor is parallel and the other perpendicular to the probe's Z axis.

Photometer viewing apertures are in the cylindrical portion of the probe body, providing adequate viewing and placing the viewing ports in an area of low entry heating. Location of the aperture in the aft bulkhead or nose cap is not desirable because of Sun aspect angles and entry heating problems.

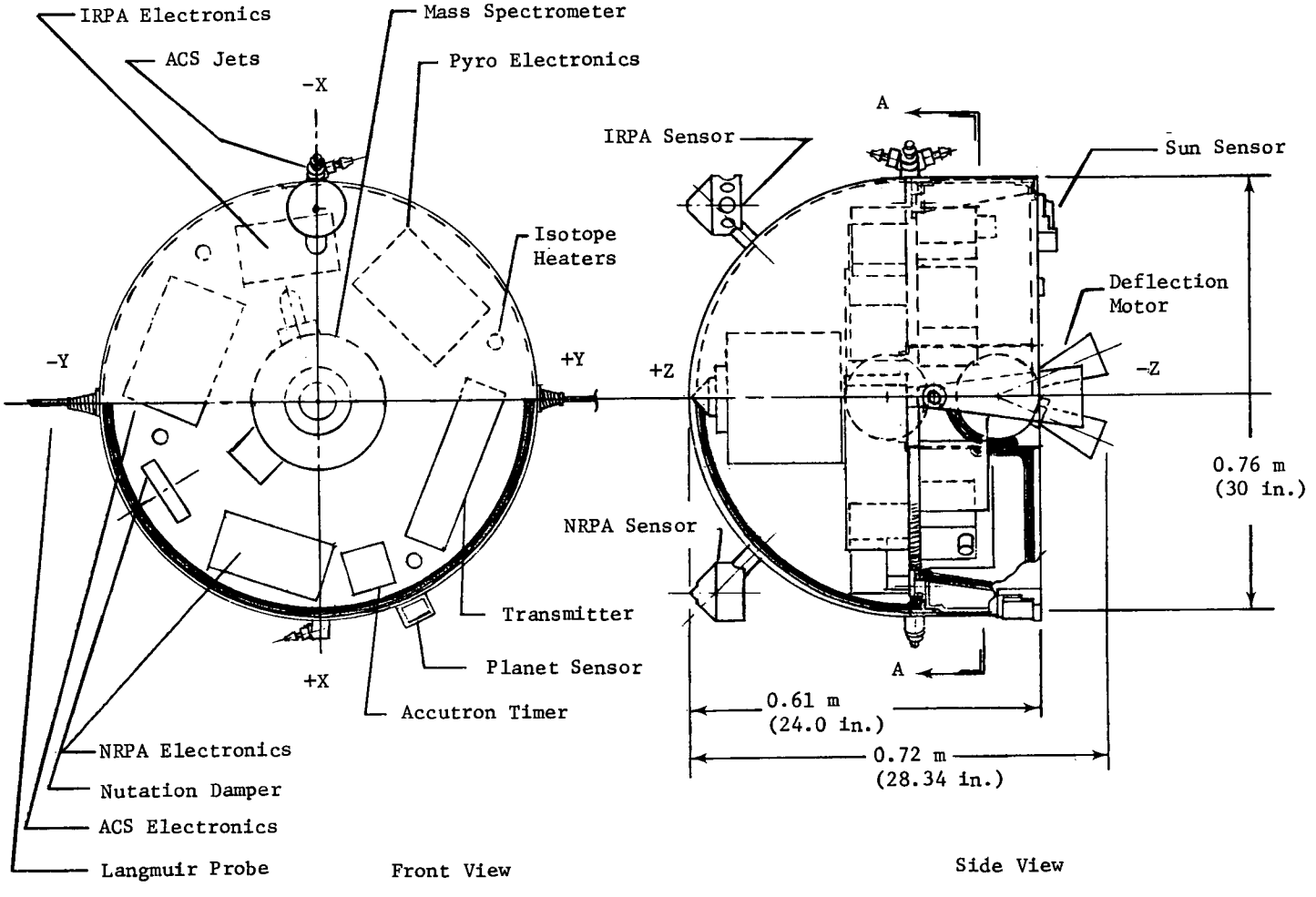

Figure V-24 Mission 3 Probe Configuration Front and Side

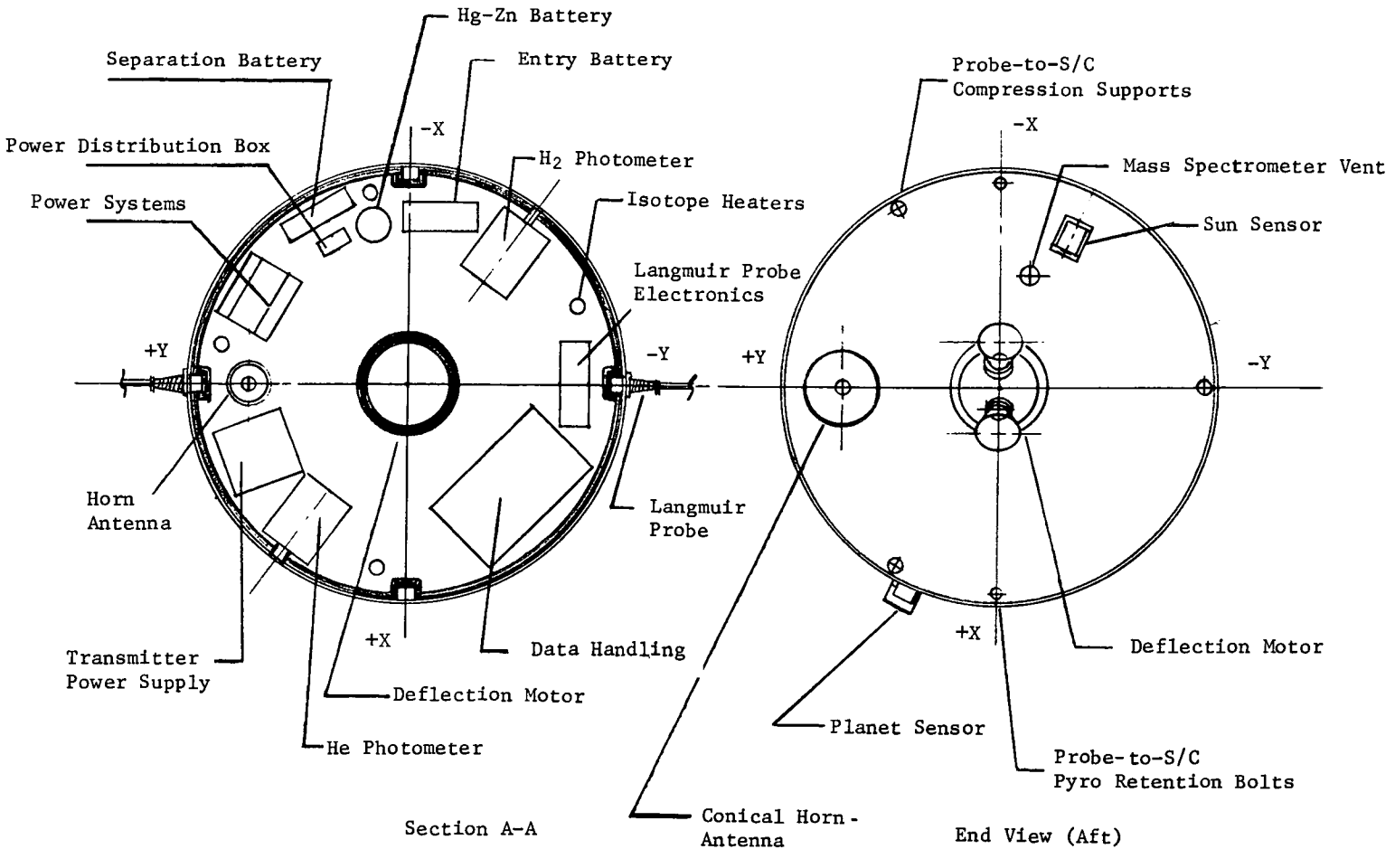

Figure V-25 Mission 3 Probe Configuration End and Section

The interrelation of components of various subsystems and the relationship of one subsystem to others are considered in the integration of internal equipment in the probe. For example, power-system components, like batteries, filters, distribution boxes, electronics, and cabling are grouped to improve the power-subsystem mass fraction. The attitude-control system with its Sun and planet sensors, nutation damper and timer, and cold-gas system for spin, despin, and precession maneuvers, requires specific locations for individual components to obtain proper inputs for controlled flight with required accuracy.

The deflection propulsion system is a dual-nozzle solid propellant motor embedded in the aft bulkhead and aligned with the probe's Z axis to achieve directional accuracy.

Location of the antenna relative to the transmitter is influenced by the desire for short direct wave-guide coupling. The transmitter power supply is near the transmitter to reduce cabling and power losses.

The pyro system is required to operate or activate other subsystems throughout the probe. Therefore, its location is more flexible than those of other systems. Pyro system equipment includes electronics, capacitors, relays, and squibs.

A thermal blanket covers the entire inner surface of the probe structure except for the equipment deck, and 12 to 15 1-W radioisotope heaters, as shown in Fig. V-25 and V-26, provide thermal control during interplanetary cruise.

Spin stabilization of the probe requires that the mass moment of inertia about the Z-Z axis (spin axis) be greater than that about the transverse axes. It is desirable that the spin-axis mass moment of inertia be greater by 20% and that mass moments of inertia about the transverse axes be equal. A further requirement is that the principal mass moment of inertia coincide with the Z-Z axis of the probe. These requirements are principally met by properly locating components and by ballasting.

Probe support and retention locations are shown on the end view in Fig. V-25. Probe weight estimates are given in Table V-33.

Table V-33 Mission 3 Weight Estimate

	kg	lb
Science	14.6	32.2
Structure & Heat Sink	14.4	31.8
Thermal Control	3.6	8.0
Guidance & Control (less propellant)	8.2	18.1
Deflection Propulsion (less propellant)	3.0	6.6
Communications	8.8	19.4
Data Handling	4.2	9.3
Electrical	11.1	24.4
Mechanisms	0.5	1.0
Pyro	3.5	7.8
Ballast	1.6	3.5
15% Design Margin	11.0	24.3
Total - Probe Coast Weight	84.5	186.4
Solid Propellant +15%	2.9	6.3
Nitrogen Gas +15%	0.5	1.2
Covers	0.2	0.5
Total - Probe Ejected Weight	88.1	194.4

a. Telecommunications - This mission has a relatively small communications range $\left(R_P = 1.94\ R_J\right)$ with small dispersions because a TOPS S/C is used. A relay antenna with a 4° beamwidth adequately covers acquisition and entry dispersions, as seen in Fig. V-26.

Design details of RF components of the telecommunications subsystem are listed in Table V-34. Note that 22 W RF are required at K-band and 7 W at X-band. An 8° conical horn is too long at X-band to fit into the probe. Therefore, a 10° horn with 1.9 dB less gain was used at X-band. There were no problems with the S/C antenna dish size. The S/C antenna does not require any position search or dispin platform because the S/C is 3-axis stabilized.

The RF system for this mission is designed for K-band transmissions.

b. Data Handling - This subsystem is similar to the subsystem described for Mission 1 (Subsection B3b). General discussion of data-handling alternative approaches and formating is in Section B of Chapter VI.

c. Power Subsystem - The power subsystem is shown in Fig. V-27. There are two power subsystems shown: (1) postseparation power source and power conditioning, and (2) entry power source, distribution, and filtering. The latter is similar to the power subsystem for Mission 1 (Subsection B3c). The postseparation subsystem provides power for pyrotechnics and attitude control required during that period. A centralized regulated multivoltage dc distribution is used because the electronics will be operated well outside the radiation belts and a more compact design can be achieved. A more detailed discussion of power-source and system alternatives is in Section C of Chapter VI.

d. Pyrotechnic Control - The electronics and implementation of pyrotechnic control is similar to that described for Mission 1 (Subsection B3d) and in the design discussion (Chapter VI, Section C). There are 12 pyrotechnic events, showing the increased complexity of this mission, with following weights and volumes for component parts.

	Electronics	Relays	Capacitor Banks
Weight, kg (lb)	0.91 (2.0)	1.14 (2.5)	0.36 (0.8)
Volume, cm^3 ($in.^3$)	1230 (75)	443 (27)	656 (40)

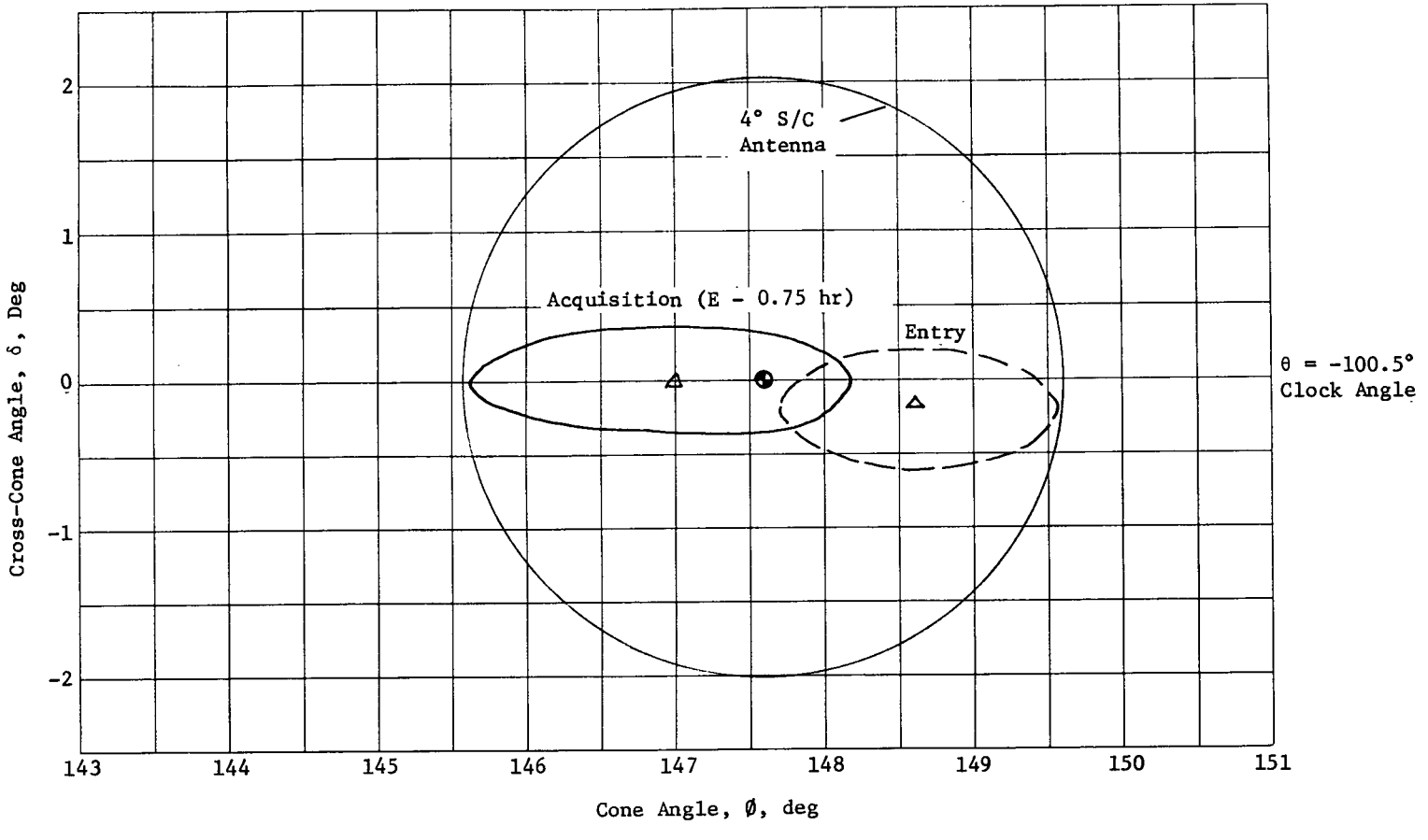

Figure V-26 Spacecraft-Antenna Acquisition Requirements for Mission 3

Table V-34 Telecommunications RF Subsystem for Mission 3

Conditions:	S/C - TOPS		Bit Rate - 1102 bps*	
			Value	
Component	Characteristic	Unit	K Band, 20 GHz	X Band, 10 GHz
Probe Conical-Horn Antenna	Electrical B/W	deg	8.0	10.0
	Max Gain	dB	25.3	23.4
	Dia	cm	12.2	19.6
		in.	4.8	7.6
	Total Length	cm	36.0	46.8
		in.	14.2	18.4
	Weight	kg	0.3	0.34
		lb	0.6	0.75
Transmitter & Power Supply	RF Power Out	W	22.0	7.0
	Overall Efficiency	%	24.0	24.0
	dc Power at 28 Vdc	W	91.5	29.1
	Total Weight	kg	7.7	7.7
		lb	17.0	17.0
S/C Dish Antenna	Electrical B/W	deg	4.0	4.0
	Max Gain	dB	32.5	32.5
	Dia	cm	27.33	54.6
		in.	10.76	21.5
	Weight	kg	1.4	2.27
		lb	3.0	5.0
	Despin		no	no
	Position Search		no	no
	Freq Acquisition	sec	67.0	35.0
	Clock Angle, θ	deg	-100.5	-100.5
	Cone Angle, ϕ	deg	147.8	147.8
S/C Receiver	System Temperature	°K	400.0	315.0
	dc Power at 28 Vdc	W	10.0	10.0
	Weight	kg	5.9	5.9
		lb	13.0	13.0

*Science plus engineering

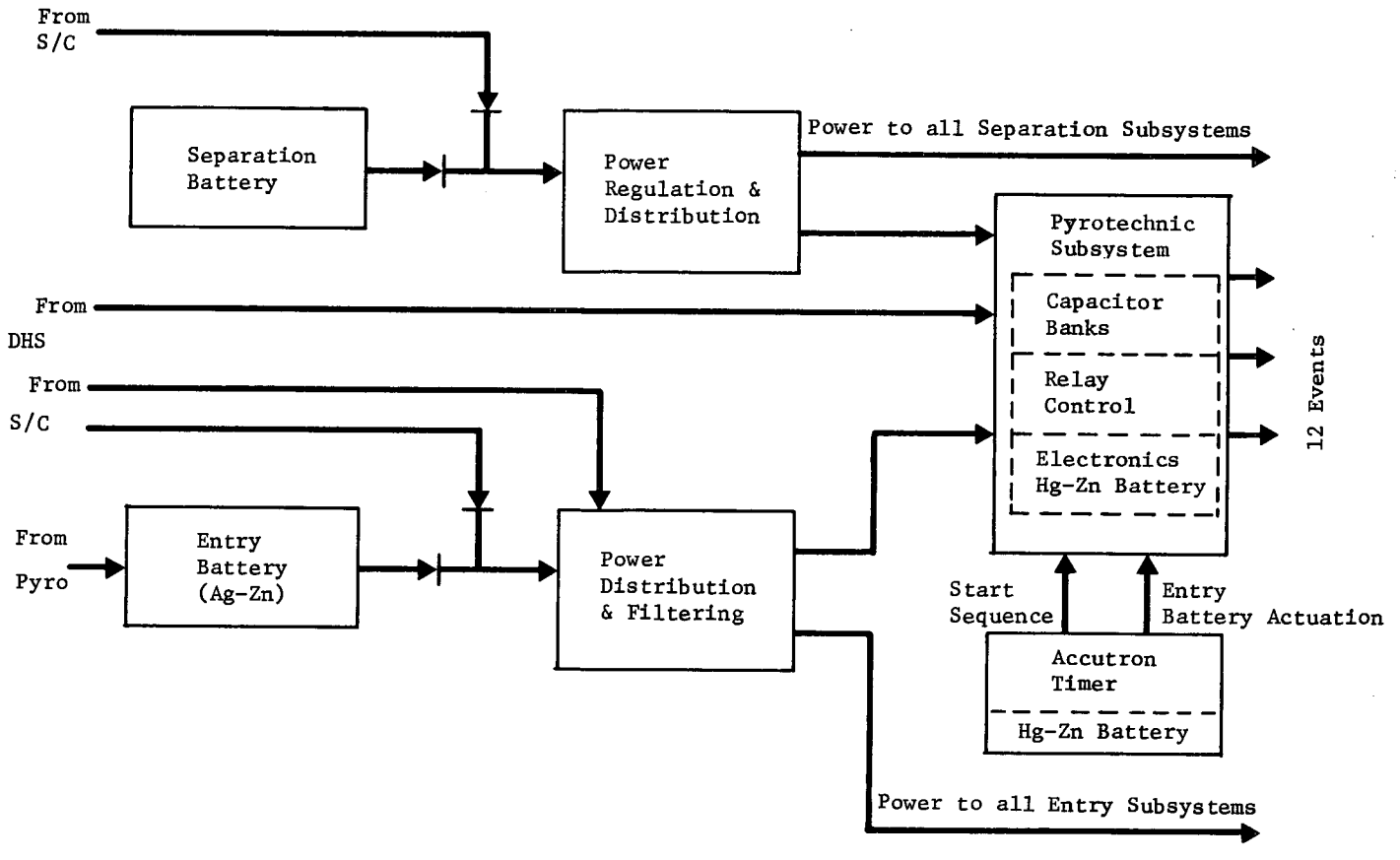

Figure V-27 Power and Pyrotechnic Subsystems for Mission 3

e. Heat Sink and Structure - The heat sink consists of a 0.76-m-dia (30-in.) beryllium hemispherical nose cap and cylindrical skin on the skirt assembly weighing 5.45 kg (12.0 lb). It is 0.40 cm (0.158 in.) thick at the stagnation point and 1.27 mm (0.050 in.) thick at the trailing edge.

The structure consists of conventional aluminum machinings, bonded aluminum honeycomb, fiberglass honeycomb, and oriented fiberglass composite structures.

f. Thermal Control - The thermal-control subsystem consists of an internally mounted multilayer insulation blanket of the same materials, thickness and number of layers as the Mission 1 probe blanket. In addition, a separate small multilayer insulation blanket will encapsulate the deflection-motor assembly during spacecraft cruise. This secondary blanket will remain with the spacecraft at probe separation. The thermal subsystem also includes radioisotope heaters located among the equipment packages and a small electric resistance heater in the deflection-motor insulation blanket. Twelve to 15 radioisotope heaters will be required. Approximately 2 W of spacecraft power will be required for the deflection-motor resistance heater. This thermal-control subsystem also includes two removable insulating aperture covers for the photometers.

g. Mechanical Subsystems - Mechanical subsystems for Mission 3 consist of the photometer aperture covers and release systems, and the probe-to-spacecraft separation system. Both are described in detail in Chapter VII, Subsection A3.

h. Propulsion (ACS, ΔV) - The Mission 3 probe incorporates a GN_2 propulsion subsystem for required probe spin-up and precession control. A dual-nozzle spherical composite-grain solid-propellant rocket motor is used to provide required deflection ΔV to the probe.

The probe is spun up to 10.47 rad/sec (100 rpm) at separation from the spacecraft. After a separation distance of 548 m (1800 ft) is attained, the solid-rocket probe deflection motor is fired, resulting in attainment of a deflection ΔV of 82.1 m/sec. At completion of the deflection maneuver, the GN_2 precession-control propulsion subsystem will precess the probe 0.63 rad (-36°). The precession subsystem is provided with solenoid valves for accurate precession control, whereas squib valves control the spin-up system.

i. Attitude-Control Subsystem - The attitude-control subsystem for this mission must spin up to 10.47 rad/sec (100 rpm) to hold attitude during the deflection maneuver, and to maneuver to the final entry attitude. The subsystem uses a Sun sensor and Jupiter sensor to obtain 3-axis reference information. These data are obtained from measurements of solar aspect angle and the angle between the spin-axis Jupiter plane and the spin-axis Sun plane. Subsystem accuracy is specified by the requirements for ΔV impulse pointing (1°) rather than communications (3°) or science (5°). A detailed discussion of alternatives, design factors, and electronics is in Chapter VIII.

4. Spacecraft Interface/Modification and Launch Vehicle

The TOPS spacecraft with the probe is launched on a Titan IIID-7-segment-D1 Centaur-Burner II. The following components are either modified or added to the spacecraft for probe support or mission operation: probe support structure, environmental enclosure, electrical interface, receiver subsystems, fixed tracking antenna, and data handling. Initial weight estimates of these modifications totaled 33.5 kg (74.0 lb). These weights were not refined when effort on use of TOPS was discontinued. The integration arrangement is shown in Fig. V-28.

G. MISSION 4 - GRAND TOUR JUN 79

The objective of this mission/system design was to incorporate a Jupiter probe as a passenger aboard a TOPS spacecraft to be launched in 1979 with postencounter objectives beyond a Jupiter flyby--Uranus and Neptune flybys.

It was found that the Jupiter flyby radius $\left(9.85\ R_J\right)$ necessary to meet postencounter objectives imposed severe constraints on the telecommunication power requirements, consequently, system definition was not carried through in detail.

Two alternative approaches were evaluated to determine the effects of modifying the probe mission objectives and constraints. The first was a reduction in data return and required transmission power; the second, sufficient reduction of flyby radius to accommodate an RF system capable of meeting the required data rate. Varying these parameters included science, mission and RF link analyses; system defintion was not included.

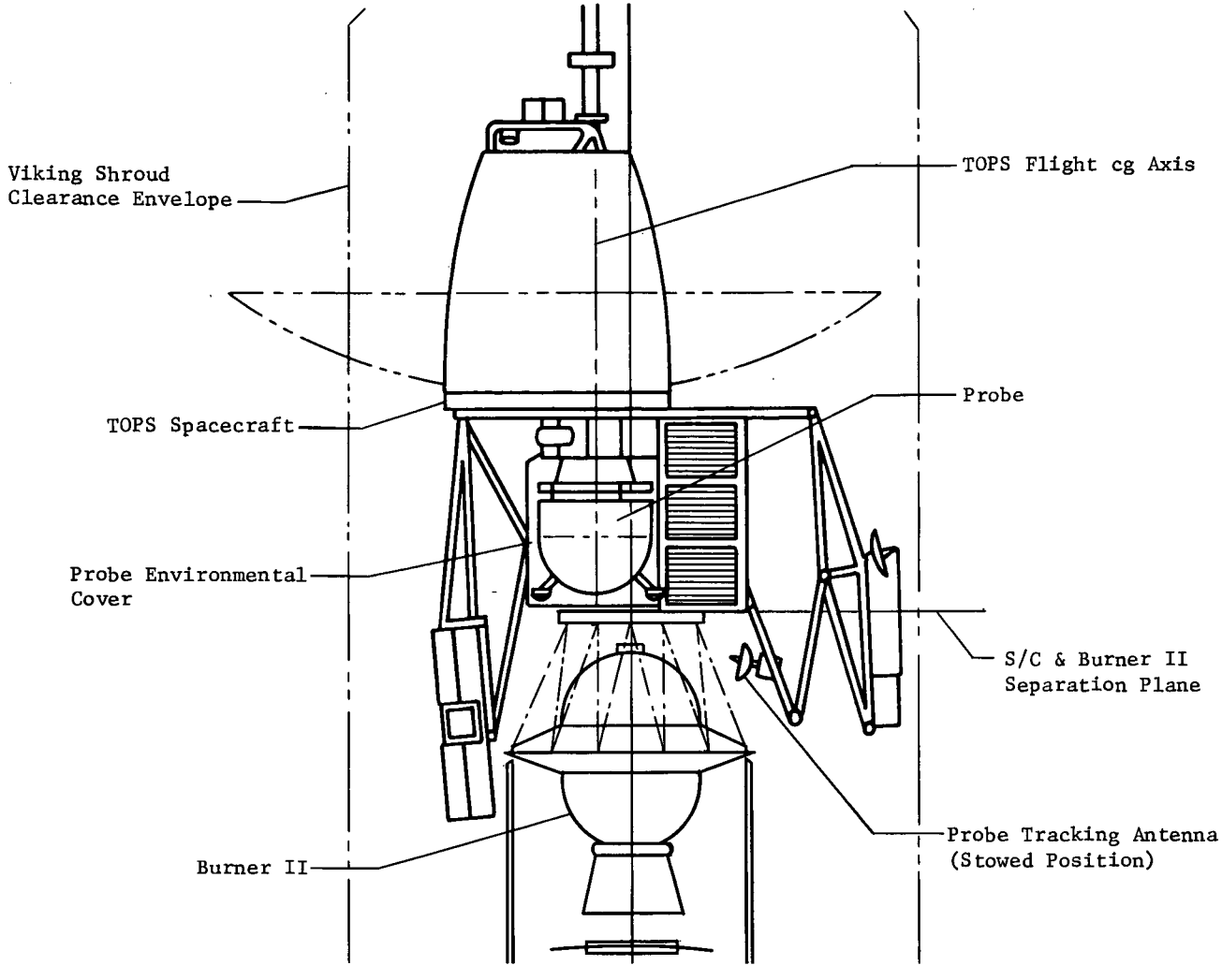

Figure V-28 Probe-Spacecraft Interface for Mission 3

The updated electron density model used in the refinement of Missions 1A, 2A, and 7 was not available for use in these analyses. Application of this model should result in the JUN 79 launch opportunity appearing more favorable as a candidate for a Jupiter probe mission. A brief evaluation of a maximum-range mission at X-band (10 GHz) (Chapter VI, Subsection A3) showed that a probe design was possible up to a S/C flyby radius of about 7 R_J. This design required a 40-W probe transmitter, which is practical at X-band.

1. Science Payload and Performance

The instrument characteristics and mission performance for Mission 4 are shown in Table V-29 in the Mission 3 discussion. Similar entry flight-path angles with identical science payloads result in identical mission performance for both Mission 3 (Section F) and Mission 4 (Section G).

2. Mission Description

The interplanetary trajectory for the standard Mission 4 JUN 79 mission was primarily selected on the basis of maximizing the launch period. This resulted in a relatively large periapsis radius at Jupiter $\left(9.85\ R_J\right)$. The minimum entry angle consistent with the 20° lighting mask constraint is $\gamma_E = -33°$ for this trajectory. The interplanetary and approach trajectories are shown in Fig. V-29.

The probe deflection mode (Mode 1) was used so as to disturb the Grand Tour trajectory as little as possible. The large periapsis radius required the large deflection radius of 50×10^6 km. The deflection ΔV and rotation angles are relatively large, as indicated in the operational sequence, shown in Fig. V-29.

Launch characteristics of the mission are indicated in Table V-35. The launch periods are 15 and 30 days, respectively, based on performance data for the Titan IIID-7-segment-Centaur with and without Burner II. Using the updated data for the Titan IIID-5-segment Centaur-Burner II, the required C_3 would be about 107 km^2/sec^2 and the launch period about 15 days.

The midcourse requirements and navigation uncertainties in Table V-36 are for a typical fast trajectory to Jupiter and were not developed specifically for the JUN 79 trajectory. However, the data should be representative of this mission.

1. Interplanetary Trajectory

LD 11/5/79

AD_J 6/8/81 TOF_J = 581 days

AD_U 3/4/86 TOF_U = 2311 days

AD_N 11/11/89 TOF_N = 3661 days

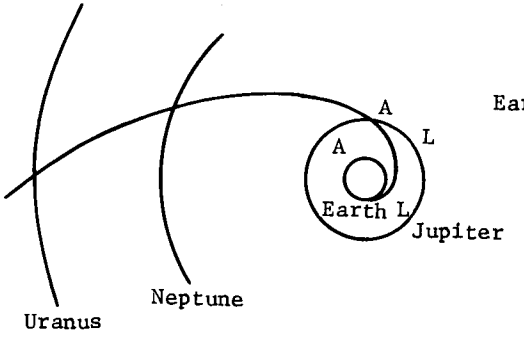

2. Approach Trajectory

R_P = 9.85

γ = 33°

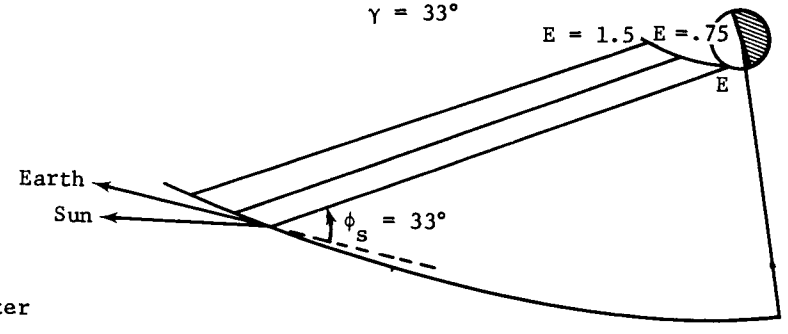

3. Deflection Maneuver

Deflection Probe

Radius = 50M km

Time = 49 days

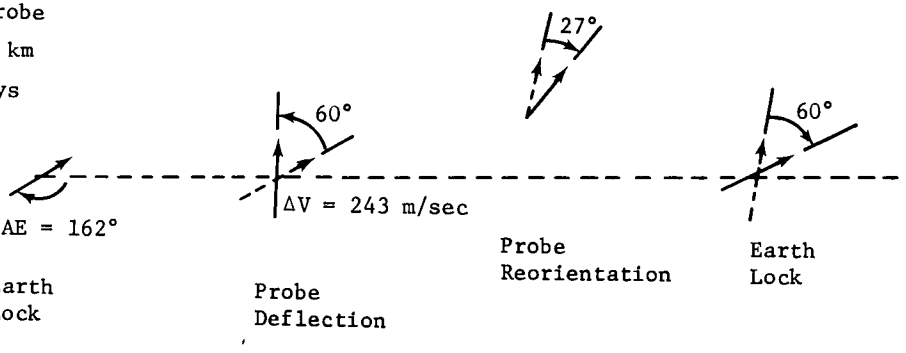

Figure V-29 Mission 4 and 4A Grand Tour 79 Trajectories

Table V-35 Summary of Launch Requirements for Mission 4 and 4A

Payload Summary	kg (lb)	Nominal Launch		Launch-Period Analysis		
Probe (15% margin)	87(194)	C_3, km^2/sec^2	104	Vehicle	Titan III/7-segment/Centaur	Burner II
S/C Mods (15% margin)	34(74)	Park Orbit Time, hr	0.9	C_3, km^2/sec^2	107	120
Spacecraft (no margin)	658(1450)	Launch Window, hr	4.1	Period, days	15	30
Adapter (15 % margin)	16(35)	DLA, deg	27			
Total	795(1753)					

Table V-36 Summary of Navigation and Guidance Analysis for Mission 4 and 4A

Midcourse Requirements, m/sec				Navigation Uncertainties, 1σ			
	Mean ΔV	σ	ΔV + 3σ		SMAA, km	SMIA, km	TOF, sec
First Midcourse	18.3	10.9	51.0	Control	975	760	148
Second Midcourse	.6	.4	1.8	Knowledge	607	340	57
Total, RSS			51.1				

Table V-37 Summary of Execution Errors and Entry Dispersions for Mission 4 and 4A

Deflection Execution Errors, 3σ			Entry Dispersions, 3σ			
	ΔV	Probe Attitude	Latitude, deg	6.6	Entry Angle, deg	4.2
Proportionality, %	1		Longitude, deg	7.8	Angle of Attack, deg	6.8
In-Plane Pointing, deg	1.4	2.0				
Out-Plane Pointing, deg	1.4	2.0	Coast Time, min	43.2		

Standard execution errors for TOPS were used for the dispersion analysis (Table V-37). The large dispersions are a result of the large deflection ΔV (243 m/sec) and large deflection radius. The angle of attack uncertainty of 6.8° (3σ) is outside the 5° requirements set by science.

Two additional versions of Mission 4 were investigated in the science and communications design area. The first, designated Mission 4B, was retargeted to a lower flyby periapsis radius of 6.6 R_J and is described in the following paragraph.

Mission 4B - The standard JUN 79 trajectory was changed slightly to reduce the flyby radius at Jupiter to a more favorable value $\left(6.6\ R_J\right)$. This led to an Earth-Jupiter flight-time reduction of 43 days, with a corresponding increase in launch energy and decrease in launch period. Minimal entry angle was $\gamma_E = -34°$, so this also suffered in the trade.

The probe deflection at 50×10^6 km was still used. The ΔV magnitude was reduced from 243 to 180 m/sec because of the decreased periapsis radius. Rotation angles were only slightly reduced. Interplanetary and approach trajectories and maneuver sequence are shown in Fig. V-30.

The reduction in launch period is evident from the data in Table V-38. The mission can no longer be flown with the Titan IIID-5-segment-Centaur-Burner II (updated). It requires the 7-segment Titan IIID with Centaur and Burner II.

The midcourse maneuver requirements and navigation uncertainties data (Table V-39) were assumed identical to those of the standard trajectory. Using the same execution error model as in the standard mission, the dispersions were reduced because of the smaller ΔV (Table V-40). However, the angle of attack uncertainty of 5.3° (3σ) is still larger than the acceptable error of 5.0°

Telecommunications - Acquisition and entry-probe dispersion ellipses can be covered with a fixed 5° S/C relay antenna. Probe antenna minimum beamwidth is 8°. The resulting K-band RF power required for a bit rate of 1024 bps is 842 W. Lowering the frequency to X-band results in a required power of 172 W for the same antenna sizes. Therefore, it was concluded that a mission with a periapsis radius of 9.84 R_J would require further refinement of the RF subsystem to lower the power required to a minimum.

1. Interplanetary Trajectory

LD 11/11/79

AD_J 5/2/81 TOF_J = 538 days

AD_U 7/26/85 TOF_U = 2086 days

AD_N 11/10/88 TOF_N = 3289 days

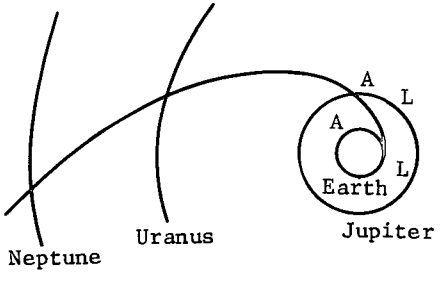

2. Approach Trajectory

$R_P = 6.6\ R_J$

$\gamma = -34.2°$

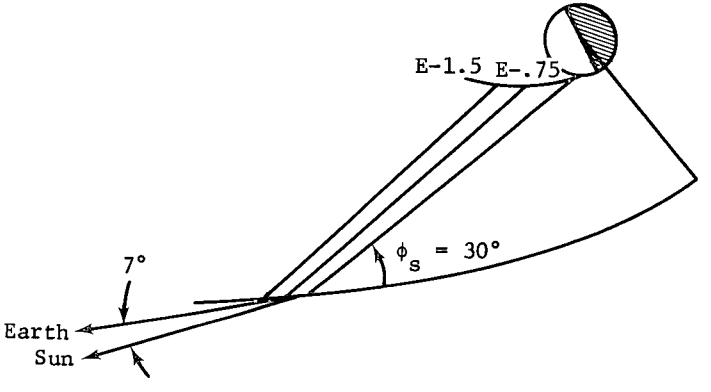

3. Deflection Maneuver

Deflect Probe

Radius = 50M km

Time = 45 days

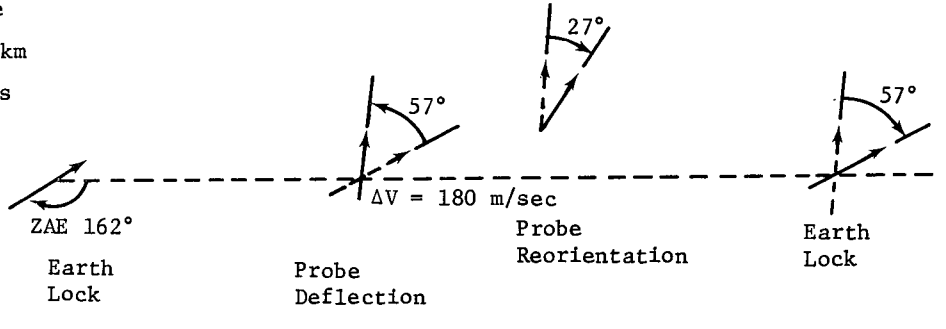

Figure V-30 Mission 4B Grand Tour 79 Trajectories

Table V-38 Summary of Launch Requirements for Mission 4B

Payload Summary	kg (lb)	Nominal Launch		Launch-Period Analysis		
Probe (15% margin)	87(194)	C_3, km^2/sec^2	112	Vehicle	Titan III/7-segment/Centaur	Burner II
S/C Mods (15% margin)	34(74)	Park Orbit Time, hr	0.9	C_3, km^2/sec^2	107	120
Spacecraft (no margin)	658(1450)	Launch Window, hr	3.8	Period, days	0	20
Adapter (15 % margin)	16(35)	DLA, deg	27			
Total	795(1753)					

Table V-39 Summary of Navigation and Guidance Analysis for Mission 4B

Midcourse Requirements, m/sec				Navigation Uncertainties, 1σ			
	Mean ΔV	σ	ΔV + 3σ		SMAA, km	SMIA, km	TOF, sec
First Midcourse	18.3	10.9	51.0	Control	975	760	148
Second Midcourse	.6	.4	1.8	Knowledge	607	340	57
Total, RSS			51.1				

Table V-40 Summary of Execution Errors and Entry Dispersions for Mission 4B

Deflection Execution Errors, 3σ			Entry Dispersions, 3σ			
	ΔV	Probe Attitude	Latitude, deg	4.8	Entry Angle, deg	3.1
Proportionality, %	1		Longitude, deg	5.6	Angle of Attack, deg	5.3
In-Plane Pointing, deg	1.4	2.0				
Out-Plane Pointing, deg	1.4	2.0	Coast Time, min	27.8		

The next step in analysis of a JUN-79 mission was to lower the S/C antenna beam width to a minimum to have maximum antenna gain in the RF link (Mission 4A). This was achieved by going to a two-position scheme for the S/C antenna, as shown in Fig. V-31. Using this method, a 3° S/C relay antenna can be used with a programmed movement of 1.5° in cone angle (ϕ) from acquisition to entry (72 min). The science bit rate was also reduced to a minimum to lower required RF power. Results are shown in Table V-41 for comparison. The increased S/C antenna gain resulted in a K-band power of 298 W required at 1024 bps. Lowering the frequency to X-band reduces the power to 62 W at 1024 bps. A reduced science payload will lower the bit rate to 791 bps, which requires 51 W at X-band. Therefore, it was concluded that a mission with a periapsis radius to 9.85 R_J results in excessive RF power requirements even at X-band with a reduced science payload.

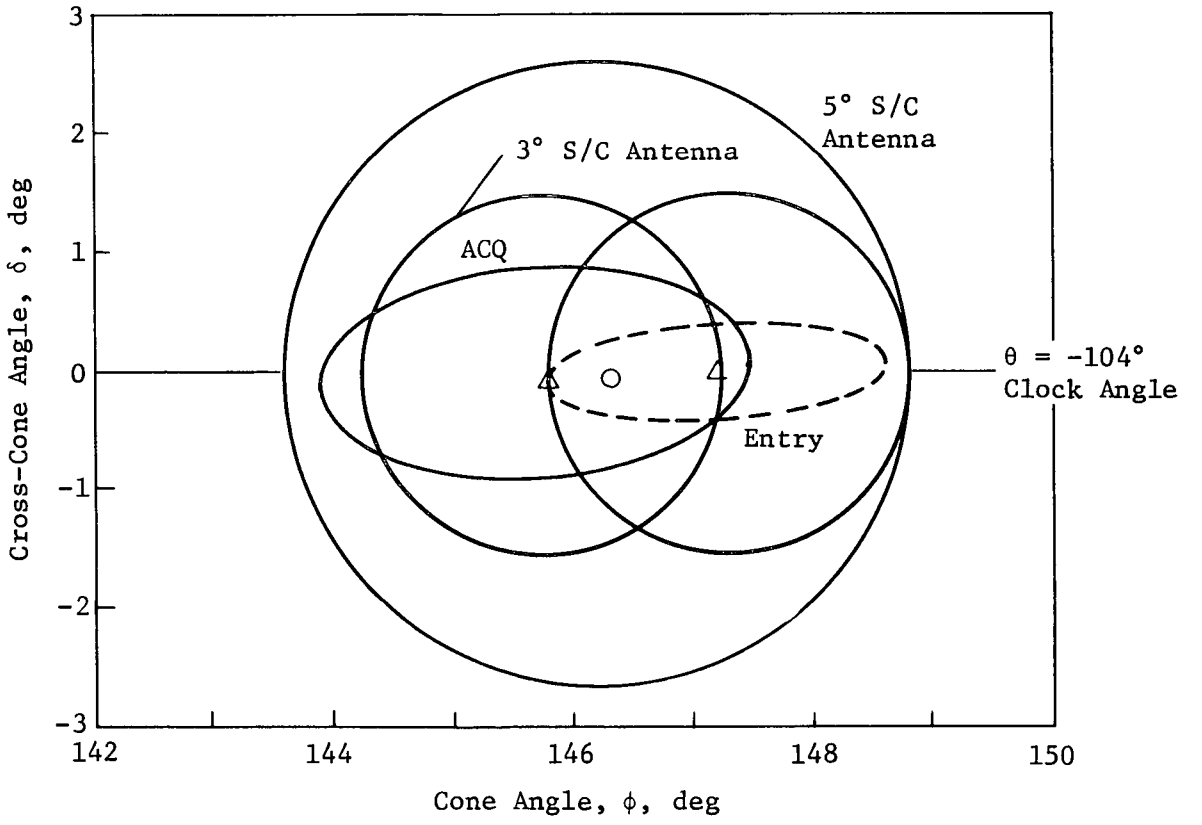

Figure V-31 Spacecraft-Antenna Requirements for Missions 4 and 4A

Table V-41 Mission 4 Telecommunications RF Subsystem

Component	Characteristic	Unit	Mission/Band					
			4		4A		4B	
			K, 20 GHz	X, 10 GHz	K, 20 GHz	X, 10 GHz	K, 20 GHz	X, 10 GHz
Probe Antenna	Beamwidth	deg	8		8		8	10
	Max Gain	dB	25.3		25.3		25.3	23.4
Transmitter	RF Power Out	W	842	172	298	62	109	35
	Bit Rate	bps	1024		1024		1024	
S/C Antenna	Beamwidth	deg	5		2.5		2.5	
	Max Gain	dB	31		36.6		36.6	
	Programmed		no		yes		yes	
	Clock Angle, θ	deg	-104		-104		-104.8	
	Cone Angle, ϕ	deg	146.2		145.5-147		148.2-149.7	
S/C Receiver	Sys Temp	°K	400	315	400	315	400	315

In a final effort to reduce RF losses, periapsis radius for the JUN 79 Mission was reduced to 6.6 R_J (Mission 4B). As seen in Fig. V-32, probe dispersions are slightly smaller than for Mission 4A (Fig. V-31), and a 2.5° S/C relay antenna was chosen with a programmed movement of 1.5° in cone angle (ϕ). Probe antenna beam width remained unchanged at 8° at K-band. For X-band, the probe beam width had to be widened to 10° to reduce the length of the horn. An 8° horn at X-band (10 GHz) is 68-cm (26.8-in.) long and cannot be packaged in the probe. A 10° X-band horn is only 46.8 cm (18.4 in.) long and can be packaged in the probe. Comparisons of RF subsystem designs for the three variations of Mission 4 are shown in Table V-41. For K-band, Mission 4B requires 109 W. Power required at X-band is 35 W RF, which is within the 1975 transmitter state of the art. The upper limit in transmitter power at X-band for the 1975 to 1980 is considered to be 40 W for deep space probes. It is concluded that the JUN 79 Mission is possible at X-band with a periapsis radius of 6.6 R_J. Space loss at higher frequencies or longer radii results in excessive RF power requirements (>40 W).

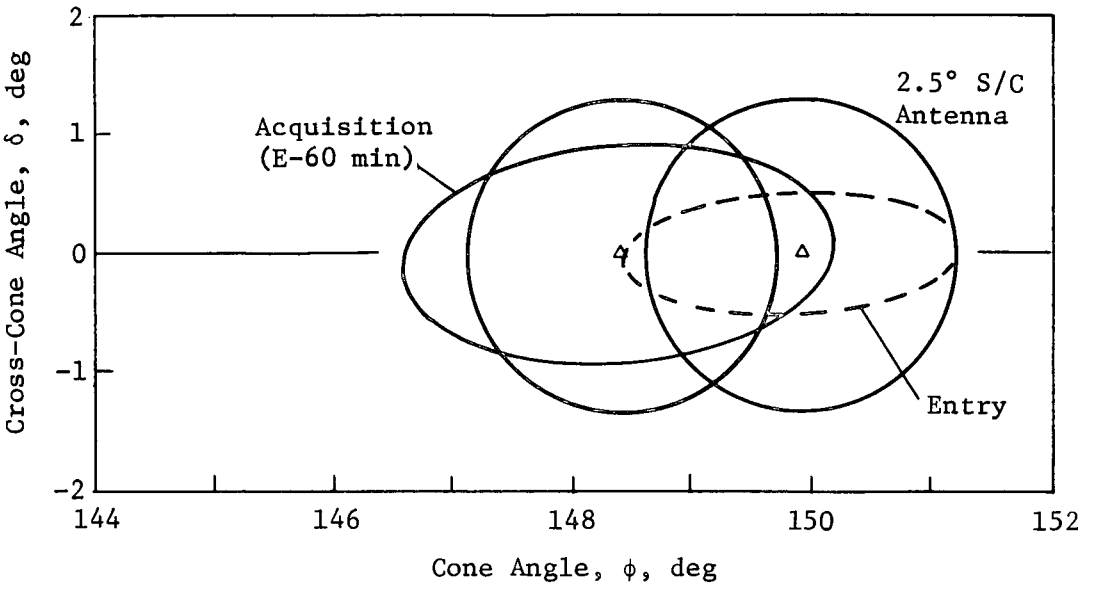

Figure V-32 Spacecraft-Antenna Requirements for Mission 4B

H. MISSION 5 - SOLAR APEX

The objective of this mission/system design was to incorporate a Jupiter probe as a passenger aboard a Pioneer spacecraft that would fly by Jupiter with a postencouter objective of flight toward the solar apex.

To minimize perturbation of spacecraft operations for postencounter objectives, probe deflection and attitude were made a probe-system functional requirement, as for the Mission 3 probe system.

System operational requirements for the spacecraft and probe are the same as those for Mission 3.

The mission sequence of events is in Table V-42 and the probe functional block diagram is the same as that of Mission 3 (Fig. V-22).

Table V-42 Mission 5 Solar Apex 78 Sequence of Events

Event	Time, hr:min:sec	Function
1	L	Launch; October 9, 1978
2	L + 02:00:00	Separate S/C system from L/V; begin S/C cruise
3	S - 05:30:00	Separate probe protective enclosure S/C power on probe; start probe checkout
4	S - 00:30:00	Complete probe checkout
5	S - 00:20:10	Enable probe battery activation
6	S - 00:20:00	Activate probe separation battery
7	S - 00:17:00	Start S/C orientation for probe release (64°)
8	S - 00:02:00	Complete S/C orientation for probe release
9	S - 00:00:30	Activate probe separation battery
10	S - 00:00:20	Switch to probe internal power; energize probe power bus energize data system; start probe sequencer begin monitor of probe engineering data; enable probe separation ordnance
11	S, L + 513 d	Separate probe (S/C power & signal)
12	S + 00:00:01	Initiate probe spin (0.91-m separation)
13	S + 00:00:17	Probe spin complete (100 rpm)
14	S + 00:10:00	Initiate probe ΔV (approx 549-m separation)
15	S + 00:10:06	Probe ΔV complete (75 m/sec)
16	S + 00:10:30	Begin probe precession (-35°); begin S/C reorientation
17	S + 00:23:00	Orient S/C (-64°) for Earth lock
18	S + 12:10:30	Probe precession complete
19	S + 12:10:40	Deactivate ACS; begin Langmuir probe decontamination
20	S + 12:22:40	Langmuir probe decontamination complete Deactivate probe power; deactivate data system
21	T - 01:21:13	Enable battery activation
22	T - 01:01:13	Activate entry battery
23	T - 00:41:13	Energize probe bus
24	T - 00:41:03	Data system on
25	T - 00:40:48	Transmitter on
26	T - 00:40:28	Enable ordnance/start probe acquisition
27	T - 00:40:18	Fire pyros at 15-sec interval
28	T - 00:38:48	Disable ordnance/start probe acquisition
29	T - 00:37:48	Complete probe acquisition/turn on instruments (ETP, IRPA, OPT)
30	T - 00:37:18	Transmit instrument engineering data (ETP, IRPA, OPT)
31	T - 00:35:18	Start data transmission (ETP, IRPA, OPT)
32	T - 00:33:45	Start transmission of engineering data (including stored)
33	T - 00:20:45	Turn on instruments (MS, NRPA)
34	T - 00:16:45	Stop transmission of engineering (housekeeping) data
35	T - 00:15:45	Transmit MS & NRPA engineering data
36	T - 00:14:45	Start data transmission (MS, NRPA)
37	T	Turbopause
38	T + 1.9 sec	Blackout
39	L + 540 days	S/C periapsis; April 1, 1980

Includes 10.25-min trajectory uncertainty, 0.3-min timer uncertainty, and 5% of time from acquisition start to T = 0.

1. Science Payload and Performance

Instrument characteristics and mission performance for Mission 5 are shown in Table V-43. The primary difference between the science-instrumnet bit rate for this and other missions is the dayglow instrument, whose data rate depends on probe spin rate. For this mission, the spin rate is 100 rpm. For a description of the contents of data words, see Chapter III, Section C under the subsection concerning the particular instrument.

On the left side of Table V-43 are the upper atmospheric and ionospheric performance, the criterion being one measurement per scale height. The lowest values are the heaviest particles of both the neutrals and ions. For a detailed discussion of these numbers, see Chapter III, Subsections D1 and D3.

2. Mission Description

Interplanetary and approach trajectories for this mission are constrained by the objective to send the spacecraft to the solar apex via a Jupiter swingby. Considerations involved are described in Chapter IV, Subsection C5. The resulting approach trajectory is inclined to Jupiter's equator about 30° and has a periapsis radius of 1.77 R_J. The minimum entry angle possible while satisfying the 20° mask-angle constraint is $\gamma_E = -34°$.

As with all missions involving post-Jupiter objectives, the probe deflection technique (Mode 1) is used. The deflection radius of 30×10^6 km results in acceptable ΔV requirements and dispersions. Interplanetary and approach trajectories and deflection sequence are summarized in Fig. V-33.

The launch characteristics are described in Table V-44. The Pioneer spacecraft and Titan IIID-5-segment-Centaur-Burner II launch vehicle is used. The mission cannot be flown without Burner II. The launch period is ample with Burner II, using either standard or updated performance data.

The midcourse maneuver requirements and navigational uncertainties (Table V-45) were developed for the specific trajectory of this mission. Midcourse maneuver requirements (to Jupiter only) are 44 m/sec. Midcourse maneuver requirements following the Jupiter swingby were not evaluated.

Table V-43 Mission 5 Science Instruments and Performance

Characteristics

Instruments	Weight, kg, lb		Power, W	Words/ Sample	Bits/ Sample	Sampling Time, sec	Science Bit Rate, bps
Langmuir Probes	1.36	3.0	3	3	24	0.5	48
IRPA	1.59	3.5	3	12	96	0.5	192
NRPA	2.27	5.0	5	14	112	0.5	224
Mass Spectrometer	5.90	13.0	15	22	176	0.4	440
Photometers	2.95	6.5	5	2	16	0.3	54
Totals	14.07	31.0	31				958

Mission Performance

Particle	Measurement/ Scale Height
H	3.3
H_2	1.7
He	0.9
H_1^+ & e^-	6.6
H_2^+	5.2
H_3^+	3.0
He^+	3.1
HeH^+	1.3

Note: Entry Flight-Path Angle, $\gamma_E = -34°$

Mission Times from

50,000 km to turbopause (min) 22.9

1000 km to turbopause (sec) 29.8

Turbopause to blackout (sec) 1.8
(minimum time below turbopause)

Mass-Spectrometer Measurements
(0.4 sec each)

Above turbopause (+20 to 0 km) = 1.50

Below turbopause (0 to -60 km) = 4.49

Total (+20 to -60 km) = 5.99

1. Interplanetary Trajectory

LD 10/9/78

AD 4/1/80

TOF 540 days

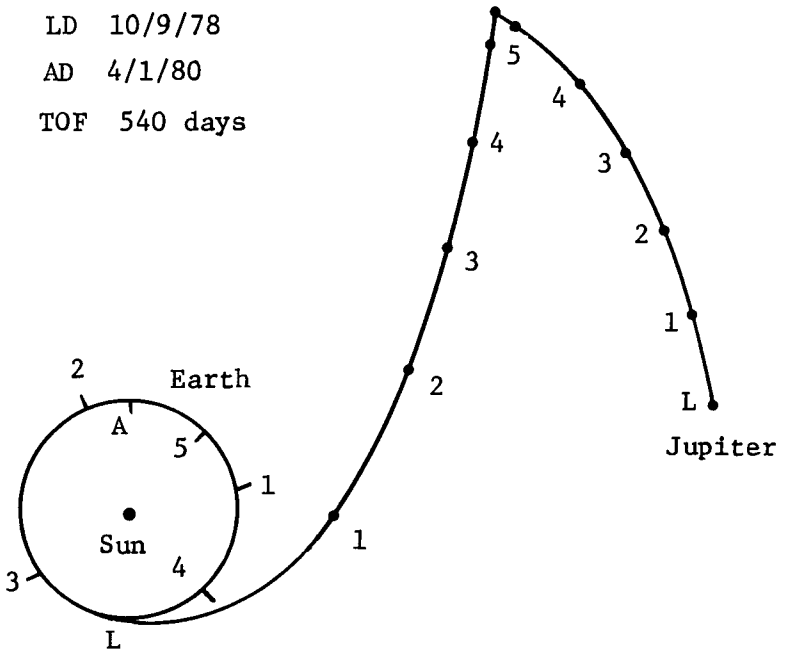

2. Approach Trajectory

$R_P = 1.77\ R_J$

$\gamma = -34°$

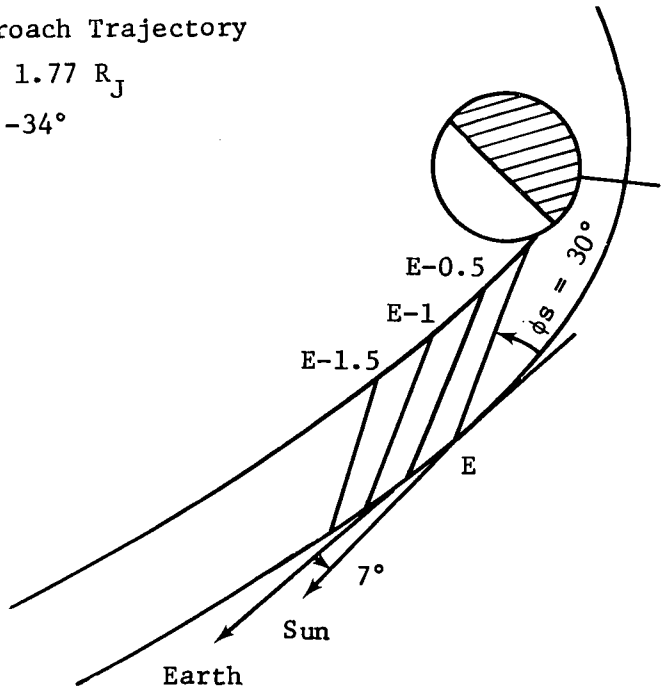

3. Deflection Maneuver

Deflect Probe

Radius = 30M km

Time = 27 days

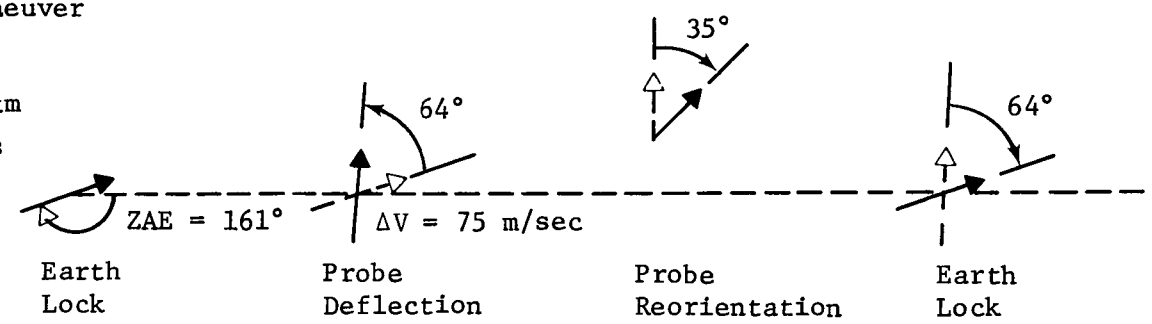

Figure V-33 Solar Apex Mission 5 Trajectories

Table V-44 Summary of Launch Requirement for Mission 5

Payload Summary	kg (lb)	Nominal Launch		Launch-Period Analysis			
Probe (15% margin)	87(194)	C_3, km^2/sec^2	111	Vehicle	Titan III/5-segment/Centaur		
						Burner II	Burner II*
S/C Mods (15% margin)	42(93)	Park Orbit Time, hr	.6	C_3, km^2/sec^2	107	132	139
Spacecraft (no margin)	254(547)	Launch Window, hr	1.1	Period, days	0	34	40
Adapter (15 % margin)	28(63)	DLA, deg	29.9				
Total	407(897)						

* Updated

Table V-45 Summary of Navigation and Guidance for Mission 5

Midcourse Requirements, m/sec				Navigation Uncertainties, 1σ			
	Mean ΔV	σ	ΔV + 3σ		SMAA, km	SMIA, km	TOF, sec
First Midcourse	13.9	9.9	43.7	Control	507	399	51
Second Midcourse	.7	.5	2.2	Knowledge	504	328	47
Total, RSS			43.8				

Table V-46 Summary of Execution Errors and Entry Dispersions for Mission 5

Deflection Execution Errors, 3σ			Entry Dispersions, 3σ			
	ΔV	Probe Attitude	Latitude, deg	2.2	Entry Angle, deg	1.9
Proportionality, %	1		Longitude, deg	2.4	Angle of Attack, deg	3.5
In-Plane Pointing, deg	3	2				
Out-Plane Pointing, deg	3	2	Coast Time, min	10.5		

Deflection execution errors used with this mission (Table V-46) are from an early model. The proportionality error is slightly optimistic and would require successful inflight calibration of the engines. Pointing errors are slightly pessimistic: more realistic values would be an in-plane error of 3.0° and an out-of-plane error of 1.0°. The probe orientation errors are realistic. These dispersions are all within required tolerances.

3. Configuration

The configuration for Mission 5 is the same as for Mission 3 except for a decrease in heat-shield thickness and weight resulting from the increase in entry angle. In addition, increased power requirements call for larger batteries. These differences are shown in the estimated weight in Table V-47.

a. Telecommunications - A 4° S/C relay antenna was selectd on a despun platform with a programmed search technique during acquisition. Figure V-34 shows the antenna initially oriented to Position 1 with receiver AGC monitored by the receiver logic circuits. The S/C antenna is then moved to Position 2 and the logic circuit compares the relative levels of the two AGC voltages. The antenna will then be moved to the position with the highest AGC voltage. Notice that Position 2 also covers most of the entry dispersion and nominal positions of the probe at acquisition and entry. The probe is expected to be in the region covered by Position 2, eliminating the need to reposition the antenna by the single-axis gimbal control during probe tracking.

Design details of the RF components of the telecommunications subsystem are listed in Table V-48. Probe antenna beamwidth was increased at X-band to maintain approximately the same horn length. At K-band, 26 W of RF power is required and 10 W at X-band. This mission was designed for K-band using smaller knowledge and control and proportionality errors with timing based on nominal end-of-mission position. If the results of the larger errors were included, it is estimated that the same antenna horn sizes could be used, with the RF power at X-band increasing to approximately 15 W.

b. Data Handling - This subsystem is similar to that for Mission 1 (Subsection B3b). Discussion of data-handling alternative approaches and formating are in Chapter VI, Section B.

Table V-47 Mission 5 Weight Estimate

	kg	lb
Science	14.6	32.2
Structure & Heat Sink	14.3	31.6
Thermal Control	3.6	8.0
Guidance & Control (less propellant)	8.2	18.1
Deflection Propulsion (less propellant)	2.7	5.9
Communications	8.8	19.4
Data Handling	4.2	9.3
Electrical	11.6	25.5
Mechanisms	0.5	1.0
Pyro	3.5	7.8
Ballast	1.6	3.5
15% Design Margin	11.1	24.4
Total - Probe Coast Weight	84.7	186.7
Solid Propellant +15%	2.6	5.8
Nitrogen Gas +15%	0.5	1.2
Covers	0.2	0.5
Total - Probe Ejected Weight	88.0	194.2

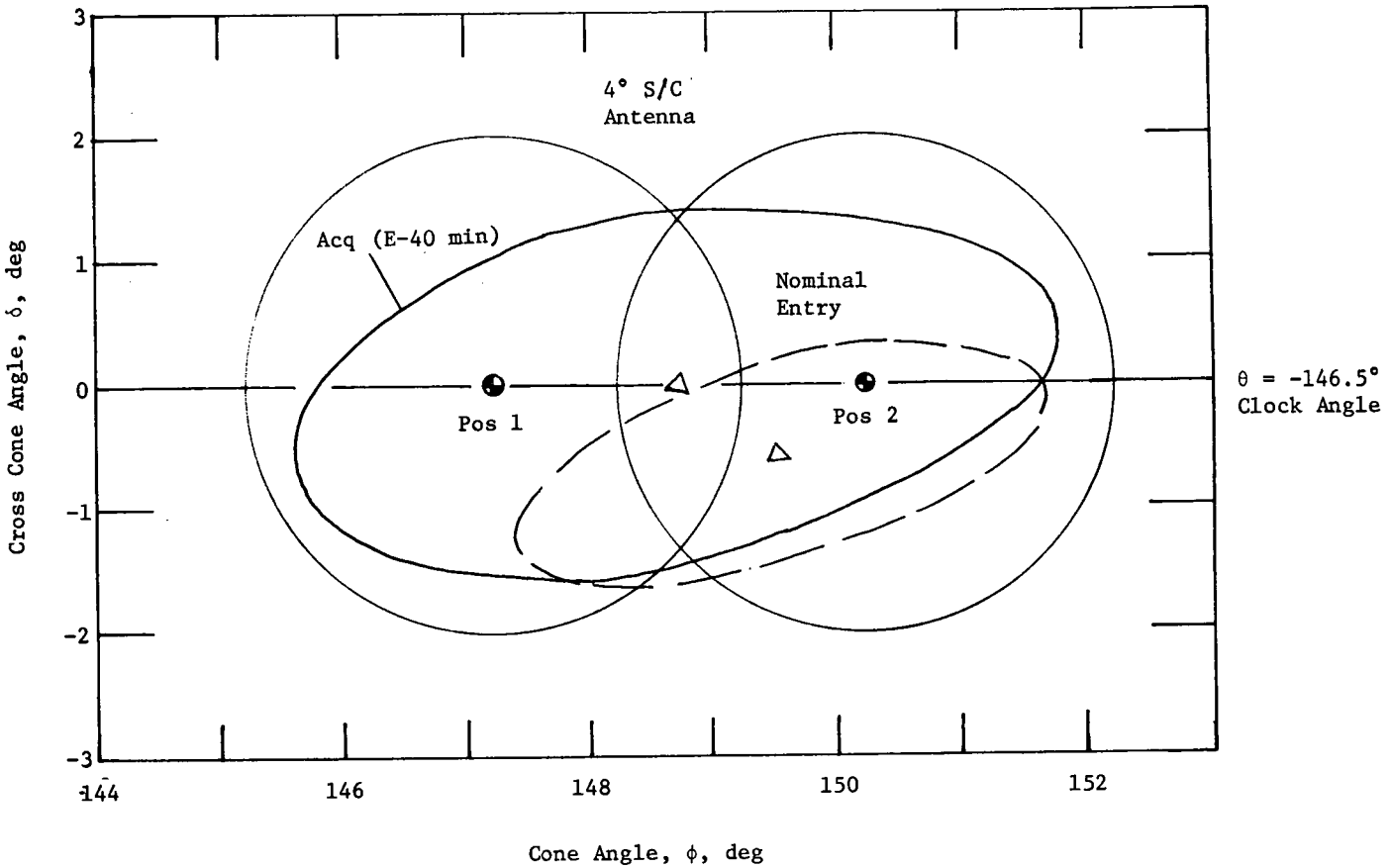

Fig. V-34 Spacecraft-Antenna Acquisition Requirements for Mission 5

Table V-48 Telecommunications RF Subsystem for Mission 5

Conditions:	S/C - Pioneer		Bit Rate - 1102 bps*	
			Value	
Component	Characteristic	Unit	K Band, 20 GHz	X Band, 10 GHz
Probe Conical-Horn Antenna	Electrical B/W	deg	8.0	10.0
	Max Gain	dB	25.3	23.4
	Dia	cm	12.2	19.6
		in.	4.8	7.6
	Total Length	cm	36.0	46.8
		in.	14.2	18.4
	Weight	kg	0.3	0.34
		lb	0.6	0.75
Transmitter & Power Supply	RF Power Out	W	26.0	10.0
	Overall Efficiency	%	24.0	24.0
	dc Power at 28 Vdc	W	108.0	41.7
	Total Weight	kg	7.7	7.7
		lb	17.0	17.0
S/C Dish Antenna	Electrical B/W	deg	4.0	4.0
	Max Gain	dB	32.5	32.5
	Dia	cm	27.33	27.33
		in.	10.75	10.75
	Weight	kg	9.54	9.54
		lb	21.0	21.0
	Despin		yes	yes
	Position Search		yes-2	yes-2
	Freq Acquisition	sec	100.0	60.0
	Clock Angle, θ	deg	-146.5	-146.5
	Cone Angle, ϕ	deg	147.2-150.2	147.2-150.2
S/C Receiver	System Temperature	°K	400.0	315.0
	dc Power at 28 Vdc	W	10.0	10.0
	Weight	kg	5.9	5.9
		lb	13.0	13.0

*Science plus engineering

c. Power Subsystem - The power subsystem is shown in Fig. V-28 in the Mission 3 description. There are basically two subsystems shown: (1) postseparation power source and power conditioning, and (2) entry power source, distribution, and filtering. The latter is similar to the power subsystem for Mission 1 (Subsection B3c). The postseparation subsystem provides power for pyrotechnics and attitude control required during that period. A centralized regulated multivoltage dc distribution is used because the electronics will be operated well outside the radiation belts and a more compact design can be achieved. A more detailed discussion of power-source and system alternatives is in Chapter VI, Section C.

d. Pyrotechnic Control - Electronics and implementation of the pyrotechnic control are similar to that described for Mission 1 (Section B3d) and in the general design discussion (Chapter VI, Section C). There are 12 pyrotechnic events, indicating the increased complexity of the mission. This results in the following weight and volume for component parts.

	Electronics	Relays	Capacitor Banks
Weight, kg (lb)	0.91 (2.0)	1.14 (2.5)	0.36 (0.8)
Volume, cm^3 ($in.^3$)	1230 (75)	443 (27)	656 (40)

e. Heat Sink and Structures - The heat sink consists of a 0.765-m (30-in.) dia hemispherical beryllium nose cap and cylindrical skin on the skirt assembly weighing 5.38 kg (11.8 lb). It is 0.39 cm (0.153 in.) thick at the stagnation point and 1.27 mm (0.05 in.) at the trailing edge.

The structure is the same as for Mission 3.

f. Thermal Control - The thermal-control system is the same as that for Mission 3.

g. Propulsion (ACS, ΔV) - The Mission 5 probe incorporates the same type of probe propulsion subsystems as those for Mission 3. For Mission 5, the probe is spun up to 10.47 rad/sec (100 rpm) by the GN_2 system at separation from the spacecraft. After a separation distance of 549 m (1800 ft), the dual-nozzle spherical solid-rocket probe-deflection motor is fired to attain a deflection ΔV of 75 m/sec. Once this has been accomplished,

the GN_2 precession-control propulsion subsystem will precess the probe 0.61 rad (-35°). Solenoid valves are incorporated in the precession subsystem for accurate precession control, whereas squib valves control the spinup subsystem.

h. Attitude Control - The attitude-control subsystem is required to spin the probe to 10.47 rad/sec (100 rpm), maintain attitude during ΔV impulse and maneuver the probe to the final entry angle. The subsystem uses a Sun sensor and Jupiter sensor to obtain 3-axis reference information. These data are obtained from measurements of solar aspect angle and the angle between the spin axis-Jupiter plane and the spin axis-Sun plane. Subsystem accuracy is specified by requirements for communications (3°). A detailed discussion of alternatives, design factors, and electronics is in Chapter VIII.

4. Spacecraft Interface/Modification and Launch Vehicle

The Pioneer spacecraft with probe is launched on a Titan IIID-5-segment Centaur-Burner II. The following components are either modified or added to the spacecraft for probe support or mission operation: probe support structure, environmental enclosure, electrical interface, receiver subsystem, despin and gimbal tracking antenna and platform, and data handling. Modification weight to the spacecraft is 42.0 kg (92.5 lb). The integration arrangement is shown in Fig. V-35.

I. MISSION 6 - JU 80

The objective of this portion of the study was to determine the feasibility of including a Jupiter probe on a 1980 spacecraft launch for a Jupiter-Uranus encounter mission. The study was limited to mission analysis.

Analysis of the launch opportunity for the JU 80 mission is shown in Chapter IV, Fig. IV-14. As the figure shows, missions with reasonable launch periods require a flyby radius greater than 15 R_J. The deflection ΔV for such a mission would be about 400 m/sec for a deflection radius of 50×10^6 km and lead to unmanageable dispersions. The communication link would require power much greater than the assumed 40-W limit for X-band. Therefore, it is not feasible to include a turbopause probe on such a mission.

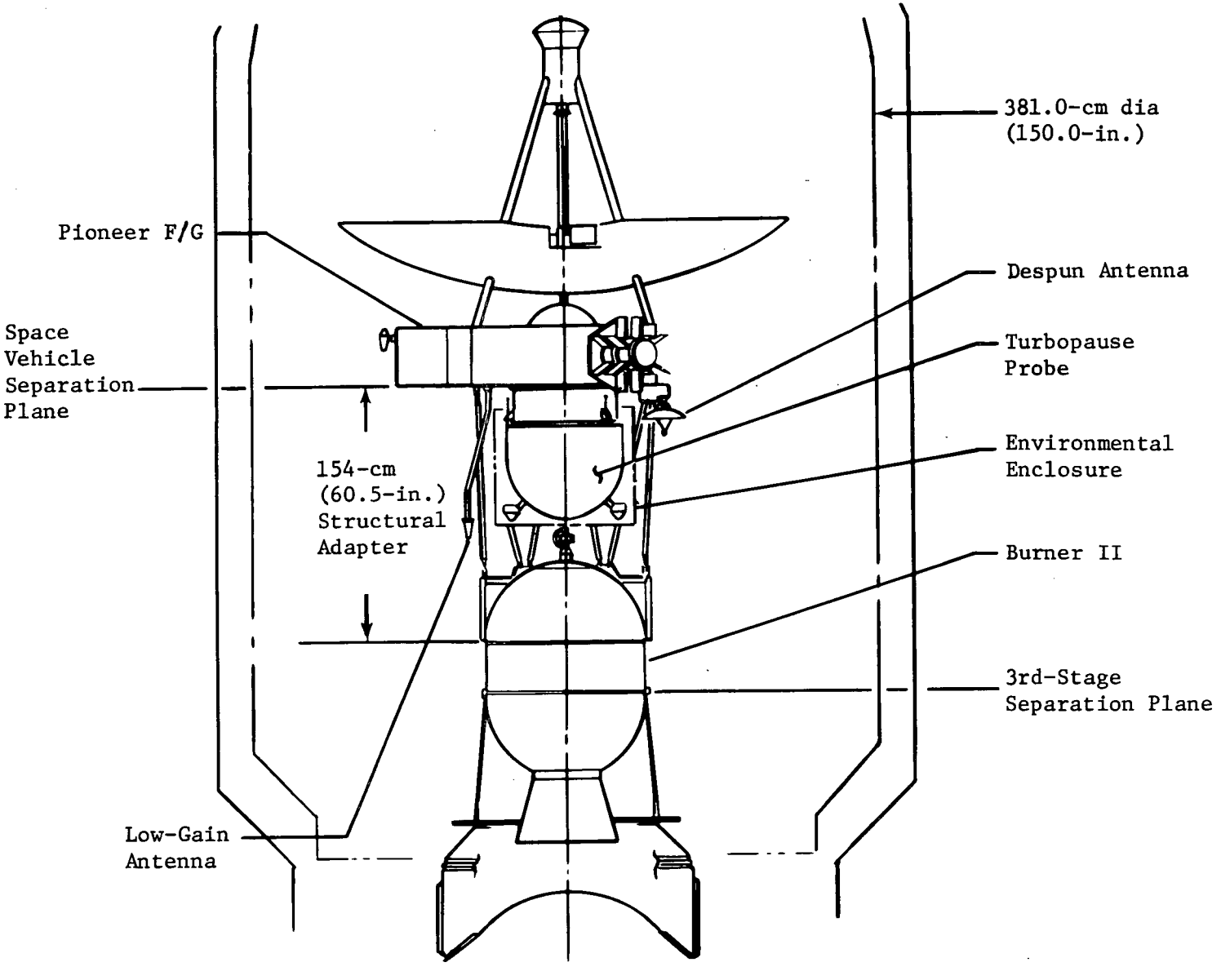

Fig. V-35 Probe-Spacecraft Interface for Mission 5

J. MISSION 7 - JS 77

The objective of this mission/system design was to take advantage of a 1977 Jupiter-Saturn launch opportunity, maintaining effective science data return.

The postencounter requirement of a Saturn flyby with the assumed spacecraft restriction for leaving the S/C trajectory undisturbed results in a system employing a probe deflection capability. This requires incorporation of a propulsion- and attitude-control system on the probe.

The system requires the spacecraft to orient itself for probe ejection, thereby establishing probe attitude. After ejecting the probe, the spacecraft reorients to Earth lock and at the end of the probe coast period, acquires the probe RF transmission, relays the data received, and continues toward its next objective (Saturn encounter).

The probe in turn, once ejected from the spacecraft, spins up, applies the required deflection propulsion (ΔV), despins, and then precesses to obtain zero angle of attack at atmospheric entry.

The remaining probe systems are those necessary to satisfy the functional requirements of science data collection, data processing, and transmission.

The mission sequence of events is shown in Table V-49, and the probe functional block diagram is Fig. V-22 (Section F) in the Mission 3 description. Figure V-36 shows the mission power profile.

1. Science Payload and Performance

Instrument characteristics and mission performance for Mission 7 are shown in Table V-50. The primary difference between science-instrument bit rate for this and other missions is the dayglow instrument, whose data rate depends on probe spin rate. For this mission, the spin rate is 20 rpm. For a description of the contents of data words, see Chapter III, Section C under the subsection concerning the particular instrument.

Table V-49 Mission 7 JS-77 Sequence of Events

Event	Time, hr:min:sec	Function
1	L	Launch; September 5, 1977
2	L + 02:00:00	Separate S/C system from L/V; begin S/C cruise
3	S - 05:30:00	Separate probe protective enclosure S/C power on probe; start probe checkout
4	S - 00:30:00	Complete probe checkout
5	S - 00:20:10	Enable probe battery activation
6	S - 00:20:00	Activate probe separation battery
7	S - 00:17:00	Start S/C orientation for probe release
8	S - 00:02:00	Complete S/C orientation for probe release
9	S - 00:00:30	Enable probe separation ordnance
10	S - 00:00:20	Switch to probe internal power; energize probe power bus energize data system; start probe sequencer begin monitor of probe engineering data;
11	S,+ 506.9d	Separate probe (S/C power & signal)
12	S + 00:00:01	Initiate probe spin (0.91-m separation)
13	S + 00:00:17	Probe spin complete (100 rpm)
14	S + 00:10:00	Initiate probe ΔV (approx 549-m separation)
15	S + 00:10:06	Probe ΔV complete (130.7 m/sec)
16	S + 00:10:30	Begin probe despin (20 rpm)
17	S + 00:10:44	Probe despin complete
18	S + 00:11:24	Begin probe precession (-31.6°); begin S/C reorientation
19	S + 00:23:00	Orient S/C (-61.8°) for Earth lock
20	S + 12:10:30	Probe precession complete
21	S + 12:10:40	Deactivate ACS; begin Langmuir probe decontamination
22	S + 12:22:40	Langmuir probe decontamination complete Deactivate probe power; deactivate data system
23	T - 01:39:01	Enable battery activation
24	T - 01:19:01	Activate entry battery
25	T - 00:59:01	Energize probe bus
26	T - 00:58:51	Data system on
27	T - 00:58:36	Transmitter on
28	T - 00:58:16	Enable ordnance/start probe acquisition
29	T - 00:58:06	Fire pyros at 15-sec interval
30	T - 00:56:36	Disable ordnance/start probe acquisition
31	T - 00:55:36	Complete probe acquisition/turn on instruments (ETP, IRPA, OPT)
32	T - 00:55:06	Transmit instrument engineering data (ETP, IRPA, OPT)
33	T - 00:53:06	Start data transmission (ETP, IRPA, OPT)
34	T - 00:52:06	Start transmission of engineering data (including stored)
35	T - 00:35:45	Turn on instruments (MS, NRPA)
36	T - 00:34:45	Stop transmission of engineering (housekeeping) data
37	T - 00:33:45	Transmit MS & NRPA engineering data
38	T - 00:32:45	Start data transmission (MS, NRPA)
39	T	Turbopause
40	T + 1.8 sec	Blackout
41	L + 557 days	S/C periapsis; March 16, 1979

Includes 26.7-min trajectory uncertainty, .54-min timer uncertainty, and 5% of time from acquisition start to T = 0.

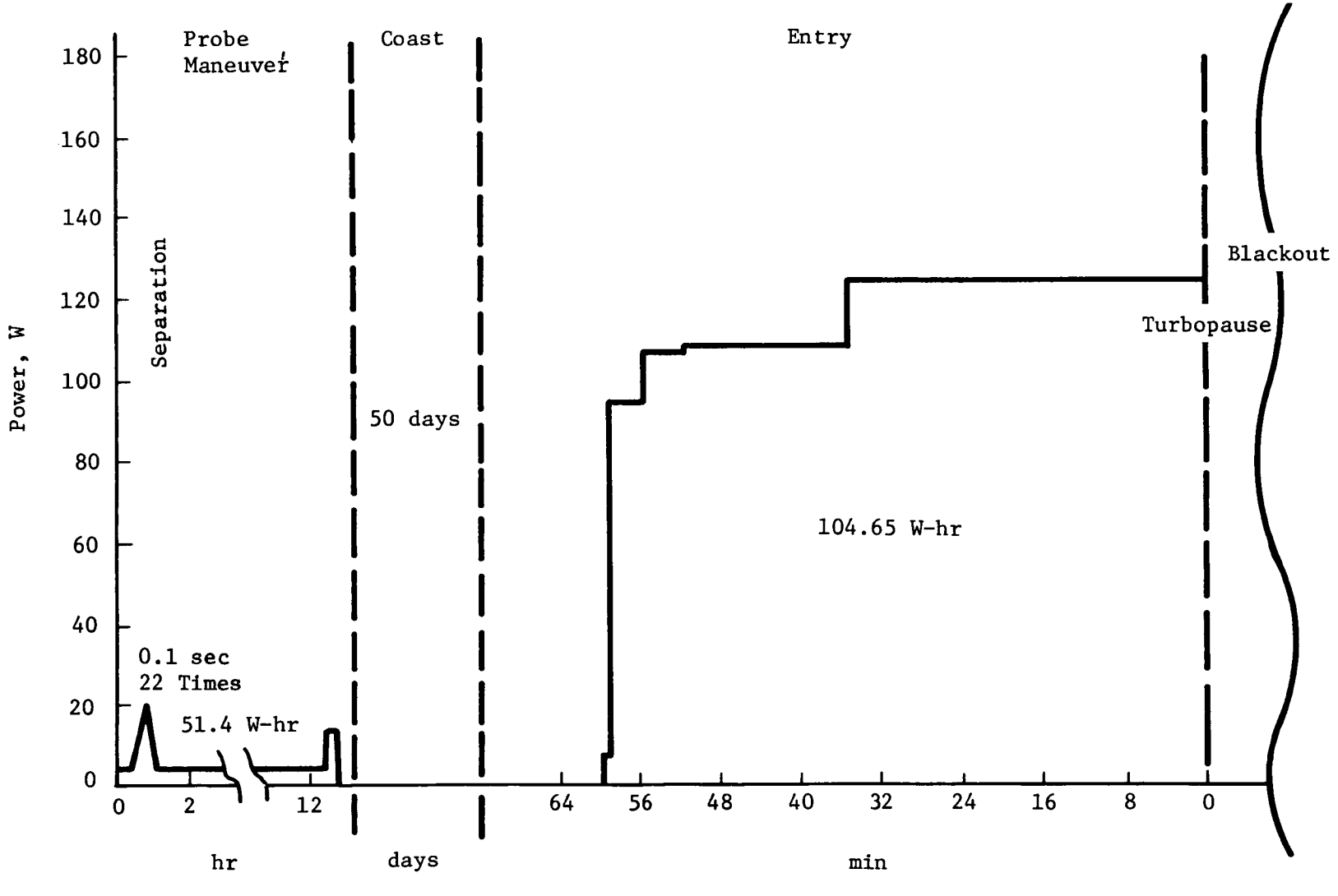

Fig. V-36 Mission 7 JS 77 Probe Power Profile

Table V-50 Mission 7 Science Instruments and Performance

Characteristics

Instruments	Weight, kg	Weight, lb	Power, W	Words/ Sample	Bits/ Sample	Sampling Time, sec	Science Bit Rate, bps
Langmuir Probes	1.36	3.0	3	3	24	0.5	48
IRPA	1.82	4.0	3	12	96	0.5	192
NRPA	2.50	5.5	5	14	112	0.5	224
Mass Spectrometer	5.90	13.0	15	22	176	0.4	440
Photometers	2.27	5.0	5	4	32	3.0	10
Totals	13.85	30.5	31				914

Mission Performance

Particle	Measurement/ Scale Height
H	3.4
H_2	1.7
He	0.9
H_1^+ & e^-	6.6
H_2^+	5.3
H_3^+	3.0
He^+	3.1
HeH^+	1.3

Note: Entry Flight-Path Angle, $\gamma_E = -33.3°$

Mission Times from

50,000 km to turbopause (min) 23.2

1000 km to turbopause (sec) 30.3

Turbopause to blackout (sec) 1.8
(minimum time below turbopause)

Mass-Spectrometer Measurements
(0.4 sec each)

Above turbopause (+20 to 0 km) = 1.53

Below turbopause (0 to -60 km) = 4.58

Total (+20 to -60 km) = 6.11

On the left side are the upper atmospheric and ionospheric performance, the criterion being one measurement per scale height. The lowest values are the heaviest particles of both the neutrals and ions. For a detailed discussion of these numbers, see Chapter III, Subsections D1 and D3.

2. Mission Description

The interplanetary trajectory for Mission 7 was determined as the JS 77 trajectory with the lowest periapsis radius possible, consistent with a 14-day launch period, assuming a MOPS sapcecraft and updated performance data for the Titan IIID-5-segment Centaur-Burner II. The requirement for a 14-day launch period is based on the minimal time interval required for a dual-launch mission. Resulting interplanetary and approach trajectories are shown in Fig. V-37. The approach trajectory has a periapsis radius of $R_P = 4.85\ R_J$. Minimal entry angle consistent with the lighting constraint is $\gamma_E = -33°$.

A probe deflection (Mode 1) was used to leave the spacecraft trajectory undisturbed. The deflection radius of 50×10^6 km was used to reduce ΔV to a reasonable value. The deflection operational sequence is indicated in Fig. V-37.

The launch analysis results are in Table V-51. The resulting launch period of 14 days was calculated assuming a 15% margin for the entire payload.

Navigation and guidance data were developed specifically for the trajectory selected. The data are summarized in Table V-52.

Execution errors in Table V-53 are consistent with projected MOPS implementation errors and probe ACS system. Entry dispersions are within allowable tolerances in all cases.

3. Configuration

The configuration for Mission 7 requires both ACS and deflection propulsion systems, with a hemispherical forward section and a cylindrical aft section. The basic probe is 0.76 m (30 in.) in diameter and 0.61 m (24 in.) long, as shown in Fig. V-38 and V-39.

1. Interplanetary Trajectory

LD 9/5/77

AD_J 3/16/79 TOF_j 557 days

AD_S 12/8/80 TOF_s 1190 days

2. Approach Trajectory

$R_P = 4.85\ R_J$

$\gamma = -33.3°$

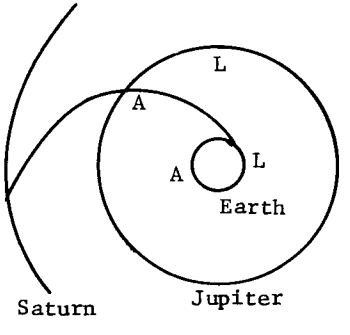

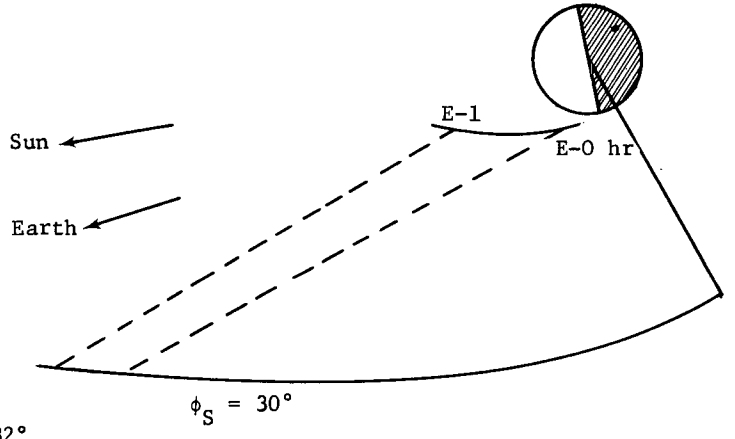

3. Deflection Maneuver

Deflect Probe

Radius = 50M km

Time = 50 days

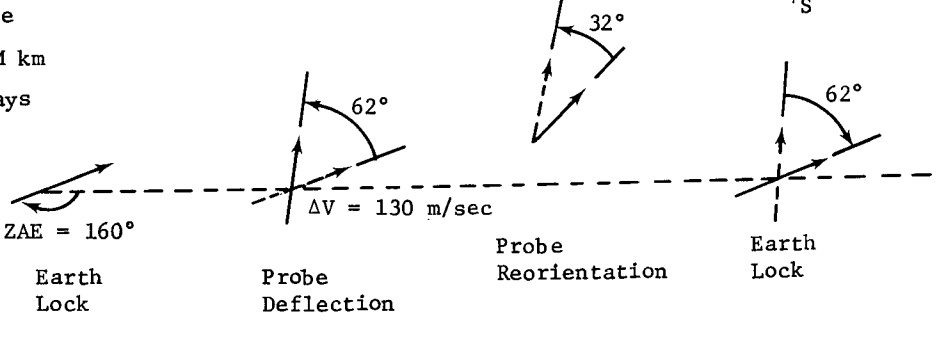

Figure V-37 Mission 7 JS 77 Trajectories

Table V-51 Summary of Launch Requirements for Mission 7

Payload Summary	kg (lb)	Nominal Launch		Launch-Period Analysis	
Probe (15% margin)	81(179)	C_3, km^2/sec^2	105	Vehicle	Titan III/5-segment/Centaur Burner II*
S/C Mods (15% margin)	25(56)	Park Orbit Time, hr	0.9	C_3, km^2/sec^2	108
Spacecraft (no margin)	664(1468)	Launch Window, hr	3.6	Period, days	14
Adapter (15 % margin)	20(44)	DLA, deg	27		
Total	790(1747)				

* Updated

Table V-52 Summary of Navigation and Guidance Analysis for Mission 7

Midcourse Requirements, m/sec				Navigation Uncertainties, 1σ			
	Mean ΔV	σ	ΔV + 3σ		SMAA, km	SMIA, km	TOF, sec
First Midcourse	18.3	10.9	51.0	Control	347	188	24
Second Midcourse	.6	.4	1.8	Knowledge	313	180	23
Total, RSS			51.1				

Table V-53 Summary of Execution Errors and Entry Dispersions for Mission 7

Deflection Execution Errors, 3σ			Entry Dispersions, 3σ			
	ΔV	Probe Attitude	Latitude, deg	1.5	Entry Angle, deg	1.7
Proportionality, %	1		Longitude, deg	1.8	Angle of Attack, deg	4.2
In-Plane Pointing, deg	2	2				
Out-Plane Pointing, deg	2	2	Coast Time, min	26.7		

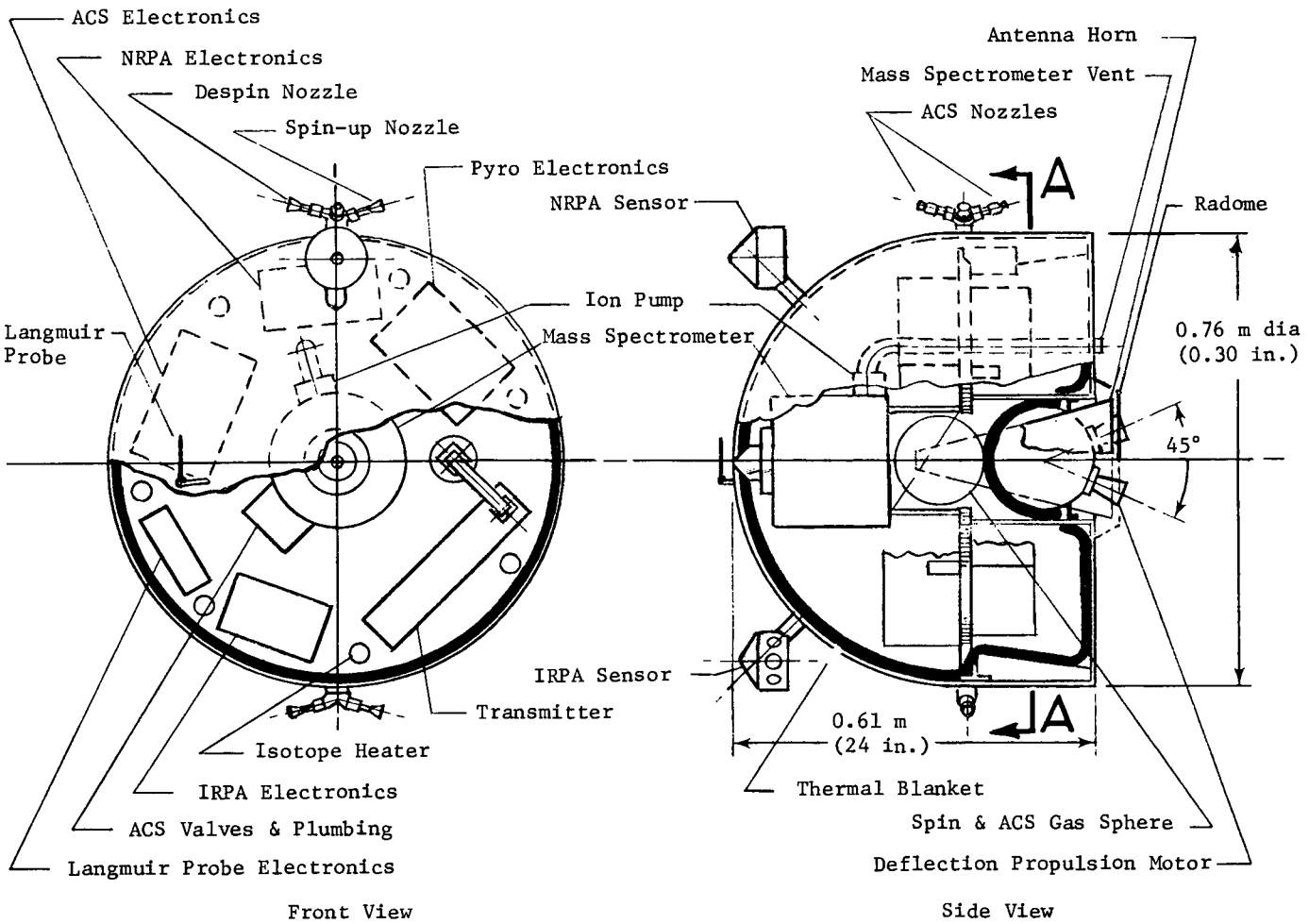

Figure V-38 Mission 7 Probe Configuration Front and Side

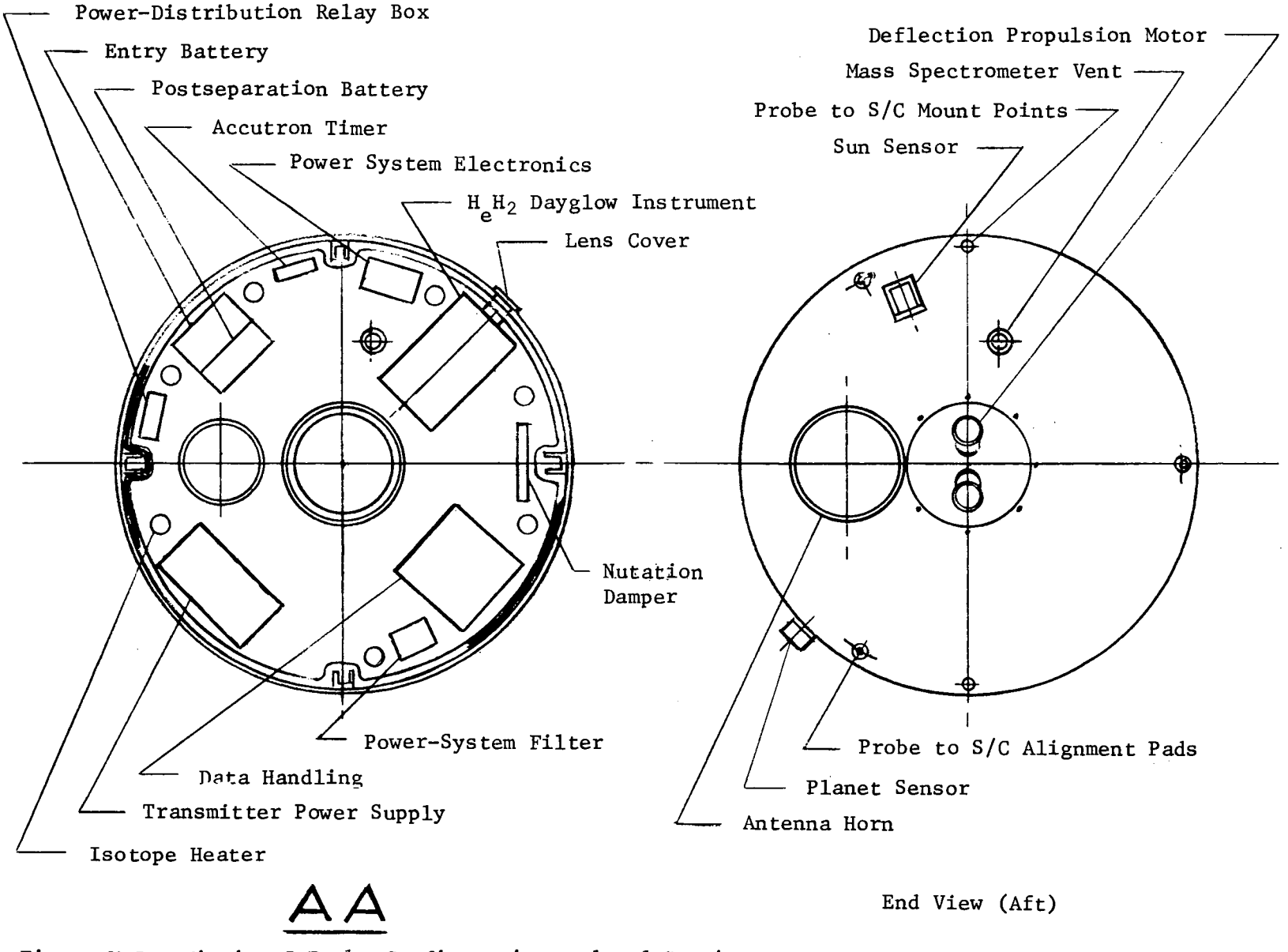

Figure V-39 Mission 7 Probe Configuration End and Section

Science experiments are integrated in the overall probe design, constrained by their functional requirements. The mass spectrometer, IRPA, NRPA, and Langmuir probes all require unobstructed access to atmospheric particles during entry. This requirement is met by placing the neutral mass spectrometer inlet directly at the nose-cap stagnation point and the RPAs at approximately 1 body radius from the Z axis at the same body station as the stagnation point of the nose cap. The mass spectrometer is vented through a 2.5-cm (0.98 in.) tube to the probe's wake, as shown in Fig. V-39.

An improved location for the Langmuir probes is 25 cm (2.56 in.) from the Z axis on the nose cap and a minimum of 6.5 cm (2.56 in.) between the sensor and the surface of the nose cap. These probe sensors are 90° to the RPA, with one sensor parallel and the other perpendicular to the probe Z axis, as shown in Fig. V-38. This arrangmenent reduces the induced voltage transients from rotation in Jupiter's magnetic field and eliminates the need for a deployment mechanism.

The spectrometer/photometer viewing aperture is in the cylindrical portion of the probe body, providing adequate viewing and placing the viewing port in an area of low entry heating. Location of the aperture in the aft bulkhead or nose cap is not desirable because of Sun aspect angles and entry heating problems.

Interrelation of components of various subsystems and the relationship of one subsystem to others are considered in the integration of internal equipment in the probe. For example, power-system components like batteries, filters, distribution boxes, electronics, and cabling are grouped to improve the power-system mass fraction.

The requirement of guidance, control, and deflection propulsion adds Sun and planet sensors, cold-gas propulsion system, post-separation battery, timer, nutation damper, and solid deflection rocket motor.

The Sun and planet sensors are shown in Fig. V-39. The nitrogen tank is mounted on the probe Z axis to preclude lateral cg travel as propellants are depleted.

The deflection propulsion system is a dual-nozzle solid-propellant motor imbedded in the aft bulkhead and aligned along the probe Z axis.

Location of the antenna relative to the transmitter is influenced by the desire for short direct wave-guide coupling. The transmitter power supply is near the transmitter to reduce cabling and power losses. Because of a large probe antenna, a thermal radome was required to control heat loss.

The pyro system must operate or activate other subsystems throughout the probe. Therefore, its location is more flexible than those of other systems. Pyro system equipment includes electronics, capacitors, relays, and squibs.

A thermal blanket covers the entire inner surface of the probe structure except for the equipment deck; 12 to 15 1-W radioisotope heaters are evenly distributed inside the probe, as shown in Fig. V-38 and V-39.

Spin stabilization of the probe requires that the mass moment of inertia about the Z-Z axis (spin axis) be greater than that about the transverse axes. It is desirable that the spin-axis mass moment of inertia be greater by 20%, and that mass moments of inertia about the transverse axes be equal. A further requirement is that the principal mass moment of inertia coincide with the Z-Z axis of the probe. These requirements are met by properly locating components and by ballasting.

Probe support and mounting locations are shown on the aft view in Fig. V-39. Probe weight estimates are given in Table V-54.

a. Telecommunications - Several iterations were made in the Mission 7 periapsis radius and operating frequency to arrive at a practical mission. Initially, an R_P of 4.85 R_j resulted in a K-band power of 125 W with an 8° horn antenna on the probe, 2° S/C dish antenna, and a bit rate of 1024 bps. R_P was next minimized at 4.46 R_J and the frequency lowered to Ku-band (15 GHz). The required power with antennas and bit rate unchanged was 26 W, which resulted in acceptable transmitter power.

Results of the wake-attenuation analysis allowed the operating frequency to be lowered and resulted in the 4.85-R_J mission being chosen with a 10° horn antenna on the probe and a 2.5° beam-width S/C dish antenna at 1024 bps. The results are listed in Table V-55 for 10 and 15 GHz. Ku-band is only shown for comparison and indicates 35 W with an 8° conical-horn antenna on the probe.

Table V-54 Mission 7 Weight Estimate

	kg	lb
Science	14.4	31.7
Structure & Heat Sink	12.6	27.7
Thermal Control	3.8	8.4
Guidance & Control (less propellant)	7.8	17.2
Deflection Propulsion (less propellant)	2.2	4.9
Communications	8.4	18.5
Data Handling	2.3	5.0
Electrical	9.9	21.8
Mechanisms	.2	.5
Pyro	3.5	7.8
Ballast	1.4	3.1
15% Design Margin	10.1	22.0
Total - Probe Coast Weight	76.5	168.6
Solid Propellant +15%	4.0	8.8
Nitrogen Gas +15%	.7	1.6
Total - Probe Ejected Weight	81.2	179.0

Table V-55 Telecommunications RF Subsystem for Mission 7

Conditions:	S/C - Pioneer		Bit Rate - 1024 bps*	
			Value	
Component	Characteristic	Unit	Ku Band, 15 GHz	X Band, 10 GHz
Probe Conical-Horn Antenna	Electrical B/W	deg	8.0	10.0
	Max Gain	dB	25.3	23.4
	Dia	cm	16.2	19.6
		in.	6.4	7.6
	Total Length	cm	46.6	46.8
		in.	18.3	18.4
	Weight	kg	0.34	0.34
		lb	0.75	0.75
Transmitter & Power Supply	RF Power Out	W	35.0	20.0
	Overall Efficiency	%	24.0	24.0
	dc Power at 28 Vdc	W	146.0	83.2
	Total Weight	kg	7.7	7.7
		lb	17.0	17.0
S/C Dish Antenna	Electrical B/W	deg	2.5	2.5
	Max Gain	dB	36.4	36.4
	Dia	cm	84.5	84.5
		in.	33.3	33.3
	Weight	kg	3.7	3.7
		lb	8.1	8.1
	Despin		no	no
	Position Search		yes-4	yes-4
	Freq Acquisition	sec	32.0	17.0
	Clock Angle, θ	deg	-92.0	-92.0
	Cone Angle, ϕ	deg	145-150.3	145-150.3
S/C Receiver	System Temperature	°K	400.0	315.0
	dc Power at 28 Vdc	W	10.0	10.0
	Weight	kg	5.9	5.9
		lb	13.0	13.0

*Science plus engineering

Total RF power is 20 W at X-band with a 10° horn on the probe. The S/C has a 2.5° dish on a single-axis gimbal with a four-position sector search, as seen in Fig. V-40 and described in Chapter VI, Subsection A4. The S/C antenna does not require a despin platform because the MOPS S/C is three-axis stabilized.

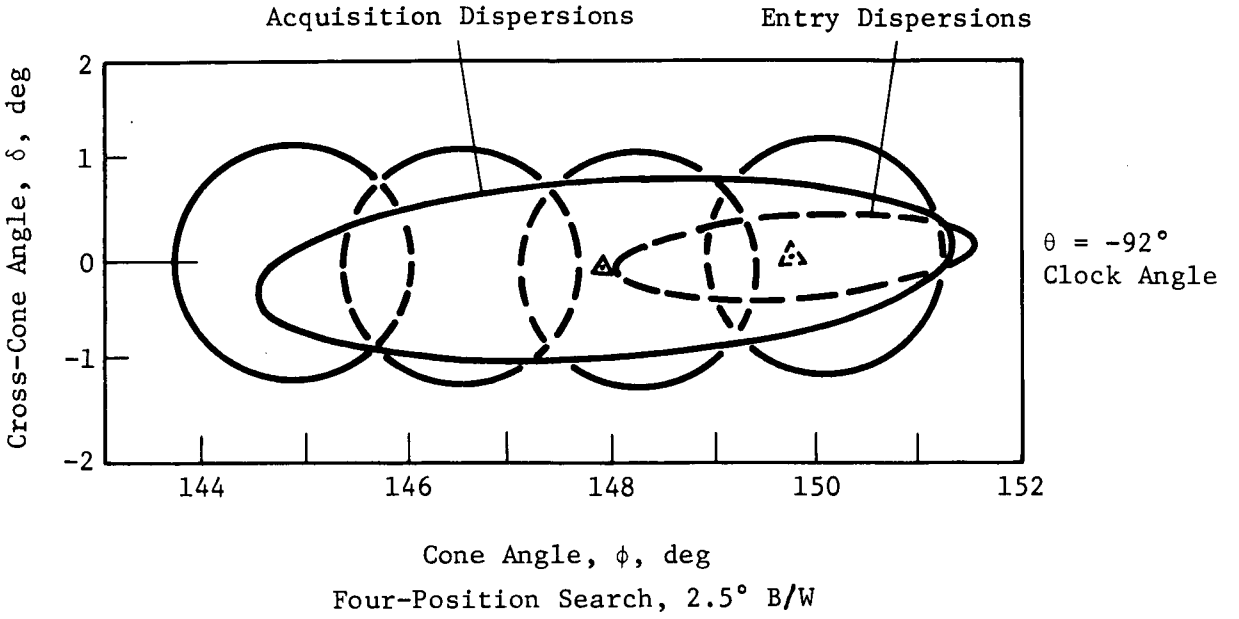

Fig. V-40 Spacecraft-Antenna Acquisition Requirements for Mission 7

b. Data Handling - This subsystem is similar to that for Mission 1 (Subsection B3b). Discussion of data handling alternative approaches and formating is in Chapter VI, Section B.

c. Power Subsystem - The power subsystem is shown in Fig. V-28. There are two subsystems shown: (1) postseparation power source and power conditioning, and (2) entry power source, distribution, and filtering. The latter is similar to the power subsystem for Mission 1 (Subsection B3c). The postseparation subsystem provides power for pyrotechnics and attitude-control required during that period. A centralized regulated multivoltage dc distribution is used because the electronics will be operated well outside the radiation belts and a more compact design can be achieved. A more detailed discussion of power-source and system alternatives is in Chapter VI.

d. Pyrotechnic Control - Electronics and implementation of the pyrotechnic control are similar to that described for Mission 1 (Subsection B3d) and in the general design discussion (Chapter VI, Section C). There are 17 pyrotechnic events, indicating the increased complexity of the mission. This results in the following weight and volume for the component parts.

	Electronics	Relays	Capacitor Banks
Weight, kg (lb)	0.91 (2.0)	1.55 (3.4)	0.45 (1.0)
Volume, cm^3 ($in.^3$)	1230 (75)	590 (36)	820 (50)

e. Heat Sink and Structures - The heat sink consists of a 0.765-m (30-in.) dia beryllium hemispherical nose cap and cylindrical skin on the skirt assembly weighing 5.4 kg (11.9 lb). It is 0.40 cm (0.157 in.) thick at the stagnation point and 1.27 mm (0.05 in.) thick at the trailing edge.

The structure consists of conventional aluminum machinings, bonded aluminum honeycomb, fiberglass honeycomb, and oriented fiberglass composite structures.

f. Thermal Control - The thermal control subsystem consists of an internally mounted multilayer insulation blanket of 72 layers of 1/4-mil Kapton polyimide film, aluminized on one side with beta glass cloth spacer material between layers. Total blanket thickness is 1.53 cm (0.6 in.). In addition, a separate small multilayer insulation blanket will encapsulate the deflection motor assembly during spacecraft cruise. This secondary blanket will remain with the spacecraft at probe separation. The thermal subsystem also includes radioisotope heaters among the equipment packages and a small electric resistance heater in the deflection-motor insulation blanket. Twelve to 15 radioisotope heaters will be required. Approximately 2 W of spacecraft power will be required for the deflection-motor resistance heater during cruise. The thermal control subystem also includes a removable insulating aperture cover for the photometer and an RF-transparent radome over the communications antenna.

g. Mechanical Subsystems - Mechanical subsystems for Mission 7 consist of the spectrometer/photometer aperture cover and release system and the probe-to-spacecraft separation system. Both are described in detail in Chapter VII.

h. Propulsion (ACS, ΔV) - The Mission 7 probe incorporates a GN_2 propulsion subsystem to provide required spin-up, despin, and precession control of the probe. As in Missions 3 and 5, a dual-nozzle spherical solid-propellant rocket motor will provide probe deflection velocity relative to the spacecraft. For this mission, the probe is spun up to 10.47 rad/sec (100 rpm) at separation from the spacecraft, after which the probe attitude is trimmed. After a separation distance of 549 m (1800 ft) is attained, the motor is fired to attain a 130.7-m/sec deflection velocity relative to the spacecraft. After this has been achieved, the probe is despun to 2.09 rad/sec (20 rpm) and precessed 0.55 rad (-31.6°). Spin and despin subsystems are controlled by actuating squib valves, whereas the precession system is controlled by solenoid valves to achieve more accurate control.

i. Attitude Control - The attitude-control subsystem for this mission is required for the trim maneuver to the attitude required for ΔV impulse, spin up to 10.47 rad/sec (100 rpm), maintain attitude during ΔV impulse, maneuver to the final entry angle, and despin to 2.09 rad/sec (20 rpm). The subsystem uses a Sun sensor and Jupiter sensor to obtain 3-axis reference information. These data are obtained from measurements of solar aspect angle and the angle between the spin axis-Jupiter plane and the spin axis-Sun plane. Subsystem accuracy is specified by the requirements for ΔV impulse pointing (1°) rather than communications (3°) or science (5°). A detailed discussion of alternatives, design factors, and electronics is in Chapter VIII.

4. Spacecraft Interface/Modification and Launch Vehicle

The MOPS spacecraft with probe is launched on a Titan IIID-5-segment Centaur-Burner II.* The following components are either modified or added to the spacecraft for probe support or mission operation: probe support structure, environmental enclosure, electrical interface, receiver subsystem, gimbal tracking antennna and platform, and data handling. Modification weight to the spacecraft is 25.2 kg (55.6 lb). The integration arrangement is shown in Fig. V-41.

---

*Lewis updated launch performance from Minutes of the OPGT Spacecraft Launch Vehicle Interface Panel at JPL, Dec 21, 1971 (approximately 61-kg (135-lb) payload increase at C_3 = 120 km^2/sec^2).

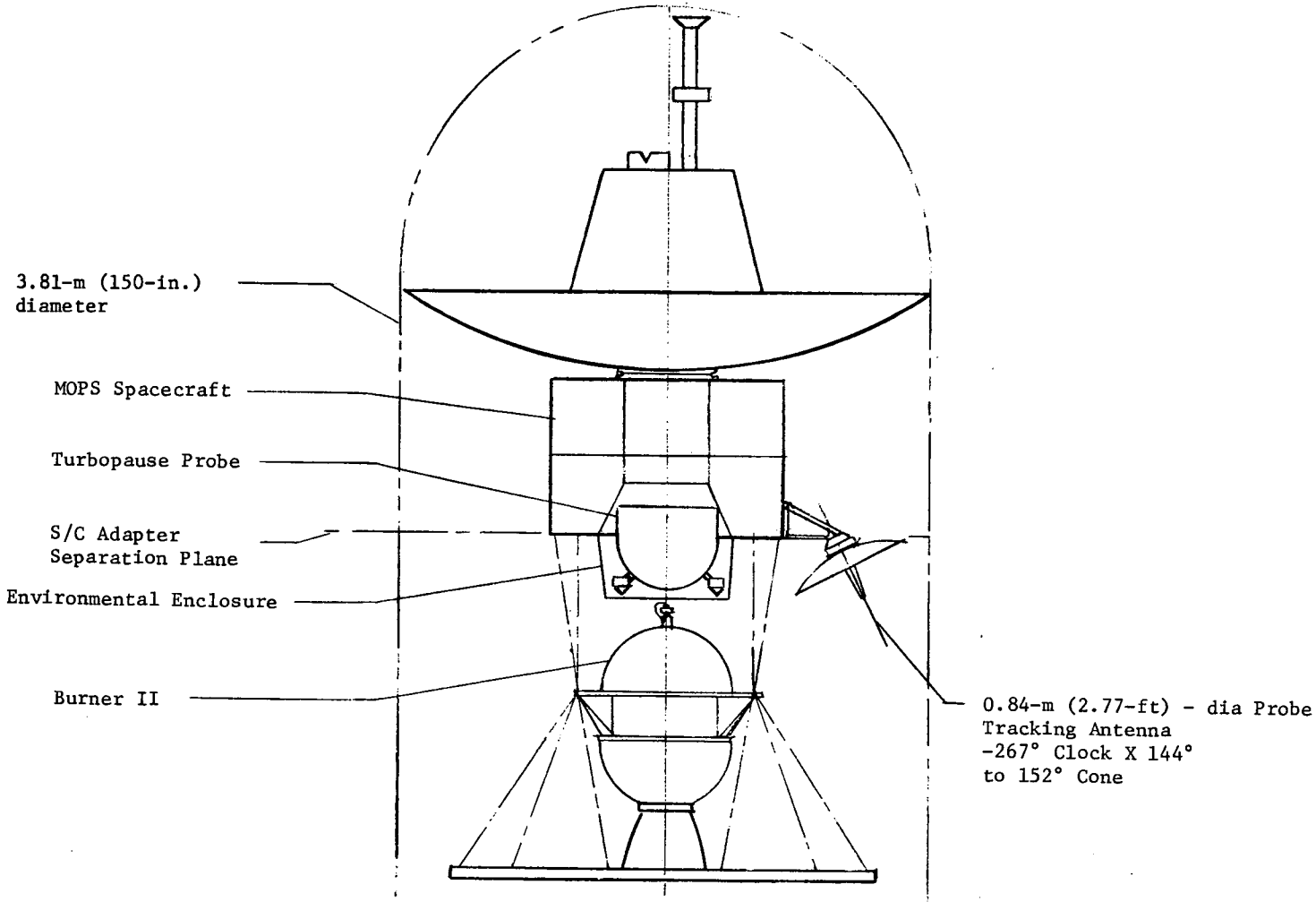

Figure V-41 Probe-Spacecraft Interface for Mission 7

K. MISSION 8 - JS 78

The objective of this part of the study was to determine the feasibility of including a Jupiter probe on a 1978 spacecraft launch for a Jupiter-Saturn encounter mission.

The study was limited to mission analyses.

The launch opportunities for a JS 78 mission were shown in Fig. IV-15. The Jupiter flyby radii for these missions are larger than 15 Jupiter radii for reasonable launch periods. Thus, these missions are not compatible with a turbopause probe mission, because the probe transmitter power requirement far exceeds the 40-W limit at X-band for large flyby radii.

L. REFERENCES

V-1. S. G. Chapin: *Jupiter Turbopause Probe Gas Physics Environment and Instrument Response Study* - Martin Marietta Report MCR-71-142, Aug 1971.

VI. TELECOMMUNICATIONS, DATA HANDLING, AND POWER

Design studies and general tradeoffs for telecommunications, data handling, and power systems are presented in this chapter. For individual mission tradeoffs, see Chapter V. General design results applicable to all missions are discussed in detail and design examples given.

A. TELECOMMUNICATION

1. Data Link Design

Telemetry data-link design is based on an RF link analysis from the data handling system on the probe to the receiver on the spacecraft. On the spacecraft, data are integrated into the spacecraft data-handling system and stored or relayed directly to Earth on the Deep Space Network (DSN) link, depending on the data handling capability of the spacecraft and mission schedules. Most missions were analyzed using 20 GHz as the carrier frequency. This was based on preliminary RF blackout calculations. Results of the nonequilibrium wake study allowed the transmission frequency to be lowered to 10 GHz. Therefore, only the three most viable missions--Probe Optimized (1A), Radiation Compatible (2A), and JS 77 (7)--were redesigned to determine power levels and RF component characteristics at X-band.

The RF link is designed to use phase-shift keying (PSK) to phase modulate (PM) the carrier with data that has been pulse-code modulated (PCM). As discussed in Subsection A4 of this chapter, a coherent link was also chosen to conserve the amount of RF power required. Therefore, total transmitter power required is the sum of the carrier tracking- and data-channel powers.

Two computer programs were employed to calculate certain key parameters of the RF link. The communications geometry program (COMGEO) provided trajectory information such as communication range, velocity, acceleration, aspect angles, and altitude versus time. These quantities were used by the communications program (PETUS) to solve for RF link parameters. Significant program results are shown in Fig. VI-1. Quantities on the left are input variables. Those on the right are calculated from the two computer programs.

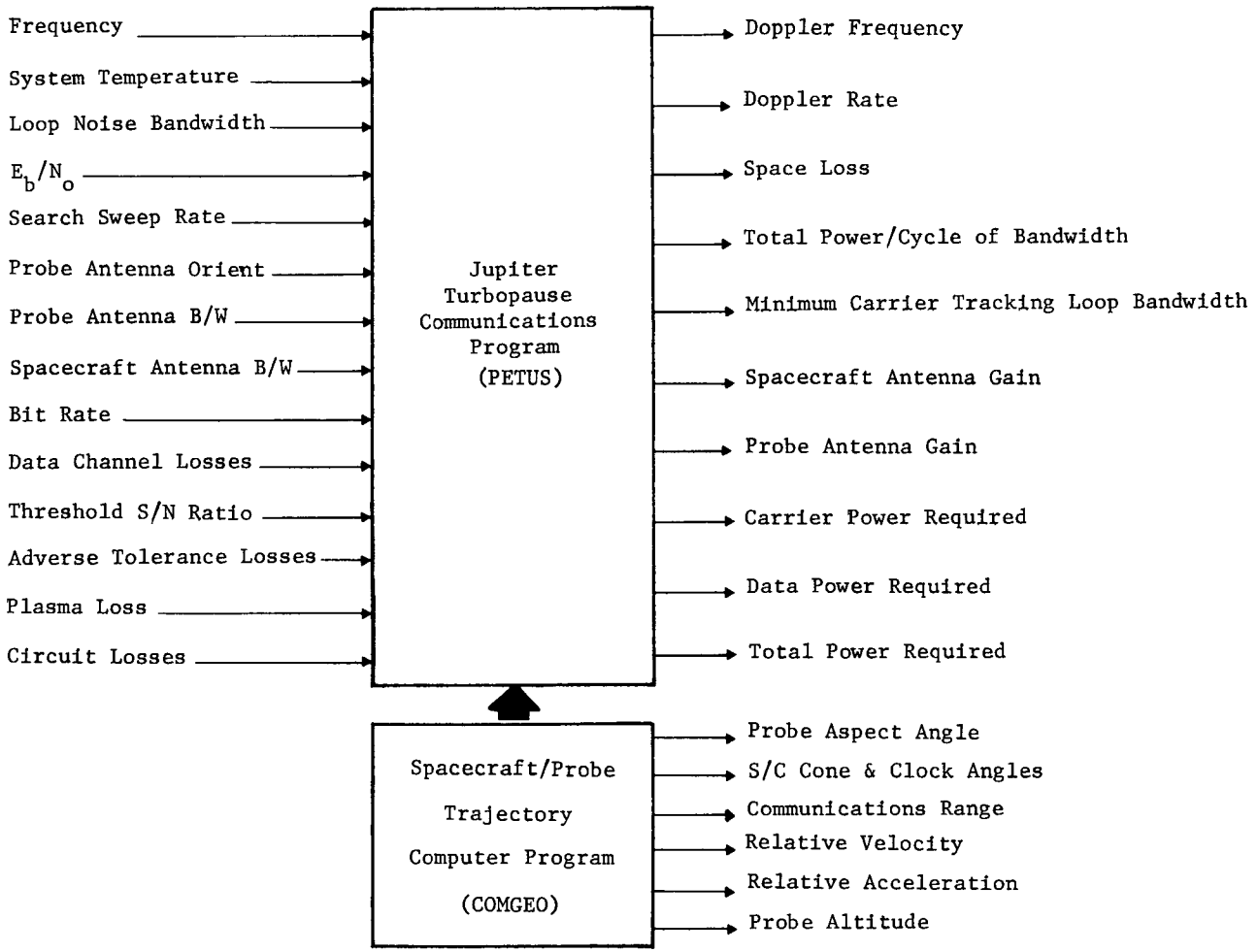

Fig. VI-1 Communications Study Program

a. Modulation and Coding - Only coded PCM/PSK/PM modulation was considered for the probe-to-spacecraft relay link because of more efficient operation. Large frequency uncertainties prohibited consideration of multiple-frequency-shift key (MFSK) operation, especially because the receiver is on board a spacecraft.

Convolutional as opposed to biorthogonal coding was selected on the basis of superior performance by as much as 1 dB, plus the fact that both the required number of symbols per bit and the bandwidth are less for the convolutional system. This results in more energy per symbol for better symbol synchronization. The two coding schemes were compared by considering a 1/3-rate, constraint-length 4 convolutional code, and a Viterbi algorithm decoder using soft decision, 4-bit symbol quantization with output delayed three constraint lengths. This was compared with both a constraint-length 4 and constraint-length 7 code generator and biorthogonal decoder. Comparative estimates of performance are given in Fig. VI-2. For the missions considered in this study, an E_b/N_o of 4 dB was used for a bit error probability of 5×10^{-5}, which corresponds to the Viterbi decoding algorithm shown in the figure.

b. RF Data Link Parameters - Parameters that comprise the RF link analysis are shown in Table VI-1 for the JS 77, Mission 7. This mission was chosen as a design example because all missions had similar values for mission-independent parameters. Space loss, antenna gains, carrier and data power, and bit rates were the major mission-dependent variables. The link is designed with 3 dB of plasma loss included so the performance margin will not be reduced to zero until after 3 dB of plasma loss has been encountered. At that point, random loss of data will become evident and increase rapidly as plasma attenuation increases.

Antenna beamwidths are based on the trajectory dispersion program that calculates the probe and spacecraft aspect angles and the 3σ deviation at the end of the mission. The spacecraft dish beamwidth was sized to cover the uncertainty ellipses at acquisition and entry, as illustrated in Fig. VI-3 and discussed in detail on page VI-34. The adverse tolerance column in Table VI-1 represents the worst-case values--the 3σ numbers for antenna pointing losses. Probe antenna adverse pointing losses include effects of pattern ripple due to asymmetry. The ratios of carrier and data power to total power are modulation losses. Data channel losses include phase jitter, doppler offset, bit-synchronization error, and demodulation losses.

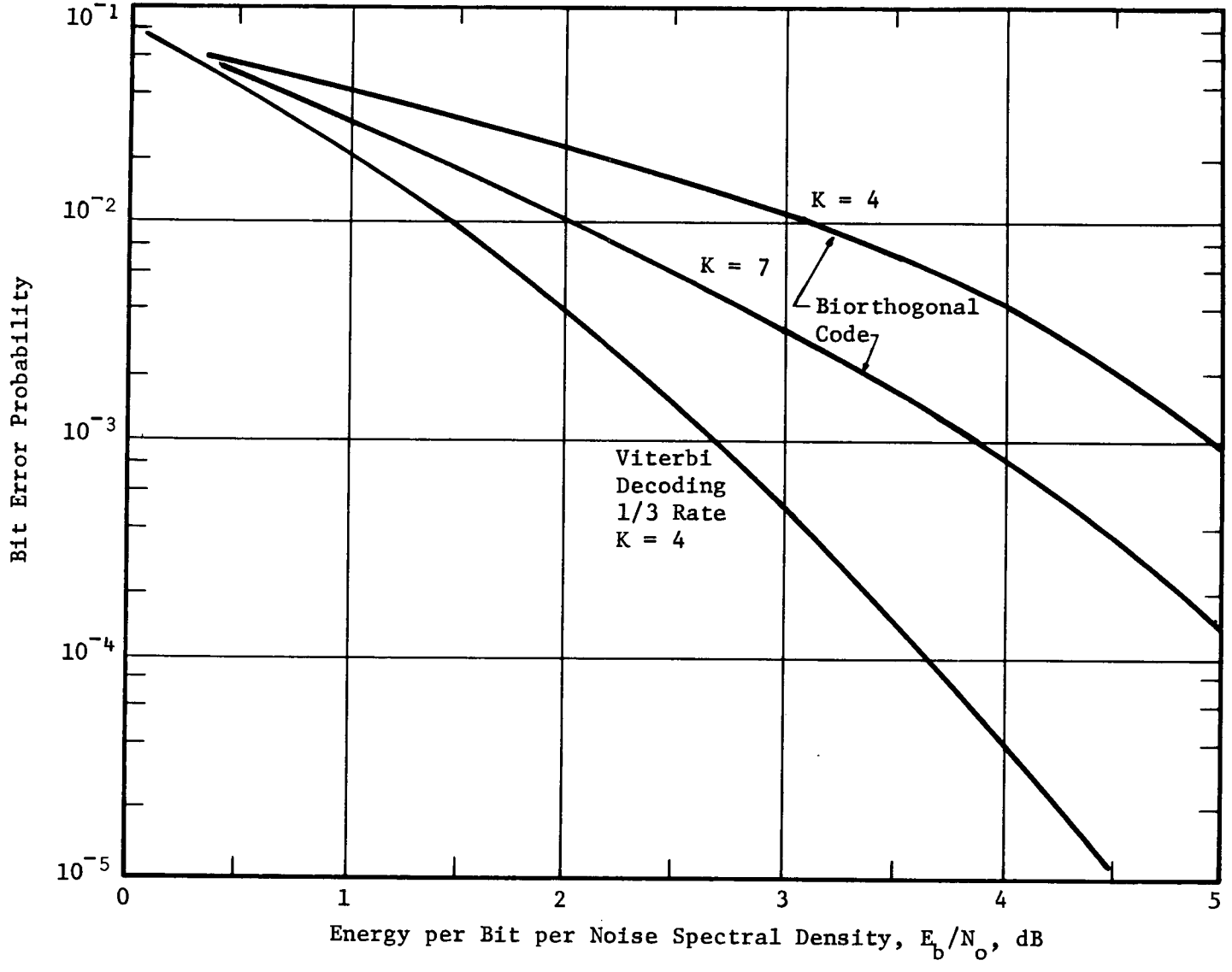

Ref: J. A. Heller: "Sequential Decoding: Short Constraint Length Codes," JPL, *Space Program Summary 37 - 54, Vol III*, December 1968, p 171 thru 177.

Fig. VI-2 Performance of Decoding Algorithms

Table VI-1 Probe Telemetry Design Control Table

Item	Parameter	Unit	Nominal Value	Adverse Tolerance	Remarks
1.	Total Transmitter Power	dBW	13.0	0.5	20 W
2.	Transmitting Circuit Loss	dB	-0.5	0.1	
3.	Transmitting Antenna Gain	dB	23.3		10° horn
4.	Transmitting Antenna Pointing Loss	dB	-1.8	0.2	PAA = 0.8°
5.	Space Loss	dB	-229.1	0.2	676,400 km
6.	Polarization Loss	dB	-0.2	0.2	
7.	Atmospheric Loss	dB	-3.0		Entry plasma
8.	Receiving Antenna Gain	dB	36.4	1.2	2.5° dish
9.	Receiving Circuit Loss	dB	-0.4	0.1	
10.	Net Circuit Loss, $\Sigma(2 \rightarrow 9)$	dB	-175.3	2.0	
11.	Total Received Power (1 + 10)	dBW	-162.3	2.5	
12.	Receiver Noise Spectral Density, N_o	dBW/Hz	-203.6	0.3	T_s = 315° K NF = 3.2 dB
13.	Carrier Tracking				
13.	Carrier Power/Total Power	dB	-5.4	0.6	
14.	Received Carrier Power (11 + 13)	dBW	-167.7	3.1	
15.	Carrier Threshold Loop Noise BW, $2B_L$	dB/Hz	21.8		150 Hz
16.	Threshold SNR, $S_c/2N_oB_L$	dB	10.0		
17.	Threshold Carrier Power, S_c, (12 + 15 + 16)	dBW	-171.8	0.3	
18.	Performance Margin (14 - 17)	dB	4.1	3.4	
	Data Channel				
19.	Data Power/Total Power	dB	-1.5	0.2	ϕ = 57.5°
20.	Radio System Loss	dB	-1.5	0.5	
21.	Subcarrier Demod Loss				
22.	Bit Sync/Det Loss				
23.	Doppler Offset Loss				
24.	Received Data Power, $\Sigma(11 + 19 \rightarrow 23)$	dBW	-165.3	3.2	
25.	Data Bit Rate, $1/T_b$	dB/bps	30.1		1024 bps
26.	Threshold E_b/N_o, S_dT/N_o, $P_e^b = 5 \times 10^{-5}$	dB	4.0		
27.	Threshold Data Power (12 + 25 + 26)	dBW	-169.5	0.3	
28.	Performance Margin (24 - 27)	dB	4.2	3.5	
29.	Nominal less Adverse Value	dB	0.7		

Specific Conditions:
1. Conditions at time of entry, JS 77 Mission (7)
2. Frequency is 10 GHz, X-band
3. Modulation - PCM/PSK/PM
4. Decoder - Viterbi algorithm, rate 1/3, soft decision, K = 4

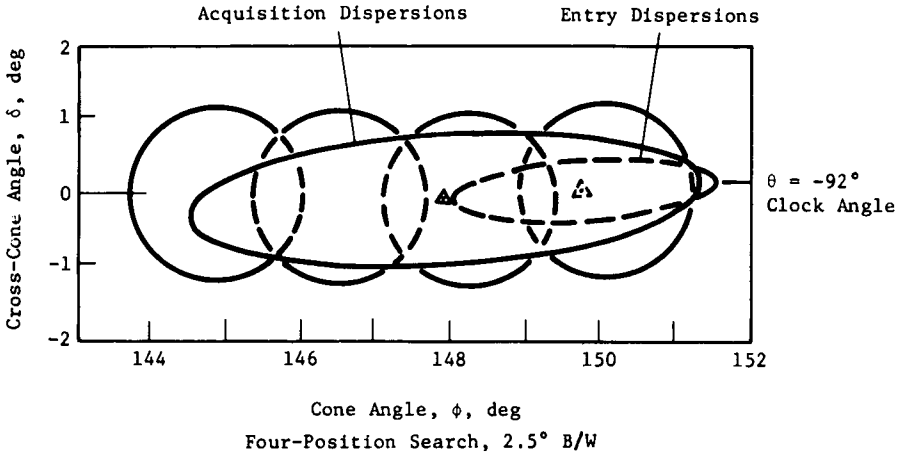

Fig. VI-3 Typical Spacecraft Antenna Acquisition Requirements

c. Maximum-Range Mission - An analysis was made to determine the maximum-range mission with practical constraints on the link design. It was assumed that at X-band (10 GHz), a reasonable power limit of 40 W would be attainable in the 1975 state of the art. Also, based on results of design and integration efforts in this study, an 8° probe antenna, a 2.5° spacecraft antenna, and a data rate of 1024 bps were assumed. The probe requires use of a parabolic dish for the 8° antenna design, which results in a 28-cm (11-in.) diameter. The antenna horn design used in the sample missions was the preferred approach for wider beamwidths of 10° or more, since wider beamwidths result in shorter, more compact antennas. However, at 8° and X-band, a horn antenna was too long to be easily integrated into the probe. The probe parabolic dish does appear practical; however, some detailed integration problems will have to be resolved. The 2.5° S/C antenna beamwidth is about the narrowest, highest-gain antenna design that will provide sufficient coverage to handle typical dispersions for the large flyby radii.

Figure VI-4 presents the results of this parametric analysis. For the assumed conditions, the maximum communications range is 5×10^5 km or 7 R_J. It should be noted that the sample missions at corresponding flyby radii show somewhat higher required RF power due to the use of the 10° beamwidth horn-antenna design.

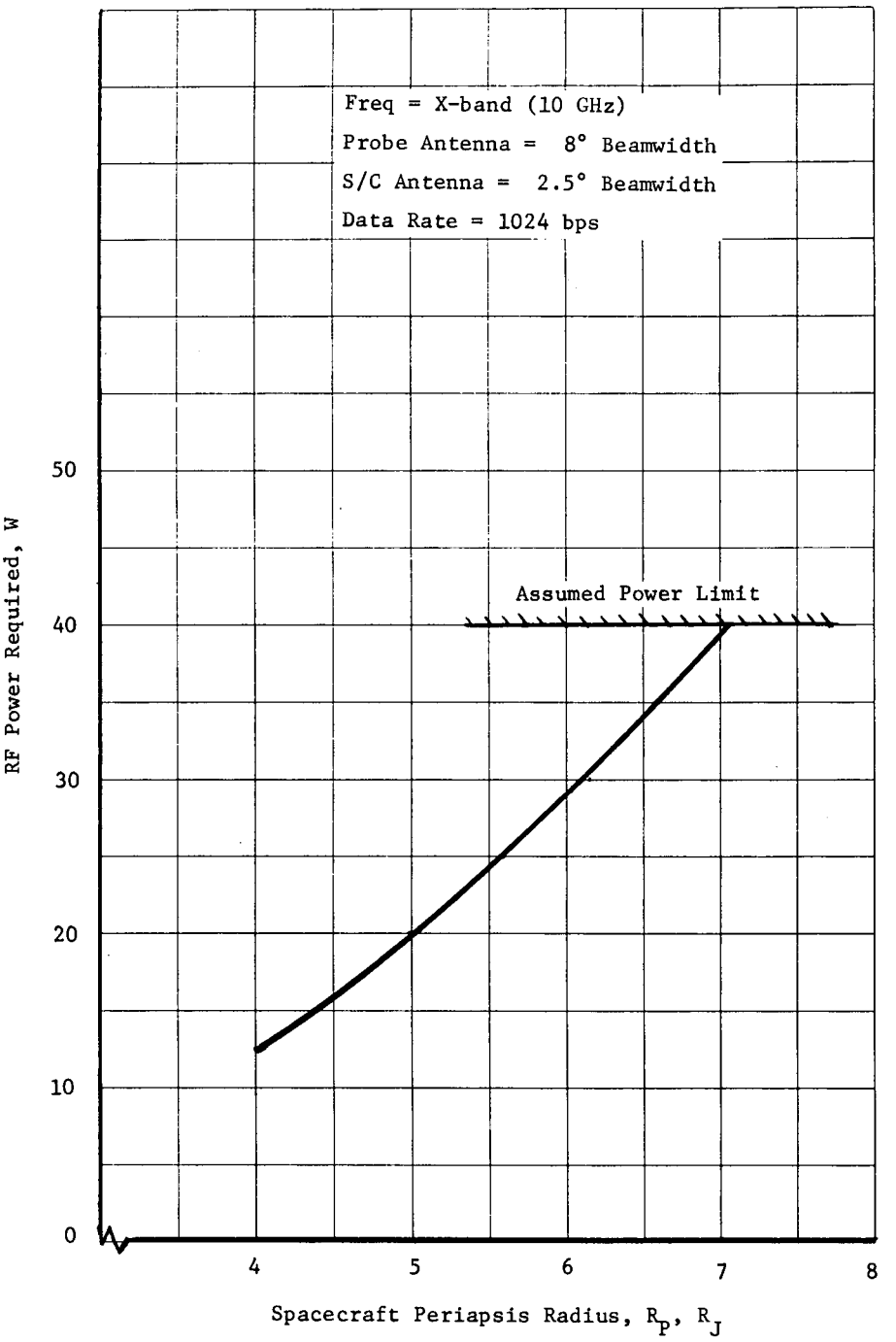

Fig. VI-4 RF Power Requirements with Range

d. Communications Geometry Tradeoff - A design tradeoff was made between minimum probe aspect angle at the end of mission and minimum communications range. Space loss at high frequencies becomes quite significant with increasing range. The deflection maneuver is different for the two trajectories, resulting in either zero aspect angle at entry or minimum range. For minimum range (side case) the aspect angle is approximately 90°. Because the probe is rotating about its spin axis, an antenna pattern that is omnidirectional in the roll plane (toroid) must be used. This considerably lowers probe gain--from 18.3 to 2.5 dB.

The side case results in decreasing space loss as the probe enters the atmosphere as seen in Fig. VI-5. Comparison of the range at entry is seen in Fig. VI-6. Therefore, side geometry optimizes the space loss problem by reducing total range at entry and decreasing the range during the mission. The decrease in space loss must be compared with the decrease in link gain resulting from a lower probe gain. This comparison was made for three cases of R_p with $R_{EJ} = 10^7$ km, and $\gamma_E = -35°$, and at K-band. Relative required power is shown in Fig. VI-7. Power difference at entry is 5 dB for 1.1 R_J and increases with periapsis radius. Therefore, if 20 W were required at K-band for the tail case, the side case would require 3.16 × 20 or 63 W. Space loss reduction did not compensate for reduction in probe antenna gain for the side case. Therefore, there is a net loss in the RF link equation that requires more transmitter power to overcome this deficit.

As a result of this trade study, a decision was made to design all missions for only the tail case, which gives minimum aspect angle (nominally zero) at probe entry. Range loss can be compensated for by using higher probe antenna gains as required.

2. Antenna Designs

a. Probe Antenna - A high-gain antenna with circular polarization is required to hold the RF link to reasonable power levels. The probe spins about its longitudinal axis to maintain attitude stability. Therefore, circular polarization will allow it to rotate without the received energy being affected by cross-polarization.

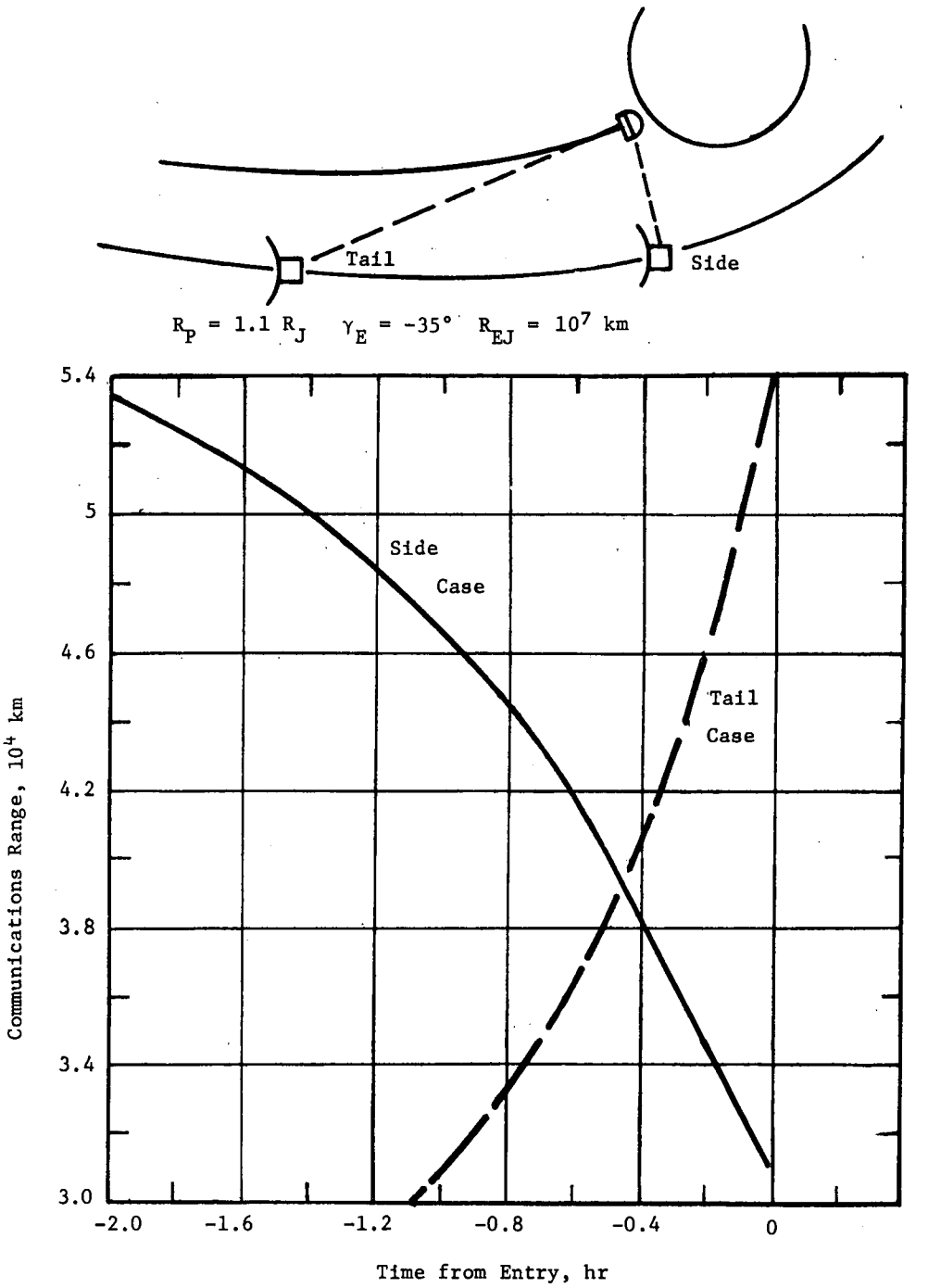

Fig. VI-5 Communications Range vs Time

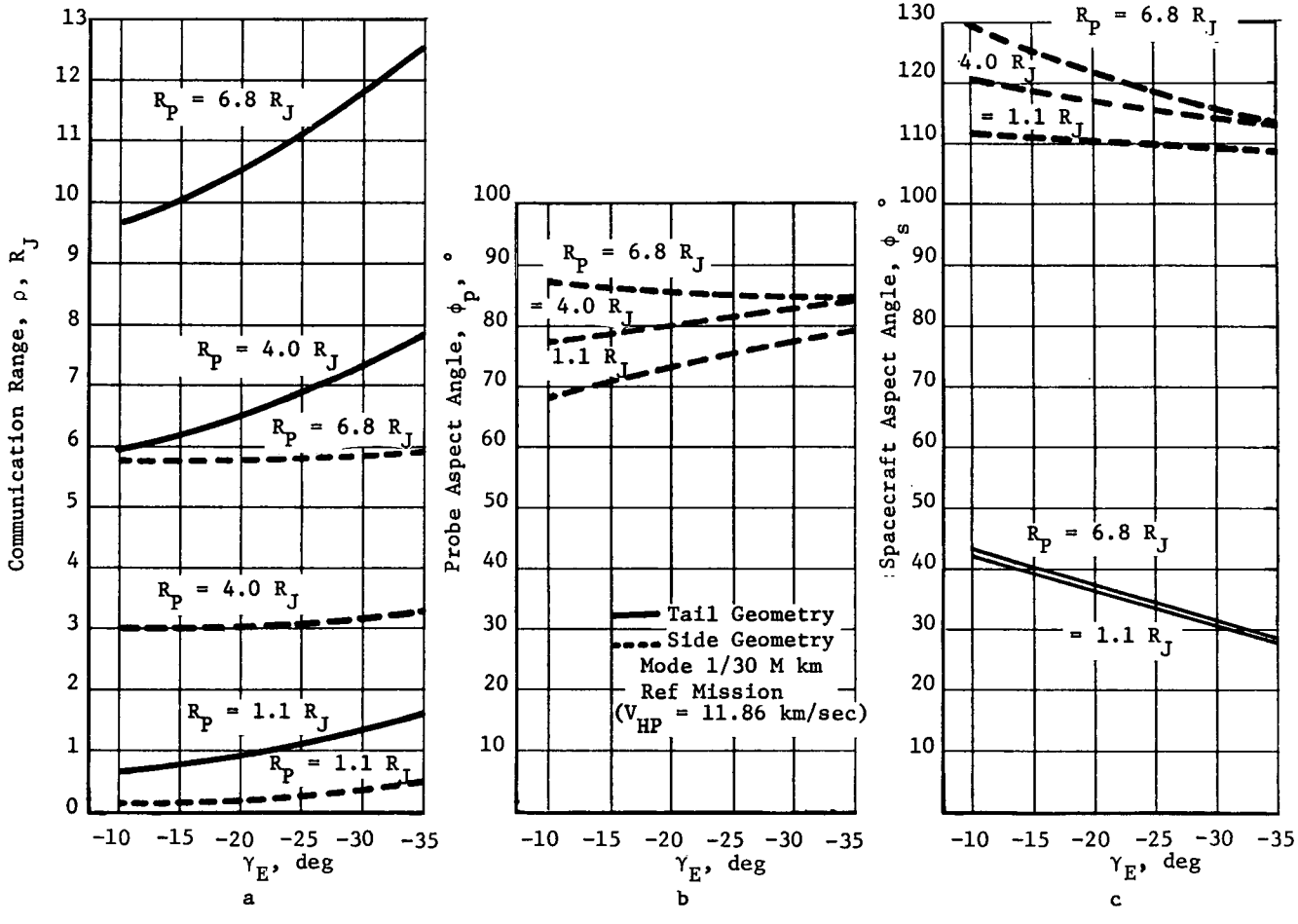

Fig. VI-6 Communication Parameter Variation with Entry Angle

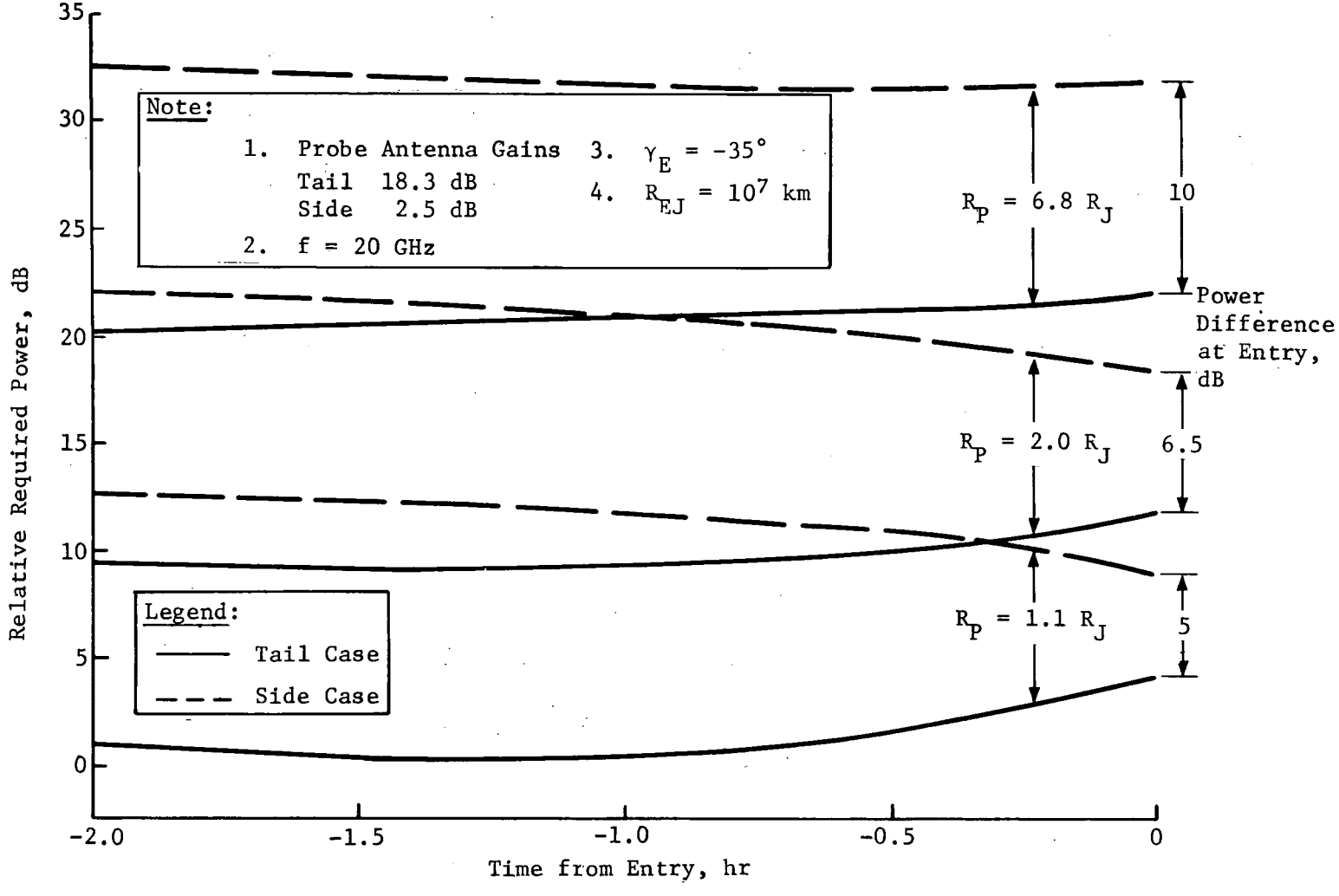

Fig. VI-7 Relative Communications Power Required for Side and Tail Geometries

Aerodynamic heating of the probe results in a steadily increasing heat rate that eventually destroys the probe. The aft bulkhead of the probe has a heat rate of approximately 6% of stagnation, which results in 500 W/cm^2 shortly before destruction. The RF subsystem is designed and packaged to withstand maximum heating because data transmission is desired as long as possible in the Jovian atmosphere. Therefore, a conical horn antenna was chosen over a parabolic dish because a dish has more exposed surface and is very sensitive to geometrical distortions of the reflector resulting from uneven heating. A horn antenna can be enclosed in the probe with only the aperture exposed to the environment. The probe can be mounted flush with the aft bulkhead or extended slightly to accommodate packaging. The aperture can be covered with a radome for thermal control.

Conical horns are the simplest antenna structure and quite compact. The length of a conical horn increases directly with power gain and can become objectionably long for high gains. Conical horns exhibit gain and directional characteristics similar to those of rectangular or pyramidal horns. Because radiation characteristics of a conical horn are determined by its dimensions in wavelengths, all dimensional data can be normalized in terms of wavelength so that sizes can be quickly determined for various frequencies.

The probe antenna was designed for minimum beamwidth for each design mission. Probe aspect angle and associated angular uncertainty were evaluated at entry and acquisition to determine the worst-case angle. Design parameters are shown in Table VI-2 for three typical missions. Worst-case angles were considered during acquisition, but RF link margins are greater due to less space loss. Therefore, probe antenna beamwidths were optimized for minimum beamwidth and maximum gain during entry, which is the worst link condition. As seen in the table, a beamwidth of 10° was chosen for the missions shown.

A conical horn is a section of a right circular cone and is usually connected to a cylindrical waveguide, as shown in Fig. VI-8. The method of excitation chosen comprises a rectangular waveguide flared into a square section where proper circular polarization is achieved. For either dominant wave (TE_{10}) excitation in a rectangular waveguide or (TE_{11}) wave excitation in a circular waveguide, the conical horn exhibits the same behavior (Ref VI-1).

Table VI-2 Probe Antenna Beamwidth Design Parameters

Parameter	Unit	Mission		
		1A	2A	7
Entry Conditions				
1. Aspect angle	deg	0.3	0.2	0.4
2. Aspect uncertainty	±deg	4.2	3.9	3.5
3. Worst-case angle	deg	4.5	4.1	3.9
4. Min probe antenna B/W for max gain	deg	10.0	10.0	10.0
5. Power loss due to adverse pointing	dB	2.5	2.1	1.8
Acquisition				
1. Time, X	E-X min	35	36	57
2. Aspect angle	deg	4.9	1.6	1.9
3. Aspect uncertainty	±deg	4.1	4.3	4.3
4. Worst-case angle	deg	9.0	5.9	6.2
5. Power loss due to adverse pointing for antenna B/W	dB	7.8	3.8	6.9

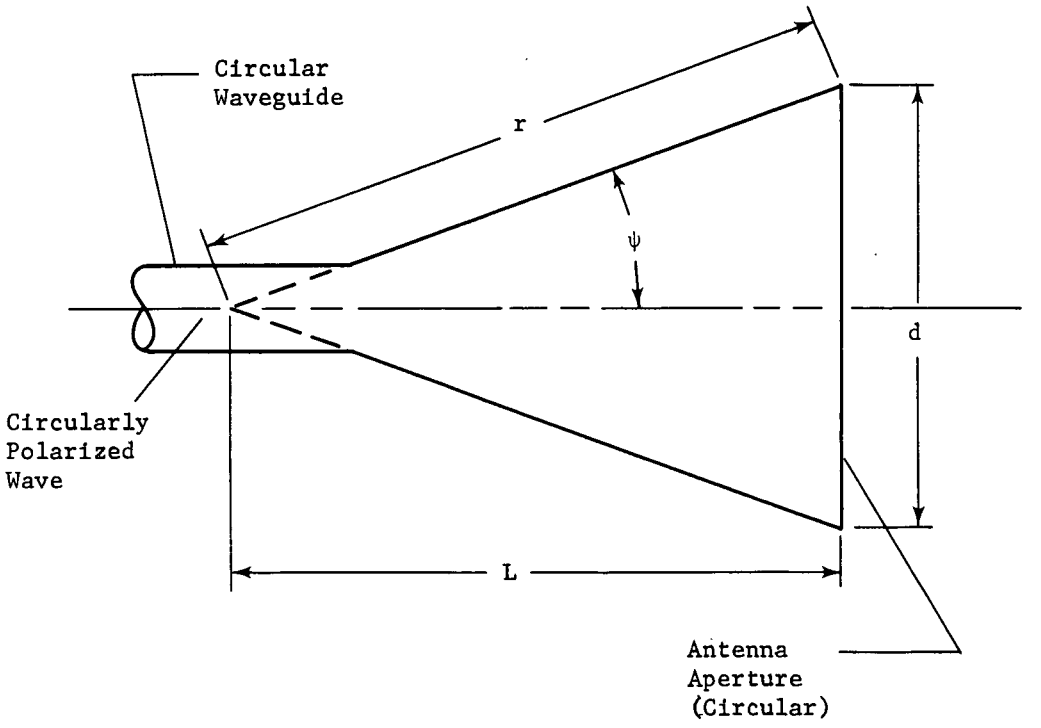

Fig. VI-8 Conical Horn Antenna Details

Antenna performance can be determined by specifying two dimensions--axial length, L, and diameter of the horn aperture, d, as indicated in Fig. VI-8. A long axial length is required to obtain uniform aperture distribution of the dominant mode with a small flare angle, ψ. From the standpoint of practical convenience, the horn should be as short as possible. An optimum horn is between these extremes and has minimum beamwidth without excessive side-lobe levels for a given length. For a fixed axial length, the axial gain increases as the aperture diameter, d, increases up to a certain optimum value. For all other values of d, the gain will be less (Ref VI-2).

The dimensions that correspond to a maximum gain for a given length are shown in Fig. VI-9. The geometrical relationships are (Ref VI-3 and VI-4):

$$\frac{r}{\lambda} - \frac{L}{\lambda} = 0.3 \qquad [VI-1]$$

or

$$\frac{L}{\lambda} = 0.3 \left(\frac{d}{\lambda}\right)^2 \qquad [VI-2]$$

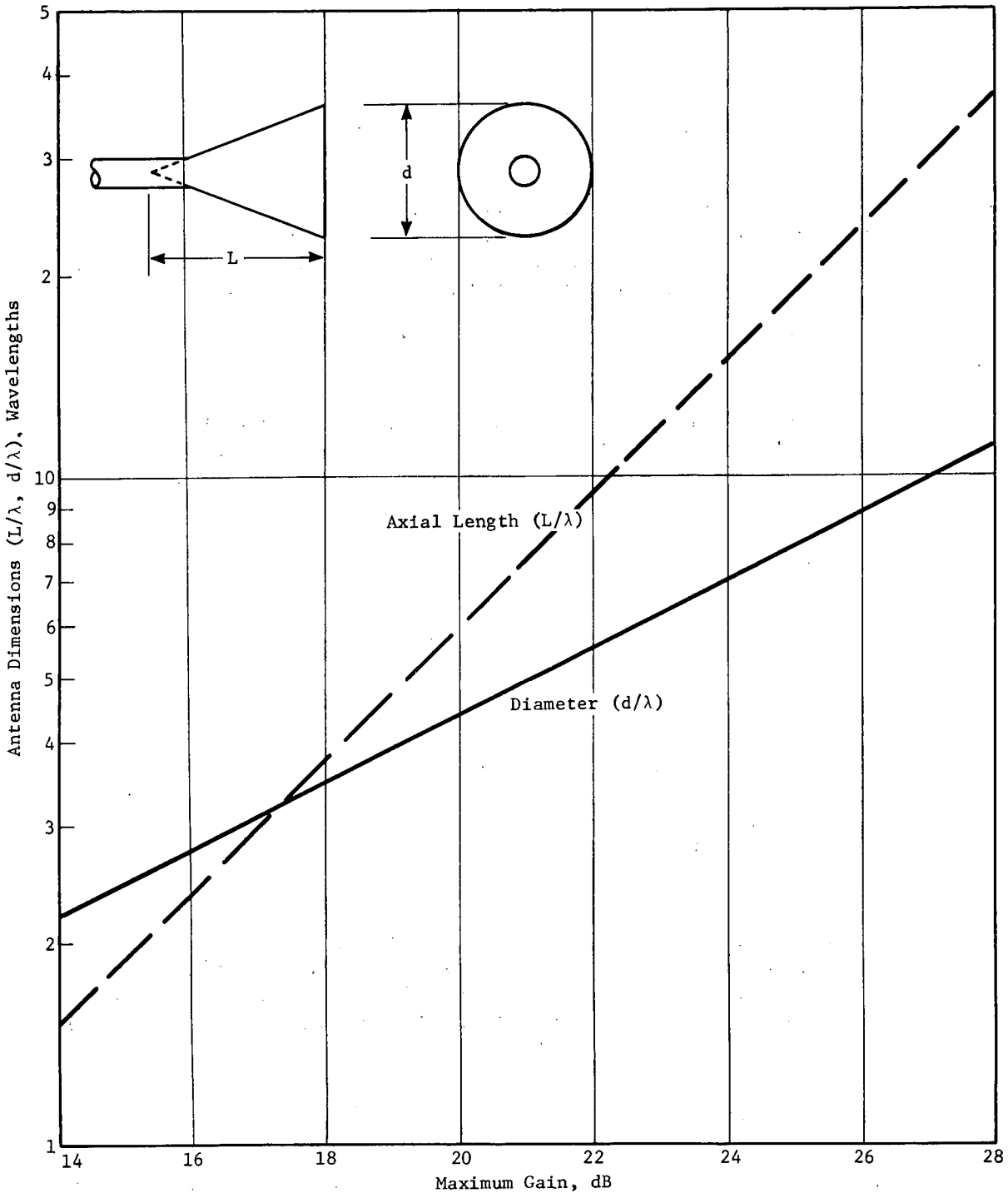

Fig. VI-9 Design Dimensions of Optimum Conical Horn Antenna As A Function of Gain

and

$$d = \sqrt{3\lambda r} \text{ or } r = \frac{d^2}{3\lambda} . \qquad [VI-3]$$

This corresponds to a maximum phase deviation of $3/8\lambda$ in the aperture wave-front. The voltage standing-wave ratio (VSWR) is in the range of 1.05:1 to 1.5:1. Frequency bandwidth is typically 50%. Half-power (-3 dB) beamwidth for circular polarization is

$$\theta_{hp} = \frac{65\lambda}{d} . \qquad [VI-4]$$

The electric and magnetic fields have equal beamwidths out to 20° from the beam axis. The effective area of an optimum conical horn is approximately 52% of its actual area. The aperture area is

$$A = \frac{\pi}{4} d^2 \qquad [VI-5]$$

and the effective area of an antenna is

$$A_e = \frac{g\lambda^2}{4\pi} \qquad [VI-6]$$

where g is the absolute power gain. The ratio

$$\frac{A_e}{A} = \frac{g}{\left(\pi\frac{d}{\lambda}\right)^2} = 0.52 \qquad [VI-7]$$

for optimum conditions and reaches a maximum value of 84% for very long horns. Only a small increase in effective area or axial gain is realized by increasing the axial length beyond two or three times the value corresponding to optimum. The maximum gain of an optimum conical horn in dB is

$$G_m = 10 \log \left[0.52 \left(\frac{\pi d}{\lambda}\right)^2\right] . \qquad [VI-8]$$

The radiation pattern is calculated from the universal radiation pattern of horns with the amplitude at ϕ proportional to $\sin \phi$. The pattern is shown in Fig. VI-10 for several beamwidths (Ref VI-5 and VI-6)

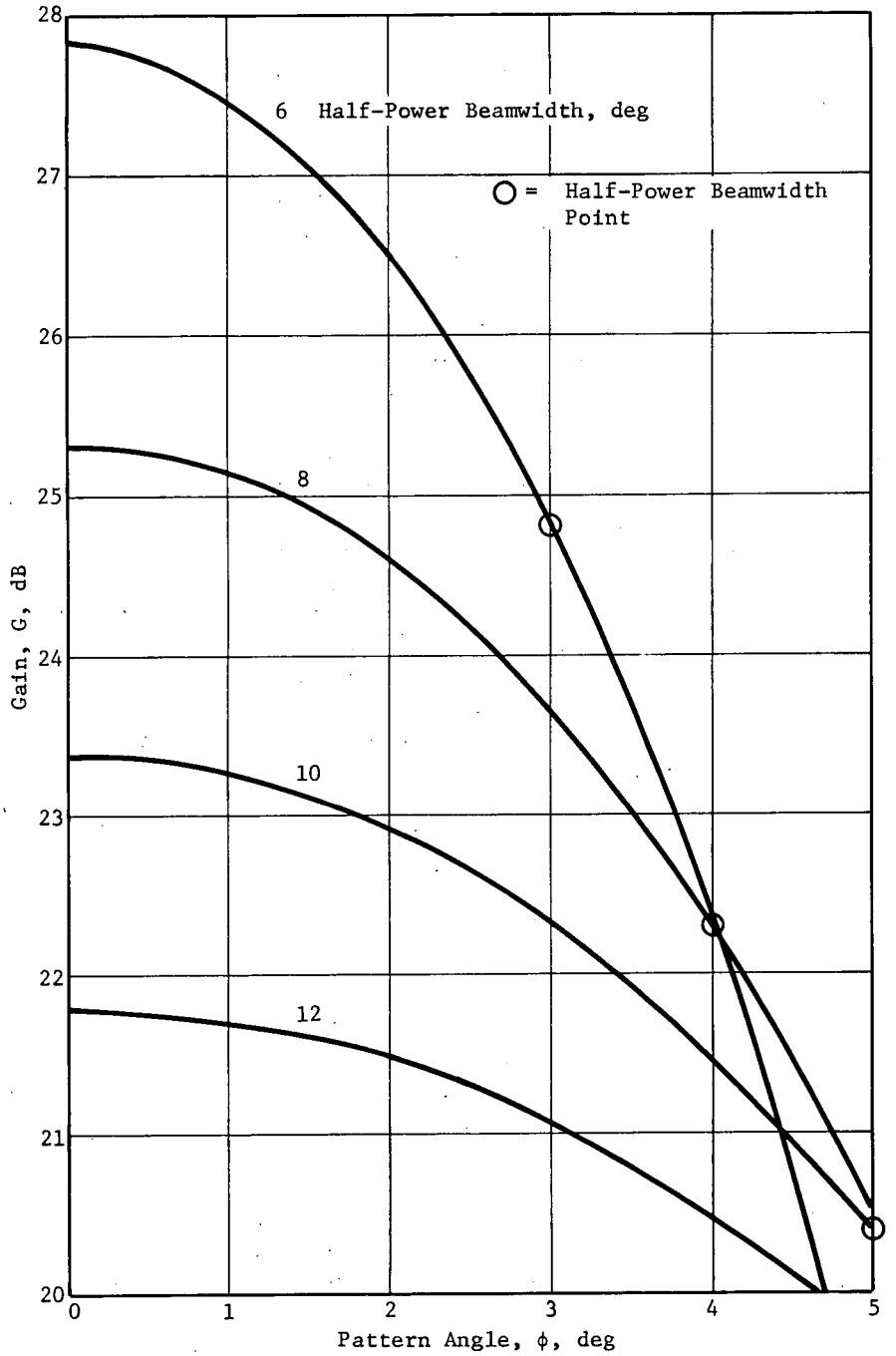

Fig. VI-10 Theoretical Optimum Conical Horn Antenna Radiation Pattern

C.6.

Table VI-3 shows dimensions of the optimum conical horn probe antenna for the design missions. As seen from the table, a beamwidth of 10° is required. The flare angle (See Fig. VI-8.) of the horn is larger than the electrical beam angle to the half-power point. The axial length, L, is defined in Fig. VI-8 and is a design measurement. The cone apex is actually located in the circle-to-square transition portion of the polarizer.

Table VI-3 Probe Antenna Design Details for X-Band

3-dB Beam, deg	Axial Gain, dB	Flare Angle, ψ, deg	Diam, d, cm	Diam, d, in.	Axial Length, L, cm	Axial Length, L, in.	Total Weight*, kg	Total Weight*, lb
10	23.4	14.4	19.5	7.68	38.0	15.00	0.34	0.75
*Total weight includes antenna and phasing section.								

The required polarization of the transmitted wave is circular. The sense is not critical and can be right-hand or left-hand as long as both the probe and spacecraft antennas are identical in sense. A transition is necessary to convert the linearly polarized wave in the rectangular waveguide to circular polarization at the apex of the conical horn. To produce the requisite space and time quadrature of the field components in the horn, the construction shown in Fig. VI-11 was used. The horn is fed from a conventional rectangular waveguide through which is transmitted a TE_{10}-mode wave, but between the horn and waveguide a transition section is interposed that displaces the horn about its axis 45° from the waveguide. The displacement is such that the wave entering the horn is resolved into two mutually perpendicular components, one of which is the TE_{01} mode, the other in TE_{10}. Thus, two fields in space quadrature are produced. By causing one component to lag by 90° with respect to the other, a circularly polarized field is radiated. This function is performed by the phasing section of the horn, in which the guide wavelength for one mode is made to differ from the guide wavelength for the other so that the phase shift is different. One method of producing a different guide wavelength is to place a longitudinal sheet of dielectric material in the phasing section so it will affect the velocity of propagation of only one of the components. The mode with the E-field line parallel to the dielectric sheet will undergo a greater phase shift per unit length than the mode with E-field lines normal to the sheet. For a thin sheet, the velocity of propagation for the normal geometry will be unaffected by its presence. Any dielectric material, such as polystyrene, Teflon,

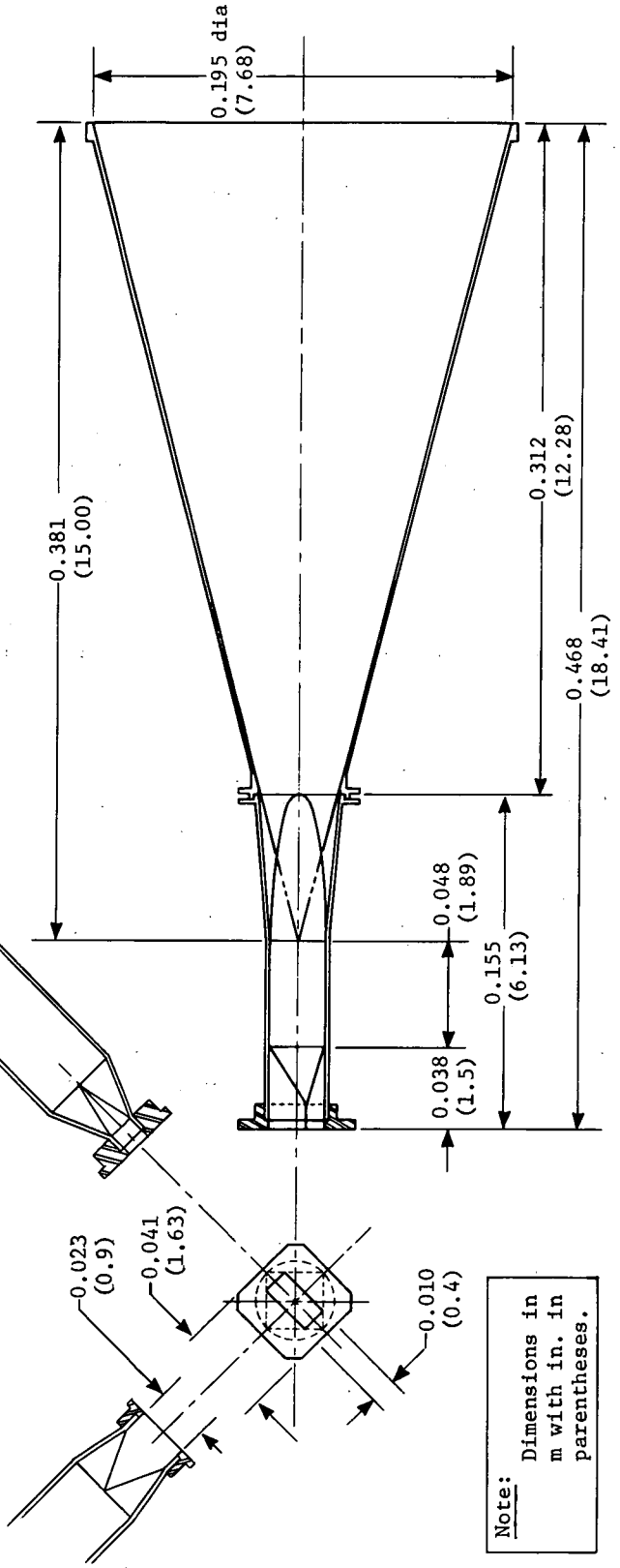

Fig. VI-11 Design Details for 10° Conical Horn Antenna at 10 GHz

PVC, or polyethylene, is suitable for the sheet. If the phasing section must withstand a higher thermal environment, a thin ceramic sheet would be satisfactory. The dielectric sheet is tapered so the sheet has V-notched ends. This makes a gradual transition from the waveguide (without dielectric) to the phasing section to minimize reflections. The dielectric sheet is designed to be 1.6λ long and 0.05λ thick. The phasing and transition sections can be precision die-cast aluminum (Ref VI-7).

The horn aperture is exposed to a high-temperature environment during entry. Therefore, the horn is beryllium and designed to withstand a maximum temperature of 800°K (∿ 1000°F). A radome over the aperture will be constructed from a suitable RF-transparent material to reduce thermal losses through the antenna. Figure VII-11 shows preliminary design details of the 10° conical horn antenna at X-band.

b. Spacecraft Antenna - The antenna selected for the spacecraft is a conventional parabolic dish with a beamwidth of 20° or less for compact design.

The dish is fed by a flared rectangular horn and is circularly polarized by a dual-mode rectangular waveguide transform section whose dimensions are selected to delay one mode by 90° relative to the other. This is a standard technique for narrowband applications. Some of the relative delay occurs in the horn itself because it is not square and its cross-polarized modes travel at different velocities. The transform section is fed by a conventional X-band rectangular waveguide (WR-90), skewed to 45° relative to the transform section so that both modes are excited equally in the section. The feed is sketched in Fig. VI-12. The transform section is shown extended for clarity. In practice, it would be bent to form part of the gooseneck feed for the dish. A flexible X-band waveguide can be used on the dish to give a compact design, as shown in the figure.

Dish antenna gain is based on an efficiency of 55% with a focal length of 0.3 (f/d) and uniform aperture illumination. The sidelobe level has maximum suppression with these conditions (> 20 dB). The maximum gain is calculated from

$$G = 10 \log_{10} \left[0.55 \, \pi^2 \left(\frac{d}{\lambda} \right)^2 \right] \qquad \text{[VI-9]}$$

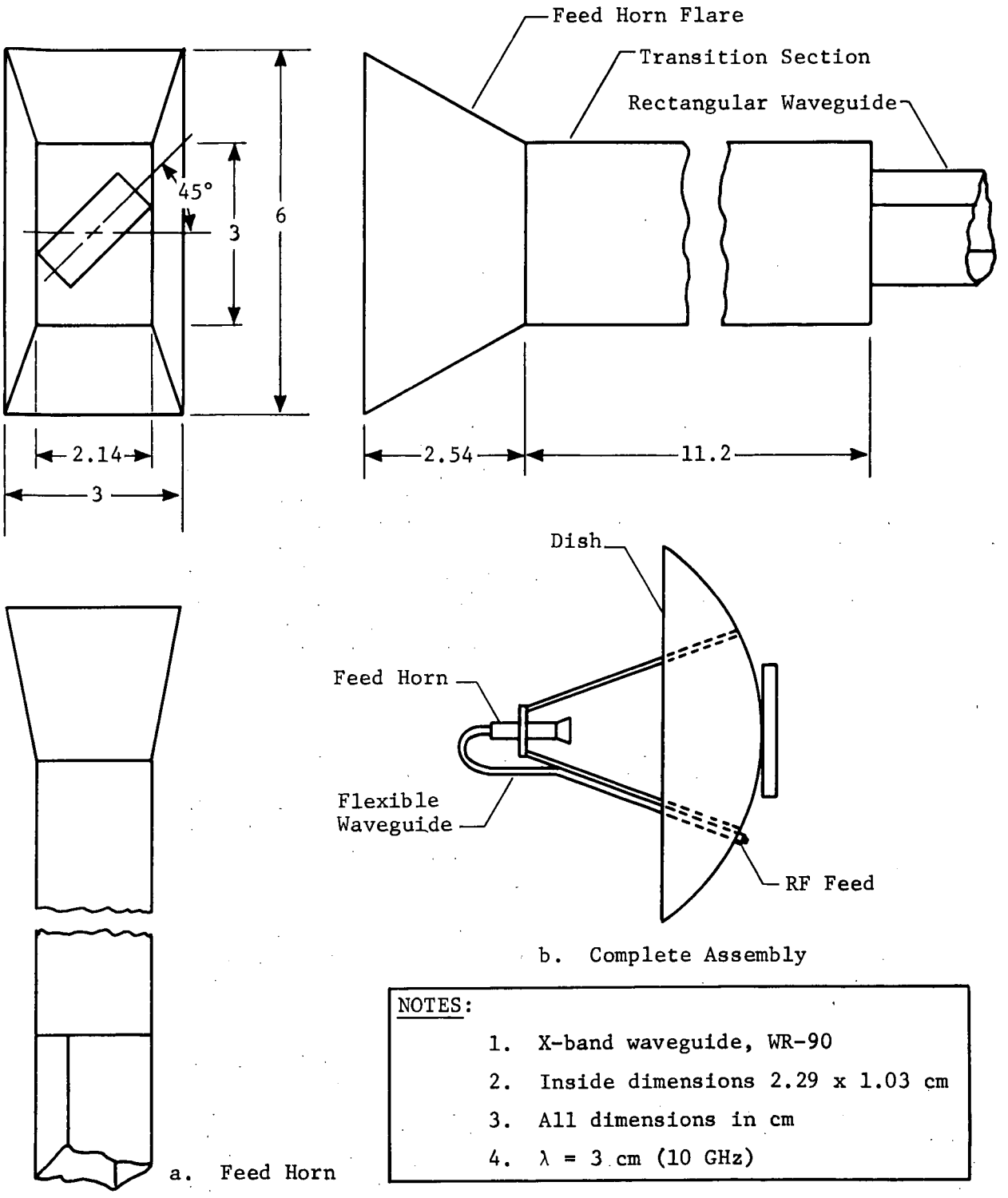

Fig. VI-12 Spacecraft X-Band Dish Antenna

where

G = dish gain, dB

d = dish diameter, cm

λ = wavelength, 30/f, cm

f = operating frequency, GHz.

The half-power (3-dB) beamwidth in degrees is symmetrical in both planes and equal to

$$\theta_{hp} = 70 \frac{\lambda}{d} \qquad [VI-10]$$

Probe position dispersions at acquisition and entry were used for each mission to determine minimum spacecraft antenna beamwidth. This gives a larger diameter from Equation [VI-10] and a larger maximum gain from Equation [VI-9] for a constant frequency (fixed wavelength). Maximum antenna gain is desired in the RF link to minimize transmitter power. Launch-vehicle payload envelope limits the spacecraft antenna size to approximately 1.5 m (5 ft) in the stowed position to clear the payload fairing. A dish with this diameter at X-band has a beamwidth of 1.5°. Therefore, a size limitation was not necessary on the spacecraft antenna.

3. Probe RF Power Sources

Nonsurvivable outer-planet probes require data transmission at high radio frequencies to overcome the effects of blackout during atmosphere entry for the greatest possible time. Transmission path loss is directly proportional to operating frequency. Therefore, required RF power increases as frequency increases to maintain a particular RF link signal margin.

Preliminary analysis of the atmosphere entry communication blackout problem indicated that frequencies in the K-band region may be required to provide a data link below the turbopause without excessive ($\geq$3 dB) attenuation. Lower frequencies will be attenuated more because plasma attenuation is inversely proportional to frequency of operation. Therefore, a data transmission system operating at K-band was initially chosen as an upper limit to consider for design missions. A detailed vendor and literature survey was made to determine the projected 1975 state of the art and an upper limit on RF power at K-band (18 to 26 GHz). The survey is described in detail in Vol III, Appendix G. The best

candidate for K-band power is a traveling-wave-tube amplifier. An upper limit is 25 W for space-qualified units by 1975. Solid-state devices may also meet the power requirements, but several development hurdles must be overcome first. In the future, if probe missions are designed for deeper penetration, higher frequencies such as K-band will be required to overcome RF blackout as long as possible.

As seen in Fig. VI-13, there are several vendors who have space-qualified traveling-wave tubes in the X-band region. Projected power levels approach 100 W at 10 GHz, which well exceeds the 20- to 30-W range required for design missions.

The amplifier operates in a straightforward manner as a subassembly of the probe transmitter, as seen in Fig. VI-14. The TWTA is waveguide coupled to the probe antenna and is the output stage of the transmitter, being fed by the modulator. The power supply is housed in a separate subassembly for small compact packaging. The power supply operates on 28- to 32-Vdc, unregulated, from the probe power bus. The amplifier package occupies 3260 cm^3 (212.5 $in.^3$) and weighs 4.5 kg (1.0 lb). The amplifier power supply occupies 2130 cm^3 (130 $in.^3$) and weighs 3.2 kg (0.70 lb). The expected overall efficiency is 24%.

4. Spacecraft Receiver Design

Postturbopause preblackout mission life can be extended by using the highest possible microwave frequency as predicted by the nonequilibrium blackout analysis. The penalty associated with increased frequency becomes significant in the K-band region for several reasons. Because the probe antenna gain and beamwidth are fixed by trajectory and dispersions, f^2 path-loss increase must be compensated for by increasing either transmitter power or spacecraft antenna gain, or both. Receiver noise temperature rises with increasing frequency, also requiring more link power. Therefore, to minimize the RF power required, a receiver with a low noise temperature was chosen.

Transistor and tunnel-diode amplifiers have a noise temperature range of 400 to 500°K at X- and K-bands, respectively. An uncooled parametric amplifier provides significantly low noise temperature at K-band that decrease even further at X-band, as seen in Fig. VI-15. The Jovian background noise temperature as seen by the spacecraft receiver over the frequency band of interest is shown as the sum of the receiver RF amplifier and antenna temperature on the spacecraft. Antenna temperature is composed of thermal disk temperature at the high end of the range, augmented by decimeter magnetosphere noise at the low end. Decimeter noise rises sharply as frequency is decreased below 17 GHz.

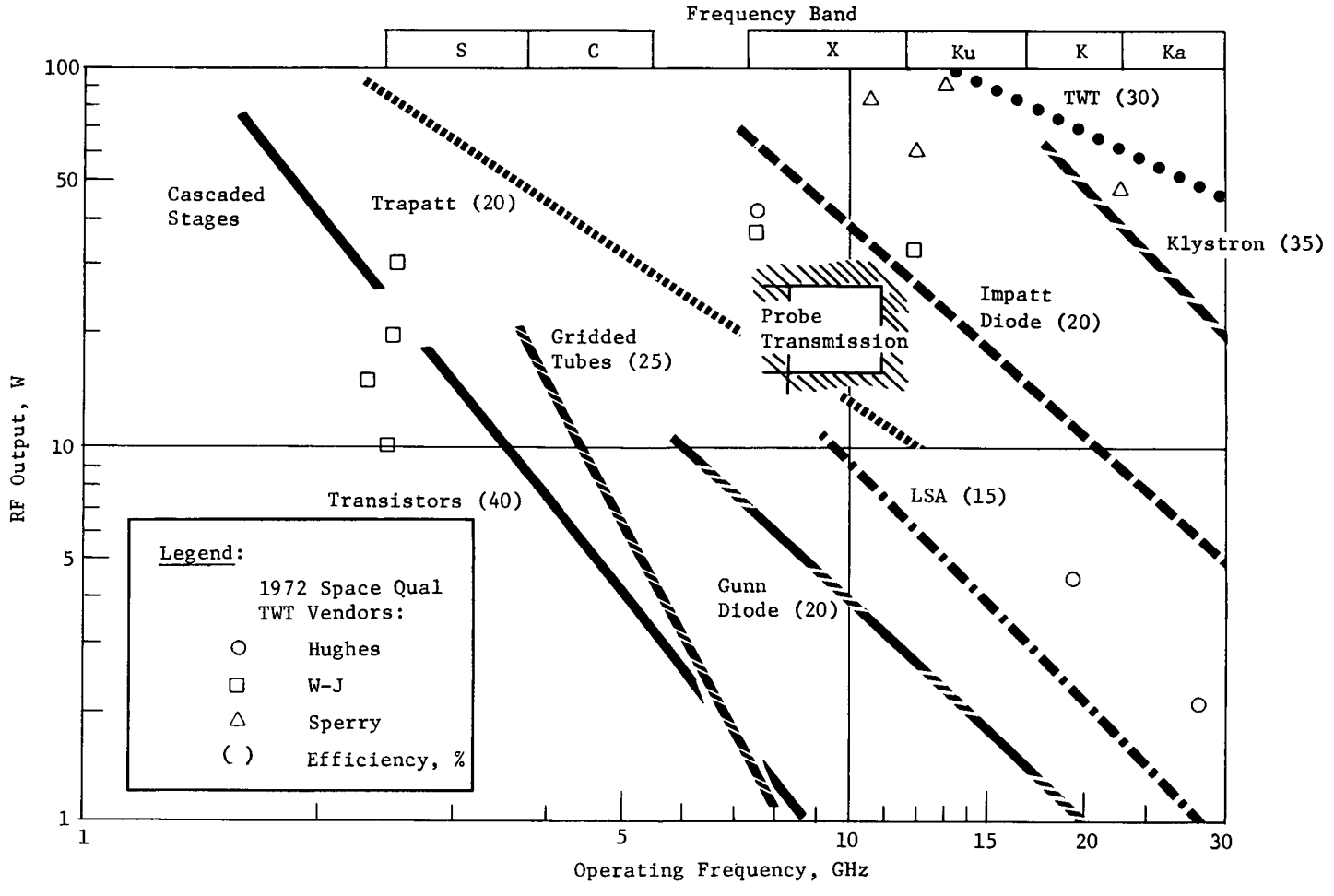

Fig. VI-13 Projected 1975 RF Power Source Capability

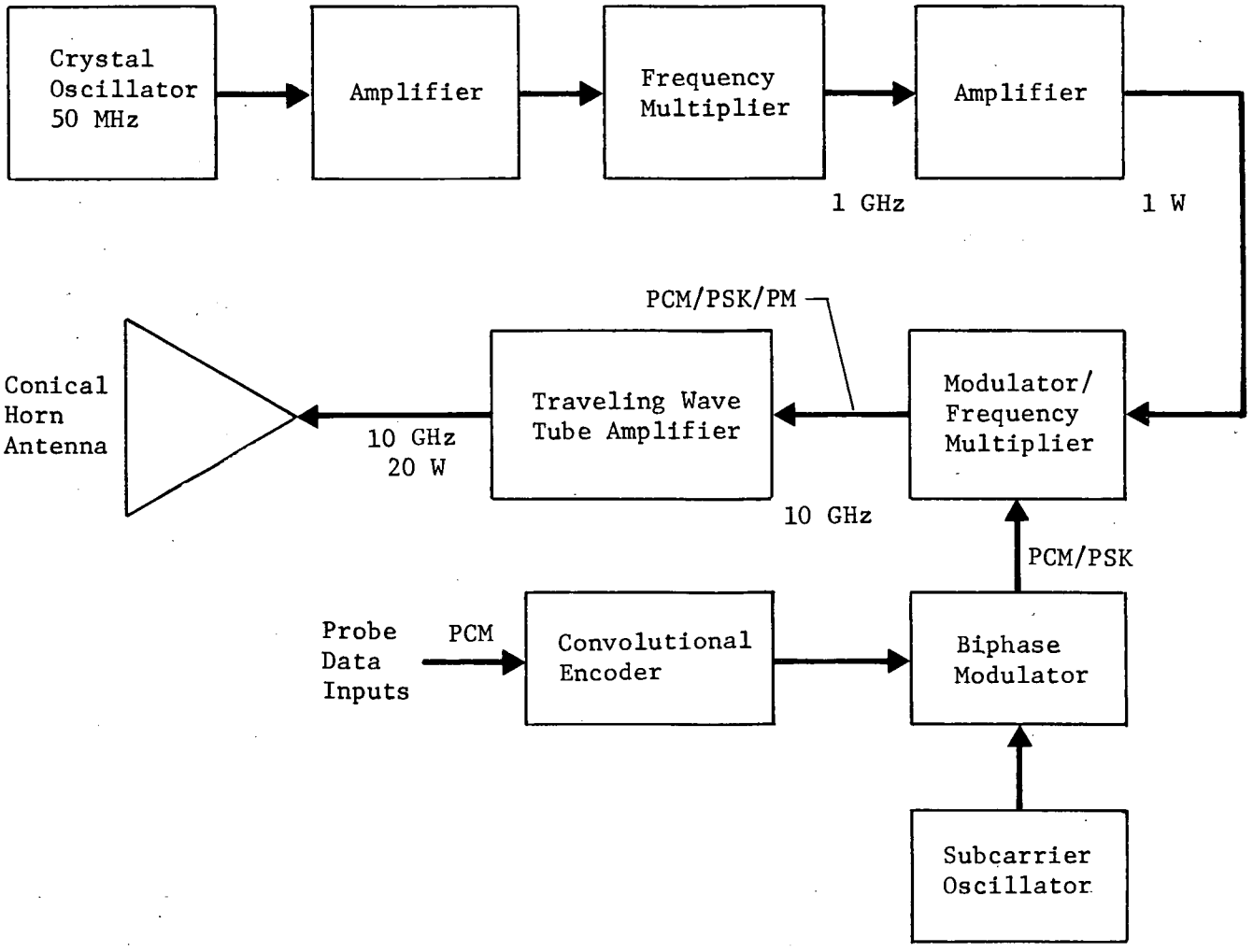

Fig. VI-14 Probe Transmitter Functional Diagram

Given this low background temperature, use of a low-noise parametric amplifier receiver front end is justified. State-of-the-art temperatures for uncooled parametric amplifiers are shown in Fig. VI-15 and are typical of space-qualified units. Amplifier noise temperatures at 18 and 26 GHz were estimated by AIL to be 228 and 207°K respectively.

a. Vendor Survey - Proposals were solicited from a number of manufacturers for a K-band parametric amplifier to be used as a receiver front end with the following characteristics:

Frequency - 18 to 26.5 GHz (K-band);

Modulation - Phase;

Bandwidth - 500 kHz minimum;

Noise Temperature - 3.5 dB (362°K);

Life - 18 months nonoperating, 48 hr operating over a 10-day period.

Proposals were received from the following:

AIL Division of Cutler-Hammer;

General Dynamics Electro Dynamic Division;

Bunker-Ramo Corp., Micromega Division;

Cubic Corporation.

The proposal from AIL is the most complete, and it probably represents the most advanced state of the art in receiver design for this frequency region. Telephone conversation with AIL personnel after receipt of their proposal provided additional technical data and permitted the refinement of certain parameters such as size, weight, and power consumption. Comments will be made on the AIL proposal, although it is not recommended that AIL be considered as a sole source for development of the parametric amplifier receiver.

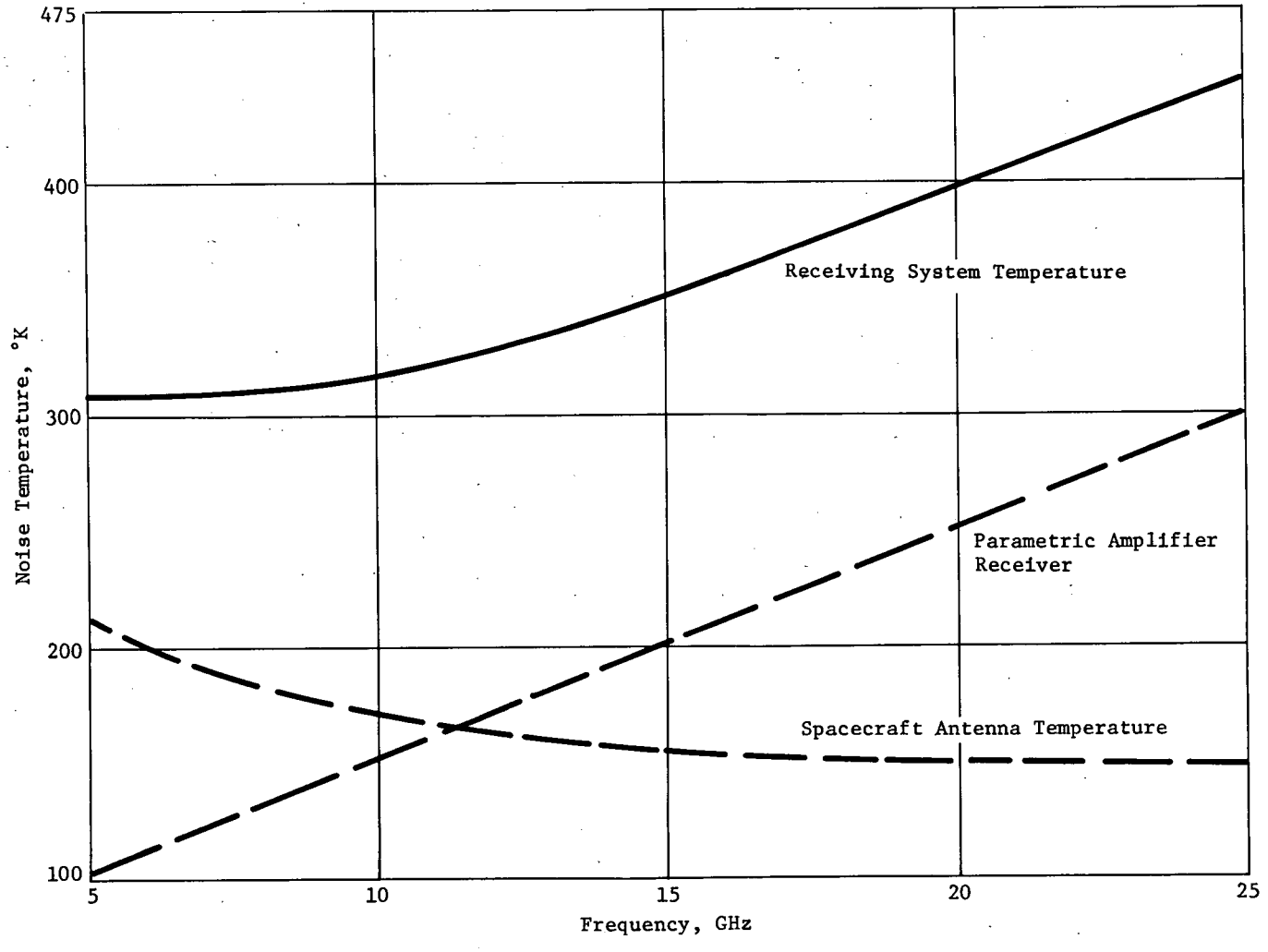

Fig. VI-15 Spacecraft Receiving System Temperatures

b. Parametric Amplifier Design - Figure VI-16 is a block diagram of the parametric amplifier proposed by AIL. A 36.5- to 40.5-GHz solid-state oscillator, followed by a varactor frequency doubler, is used as a pump. About 250 mW of pump power are required at the fundamental frequency. Total power consumption for the parametric amplifier will not exceed 7 W. Total weight will be 0.9 to 1.35 kg (2 to 3 lb) and occupy 1066 cm^3 (65 $in.^3$). Amplifier gain is about 15 to 20 dB, so a single-stage amplifier is sufficient to achieve the receiver noise figure.

The spacecraft must provide a thermal environment of ±10°C change at an operating temperature of 50°C to provide a gain stability of ±1 dB. A ±20°C change will increase the gain stability to ±5 dB, which is excessive. Therefore, receiver temperature control must be provided by the spacecraft. The solid-state pump source is powered by a 28 ±5 V input voltage from the spacecraft power source, and a dc-to-dc converter transforms this to 40 V at 300 mA for operation of the pump source. In addition, the source provides a regulated bias voltage for the parametric amplifier. A dc power input of 7 W for this supply would be required. No problems are foreseen in meeting the environmental requirements specified as long as temperature control is provided by the spacecraft.

Reduction of signal frequency to X-band (8.4 to 10 GHz) provides both a lower noise temperature and a more efficient parametric amplifier because of the availability of more efficient pump sources in this frequency range. Design details of the parametric amplifier would remain essentially the same at X-band, with the package size and weight 10% greater.

c. Receiver Design - The balance of the receiver circuit is conventional phase-lock design. A double conversion receiver is recommended. A noise figure of about 8 dB is readily achievable at this frequency. This will cause negligible degradation of the noise temperature given by the parametric amplifier.

The frequency acquisition and tracking system will be considered next. Doppler frequencies and rates, velocities, accelerations, and 3σ uncertainties were calculated from communications geometry and entry dispersion computer programs. The doppler frequency is a function of carrier frequency and velocity. It is expressed by

$$f_d = \frac{\dot{r} f}{c} = \frac{10 \dot{r} f}{3} \qquad [VI-11]$$

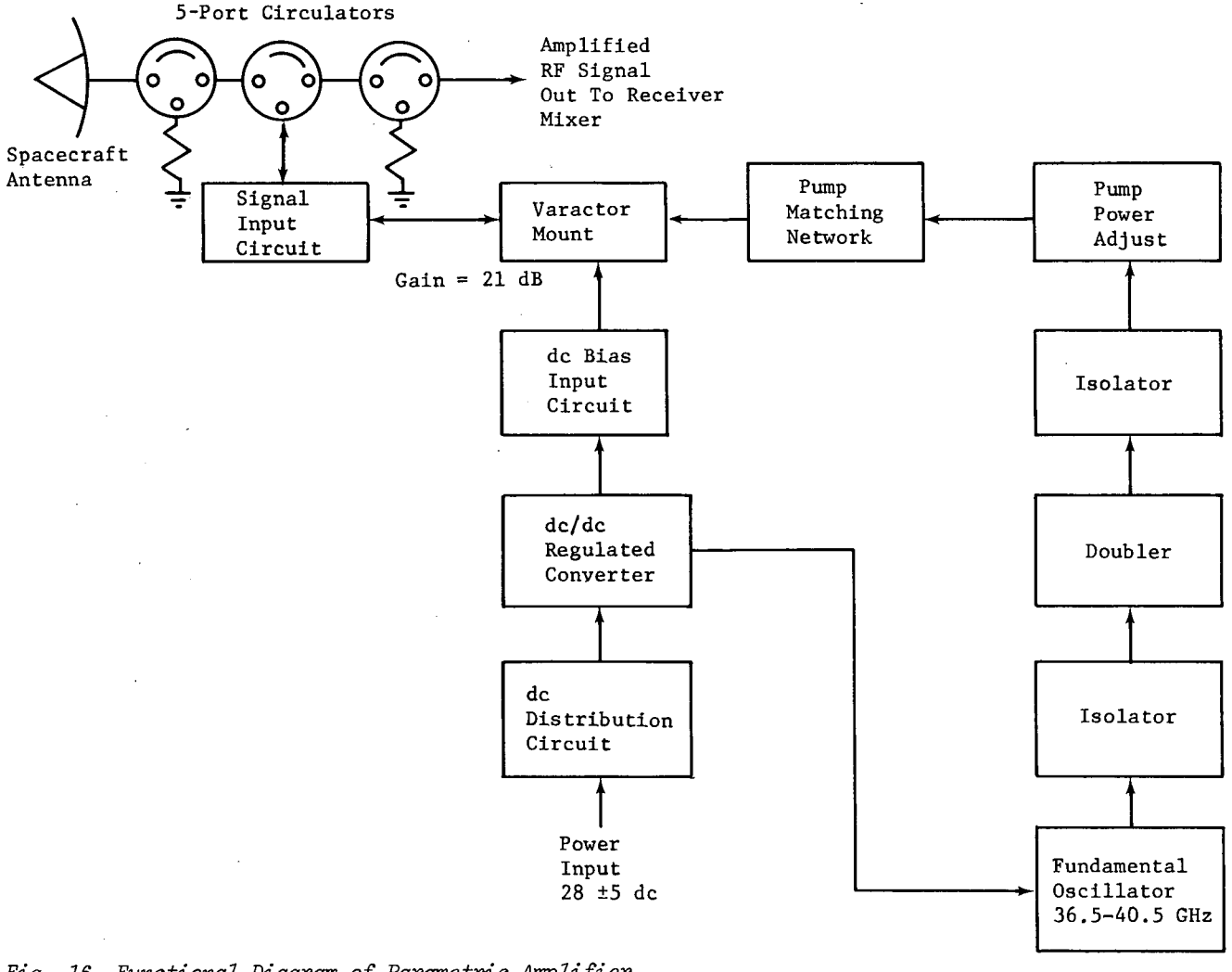

Fig. 16 Functional Diagram of Parametric Amplifier

where

f_d = doppler frequency, kHz

$\dot{r}$ = velocity, km/s

f = RF frequency, GHz

c = velocity of light, km/s

The doppler rate is expressed in a similar manner by

$$\dot{f}_d = \frac{\ddot{r}\, f}{c} = \frac{10\, \ddot{r}\, f}{3} \qquad \text{[VI-12]}$$

where

$\dot{f}_d$ = doppler rate, kHz/s

$\ddot{r}$ = acceleration, km/s^2.

Uncertainties in doppler frequency and rate are calculated from the 3σ values of velocity and acceleration. The 3σ values are used in Equations [VI-11] and [VI-12] for $\dot{r}$ and $\ddot{r}$ to determine corresponding doppler frequency and doppler rate uncertainties. An additional doppler frequency uncertainty is that due to relative drift between probe and spacecraft oscillator frequency references. This is taken at ±2 parts in 10^6 for a 3σ value and results in 20 kHz at 10 GHz. Total doppler frequency uncertainty, then, is the sum of doppler frequency due to 3σ variation in velocity, Δf_d, and doppler frequency due to relative frequency drift, Δf. So

$$\Delta f_t = \Delta f_d + \Delta f. \qquad \text{[VI-13]}$$

In a similar manner, doppler rate uncertainty, $\Delta \dot{f}_d$, is due to 3σ variation in acceleration and must be lower than the frequency search rate by at least a factor of 10. This prevents frequency variation from exceeding sweep rate.

Mission parameters associated with frequency acquisition are shown in Table VI-4 for three typical missions. Conditions at acquisition and entry are shown for comparison, but frequency search will normally be initiated during acquisition, which occurs up to 1 hr before atmosphere entry. Nominal doppler frequency for a 10-GHz carrier ranges from 735 to 241 kHz at acquisition. At acquisition, maximum total frequency uncertainty is ±86.6 kHz for the radiation-compatible mission (2A). This is the uncertainty that must be searched in the initial acquisition process. As seen from the table, the uncertainty in doppler rate is only 12 Hz/sec.

Table VI-4 Frequency Acquisition Parameters

Parameter	Symbol	Unit	Mission No.					
			1A		2A		7	
			Acquisition	Entry	Acquisition	Entry	Acquisition	Entry
Time		E-X min	38		36		57	
Doppler frequency	f_d	kHz	241	570	735	1374	485	1403
Doppler rate	$\dot{f}_d$	Hz/s	120	210	230	470	100	520
Range	r	10^6 m	52.5	73.3	492	547	588	676
Velocity	$\dot{r}$	km/s	6.	17	18.2	41.1	16	42.1
3σ velocity	$\Delta\dot{r}$	±km/s	1.2	1.2	2	0.6	6.3	0.4
Acceleration	$\ddot{r}$	m/s^2	-3.3	-5.3	-0.2	-0.3	-0.1	-0.2
3σ Acceleration	$\Delta\ddot{r}$	±m/s^2	0.4	0.9	0.04	0.09	0.03	0.04
Doppler frequency	Δf_d	±kHz	40	40	66.6	20	17	11.3
Frequency drift	Δf	±kHz	20	20	20	20	20	20
Total frequency uncertainty	Δf_t	±kHz	60	60	86.6	40	37	31.3
Δ Doppler rate	$\Delta\dot{f}_d$	Hz/s	12.3	30	1.3	3	1	1.3
Min track loop bandwidth	W_c	Hz	105	110	111	121	105	124
Search time for s.2 kHz/s rate	t_a	sec	27	27	39	18	17	14

Note: Doppler values are based on f = 10 GHz.

Frequency acquisition operates in the following manner. Nominal doppler frequency is preprogrammed into the receiver frequency reference so that its free-running frequency corresponds to estimated signal frequency. This program is loaded on command from Earth shortly before probe/spacecraft separation to provide the latest doppler frequency estimate. After the transmitter is turned on, frequency search through the uncertainty region of Δf_t is initiated. The search rate is fixed by the phase-lock-loop (PLL) noise bandwidth. A rule of thumb is

$$R = 0.1\ B_n^2 \qquad \text{[VI-14]}$$

where

R = search rate, Hz/s

B_n = PLL noise bandwidth, Hz.

The current design uses 150 Hz for B_n, which gives a search rate of 2.25 kHz/s. Doppler rate uncertainty, $\Delta \dot{f}_d$, must be subtracted from this to give a usable search rate. This uncertainty is approximately 30 Hz/s. The usable search rate is 2.22 kHz/s. At this rate, the uncertainty region can be searched in 86.7/2.22 or 39 sec. The PLL can be designed with any loop noise bandwidth desired, but there is a tradeoff between B_n, carrier power, and search time. For instance, if B_n = 100 Hz, R = 1 kHz, search time = 87 sec, and the carrier power will be lower by 2 W or less. The design goal was to minimize search time, t_a. Therefore, a loop noise bandwidth of 150 Hz was selected, which gives R = 2.22 kHz and frequency acquisition times in the range of 30 to 40 sec.

Once lock-on has been achieved, loss of lock is relatively unlikely. However, there must be a contingency plan to cope with signal dropout in case it does occur. Because the uncertainty region remains nearly constant throughout the mission, a complete search would take about the time required for initial acquisition. However, this uncertainty can be greatly reduced by using information gained during lock-on. A simple first-order or slope-matching predictor would probably reduce the uncertainty to an estimated 1/10 of the initial uncertainty. This would reduce the reacquisition time to around 4 sec. A block diagram of the receiver is shown in Fig. VI-17. The receiver operates on 28 Vdc, requires 10 W, and weighs 5.9 kg (13 lb).

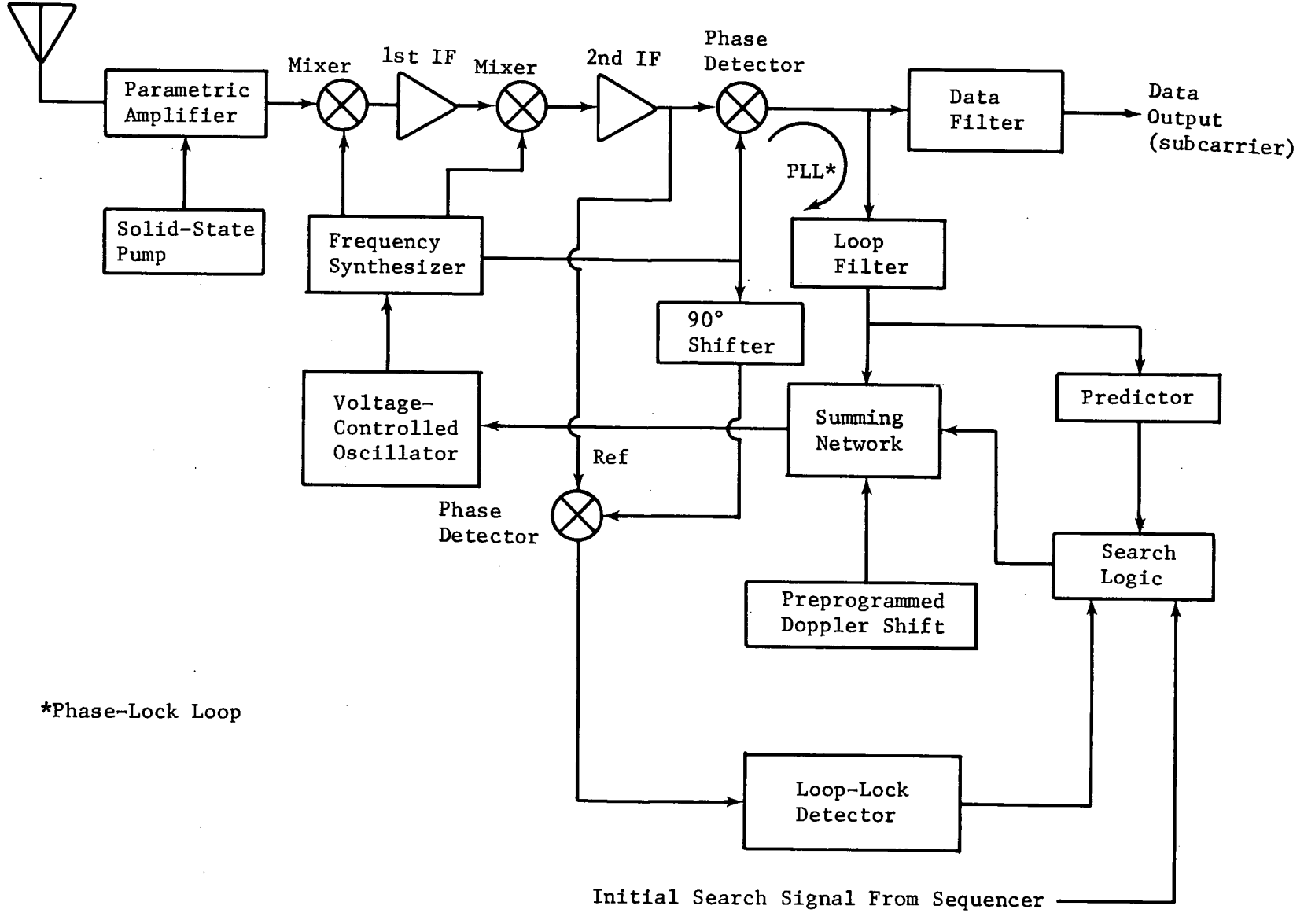

Fig. VI-17 Receiver Block Diagram

Certain missions with large periapsis radii require a high spacecraft antenna gain, resulting in a beamwidth of 2 to 3° to hold the RF power to an acceptable level. Probe dispersions at acquisition and entry are larger than the beamwidths, so a position search must also be performed to direct the spacecraft antenna at the probe. Several techniques were considered in an attempt to arrive at a reliable and economical system. The most reliable system is an autotrack receiver that uses a dish antenna with a Cassegrain feed. The antenna has four outputs, one for each quadrant of the antenna beam. They are mixed at the receiver input circuitry and sent to sum and difference receivers. Feedback loops are designed so the antenna follows or tracks the probe signal and maintains the probe in the center or very nearly in the center of the beam. A multiple-beam spherical reflector antenna also has a wide scanning capability with a narrow beam because the beam position can be moved by moving the feed position relative to the reflector. This type of system would greatly increase cost, complexity, and weight of the spacecraft antenna and receiver system.

Another technique is a simple spacecraft dish antenna with a single receiver and a preprogrammed cone-angle search program with logic circuits attached to the receiver AGC voltage. Two such missions that require a position search system are shown in Fig. VI-18 for the JS 77 Mission (7) and radiation-compatible mission (2A). At acquisition, the probe will be somewhere in the dispersion ellipse. The spacecraft antenna is moved to the first sector position, and the logic circuit records the AGC voltage. The same steps are repeated for other positions, and the antenna is returned to the position with the highest AGC voltage. Elevation (cross-cone) angle changes are very small, and position searches in that plane are unnecessary.

As discussed in Chapter IV, Subsection F2, a probe in the left half of the ellipse at acquisition will end its mission in the left half and not move to some other random position. This fact is very helpful because the final position of the probe will be known at entry, based on probe location at acquisition. Antenna position logic will have different movement rates for the cone angle for different cone-angle positions. For instance, in Mission 7, a probe acquired in Position 1 will cause the antenna to move faster (cone angle deg/min) than one acquired in Position 3. At each antenna position, the aforementioned frequency search will also have to be performed. As seen in Table VI-4, frequency search time for Mission 7 is only 17 sec. Therefore, a four-position sector search in frequency and position could be made in

2 min or less. Also noted from Fig. VI-18, if the probe were acquired in Sector 4, it would probably not require any additional movement to follow the probe to entry because the entry dispersion ellipse is within the right end of the acquisition dispersion ellipse. This semiactive programmed tracking technique greatly simplifies spacecraft antenna and receiver subsystems and provides a reliable positioning system that shows cost and weight savings over a monopulse radar technique.

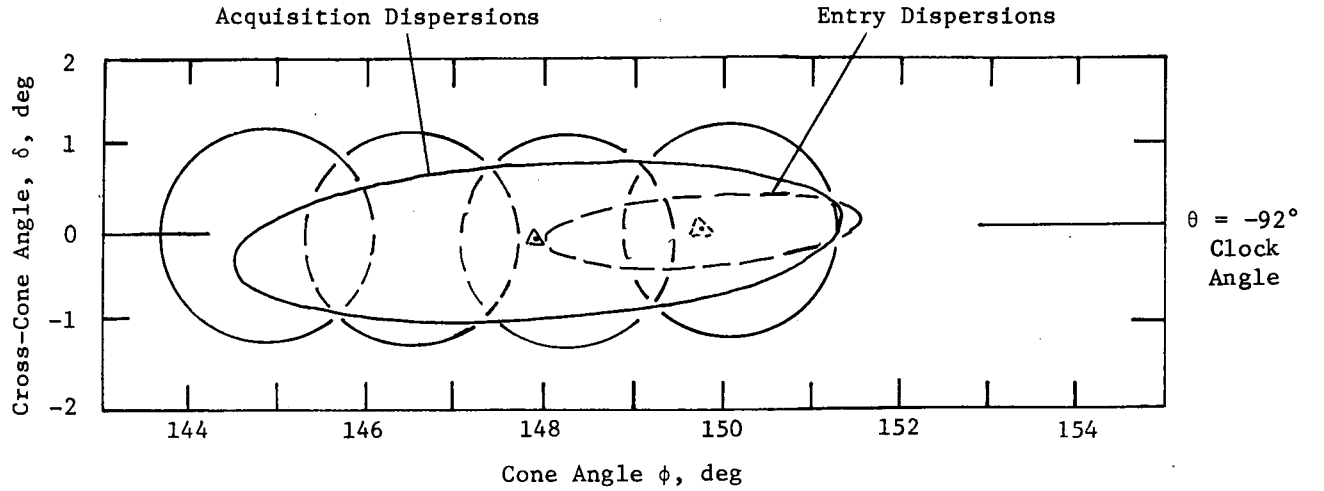

a Mission 7 4-Position Search, 2.5° B/W

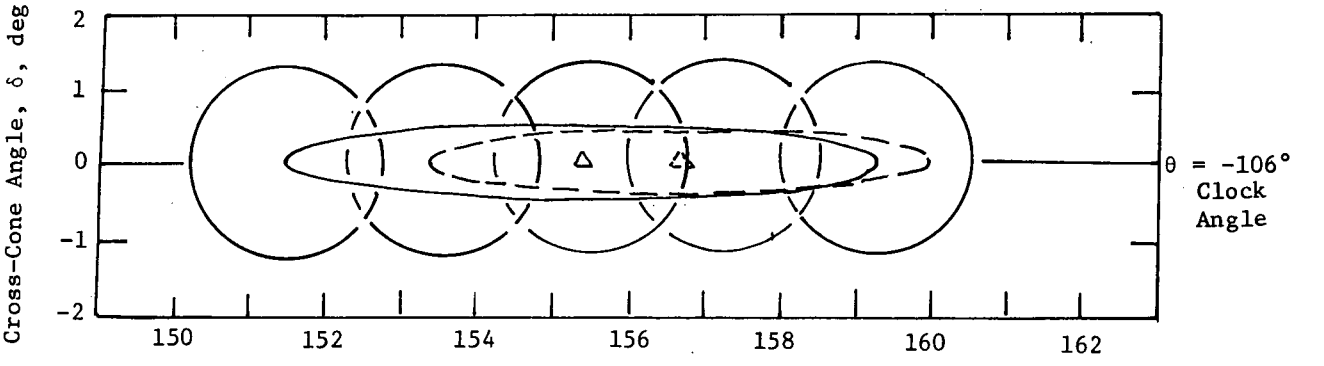

b Mission 2A 5-Position Search, 2.5° B/W

Note: Δ = nominal position

Fig. VI-18 Spacecraft/Antenna Acquisition Requirements

e. Coherent vs Noncoherent Communications - Three general types of communication systems can be considered for the probe-to-spacecraft link in the turbopause probe mission. These are a coherent phase-locked system, a noncoherent system without frequency tracking, and a noncoherent system with servocontrolled frequency tracking. Block diagrams of the three receivers are shown in Fig. VI-19 and VI-20.

The coherent system requires the least transmitter power of the three. It also requires an initial frequency search and lockon of the phase-lock loop (PLL) as described in Subsection 4d. The search and lockon procedure must be reinitiated if signal lock is lost during the mission. If loss of lock occurred near the end of the mission, reacquisition might not occur soon enough to receive the data from the critical last few seconds of the mission. It is also conceivable that initial lockon might never occur because of some malfunction, causing the whole mission to be lost.

A true loss of lock must be distinguished from a cycle-slipping event. The latter has a small probability of occurring during the mission. This would only cause a brief transient ($\sim$1/50 sec) in the data stream, resulting in a short burst of bit errors. Loss of lock would require a disturbance for perhaps a few seconds, sufficient to cause the frequency of the incoming signal and loop to drift apart by an amount greater than the loop pull-in range. If this occurred, reacquisition time would be 15 to 30 sec.

It is difficult to estimate a probability for the occurrence of these malfunctions. The probability of random equipment failure can presumably be made acceptably low and largely independent of the type of communication system used. Environmental effects are largely unknown, but lightning-like discharges, for example, would probably not occur at altitudes above the cloud tops.

We can only assume that the probability of a loss of lock during the critical last few seconds of the mission is small. It would, of course, be desirable to remove the uncertainty of a lockon system if the resulting weight penalty is not too high. A procedure for determining this penalty is outlined below. A sample calculation is also given for 20 GHz.

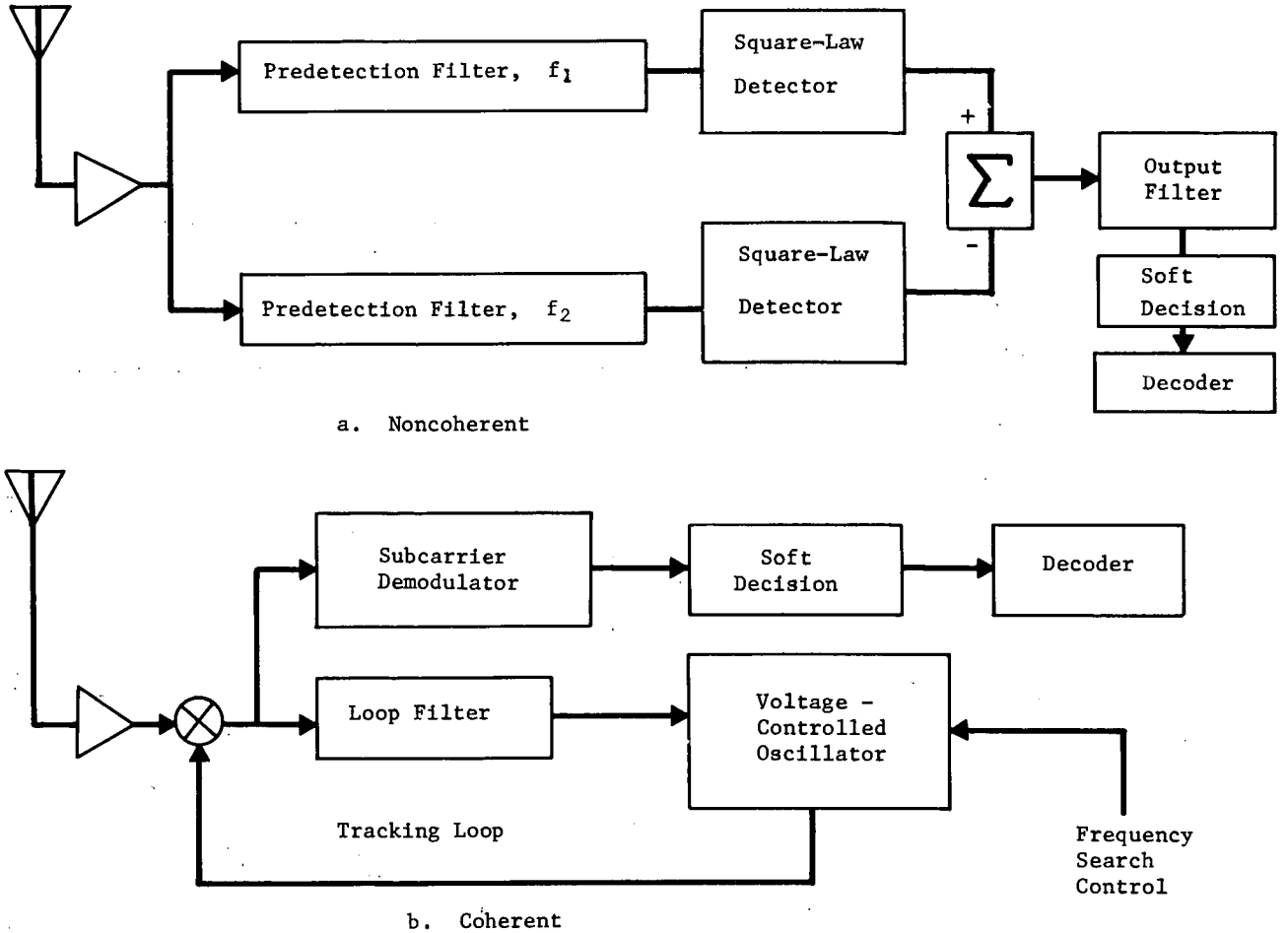

Fig. VI-19 Noncoherent And Coherent Receivers

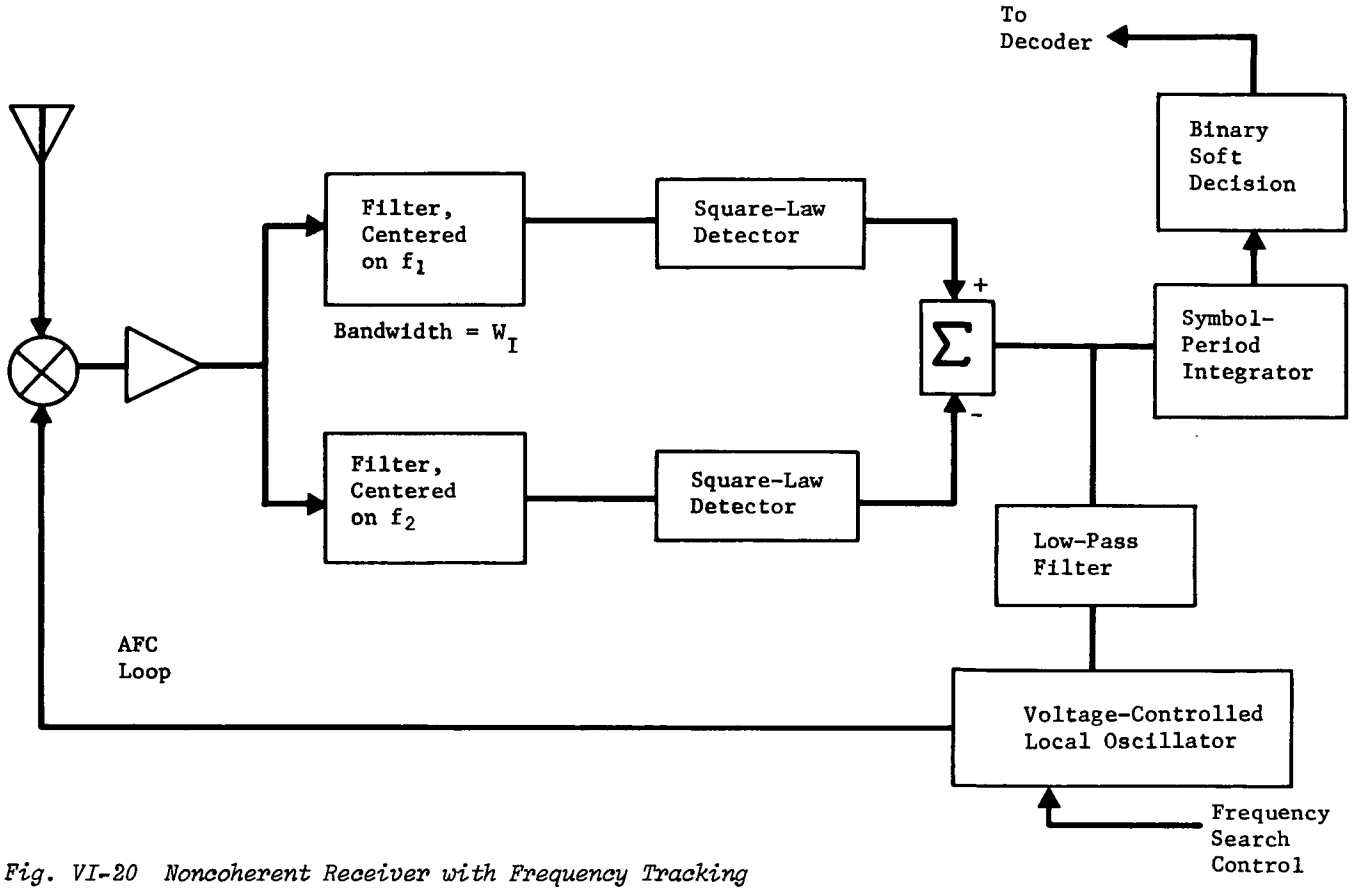

Fig. VI-20 Noncoherent Receiver with Frequency Tracking

Given a specific link with a specified transmission frequency, f, the first step is to make a conventional link calculation for a coherent link. The details of this calculation will not be covered here. This calculation will determine P_c, required transmitter power for a coherent link; L_R, noisy reference loss factor; and L_M, modulation loss factor. A value of E_b/N_o will be specified based on the assumed coding-decoding system. We will assume E_b/N_o = 2.5 or 4 dB. Next, it will be necessary to compute S_{cc}, effective channel E_b/N_o for the coherent link, augmented to cover modulation and noisy reference losses.

$$S_{cc} = \frac{E_b/N_o}{L_R L_M} = \frac{2.5}{L_R L_M} . \qquad [VI-15]$$

The next step is to compute an equivalent channel E_b/N_o for nontracking noncoherent link, S_{cn}, for comparison with S_{cc}.

A two-frequency FSK system using the same code and requiring the same effective E_b/N_o as the coherent system has been assumed. Performance of noncoherent systems can be improved by a factor approaching 2:1 by using a large (say 32) number of frequencies, assuming the same level of encoder-decoder complexity. However, transmitter and receiver complexity increases sharply if a large number of frequencies are used. It was concluded that the two-tone system sketched in Fig. VI-19 would be more appropriate for a probe-to-spacecraft relay link.

The most important factor in this computation is the frequency uncertainty. This uncertainty has two parts, oscillator instability and doppler uncertainty. The former is assumed to be $2 \times 10^{-6} f$ ($\pm 3\sigma$), which assumes a temperature range of 247 to 330°K (-15 to +135°F). Total range of doppler frequency during the 1-hour mission is very large (See Table VI-4.), and noncoherent system performance would be impossibly degraded by including this whole range in frequency uncertainty. This is avoided by using preprogrammed open-loop tracking of estimated or nominal doppler frequency, computed from range rates given by the trajectory. Doppler uncertainty is then given by the dispersion in range rate, computed from the trajectory dispersion program, as a function of time. Worst-case dispersion (which generally occurs at the end

of the mission) must be used. Total uncertainty is then used to fix the predetection bandwidth, W_I, from Equation [VI-13], or

$$W_I = ff_t = (2 \times 10^{-6} + 3.33\ \dot{r})\ f. \qquad \text{[VI-16]}$$

Signaling bandwidth, W_o, is 1/2 the bit rate, R, multiplied by the bandwidth expansion, V, given by the code. This is 3:1 for the code assumed, or

$$W_o = \frac{V}{2}R = \frac{3}{2}R. \qquad \text{[VI-17]}$$

The ratio $G = W_I/W_o$ is then computed. The results given below assume G >> 1, which will be the case for all links of interest to this program. Predetection SNR(X) is equal to

$$X = \frac{2\ S_{cn}}{GV} = \frac{2\ S_{cn}}{3G}. \qquad \text{[VI-18]}$$

Postdetection SNR for a two-channel comparison and a square-law detector is

$$SNR_{pd} = \frac{X^2}{2 + 2X}. \qquad \text{[VI-19]}$$

Output SNR is equal to

$$SNR_o = 0.5\ G\ \left(SNR_{PD}\right)\ . \qquad \text{[VI-20]}$$

This must equal 2/V times the desired E_b/N_o or, for our case of E_b/N_o = 2.5 and V = 3, it must equal 1.667.

Combining Equations [VI-18] through [VI-20] and equating SNR_o to 1.667 gives

$$S_{cn} = 5 + \sqrt{25 + 15G} = 5 + \sqrt{25 + \frac{10W_I}{R}}\ . \qquad \text{[VI-21]}$$

Equation [VI-21] can be used to find the required transmitter power for a noncoherent link, P_n, from

$$\frac{P_n}{P_c} = \frac{S_{cn}}{S_{cc}} \qquad \text{[VI-22]}$$

Next, consider the noncoherent system using closed-loop frequency tracking, as seen in Fig. VI-20. A frequency-tracking servo or AFC loop is somewhat simpler than the PLL required for a coherent system. It can be searched at a higher rate, reducing required search time for initial or reacquisitions, and it does not have the cycle-slipping problem. However, it is a closed-loop tracking system, so the uncertainty of possible loss of track during the crucial part of the mission is not eliminated. Because this uncertainty is largely subjective in either case, there is not much incentive to use the noncoherent system. However, it was given a quick look.

Generally, a split-phase signaling format must be used for an AFC receiver to avoid imbalances caused by possible long strings of data that are mostly zeros or mostly ones. This doubles the signaling bandwidth to 6R for a V = 3 code. Because the AFC loop will not be perfect, it is prudent to double this and use $W_I = 12$ R. Putting this value into Equation [VI-21] gives

$$S_{ct} = 17.9. \qquad \text{[VI-23]}$$

Transmitted power for this system is given by

$$\frac{P_t}{P_c} = \frac{S_{ct}}{S_{cc}} = \frac{17.9}{S_{cc}}. \qquad \text{[VI-24]}$$

The relay link considered early in the study was used as a sample calculation. The parameters of the coherent link are

f = 20 GHz (K-band)

R = 750 bps

P_c = 20 W

L_M = -1.5 dB = 0.707

L_R = -3.0 dB = 0.5

This gives S_{cc} = 7.07 from Equation [VI-15]. The worst-case 3σ velocity uncertainty, $\dot{r}$, was ±0.518 m/sec. This gives W_I = 2.15 × 10^5 Hz from Equation [VI-16], S_{cn} = 58.8 from Equation [VI-21], and P_n = 166 W from Equation [VI-22]. Equation [VI-24] gives 50.5 W for the tracking noncoherent system.

These results suggest that the penalty for using a nontracking noncoherent system is prohibitively high, but consider the conditions at 10 GHz. This would drop path loss by a factor of 4, reducing P_c to 5 W if the same probe antenna gain could be used. It would halve W_I to 1.08 × 10^5 Hz, giving P_n = 30.6 W.

A very crude estimate of the consequence of these power levels on probe weight can be made by assuming RF power generation at 25% efficiency, battery capacity at 55 W-h/kg, mission duration 1.5 hr, and then doubling resulting weight to account for additional probe structure, cabling, and heat-sink weight. This results in a weight penalty of 31.8 kg for the 20-GHz case and 5.5 kg for the 10-GHz case. The latter weight might be an acceptable penalty to pay for the greater reliability of the nontracking noncoherent system.

RF link calculations for design missions at X-band indicate that antenna gains also had to be changed because of increased trajectory dispersions and probe antenna size limitations. Therefore, X-band power levels are still in the 20-W region. From Equation [VI-22], noncoherent power, P_n, is now 122.4 W and the weight penalty is also severe. Therefore, it is concluded that a coherent system provides optimum power and weight levels.

f. False Lock, Coherent Relay Link Receiver - There are two categories of false signals onto which the coherent receiver phase lock loop (PLL) could lock. There are extraneous received signals and spurious signals generated in the spacecraft. For locations remote from Earth, the first of these reduces to signals radiated from the DSN and spurious signals, including sideband signals, radiated by the probe. DSN signals can be readily avoided by proper frequency selection.

The probability of locking onto a sideband can be reduced to a negligible level by proper design of the signaling format. This is accomplished by modulating a subcarrier with the data stream, using a suppressed-carrier modulation format such as biphase ±90°

PSK using either a sinusoidal or a squarewave subcarrier. This does not prevent the appearance of specular components in the spectrum, taken over a short averaging time, because of the occurrence of a string of data that are predominantly zeros. However, long strings of zeros or ones can be avoided by the use of error-correcting data encoding selected in part for this purpose. If these techniques are used, lockon to a sideband would probably not occur at all. At worst, it could only occur momentarily. After this was lost, the receiver would resume searching until it locked onto the desired carrier.

False lock on spurious signals generated in the spacecraft is a more serious problem. The relay link receiver will be a double conversion receiver, with the first IF somewhere in the UHF band and the second IF at a few MHz. There will be other RF equipment on board, such as the transponder used to communicate with the DSN. Therefore, there will be several signal sources on board, including local oscillators in both the relay receiver and transponder receiver and, most important, the high-powered transponder transmitter. Generation of sum-difference signals in various circuit nonlinearities, especially mixers, is possible. These signals will have frequencies given by

$$Mf_i \pm Nf_j \qquad \text{[VI-25]}$$

where M and N are integers, and f_i and f_j are the frequencies of the various signal sources on board. If any of these frequencies falls within the passband of either of the relay link receiver IF bands any time during acquisition, spurious lockon is a possibility. Because the search is mechanized by varying one of these frequencies (the first local oscillator, LO, in the relay link receiver), any components of Equation [VI-25] involving this frequency source will search M times the search range. This search range could be as much as 500 kHz, depending on trajectory dispersions. Therefore, at some point in the search, the potential is quite high for occurrence of an acceptable spurious signal of the form given by Equation [VI-25].

Two steps must be taken to minimize this problem. First, standard techniques for controlling the level of radio frequency interference (RFI) in a vehicle must be used. This includes careful design, layout, isolation, shielding of RF components, and filtering of power supply leads. This will help reduce the level of spurious signals below the loop lockon threshold.

The second step is proper selection of LO and IF frequencies in the relay link receiver. This can be accomplished by a computer search of signal components of the form given by Equation [VI-25], varying signal frequencies that are within the designer's control (LO frequencies) and determining if any components fall within the IF passbands at any point in a simulated frequency search. The strength of these components decreases with increasing M and N. It is generally not necessary to carry the search beyond M and N = 7. The RFI environment in the spacecraft cannot be completely predicted. It is necessary to build a model, using standard RFI suppression techniques, and then measure the environment with all RF systems operating. This type of problem occurs to some degree in the design of any space vehicle, and its solution is within the current state of the art.

5. Plasma Attenuation of RF Signals

During entry of the hemisphere-cylinder probe into the Jovian atmosphere, a plasma will surround and trail the probe. The conical horn antenna is located on the rear bulkhead of the probe (as shown in Fig. VI-21) and propagation takes place to the rear in the direction of the negative roll axis through the ionized wake. The probe analyzed in the wake study was 0.763 m (30 in.) in diameter. The horn antenna is circularly polarized and operates at 10 GHz with a 3-dB beamwidth of 10° in both planes. Effects of the ionized wake on communications were investigated to determine when RF blackout occurs at various frequencies.

Plasma properties of the ionized wake must be known before effects of the plasma can be considered. Determination of these properties was a formidable task in itself, as described in Chapter X, because it required a detailed analysis of aerodynamic flow fields, which depend on Jovian environment and chemical reaction rates of atmospheric constituents. From the nonequilibrium flowfield analysis, electron density and collision frequency contours were determined in the near and far wake where plasma/RF interaction occurs for the configuration shown in the figure.

RF signals transmitted from the probe are affected by interaction of electromagnetic waves with plasma particles, premarily electrons. The interference is characterized by reflection and absorption, attenuation losses due to collisions, and phase shift and refraction. Reflections are most pronounced at plasma-atmosphere interfaces and in regions of rapidly varying electron density.

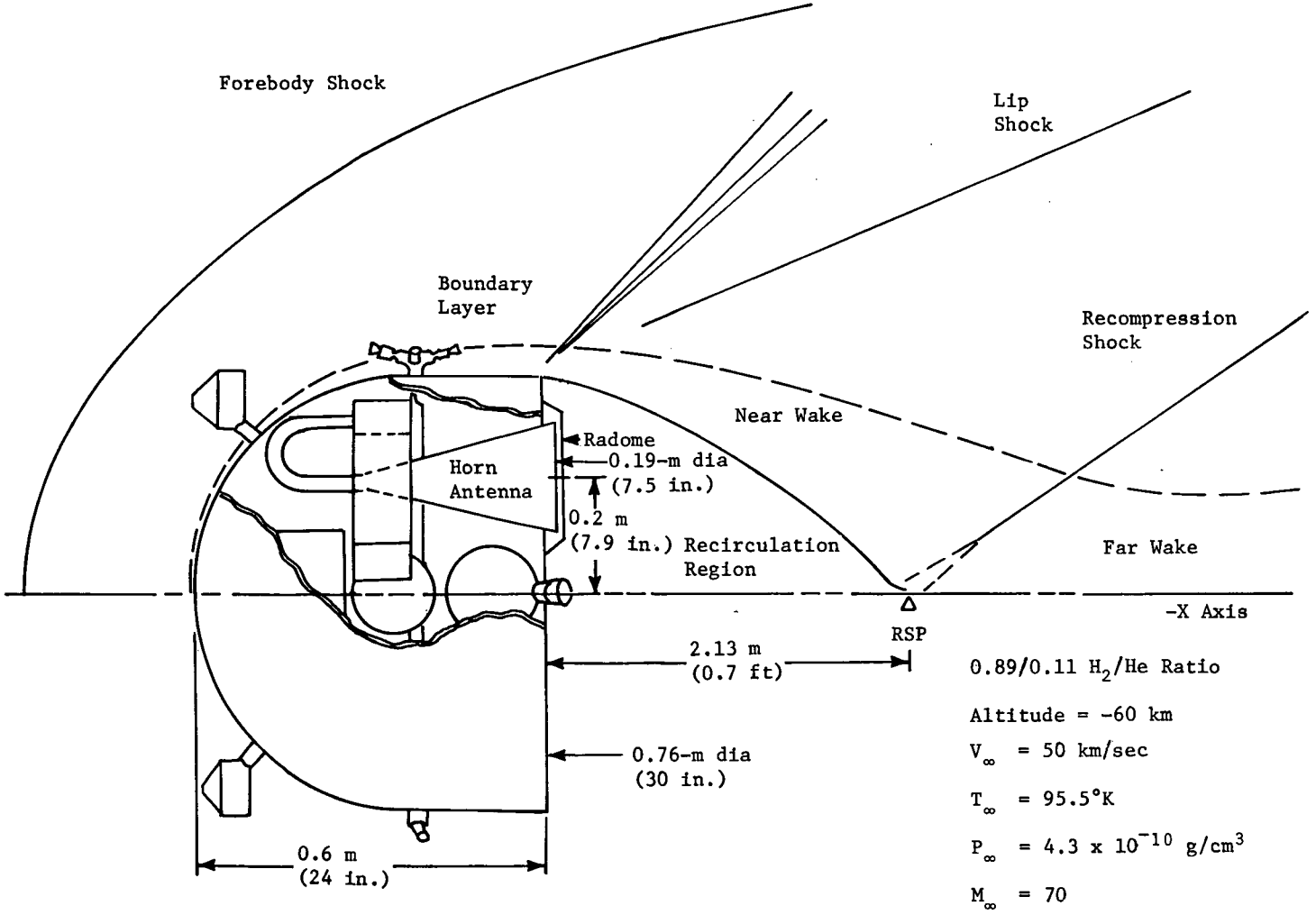

Fig. VI-21 Layout of Probe Antenna For Wake Study

Transmission of RF signals through plasma depends on the angle of transmission through the plasma, frequency, transmitted power, antenna radiation characteristics, polarization of the wave, and location of the antenna on the probe. Plasma can also cause antenna mismatch (i.e., alter input impedance) and electrical breakdown of the antenna, with resultant distortion of the radiation pattern. As the probe descends further into the atmosphere, electron density increases to a point where plasma properties are at a level to severely attenuate, reflect, or refract the transmitting signal. The RF link has been designed with enough RF power to operate with a plasma loss of 3 dB. Losses in excess of 3 dB will result in data dropout, first on a random basis, and finally, complete loss of data occurs along with carrier dropout through the coherent RF link.

a. Electromagnetic Properties of a Plasma - Electromagnetic properties of shock-induced plasma are defined by the complex dielectric coefficient, which in turn determines the attenuation, phase, and reflection coefficients of the propagation constant. Plasma is a conducting medium and its finite conductivity has a complex value. For a linear plasma with no net change present ($\nabla \cdot E = 0$), with a permittivity, ε_p, and conductivity, σ; Maxwell's first equation relating the electric and magnetic field intensity is

$$\nabla \times H = \varepsilon_p E + \sigma E. \qquad \text{[VI-26]}$$

For sinusoidal variation of E, we have

$$\nabla \times H = \left(\varepsilon_o - \frac{j\sigma}{\omega}\right) E. \qquad \text{[VI-27]}$$

From Equation [VI-27], it is apparent that a partially conducting dielectric can be considered as a dielectric that has a complex dielectric constant, ε_p, where

$$\varepsilon_p = \left(1 - \frac{j\sigma}{\omega\varepsilon_o}\right) \varepsilon_o \qquad \text{[VI-28]}$$

and

σ = conductivity, mho/m

ω = angular frequency, rad/s

ε_o = free-space permittivity, $10^{-9}/36\pi$, F/m.

Consider next the phenomenon of space-change oscillations. The physical nature of plasma oscillations can be seen in terms of a simplified natural physical resonance. The model considers a uniform gas of density, N_e. If an external perturbation occurs, the electrons are set into harmonic motion. Frequency of motion is critical and defined as the plasma frequency, f_p. Plasma frequency varies directly with the square root of the electron density and is expressed as:

$$\omega_p = 2\pi f_p = \sqrt{\frac{q^2 N_e}{\varepsilon_o m}} \qquad \text{(rad/s)} \qquad \text{[VI-29]}$$

and

$$f_p = 8979\sqrt{n_e} \qquad \text{(Hz)} \qquad \text{[VI-30]}$$

where

q = electron charge, 1.6×10^{-19} C

N_e = electron density, m^{-3}

n_e = electron density, cm^{-3}

m = electron mass, kg

ε_o = free-space permittivity, $10^{-9}/36\pi$ F/m.

At this frequency, reflection starts as the operating frequency is progressively lowered. In the limit of low electron collision frequency, or low gas density, the equation determines the minimum usable frequency. The relationship of electron density to plasma frequency is shown in Fig. VI-22. The relative influence of operating frequency, collision frequency, and plasma frequency on RF attenuation is shown in Fig. VI-23. Note that plasma frequency is the point where plasma absorption begins if the collision frequency is low (collisionless plasma). The phase constant undergoes violent variations near the plasma frequency. To select the proper operating frequency, electron density and electron collision frequency distributions over the entire trajectory should be known in the hypersonic wake. This was impractical to determine at several altitudes, and only one critical altitude was selected--60 km below the Jovian turbopause. This altitude was chosen from a science mission standpoint. (Chapter III describes the science requirements in detail.)

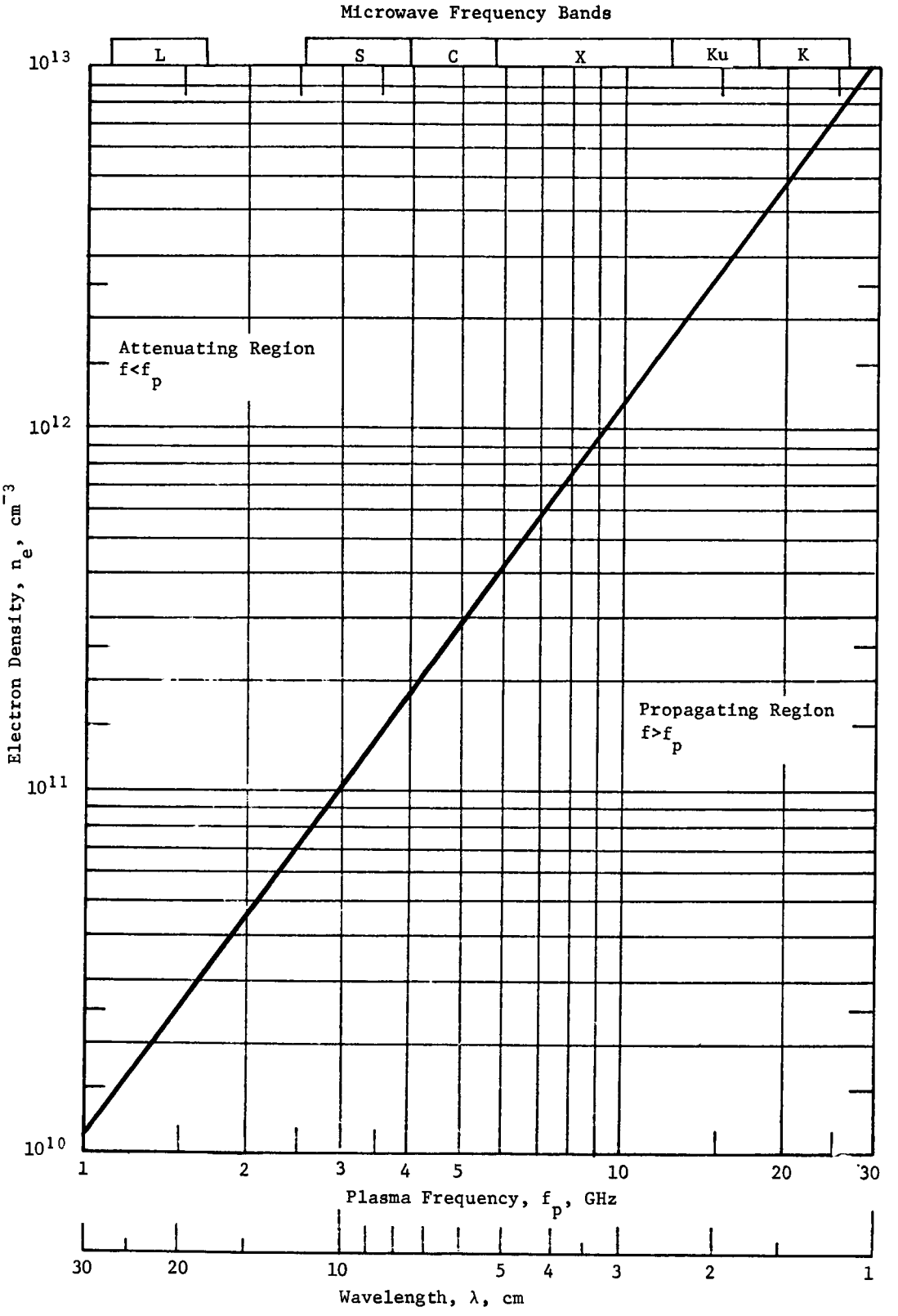

Fig. VI-22 Plasma Frequency Versus Electron Density

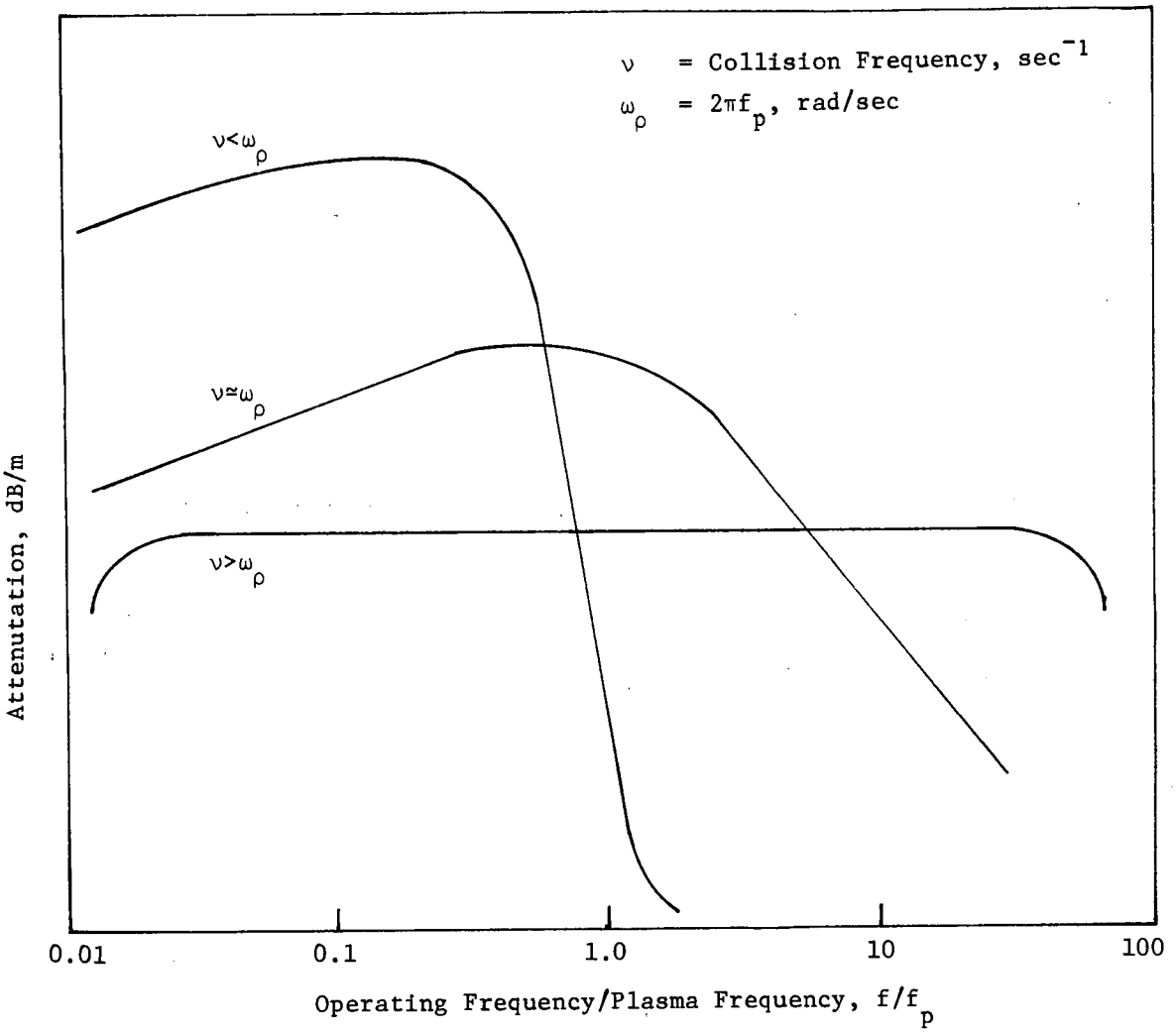

Fig. VI-23 Influence of Operating, Collision, and Plasma Frequencies on Attenuation

Particle collision rate, ν_c, is the basic parameter that determines electrical conductivity of plasma. Collisions between all possible species must be considered, although some may prove insignificant. For instance, with weakly ionized gases, only electron collisions with neutrals need be considered. Collisions can be regarded as discrete events, hence

$$\nu_c = \frac{\text{mean electron velocity}}{\text{mean free path of electron}} . \qquad [VI-31]$$

The electron velocity is a nonlinear function of electron temperature and mass. The electron mean free path is given by

$$\lambda = \left[\sum_{j=1}^{N} n_j Q_j \sqrt{1 + \frac{m_e}{m_j}} \right]^{-1} \qquad \text{[VI-32]}$$

where

λ = electron mean free path.

The electron velocity is given by

$$v_e = \sqrt{2kT/m_e} \qquad \text{[VI-33]}$$

The collision frequency of electrons for momentum transfer with other species of plasma is given by

$$\nu_c = \frac{v_e}{\lambda_e} = \sqrt{\frac{2kT}{m_e}} \left[\sum_{j=1}^{N} n_j Q_j \sqrt{1 + \frac{m_e}{m_j}} \right] \qquad \text{[VI-34]}$$

where

v_e = electron velocity, m/sec

n_j = species number density, m^{-3}, with which electrons collide

Q_j = electron collision cross-section for momentum transfer with the j-th species, m^2

T = electron temperature, °K

m_e = electron rest mass, kg

m_j = species mass, kg

N = number of species

k = Boltzmann's constant, 1.38×10^{-23} J/°K.

The method of calculating collision frequency is further described in Chapter X.

In conclusion, it would be well to review the conditions that describe the hypersonic plasma considered. At the altitude chosen, the probe has a strong shock and is traveling at a high Mach number ($M \simeq 70$). There is a highly ionized plasma, but the collision rate is at least three orders of magnitude lower than local plasma frequencies. No static magnetic field is present, and the plasma is also considered to be isotropic within the wake model. The total plasma is neutral, and therefore contains no net charge over macroscopic volumes. Electron density and collision frequency profiles in the wake are axisymmetric and are represented by a cylindrically stratified plasma. The probe antenna was considered to be on the probe roll axis for purposes of slab calculations. In the near-wake recirculation region, gas pressure is very low, and electron density and collision rate are quite low. The far wake begins 2.8 body diameters aft of the probe baseplate where a strong recompression shock produces a sharp increase in electron density and collision rate that has a maximum value on the roll axis and decreases in both radial and axial directions. (See Fig. VI-24.)

b. Microwave Propagation Analysis - A computer program determined transmission and reflection coefficients of inhomogeneous planar plasma slabs with arbitrary electron density and collision frequency profiles normal to the slabs. Propagation is analyzed by representing the wake plasma as several adjacent homogeneous slabs that approximate the time variation in plasma characteristics. Simple ray theory (small wavelength) is used and propagation is by plane electromagnetic waves normally incident upon a plasma whose gradient (dielectric constant) is parallel to the direction of propagation. The mathematical model represents actual plasma by a number of parallel contiguous slabs whose electrical properties are homogeneous and isotropic in each slab.

Profiles of electron density (plasma frequency) and collision frequency through the near and far wake are used to determine dielectric characteristics of the plasma. A typical slab approximation is shown in Fig. VI-25. The electrical properties of the wakes shown in the figure are for the roll axis of the probe and represent the worst-case values for the axial-viewing probe antenna.

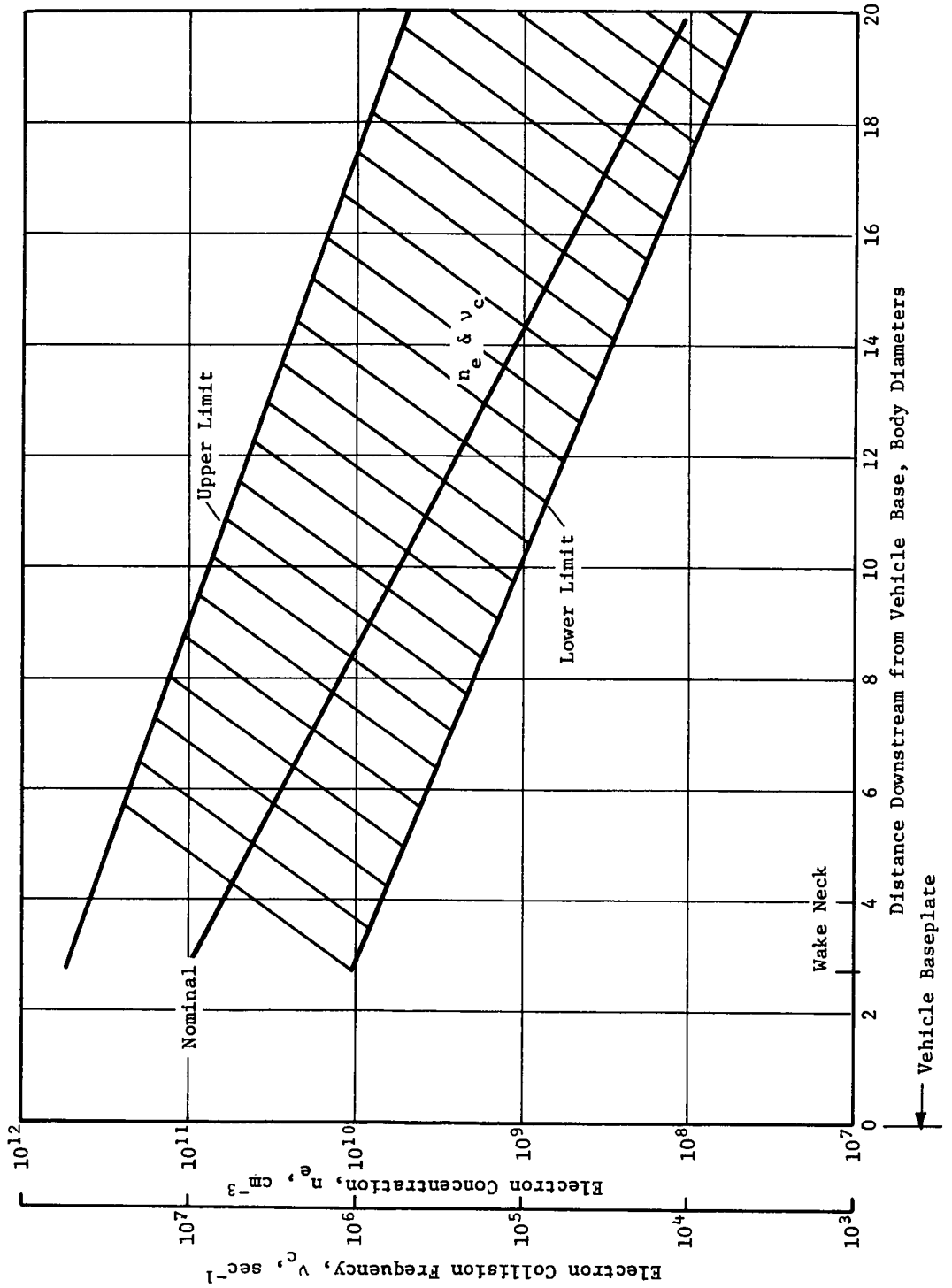

Fig. VI-24 Centerline Distributions of Wake Electron Density and Collision Frequency

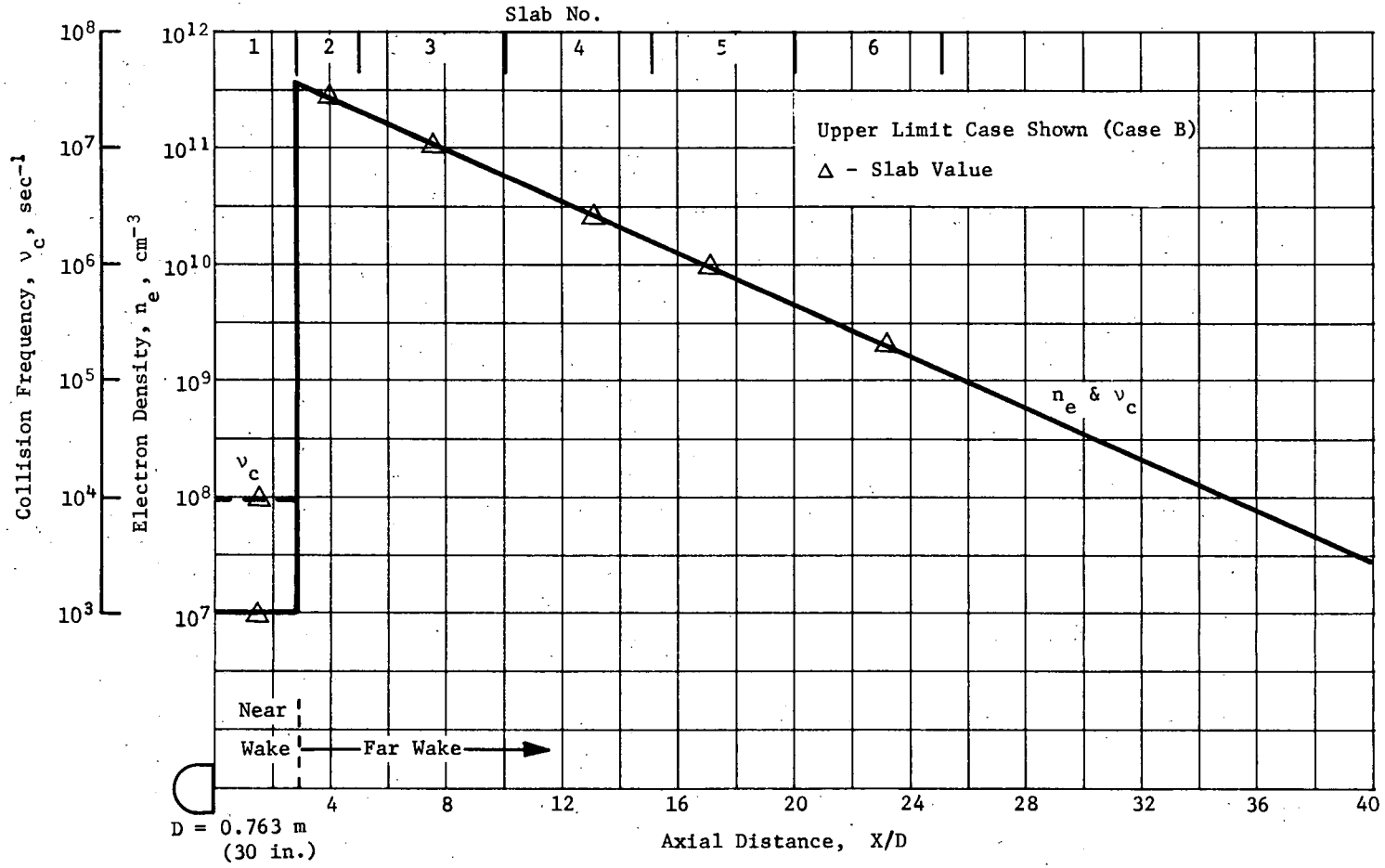

Fig. VI-25 Typical Slab Model of Probe Hypersonic Wake

Assume an electromagnetic wave normally incident upon a layered dielectric. Part of the energy is transmitted into the first slab and a portion may be reflected. The transmitted energy is partially absorbed and the remainder is incident upon the second interface. A portion of this energy is now transmitted into the second slab and part is reflected back into the first slab, etc. Thus, each elemental wave in the slabs gives rise to two new waves, one that is transmitted into the next slab and one that is reflected back. The wave in each slab then consists of a forward-traveling and backward-traveling wave. A computer program is used to make the necessary calculations and determine attenuation through the slabs at a particular operating frequency for a given electron density and collision frequency.

c. Hypersonic-Wake Plasma Blackout Calculation - Values of electron density and collision frequency based on the nonequilibrium wake analysis were used in the slab attenuation computer program to determine the extent of plasma attenuation. A description of the probe model, wake conditions, and simplifications concerning the slab analysis have been discussed previously. Electrical parameters of the wake model were determined for only one altitude (60 km below the turbopause) because an extensive set of computer programs is required to develop the wake properties. Most of the aerophysics study was concentrated in developing the computer programs (See Chapter X.) required to investigate and calculate plasma properties of the wake.

Nominal calculated values of electron density and collision frequency were used in the slab attenuation for the near and far wake at an altitude of 60 km below the turbopause. The values are shown in Table VI-5. Using the nominal values, resulting RF attenuation at 20 GHz was 0.002 dB and 0.01 dB at 10 GHz. The nonequilibrium wake analysis was very complex, with several assumptions required to complete the calculations. One of the major areas of uncertainty is in the constituent reaction rate assumptions, as discussed in Chapter X. Because of these uncertainties, there is a half-order magnitude of uncertainty in the plasma parameters calculated from the study. An upper-limit case was next considered to account for this uncertainty with the plasma properties listed in Table VI-5 for Case B. The results are shown in Fig. VI-26 and show 0.12 dB loss at 20 GHz through the wake. The nominal value (Case A) is not shown in the figure because it was less than 0.1 dB for the lowest frequency shown. Case B indicates a plasma loss of 0.6 dB at 10 GHz. Case B also shows that the probe wake plasma will attenuate RF signals less than 3 dB in the range of interest (10 to 20 GHz) at 60 km below the turbopause, using the upper-limit plasma parameters.

Table VI-5 Probe Wake Plasma Parameters

Parameter	Unit	Case				
		A	B	C	D	E
Wake Condition		Nominal	Upper Limit	← Iterations →		
Near wake, n_e, (Slab 1)	cm^{-3}	10^6	10^7	5×10^7	6×10^7	8×10^7
Near wake, ν_c, (Slab 1)	sec^{-1}	2.5×10^3	10^4	5×10^4	6×10^4	8×10^4
Near-wake thickness (Slab 1)	m	2.14	2.14	2.14	2.14	2.14
First far wake max, n_e, (Slab 2 left edge)	cm^{-3}	10^{11}	5.5×10^{11}	10^{12}	2×10^{12}	3×10^{12}
First far wake max, ν_c, (Slab 2 left edge)	sec^{-1}	10^7	5.5×10^7	10^8	2×10^8	3×10^8
First far wake avg, n_e, (Slab 2 center)	cm^{-3}	6×10^{10}	4×10^{11}	7×10^{11}	1.5×10^{12}	2×10^{12}
First far wake avg, ν_c, (Slab 2 center)	sec^{-1}	6×10^6	4×10^7	7×10^4	1.5×10^8	2×10^8
First far wake avg, f_p, (Slab 2 center)	GHz	2.3	5.8	7.7	11.0	13.0
First far wake, d, slab thickness (Slab 2)	m	1.68	1.68	1.68	1.68	1.68

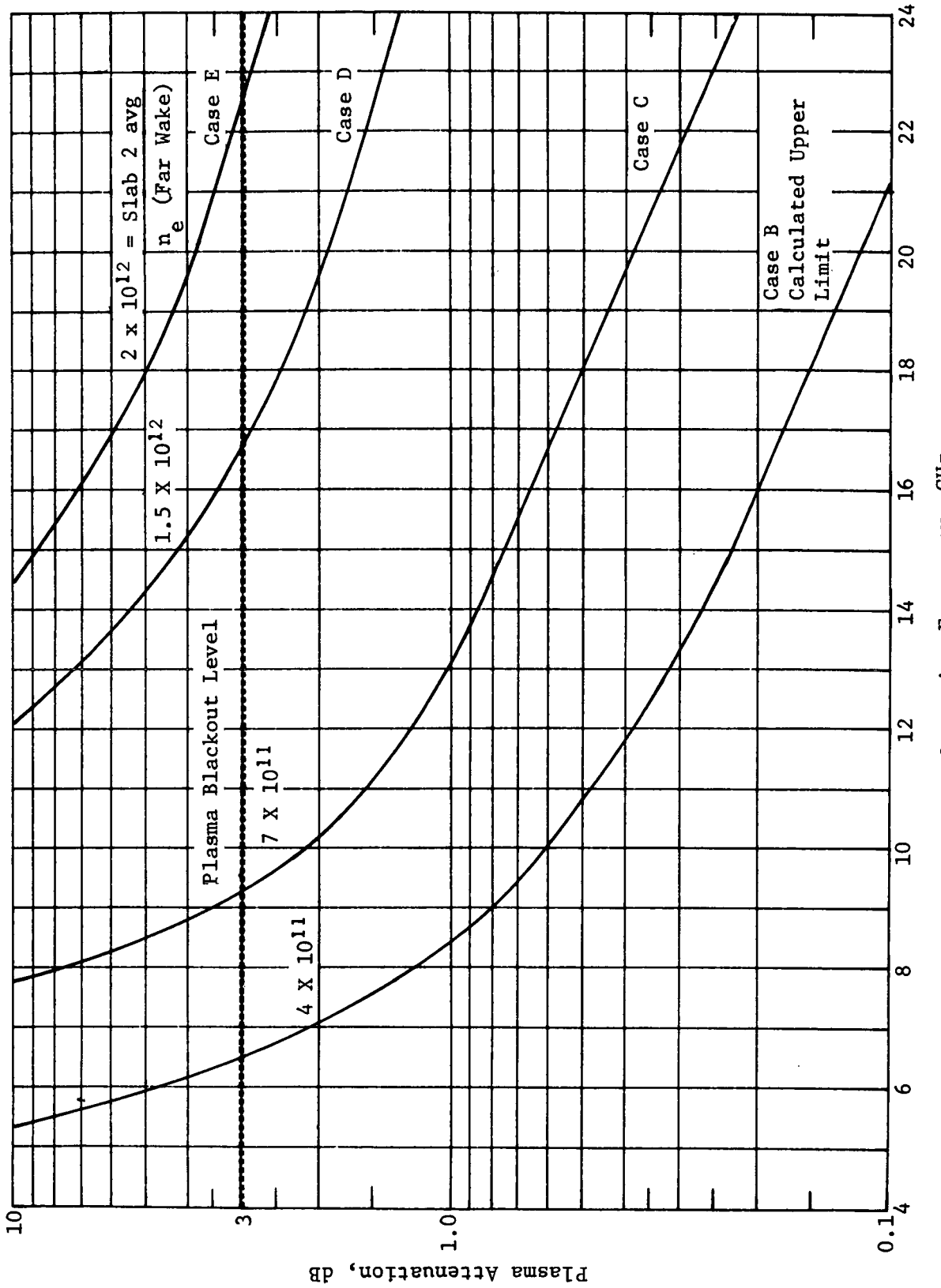

Fig. VI-26 Probe Wake Attenuation Versus Frequency for Plasma Cases

The next question to answer was: "What is the lowest frequency that will be attenuated 3 dB at approximately -60 km?" To extend the plasma parameters to higher values, Cases C through E were investigated to determine the cutoff frequencies. These cases represent deeper penetration into the atmosphere. Maximum values of n_e and ν_c in the first far-wake slab that result in 3-dB attenuation were determined from the three cases shown in Fig. VI-26 and plotted in Fig. VI-27. As discussed previously, the nonequilibrium flow analysis was performed only at one altitude; namely, -60 km. The plasma parameters are shown in Fig. VI-28 with a band of uncertainties due to variations in basic assumptions made, as mentioned previously. The slope of the curves was estimated for nonequilibrium conditions for other altitudes. This figure relates the maximum value of plasma parameters in the far wake to Jovian altitude. Figures VI-27 and VI-28 were used to develop Fig. VI-29, which relates the 3-dB blackout altitude to RF frequency. This figure is based on the upper-limit case of the nonequilibrium flow analysis shown in Fig. VI-28. Figure VI-29 shows that 20 GHz will black out at -72 km and is lower than the design goal of -60 km. From this curve, the decision was made to move the operating frequency from 20 GHz to 10 GHz. As seen, the probe will still penetrate to approximately -65 km before RF blackout ($\geq$3 dB attenuation) occurs at 10 GHz (X-band). There is still a fair amount of conservatism involved because the upper-limit flow analysis was used, and 8 GHz is the actual frequency for blackout at -60 km.

B. DATA HANDLING

1. Requirements and Assumptions

a. Prelaunch Checkout - It is assumed that the probe payload and supporting equipment will be checked out by the spacecraft checkout system, thereby avoiding AGE connections to the probe in the launch configuration.

b. Preseparation Checkout, Calibration, and Programming - Before separation, the operational readiness of the probe will be determined by the spacecraft data system. Presumably, the spacecraft will interrogate the probe through a stored program that will also compile a report for the DSN. From the spacecraft data return, the DSN will determine the operational readiness of the probe, calibration status of the science instruments, and drift function of the spacecraft clock.

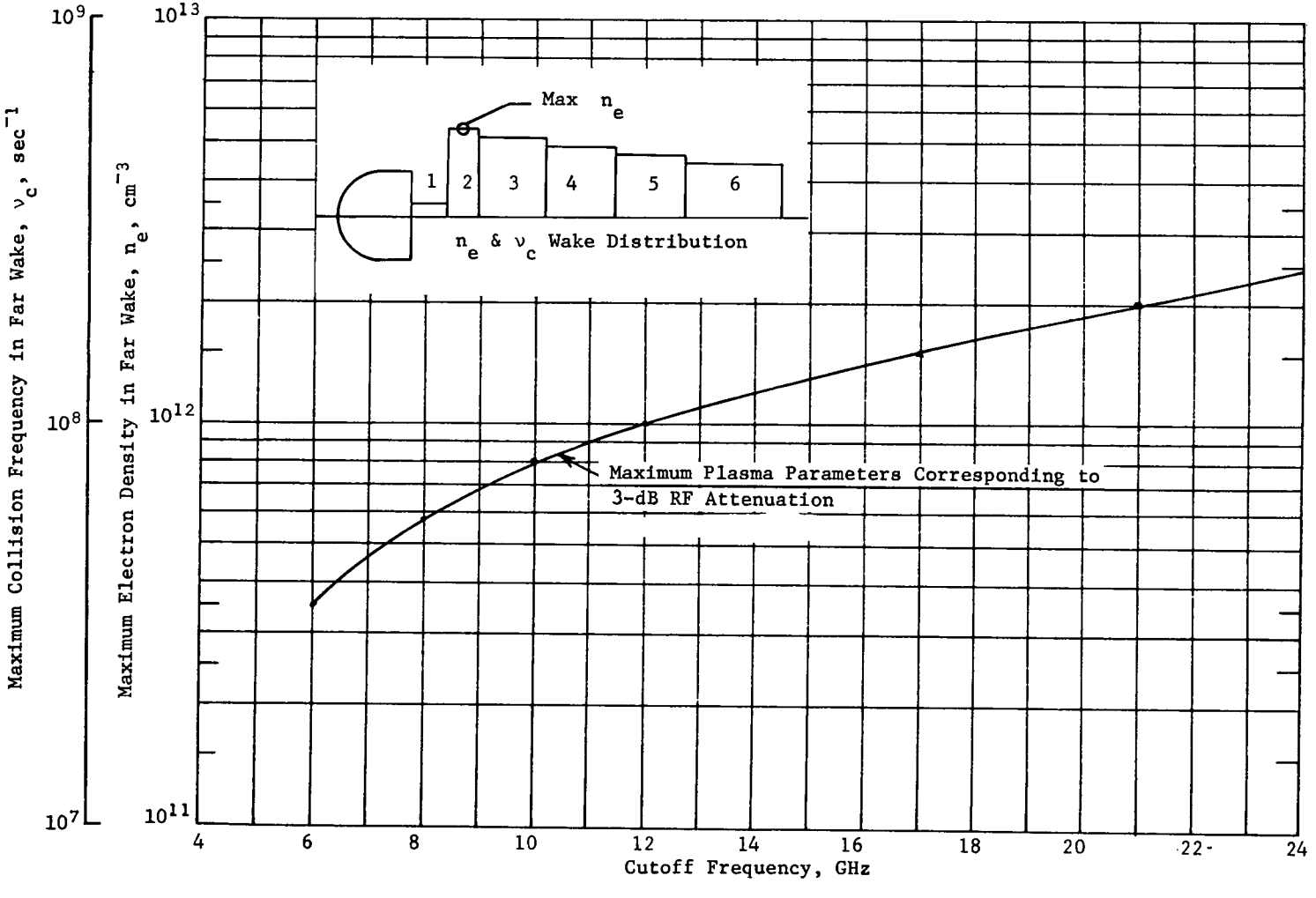

Fig. VI-27 Maximum Far-Wake Plasma Parameters for RF Blackout

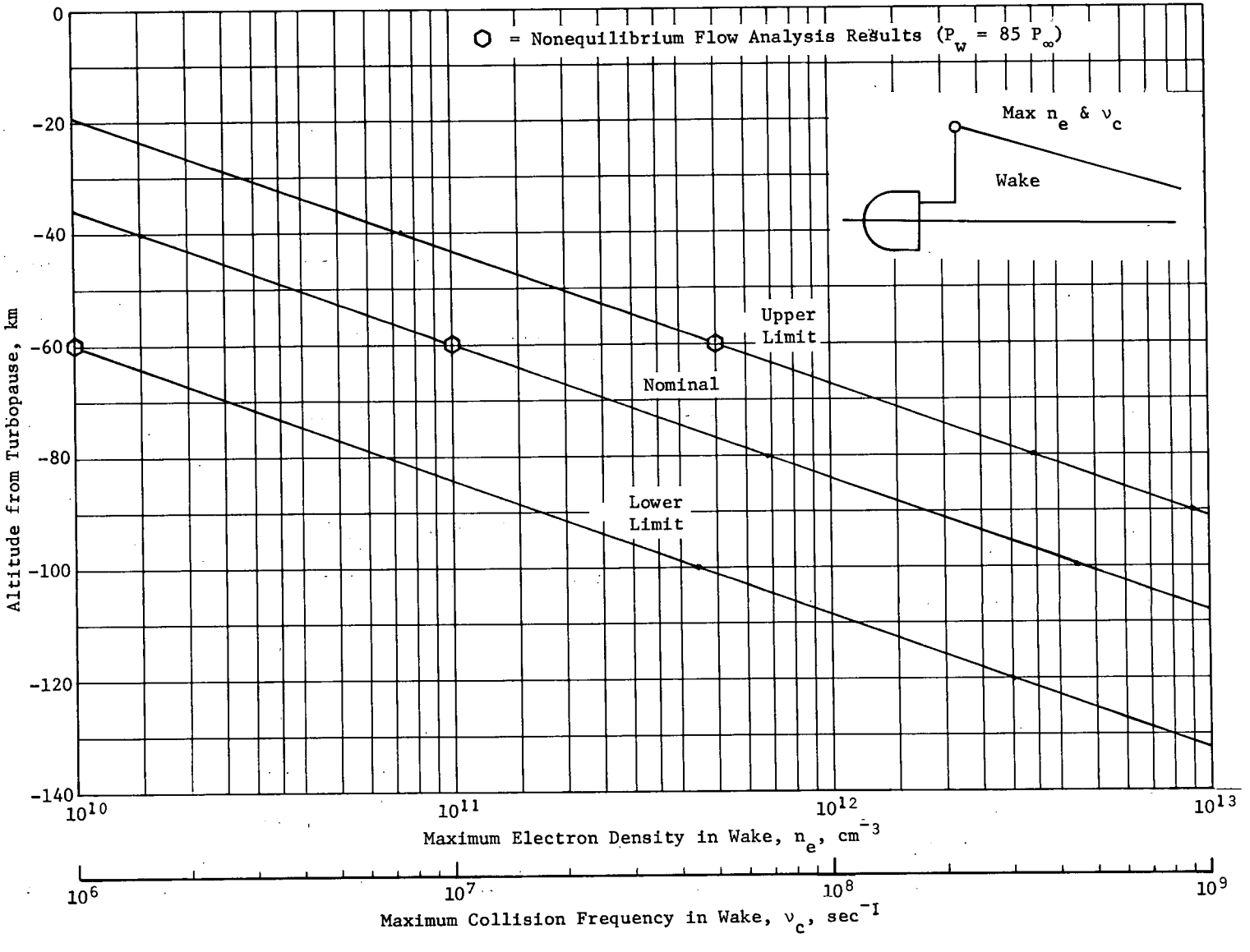

Fig. VI-28 Nonequilibrium Wake Plasma Parameters

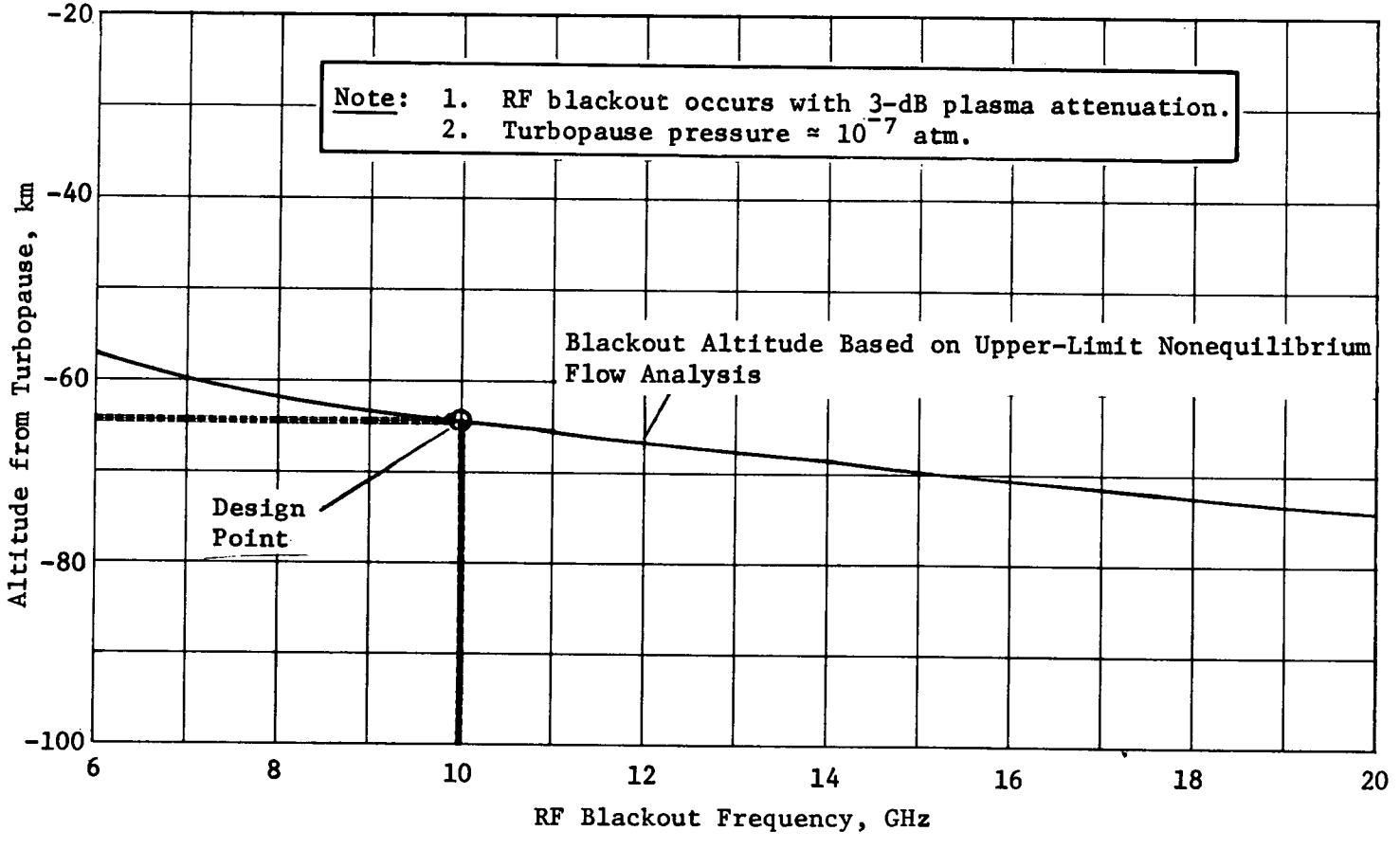

Fig. VI-29 Blackout Altitude versus RF Frequency

From analysis of these data and determination of the spacecraft ephemeris, the DSN will generate any required changes to the prestored probe mission program sequences, compute any vernier functions needed by the instruments, and compile parameter changes needed to optimize the separation and postseparation maneuvers. These new probe program entries will be tagged and communicated to the spacecraft which, in turn, will compile them for loading and verification. The spacecraft will then notify the DSN that the program changes have been properly loaded into the probe program storage and verified. (It is noted that the above description assumes an alterable probe program storage. In view of the inflexibility and relatively high recurring costs associated with a predetermined, hard-wired program, this would seem to be a prudent assumption.)

c. Probe Control - Control functions required aboard the probe are event sequencing, attitude control, and instrument control. Pending further study, it may also be necessary to employ some form of adaptive instrument control and/or adaptive data processing (data compression) to optimize information return from the probe.

The requirements and assumptions of *a*, *b*, and *c* above suggest the spacecraft/probe interface configuration shown in Fig. VI-30.

d. Data Processing on Probe - As mentioned in *c* above, data compression is a possibility. In addition, there are the normal data-processing functions of signal conversion, data formating, and output coding for the communications link.

e. Data Processing on Spacecraft - Probe data are either stored aboard the spacecraft for subsequent transmission or relayed from the spacecraft to the DSN in real time, depending on the communications-link capability. Storage is required if the Earth link cannot support real-time transmission of the probe data or simultaneous transmission of both probe and spacecraft data, depending on mission configuration. It is likely that real-time data transmission can occur for Jupiter and possibly Saturn, depending on which spacecraft is employed, but that tape storage is needed for Uranus and Neptune because of the reduced link capability.

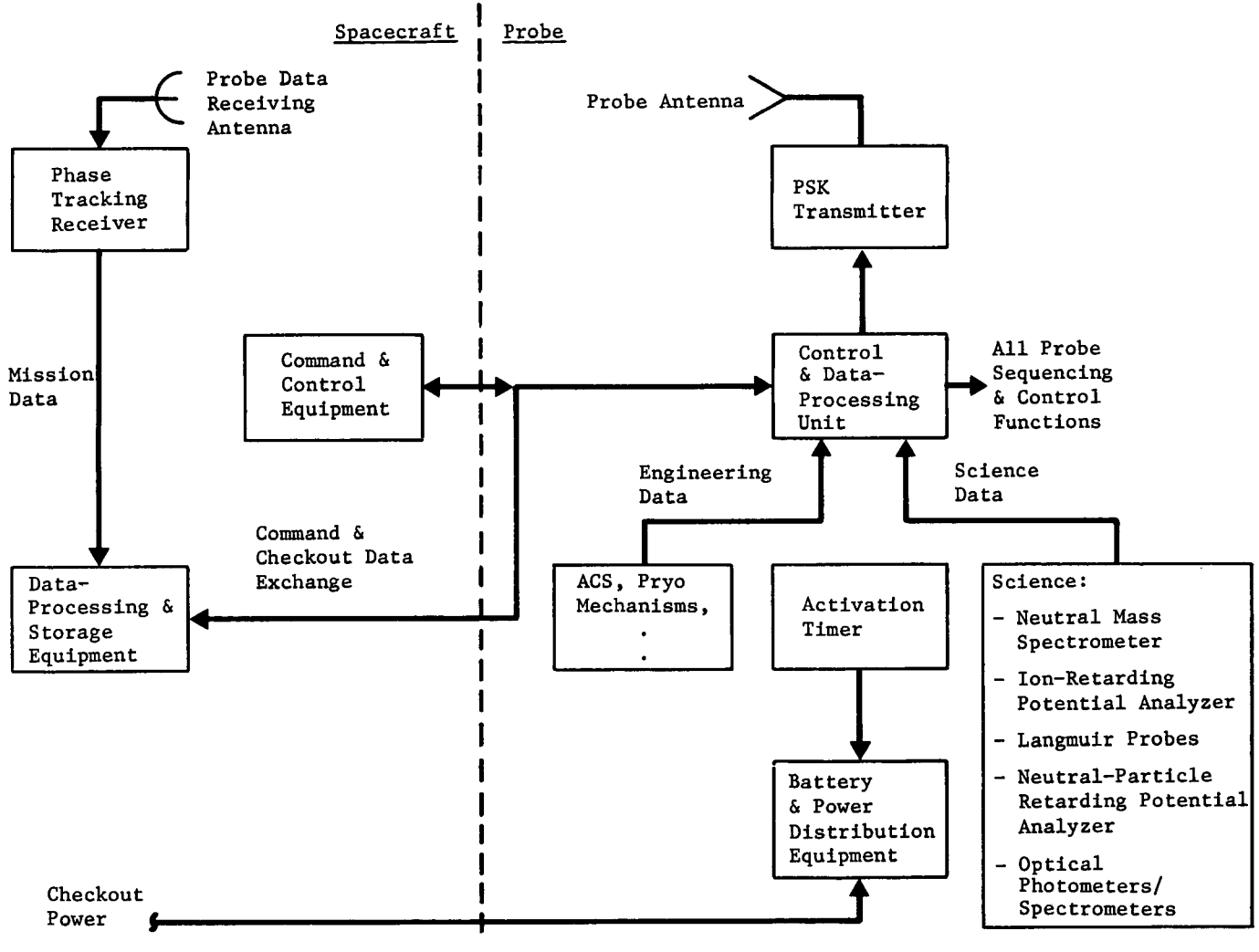

Fig. VI-30 Jupiter Spacecraft/Turbopause Probe Interfaces

f. Data Processing on Earth - Data processing on Earth will probably consist of nonreal-time computer processing of tape-recorded signals with the following possible signal transfer options:

1) Demodulate and decode in the spacecraft and recode for Earth link;

2) Demodulate only in the spacecraft, sample, and recode for Earth link;

3) Sample unmodulated signal in the spacecraft and recode for Earth link.

2. Probe Hardware Tradeoffs

a. Instrument versus Centralized Signal and Data Processing - The question is how independent the instruments should be with respect to control and signal-processing functions. At one extreme is the case in which the instrument receives a start pulse and outputs formated digital data periodically. This requires that the instrument contain timing, sequencing, and signal- and digital data-processing functions. At another extreme is the case in which the instrument contains only the special circuitry associated with intimate control of physical parameters and amplification of low-level output signals. The advantages of the latter, of course, are lower instrument weight, power, and cost, and greater system flexibility. Weight and power are reduced in proportion to the amount of circuitry because the probe data-processing unit must contain signal-processing and conversion equipment for housekeeping data, regardless of how the instruments are configured. Cost is reduced by eliminating separate development of this common-function equipment for each instrument. The system flexibility aspect can be a very important item, especially in view of the desirability of adapting the instrument/data system to a variety of missions.

An example of how the centralized system might be configured is given later, in Subsection 3.

b. Special versus Computer Processor - The question is whether to design a special-purpose processor to provide probe control and signal- and data-processing functions or whether to implement these functions by a combination of computer and interface electronics.

Estimates were made for the two approaches. Figure VI-31 is a block diagram of a control and data processor unit (CDPU). This unit supplies all control and processing functions not in the instrument and attitude-control hardware. A computerized version of the same functional hardware is shown in Fig. VI-32, the adaptive control and data processing group (ACDPG). The ACDPG consists of the computer and a processor interface unit (PIU) that includes all functional blocks in Fig. VI-32 except the computer. The selected computer is a nonredundant version of the advanced onboard processor (AOP) being considered by Martin Marietta for the spacecraft. It employs a plated-wire memory and bipolar (non-MOS) LSI circuits. A comparison of the weight, size, and power of the two versions is given below.

	CDPU	ACDPG Computer	ACDPG EDP	ACDPG Total	Δ over CDPU
Weight, kg (lb)	2.3 (5.0)	6.4 (14.0)	1.3 (2.8)	7.7 (16.8)	5.4 (11.8)
Size, cm^3 ($in.^3$)	2510 (153)	4500 (275)	1470 (90)	5980 (365)	3470 (212)
Power, W	11.5	14.0	1.4	15.4	3.9

The increase of 5.4 kg (11.8 lb) and 3.9 W of the computerized version over the CDPU version would be traded off against the savings in weight, power, and development costs that could be realized in the science instruments and attitude-control system by use of a system like the ACDPG. Also, the AOP computer is designed for use in a redundant configuration. Although the hardware estimate used here represents a single-thread arrangement of AOP modules, some of the electronics in these modules are dedicated to redundancy combining functions. Hence, it could be expected that the actual weight and power could be reduced by 10 to 30% from that given for the computer.

3. Output Data Formating

Figure VI-33 shows the mission data profile and event timeline relationship. It is recognized that the most valuable data are obtained from the neutral mass spectromater (NMS) immediately before entry. In devising an output data format, then, it is important to minimize the time delay between acquisition of NMS data samples and outputting these samples on the probe-to-spacecraft data link. An example of an output data format that favors minimization of delay for both NMS and NRPA data is shown Fig. VI-34.

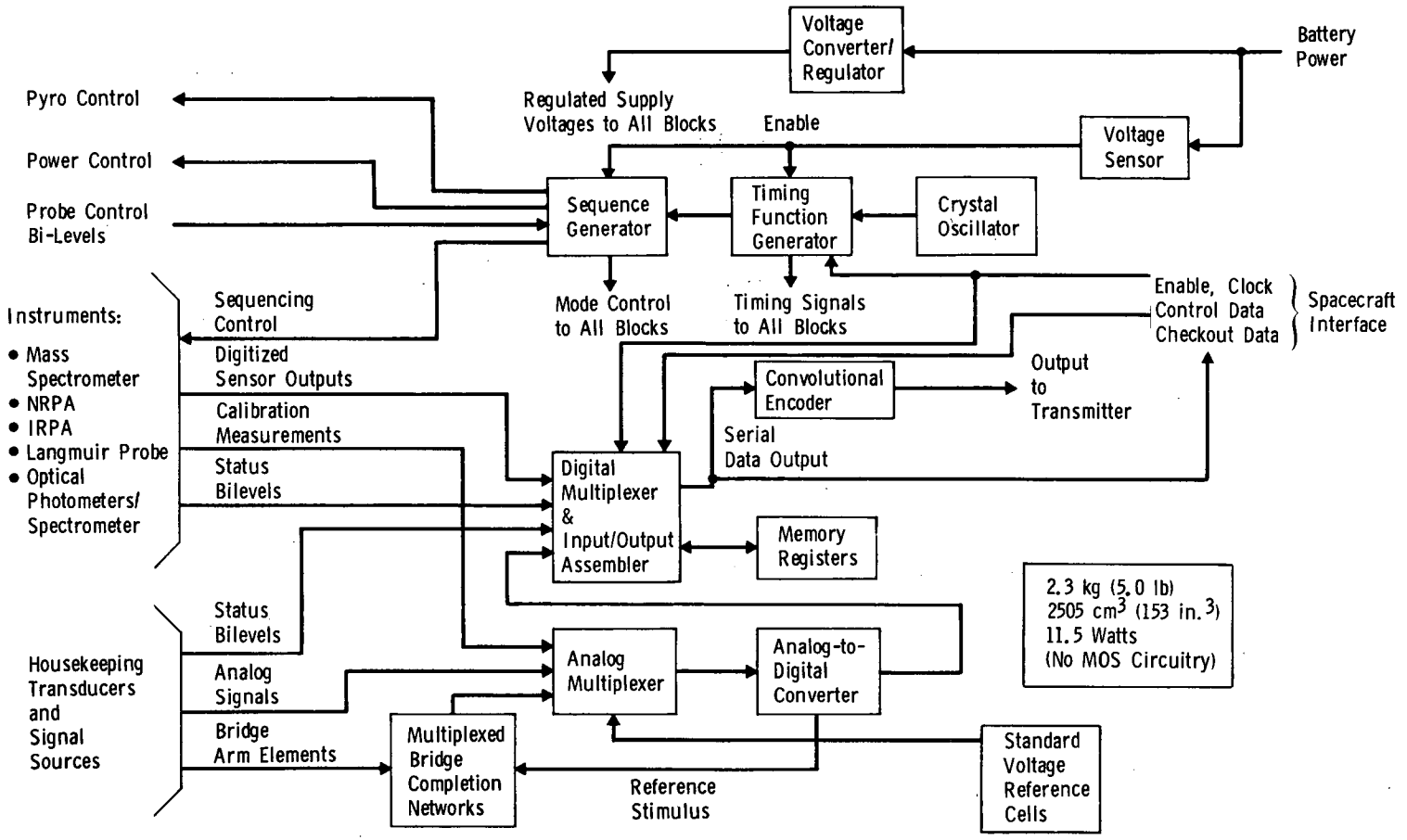

Note: This unit provides fixed control sequences and data formats. It could be made programmable by adding a plated-wire memory card. Arithmetic hardware would be required for it to perform adaptive control and data processing functions.

Fig. VI-31 Turbopause Probe Control/Data Processing Unit (CDPU)

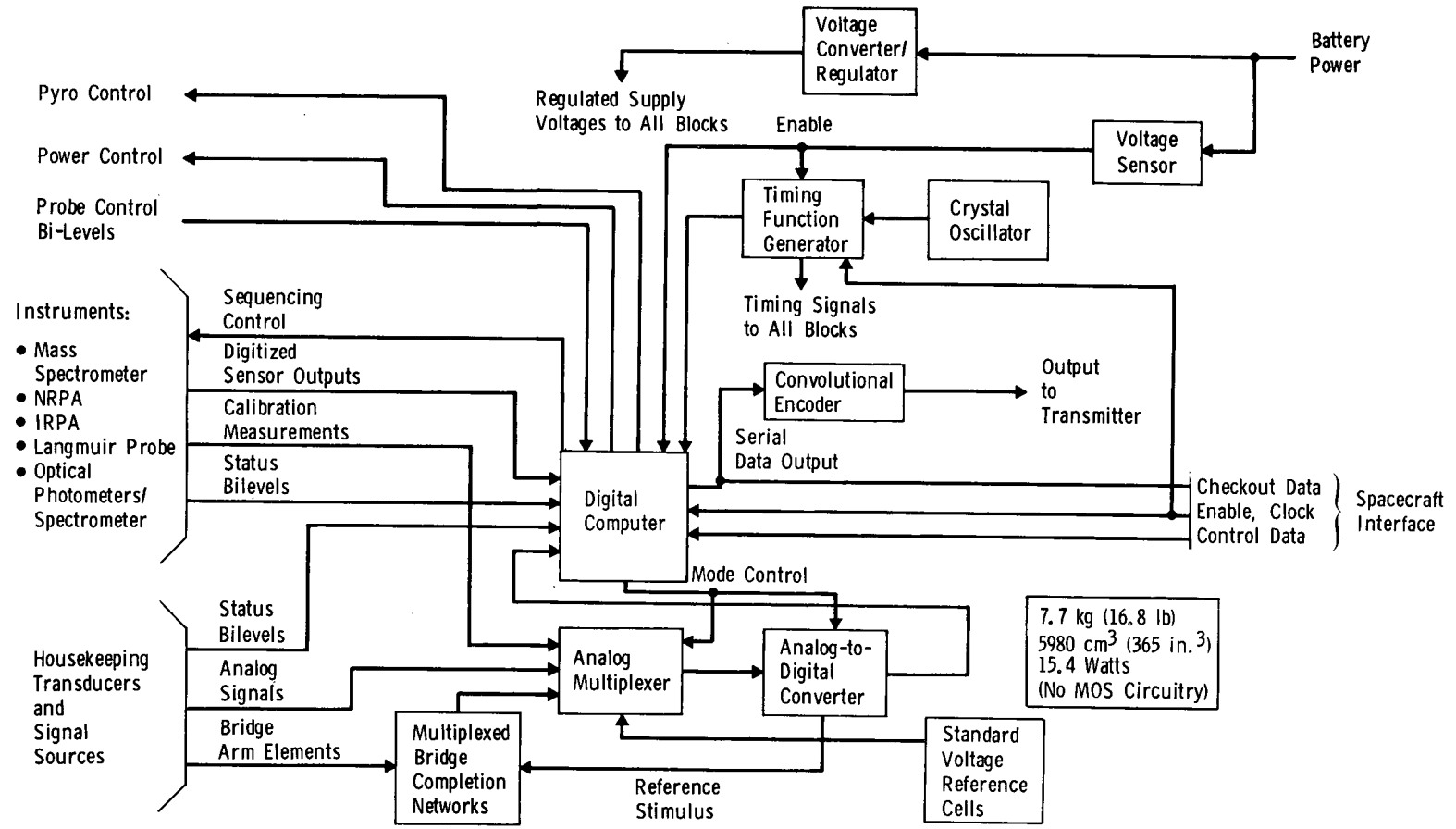

This equipment group consists of two units: a digital computer with approximately 8K words of memory and the remaining functions housed as a data processor unit (DPU). The equipment provides adaptive control and data processing functions which are software programmable.

Fig. VI-32 Turbopause Probe Adaptive Control/Data Processing Group (ACDPG)

FOLDOUT FRAME 1

FOLDOUT FRAME 2

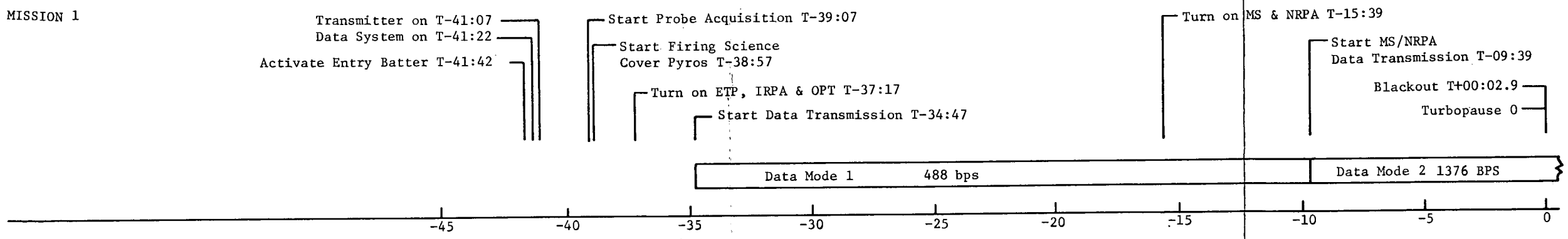

Fig. VI-33 Typical Mission Data-Profile/Timeline Relationship

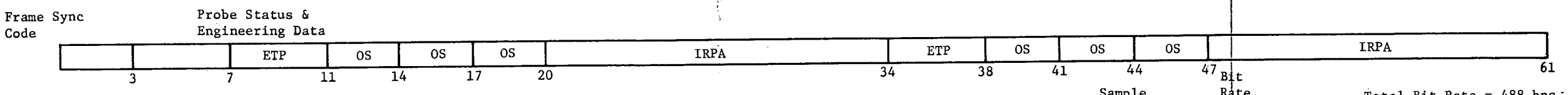

Data Mode 1 Frame Format
1-sec Frame Duration
One Square = One 8-bit Word

Data Source	Words/Sample	Bits/Sample	Samples/Frame	Sample Interval, sec	Bit Rate, bps
ETP	4	32	2	0.5	64
OS	3	24	6	0.1666	144
IRPA	121 + 2V = 14	112	2	0.5	224
FS & Eng	7	56	1	1.0	56
					488

Total Bit Rate = 488 bps

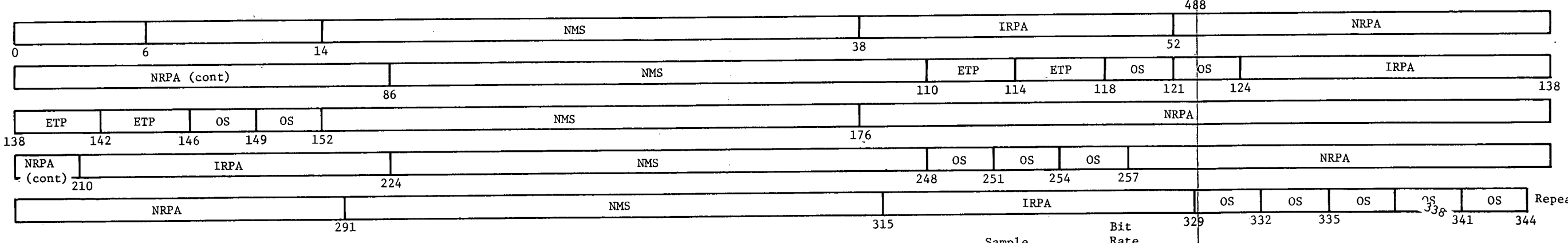

Data Mode 2 Frame Format
2-sec Frame Duration
One Square = One 8-bit Word

Data Source	Words/Sample	Bits/Sample	Samples/Frame	Sample Interval, sec	Bit Rate bps
ETP	4	32	4	0.5	64
OS	3	24	12	0.1666	144
IRPA	121 + 2V = 14	112	4	0.5	224
NMS	24	192	5	0.4	480
NRPA	301 + 4V = 34	272	3	0.6666	408
FS & Eng	14	112	1	2.0	56
					1376

Total Bit Rate = 1376 bps

Fig. VI-34 Data-Frame Formats

The data Mode 1 format is for data transmission over approximately the first 25 min of data timeline. During this period, the ETP, IRPA and optical spectrometer and/or photometers are acquiring data. The data Mode 2 format is for data transmission when NMS and NRPA data are also being acquired. Sampling intervals are compatible with science requirements.

4. Space Hardware Tradeoffs

As noted in Subsection 1, probe data may be relayed in real time from the spacecraft to the DSN or stored on the spacecraft for delayed transmission, depending on probe mission and spacecraft design. Also, as noted in Subsection f, there are three data-transfer options, not considering the spacecraft storage option.

1) Decoding on the spacecraft;

2) Demodulating but not decoding;

3) Transfer of the original undemodulated signal.

Option 1 has only on advantage, which is far outweighed by the disadvantages. It is assumed that convolutional encoding will be performed at the probe on the output data stream and a Viterbi decoding algorithm used to decode received data. By decoding on the spacecraft, the smallest amount of storage would be required, compared to the other two options. This advantage disappears, of course, if storage on the spacecraft is not required. The main disadvantage is that only one real-time decoding pass can be made at the data. This would also very likely require additional power to guarantee adequate data demodulation for real-time decoding. The second option avoids single-pass decoding disadvantage, but at the expense of considerably more data generated at the receiver output. It would also require somewhat more power, perhaps 1 dB, than Option 3 because Option 2 is essentially a one-time demodulation pass (in real time).

Option 3 has the advantage that it can be demodulated repeatedly, using computer programs operating on its tape record. Following this, it can be decoded repeatedly by computer programs. Both operations can be done with continually improved accuracy (to some limit).

To summarize, assuming the following parameters:

1) 1376 original information bps;

2) Rate 3 convolutional encoding, (V = 3);

3) PSK/PM modulation, 5-kHz subcarrier (giving an 8.26-kHz transmitted subcarrier bandwidth);

4) 4-bit encoding of signals at the receiver (constraint length, K = 4).

Receiver data output rates for the three options are:

1) Decoding with 4-bit soft decision quantization - 5504 bps;

2) Demodulation only - 41.3 kbps;

3) Predemodulation - 92 kbps.

For a 61-min data transmission time, bit totals are respectively:

1) 2×10^7

2) 1.51×10^8

3) 3.37×10^8.

Hence, if storage is required, a tape recorder must be used, regardless of which option is selected. This is because a plated-wire memory for storage of 20,000 k bits would very likely exceed 100 pounds. The amount of tape required for any of these options is relatively small considering that storage capacities of well over 10^{10} bits for an air transport and 10^9 bits for a fluid-filled transport are about right for a 40-lb recorder.

5. Recommendation for Future Study

a. Instrument/Processor Interfaces - The most pressing need is to establish interfaces that give the optimum system. More study is needed with respect to instrument functions versus central-processor functions.

b. Attitude Control - An estimate of attitude-control electronics hardware is necessary to assess the weight and power savings that could be obtained by using a computer like the AOP.

c. Adaptive Control and Data Processing - Some estimates need to be made of potential performance gain (science information return) that could be achieved from likely forms of adaptive instrument control and adaptive data processing.

d. Spacecraft/Probe Interfaces - Based on projected TOPS, Pioneer, and DSN capabilities, design estimates are needed for implementation of preseparation checkout, calibration, and programming functions (Subsection 1b) to assess the effects on probe data-system design.

C. ELECTRICAL POWER AND PYROTECHNIC SUBSYSTEMS

1. Power Subsystem

Power requirements for the probe components are listed in Table VI-6. The power-system design approach for each probe is essentially the same, although it should be noted that probe missions that do not require an attitude-control maneuver do not have a postseparation power system.

Table VI-6 Probe-Component Power Requirements

Data management	11.5 W	RF subsystem	83.2 W
Pyrotechnics	0.5 W[a]	ACS electronics	1.5 W
Instrument engineering	1.0 W	Sun sensor	2.0 W
Vehicle engineering	1.0 W	Jupitor sensor	1.0 W
Accutron timer	b	Langmuir probe	3.0 W
Nutation damper	c	IRPA	3.0 W
Mass spectrometer	15.0 W	NRPA	5.0 W
Photometer/spectrometer	5.0 W		

[a]Does not include power from self-contained Ag-Zn battery for first preentry event (remotely activated battery event).

[b]No power required.

[c]Self contained Ag-Zn battery.

a. Postseparation Power Subsystem - This subsystem provides power for the attitude-control, data-handling, and pyrotechnic subsystem for the approximate 12-hr postseparation period allowed for the probe attitude-control maneuver. The power subsystem consists of a power source, conversion and regulating equipment. It is activated by the spacecraft before separation. The subsystem will also be activated by spacecraft power during preseparation checkout.

b. Entry Power Subsystem - This subsystem will provide power to the data-handling, communication, science, and pyrotechnic subsystems. The distribution system will consist of relays and power-isolation filters to deliver unregulated battery power to the various components. Power conditioning and regulation will be implemented in the individual components as required. This approach is used for the entry configuration to minimize the possibility of common-mode failures and to permit use of lower-power transistors that tend to be less radiation sensitive. Silicon-controlled rectifiers (SCR) are avoided in favor of relays for similar reasons. A functional block diagram of the power and electrical subsystems is shown in Fig. VI-35.

c. Power Source - There are three fundamentally different power source requirements--probe bus power source, Accutron timer power source, and preentry pyrotechnics power source. The timer and preentry pyrotechnic power sources have requirements for long life and very low capacity. The probe bus power source is required to meet much higher power requirements but has an active life of less than 12.5 hr. Selection of battery type to supply bus power is discussed below.

d. Probe Bus Power Source - Although consideration has been given to various power sources such as RTGs, solar cells, and gas generators, for the probe, the choice rapidly narrows to some type of battery. An evaluation of various types has been made and is based on the following mission/test profiles.

1) Ni-Cd Secondary - Discharged

   a) Fly discharged 526 days at 50 to 80°F

   b) Condition battery at C/10 or greater

   c) Hold open circuit at less than 70°F for 20 days

   d) Discharge between 40 and 110°F for 2 hours or less.

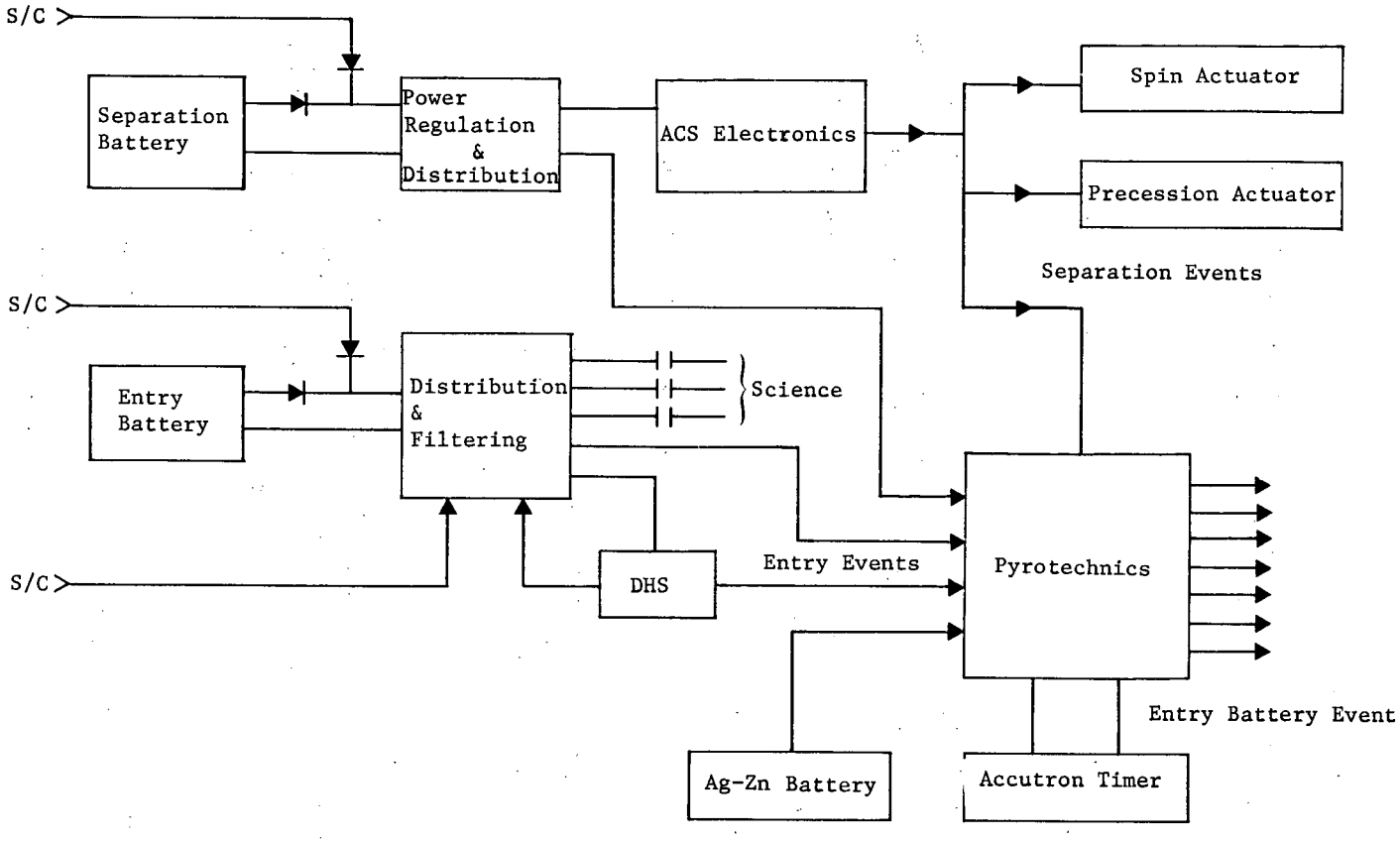

Fig. VI-35 Power Subsystem

2) Ni-Cd Secondary - Charged

   a) Float charge for 526 days at C/100 or greater (loss of expected at temperatures less than 68°F)

   b) Hold charged on open circuit at less than 70°F for 20 days

   c) Discharge between 40 and 100°F for 2 hr or less.

3) Ag-Zn Remotely Activated - Conventional Design

   a) Assume two batteries, postseparation battery (3-hr life) and entry battery (40-min life); tubular-reservoir standard gas generator activator; common manifold fill

   b) Standard design capable of satisfying requirements for up to 24-hr activated life.

4) Ag-Zn Remotely Activated - Pile Construction

   a) Assumptions as above, but with diaphragm activator mechanism

   b) Design capable of satisfying requirement for 5-hr activated life; some development needed if activated life is to be extended.

5) Ag-Zn Secondary

   In all probability, the only other design that would meet the requirement would need irradiated and linked separator material. General Electric Test Report 67SD337 offers the best data to date. The test for Venus Planetary Explorer (by Martin Marietta) will be performed on similar cells.

6) Ag-Zn Secondary - Float Charge

   a) High decay rate, expect a loss of approximately 3% per month (approximately 54% total)

   b) During a 30-day charge stand, expect a 5% loss.

7) Ag-Zn Secondary - Open-Circuit Stand

   a) Assumed charged at launch and left open circuit at 50°F for 526 days

   b) Battery would lose all capacity and need recharge

   c) Expect a permanent loss of 26% on recharge

   d) Expect 5% loss during 30-day charged stand.

8) Ag-Zn Discharge Stand

   a) Expect a loss of 17% on recharge

   b) Expect a 5% loss after 30-day charge stand.

e. Evaluation - Based on the above decay and degradation rates, tests, and Ref VI-8 and VI-9, the curves in Fig. VI-36 were generated. It should be noted that all Ag-Zn secondary batteries would need separator development for this application. The pile construction battery would need known minor modifications and packaging for life beyond approximately 5 hr. The Ni-Cd batteries have the highest reliability but are excessively heavy. Based on these considerations and the need for critical recharge and conditioning control for secondary batteries, the remotely activated Ag-Zn battery was selected for this application. Consideration of standard versus pile construction indicated approximately 50% weight could be saved with the latter. The state of the art indicates that all development necessary for this application should be completed and available for the pile construction battery by 1975. Based on the above, a pile-construction battery has been recommended for this application and the weights indicated in Fig. VI-36 have been used in the current estimates.

f. Long-Life Remotely Activated Batteries - An alternative approach would use standard remotely activated batteries with some modifications for longer life. This would eliminate a significant problem of energizing pyrotechnics after postseparation coast. The degradation and life characteristics are, in general, applicable to all primary Ag-Zn designs. The fill manifold is a development for standard construction.

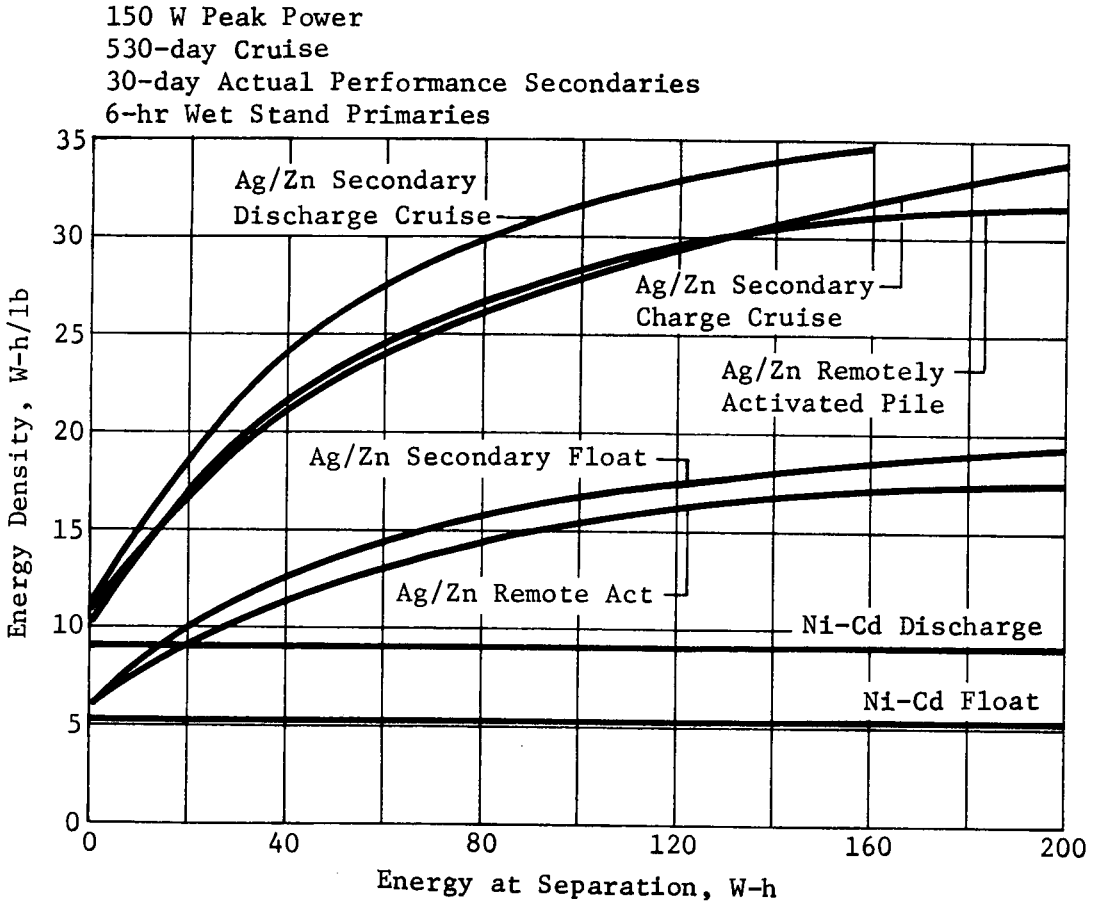

Fig. VI-36 Power-Source Tradeoff

C.7

g. Remotely Activated Ag-Zn Oxide Batteries

1) General Description

Current designs of remotely activated batteries for space application generally employ an electrolyte reservoir separated from the dry cells by a frangible diaphragm. Activation is accomplished by initiating a trigger mechanism or explosive squib that introduces pressurized gas to the electrolyte compartment, thus forcing the electrolyte into the battery cell compartment. Present design efforts focus on ensuring that sufficient electrolyte is forced into the cells and effective venting of residual electrolyte and pressurant.

Typically, separator materials used in standard designs are not semipermeable membranes that permit long activated life, but hydrophylic nonwoven materials capable of fast activation. Activated stand life exceeding 24 hr should not be expected.

2) Dry Stand Loss

Dry storage loss is a function of humidity control, temperature, plate processing, and particularly, cell materials and fabricating techniques. Most battery manufacturers are aware of these problems and have solved them. Typical data on the Poseidon Missile Program indicates no loss of capacity during a 91-month storage.

Losses usually result from loss of peroxide on the positive, which is accelerated at high temperature. Figure VI-37 shows the effect of temperature and that capacity at any temperature will decay to a minimum of 50% of rated, depending on storage time.

3) Activated Stand Life

There are two major problems in extending activated stand life of remotely activated batteries.

Electrolyte Paths - Standard designs use a manifold across the cells that permits simultaneous activation of all cells. After activation, the manifold may remain flooded and, at best, high-resistance electrolyte paths exist between cells. Resulting potentials between cells are high enough to permit Zn precipitation along the electrolyte paths, resulting in massive shorts and subsequent discharge of the battery.

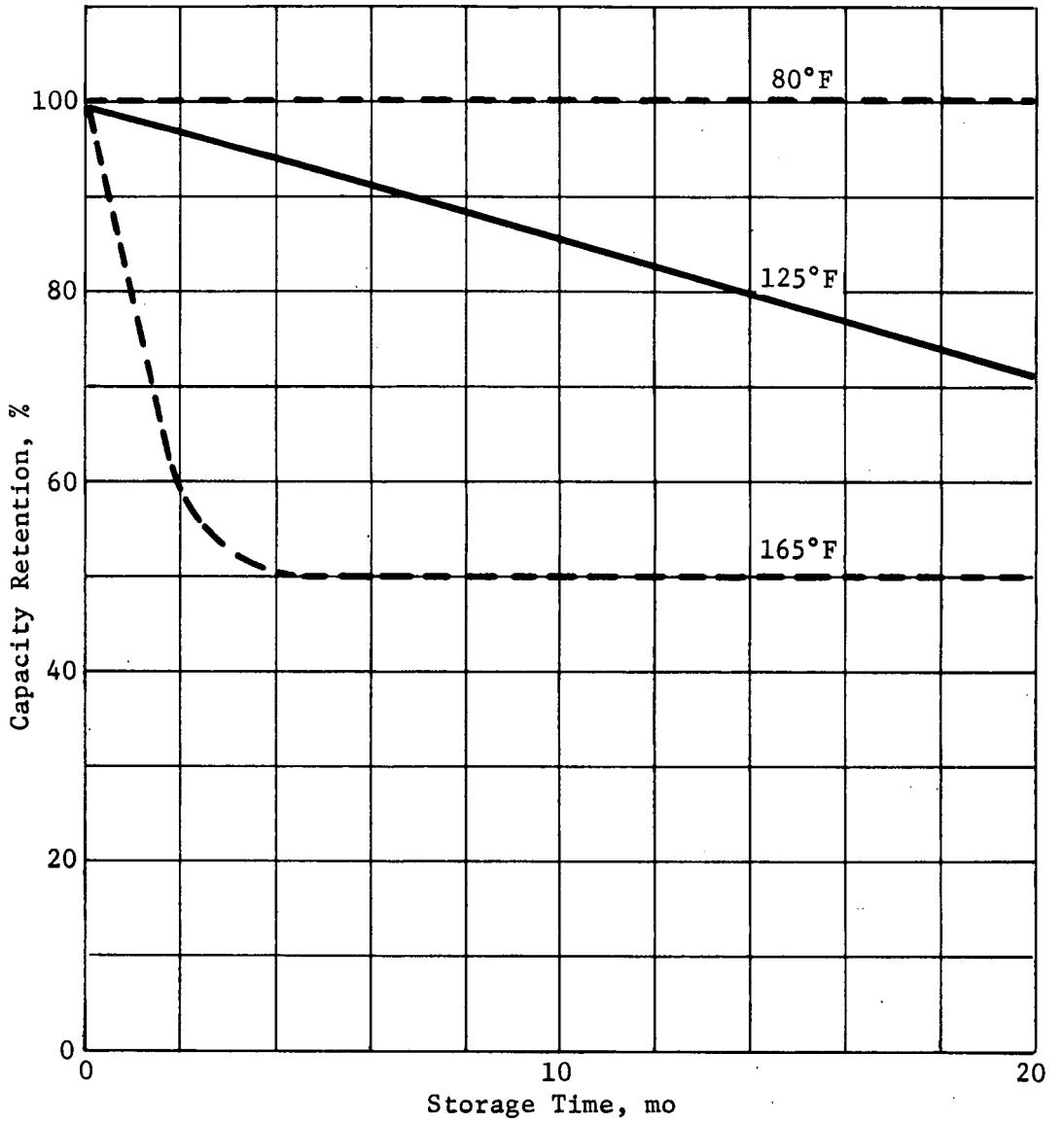

Fig. VI-37 Dry-Storage Charge-Retention Characteristics

Separator Material - Absorbent separators in remotely activated batteries serve two major purposes: activation times of less than 2 sec, and a higher current density (i.e., voltage current characteristics). The major disadvantage is that it is not a semipermeable membrane and oxidation occurs at a high rate, resulting in self-discharge.

4) Weight Shift Due to Activation

Upon activation, electrolyte transfers from the reservoir to the cells. The quantity of electrolyte varies with capacity and separator material. As a rule of thumb, 4.2 ml/A-h/cell or 5.9 gm/A-h/cell can be used (e.g., 20 A-h 20-cell battery - 2,360 gm KOH.

The weight shift depends on the battery design. With a tubular reservoir wrapped around the cell pack as described in the Eagle Picher data (Ref VI-10), electrolyte would transfer from the periphery to the center of the black box. In the case of a higher-energy-density design, as shown in Fig. VI-38, transfer approximates a shift from the top half of the black box to the bottom half.

5) Design Concepts for Long Wet Stand

A 7-day wet stand life has been achieved with the design shown in Fig. VI-39 and VI-40.

Figure VI-39 shows a high-energy-density design in which the cell case is a half shell. High-energy density is achieved by elimination of the double cell wall resulting from normal cell construction. The center wall also can be as thin as 0.0254 cm (0.01 in.).

The half shells are assembled so that the flexible member is directly below the open section. Design tolerances provide a crude seal at this point. When the battery is activated through the manifold, activation pressures deflect the flexible member, permitting electroylte to enter the cell. At equilibrium conditions, a pressure balance occurs across the flexible member and the joint closes causing very high resistance paths between cells, which minimizes electrolyte shorts.

To eliminate cell degradation caused by separator breakdown, a semipermeable membrane would be included in the cell pack. Activation times would increase to 20 sec and wet stand life to 7 days.

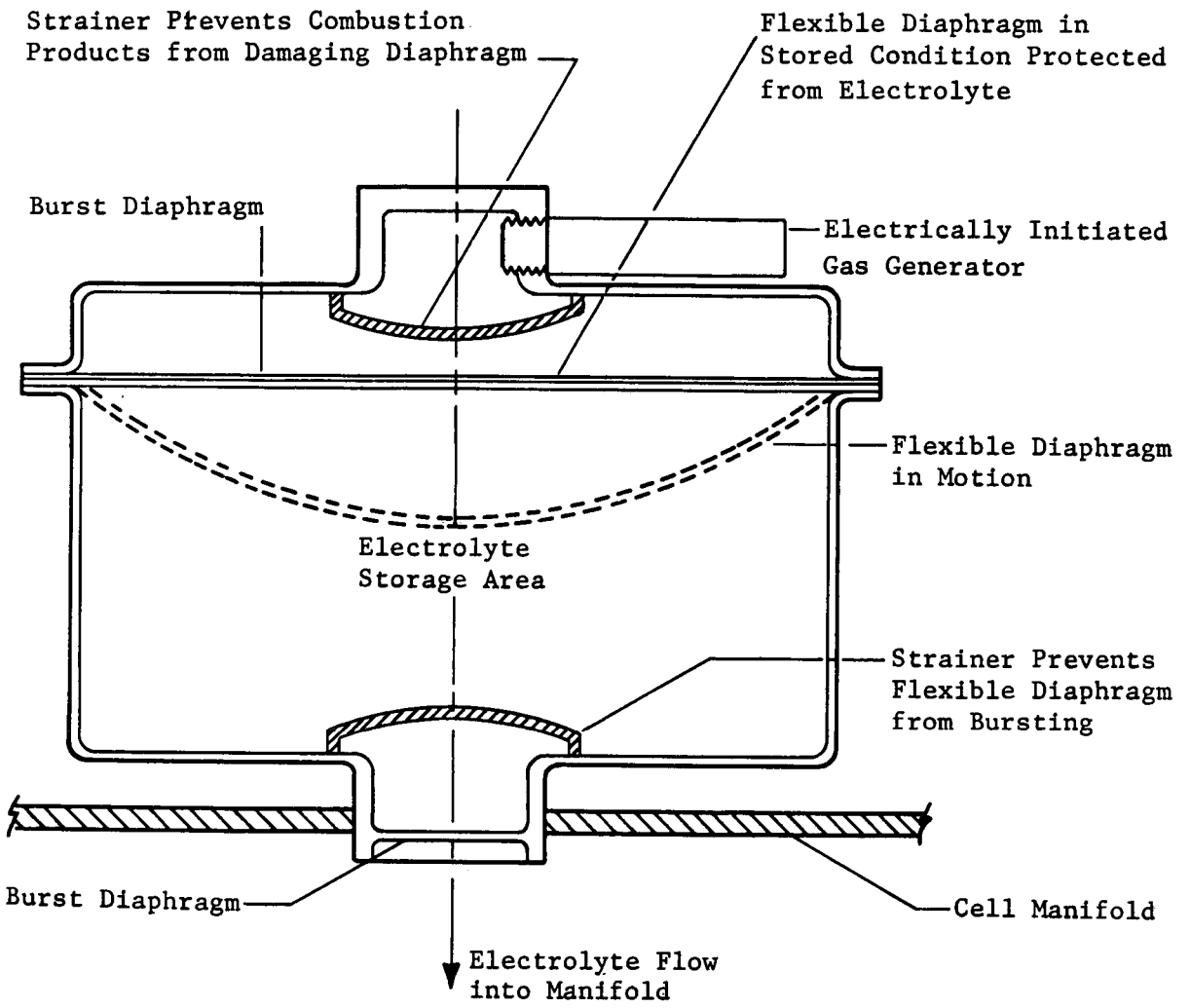

Note: Gas generated by initiator increases internal pressure of mechanism until burst diaphragms open. Electrolyte flows into manifold under pressure of distending flexible diaphragm.

Fig. VI-38 High-Energy-Density Activation Mechanism for Ag-Zn Batteries

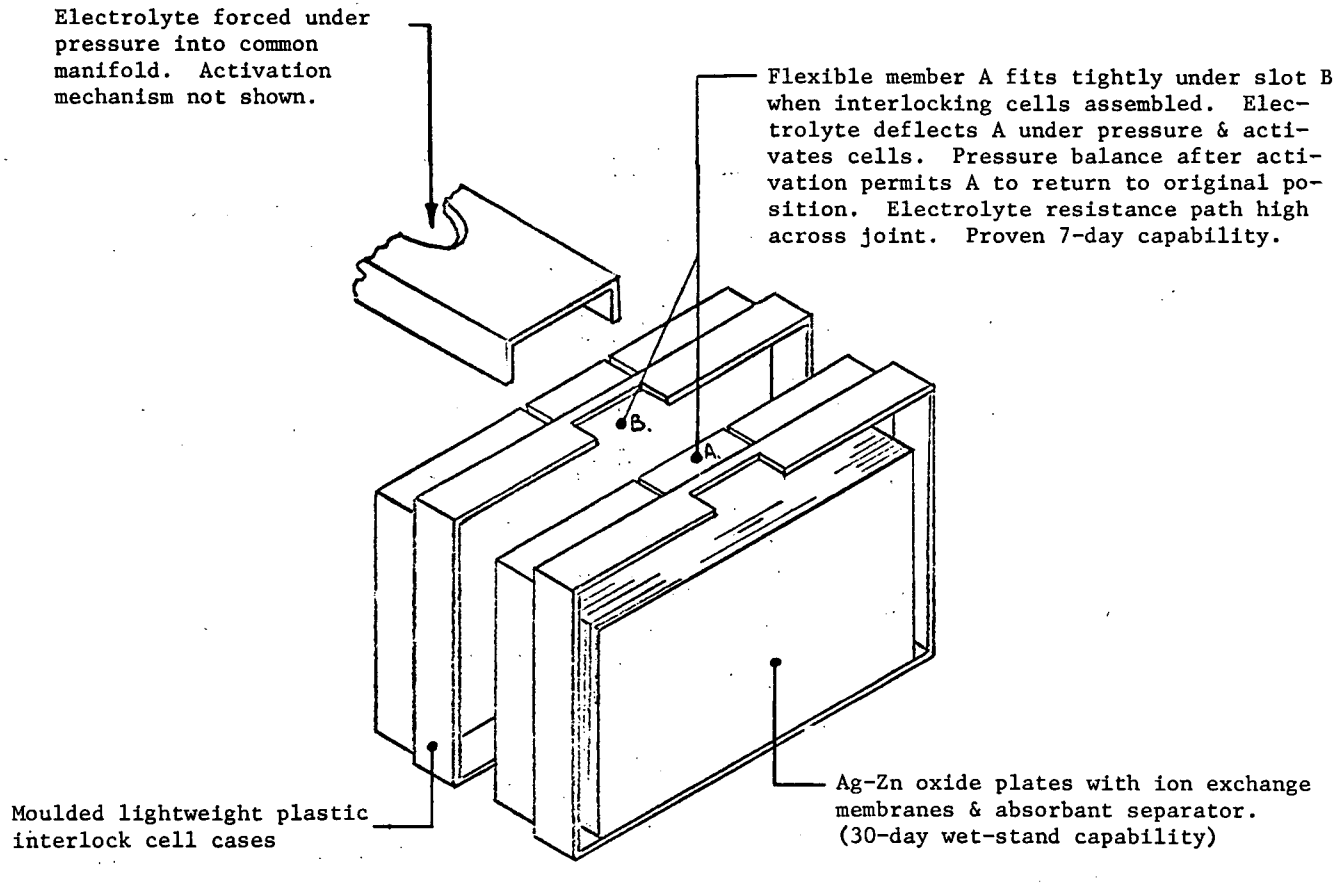

Note: System designed & qualified for 7-day wet-stand requirement.

Fig. VI-39 Remotely Activated 30-Day Wet-Stand Design Concept 1

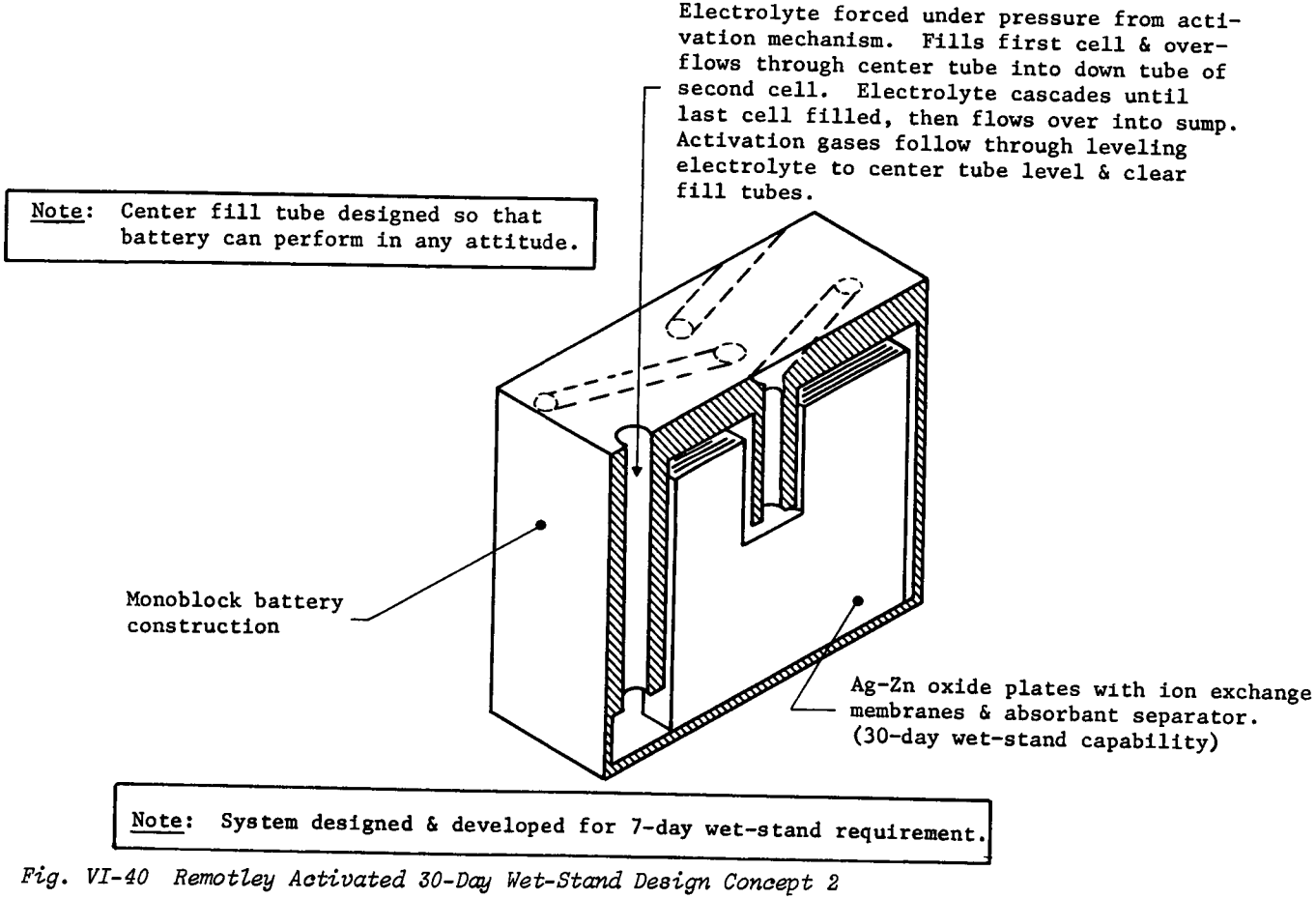

Fig. VI-40 Remotley Activated 30-Day Wet-Stand Design Concept 2

Figure VI-40 shows a more conservative design that increases energy density, but eliminates intercell shorting. Electrolyte enters Tube A and enters the first cell at the level of Tube B. It travels up Tube B across to the next cell and down Tube A of the second cell. This process is repeated until the last cell is filled. Excess electrolyte continues to move into a final compartment where it is centrifuged into an absorbent material. The activation mechanism is designed so activating gases follow through with the electrolyte and purge the tubes and intercell paths of electrolyte. This design, like the other, will operate in any attitude. As before, separator material would be changed to a semipermeable membrane.

Both designs were developed for the Royal Aircraft Establishment, England, for a 7-day activated mission. It is expected that the design in Fig. VI-40 could exceed this requirement, but a 30-day stand would be a marginal concept. Conceptually, a revised design would be capable of providing a 30-day wet stand with a high degree of confidence.

6) watt-Hour Design Margins

If it is assumed that electrolyte leakage paths can be eliminated and the whole design concept is based on this assumption, the following margins can be applied when sizing the battery.

With up-to-date design methods, a 40-W-h/lb battery can be manufactured.

Start with 40 W-h/lb.

Apply degradation rates:

a) Dry stand loss 3% per year below 90°F; it would be undesirable to fly the battery at a higher temperature;

b) Activated stand loss 0.5% per day;

c) If sterilization is required, loss is 25%, with nor further loss due to dry-charged stand.

Items a) and b) can be supported by characteristics of primary Ag-Zn batteries like those used on Titan III and Biosatellite, and torpedo batteries. Item c) causes loss of perioxide, which in a normal design would be 50%. However, because this loss is known, the Zn plate capacity would be reduced accordingly, and the weight gained would be transferred to the positive plate.

7) Temperature Performance Activated

Normal operating temperatures should be 30 to 80°F. However, if load requirements are known, the battery could be designed to perform at lower temperatures, around 10°F. The high-temperature restraint is not required on discharge, but has a degrading factor on the stand.

2. Pyrotechnic Subsystem

The pyrotechnic subsystem is similar to designs already applied to several space vehicles like Mariner and Viking. Specific constraints and devices considered for this design were principally derived from Viking, which has severe restrictions on weight and a radiation environment. The pyrotechnic subsystem consists of power-conditioning equipment, relay switching control, control logic, and capacitor banks for high-pulse discharge.

The pyrotechnic control system derives power and initiating signal from several sources.

1) Separation events - Initial charging of the capacitor banks and initiation signal are provided by the spacecraft. After the postseparation battery has been activated, power is then derived from the probe postseparation battery.

2) Postseparation events - Power is derived from the probe post-separation battery and initiation signals from the probe data-management system.

3) Preentry battery event - Power is derived from a 40-V Hg-Zn battery. This is the only function for this battery, which must maintain the capacitors on charge for about 20 min. The initiation signal is derived from the electromechanical (Accutron) timer.

4) Preentry events - Power is derived from the probe preentry battery. Initiation signals are provided by the data management system.

a. Power - Except for the entry battery pyro event, all power conditioning required in the pyrotechnic control subsystem is generated by an internal power supply. Outputs are not regulated and have a tolerance of ±10%. The outputs consist of two 40-V windings completely isolated from each other and from all other windings. Voltages, which are provided for internal use, are:

Capacitor charging	+40
Relay switching	+28
Logic circuitry	+5
Digital interface circuitry	±5

The supply has an output capability of approximately 50 W and a standby power dissipation of 450 mW. Because the supply is essentially in the standby condition at all times, except for approximately 5 sec after each event, the assumed average power requirement is 0.5 W.

b. Relay Assembly - Magnetic latching relays are used for pyro firing functions as well as for safing and arming. This is a deviation from the Viking approach, which uses SCRs for firing. The modification results from the suceptibility of SCRs to the high-radiation environment near Jupiter. The relay selected for this purpose and for estimated weight and size is Potter Bromfield Type HL 4125 (MIL-R-5757). The relays weigh 0.029 kg (0.063 lb) with a volume of 11.12 cm^3 (0.68 $in.^3$). The present configuration assumes one relay for each side of the redundant squib and one for safing and arming in the common lead. This approach requires three relays for each event.

Considerations to be evaluated for this design are the effect of contact bounce on the operation of the squib, possible fusing of contacts (which would leave the capacitor banks connected to the squib circuit), and testing problems. The contact fusing problem could be eliminated by adding another relay for each event and performing safing and arming directly in series with the contacts of the initiator relay. An alternative configuration could use the common-lead relay for firing. However, this would accentuate the effects of contact bounce on the performance reliability. Testing may be a severe problem because the first operation is likely to cause significant damage to relay contacts. A simulated test that measures contact bounce and contact resistance may be sufficient. The effect on the squibs cannot be predicted at this time. The manufacturer is reluctant to reduce the specification on contact bounce below 2 msec. Firing time of the squib is approximately 0.4 msec and further study will be required to evaluate this problem. Present Viking design calls for operation of the relay with 8 to 18 V applied across the coil. A 1600-Ω coil design ensures sufficient power to operate the relay from the low-energy Hg-Zn battery, which initiates the preentry phase of the mission.

c. Capacitor Banks - Each capacitor bank contains six 82 μF capacitors rated at 50 V. These wet-slug tantalum capacitors are required to deliver 150 mJ in 5 msec into a 1-Ω circuit. Each capacitor bank is required to fire six initiators, one at a time. No two initiators can be fired by a capacitor bank within a 12-sec period. The design is planned to permit charging all capacitor banks from either side of the power supply through charging resistors. Failure of one or several banks will not produce a serious load on the power supply. One possible exception to the resistive cross connection may be the capacitor banks that fire the entry battery pyrotechnics because these are energized by a low-capacity long-life Hg-Zn battery.

The design and application of the pyrotechnic subsystem does not depart significantly from state-of-the-art designs, and in particular, the Viking design. One aspect that must be given further consideration, because of the nature of the probe mission profile, is the conditioning of the pyrotechnic capacitor banks. Because the various probe designs will have been electrically quiescent for approximately 18 months before separation, the capacitor banks will need to be reconditioned for approximately 1 hr. A more critical requirement will occur after the quiescent coast period. This represents a significant problem because of the lack of available power. The design approach is to provide a 40-V Hg-Zn battery that will provide charging current and maintain charge for approximately 20 min on two capacitor banks. These capacitor banks will then provide the energy to fire the entry pyrotechnic. The actuator that initiates the capacity charging and provides the firing control will be mechanically closed by contacts in the electromechanical (Accutron) timer. A 40-V battery will be used to avoid the need for power conditioning. The only function of this battery is to provide charge current to the capacitor banks, leakage current during the conditioning period, and power to operate the relay initiator logic.

d. Interface - Except for the entry battery pyrotechnic event, all pyrotechnic event control will be provided through the data management subsystem. The control signal will be in the form of parallel digital address, enable, fire, and safe commands. The pyrotechnic subsystem will be enabled by applying power through a power control relay in the power distribution control.

D. REFERENCES

VI-1 A. P. King: "The Radiation Characteristics of Conical Horn Antennas," *Proc. IRE*, Vol 38, March 1950, p 249 thru 251.

VI-2 R. E. Collin and F. J. Zucker: *Antenna Theory, Part I*, McGraw-Hill, 1969, p 644 thru 646.

VI-3 J. D. Kraus: *Antennas*, McGraw-Hill, 1950, p 371 thru 381.

VI-4 H. Jasik: *Antenna Engineering Handbook*, McGraw-Hill, 1961, p 10.1 thru 10.13.

VI-5 M. G. Schorr and F. J. Beck: "Electromagnetic Field of the Conical Horn," *Journal of Applied Physics*, Vol 21, August 1950, p 795 thru 801.

VI-6 G. C. Southworth and A. P. King: "Metal Horns as Directive Receivers of Ultra-Short Waves," *Proc IRE*, Vo. 27, February 1939, p 95 thru 102.

VI-7 H. J. Reich: *Very High-Frequency Techniques*, Vol 1, McGraw-Hill, 1947, p 153 thru 157.

VI-8 "Evaluation Program for Spacecraft Secondary Cell," (Prepared for GSFC Contract W12,397) Quality Evaluation Laboratory NAD Crane, Indiana.

VI-9 C. F. Palandati: "Electron Radiation Effects on Silver Zinc Cells," X-716-68-136. GSFC, 1968.

VI-10 E. M. Morse: "Eagle-Picher Silver Zinc Automatically Activated Batteries," Bulletin No. 101, Eagle-Picher.

VII. PROBE MECHANICAL SUBSYSTEMS

The mechanical subsystems include structures, mechanical, thermal control, and propulsion.

The primary structural elements are the beryllium nose cap, cylindrical skirt assembly, and rocket motor mount. Mechanical systems used on the probe are the probe-to-spacecraft structural separation and removable lens cover for the photometer experiment.

In the interests of simplicity and reliability, probe thermal control is passive, using multilayer insulation, finishes, and radioisotope heaters. Thermal control of the probe while on the S/C will be discussed in Chapter IX, and the probe alone will be discussed here. A trade study to determine whether the multilayer insulation blanket should be outside or within the structure was done, and thermal inertia was traded against isotope heaters as a means of maintaining temperature during coast.

Selection of the propulsion subsystems was based on both cost and weight considerations. A parametric study was conducted that related total system weight to total impulse for cold-gas (N_2), hydrazine catalyst, and solid propulsion subsystems. This study provided the basic data necessary to select the deflection propulsion subsystem. A cold-gas propulsion system was selected for the other propulsion requirements--spin, despin, and precession.

A. STRUCTURES AND MECHANICAL

1. Heat Sink

The primary functional requirement is to protect the probe and its systems from degradation caused by entry heating from turbopause to end of mission. Other requirements are to enclose the electrical and science equipment, support the insulation blanket, survive launch loads, support the RPAs and Langmuir probes.

To meet the primary requirement, the heat shield must withstand both high heating rates and a large amount of heat. Because of these demands, and the need to minimize weight, beryllium was selected. It is uniquely high in specific heat (1.67 J/kg °K at room temperature, 2.93 J/kg °K at 920°K), low in density, and high in strength-to-density ratio. All these characteristics are desirable to meet design requirements. Ablator-protected structures were not considered because of the contamination of mass spectrometer samples and optical instrument window. The heat sink consists of a hemispherical nose cap and cylindrical skirt. Thermal response of the heat sink to entry heating was computed for entry angles of -15, -25, and -35°. Stagnation, 30° off stagnation, 90° off stagnation, and the leading edge of the cylindrical skirt were analyzed.

Selection of heat-sink thickness for each altitude is based on thermal deformation criteria, front face melting, and strength considerations.

a. Thermal Analysis - Figure VII-1 shows the geometry of the heat sink. The nose cap is 76.2 cm (30.00 in.) OD and the skirt length is 23 cm (9.00 in.). The nose cap is constant thickness from Point A to Point B, then tapers linearly to Point C. Point D, the leading edge of the cylindrical skirt, is the same thickness as Point C and is constant thickness.

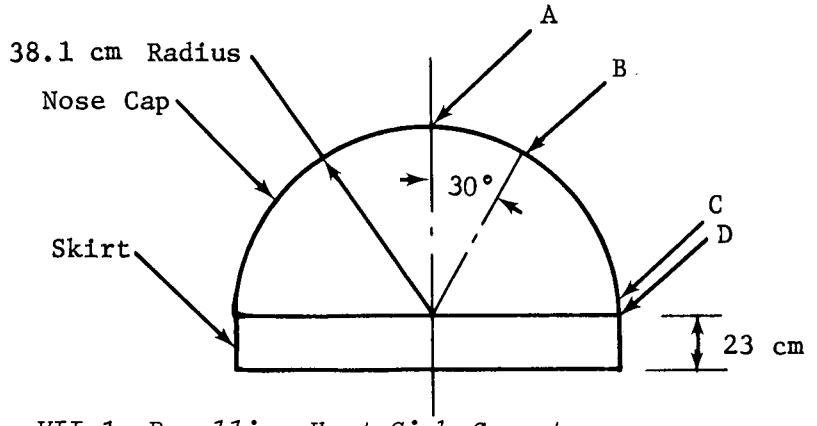

Fig. VII-1 Beryllium Heat-Sink Geometry

The stagnation heat load versus altitude is developed in Chapter X, and heating distribution for a 0.765-m-dia (30-in.-dia) hemisphere is given in Fig. VII-2 and VII-3. Heating is primarily convective over the range of altitudes considered in this study.

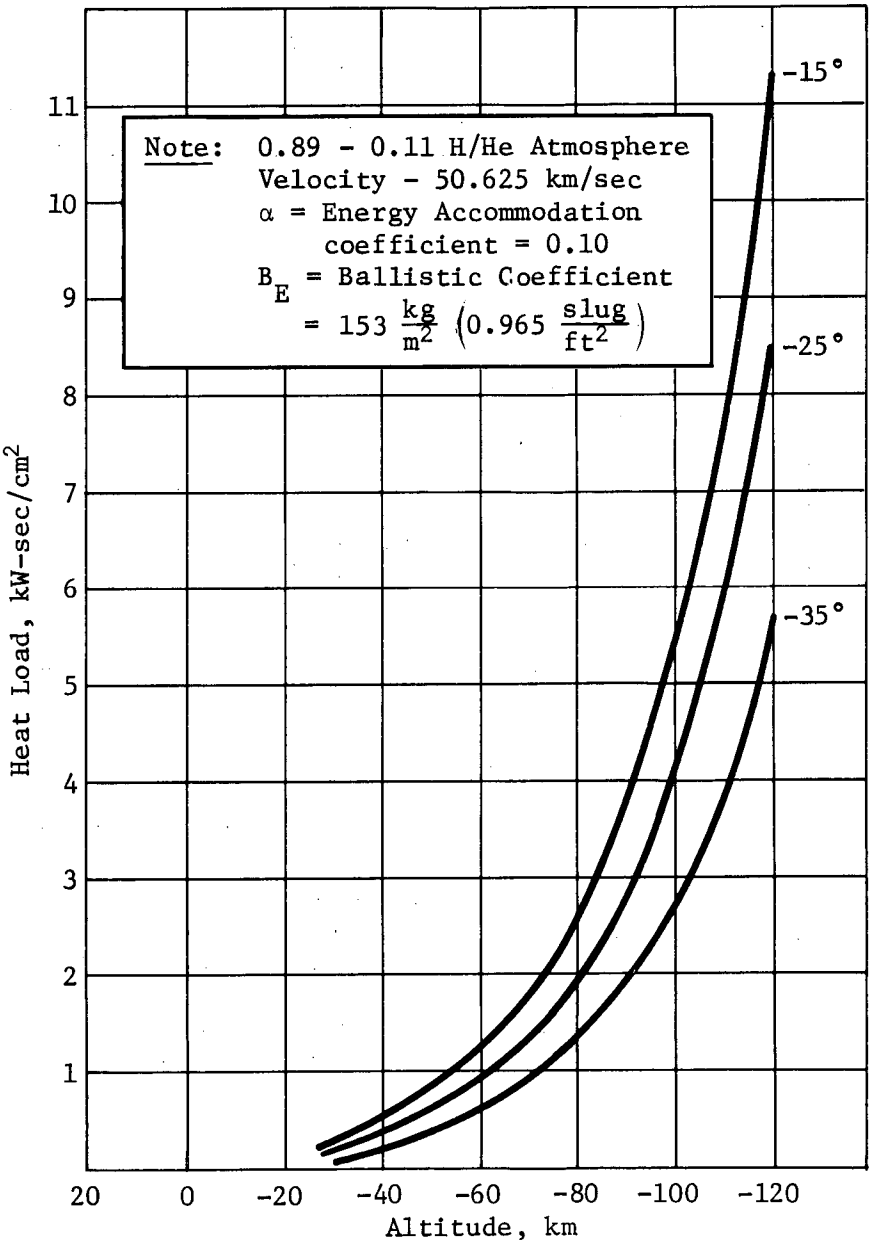

Fig. VII-2 Stagnation-Point Total Heat Load, Hemisphere Configuration

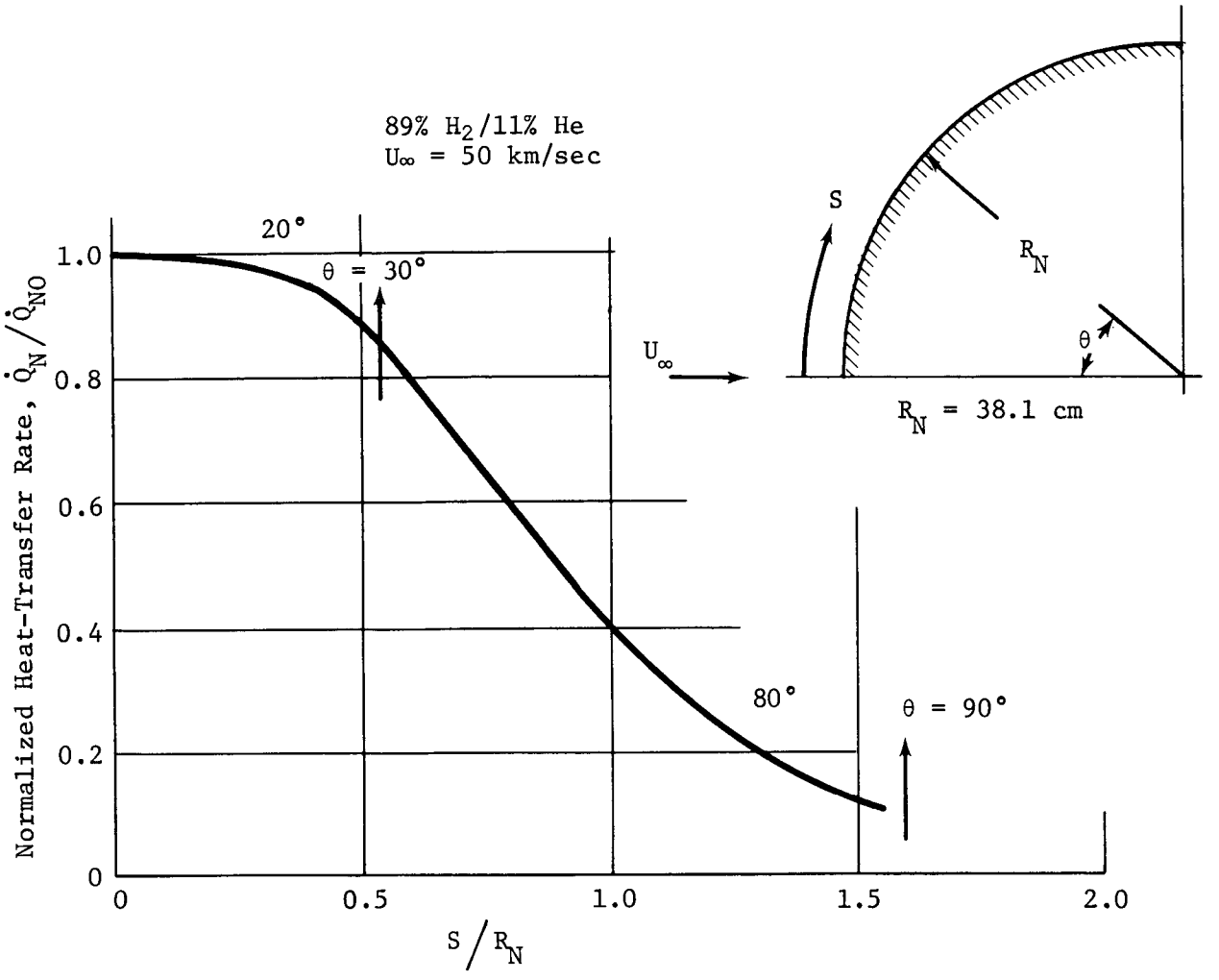

Fig. VII-3 Continuum Flow Analysis, Off-Stagnation Point Heating

The thermal response of Points A through D is computed using a generalized heat-transfer program, Martin Marietta Integrated Thermal Analysis System (MITAS). A one-dimensional analysis determs the temperature distribution through the thickness of the heat sink, using a 10-element model with resistance and capacitance, radiation of the external element, and adiabatic backface.

A matrix of heat-sink thickness versus entry angle for Points A through D used in the study is shown in Table VII-1. The results of this analysis is shown in Fig. VII-4 through VII-9. Figure VII-4 presents the thermal response of the heat sink at -15° entry angle at Points A and B for front face and back face, and mid-thickness of Point A for both -60 km and -70 km as a function of heat-sink thickness. Figure VII-5 presents similar data for -80 km and also provides frontface and backface temperatures of Points C and D (skirt) for -60 km and -70 km. Figures VII-6 and VII-7 present similar information for -25° entry angles, and Fig. VII-8 and VII-9 for -35° entry angles.

Table VII-1 Matrix of Thicknesses and Entry Angles Used in Parametric Study

Point	Thickness		Material	Entry Angle		
	cm	in.		35°	25°	15°
A	1.27	0.50	Be			X
	1.0	0.40			X	X
	0.76	0.30		X	X	X
and	0.63	0.25		X	X	X
	0.51	0.20		X	X	X
	0.38	0.15				
B	0.20	0.08				
C	0.23	0.090	Be	X	X	X
	0.20	0.080		X	X	X
and	0.17	0.070		X	X	X
	0.15	0.060		X	X	X
D	1.27	0.050		X	X	X

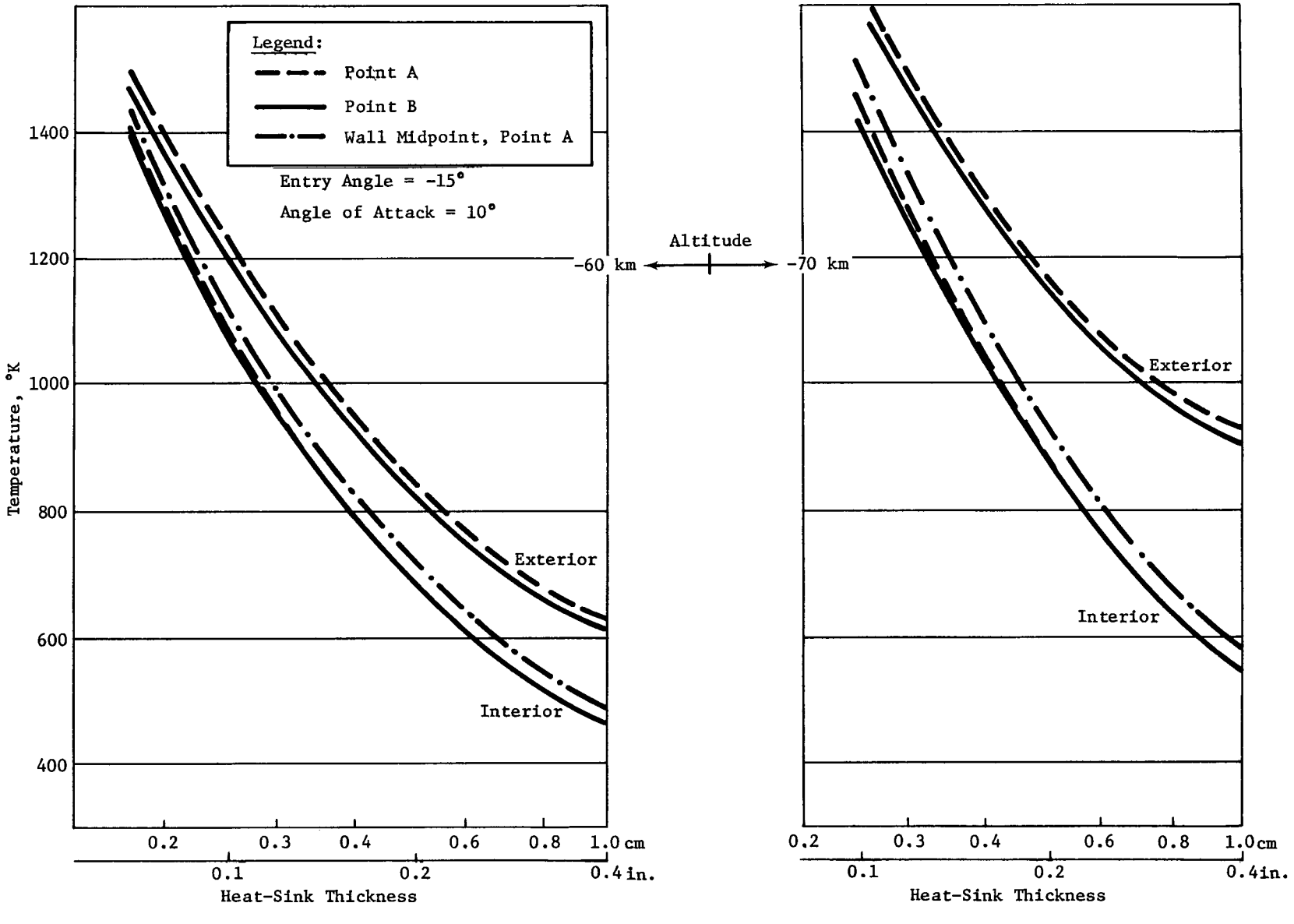

Fig. VII-4 Thermal Response of Heat Sink at -15° Entry Angle

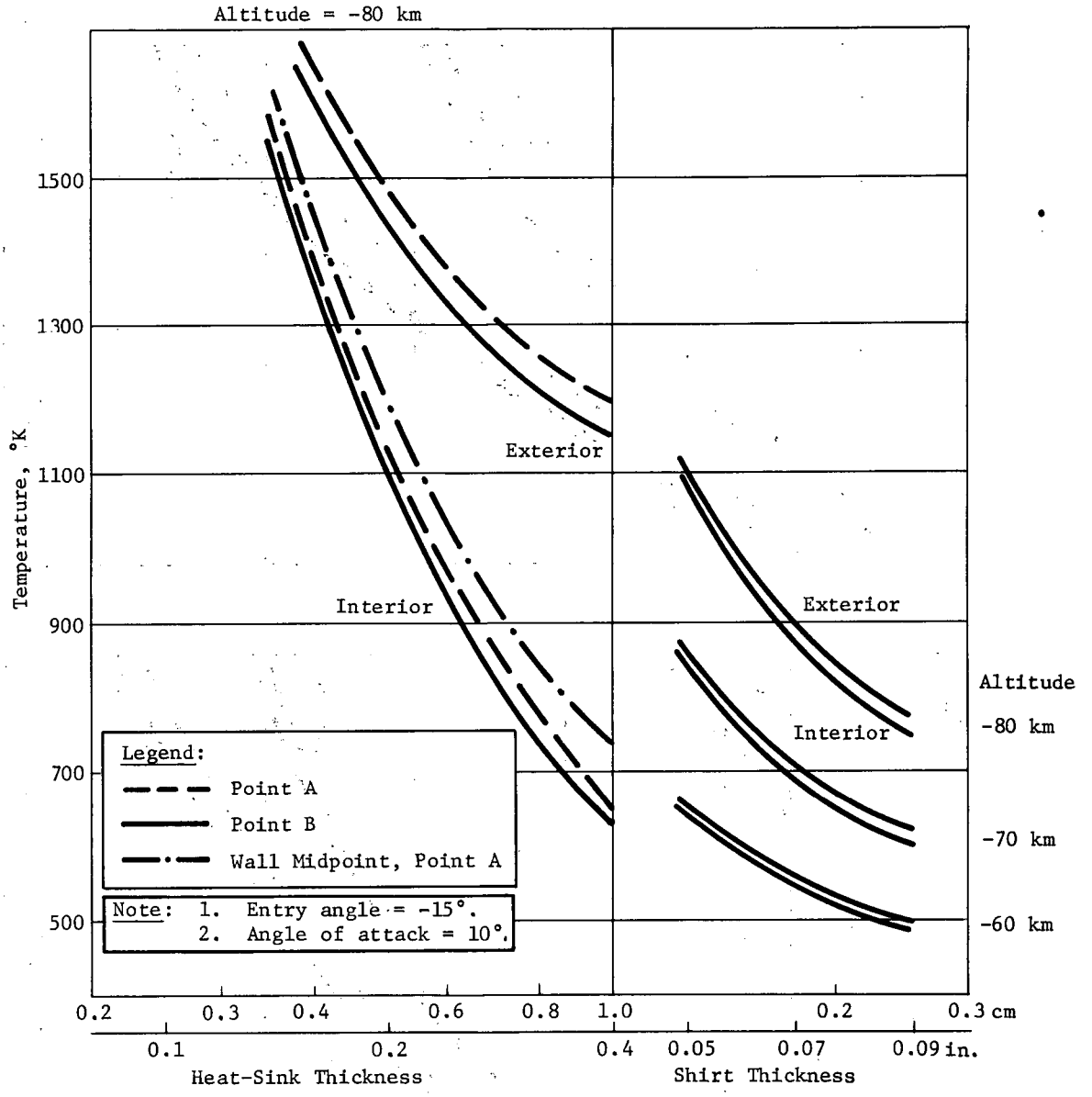

Fig. VII-5 Thermal Response of Heat Sink and Skirt at -15° Entry Angle

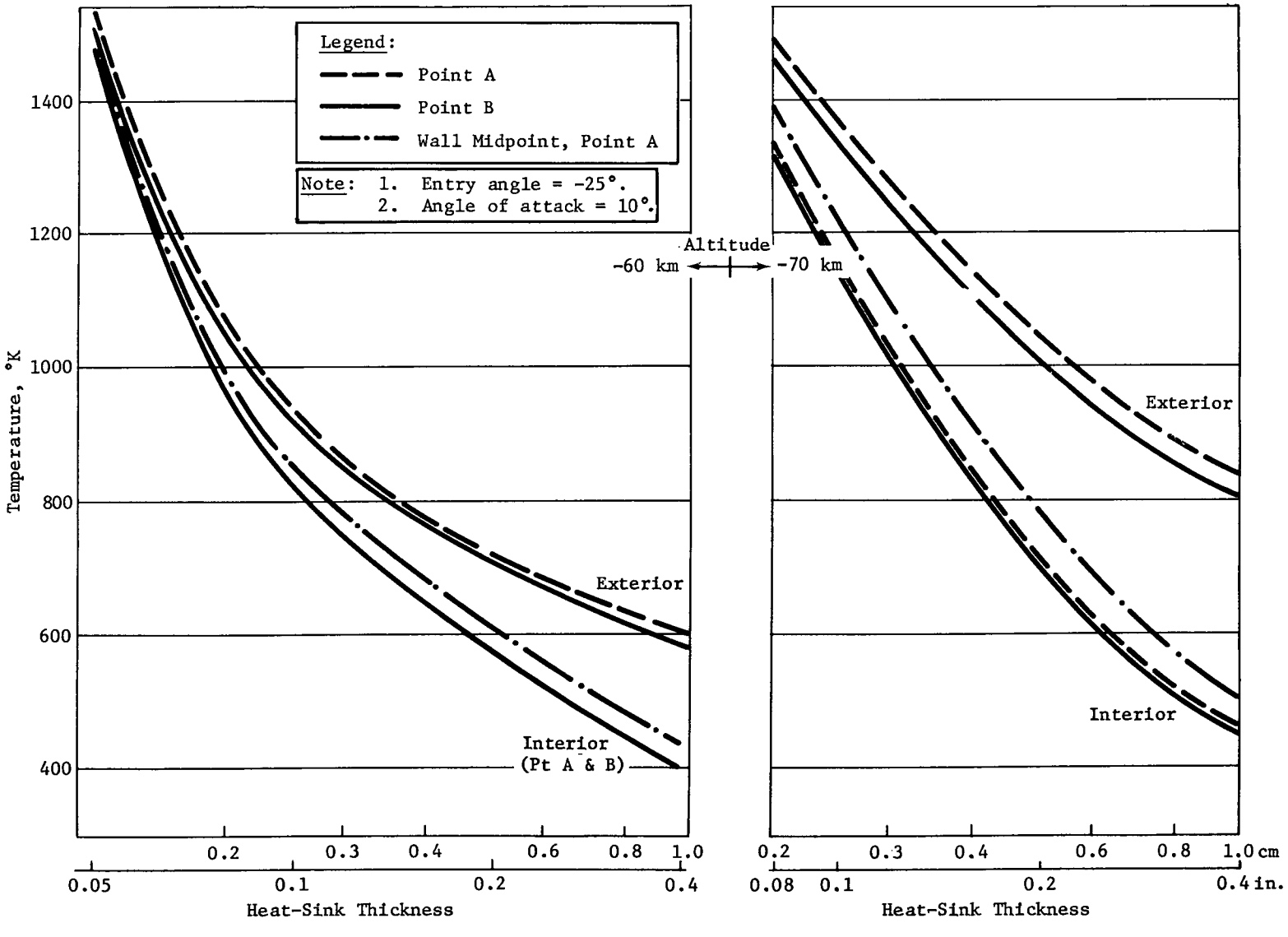

Fig. VII-6 Thermal Respone of Heat Sink at -25° Entry Angle

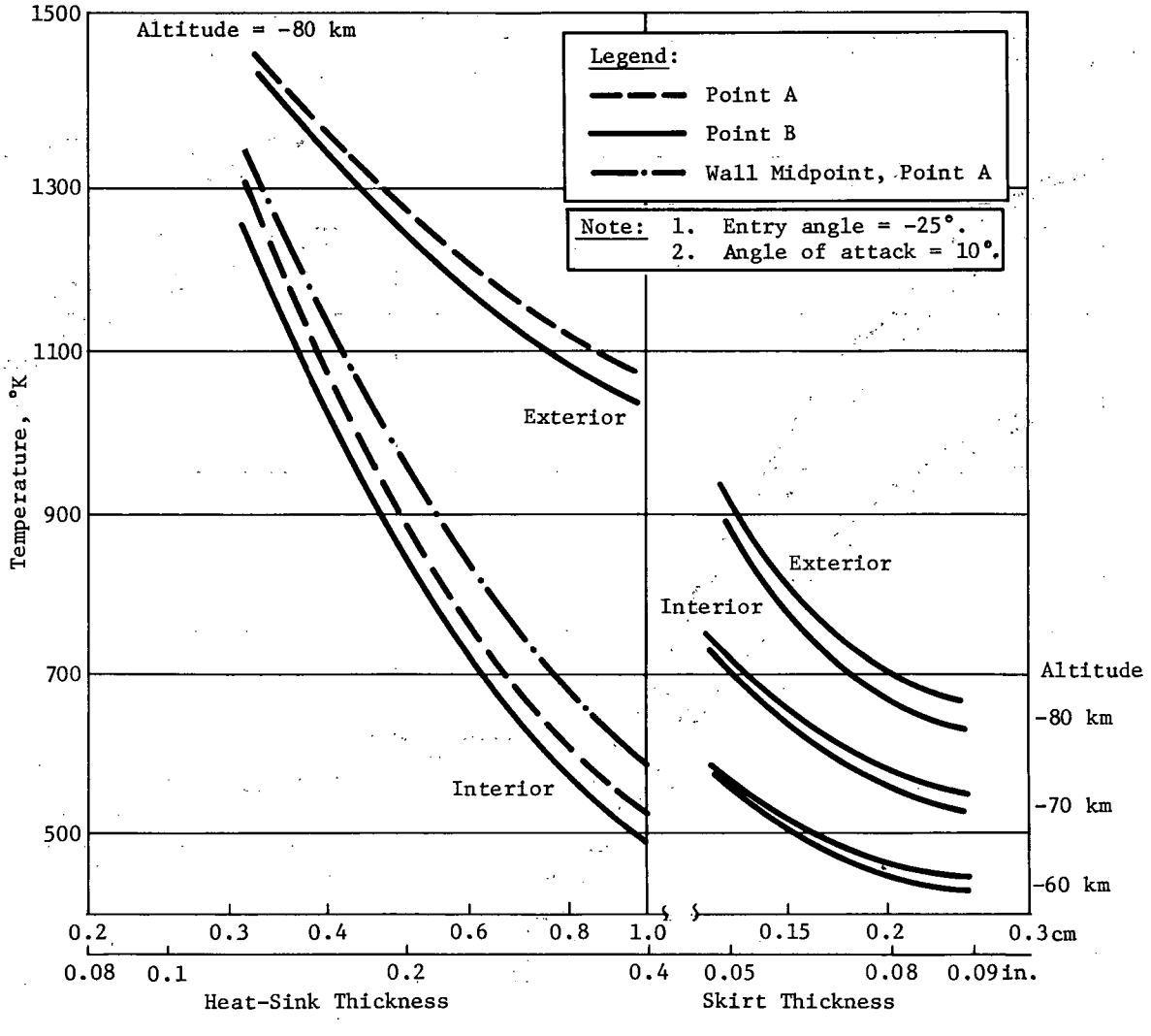

Fig. VII-7 Thermal Response of Heat Sink and Skirt at -25° Entry Angle

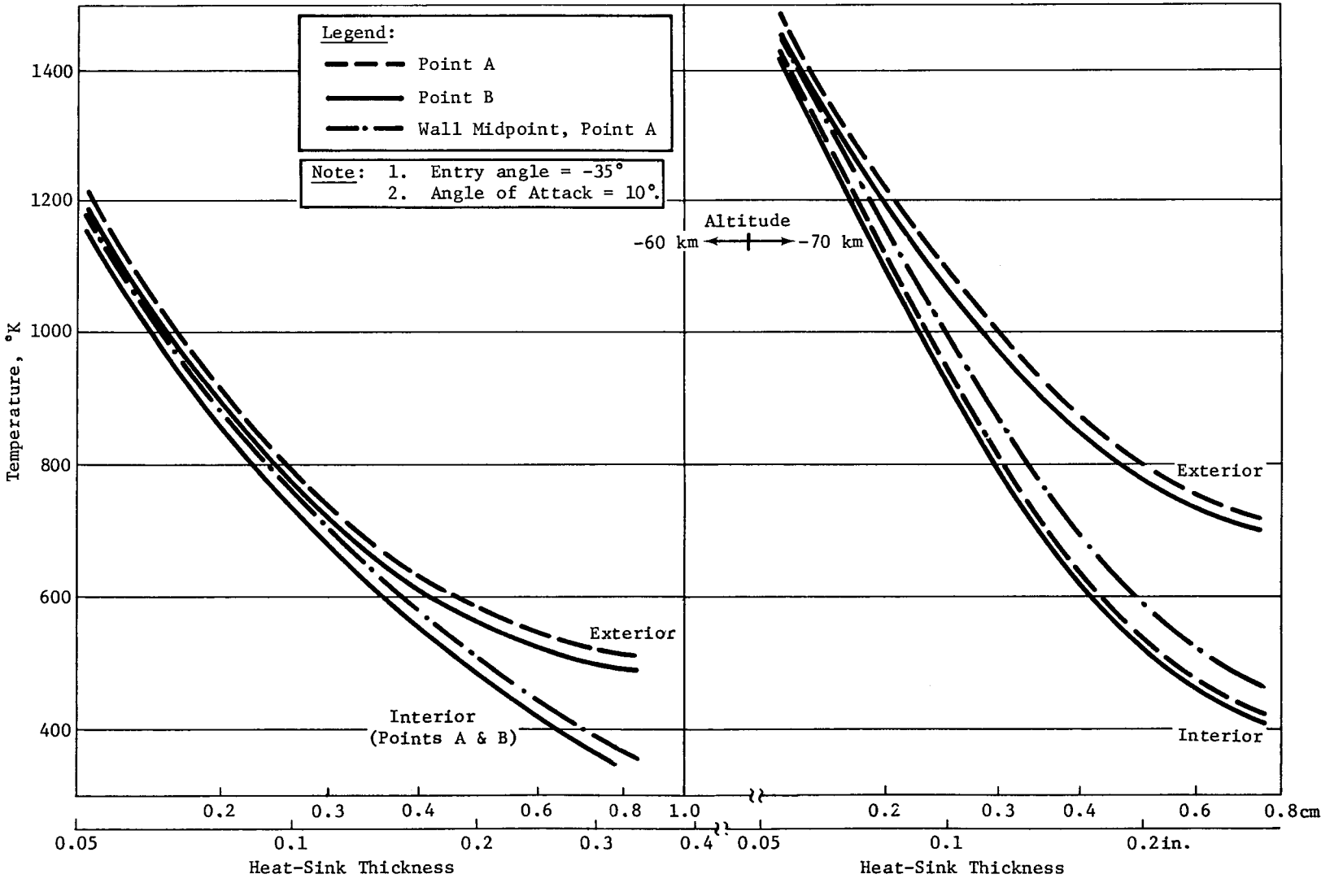

Fig. VII-8 Thermal Respone of Heat Sink at -35° Entry Angle

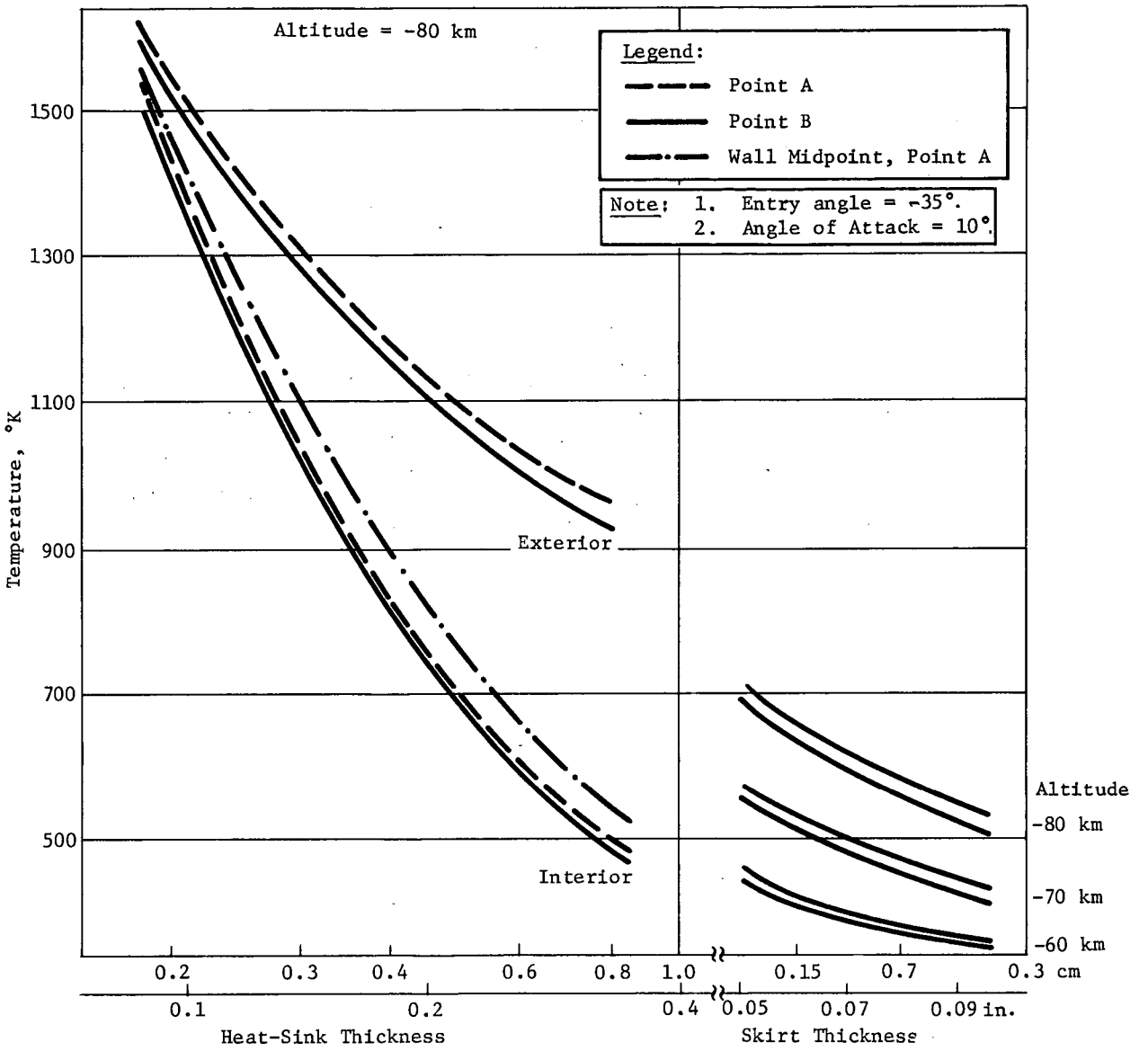

Fig. VII-9 Thermal Response of Heat Sink and Skirt at -35° Entry Angle

b. Evaluation of Thermal Effects on Heat Sink - Modes of failure induced by the entry heating considered are:

1) Thermal stresses and strength at temperature;

2) Surface melting;

3) Backface temperature effects.

Thermal stresses during entry heating are accentuated by the extremely short temperature rise time. Figure VII-10 presents a typical entry with a -35° entry angle. At 50-km/sec entry velocity, the altitude rate is -30 km/sec. This results in approximately 2.6 sec from onset of heating to structural failure. This rapid heating appears to present a problem in thermal stress.

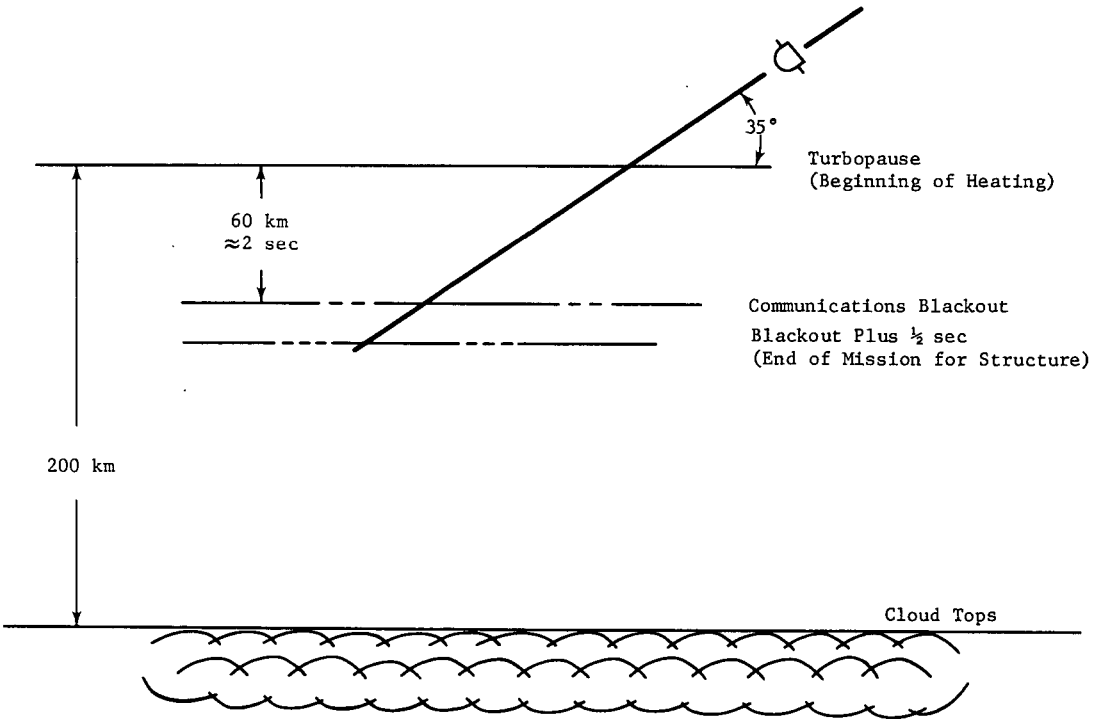

Fig. VII-10 Typical Entry of Jupiter Turbopause Probe

The thermally induced stresses for a -35° entry angle were investigated using the Martin Marietta SA005 computer program. The program determines displacements and stresses within plane or axisymmetric solids with nonlinear material properties by replacing the

continuous body with elements of triangular or quadrilateral cross section. Stresses and strains for a nose cap with a 0.51-cm (0.20-in.) thickness at Points A and B and 1.8 mm (0.070 in.) at Point C were analyzed at -70 km and -80 km. (See Appendix A, Vol III.)

A section of the spherical cap was modeled using 528 elements and 686 nodes. Resulting stresses are presented in Fig. VII-11 and VII-12. The outer surface of the shell is in compression caused by greater thermal expansion of the outer surface and restraint by the cooler backface. The backface is in tension. The peak tension stress is $238.0 \times 10^6 \frac{N}{m^2}$ (34,480 psi) at 33° from stagnation for -70 km and moves around to 47° and $253.0 \times 10^6 \frac{N}{m^2}$ (37,340 psi) for -80 km. The peak tensile deformation found was 0.0014 m/m.

A complete parametric study using the SA005 program was beyond the scope of this study; therefore, the following method was employed.

The thickness was selected to maintain a temperature so that the beryllium has a minimum of 3% elongation to failure or a minimum of 20% of room-temperature strength for the material stressed in tension. If outer-surface melting occurs before the above criteria are met, thickness will be set by the melting criteria. The minimum thickness considered was 1.27 mm (0.050 in.).

The above criteria are considered reasonable and conservative based on the small amount of deformation found in the finite element analysis (0.0014 m/m) and also because externally applied loads are negligible. At -100 km, aerodynamic decelerations are on the order of 9.75 m/sec^2.

The backface temperatures at -80 km at -15° entry angle are a maximum of 930°K. A high-temperature insulator such as Refrasil or Q felt will be installed between the heat sink and the Kapton multilayer insulation, which degrades at 645°K. To protect the Kapton at this condition, 1.5 mm of Q felt at 80 kg/m^3 (5 lb/ft^3) is required. This weight is negligible.

Figure VII-13 presents the beryllium properties of interest. The heat-sink thickness and weight are shown in Table VII-2 and Fig. VII-14.

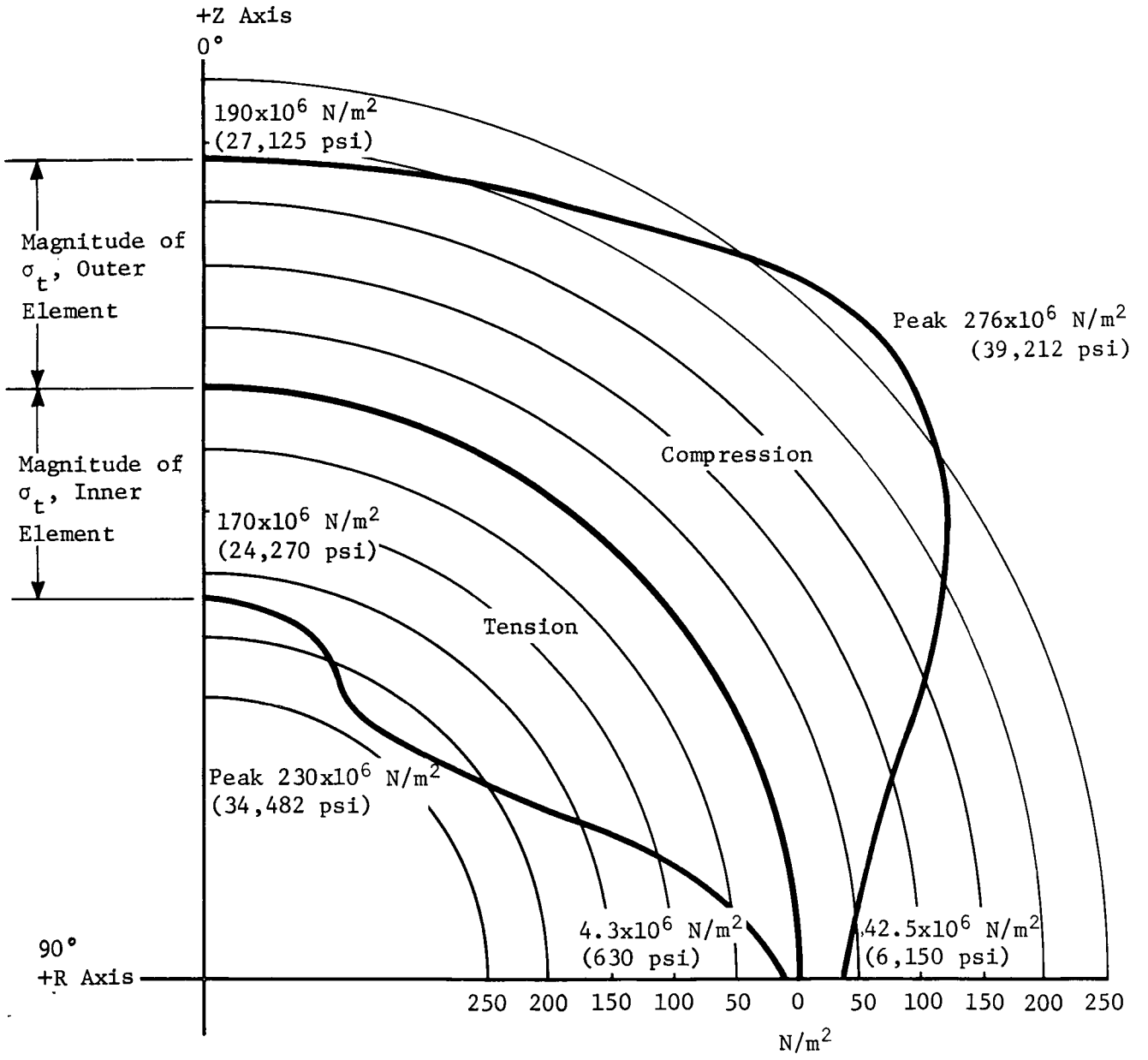

Fig. VII-11 Tangential Stress, σ_t for Outer and Inner Elements at Altitude of 70 km below Turbopause

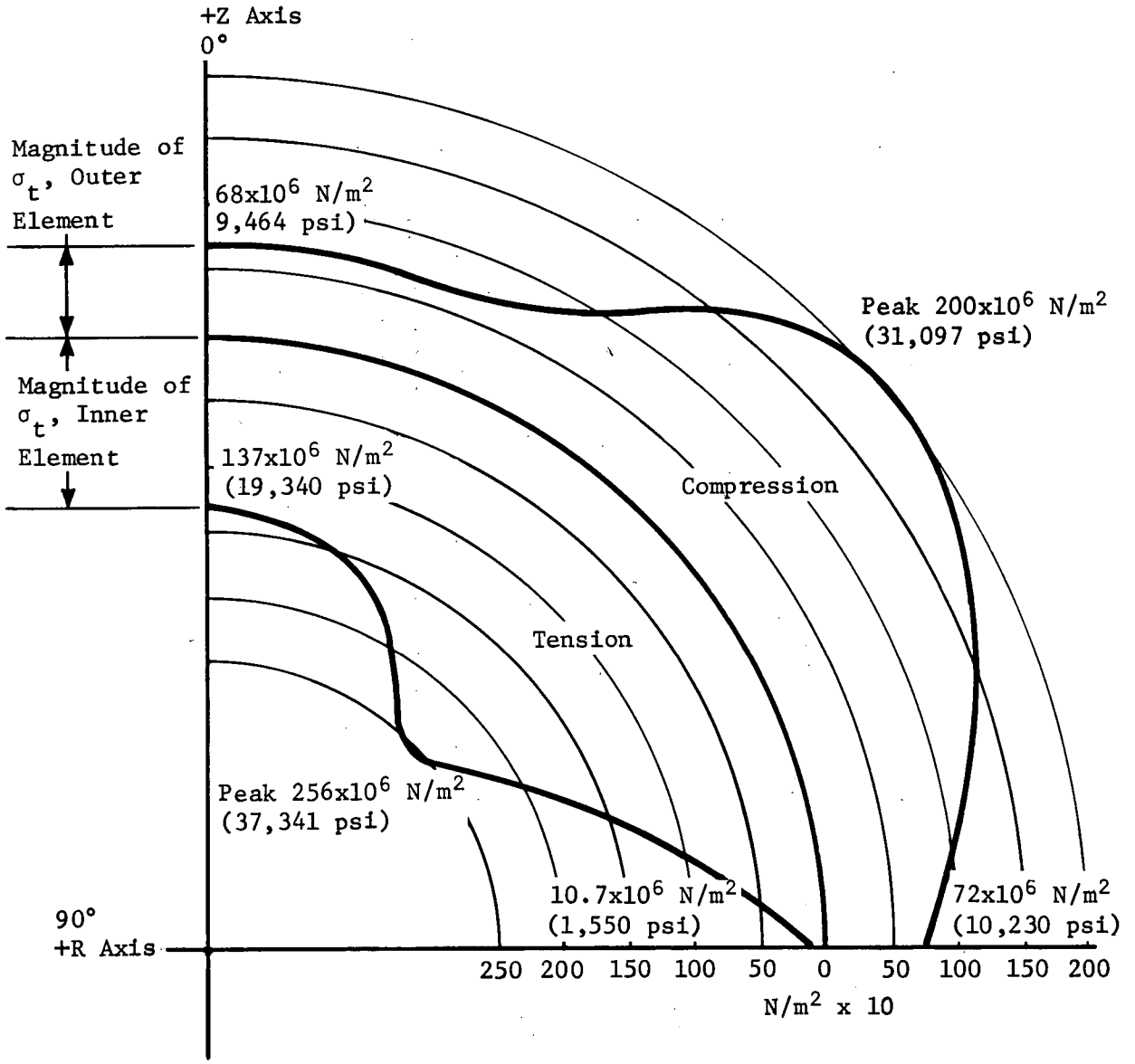

Fig. VII-12 Tangential Stress, σ_t for Outer and Inner Elements at Altitude of 80 km below Turbopause

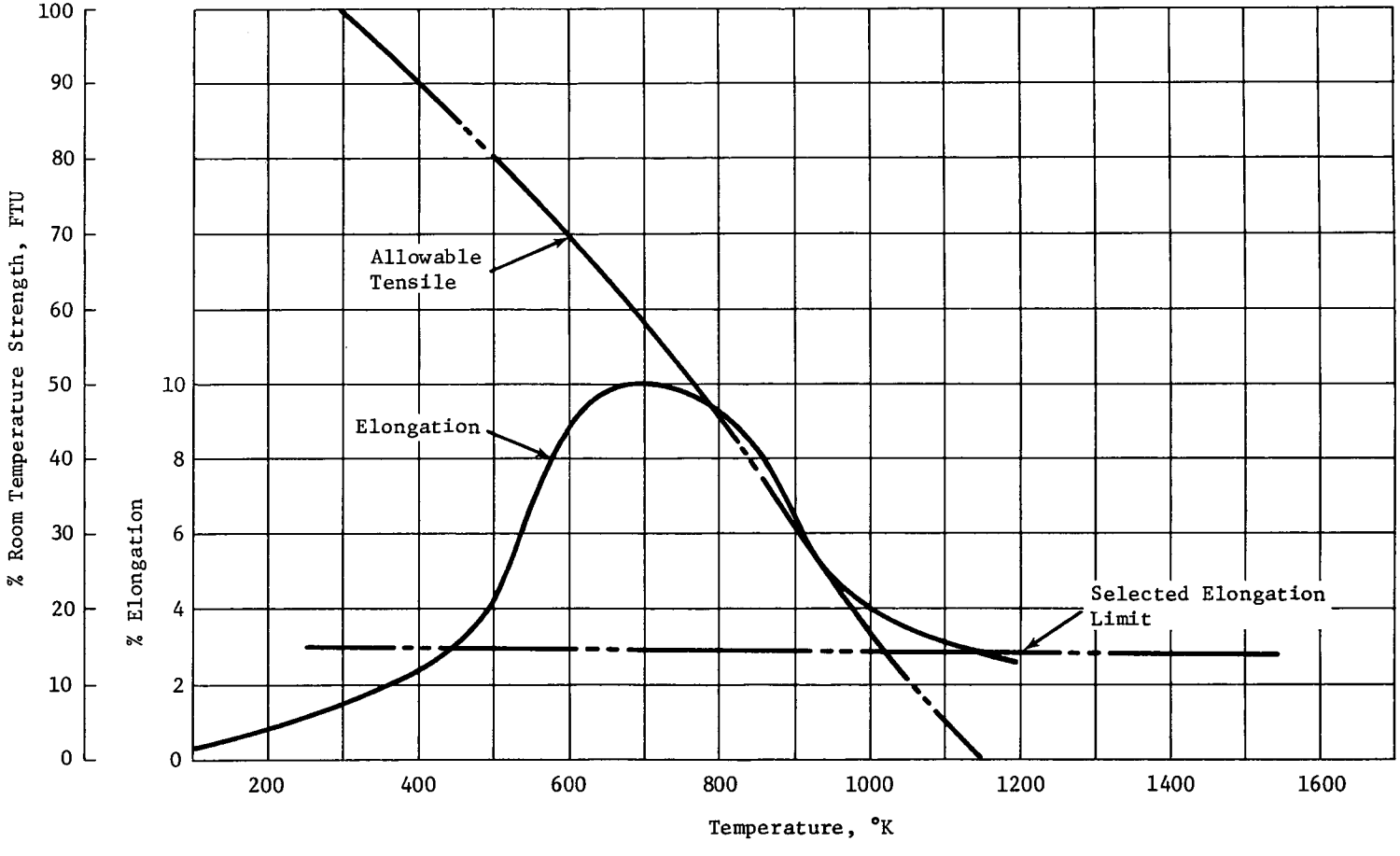

Fig. VII-13 Effect of Temperature on the Elongation of Beryllium

Table VII-2 Heat Sink Thickness versus Entry Angle and Altitude

Entry Angle	Altitude, km	Thickness, in., cm			
		A & B		C & D	
-15°	-80	0.252	0.645	0.062	0.158
	-70	0.190	0.480	0.050	0.130
	-60	0.165	0.320	0.050	0.130
-25°	-80	0.195	0.495	0.050	0.130
	-70	0.145	0.370	0.050	0.130
	-60	0.085	0.216	0.050	0.130
-35°	-80	0.148	0.377	0.050	0.130
	-70	0.106	0.270	0.050	0.130
	-60	0.069	0.176	0.050	0.130

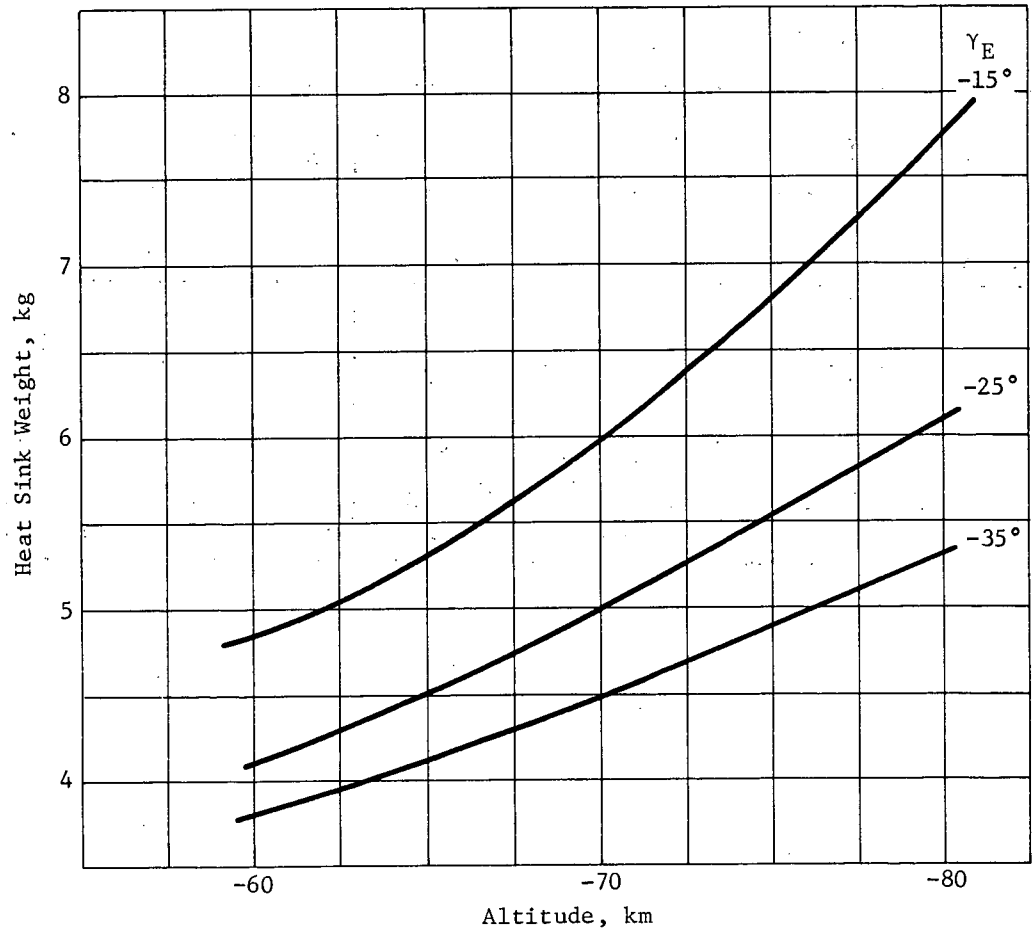

Fig. VII-14 Heat-Sink Weight vs Altitude, Cap Plus Skirt

c. Conclusions

1) A rigorous analysis of the heat sink was beyond the scope of this study. To perform a complete parametric analysis, bi-axial material properties must be obtained.

2) Low entry angles penalize probe weight, but survival to -80 km appears reasonable down to a 15° entry angle.

2. Structures

a. Design Loads - Design loads for the probe primarily result from launch accelerations. Entry decelerations are only 1.25 g at burnout. A summary of the launch load factors is presented in Table VII-3. Longitudinal accelerations are those experienced at Burner II burnout. Lateral accelerations occur at liftoff for the Viking payload and are considered representative. The 1.25-g lateral load factor is associated with a 1.5-cps vibration.

Table VII-3 Launch Load Factors

	Mission						
	1	2	3	5	1A	2A	7
Longitudinal Acceleration, g	18.5	18.5	9.0	17.5	18.5	18.5	9.0
Lateral Acceleration, g	1.25	1.25	1.25	1.25	1.25	1.25	1.25
Launch Vehicle	TIIID/ 5-Seg Centaur Burner II	→	TIIID/ 5-Seg Centaur Burner II	TIIID/ 5-Seg Centaur Burner II	→	→	→
Spacecraft	Pioneer	Pioneer	TOPS	Pioneer	Pioneer	Pioneer	MOPS

The design conditions for the structural assemblies are given in Table VII-4.

Table VII-4 Design Conditions for Structural Assemblies

Structural Assembly	Design Condition
Heat Sink	Entry Heating Pulse (See Subsection VII A1.)
Skirt Assembly	Launch Loads (Except for Be Skin which is Sized by Heating or Min Gauge Depending on Entry Angle (See Subsection VII A1.)
Deflection Motor Mount	Deflection Motor Thrust
RPA Masts	Entry Heating

b. Description - The structural interface between the probe and probe spacecraft adapter is shown in Fig. VII-15. All tension loads are transmitted across the interface by two bolts, 180° apart, at two primary longerons. Compression loads are transmitted at three equally spaced points, one a primary longeron 90° from the tension bolts, and two secondary longerons. Two shear pins adjacent to the tension bolts assure accurate probe positioning and transmit lateral shear loads.

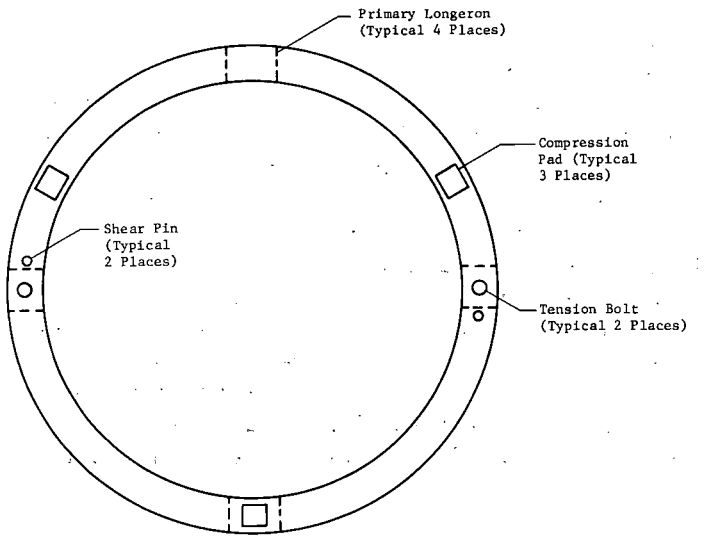

Fig. VII-15 Probe/Spacecraft Structural Interface

For all missions studied, the structural elements shown in Fig. VII-16 and VII-17 meet configuration and structural requirements. Basic diameters evolved to 0.714 m (38 in.) and 0.764 m (30 in.) for simple and complex probes, respectively. The simple probe design does not require an attitude-control system, separation battery, deflection propulsion system and motor mount, and can therefore be smaller. Figure VII-16 presents the structural elements for the complex probe. The structure is divided into three assemblies--nose cap, rocket motor mount, and skirt assembly. The skirt assembly consists of the equipment shelf, main ring frame, primary longerons, secondary longerons, aft ring frame, and aft bulkhead.

The nose cap is primarily a heat sink and is sized for that function rather than for loads.

The rocket motor mount is an assembly of aluminum rings and a glass/epoxy composite cylinder. The glass/epoxy was selected because of good strength and low thermal conductivity that is essential to reduce heat loss from the compartment during coast. The glass/epoxy cylinder is designed for the compression load of deflection engine firing.

The equipment shelf is a circular bonded aluminum honeycomb structure supported at four points by the four primary longerons. A plastic insert is provided at each of these structural pickup points to increase thermal resistance, and thus, conserve thermal energy during coast. Science, electronic, and propulsion components mount on both forward and aft surfaces of the equipment shelf.

The main ring frame is machined aluminum alloy that serves to react moments about the primary longerons caused by lateral loads on the equipment shelf and to shear these lateral loads into the beryllium skin of the skirt assembly. The aft ring frame similarly shears the load out of the beryllium skin into the shear pins at the separation interface. At the forward and aft edges of the beryllium skin, the ring frames form coaxial-hoop continuous rings inside the skin. Large changes in temperature that will occur after manufacture cause thermal stresses to develop at this interface. For beryllium, the cold extreme is 117°K (-250°F) and the hot extreme is 950°K (1240°F). A preliminary simplified analysis, which did not account for the tie from the main ring frame to equipment shelf, indicates a differential expansion of 1.65 mm (0.065 in.) in the cold case for beryllium and aluminum.

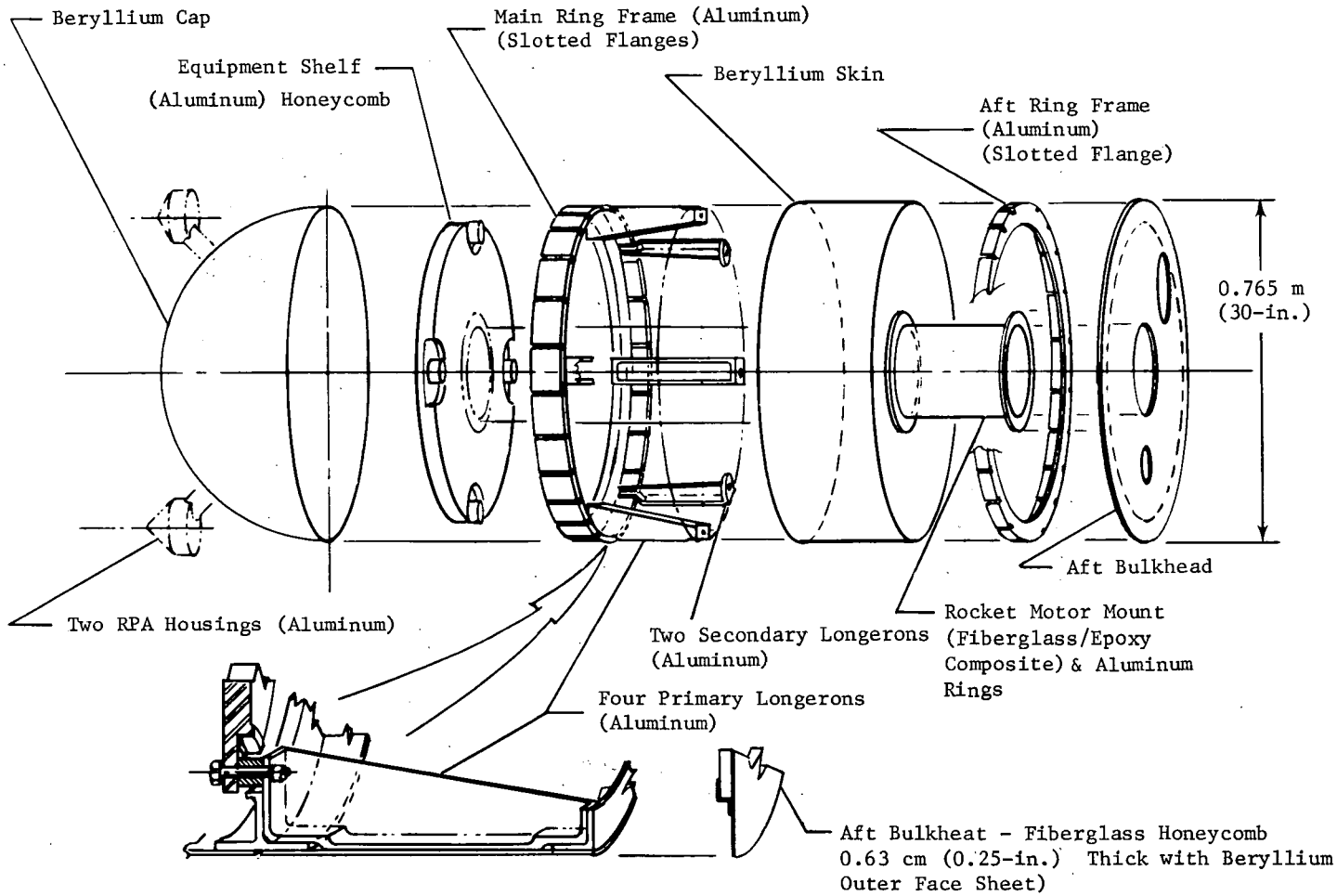

Fig. VII-16 Jupiter Turbopause Complex Probe Structure

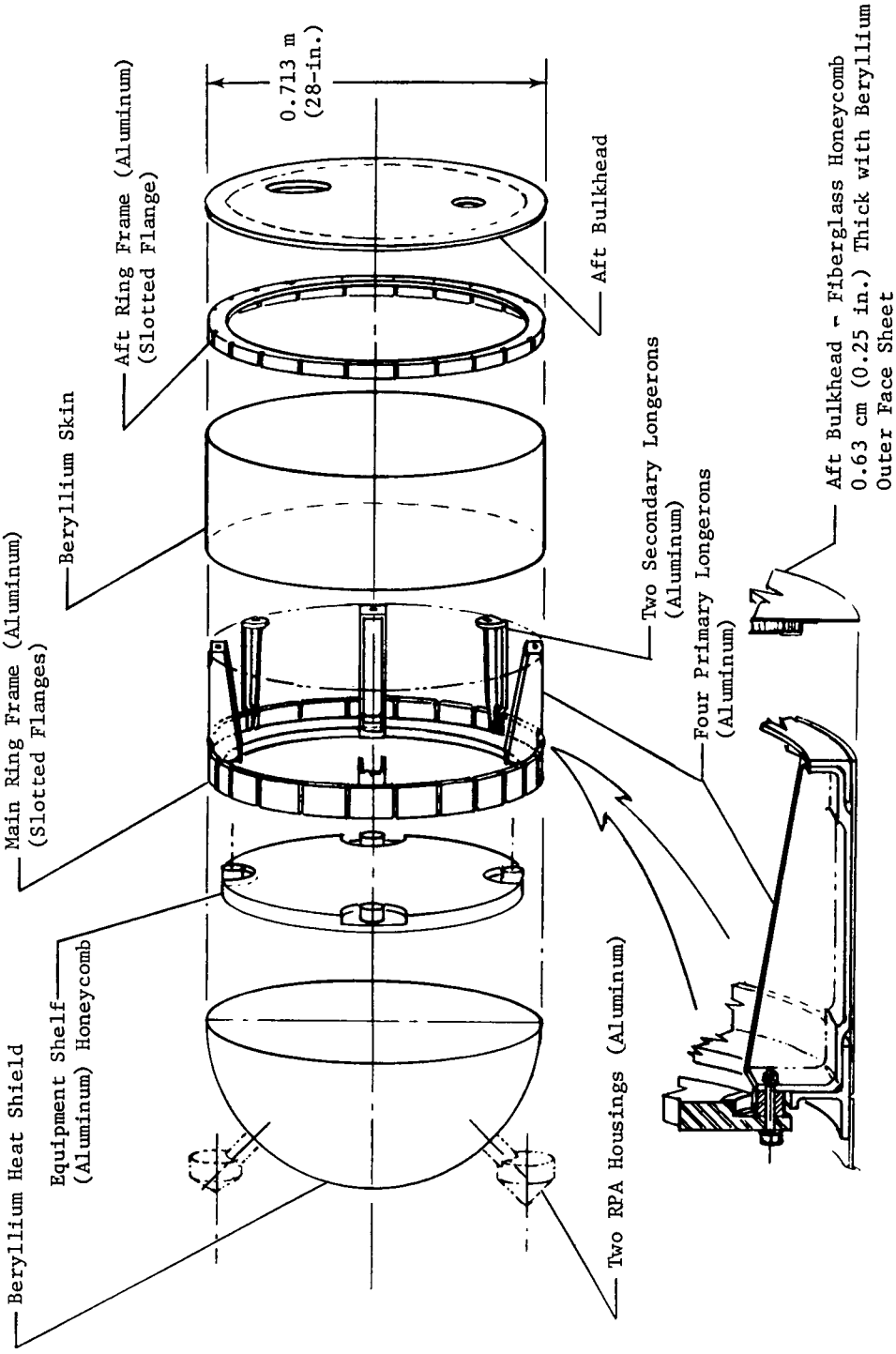

Fig. VII-17 Jupiter Turbopause Simple Probe Structure

Similarly, for beryllium and titanium, the differential was 0.20 mm (0.008 in.). The cold case places the beryllium in compression. Therefore, the joining fasteners would be in tension. With the fasteners in tension and the beryllium in compression, inter-fastener buckling must be investigated. In the high-temperature case, analyses are complicated by the difficulty of predicting thermal coupling of the beryllium to the main frame flange. To avoid these problems, the slotted-frame flange design was selected.

The primary longerons are aluminum alloy machined bathtub fittings riveted to the ring frames and beryllium skin. The forward end bolts to the equipment shelf and the aft end is fitted with a bolt catcher (in two cases) and with a pressure pad (in two cases). Two of the primary longerons carry all tension loads from the probe to the probe/spacecraft adapter.

The secondary longerons are machined aluminum alloy tee fittings. They are riveted to the beryllium skin and carry compression loads across the probe/spacecraft interface, along with one primary longeron.

The aft bulkhead is a fiberglass honeycomb composite structure with a beryllium outer face skin to reduce the thermal response during entry. It closes the equipment compartment and stabilizes the aft ring frame. Large circular cutouts are necessary for the deflection motor nozzle and probe conical horn antenna.

c. Weight - The analysis that sized the nose cap is presented in Subsection A1. This analysis also set the thickness of the beryllium skirt skin at 1.27 mm (0.050 in.) minimum. A free-body static analysis of the skirt structure under launch longitudinal and lateral loads shows that all shear flows in the beryllium skin are small compared to capability, 8700 N/m (50 lb/in.) load.

The weight of the remaining structural elements is presented in Table VII-5 for both 0.71-m (28 in.) and 0.76-m (30 in.) dia probes.

The motor mount is designed by the deflection motor thrust, which loads the structure in compression. The thrust load is approximately 1110 N (250 lb). A 0.18-m (7.0-in.) diameter fiberglass tube with 0.51-mm (0.020-in.) walls would be expected to carry 8,400 N (1,900 lb), so the design of the mount is basically dictated by minimum gage considerations.

Table VII-5 Structure and Weight Estimate Summary

Item	Description	Weight			
		0.713-m dia		0.765-m dia	
		lb	kg	lb	kg
Engine Mount	Aluminum rings (3) 18-cm dia fiberglass/epoxy cylinder 18 cm long	0.0	0.0	1.5	0.68
Skirt Assembly					
Main ring frame	Aluminum 1.06 cm^2 (0.165 $in.^2$) (1)	1.5	0.68	1.6	0.73
Aft ring frame	Aluminum 0.65 cm^2 (0.10 $in.^2$) (1)	0.9	0.41	1.0	0.46
Primary longeron	Aluminum (4)	2.2	1.00	2.0	0.91
Secondary longeron	Aluminum (2)	0.2	0.09	0.2	0.09
Aft bulkhead	Fiberglass honeycomb panel, 0.63 cm thick (0.25 in.) 0.76 mm thick (0.030 in.) Be outer skin on aft face	3.7	1.68	4.2	1.91
Equipment shelf	1.9 cm thick, 0.25-mm face, 77 kg/m^3 core density (0.75 in. thick, 0.010-in. skins, 4.8 lb/ft^3 core density)	4.6	2.1	5.3	2.40

The ring frames are 1.27 mm (50 mil) basic thickness with some additional cap area on the main ring frame to carry the moments introduced by the longerons. The skin shear flow is approximately 1210 N/m (7 lb/in.) and the longeron induced moment approximately 21.4 N-m (190 in.-lb).

The weight of the primary longerons is established more by such functional requirements as wrench clearance and bolt-catcher dimensions than loading. The maximum limit load identified as the main longeron is approximately 7800 N (1530 lbf).

The aft bulkhead weight is composed primarily of the 0.76 mm (30 mil) beryllium outer skin and the adhesive used to join the assembly. These items alone account for 20% of the weight. A core density of 64 kg/m^3 (4 lb/ft^3) was assumed.

The equipment shelf was analyzed as a beam with equipment uniformly distributed. To account for dynamic amplification, a load factor of 35 g was used. This resulted in a peak bending moment of 1020 N-m (9000 in.-lb) or 14.2 N-m/cm (320 in.-lb/in.) of width. These loads resulted in a design selection of 1.9 cm (0.75 in.) panel thickness, 0.25 mm (10 mil) face sheets, and 77.0 kg/m^3 (4.8 lb/ft^3) aluminum core.

3. Probe Mechanical Subsystems

The mechanical subsystems consist of a photometer aperture cover and a spacecraft/probe structural separation system.

The purpose of the photometer aperture cover is to protect the photometer sensor from damage and contamination during launch and flight modes (Fig. VII-18). It fits into a machined fitting, which is part of the external structure of the probe. This fitting supports the cover, cover deployment device, and a sealing surface for the metal bellows closeout between the photometer and external structure of the probe. The cover is retained in the fitting by four integral tabs on the inside diameter of the retaining ring. These tabs will bend when the pyro pin pusher is activated, apply a prying load on the cover lever, releasing the cover from the probe structure.

The spacecraft/probe structural separation system must serve two functions. The first is to provide structural load paths between the S/C and probe for launch loads that separate on command, and second, to provide energy for the separation of the probe from the spacecraft.

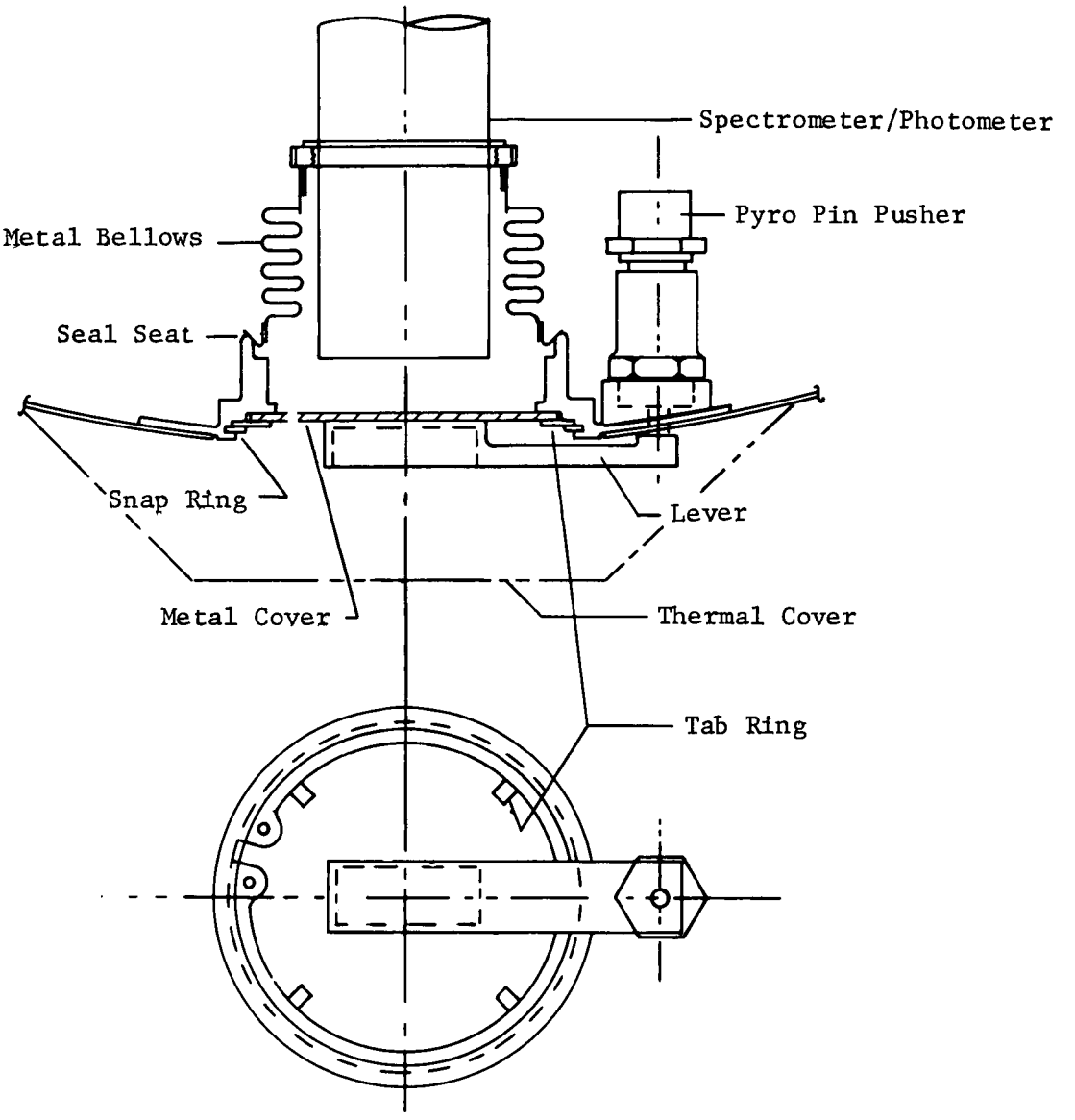

Fig. VII-18 Spectrometer/Photometer Cover

During launch, the separation system must transmit loads produced by a large longitudinal acceleration (9 to 18.5 g, depending on the S/C) and a small lateral acceleration ($\sim$ 1.25 g). Longitudinal acceleration of launch produces a tension load on the separation system. An additional small tension load is produced by the separation springs. For a description of how these loads are carried see Subsection A2b.

The tension load-carrying interface members are the two tension bolts and pyro separation nuts. They carry the longitudinal load and component loads due to side load. The tension bolts are attached to two primary longerons in the probe, and the pyro-activated retention nuts are mounted on the spacecraft adapter ring as shown in Fig. VII-19. Side loads are transferred by two positioning shear pins on the same primary longerons as the tension bolts. The two longerons are equipped with bolt catchers to prevent damage to the probe when the pyro-activated retention nuts release the tension bolts during separation of the probe from the spacecraft. The separation spring cartridges are in the compressed position and serve as a three-point compression load path across the interface for the probe during the launch and flight modes.

The end of the spring cartridges that interface with the probe are conically shaped pins for easy disengagement during separation. They fit into sockets in the back of the probe to ensure that there is no relative lateral motion between S/C and probe during ejection. At ejection, the spring cartridges supply a relative separation velocity of 0.91 m/sec (3 fps) with a 10.2 cm (4 in.) stroke. Each spring exerts a load of approximately 178 N (40 lb). These cartridges have a centerline guide rod with an L/D bearing overlap of approximately 5:1 for stability. The spring cartridges have an adjustable stroke to compensate for manufacturing tolerances, assuring that all three units have equal energy, thereby minimizing tip rate during separation.

4. Mass Properties

Weight estimates for each mission are reported in Chapter V. Center-of-gravity location, mass moments of inertia, and inclination of principal axes were computed for early versions of Missions 1, 2, and 3. The results are summarized in Table VII-6. The cg location is referenced to the stagnation point of the probe.

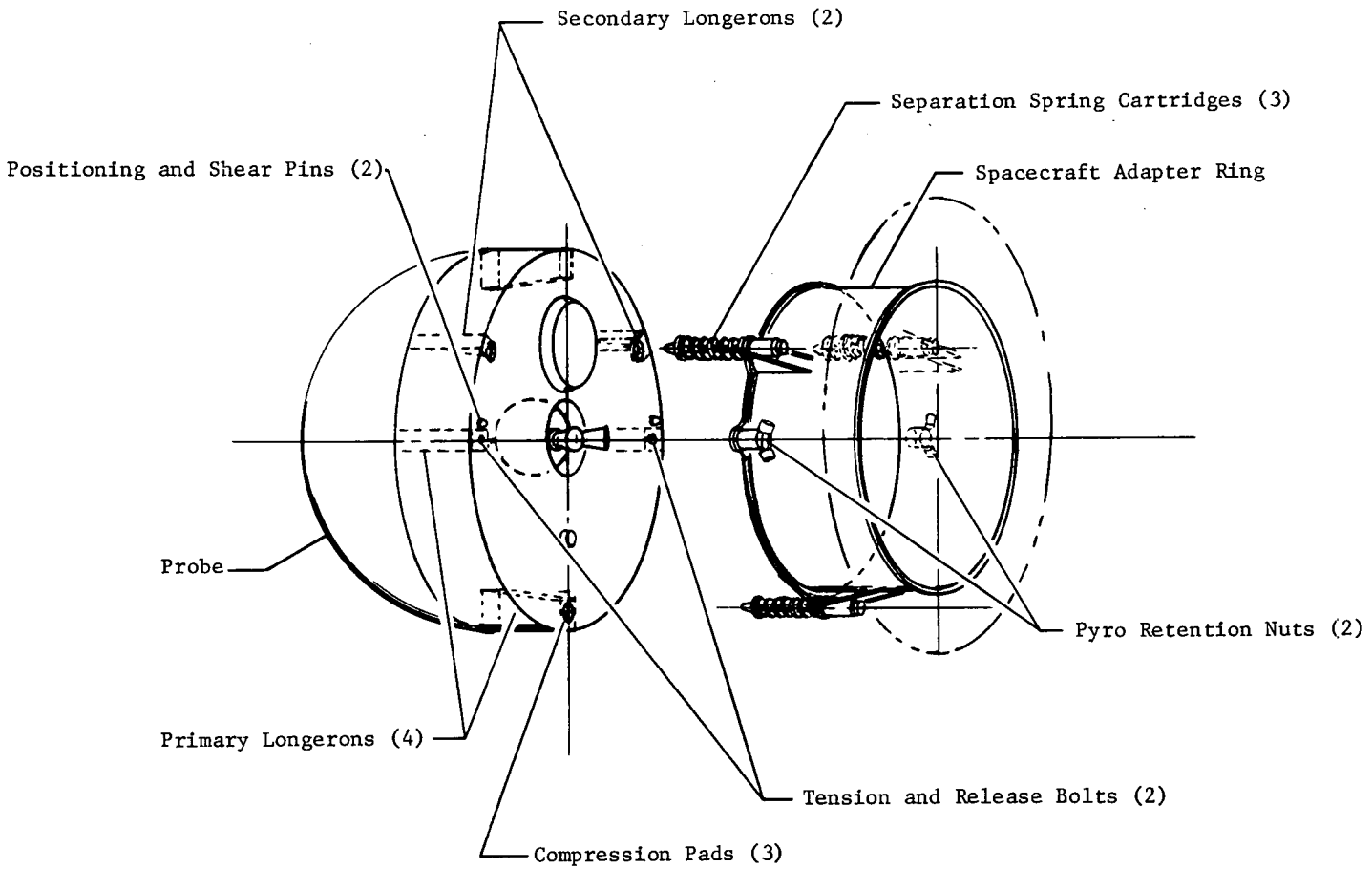

Fig. VII-19 Jupiter Turbopause Probe/Spacecraft Support and Separation System

Table VII-6 Summary of Mass Properties Analysis

	Units	Mission		
		1	2	3
Weight	kg (lb)	53.0 (117.23)	54.5 (120.07)	73.0 (159.62)
cg location				
X	m (in.)	0.0 (0.0)	0.0 (0.0)	0.0 (0.0)
Y	m (in.)	0.0 (0.0)	0.0 (0.0)	0.0 (0.0)
Z	m (in.)	0.33 (12.81)	0.33 (12.86)	0.372 (14.66)
Moment of inertia	$kg\text{-}m^2$ ($lb\text{-}in.^2$)			
Im X-X		12.6 (8844)	12.6 (8847)	19.0 (13,368)
Im Y-Y		12.6 (8844)	12.6 (8845)	19.0 (13,317)
Im Z-Z		15.8 (11,076)	15.8 (11,009)	24.8 (17,310)
Principal moments of inertia	$kg\text{-}m^2$ ($lb\text{-}in.^2$)			
Im lateral		13.3 (9301)	12.9 (9063)	19.7 (13,715)
Im lateral		12.0 (8387)	12.3 (8629)	18.5 (12,969)
Im longitudinal		15.8 (11,076)	15.8 (11,009	24.8 (17,310)
Angle between IM Z-Z & spin axis	deg	0.02	0.03	0.01
Ballast total	kg (lb)	1.95 (4.3)	1.90 (4.16)	2.4 (5.27)

In all cases, mass moment of inertia in spin is at least 25% greater than that in pitch and yaw. Total ballast required to make $I_{xx} = I_{yy}$ and make the principal spin axis align with the geometric spin axis is shown on the last line. It is felt that these values can be reduced somewhat by detailed equipment installation studies.

The mass properties for Missions 1A, 2A, 5, and 7 are similar to those for Missions 1, 2, and 3.

5. Micrometeoroid Penetration Analysis

Probe susceptibility to the micrometeoroid environment from Earth to Jupiter was analyzed using the environmental model defined by NASA SP-8038. (See Chapter III Section D.) For the analysis, the probe was mounted on both Pioneer and TOPS, as shown in Fig. VII-20.

Specific mass of the equipment compartment shell assumed for the analysis varied between 1.14 gm/cm^2 at the nose of the heat shield to 0.28 gm/cm^2 at the opposite end. For the bumper (environmental cover), a specific mass of 0.14 gm/cm^2 was used with a spacing of 3.8 cm (1.5 in.).

Table VII-7 presents the result of the study for the case without a bumper. Table VII-8 presents the result of the study using a 0.5-mm (0.020-in.) aluminum bumper. Table VII-9 presents the vulnerability of the bumper itself to the environment.

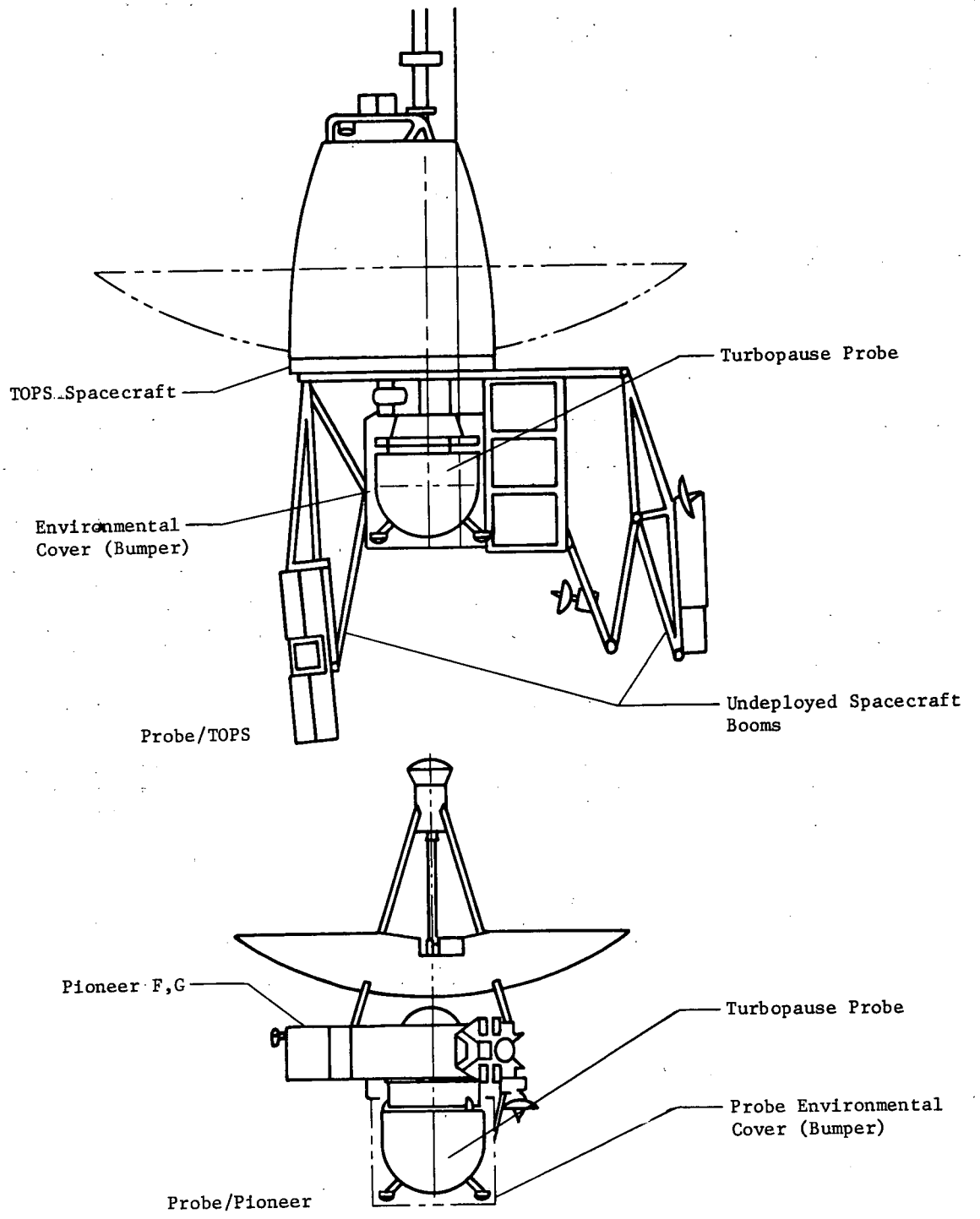

Fig. VII-20 Probe/Spacecraft Geometries

Table VII-7 Inherent Survivability of Jupiter Turbopause Probe in Meteoroid Environment, Cruise Phase Only

Bus	Location	Number of Penetrations			Probability of No Penetrations		
		Cometary	Asteroidal	Total	Cometary	Asteroidal	Total
TOPS	Forward compartment	1.566×10^{-4}	6.084×10^{-3}	6.241×10^{-3}	0.999843	0.99393	0.99378
	Aft compartment*	1.776×10^{-2}	1.311×10^{-1}	1.488×10^{-1}	0.98239	0.87716	0.861713
	Total spacecraft	1.792×10^{-2}	1.371×10^{-1}	1.551×10^{-1}	0.98225	0.87184	0.85636
Pioneer	Forward compartment	1.989×10^{-4}	7.726×10^{-3}	7.925×10^{-3}	0.999801	0.99230	0.99212
	Aft compartment*	2.365×10^{-2}	1.745×10^{-1}	1.982×10^{-1}	0.97663	0.83986	0.8204
	Total spacecraft	2.385×10^{-2}	1.822×10^{-1}	2.061×10^{-1}	0.97644	0.83341	0.81376

*Most vulnerable region is rear face of aft compartment.

Table VII-8 Survivability of Jupiter Turbopause Probe when Protected from the Meteoroid Environment by a Cylindrical Housing, 0.051 cm Aluminum, 3.8 cm Off Walls

Bus	Location	Number of Penetrations			Probability of No Penetrations		
		Cometary	Asteroids	Total	Cometary	Asteroids	Total
TOPS	Forward compartment	1.455×10^{-5}	1.062×10^{-3}	1.077×10^{-3}	0.9999854	0.99894	0.99892
	Aft compartment*	7.149×10^{-5}	2.986×10^{-3}	3.057×10^{-3}	0.9999285	0.99702	0.99694
	Total probe	8.604×10^{-5}	4.048×10^{-3}	4.134×10^{-3}	0.9999140	0.99596	0.99587
Pioneer	Forward compartment	1.848×10^{-5}	1.348×10^{-3}	1.366×10^{-3}	0.9999815	0.99865	0.99863
	Aft compartment*	9.520×10^{-5}	3.976×10^{-3}	4.071×10^{-3}	0.9999048	0.99603	0.99593
	Total probe	1.137×10^{-4}	5.324×10^{-3}	5.438×10^{-3}	0.999886	0.99469	0.99456

*Most vulnerable region is rear face of aft compartment.

Table VII-9 Vulnerability of Cylindrical Housing, Jupiter Turbopause Probe, 0.051 cm Aluminum

Bus	Number of Penetrations			Probability of No Penetrations		
	Cometary	Astroids	Total	Cometary	Asteroids	Total
TOPS	0.741	2.422	3.163	0.47657	0.08872	0.04228
Pioneer	0.987	3.225	4.212	0.37274	0.03974	0.01481

B. THERMAL CONTROL

1. Selection of Thermal Control

Thermal control must be provided to ensure that all probe systems will be maintained within acceptable temperature limits before arrival at Jupiter and during the science-return portion of the mission. For thermal analysis, the turbopause mission was divided into three phases:

1) Preseparation cruise, during which the probe is being carried by the spacecraft;

2) Postseparation coast, when the probe has been separated from the spacecraft;

3) Entry, when the probe's equipment is activated. (See Fig. VII-21.)

The most critical probe temperatures during the mission are the minimum temperature experienced at the end of postseparation coast and the maximum TWT amplifier temperature reached during entry. Because the probe equipment temperature at the end of coast will equal its temperature at the beginning of the entry phase, these temperatures must be above the minimum required for probe operation (272°K lower limit). During the probe entry phase with equipment in operation, the primary thermal problem is dissipating the waste heat from the TWT amplifier (343°K upper limit).

Two candidate thermal-control configurations were chosen and analyzed (Fig. VII-22 and VII-23). The basic approach was to use high-performance multilayer insulation to reduce heat losses and isolate the probe interior from the space enviornment. The insulation is supplemented with small amounts of internally generated heat to maintain the probe equipment temperature within allowable limits and above the minimum temperature required at the beginning of entry.

The candidate configurations considered were internal and external probe insulation concepts.

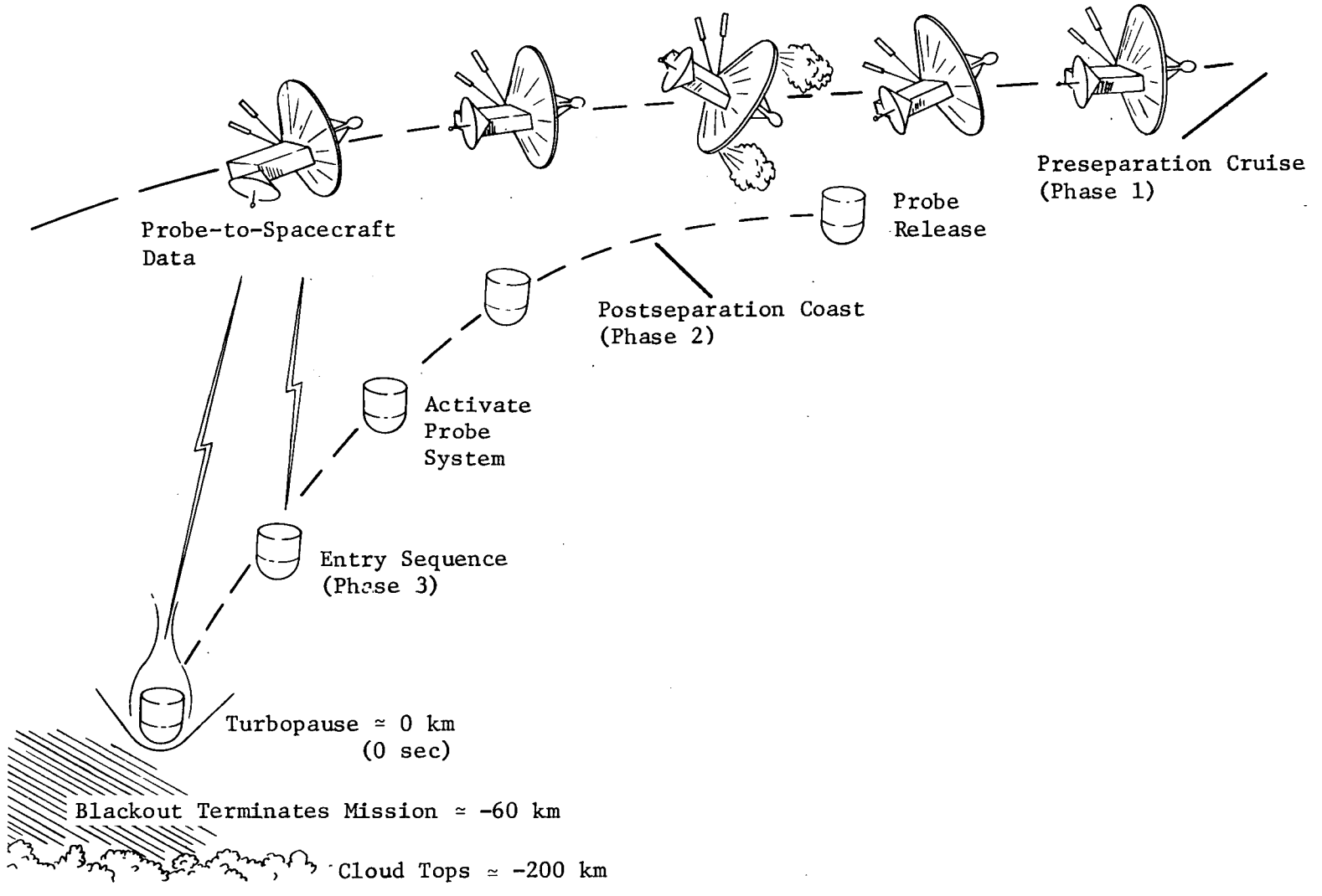

Fig. VII-21 Probe Release/Entry Sequence

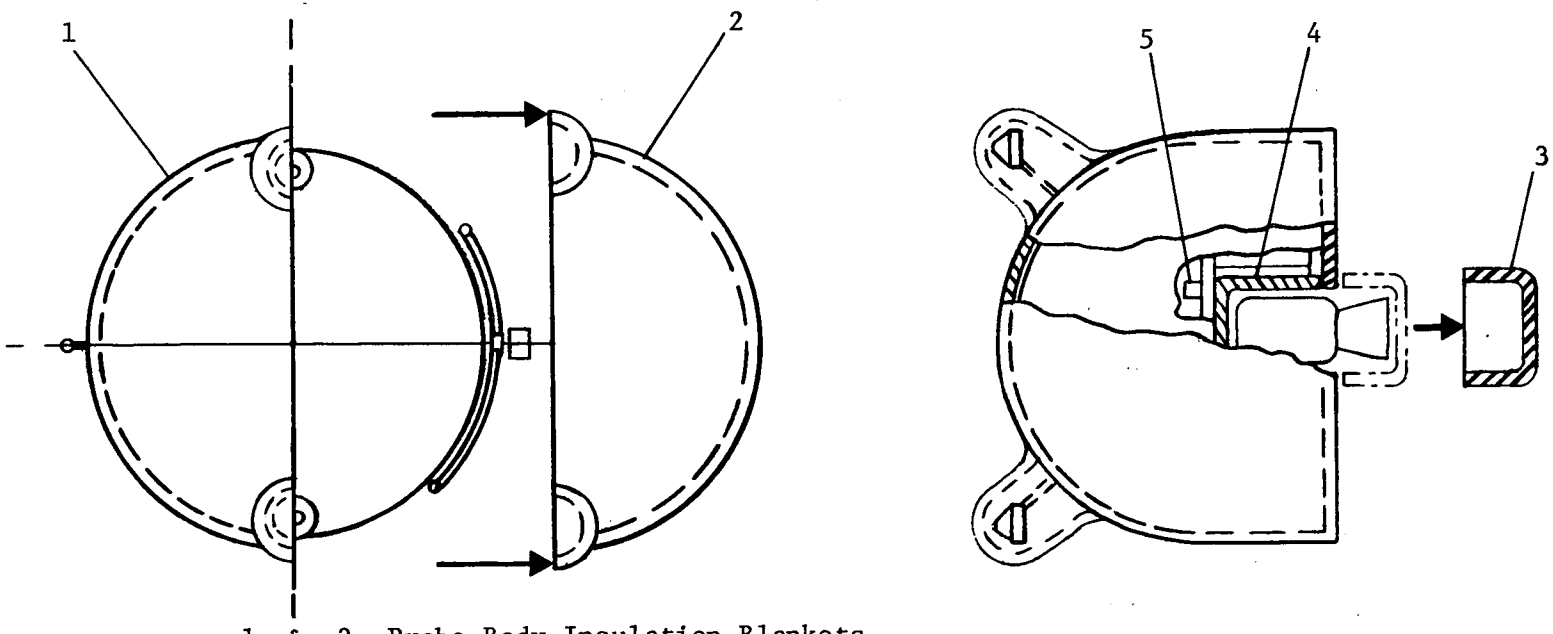

1 & 2 Probe Body Insulation Blankets
Blankets Penetrated By:

ACS/Spinup Jet Feeds,
Sun Sensors,
Probe-to-Spacecraft Attach Points

3 ΔV Rocket Motor Spacecraft-Mounted Multilayer Insulation

4 Fixed Blanket, Insulates Probe after Probe Ejection

5 Internal Heat Source, Radioisotope Heater

Fig. VII-22 External Insulation Design Configuration

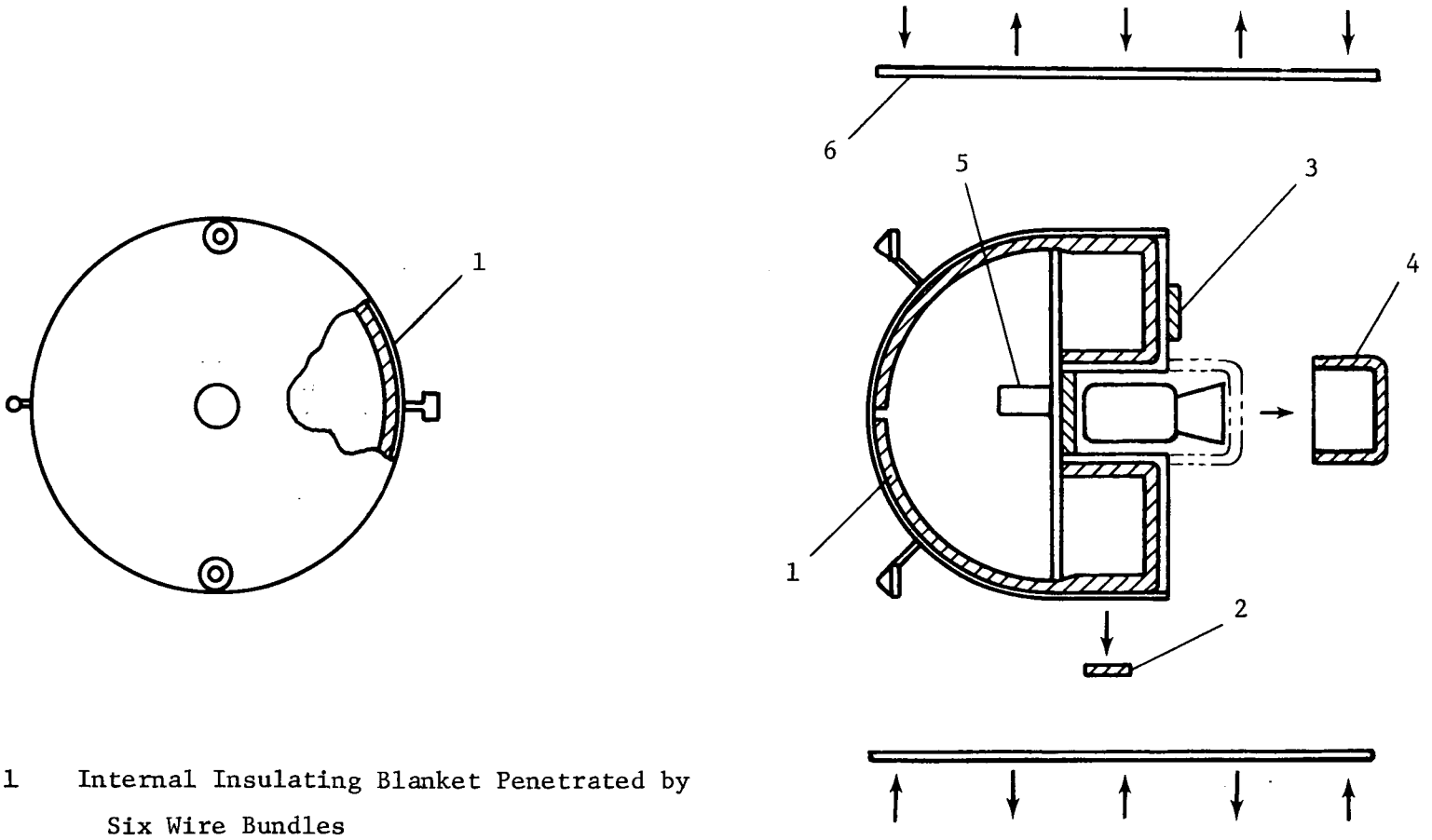

1 Internal Insulating Blanket Penetrated by

- Six Wire Bundles
- ACS Tubing
- Primary Longeron Attachment Points
- Science Ports

2 Photometer Cover

3 RF-Transparent Horn Antenna Insulating Cover (long-range communications missions only)

4 ΔV Rocket Motor Spacecraft-Mounted Multilayer Insulation

5 Internal Heat Source, Radioisotope Heater

6 Environmental Cover Provided by Spacecraft

Fig. VII-23 Internal Insulation Design Configuration

The advantages and disadvantages of the two configurations are summarized as follows.

a. External Insulation Characteristics -

1) Thermal shorts through insulation minimized;

2) Probe needs no independent heat source if coast period is limited to 8 days;

3) No separate Sun shield required;

4) Insulation blanket provides protection for science instrument apertures during prelaunch, launch, and coast;

5) Insulation blanket limits probe access and makes probe/spacecraft structural interface difficult;

6) The requirement to jettison the insulation blanket introduces a mission failure mode.

b. Internal Insulation Characteristics -

1) Thermal shorts reduce overall insulation efficiency;

2) Probe requires independent internal heat source for coast periods greater than 4 days;

3) Pioneer thermal environment requires Sun shield;

4) Science aperture covers may be required;

5) Probe access and structural interface problems minimized;

6) A bare heat shield is guaranteed at entry.

A thermal-control coating on the outside of the probe was ruled out because entry heating would prematurely terminate the mission by surrounding the probe with a cloud of decomposed coating material. The coating function can be provided by a separate Sun shield when internal insulation is used, or a solar reflective coating on the jettisonable blanket if external insulation is used.

Internal insulation was chosen for the thermal design for all missions. The reasoning that led to this choice is summarized below.

1) A source of mission unreliability is eliminated because insulation jettisoning is not required.

2) The external insulation configuration requires merely a coat of solar reflective paint on the jettisonable insulation for protection from the Sun, thus giving it a weight advantage over the internal configuration, which needs a separate Sun shield. However, the Sun shield doubles as a meteoroid bumper, which is desirable in any case.

3) Limiting the coast period to 8 days would be poor design strategy. Thus, an independent heat source is required for either configuration.

4) The additional heat required for internal insulation can be provided by isotope heaters at approximately the same weight penalty as jettisonable external insulation.

In addition to the insulation blanket and internal heaters, the thermal control subsystem will require the following components:

1) A photometer aperture cover that can be removed before entry;

2) For missions requiring a probe deflection maneuver, a secondary insulation blanket that encapsulates the deflection motor assembly. This blanket remains with the spacecraft because the deflection motor is used just after separation;

3) An electric heater located within the deflection motor insulation blanket. This heater will use spacecraft-supplied power (less than 5 W) to maintain the deflection motor temperature at 294°K (70°F) before separation.

4) An RF-transparent insulating radome to cover the communications antenna for long-range communication (large-antenna) configurations.

2. Analysis of Reference Mission

Jupiter turbopause probe thermal-subsystem performance was analyzed using a finite-element thermal mathematical model that simulated the probe and the probe-spacecraft combination. A simulation of the thermal environment, containing all thermally significant events from spacecraft/booster separation until Jupiter atmospheric entry, was included in the model. The entry heating phase was discussed separately (Subsection VII A1).

The following probe configurations and spacecraft/probe combinations were analyzed and led to the reference configuration definition:

1) Bare probe with internal insulation/Pioneer;

2) Probe/environmental cover/Pioneer combination with internal insulation;

3) Probe/environmental cover/TOPS combination with internal insulation;

4) Bare probe with external insulation/Pioneer.

The finite-element probe model consisted of 11 nodes and 28 conductors. For the cruise mode, the probe model was joined with a simplified spacecraft thermal model, resulting in a total of 23 nodes and 67 conductors for the combination. The model contained logic to simulate the cruise thermal environment, probe separation and coast, and probe operation with operating equipment heat dissipation. Thermally significant events such as insulation or instrument-cover jettisoning were also accounted for. In addition to the thermal subsystem analysis, the probe model was used as a design aid for structural details where insulation penetrations degraded thermal performance.

Before spacecraft separation, the probe's thermal environment consists of the deep-space heat sink, as modified by view blockage by the spacecraft, and solar flux early in the cruise mode, again modified by spacecraft shadowing. A second consideration is the radiant heat interchange with the spacecraft.

Figure VII-24 illustrates the solar flux environment throughout cruise in terms of spacecraft orientation and solar intensity as a function of cruise time. The Sun-oriented TOPS spacecraft will shade the probe from solar radiation except for brief midcourse corrections. The Earth-oriented Pioneer will allow solar heat to the probe for the first 15 to 20 days of cruise, at a time when solar flux is relatively high.

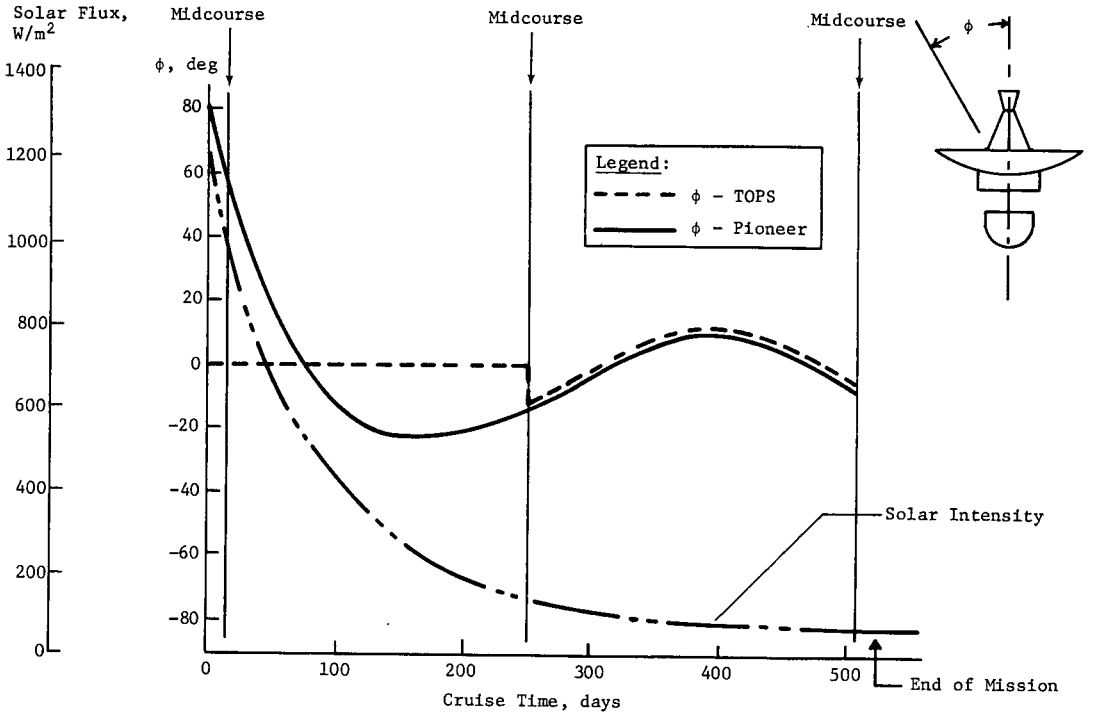

Figure VII-24 Probe Cruise Thermal Environment

For the reference-mission thermal analysis, the first midcourse correction was defined as 1 hr of solar impingement at 1025 W/m^2 (325 $Btu/hr-ft^2$) from the probe's most thermally sensitive angle. Later midcourse maneuvers were not analyzed because of lower solar intensity. The reference mission power profile used for analysis is presented in Fig. VII-25. During transmitter operation, it was assumed that 25 W of the transmitter's 85 W was being radiated as RF energy.

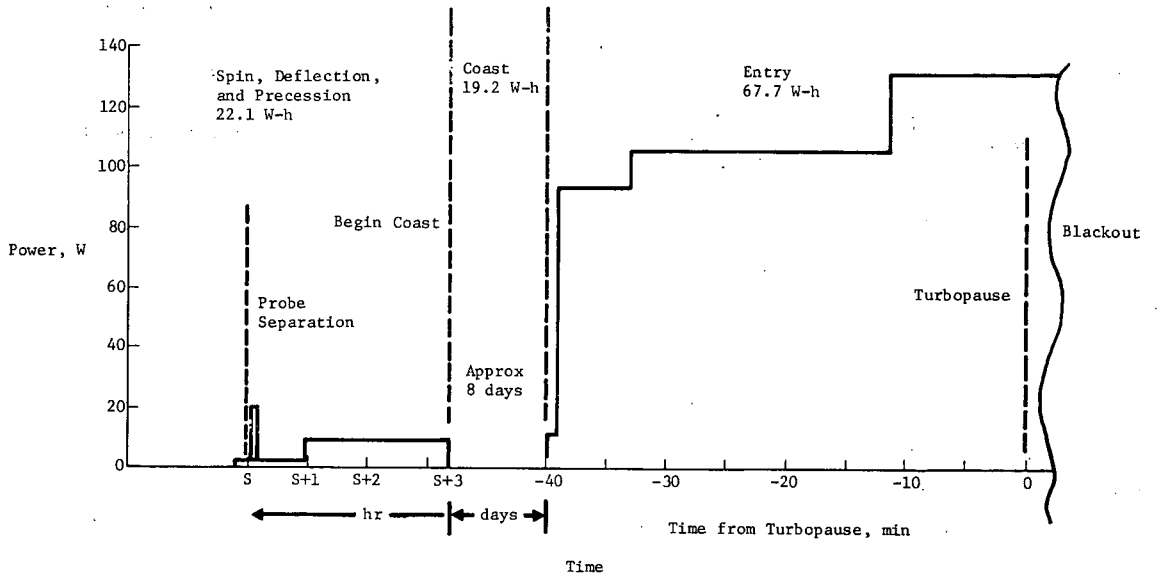

Fig. VII-25 Reference Mission Power Profile

Results of the reference mission thermal analysis are shown in Fig. VII-26 and VII-27. Internal equipment temperature was maintained well within the allowed limits throughout the cruise and coast mission phases with 4 and 8 W internal power for the external and internal configurations, respectively. These power levels were chosen presuming the use of radioisotope heaters whose output could not be changed during the mission. If spacecraft electrical heat were used, thermostatic heater control would be used to maintain the probe at its minimum allowable temperature during cruise. Probe temperature would then be brought to a maximum just before separation, and for the external insulation case (Fig. VII-26), the probe's thermal mass would be sufficient to maintain an internal equipment temperature above the minimum allowable limit during an 8-day coast with no additional internal heat. For the internal insulation configuration (Fig. VII-27), this scheme is feasible for coast periods up to 4 days.

The cruise mode analysis was run for both probe/TOPS and probe/Pioneer combinations, with a negligible difference in results. Figures VII-26 and VII-27 can be considered correct for either spacecraft combination. In addition, an assumed 1-hr midcourse correction results in a temperature rise of less than 5°F inside the probe.

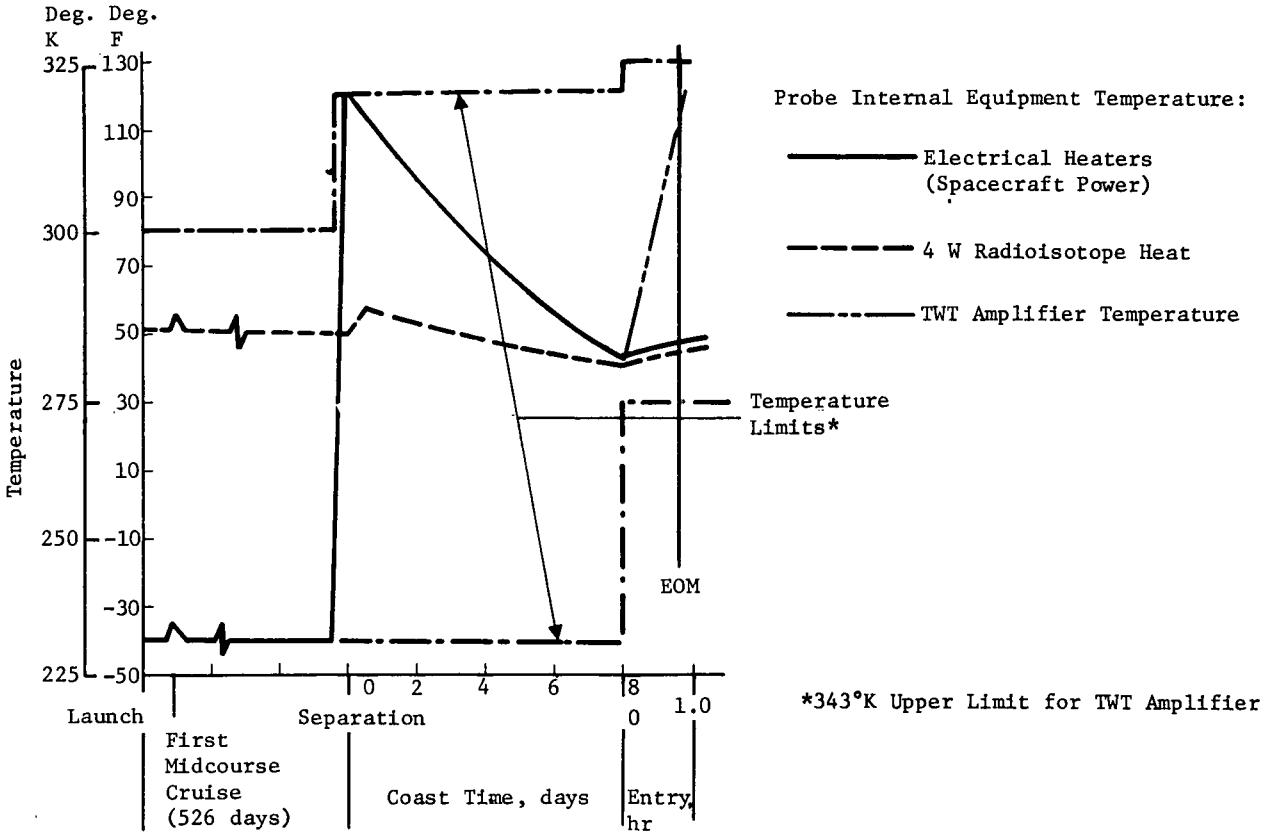

Figure VII-26 External Insulation Configuration Thermal Analysis Results

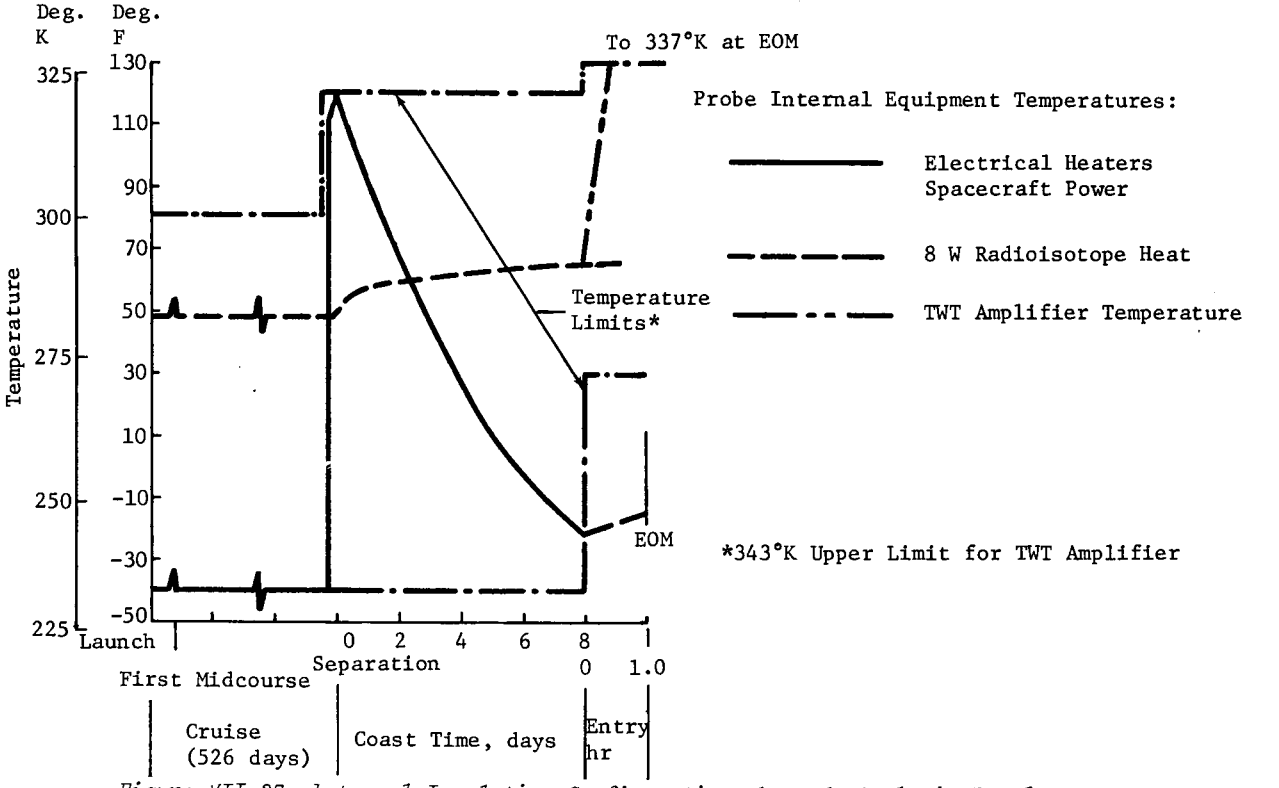

Figure VII-27 Internal Insulation Configuration Thermal Analysis Results

During the probe entry phase with equipment operating, the primary thermal problem is dissipating waste heat from the TWT amplifier. This component remained below its allowable limit of 343°K (158°F) for the 42-min reference mission power-on time with only conduction and radiation cooling. If communication power requirements were increased however, as for a 2 or 3 R_J communication distance, additional TWT amplifier thermal control would be required. This commonly is done with a wax-type phase-change material that melts at about 100°F. Approximately 0.018 kg (0.004 lb) of this material would be required per watt-hour of transmitter dissipation.

3. Analysis of Missions 1, 1A, 2, 2A, 3, 5, 7

A probe thermal analysis was performed for the spacecraft and probe design configurations defined for Missions 1, 1A, 2, 2A, 3, 5 and 7. (See Table VII-10.) The purpose was to ensure that all probe systems would be maintained within allowable temperature limits throughout the missions. As in the reference mission, the pivotal temperature is the steady-state equipment temperature at the end of the coast. The subsystem is designed so this temperature is safely above the lower limit for equipment operation. This allows the most leeway for temperature rise from equipment operation during the entry phase.

The thermal design concept for all missions investigated consisted of a high-performance multilayer insulation blanket to isolate the probe interior and conserve internal heat supplied by radioisotope heaters. The internal insulation configuration was chosen for all missions. As previously discussed, the use of thermal-control coatings on the probe exterior is not desirable. During the spacecraft cruise phase, however, the probe is housed in a cylindrical enclosure that shields the probe and provides a thermal coating.

The basic probe configurations consist of a 0.712-m (28-in.) probe design with no propulsion system (Mission 1, 1A, 2 and 2A), and a larger 0.762-m (30-in.) dia probe design that includes a propulsion system, Sun and planet sensors, and an attitude control system (Missions 3, 5 and 7). Figure VII-28 shows the basic probe designs.

Table VII-10 Mission Definitions

	Mission No. and Title						
	1	1A	2	2A	3	5	7
	Probe Optimized	Probe/Sci Optimized	Radiation-Compatible	Radiation-Compatible	JUN 78	Solar Apex	JS 77
S/C	Pioneer	Pioneer	Pioneer	Pioneer	TOPS	Pioneer	MOPS
Launch Date	10/21/78	10/21/78	10/13/78	10/13/78	10/3/78	10/9/78	9/5/77
Flight time, days	797	760	655	655	576	540	557
Periapsis radius, R_J	1.1	1.1	4.0	4.0	1.94	1.77	4.85
Deflection mode	S/C	S/C	S/C	S/C	Probe	Probe	Probe
Deflection radius $\times 10^6$ km	30	30	50	50	30	30	50
Coast time, days	42	10.9	60	60.3	29	27	50.1
ΔV, m/sec	16	16	101	101	82	75	130.7
γ_E, deg	-21	-23.2	-29.0	-29.0	-33.0	-34.0	-33.3

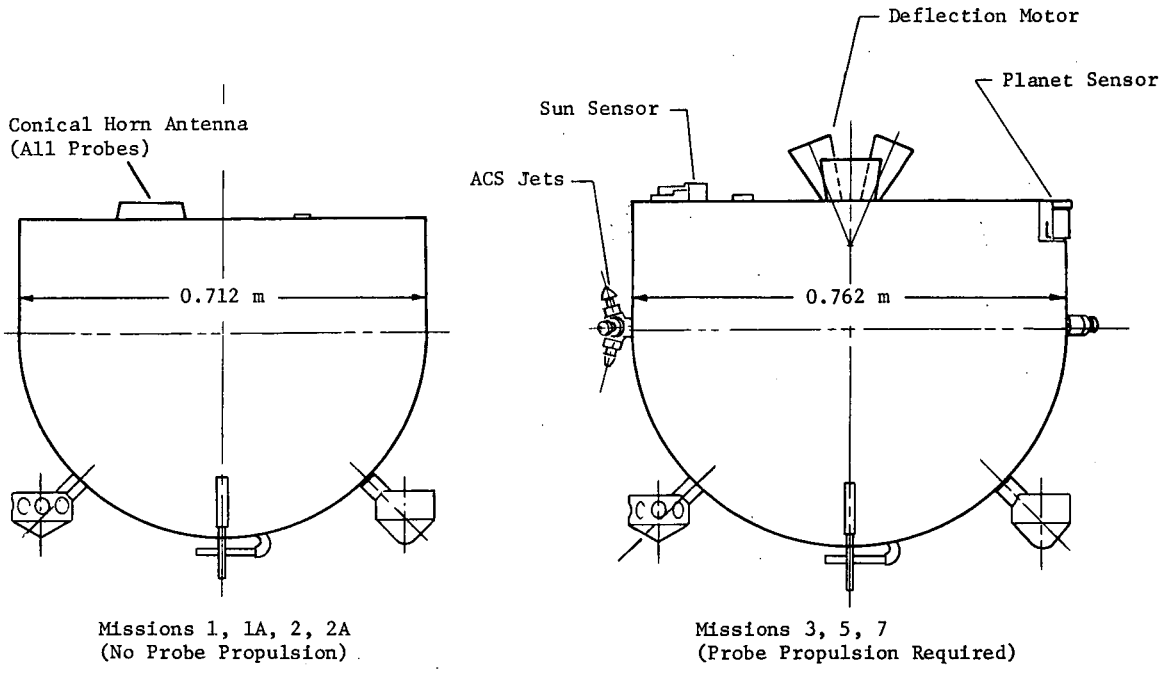

Fig. VII-28 Probe Configuration Comparison

To analyze the probe's thermal performance, a finite-element thermal math model was constructed for the probe and probe/spacecraft combination for each mission investigated. The probe thermal model consisted of nine nodes and 19 associated conductors plus three additional nodes and four additional conductors to simulate the probe propulsion system. Figure VII-29 is a schematic showing the resistance-capacitance thermal network representing the probe model. For the cruise mission phase, the probe was joined to a simplified spacecraft model, resulting in a total of 19 nodes and 69 conductors for Mission 1, 1A, 2 and 2A, and 22 nodes and 75 conductors for Missions 3, 5, and 7. The geometric thermal model used to compute radiant probe spacecraft interchange is presented in Fig. VII-30.

The probe thermal/structural data used to perform the thermal subsystem analysis for each mission are presented in Table VII-11. Considerable care was exercised to account for all heat losses through penetrations in the thermal blanket. Likewise, the actual design of the structural details minimized heat leak paths by avoiding metallic contacts to the probe shell and using low-conduction materials wherever possible. The insulation blanket itself, however, presented the biggest uncertainty in determining probe heat losses.

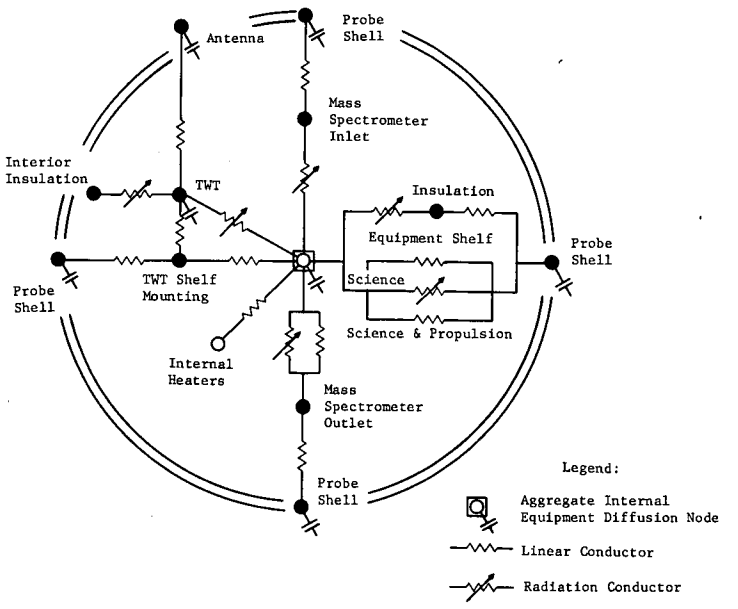

Fig. VII-29 Schematic of Basic Probe Thermal Model Used to Perform Turbopause Mission Thermal Analysis.

To accurately evaluate insulation performance, two applicable data sources on multilayer insulation were obtained and evaluated and an analytical expression representing the insulation conductivity obtained and incorporated in the thermal model (Appendix I, Vol III.)

To determine the radioisotope heater power required, Missions 1 and 3 were selected to represent the two basic probe configurations (i.e., with and without a probe propulsion system). These missions were evaluated parametrically by varying insulation thickness and determining internal heater power required to maintain a steady internal equipment temperature of 283°K (50°F). The 283°K equipment temperature is the desired probe temperature at the end of the coast phase before Jupiter entry.

Figure VII-31 presents the internal radioisotope-heater power requirement as a function of the multilayer insulation thickness for Missions 1 and 3. These results indicate that 10 W of heater power should be adequate to maintain the desired probe temperatures for Mission 1, 1A, 2 and 2A, and 14 W should be adequate for Missions 3, 5 and 7.

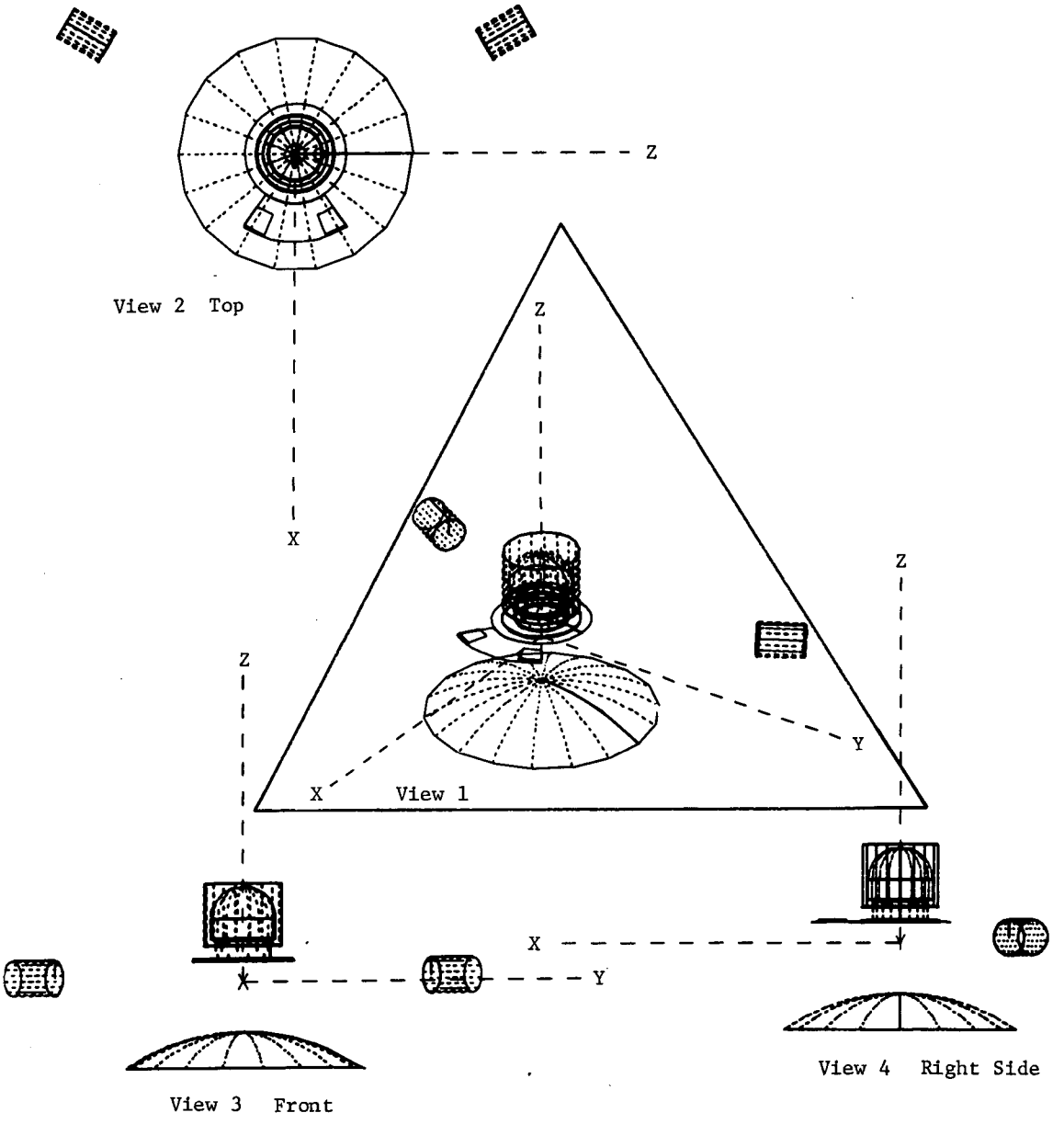

Fig. VII-30 Geometric Thermal Model of Probe/Spacecraft Combination

Table VII-11 Probe Thermal Analysis Data

Thermal/Structural Data		Mission 1	Mission 1A	Mission 2	Mission 2A	Mission 3	Mission 5	Mission 7
a Surface Area,	m^2	1.646	1.646	1.646	1.646	1.889	1.889	1.889
b Aft Bulkhead Area,	m^2	0.398	0.398	0.398	0.398	0.430	0.430	0.430
c Antenna Horn Exit Area,	m^2	0.008	0.030	0.013	0.030	0.013	0.013	0.030
d Externally Exposed Antenna Area,	m^2	0.008	0.030	0.013	0.030	0.040	0.040	0.056
e Antenna Radome Thickness,	cm	None	1.27	None	1.27	None	None	1.27
f TWT Amplifier Standoff,	cm	3.81	0.127	5.72	0.127	1.27	1.27	0.127
g Mass Spectrometer Vent Length,	cm	20.3	20.3	20.3	20.3	38.1	38.1	38.1
h Internal Insulation Thickness,	cm	1.52	1.52	1.52	1.52	1.42	1.42	1.42
i Science Penetration Conductance,	W/°K	0.0014	0.0014	0.0014	0.0014	0.0017	0.0017	0.0017
j ACS & Propulsion Conductance,	W/°K	N/A	N/A	N/A	N/A	0.0446	0.0446	0.0446
k Equipment Shelf Penetration,	W/°K	0.0033	0.0033	0.0033	0.0033	0.0033	0.0033	0.0033
l Mass Spectrometer Inlet Penetration,	W/°K	0.1587	0.1587	0.1587	0.1587	0.1587	0.1587	0.1587
m Mass Spectrometer Outlet Penetration,	W/°K	0.0044	0.0044	0.0044	0.0044	0.0044	0.0044	0.0044
n Probe - S/C Mount Conductance	W/°K	0.0391	0.0391	0.0391	0.0391	0.0391	0.0391	0.0391
o Antenna - Amplifier Conductance,	W/°K	0.0164	0.0115	0.0142	0.0115	0.0142	0.0142	0.0115
p TWT Shelf - Interior Conductance,	W/°K	0.0785	0.0785	0.0785	0.0785	0.0785	0.0785	0.0785
q TWT Shelf - Probe Shell Conductance,	W/°K	0.0008	0.0008	0.0008	0.0008	0.0008	0.0008	0.0008
r Science Penetration Radiation,	$W/°K^4$	0.0010σ*	0.0010σ	0.0010σ	0.0010σ	0.0020σ	0.0020σ	0.0020σ
s Interior - Insulation Radiation,	$W/°K^4$	0.0771σ	0.0771σ	0.0771σ	0.0771σ	0.0892σ	0.0892σ	0.0892σ
t Mass Spectrometer Inlet Radiation,	$W/°K^4$	0.0017σ	0.0017σ	0.0017σ	0.0017σ	0.0017σ	0.0017σ	0.0017σ
u TWT - Interior Radiation,	$W/°K^4$	0.0985σ	0.0985σ	0.0985σ	0.0985σ	0.0985σ	0.0985σ	0.0985σ
v TWT - Insulation Radiation,	$W/°K^4$	0.0041σ	0.0041σ	0.0041σ	0.0041σ	0.0041σ	0.0041σ	0.0041σ
Capacitance Data								
a Internal Capacitance,	W-h/°K	2.530	3.044	2.603	3.036	4.005	4.005	4.357
b Probe Shell Capacitance,	W-h/°K	1.455	1.504	1.358	1.462	1.556	1.556	1.517
c TWT Amplifier Capacitance,	W-h/°K	0.326	0.326	0.358	0.326	0.358	0.358	0.326
d Conical Antenna Capacitance,	W-h/°K	0.073	0.110	0.103	0.110	0.103	0.103	0.110
e Deflection Propulsion Motor,	W-h/°K	N/A	N/A	N/A	N/A	0.127	0.127	0.127
Power Data								
a Average Equipment Power,	W	47	43	55	50	50	54	57
b Equipment Energy Dissipation,	W-h	32.5	28.6	59.1	31.9	35.2	46.4	52.1
c TWT Amplifier Power,	W	50.0	83.2	83.2	83.2	91.5	108.0	83.2
d TWT RF Energy Dissipation,	W-h	8.2	13.4	21.2	12.7	15.3	22.3	18.3
e TWT Electrical Energy Dissipation,	W-h	26.0	42.3	67.2	40.0	55.2	70.5	57.6
f Total Probe Energy Dissipation,	W-h	66.7	84.3	147.5	84.6	105.7	139.2	132.0

*$\sigma = 5.669 \times 10^{-8}$ W/m^2 $°k^4$

C.8

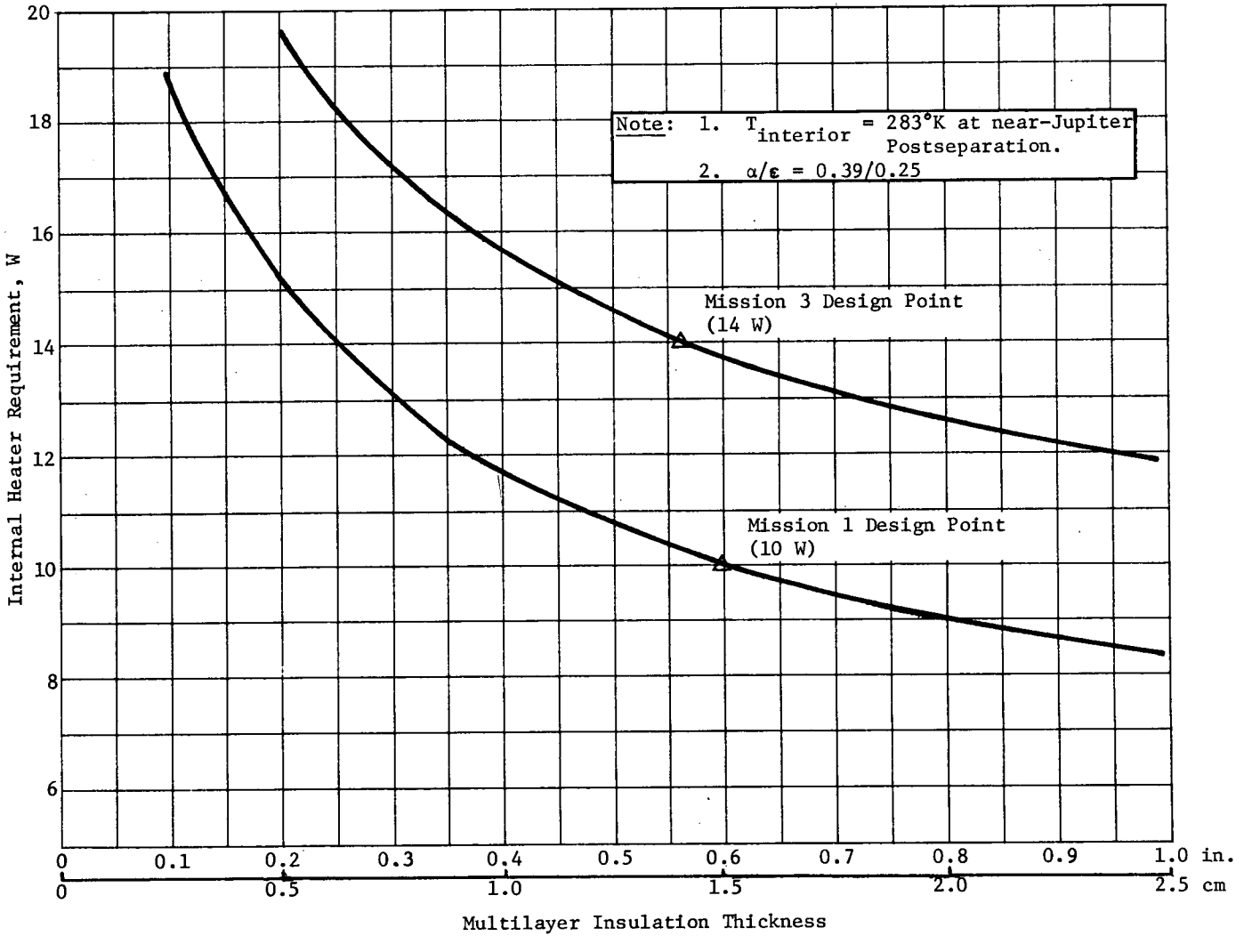

Fig. VII-31 Turbopause Probe Insulation Thickness vs Radioisotope Heater Power Required

Heater power requirement for Mission 3 (14 W) is considerably larger than that of the reference mission, even though the configuration is very similar. This results from the reference mission analysis being based on a low-emissivity (0.05) probe exterior. It was found by optical-property measurement of a sample of platinum-plated beryllium that this emissivity will actually be approximately 0.25, so the Mission 1 and 3 analyses were based on the higher value. The sensitivity of the thermal design to this value is discussed in Appendix J, Vol III.

The insulation thickness was chosen to achieve a reasonable compromise between heater power and insulation bulk. Appendix J (Vol III) shows the sensitivity of heater power to insulation thickness. If the insulation thickness were doubled from the design points chosen, a heater power saving of only 2 to 3 W results. Final selection of the number of radioisotope heaters will be made on the basis of thermal tests.

A summary of probe heat losses for Mission 1 and 3 probe configurations is presented in Fig. VII-32.

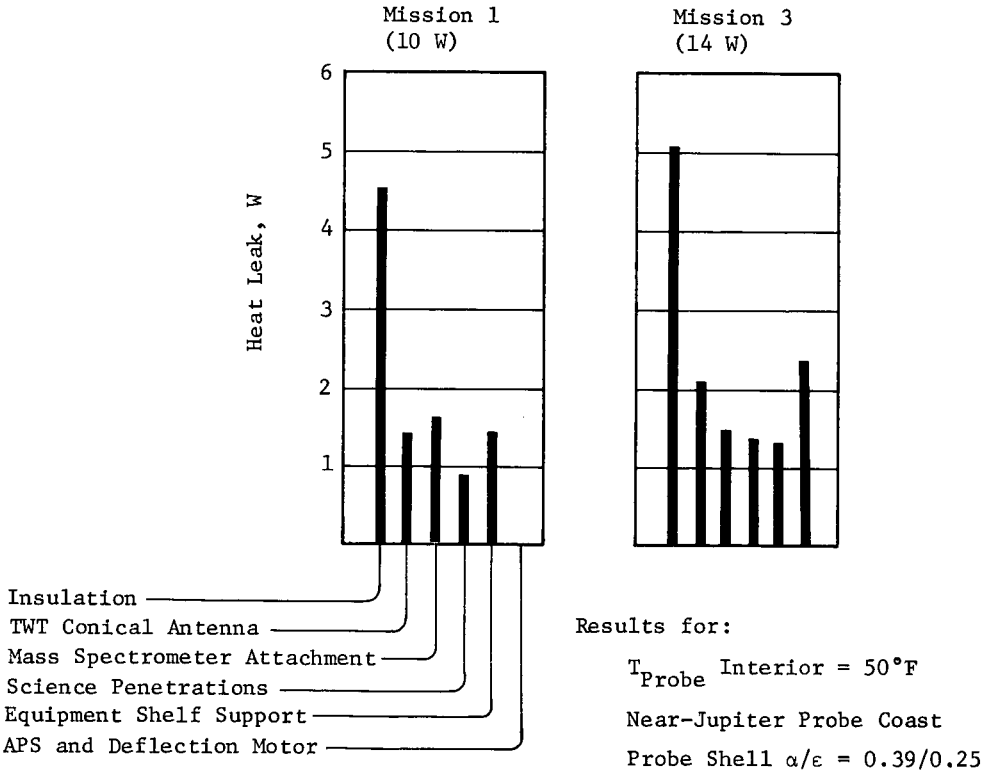

Fig. VII-32 Summary of Probe Configuration Heat Losses

The results of the thermal analyses are summarized and presented in Table VII-12. These results include probe equilibrium temperatures during the preseparation phase, equilibrium temperatures during the postseparation coast, and transient temperatures during the Jupiter entry sequence before aerodynamic heating. The table contains results for all missions investigated and includes applicable temperature limits for each mission phase analyzed. Power profiles used to perform the entry sequence analysis have been discussed in Chapter V. A breakdown of the probe's energy dissipation was also presented in Table VII-11. During transmitter operation, radiated RF energy was not included as thermal heat dissipation.

During probe entry, the primary thermal problem is dissipating waste heat from the TWT amplifier. This component remained well below its allowable upper temperature limit 343°K (158°F) for the mission configurations analyzed. But, if communication power requirements or "on time" should be increased, the TWT amplifier or "on time" should be increased, the TWT amplifier could require additional thermal protection. As discussed in Subsection 2, thermal protection could be supplied by using a wax-type phase-change material that melts at about 217°K (100°F).

For the turbopause missions requiring the larger antenna (Missions 1A, 2A, and 7), the thermal design includes a 1.27-cm (1/2-in.) radome cover. This cover is necessary to maintain probe heat losses at levels experienced for equivalent probe configurations. A restriction in the use of the radome cover would require an increase in the internal heater power requirement for these missions.

In addition to thermal protection required for the probe's interior, approximately 5 W of additional heater power will be needed to maintain the deflection motor temperature above the limit required for ignition (283°K lower limit). Because the deflection motor is fired immediately after separation, this heat can be supplied by a controlled electric heater powered by the spacecraft.

Table VII-12 Internal Insulation Configuration Thermal Analysis Results

	Allowable Temperature Limits, °K	Mission 1 (10 W), °K °F	Mission 1A[a] (10 W), °K °F	Mission 2 (10 W), °K °F	Mission 2A[a] (10 W), °K °F	Mission 3 (14 W), °K °F	Mission 5 (14 W), °K °F	Mission 7[a] (14 W), °K °F
Preseparation Phase								
Probe interior	233/300	283 49	286 54	283 50	286 54	290 63	290 63	293 68
TWT amplifier	233/354	280 44	283 50	280 45	283 50	287 57	287 57	291 64
Antenna	N/A	254 -3	256 1	251 -7	256 1	246 -17	246 -17	254 -2
Probe shell	N/A	179 -138	179 -137	179 -138	179 -137	189 -120	189 -120	188 -119
Deflection motor (prestart)	283/300	--- ---	--- ---	--- ---	--- ---	294 70	294 70	294 70
Postseparation Coast								
Probe interior	272/300	283 50	282 47	281 46	282 47	283 50	283 50	284 52
TWT amplifier	264/343	280 45	279 42	277 39	279 42	279 43	279 43	281 46
Antenna	N/A	254 -2	236 -34	240 -27	236 -34	231 -44	231 -44	226 -53
Probe shell	N/A	181 -134	180 -135	180 -135	180 -135	182 -132	182 -132	182 -132
Entry Phase[b]								
Probe interior	272/322	287 57	286 54	289 60	286 55	286 55	288 58	289 60
TWT amplifier	264/343	302 83	310 99	321 119	310 99	313 104	326 126	321 117
Antenna	---	256 1	238 -32	244 -21	238 -32	232 -42	233 -40	228 -49
Power dissipation	---	66.7 W-h	84.3 W-h	147.5 W-h	84.6 W-h	105.7 W-h	139.2 W-h	132.0 W-h

Note: [a]Antenna radome required to reduce antenna heat losses.
[b]Temperatures attained just before aerodynamic heating.

C. PROPULSION

1. Selection of Subsystems

Probes for Missions 3, 5 and 7 require ACS and deflection ΔV propulsion subsystems.

a. ACS Propulsion - The maximum total impulse required for ACS propulsion (including spinup and despin) will not exceed 489 N-sec (110 lbf-sec). Figure VII-33 indicates that cold gas systems or a Tridyne system will be the lightest system for such a low total specific-impulse requirement. A Tridyne system is a hot gas system that is not flight qualified. It is considerably more expensive than a GN_2 system. GN_2 systems have many flight-qualified components from which to design a probe ACS propulsion system. For these reasons, Tridyne systems were dropped from consideration in favor of cold gas systems. Figure VII-34 indicates that the weight of a GN_2 system is very competitive with other cold gas propellant systems. Selection of a GN_2 cold gas propulsion subsystem for ACS (including spin and despin) application resulted from its relative simplicity and the availability of developed hardware.

The GN_2 system is pressure regulated and sealed by redundant squib valves except for a maximum of 12.5 hr after separation of the probe from the spacecraft. During this period, redundant solenoid valves will be the primary source of system leakage. For the long-term locked-up storage period during the Earth-Jupiter traverse, welds between the GN_2 storage tank and closed squib valves are the major leakage sources. A weld joint was assumed to leak He at 3×10^{-7} scc/hr and a solenoid valve at 1 scc/hr, according to Martin Marietta test and flight data. Considering these leakage rates and the required restoring-force GN_2 requirement, total leakage would be approximately C.1 grams. Leakage from the GN_2 propulsion subsystem was therefore considered to be negligible.

The weight of a GN_2 system (based on Ref VII-1 data and presented in Appendix C, Vol III) has been considerably reduced by using tank weights based on fracture mechanics and cryogenic proof-pressure testing techniques. This approach estimates the tank weight to be approximately 1.1 times the weight of GN_2 to be contained. A tank weight factor about three times the weight of GN_2 contained results from using Ref VII-1. The GN_2 propellant was assumed to have a delivered specific impulse of 705 N-sec/kg (72 lbf-sec/lbm).

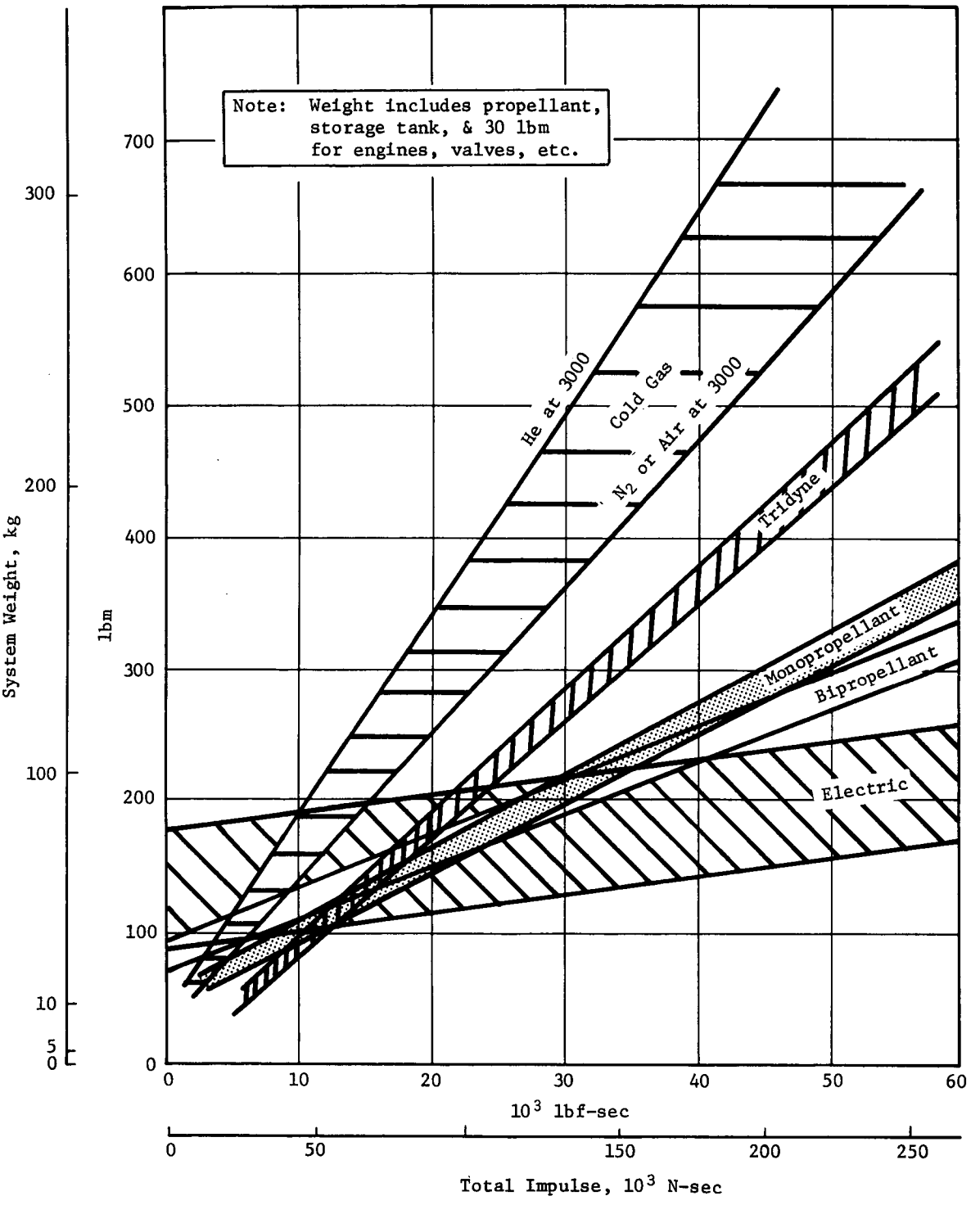

Fig. VII-33 System Weight Comparison (Ref VII-3)

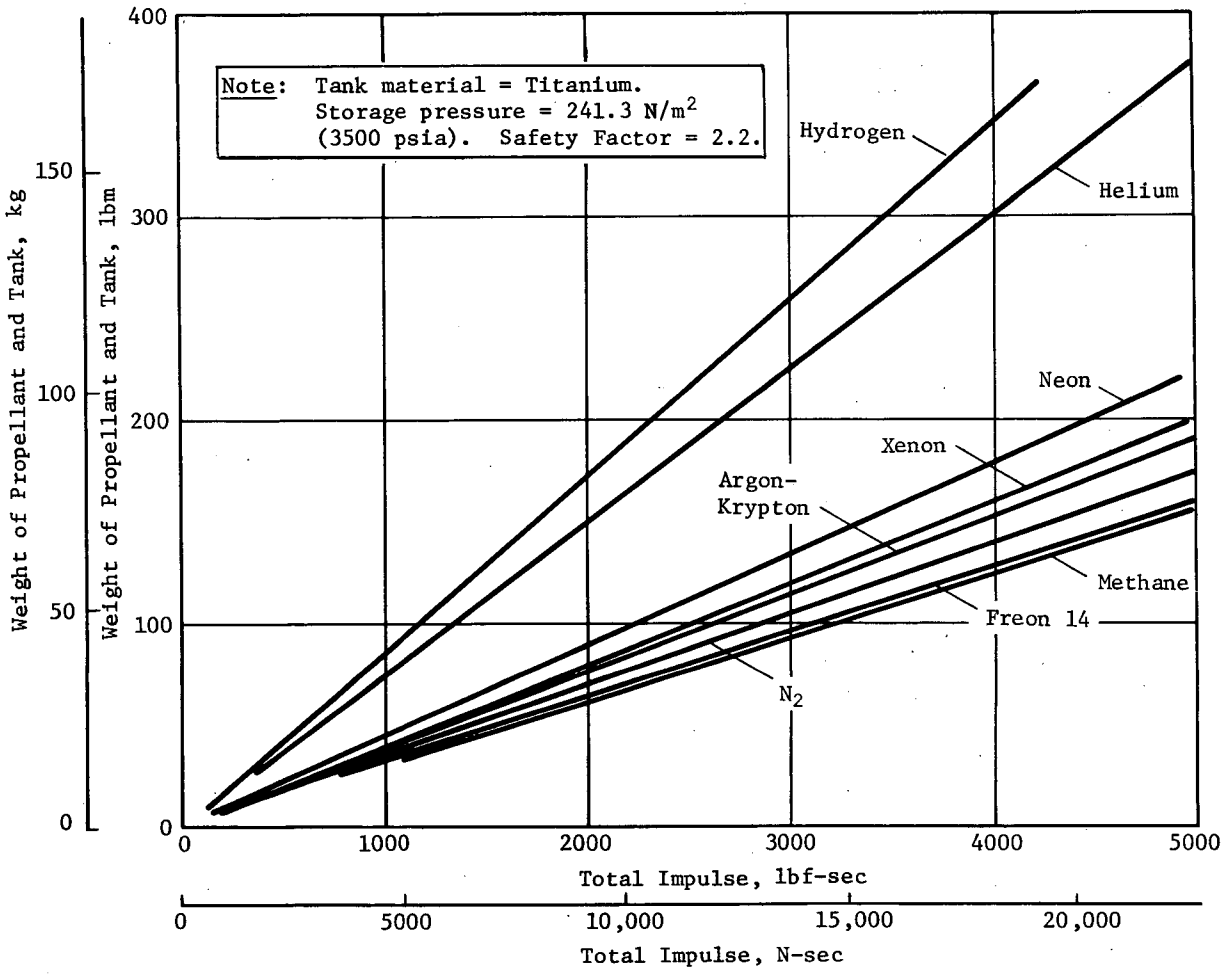

Fig. VII-34 Weight Characteristics of Cold Gas Systems (Ref VII-2)

This is in agreement with data presented in Ref VII-2 for cases in which pulse rates are less than 0.02 sec. The GN_2 propellant computed for actual use was multiplied by 1.3 to compensate for tank residuals and line and component residuals.

b. Deflection Propulsion - Solid-propellant rocket motors were selected for probe deflection because of their simplicity, reliability, and high performance. Two potential problems arise from using solid rocket motors in this application. One is the relatively high thrust associated with solid motors for a given total impulse. This high thrust and the thrust-vector misalignment, caused by motor manufacture and installation tolerances, requires high spin rates to limit probe nutation to tolerable levels. Using a lower burning rate high-performance propellant results in deflection motors with lower thrust and longer burning time, which reduces the potential for significant nutation. Typical of such propellant development is Thiokol's TPH-3135 formulation. Use of this propellant would essentially double burning time without sacrificing performance. Data from Thiokol indicate that this propellant is suitable for use in spherical motors, resulting in near-neutral thrust time characteristics. Spherical motors were considered for Missions 3, 5, and 7 because they generally have better propellant fractions than cylindrical designs. The Mission 7 motor uses the slower burn-rate propellant. Data on slower burning propellant was not available at the time of Missions 3 and 5 motor design.

The other potential problem is associated with impingement on the spacecraft of solid particulate matter in the nozzle exhaust plume. A study of the impingement was made and is incorporated as Appendix B, Vol III. Results of this study indicate that plume impingement problems can be avoided by going to dual-nozzle motors in which nozzle centerlines are separated by at least 40°. Probe motor designs use a separation angle of 45°. Estimates from motor manufacturers indicate no difference in development cost between single- and dual-nozzle motors.

A delivered vacuum specific impulse of 2809 N-sec/kg (287 lbf-sec/lbm) was suggested by solid-motor manufacturers for these applications, with composite propellants for long vacuum exposure before ignition of the motor. The use of a double-base propellant requires sealing the chamber with a scored plug assembly at the throat to maintain a dry N_2 atmosphere before ignition. This requirement would introduce a potential failure mode.

2. Selected Subsystems Description

The ACS and deflection-velocity probe propulsion systems' characteristics for Missions 3, 5, and 7 are presented in this section.

a. Deflection Propulsion Subsystem - Propellant quantities for deflection velocity attainment were based on:

$$\ln\left(\frac{W_I}{WF}\right) = \frac{\Delta V}{I_{SP}g} \qquad \text{[VII-1]}$$

where

W_I = initial probe weight,

W_F = final probe weight after achieving deflection velocity,

ΔV = deflection velocity,

I_{SP} = propellant specific impulse.

Solution of this equation results in the determination of W_F based on initial probe weight. The difference between W_I and W_F is the propellant weight, W_P, expended.

Referring to Fig. VII-35, motor mass fraction for a single-nozzle motor can be determined, once the contained propellant is known. Because the motor has dual nozzles whose centerlines are separated by an angle of 0.785 rad (45°), actual propellant required is the computed W_F divided by the cosine of half the angle between the dual nozzle centerlines. The single-nozzle motor inert weight can now be computed by taking the quotient of the contained propellant divided by the mass fraction.

Several solid-propellant rocket-motor manufacturers were consulted to determine the effect on mass fraction of incorporating two half-thrust nozzles on the motor instead of a single full-thrust nozzle. For the dual-nozzle sizes employed, it was suggested that a weight of approximately 0.453 kg (1 lbm) be added to the single-nozzle motor inert weight to arrive at a dual-nozzle motor mass fraction.

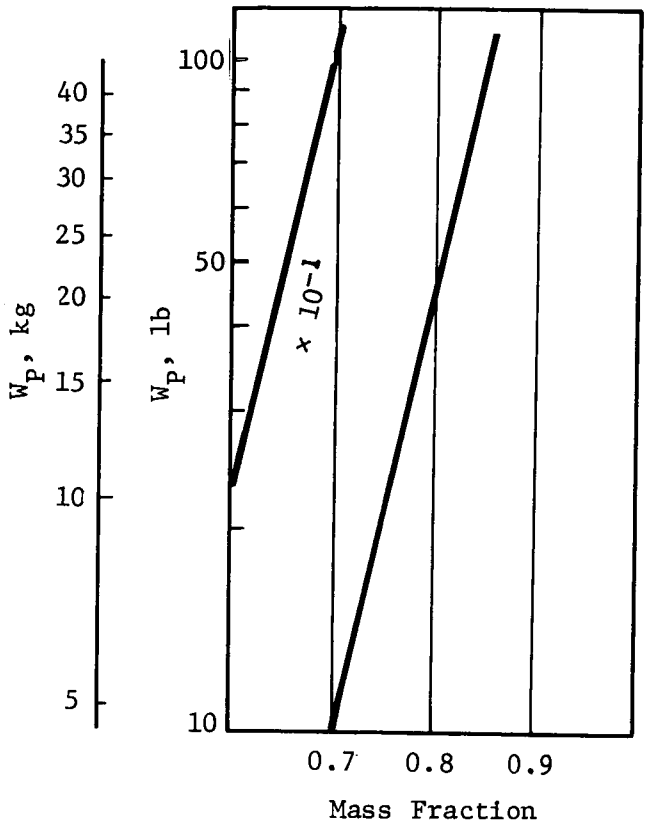

Fig. VII-35 Small Solid-Propellant Rocket-Motor Mass Fraction versus Propellant Weight

Solid-rocket motor dimensions and burn times were calculated based on procedures in Ref VII-4. A thrust coefficient of 1.78 and chamber pressure of 3.654×10^6 N/m^2 (530 lbf/in.^{2}) were assumed. A burn rate of 0.716 cm/sec (0.282 in./sec) was assumed for the faster burning-rate propellant and 0.487 cm/sec (0.20 in./sec) for the slower burning-rate propellant. Based on these assumptions, it was possible to compute the nozzle dimensions. The resultant spherical dual-nozzle deflection-motor characteristics are presented in Table VII-13.

Table VII-13 Spherical Dual-Nozzle Deflection-Motor Characteristics

Item	Unit of Measure	Mission		
		3	5	7
ΔV	m/sec	82.1	75	130.7
W_P	kg (lbm)	2.37 (5.23)	2.17 (4.78)	3.49 (7.7)
I_{SP}	N sec/kg (lbf sec/lbm)	2809 (287)	2809 (287)	2809 (287)
I_T	N sec (lbf sec)	6670 (1500)	6100 (1370)	9840 (2210)
P_C	N/m^2 ($lbf/in.^2$)	3.654×10^6 (530)	3.654×10^6 (530)	3.654×10^6 (530)
λ	——	0.59	0.59	0.61
$W_{loaded\ motor}$	kg (lbm)	4.02 (8.86)	3.67 (8.1)	5.71 (12.6)
t_b	sec	5.6	5.5	9.8
F/nozzle	N (lbf)	596 (134)	554 (124.5)	503 (113)
A_{throat}	cm^2 ($in.^2$)	0.92 (0.142)	0.85 (0.132)	0.77 (0.120)
ϵ	——	40	40	40
A_{exit}	cm ($in.^2$)	36.6 (5.68)	34.1 (5.28)	31.0 (4.80)
D_{motor}	cm (in.)	13.5 (5.5)	13.2 (5.4)	15.6 (6.4)
$L_{nozzle\ exposed}$	cm (in.)	10.2 (4.18)	9.9 (4.06)	5.8 (2.38)
L_{motor}	cm (in.)	24.6 (9.68)	24.0 (9.46)	22.3 (8.78)

b. ACS Propulsion Subsystem - For Missions 3 and 5, the GN_2 ACS propulsion subsystem is required to provide a probe spinup of 10.47 rad/sec (100 rpm) on separation of the probe from the spacecraft. After a distance of 548 m (1800 ft) between probe and spacecraft, the probe deflection motor is fired. On completion of this firing, the probe is precessed 0.63 rad (-35°) for Mission 3 and 0.61 rad (-35°) for Mission 5 by the GN_2 ACS propulsion subsystem.

The GN_2 ACS propulsion subsystem for Mission 7 provides for a probe spinup of 10.47 rad/sec (100 rpm) on separation of the probe from the spacecraft. Once a distance of 548 m (1800 ft) separates probe and spacecraft, the deflection motor is fired. On completion of this firing, the probe is despun to 2.09 rad/sec (20 rpm) and precessed 0.55 rad (-31.6°).

Schematics of the GN_2 systems and component weight estimates are presented in Fig. VII-36 for Missions 3 and 5 and in Fig. VII-37 for Mission 7. Component weight estimates were obtained from Ref VII-1. Table VII-14 presents probe characteristics and various spinup, despin, and precession subsystem characteristics and propellant requirements for the GN_2 ACS propulsion systems incorporated in Missions 3, 5, and 7 probes.

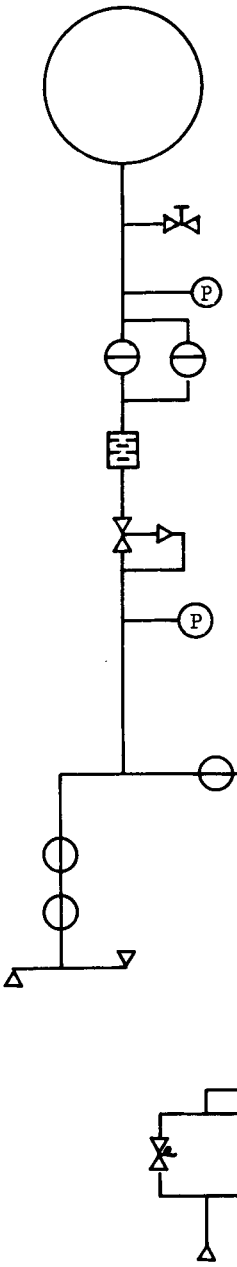

	kg	lbm
Tank	0.513	1.13
GN_2	0.467	1.03
Fill Valve	0.113	0.25
Pressure Transducer (2)	0.227	0.50
NC Squib Valve (2)	0.227	0.50
Filter	0.59	0.35
Regulator	0.182	0.40
Lines	0.113	0.25
NO Squib Valve (4)	0.454	1.00
Thruster (4) 0.445 N (0.1 lbf)	0.182	0.40
Solinoid Valve (4)	0.363	0.80
Total	3.00	6.61

Fig. VII-36 ACS/Spin Propulsion Subsystem Schematic and Weights for Mission 3 and 5 Probes

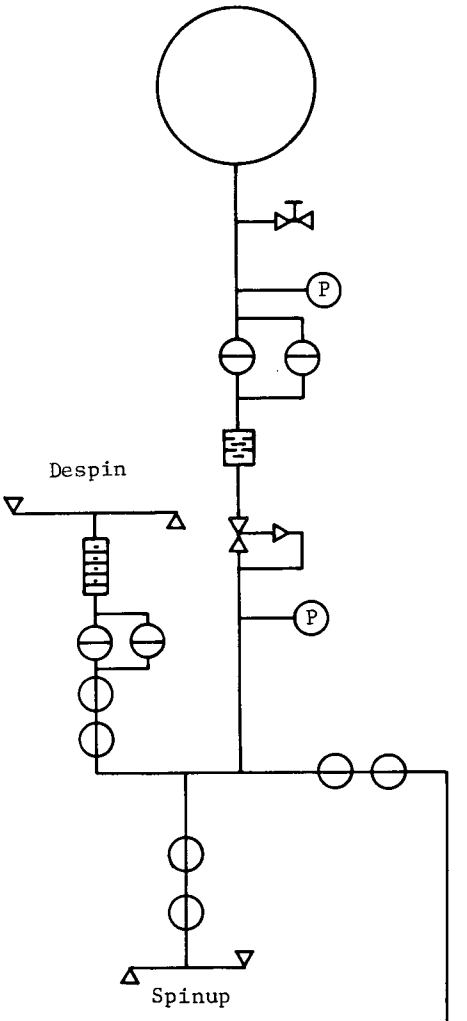

	kg	lbm
Tank	0.685	1.51
GN_2	0.622	1.37
Fill Valve	0.113	0.25
Pressure Transducer (2)	0.226	0.50
NC Squib Valve (4)	0.454	1.00
Filter (2)	0.318	0.70
Regulator	0.182	0.40
Lines	0.113	0.25
NO Squib Valve (6)	0.680	1.50
Thruster (6) 0.445 N (0.1 lbf)	0.272	0.60
Solenoid Valve (4)	0.363	6.0
Total	4.03	8.88

Fig. VII-37 ACS/Spin Propulsion Subsystem Schematic and Weights for Mission 7 Probe

Table VII-14 Probe ACS/Spin Propulsion Subsystem GN_2 Requirements

Item	Unit	Mission	
		3 and 5	7
Probe I_Z	kg m^2 (slug ft^2)	5.15 (3.8)	5.15 (3.8)
Spin Subsystem			
$\Delta\omega$	rad/sec (rpm)	10.47 (100)	10.47 (100)
Arm	m (ft)	0.382 (1.25)	0.382 (1.25)
Nozzles (2)	N ea (lbf ea)	0.445 (0.1)	0.445 (0.1)
t_b	sec	159	159
W_p required	kg (lbm)	0.20 (0.44)	0.20 (0.44)
Precession Subsystem			
θ	rad (deg)	0.61 (-35)	0.56 (-32)
W_p required	kg (lbm)	0.16 (0.35)	0.12 (0.27)
Despin Subsystem			
$\Delta\omega$	rad/sec (rpm)	N/A	8.36 (80)
Arm	m (ft)	N/A	0.382 (1.25)
Nozzles (2)	N ea (lbf ea)	N/A	0.445 (0.1)
t_b	sec	N/A	127
W_p required	kg (lbm)	N/A	0.16 (0.35)
Σ W_p (GN_2) = Σ W_p required × 1.3 margin	kg (lbm)	0.47 (1.03)	0.62 (1.37)

D. PROBE CONFIGURATION

Both blunt and sharp configurations were considered for the entry probe. These shapes are shown in Fig. VII-38, in which the blunt shape is represented by the hemisphere/cylinder and the sharp configuration by the cone.

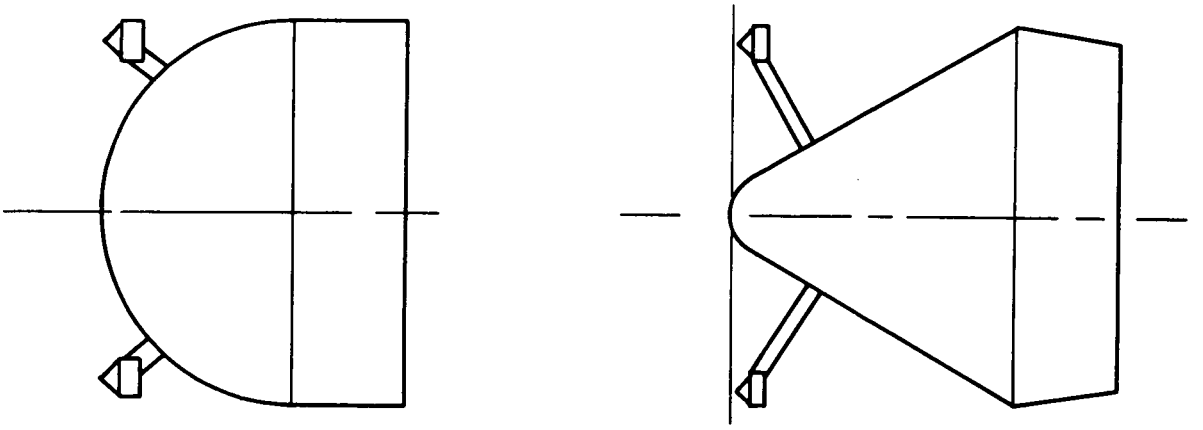

a Hemisphere/ Cylinder Configuration

b Cone Configuration

Fig. VII-38 Hemisphere/Cylinder and Cone Configurations

There are four basic criteria for comparison of these classes of configurations for the turbopause probe mission:

1) Location of science instruments relative to the probe surface for minimum measurement interference;

2) Sufficient roll inertia relative to pitch and yaw to maintain spin stability;

3) The effect of shape on the number of electrons generated in the wake, and thus, the blackout condition;

4) Local aerodynamic heating.

1. Science Instrument Interference

From the standpoint of instrument interference, no particular advantage could be found with one configuration compared to the other. The mass spectrometer is located with its inlet at the stagnation point in both cases in which minimum interference is experienced. The IRPA and NRPA instruments are best placed forward on booms even with the stagnation point and outboard, as

shown. This requires longer booms for the cone shape; however, no particular problem is involved. The ETP and photometers can be mounted in equivalent locations.

2. Roll Inertia

Because the probe depends on spin stabilization over a long period, roll moment of inertia must be at least 1.1 times more than the inertia of the transverse axes, and preferably 1.2 times more. Integration layouts of identical probe systems were prepared with hemisphere/cylinder and conical bodies. Despite the fact that the diameter of the conical design was increased by 5 cm (2.0 in.), the spin to transverse mass moment of inertia was only 1.07 compared to 1.20 for the hemisphere/cylinder. An additional factor considered is that it is difficult to use the cone volume efficiently for packaging equipment. Therefore, installation of equipment to provide proper inertia ratios for spin stabilization definitely favors the blunt hemisphere/cylinder configuration.

From a structural and mechanical viewpoint, no characteristics were found that favor one configuration.

3. Electron Density in the Wake

Communications blackout is a direct function of electron density in the wake. The blunt shape develops and extensive normal shock region that generates extremely high shock temperatures and associated electrons that carry into the wake. A highly complex series of aerophysics computer programs were run to evaluate this condition, and the results are reported in Chapter X. Because of its relatively sharp nose, the cone shape will develop a small normal shock region, and therefore, a smaller number of electrons will be generated about the stagnation area in this region. However, there are reasons to believe that there may be compensating flow-field actions as the flow is carried around the body into the wake (Chapter X), and the resulting wake electron density for the sharp cone may remain nearly as high as that for the blunt hemisphere. Complete evaluation of the cone flow field was beyond the scope of this study. However, an evaluation similar to that for the hemisphere will be required to resolve this question.

4. Aerodynamic Heating

Initial aerodynamic heating is primarily convective heat transfer. Because convective heating is a direct function of $1/\sqrt{\text{nose radius}}$, the sharp cone will experience considerably higher stagnation-point heating than the hemisphere. However, most of the significant heating occurs after communications blackout, and therefore,

is not a primary design factor. Local heating at the mass spectrometer inlet (stagnation point) should be checked to see that no contamination or melting of the inlet occurs before the end of the mission. Preliminary analyses indicate that this will not be a problem.

In summary, based on analyses completed within the scope of the study, the hemisphere/cylinder configuration has the clear advantage in the area of spin stabilization and equipment packaging. Additional aerophysics analysis is warranted for evaluation of electron density in the wake because the cone may show an advantage there. No particular advantage for either shape is seen in the areas of instrument interference, structural/mechanical design, and aeroheating.

E. REFERENCES

VII-1 Lee B. Holcomb: *Satellite Auxiliary Propulsion Techniques*, JPL NASA TR 32-1505, Nov 1, 1970.

VII-2 *Auxiliary Propulsion Survey - Part III Survey of Secondary Propulsion and Passive Attitude Control Systems for Spacecraft*, APL-TR-68-67, Part III, September 1968.

VII-3 *Attitude Control Engine Evaluation*, Martin Marietta TM 1661-66-10, Dec 1966.

VII-4 *Spherical Rocket Motors*, Thiokol Chemical Corporation, EB7-64, Jan 1965.

VIII. PROBE ATTITUDE CONTROL

This chapter discusses the probe attitude-control system requirements and design implementation approach. Mission study results showed that two basic probe designs are required depending on the type of mission flown. On certain missions, the probe does not require attitude control or deflection propulsion and is, therefore, a very simple design. Other missions require both ACS and propulsion on the probe, with attendant probe complexity.

There are three fundamentally different sets of attitude-control requirements for the defined mission profiles, and these are listed below.

Mode 1 (Probe Deflection) - The spacecraft releases the probe in the attitude required for the deflection ΔV. The probe fires the ΔV, which puts it on the desired impact trajectory and establishes the required communications geometry. The probe then reorients itself to the attitude required for zero angle of attack at entry.

Mode 2 (Shared Deflection) - The spacecraft releases the probe in the proper attitude for zero angle of attack at entry. The probe fires a ΔV in that direction so that it is displaced to the entry site. The spacecraft then speeds up to achieve the required communications geometry at entry.

Mode 3 (Spacecraft Deflection) - The spacecraft trajectory is targeted to impact the entry site. The spacecraft releases the probe in the proper attitude for zero angle of attack. The spacecraft then orients itself and firest a ΔV to establish the desired flyby trajectory and communications geometry.

A. ATTITUDE-CONTROL ERROR ANALYSIS

Critical parameters affecting mission success are correct placement and magnitude of the ΔV impulse vector determines probe trajectory in time and space, is the principal factor in locating the probe at acquisition, and influences communications aspect angles and doppler shift.

Final pointing attitude of the probe is constrained by scientific experiments and communications aspect angle. Aspect angle is normally the more severe attitude constraint for these missions. The following is a discussion of sources of various errors and their influence on attitude-control requirements. Errors developed for each mission are tabulated in the mission analysis, Chapter IV Section F. Numerical results will be developed here only for those aspects required to define attitude control requirements.

Case 1 (Mode 3 - Spin-Stabilized Spacecraft) - The spacecraft provides velocity impulse and final pointing of the probe for this type of mission. All trajectory errors are derived from spacecraft tolerances. Because the probe is released spinning in its final attitude, attitude errors are a function of spacecraft attitude errors and tipoff rates. Final attitude of the probe is determined by the orientation of its angular momentum vector because a passive damper is included in the probe design to remove nutation. The attitude errors for the probe are then

$$\theta_{epl} = \theta_{es}$$

$$\theta_{ep2} = \tan^{-1} \frac{\omega_{es} I_t}{\omega_z I_z}$$

θ_{ep} = probe attitude error, rad

θ_{es} = spacecraft attitude error, rad

ω_{es} = tipoff rate, rad/sec

ω_z = nominal probe spin rate, rad/sec

I_z = probe spin axis moment of inertia

I_t = probe transverse axis moment of inertia

$I_t = I_x = I_y$

$I_z > I_t$

Because these errors are random, they are combined statistically in the mission analysis programs and will not be manipulated further here.

Case 2 (Mode 1 - Spin-Stabilized Spacecraft) - The spacecraft provides pointing for the ΔV impulse and spinup to 40 rpm before separation in the case of the Pioneer S/C. The probe continues spinup to 100 rpm, provides ΔV impulse with a solid rocket motor and an attitude maneuver to the final orientation. Initial errors involved in these maneuvers are similar to the errors for Mode 3.

$$\theta_{ep1} = \theta_{es}$$

$$\theta_{ep2} = \frac{\omega_{es} I_t}{\omega_z I_z}$$

The remaining errors, which are significant parameters of this mission, are momentum vector error $\left(\theta_{ep3}\right)$ caused by spin-jet misalignment and velocity-vector error $\left(\theta_{ep4}\right)$ during ΔV thrusting resulting from misalignment of the solid rocket motor. These errors are discussed in Ref VIII-1.

The values are given by

$$\theta_{ep3} = K_3 \eta + K_4 \omega_z$$

$$\theta_{ep4} = \frac{Fr}{I_z \omega_z^2} \text{ (limiting case)}$$

$\eta = T_t / T_a$ ratio of cross-axis torque to axial torque. (This term arises from misalignment of the spin jets.)

K_3 = coefficient from reference (See discussion below.)

K_4 = coefficient from reference (See discussion below.)

r = axial thrust misalignment (See Table VIII-1.)

Table VIII-1 Probe Tolerances Contributing to Attitude Disturbance

Structural Tolerance (3σ)	
Nozzle/flange	0.0254 cm
Flange	0.0762 cm
Mounting surface	0.1°
cg location	0.038 cm
Thrust Motor	
Thrust vector	0.1150°
Axial Thrust Misalignment	0.140 cm*
Radial Thrust Misalignment	0.140 cm*
Spin Thrust Misalignment	0.095 cm†

*RSS
†RSS (two thrusters)

The coefficient K_4 is a Fresnal integral that is plotted in the reference. Although the computer plot in the reference is with respect to some specific vehicle parameters, they are combined so that the curves can be normalized and applied to all vehicles. The coefficient K_3 is a double Fresnal integral that does not yield to attempts to normalize. However, the value of K_3 is bounded, and approximate solutions can be obtained.

After the ΔV impulse event, the attitude control subsystem maneuvers to the final orientation. The accuracy of this maneuver is required to be 2° or 3°, depending on the specific mission. A description of the attitude-control geometry and subsystem is provided in Subsection C6.

Case 3 (Mode 1 - Three Axis-Stabilized Spacecraft) - The spacecraft is a three-axis stabilized vehicle in this mission profile. Two alternative designs for probe release were considered. The obvious approach of using a spin table has a number of disadvantages: interaction with the spacecraft stabilization system, difficulty in achieving sufficiently low tipoff rates, weight, and the cost of the development and space qualification of a long-life precision mechanism. Because of these considerations, a nonspinning separation mode was selected. The alternatives then presented consisted of spinning up immediately after separation or using the probe attitude-control system to implement ΔV impulse pointing and spinup. The analysis of the first of these alternatives follows.

Angular momentum increase

$$\dot{\overline{P}} = M\hat{k}$$

where

$\dot{\overline{P}}$ = angular momentum

M = spin torque

$\hat{k}$ = unit vector along spin axis

Angular precession rate

$$\omega_p = \overline{P} / I_t$$

Motion of the k axis

$$\dot{\hat{k}} = \overline{P} / I_t \times \hat{k}$$

$$\ddot{\overline{P}} = M \dot{\hat{k}}$$

$$\ddot{\overline{P}} = \frac{\overline{P} \times \dot{\overline{P}}}{I_t}$$

Letting

$$\overline{P} = \hat{x}\, p_x + \hat{y}\, p_y + \hat{z}\, p_z$$

$$\dot{\overline{P}} = \hat{x}\, \dot{p}_x + \hat{y}\, \dot{p}_y + \hat{z}\, \dot{p}_z$$

$$\dot{p}_z \approx M \qquad p_z \approx Mt$$

Then

$$\ddot{p}_x = \frac{M}{I_t} \left(p_y - t\dot{p}_y \right)$$

$$\ddot{p}_y = \frac{M}{I_t} \left(t\dot{p}_x - p_x \right)$$

$$\dddot{p}_x = \left(\frac{M}{I_t} \right)^2 \left(tp_x - t^2\, \dot{p}_x \right)$$

$$\dddot{p}_y = \left(\frac{M}{I_t} \right)^2 \left(tp_y - t^2\, \dot{p}_y \right)$$

The series solution of these equations

$$u = A_0 + A_1 t + A_2 t^2 + \ldots + A_n t^n$$

$$A_{n+4} = \frac{-\left(M / I_t \right)^2 (n - 1)}{(n + 4)\ (n + 3)\ (n + 2)}$$

For the x component

$$p_x(0) = \omega_{es} I_t \qquad \dot{p}_x(0) = 0 \qquad \ddot{p}_x(0) = 0 \qquad \dddot{p}_x(0) = 0$$

and

$$p_y(0) = 0 \qquad \dot{p}_y(0) = 0 \qquad \ddot{p}_y(0) = \frac{-M\, p_x(0)}{I_t} \qquad \dddot{p}_y(0) = 0$$

$$p_x = p_x(0)\left[1 + \sum_{n=1}^{\infty} (-1)^{n+1} \frac{\left(P_z\right)^{4n}}{\left(MI_t\right)^{2n}} \frac{(4n-2)!}{(4n)!\left(2^{2n-1}\right)(2n-1)!}\right]$$

or

$$p_x = p_x(0)\left[1 + \sum_{n=1}^{\infty} b_n \left(P_z\right)^{4n}\right]$$

And the displacement of the angular momentum vector in the x direction from the effect of initial rates on spin-up is

$$\theta_x = \theta_{ep2}\left[1 + \sum_{n=1}^{\infty} b_n \left(p_z\right)^{4n}\right]$$

A similar series can obviously be generated for θ_y. However, when it is considered that the total error budget now includes not only the previously defined errors θ_{ep1}, θ_{ep2}, and θ_{ep3}

but also $\theta_{ep2} \sum_{n=1}^{\infty} b_n \left(p_z\right)^{4n}$ and θ_{ep0}

where

$$\theta_{ep0} = \omega_{es}\, t_o$$

and

t_o = time from separation to spinup,

it becomes obvious that, with realizable tipoff rates (1 to 3°/sec), accurate placement of the ΔV impulse vector is impractical. Based on this reasoning, an approach that requires probe subsystems to supply pointing accuracy for velocity impulse was selected. This will require the probe attitude-control subsystem error to be less than 1° for this function.

B. SPIN RATE

Effectiveness of spin stabilization is directly related to the magnitude of disturbance torques. Axial thrusters for trajectory correction are a major source of disturbance torque because the thrust vector may not pass through the center of mass. If structural tolerances are considered fixed, increased axial thrust will result in increased body-fixed torques. In general, the magnitude of attitude disturbance is directly proportional to thrust level and inversely proportional to the square of the spin rate. These relationships are illustrated in Fig. VIII-1 through VIII-3.

The reliability and economy of solid rocket motors compared to other propulsion systems justifies consideration of these devices in a simple planetary entry probe. The higher thrust level of solid rocket motors will require higher spin rates to maintain desired pointing accuracy. A review of electronic-component and attitude-control dynamics limitations has been made to establish conservative upper limits for the entry probe spin rate.

1. Mechanical Stress

Acceleration stress from angular velocity and radial position is illustrated in Fig. VIII-4. Angular velocity necessary to produce acceleration stresses comparable to the launch sequence maximum (16.9 g) at the periphery of the probe is 20.8 rad/sec.

The effect of the acceleration field on components of electronic subsystems has been reviewed. Two components were found to have operating constraints at accelerations less than 16.9 g.

Remotely activated batteries must be oriented in the vehicle so the acceleration forces assist the flow from the reservoir to the cells. This is necessary to prevent any reverse flow of electrolyte, which would create conduction paths and short the cells.

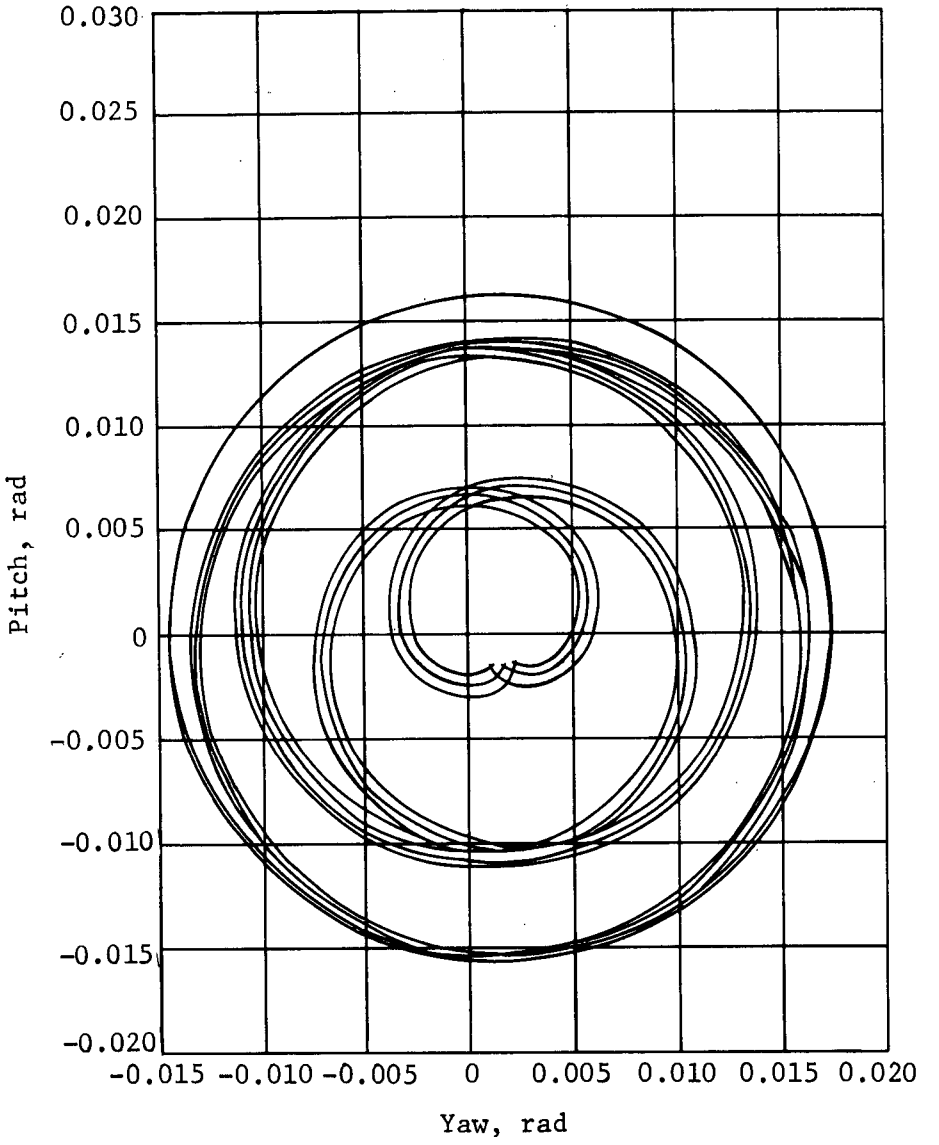

Fig. VIII-1 Typical Spin Axes Displacement with Axial Thrust-Induced Body-Fixed Torque

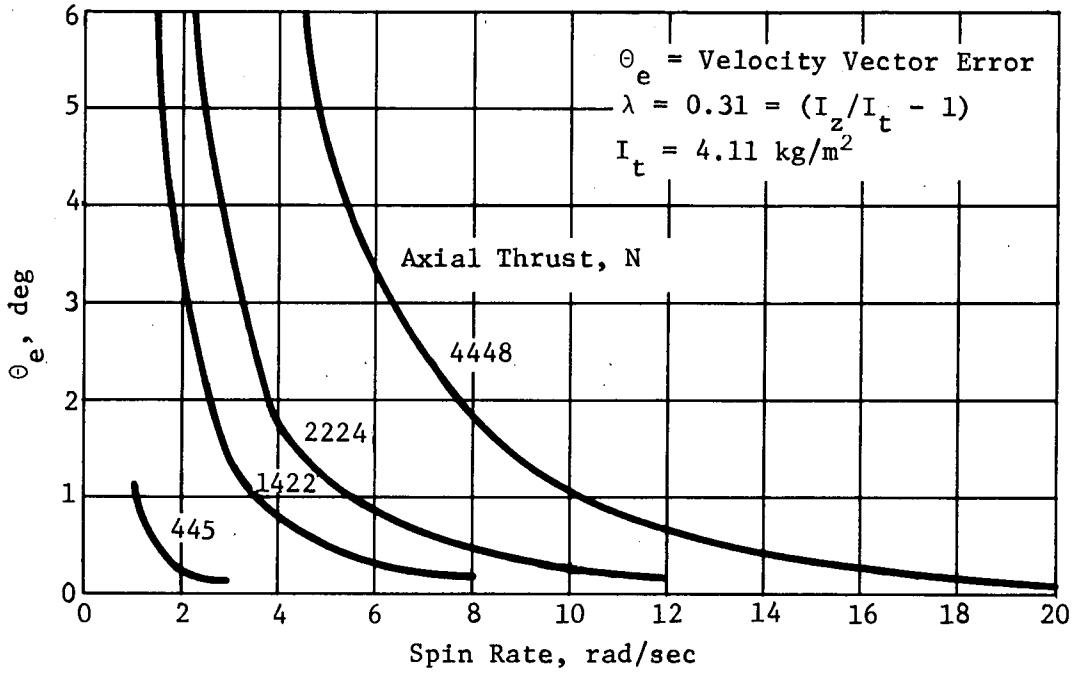

Fig. VIII-2 Velocity Vector Error Due to Body-Fixed Torque

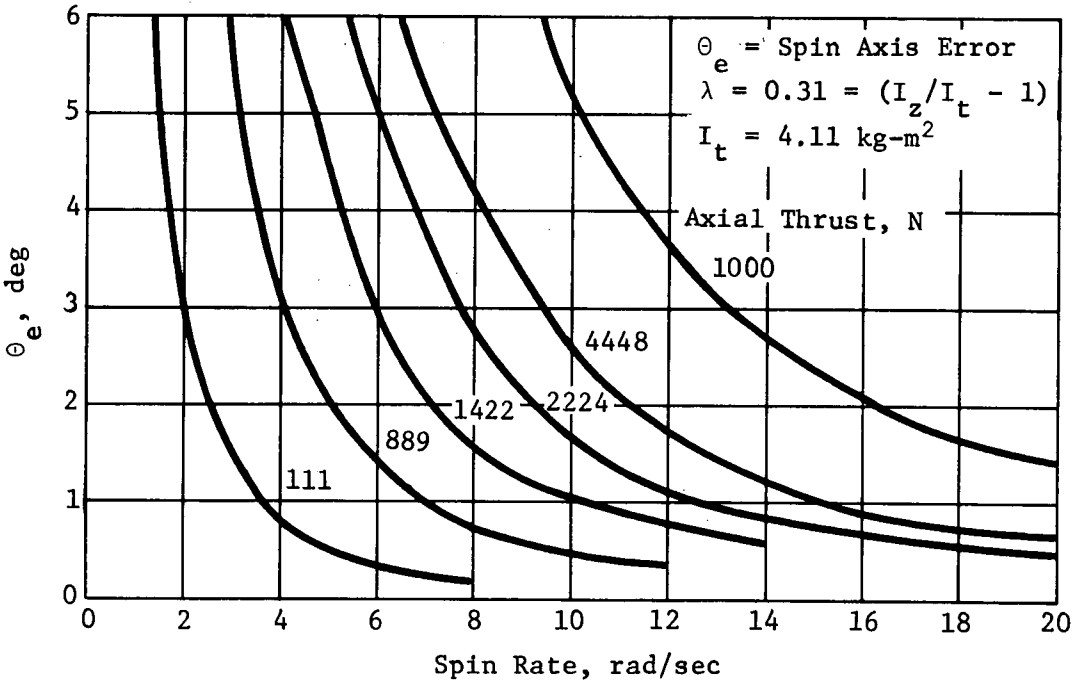

Fig. VIII-3 Axial Thrust-Induced Nutation

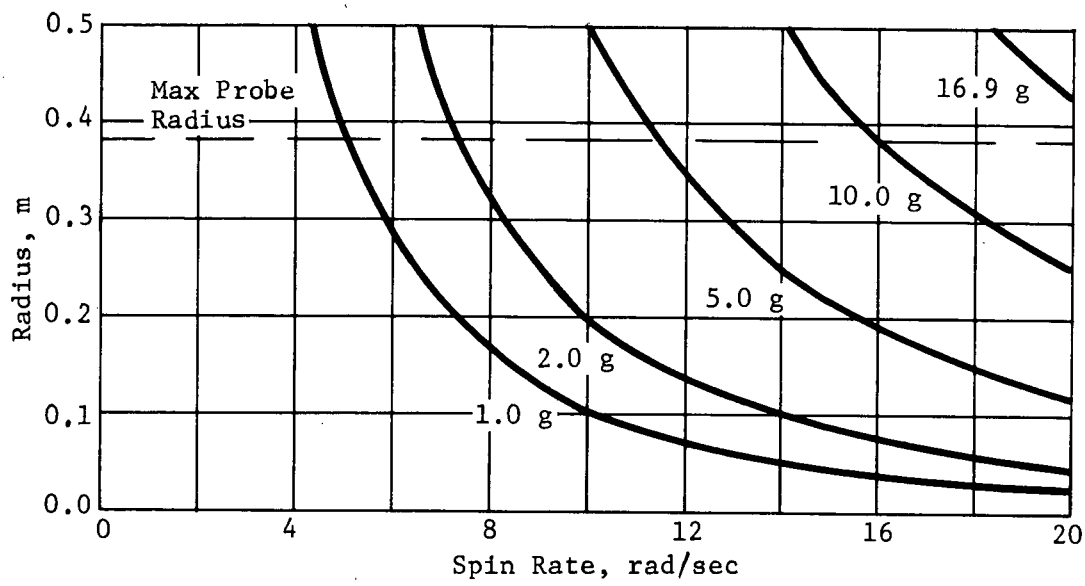

Fig. VIII-4 Rotating Vehicle Acceleration Field

Latching relays are expected to be used for pyrotechnic events that take place at near-Jupiter distances (i.e., entry phase) Relays being considered for Viking (Potter Bromfield HL-4125) are required to operate in a 5-g field along any axis with less than 10 μsec contact chatter. This specification is considered conservative, and the relay should meet specifications in a 20-g field.

2. Performance Factors

a. Propellant - Use of increased angular rates will require more propellant for attitude maneuver as well as spinup. Required total impulse is directly proportional to the spin rate and is given by

$$(IMP)_T = \frac{(e + 1.2\theta)\ \omega I_z}{er}$$

Θ = maneuver angle

ω = angular rate

I_z = moment of inertia about the spin axis

r = moment arm for spin and precession jets

e = precession thruster efficiency.

A factor of 20% is included in the attitude maneuver to account for nutation correction. No factor is included for leakage and ullage. The value of θ is zero for mission profiles that do not require an attitude maneuver.

b. Precession Control - Angular rate affects maximum impulse per rotation, number of solenoid (jet) cycles, control range, and total impulse, as previously noted. Jet efficiency is the ratio of effective impulse to total impulse and is a function of firing angle. Firing angle is usually limited to 45° (e = 0.975). Angular rate is limited to the value at which minimum solenoid cycle time (minimum bit) prescribes a firing angle equal to the maximum allowable firing angle. Control range is the ratio of the difference between the minimum bit and the maximum impulse per cycle to the maximum impulse per cycle.

The above study indicates no significant obstacle at spin rates below 200 rpm. At this angular velocity, acceleration forces are equal to the maximum launch environment force. Higher rates could be used by locating fragile components near the axis of rotation.

The effect of velocity-induced electric fields in combination with high spin rates produces current flow in the Langmuir probe sensors. This indicates that it will be necessary to despin to about 20 rpm before operating this instrument.

The purposes of increasing the spin rate are achieved at approximately 100 rpm. Because the probe mass and criticality of design tolerances increase with spin rate, 100 rpm is recommended.

C. ATTITUDE-CONTROL DESIGN

Several alternative approaches were considered to meet attitude-control requirements. Principal considerations in the survey of possible systems were simplicity, reliability, and use of available components, because these asepects have a direct effect on cost. A few of these alternatives are briefly discussed in this section.

1. Offset Thrust

The conditions described for mission profiles that require attitude control indicate that two attitude positions are required: orientation for ΔV impulse, and final position for entry. It has been considered that, if the ΔV impulse could be applied at an angle with respect to the spin axis, the probe could be separated with spin in the final attitude and no maneuver would be required. This approach could be implemented in one of two ways:

1) A combination of axial thrust and an impulse at right angles to the spin axis;

2) Use of an offset solid rocket motor with a firing time that is small compared to the time of rotation.

However, both approaches would require precise timing functions that would have to be derived from at least a Sun sensor. Furthermore, effects of offset tolerances and the transverse component of the thrust would produce unacceptable attitude errors, and further attitude corrections would be required.

2. Stored Momentum

This approach would use a small flywheel operated at high speed. The angular momentum vector of the wheel would be exactly that required to correct the position of the probe angular momentum vector from the ΔV impulse direction to the final position. The wheel would be positioned before separation and spinup. Once positioned, the wheel would be released on free gimbals. The probe would then be spun up, released, and the solid rocket motor fired. After completion of the ΔV impulse, the wheel could be locked to the probe spin axis and eventually stopped with respect to the probe frame of reference by friction, resulting in complete transfer of wheel angular momentum to the probe.

The problems arising with this approach are basically:

1) The possibility of undesirable transfer of momentum from the wheel to the probe before or during ΔV impulse;

2) The presence of high-energy storage in the wheel could result in the probe eventually achieving an attitude of 180° from that desired.

Basically, the first problem is the most serious. The free gimbals would be stressed during ΔV impulse. Consideration was given to providing some drive to a gimbal oriented along the spin axis to overcome biased friction from the probe spin. However, even if this approach were considered feasible, an expensive development and qualification program would be required for a precision gimbal development.

3. Open-Loop Control

This system would consist of a stored series of timed precession impulses. Because orientation of the probe and final attitude are well known, the attitude maneuver could be precisely specified. The final error would then include the disturbance to the angular momentum vector caused by the ΔV impulse. This approach could not be used for missions that require attitude trim before firing the solid rocket motor. This method was discarded because it is not feasible to meet the knowledge requirements on probe spin rate and phase. At least a Sun sensor would be required. Because these sensors are available to yield Sun aspect angle as well as Sun crossing time for phasing, a closed-loop system could be used that would provide greater reliability and probably lower cost when testing, and less critical precision requirements are considered.

4. Simple Closed-Loop Single-Axis Maneuver

This approach is a natural outgrowth of the open-loop system. It would use a Sun sensor that provides a measurement of solar aspect angle as well as Sun crossing time. The maneuver sequence would consist of firing a preprogrammed set of precession impulses immediately after the ΔV impulse maneuver. These pulses could be offset in phase so that an essentially two-axis maneuver could be achieved, although only the maneuver angle with respect to the Sun line (i.e., solar aspect angle) could be measured. After the

initial maneuver, some time (several hours) would elapse while the damper removed residual nutation. A measurement of solar aspect angle would then provide information for further maneuvers.

5. Closed-Loop Two-Axis Maneuver

This design approach uses a Sun sensor to measure solar aspect angle and Sun crossing time and a Jupiter sensor to measure Jupiter crossing time. The sequence of the maneuver would be similar to the single-axis system. Immediately after ΔV impulse maneuver, a preprogrammed series of pulses would orient the probe near its final position. Then, after a waiting period of several damper time constants, measurements would be made of solar aspect angle (clock angle) and the angle between the Sun and Jupiter measured about the spin axis of the probe (cone angle). These measurements would then be used to develop subsequent precession programs to finalize the probe's position. Because of residual nutation, it is not considered desirable to continuously drive the probe to minimize the final error. For this reason, the maneuver would occur in a series of steps, as described above. For this approach, there are certain constraints on the relative position of the Sun and Jupiter, as discussed below. This system, using attitude sensors, can also be used to trim probe attitude before the ΔV impulse. Because it represents a minor increment in complexity over a single-axis system and has inherently greater flexibility and capability, it has been the system that has received major consideration. For missions in which the single-axis system may be preferred, it would be a minor consideration to reduce the two-axis maneuver system to a single-axis system.

6. Two-Axis Closed-Loop Geometry

As previously described, the simple probe sensor system defined for the turbopause mission can measure solar aspect angle and the angle between two planes. The line of intersection of the planes is the spin axis of the probe. The spin axis, probe-Sun vector, and probe-Jupiter vector describe the position of the two planes, respectively. The geometric relationships are shown in Fig. VIII-5. As noted in the figure, measurement of the solar aspect angle effectively locates the probe spin axis on a cone in inertial space. The location of the spin axis on the cone must then be determined, although in the applications under consideration, this location will be predictable within a few degrees. Figure VIII-6 elaborates on the measurements that must be performed.

Fig. VIII-5 Attitude-Control Geometry

Fig. VIII-6 Attitude-Control Measurement, β Plane

In Fig. VIII-6, a nomograph is shown to illustrate how the angle between Jupiter and the Sun measured about the spin axis, β, varies with the position of the probe spin axis on the surface of the cone, θ. The angle β is also influenced by Jupiter aspect angle, ϕ. However, this angle is not shown because the sensory sensory system does not measure it. A complete expression for the reslationship between α, β, θ, and ϕ is

$$\tan \beta = \frac{\sin \alpha \sin \theta}{\sin \alpha \cos \theta \cos \phi - \cos \alpha \sin \phi}$$

The cone itself is symmetrical in space with respect to the probe Sun line and has a half angle equal to the solar aspect angle, α. The values shown are applicable to Mission 3. Geometric problems are encountered for some geometries. These are illustrated in Fig. VIII-6 for a value of $\alpha = 57.3°$. For this condition, the Jupiter aspect angle with respect to the spin axis is less than the solar aspect angle and the probe-Jupiter vector lies within the cone shown in Fig. VIII-5. The effect of this geometry is to make θ double-valued for any allowable value of β. The minimum value of β (i.e., β'), which will be measured (subject to the constraint $\alpha = 53.7°$) results in a condition for which changes in θ result in no change in β. This means that the system gain described functionally by $\beta = f(\theta)$ is zero. Values of θ near this condition cannot be measured by this system. However, values of θ and β for this mission are close to 180°, and this singular condition is not a problem. The final position for this mission involves a value of $\alpha = 20.9°$. Under these circumstances, the probe-Jupiter vector lies outside the solar aspect cone and θ is single-valued for any particular value of β. Furthermore, β now has a minimum value of zero (i.e. all values of β are allowable). The effect of the constraints on the mission results in a sensory system gain of 0.67 near the final attitude desired ($\alpha = 20.9°$). Sensory system gain is in general greater than one for values of θ near zero and less than one for values of θ near 180°.

Other geometric problems that may arise with this system occur if the solar aspect angle or Jupiter aspect angle approach zero. For geometries in which these angles are less than a few degrees, a simpler system can be used that merely points the spin axis at the reference. However, for aspect angles greater than a few degrees and less than approximately 15°, difficulty may be encountered in obtaining the proper accuracy of measurement because of the finite window of the sensors and the natural polar coordinate system inherent with this configuration.

7. Sensors

The requirement is for a three-axis attitude determination of a spin-stabilized spacecraft at approximately 10^7 km from Jupiter. For the mission discussed, the probe is relatively near the line between Jupiter and the Sun. Jupiter will be nearly full-phase and approximately 0.4° apparent diameter as seen from the probe. accuracy of angular measurements within 0.5° is considered adequate.

The design approach uses two sensors, one to obtain two-axis information from the Sun, the other to furnish third-axis information by sensing Jupiter.

The Sun sensor will measure the angle between the spacecraft spin axis and the Sun. This can be a 9-bit digital output (with the Adcole Corp. instrument), or linear analog output (with the Honeywell Radiation Center instrument). The second axis is determined by the direction of the Sun when the plane containing the instrument's optical axis and the spacecraft spin axis crosses the Sun. This is indicated by a pulse output from the Sun sensor. This Sun sensor and its electronics will weigh a maximum of 1.59 kg and require a maximum of 2 W if the instrument is to cover the whole celestial sphere on each revolution about the spacecraft spin axis. These numbers can be lowered if miniaturized integrated circuitry is used and if the spin-axis-to-Sun angle is constrained within certain limits.

8. Jupiter Sensor

The electromagnetic radiation from Jupiter consists mainly of three classifications:

1) Reflected light from the Sun, essentially in the wavelength band from 0.3 to 1.5 μ, with peak at approximately 0.5 μ. This is in the visual and near-infrared region. The apparent shape of Jupiter in this radiation will vary from a thin crescent to a fully illuminated disc, as a function of the phase angle between the line of sight from the instrument to Jupiter and the line from Jupiter to the Sun.

2) Energy radiated by the planet as a black body, from its own temperature. Because Jupiter has a significant atmosphere and a relatively high rotational speed (approximately 10 hr/rev), temperature over the entire apparent surface is relatively constant at approximately 130° K. Its black-body

radiation is essentially in the wavelength band from 5 to 30 μ, peaking at about 11 μ. It is relatively constant from about 8 to 14 μ. Jupiter's apparent shape in this radiation will be the nearly circular shape of an oblate spheroid.

3) Radio-frequency radiations in the wavelength band longer than 3 cm. This radiation seems to be associated with varying but discrete sources on the planet, and is therefore not suitable for sensing the plane for determination of its center.

There are many sensors that can detect reflected solar radiation, and their relative usefulness depends on the specific purpose of the instrumentation as well as their own intrinsic properties. Some of the more frequently used materials are summarized in the following tabulation.

Material	Wavelength at peak response	Remarks
Photocathodes: (Usually in photomultiplier tubes)		
S-1	1 μ	
S-11	0.43 μ	
S-20	0.42 μ	Highest response
Others		
Silicon	1 μ	Photo conductive & photovoltaic
Selenium	0.8 μ	
Gallium Arsonide	0.8 μ	
Copper-Cupric Oxide	0.5 μ	
Cadmium Sulphide	(visual)	

At least three materials are sensitive in the range of Jupiter's black-body radiation. These are Mercury-doped germanium operating at 28°K, gold-doped germanium, at 60°K, and copper-doped germanium at 4.2°K. Zinc-doped germanium at 4.2°K covers the

desired range at lower sensitivity; it is more useful at somewhat longer wavelengths. The disadvantage common to these materials is that they must be operated at very low temperatures. This often adds prohibitive weight for spacecraft applications, but the low temperatures available in space can conceivably be used to advantage for these detectors.

Based on the above, the device selected for a Jupiter sensor will consist of a silicon sensitive element and possibly a lens system. A survey should be made of available Sun sensors to establish whether an available component could be used for this application.

9. Electronics

The functional block diagram in Fig. VIII-7 is representative of the electronics for all missions requiring an attitude-control system. The functions required of the ACS electronics are listed below.

1) Process the solar aspect-angle information. The data output of the solar aspect sensor is generally analog or digital gray code. In either case, it would be converted to binary digital for processing in the logic. The solar aspect output can be used as a measure of nutation by establishing maximum and minimum attitude angles, as will be discussed in 4) below.

2) The pulse output from the Sun sensor is generated when the Sun crosses the sensor's optical axis. Processing this pulse will consist of establishing its center by selecting the point at which the derivative (slope) is zero (maximum amplitude) or averaging the time between preselected amplitudes. Some study must be made of the effect of the greatly increased solar range on this pulse. It is distinctly possible that solar intensity near Jupiter may be decreased by factors other than range because recent data from the Mariner flights indicate a discrepancy between measured and expected illumination. The Sun pulse is used to control the sector logic as well as provide attitude information in combination with a similar Jupiter pulse.

3) The pulse derived from the Jupiter sensor when the planet crosses the optical axis of the sensor is essentially similar to the Sun pulse described above, and processing will be the same.

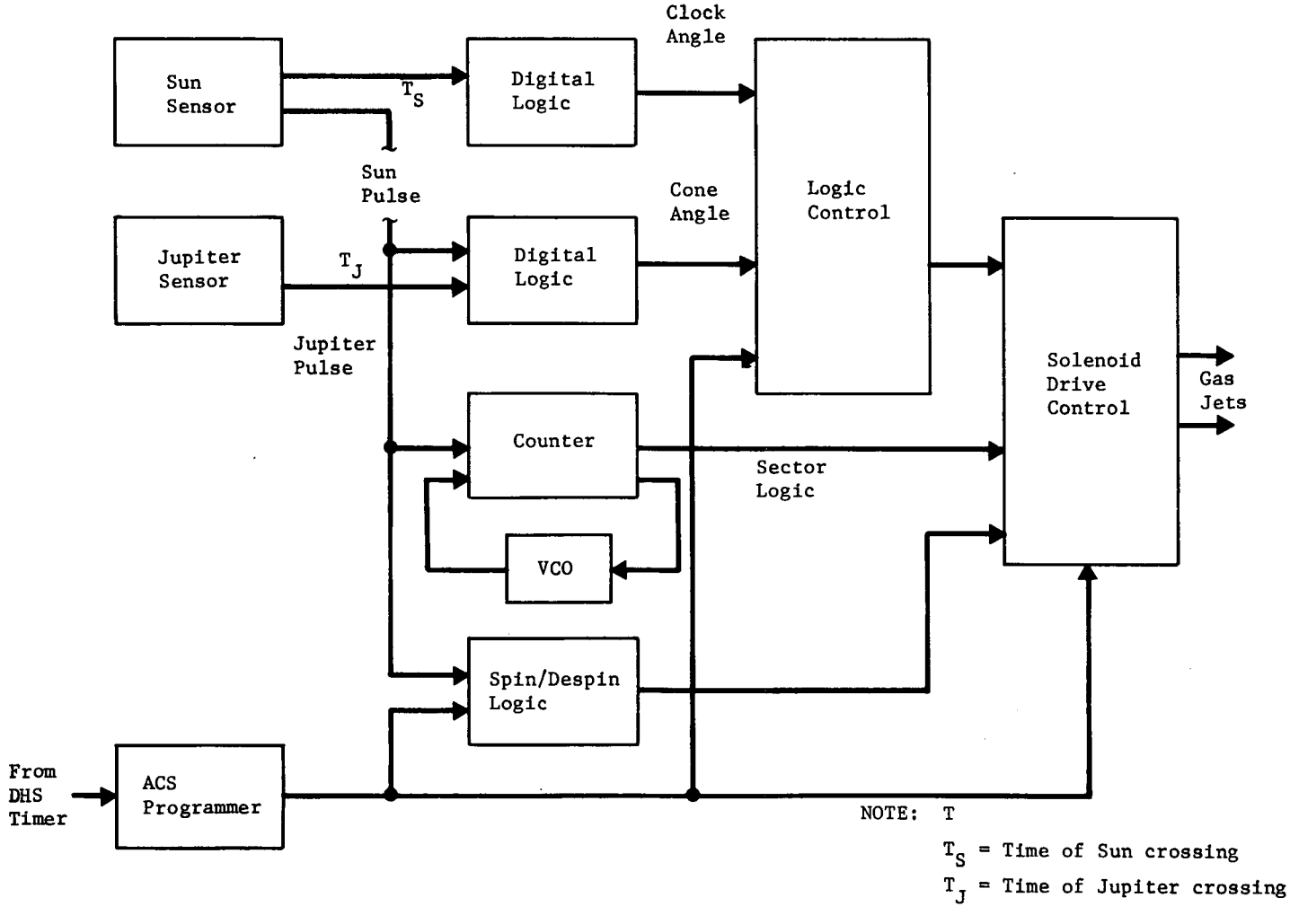

Fig. VIII-7 Attitude-Control System

4) Sector logic will be used to establish correct precession jet-firing intervals. There are two obvious approaches to this logic. A counter can be used to measure the period of revolution. Simple binary division and addition processing can then be used to establish angular position of the probe at any time during the next revolution on the basis of the content of the register. Because the measured period of rotation will be updated every revolution, the basic timing oscillator would have no critical nominal frequency requirements and reasonable drift requirements, resulting in a simple economical design for this element. However, digital processing would be increased over a voltage-controlled oscillator approach. The use of a VCO would permit the sector logic to be hard wired. This system generates the proper sector logic by driving the oscillator so the count register approaches a fixed value for every revolution. Angular position of the probe is determined when this counter reaches some preset value. This is the preferred approach for this function because required development is decreased. This method has been applied to several recent vehicles. Furthermore, a reasonably accurate clock will be needed for missions with despin requirements to ensure that allowable minimum angular rate is maintained.

5) A nominal functional block diagram of the solar aspect processing is shown in Fig. VIII-8. At predetermined intervals, a series of solar aspect angles will be measured and the maximum and minimum selected. This is necessary because nutation will be present. If the difference between these angles is too great, indicating excessive nutation, another waiting interval will be initiated. If the difference between the maximum and minimum angle is small enough, the attitude will be evaluated. The evaluation will consist of summing the maximum and minimum measurements to obtain a measurement related to the mean value representative of the position of the angular momentum vector. This value is then compared to a preset attitude command and the sign and magnitude of the error are established. A similar function provides an evaluation of the spin-axis cone angle. The difference in the content of the revolution period-count register between the Sun and Jupiter pulse is compared with the total revolution period. This provides a measurement of the angle β through which the probe rotates between pulses, and establishes the position of the probe on the space cone defined by the solar aspect angle.

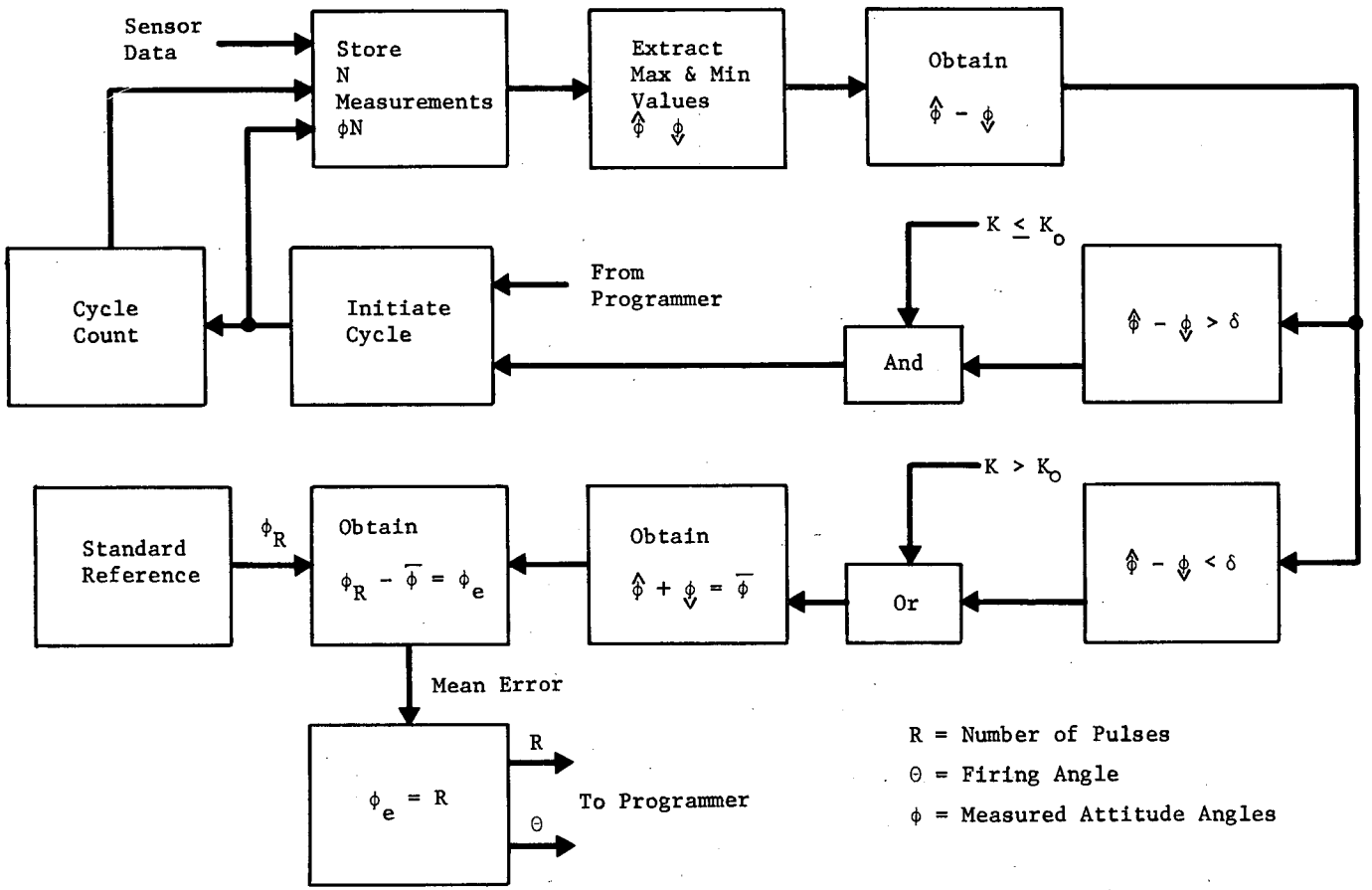

Fig. VIII-8 Precession Logic

An averaging similar to that provided by the solar aspect logic is performed and the results compared with a preset command. The resultant angular errors are then used to program the timing of the precession events and pulse width. When the indicated error decreases below the allowable maximum error, the ACS signals the data management system that the maneuver is complete and the precoast shutdown sequence is initiated.

The attitude-control logic may be implemented by COSMOS within the 1975 state of the art. Because this is a critical maneuver, with this design, there is no method by which the success of the maneuver can be evaluated and readjusted by spacecraft or ground command, it is recommended that 100% redundant majority logic be used. The use of COSMOS will alleviate the power penalty that might otherwise be incurred. The Jupiter range at which this maneuver takes place is sufficient to ignore the effects of the Jupiter radiation belts.

The precession pulses will be implemented by pneumatic jets driven by appropriate power amplifiers. These amplifiers should be designed to require low power during standby.

The required vehicle maneuver is relatively simple, and consequently, the electronics presents no design problem. Some further studies may be required to evaluate the effects of nutation on subsystem performance.

10. Damper

A viscous ring damper was selected for the mission because of its mechanical simplicity. This type of damper has been applied to several designs such as VELA, LES, Intelsat III, COMSAT, TIROS. It has advantages of no moving parts; no threshold of performance; insensitivity to changes in spin rate, mass properties, and temperature; does not affect probe static or dynamic balance; and it does not have critical mounting or geometry requirements. Its principal disadvantages are size and weight, which are inversely related to rather long time constants. In case the viscous ring damper proves impractical, a tuned wheel can be used, which is much smaller but would increase cost. The performance of the viscous damper has been analyzed (Ref VIII-2) and the time constant, τ, is given by

$$\tau = \frac{2\pi I_z}{F(\gamma)\ m\ R^2\ (1+\lambda)^2\ \omega}$$

I_z = spin moment of inertia

I_t = transverse moment of inertia

$F(\gamma)$ = function of wobble Reynolds number ≈ 1

m = mass of fluid

R = radius of ring

$\lambda = I_z / I_t - 1$

ω = angular rate of probe.

With the constants appropriate to the various turbopause probes with dynamic attitude control, it appears that time constants on the order of 1 hr are feasible with a 12-cm-dia damper. Because the period during which the ACS system must be active may be as long as 12 hr, this would appear adequate. With a vehicle operating at 5 rpm, the damping period would extend to 20 hr. This is not a problem because the ACS does not depend on damping for missions with this angular rate. Furthermore, initial nutation would only be caused by tip-off rates, and approximately 7 days are available for damping.

D. REFERENCES

VIII-1 R. S. Armstrong: *Errors Associated with Spinning-up and Thrusting Symmetric Rigid Bodies*, JPL TR 32-644, 1965.

VIII-2 J. V. Dedor *et al.*: *Explorer XXXV Attitude Control System*, GSFC, NASA TN D-5187, 1969.

IX. SPACECRAFT INTERFACE AND MODIFICATIONS REQUIREMENTS

The addition of a probe to a spacecraft has a potential for affecting many aspects of the analysis and design of the spacecraft, its integration with the launch vehicle, and its mission.

The presence of the probe requires that the spacecraft design and analysis be modified by changes in structural design loads, mass properties, and thermal performance. Aspects of the integration of the spacecraft with the launch vehicle, which are influenced by the probe, are relocation of the spacecraft in the fairing envelope, changes to the launch vehicle/spacecraft adapter, modification of spacecraft dynamic response to the launch environment, changes to space requirements in the fairing caused by added equipment, and increased payload weight. Spacecraft mission modifications required by the presence of a probe vary considerably as a function of probe complexity. Generally speaking, the simpler the probe, the greater the effects on the spacecraft mission.

During the study, effects of a probe on the Pioneer, TOPS and MOPS spacecraft were evaluated. Pioneer and MOPS received the major emphasis because of contract redirection. Table IX-1 presents the spacecraft used for each mission study.

Table IX-1 Launch Load Factors

	Mission 1	2	3	5	1A	2A	7
Launch Vehicle	Titan IIID-5-seg Centaur-Burner II		7 seg	5-seg	←5-seg→		
Spacecraft	Pioneer	Pioneer	TOPS	Pioneer	Pioneer	Pioneer	MOPS

The scope of the study precluded an evaluation of all factors mentioned above. Evaluation of spacecraft interfaces and modifications was limited to conceptual integration layouts, thermal analysis of the probe on the spacecraft, evaluation of the thermal effect of the probe on the Pioneer, identification of spacecraft-supplied power requirements, analysis of a communications link with the probe, and an evaluation of the spacecraft propulsion subsystem.

A. PIONEER

1. Integration

Figure IX-1 presents a layout study of the simple (no deflection motor) probe on the Pioneer spacecraft on the Titan IIID-5-Segment Centaur-Burner II launch vehicle with the Viking fairing. Above the Centaur stage is a spin table, TEM-364-4 (Burner II) solid motor, spacecraft/probe structural adapter, and Pioneer. Below the spacecraft on the spacecraft Z axis are a probe adapter and probe. After Centaur burnout, the TEM-364-4 motor and payload above it are spun up and separated. The TEM-364-4 is fired and separates at the space-vehicle separation plane.

The Pioneer without probe adapts to the TEM-364-4 by a cylindrical adapter similar to the one used for the probe. Because of incorporation of the probe, the spacecraft system/TEM-364-4 adapter interfaces at the corners of the hexagonal Pioneer equipment compartment.

The cylindrical adapter on the spacecraft Z axis, which formerly adapted to the TEM-364-4 solid rocket motor, is modified to accept the probe and its structural separation system and electrical connector. In addition, it must accept the environmental cover and its associated structural separation and separation spring system. The Pioneer/probe structural adapter must also support the insulation blanket, which thermally controls the solid rocket deflection motor on the probe during cruise (for those probes that include a propulsion subsystem).

The effect of the probe on spacecraft-system mass properties requires evaluation, particularly because Pioneer is a spin-stabilized spacecraft. Addition of the probe on the Z axis will increase the X and Y axes mass moments of inertia. An evaluation of this effect will be required. Location of the probe on the Z axis was made practical by information received from TRW that spacecraft cruise cg could be readily located on the Z axis rather than 0.19 m (7.6 in.) laterally offset, as now defined. Table IX-2 presents an estimate of the weight effect of the probe system on Pioneer for Missions 1, 1A, 2, 2A, and 5.

Note that Missions 2 and 2A require a small increase in spacecraft propellant, which requires a propellant tank modification. This modification has a minor effect on spacecraft weight and design.

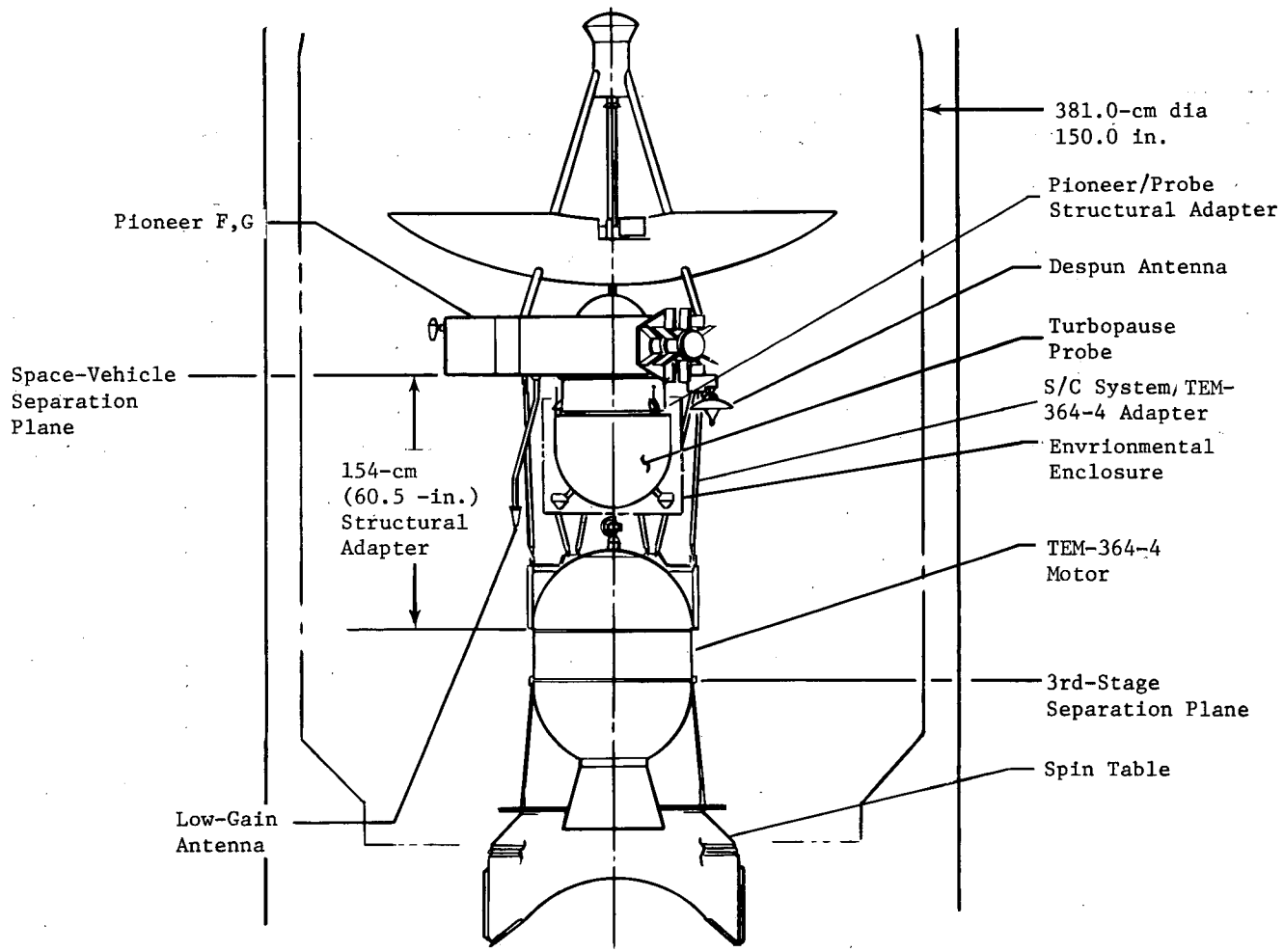

Fig. IX-1 Probe Pioneer F-G Interface, Mission 1

Table IX-2 Weight Estimates of Pioneer Spacecraft Modifications

Item \ Mission	1, kg	(lb)	1A, kg	(lb)	2, kg	(lb)	2A, kg	(lb)	5, kg	(lb)
Environmental Enclosure	4.5	(10.0)	4.5	(10.0)	4.5	(10.0)	4.5	(10.0)	4.5	(10.0)
Probe & Environmental Enclosure Mount & Separation Spring	4.5	(10.0)	4.5	(10.0)	4.5	(10.0)	4.5	(10.0)	4.5	(10.0)
Electrical Mounting Brackets & Wire Bundles	3.4	(7.4)	3.4	(7.4)	3.4	(7.4)	3.4	(7.4)	3.4	(7.4)
Antenna/Drive/Bracket	10.0	(22.0)	1.4	(3.0)	11.5	(25.3)	13.5	(30.0)	10.5	(23.1)
Receiver System	5.9	(13.0)	5.9	(13.0)	5.9	(13.0)	5.9	(13.0)	5.9	(13.0)
Data Handling System	6.8	(15.0)	6.8	(15.0)	6.9	(15.0)	6.8	(15.0)	6.8	(15.0)
Spacecraft Propellant					5.8	(12.3)	4.4	(9.7)		
Thermal Blanket	0.9	(2.0)	0.9	(2.0)	0.9	(2.0)	0.9	(2.0)	0.9	(2.0)
Subtotal	36.0	(79.4)	27.4	(60.4)	43.3	(95.5)	43.9	(97.1)	36.5	(80.5)
Margin ∿ 15%	5.4	(11.9)	4.1	(9.0)	6.0	(14.3)	6.3	(14.5)	5.5	(12.0)
Totals	41.4	(91.3)	31.5	(69.4)	49.3	(109.8)	50.2	(111.6)	42.0	(92.5)

2. Probe/Spacecraft Thermal Integration

A thermal analysis was performed to investigate the effect of the turbopause probe on the spacecraft's thermal performance. Because the interface between probe and spacecraft causes the probe and probe shield to partially block the spacecraft louver assembly view to space, it was necessary to evaluate the spacecraft louver's heat-rejection capability.

For the TOPS spacecraft, louver assemblies are on both the +Y and -Y sides of the electronic equipment compartment. Because the probe is not mounted directly in front of either louver assembly, no significant blocking occurs, and only a minor decrease in heat rejection capability would result. TOPS is also Sun oriented and therefore shades the probe, except during brief midcourse corrections. During these corrections, however, the probe could reflect varying amounts of sunlight into the louver panels, thus briefly reducing their heat-rejection capability.

For Pioneer, the probe and environmental cover are directly above the equipment-bay louver assemblies, as shown in Fig. IX-2. The spacecraft/probe radiant interchange was analyzed using the Mission 3 probe configuration, which represented the largest probe diameter. Results of the thermal analysis include maximum heat-rejection capability of the equipment-bay louver assemblies as a function of the effective louver-radiator temperature for both unmodified Pioneer (no probe) and Pioneer/probe combination. (See Fig. IX-3.)

The results indicate approximately 25% reduction in the heat-rejection capability of the equipment-bay louver assemblies. The maximum heat-rejection rate of these assemblies, therefore, becomes 75 W, assuming an upper limit of 50°F for the louver radiator. The reduction in performance identified applies only to the equipment-bay louver assemblies. The science bay louver assembly will be unaffected by the probe's presence.

If the heat-rejection requirement of the spacecraft during cruise (with probe on board) is greater than 75 W (assuming the 50°F upper limit), modification will be required to increase the equipment-bay radiator area.

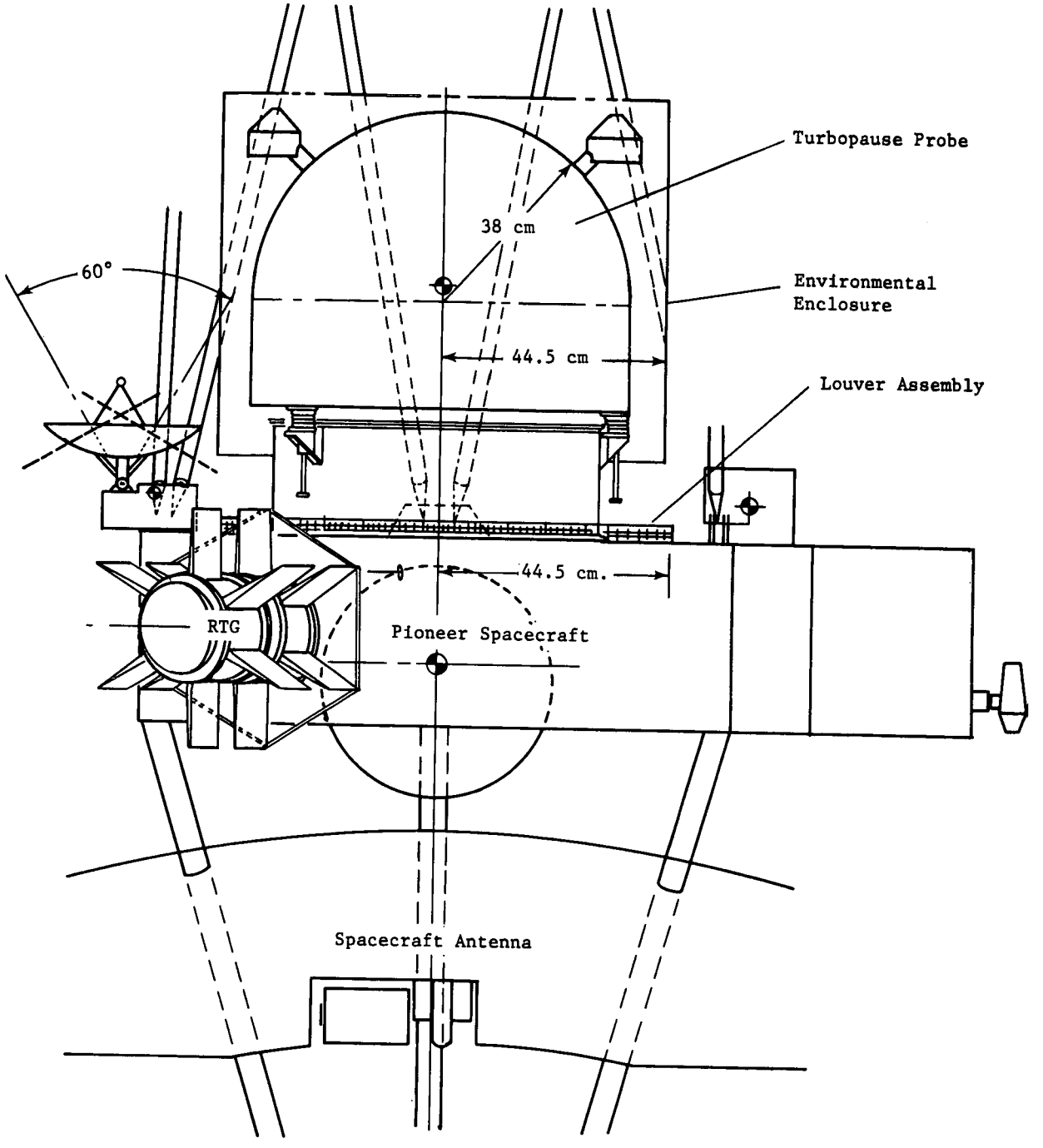

Fig. IX-2 Pioneer Spacecraft and Stowed Turbopause Probe

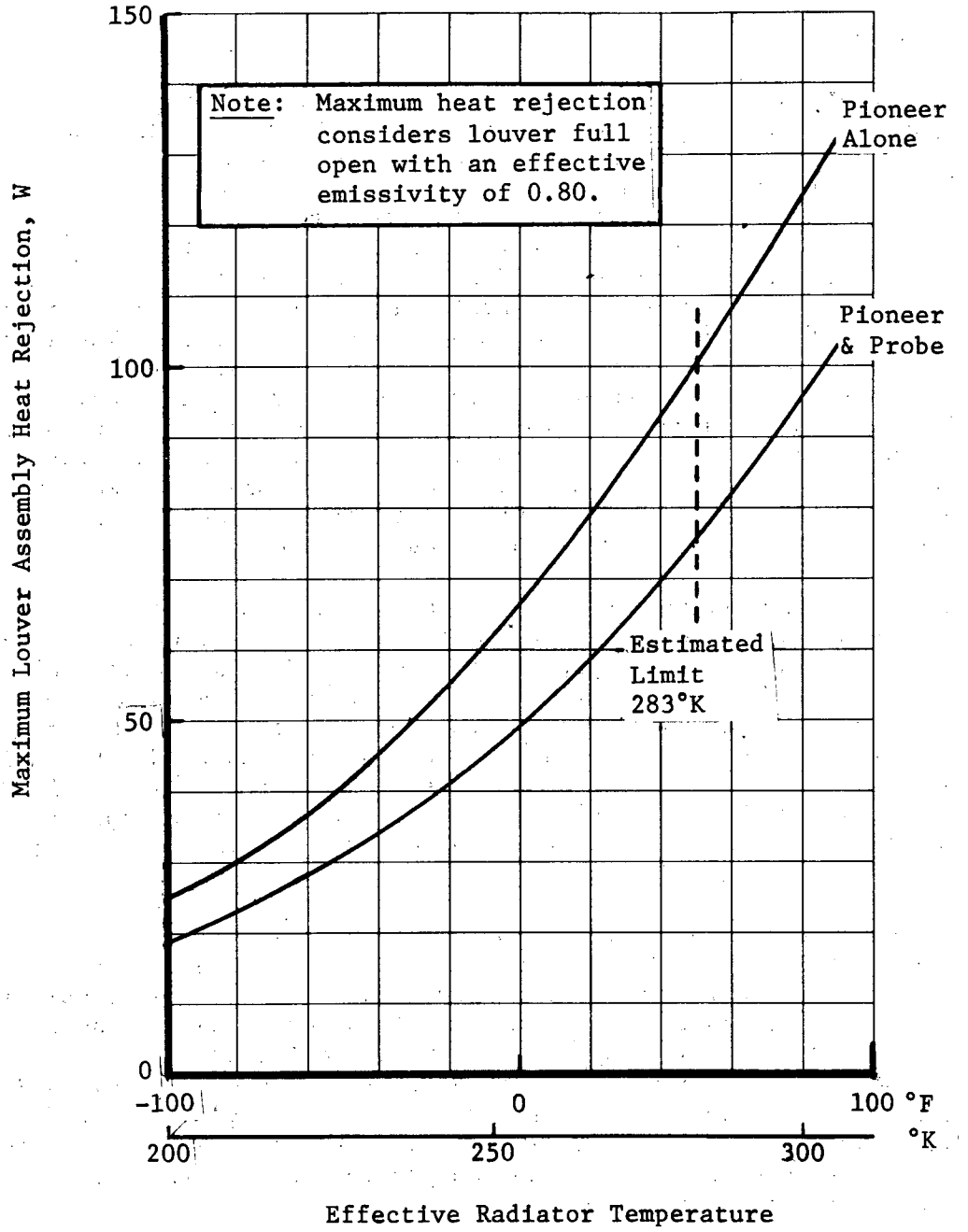

Fig. IX-3 Thermal Analysis Results--Louver-Assembly Heat Rejection vs Effective Radiator Temperature

3. Propulsion

Probes for Mission 1, 1A, 2, 2A, and 5 are carried by Pioneer spacecraft from Earth to near Jupiter. The probe on Mission 5 provides its own spin-up and deflection velocity after it is freed from the spacecraft.

Probes 1, 1A, 2, and 2A are carried by the spacecraft on a trajectory targeted to enter the Jupiter atmosphere. At a distance from Jupiter specified by the particular mission, the spacecraft is properly oriented, spun up, and the probe released. The spacecraft is then despun, reoriented, and a deflection velocity imparted to put it on the prescribed Jupiter flyby trajectory. The propulsion subsystems of the Pioneer spacecraft must provide the spin, despin, and deflection velocities for the spacecraft with the added weight of spacecraft modifications. The spin up maneuver will include the probe weight. The ΔVs and propellant margins required are listed in Tables IX-3 and IX-4.

The propulsion subsystems of the Pioneer are assumed to use a hydrazine catalyst system incorporating a GN_2 blowdown pressurization system. A total propellant weight of 25.7 kg (60.5 lbm) is initially stored aboard the spacecraft. For the Earth-to-Jupiter midcourse correction, a delivered propellant specific impulse of 2150 N sec/kg (220 lbf sec/lbm) was assumed. For all other propulsion functions, a delivered specific impulse of 1860 N sec/kg (190 lbf sec/lbm) was assumed. The decreased specific impulse is assumed to be due to the blowdown characteristics of the propulsion system.

Based on these propellant performance characteristics, spacecraft, spacecraft modifications, probe weights, and sequence of events, Tables IX-3 and IX-4 were developed. Table IX-3 presents numerical values in English units and Table IX-4 in metric units. As can be seen, Missions 1, 1A, and 5 can be accomplished with the 27.5 kg (60.5 lbm) of propellant carried by the Pioneer. Missions 2 and 2A would require slightly more propellant (or higher-performance propellant). TRW has indicated that larger propellant tanks could easily be accomodated in the present design with little effect on Pioneer systems.

Table IX-3 Pioneer Spacecraft Application (English Units)

	1	1A	2	2A	5
Pioneer S/C (lbm)	547.0	547.0	547.0	547.0	547.0
Pioneer modifications	91.3	69.4	109.8	111.6	92.5
Probe	134.6	131.9	136.7	130.7	194.2
W S/C initial	772.9	748.1	793.5	789.3	723.7
ΔV E-J (m/sec)	100	100	100	100	100
W_E E-J (lbm)	35.0	34.0	35.3	35.3	32.8
Probe garage	10	10	10	10	10
Spin-up S/C from 4.8 rpm to	37.5	20	37.5	20	NA
W_P spin-up	3.38	1.58	3.38	1.58	NA
Separate probe	134.6	131.9	136.7	130.7	194.2
Despin S/C to (rpm)	4.8	4.8	4.8	4.8	NA
W_P des pin	3.38	1.58	3.38	1.58	NA
W S/C at deflection	586.5	569.0	604.7	609.7	486.7
ΔV S/C deflection (m/sec)	16.1	54.6	101.3	101.3	NA
W_P S/C deflection	5.0	16.5	31.2	31.7	NA
W S/C final	581.5	552.5	573.5	578.0	486.7
W S/C Available Propellant	60.5	60.5	60.5	60.5	60.5
W_P E-J	35.0	34.0	35.3	35.3	32.8
W_P spin & despin	6.76	3.16	6.76	3.16	NA
W_P deflection ΔV	5.0	16.5	31.2	31.7	NA
W S/C propellant remaining	13.7	6.8	-12.8	-9.7	28.7

Note: All units lbm unless otherwise noted

Table IX-4 Pioneer Spacecraft Application (Metric Units)

	1	1A	2	2A	5
Pioneer S/C	248.2	248.3	248.3	248.3	248.3
Pioneer modifications	41.4	31.5	49.3	50.2	42.0
Probe	61.1	59.6	61.9	59.3	88.2
W S/C initial	350.9	339.2	359.5	357.8	328.6
ΔV E-J (m/sec)	100	100	100	100	100
W_P E-J	15.9	15.4	16.0	16.0	14.9
Probe garage	4.5	4.5	4.5	4.5	4.5
Spin-up S/C from 0.5 rad/sec to	3.93	2.09	3.93	2.09	NA
W_P spin-up	1.5	0.7	1.5	0.7	NA
Separate probe	61.1	59.6	61.9	59.3	88.2
Despin S/C to (rad/sec)	0.5	0.5	0.5	0.5	NA
W_P despin	1.5	0.7	1.5	0.7	NA
W S/C at deflection	266.3	258.3	274.1	276.6	221.0
ΔV S/C deflection (m/sec)	16.1	54.6	101.3	101.3	NA
W_P S/C deflection	2.3	7.5	14.2	14.4	NA
W S/C final	264.0	250.8	259.9	262.2	221.0
W S/C available propellant	27.5	27.5	27.5	27.5	27.5
W_P E-J	15.9	15.4	16.0	16.0	14.9
W_P spin and despin	3.0	1.4	3.0	1.4	NA
W_P deflection ΔV	2.3	7.5	14.2	14.4	NA
W S/C propellant remaining	6.3	3.2	-5.7	-4.3	13.0
Note: All units kg unless otherwise noted					

4. Spacecraft Power

Three primary requirements for S/C power have been identified. They are power for thermal control of the probe deflection propulsion system, thermal control of the receiver crystal, and power for the communications and data handling system. Other requirements for S/C power are probe checkout, pyro firing, antenna drive, and S/C spin-up and despin.

Maintaining the probe deflection propulsion motor at 294°K will require 2 to 3 W of electricity from the spacecraft. A thermostatically controlled 5-W heater would provide an acceptable solution.

The S/C receiver crystal should be maintained at 50 ±10°C for stable operation. This will require approximately 10 W.

Requirements for the communications and data handling system for real-time transmission are 10 W. The time power is required is summarized in Table IX-5 for all Pioneer missions. This system requires 28 ±5 V.

For mission on which data storage is required, an additional 25 W will be required for a tape recorder.

5. Communications

The communications subsystems supported by an interface with Pioneer are the antenna, antenna despin driver (if used), receiver, and data handling.

The antenna requires accurate pointing for probe tracking. For this study, a deadband of 0.25° 3σ was used. For all Pioneer missions (except 1A), a despin drive is required to counterrotate the antenna at the spin speed of the S/C. For 1A the S/C antenna aspect angle is so small that a fixed antenna installation is used. The relay antenna installation is shown in Fig. IX-1.

The receiver and data handling system require a mounting location compatible with the thermal control and micrometeoroid hazard considerations.

Table IX-5 Power Requirements Time Summary for Communications and Data Handling

	Mission				
	1	1A	2	2A	5
S/C Receiver On time (min:sec)	T - 38:16	T - 40:10	T - 48:46	T - 38:2	T - 40:48
S/C Receiver Off time (min:sec)	T + 0:2.9	T + 0:2.6	T + 0:2.1	T + 0:2.1	T + 0:1.9
ΔT Trajectory Uncertainty (min:sec)	1:54	5:31	15:24	5:7	10:15
Totals	40:12.9	45:43.6	64:12.1	43:11.1	51:4.9

B. MODIFIED OUTER-PLANET SPACECRAFT (MOPS)

1. Integration

The current MOPS configuration as designed by Martin Marietta can carry a deep survivable probe or Jupiter turbopause probe with only minor modifications. Three machined fittings are required to adapt to the turbopause probe. Figure IX-4 is an overall view of the MOPS S/C with the probe mounted in the center of the hexagonal equipment compartment. Figure IX-5 shows additional structural and mechanical details of probe attachment and the S/C-mounted probe antenna.

Attachments shown on Fig. IX-5 incorporate hi-shear separation nuts and probe ejection springs at three locations around the base of the probe. The probe is mounted along the Z (roll)-axis of the spacecraft, and therefore imparts little disturbing moments or imbalance at probe/spacecraft separation. Access to the probe attachment hardware is provided through access plates on the spacecraft. A honeycomb cover is permanently attached to the spacecraft to protect critical areas of the probe from meteoroids.

The probe tracking antenna, a 2.7-ft-dia parabolic dish, is between the +X and Y axes. It is locked in a stowed position for launch, and deployed to an operational position of 148° (cone angle) after Burner II separation. A single-axis gimbal mechanism permits a rotation of ±5° in 2° steps for tracking in the ecliptic plane. An estimate of the weight effect of these modifications is shown in Table IX-6.

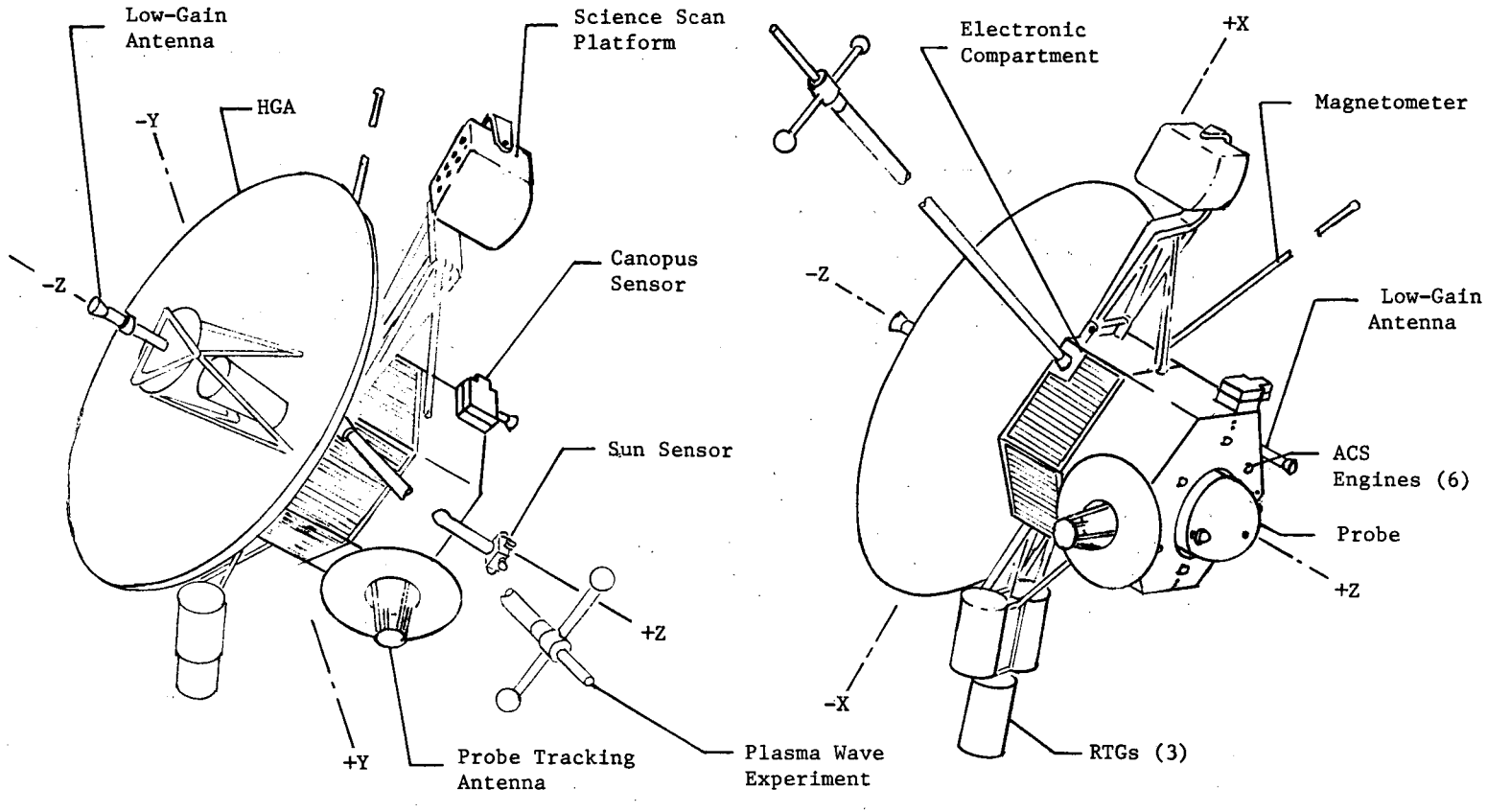

Fig. IX-4 Spacecraft Configuration for Modified Outer-Planets Mission

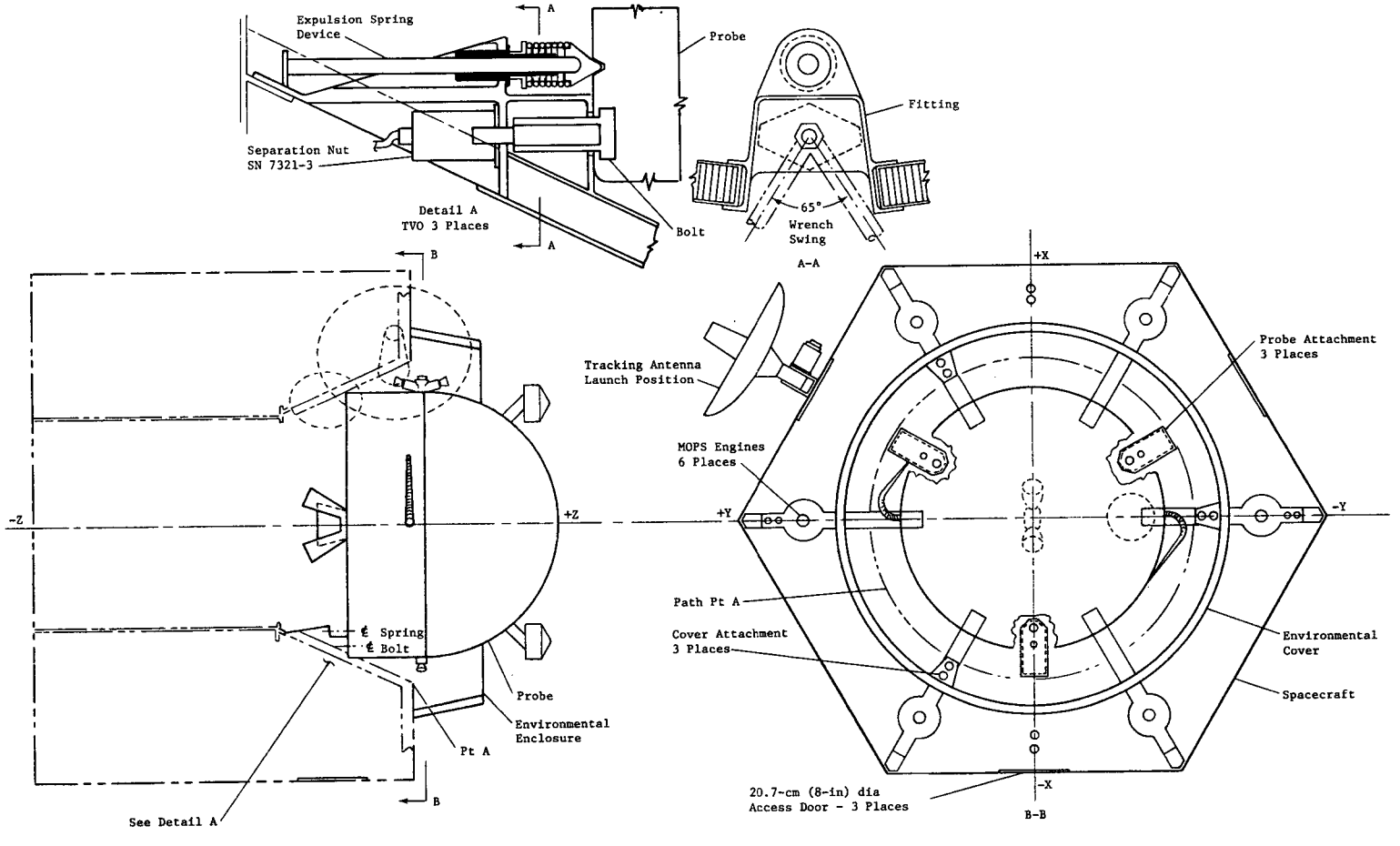

Fig. IX-5 MOPS/Turbopause Probe Configuration Interface

Table IX-6 Weight Effects of Spacecraft Modification, MOPS JS 77 Mission

	kg	lb
Probe Structural Support & Environmental Enclosure	12.4	27.3
Radio Receiver & Antenna	9.6	21.1
Subtotal	22.0	48.4
Contingency 15%	3.3	7.2
Total	25.3	55.6

C. THERMOELECTRIC OUTER PLANET SPACECRAFT (TOPS)

Consideration of the TOPS as a vehicle for the Jupiter turbopause probe was discontinued upon redirection during the study, therefore analytical integration effort was limited.

The results of thermal integration are mentioned in Subsection A2, and Table IX-7 shows a preliminary estimate of the spacecraft modifications required to carry a probe on a JUN 78 mission.

Table IX-7 Weight Effects of Spacecraft Modification, JUN 78 Mission

	kg	lb
Probe Structural Support & Environmental Enclosure	14.2	31.4
Radio Receiver & Antenna	15.0	33.0
Subtotal	29.2	61.4
Contingency 15%	4.4	9.6
Total	33.6	74.0

X. AEROPHYSICS

During entry into the Jovian atmosphere, communication from the entry probe to the spacecraft will occur along a line passing through the wake of the flow field, aft of the entry probe. Therefore, prediction of the degree of signal attenuation and the onset of blackout requires determination of the distribution of both electron density and electron collision frequency in the wake.

For an altitude envelope from 60 to 100 km below the turbopause, entry-probe flow fields have been thermochemically analyzed to predict both plasma properties distributions and aeroheating effects. A decription of the analyses, with a discussion of the results and their effects on the mission, are presented in this chapter.

A. NONEQUILIBRIUM FLOW ANALYSIS

1. Rationale for Analysis

Figure X-1 shows the various flow regimes encountered by the entry probe as a function of altitude (Ref X-1). Note that at 60 km below the turbopause, the entry probe is well into the continuum flow regime. At the high entry velocity (50 km/sec), a bow shock wave is formed forward of the body. The sudden increase in gas temperature caused by the shock wave is sufficient to cause dissociation of the molecular H_2 and subsequent ionization of the atomic H and He. It is the passage of this partially ionized gas over the entry vehicle and into the wake that will cause electromagnetic signal attenuation and, subsequently, communication blackout, thereby terminating the mission.

The strength of the bow shock wave and thermochemical state of the shock layer will determine electron density and collision frequency throughout the flow field. Results of a previous study (Ref X-2) indicate that, at 60 km below the turbopause, the forebody flow field is in thermochemical nonequilibrium. Hence, a nonequilibrium analysis has been performed and compared with equilibrium analytical results.

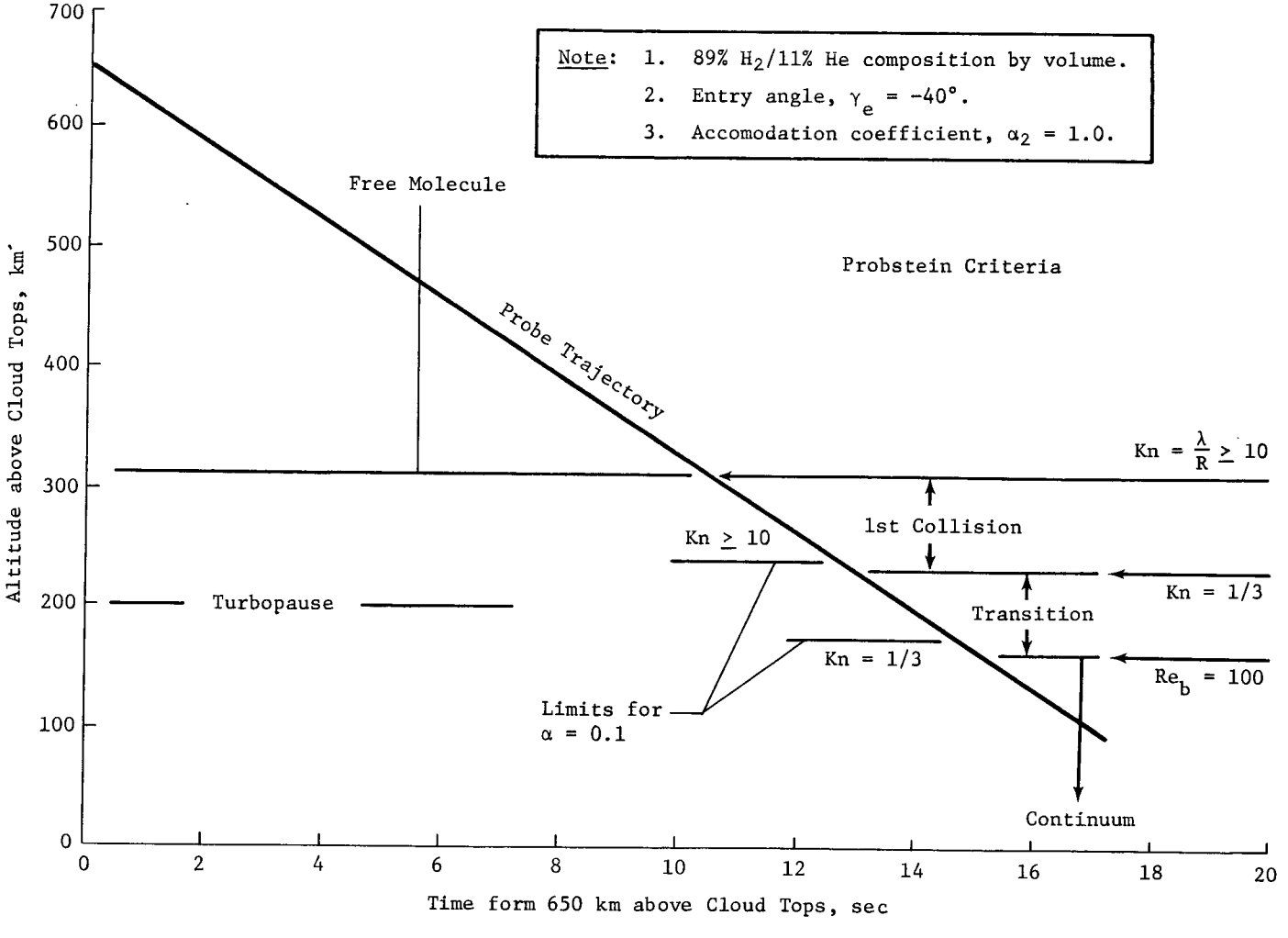

Fig. X-1 Probe Flow-Field Regime Delineation

Figure X-2 shows the various flow-field regions of the entry probe during continuum flow. While it is the body boundary-layer flow that forms the viscous near and far wakes aft of the probe, analysis of the inviscid body flow field is required to determine boundary-layer edge conditions. Having done so, the boundary-layer analysis is then performed to set the initial conditions for the free shear-layer (near-wake) analysis. Reattachment of the near wake (aft of the shear layer and recirculation region) causes a sudden recompression of the flow field. This results in formation of a recompression shock wave (Ref X-3) and further creates nonequilibrium effects in the far wake. This type of coupled analysis assures that the wake-plasma properties distributions are consistent with overall vehicle geometry and material composition as well as with entry velocity and consequent forebody bow shock strength.

2. Nonequilibrium Inviscid Forebody Analysis

The inviscid forebody flow-field analysis has been performed using an inverse method (Ref X-4) with finite rate chemistry. The advantage of the inverse method is that it gives detailed results at field points throughout the inviscid shock layer. Ambient atmospheric composition 60 km below the turbopause is 89 mole % molecular H_2 and 11 mole % He. Therefore, the principal reactions of importance to electron production in the inviscid flow field are the dissociation of molecular H_2 and the subsequent ionization of both atomic H and atomic He. As a result, analysis of the flow-field model involved development of a reaction-rate model and integration of flow-field equations for conservation of mass, momentum, energy, and chemical species, throughout the inviscid hypersonic shock layer.

a. Analysis - Table X-1 shows the chemical kinetic reaction model used in the analysis. Details of the computational procedure are given in Appendix H (Vol III). Because experimentally verified reaction-rate data were not available for the gas composition and energy range of interest (e.g., shock Mach No. = 70.0), rates used result from theoretical analysis using proven analytical techniques (Ref X-5). To check the reliability of the reaction rate model, nonequilibrium normal shock analysis was performed using these same rate constants in the postshock flow field. Results indicate that the thermochemical state of the gas converged to the predetermined equilibrium state over a large range of entry (freestream) conditions. Therefore, justification of the rate-constant model is that it works successfully for the conditions of interest.

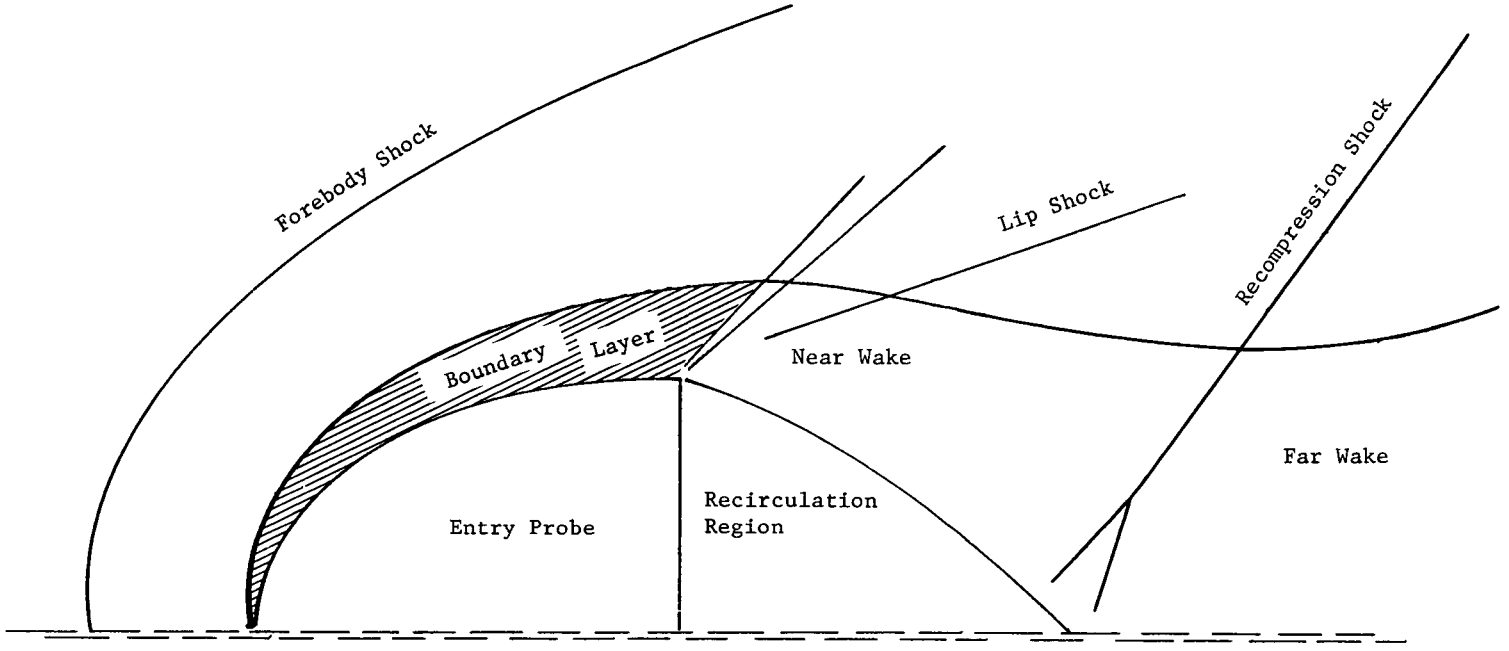

Fig. X-2 Continuum Flow-Field Regions Surrounding Jovian Entry Probe

Table X-1 Chemical Kinetic Reaction Model for Jovian Turbopause Entry Probe Inviscid Flow-Field Analysis

Reaction	Rate Constant (K_f)
$H_2 + M \underset{}{\overset{K_f}{\rightleftharpoons}} 2H + M$	$1.43 \times 10^{14}\ T^{-0.82}\ e^{-51957/T}$
$H + M \overset{K_f}{\rightleftharpoons} H^+ + e + M$	$7.522 \times 10^{11}\ T^{0.5}\ e^{-158000/T}$
$He + M \overset{K_f}{\rightleftharpoons} He^+ + e + M$	$1.096 \times 10^{11}\ T^{0.5}\ e^{-285200/T}$
Note: Units on rate constants are $\left(\frac{cc}{mole\text{-}sec}\right)$.	

b. Results - Figure X-3 gives the resultant nonequilibrium electron density at the entry-vehicle stagnation point. Note that nonequilibrium of the flow field yields a lower electron population than would result if the flow field were in an entirely equilibrium state. This is essentially because energy absorbed by dissociation of molecular H_2 results in a lower translational temperature throughout the nonequilibrium flow field.

Because the nose-stagnation region has the highest flow-field temperature (and electron concentration) the results at the stagnation point provide an upper bound to electron population throughout the rest of the flow field. However, these results are for inviscid flow and will be modified somewhat by the presence of the boundary layer, as will be shown in a subsequent discussion of boundary-layer results. Figure X-4 illustrates the decay of electron concentration from expansion cooling of gas along a stream line paralleling the body contour. The electron concentration profile resulting from equilibrium analysis (Ref X-6) is included in the figure to demonstrate that throughout the inviscid flow field, nonequilibrium effects relieve the entry-communication signal-attenuation problem. This will become more evident as the boundary-layer flow and resulting wake flow fields are considered.

60 km Below Turbopause

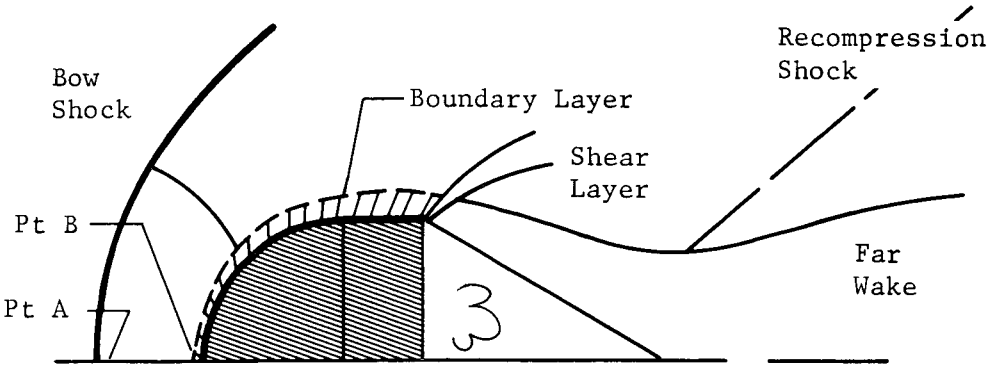

Nonequilibrium Electron Concentration

Electrons/cm^3

Pt A	Pt B
5.4×10^{10}	1.1×10^{12}

Fig. X-3 Nonequilibrium Electron Concentration along Forebody Stagnation Streamline

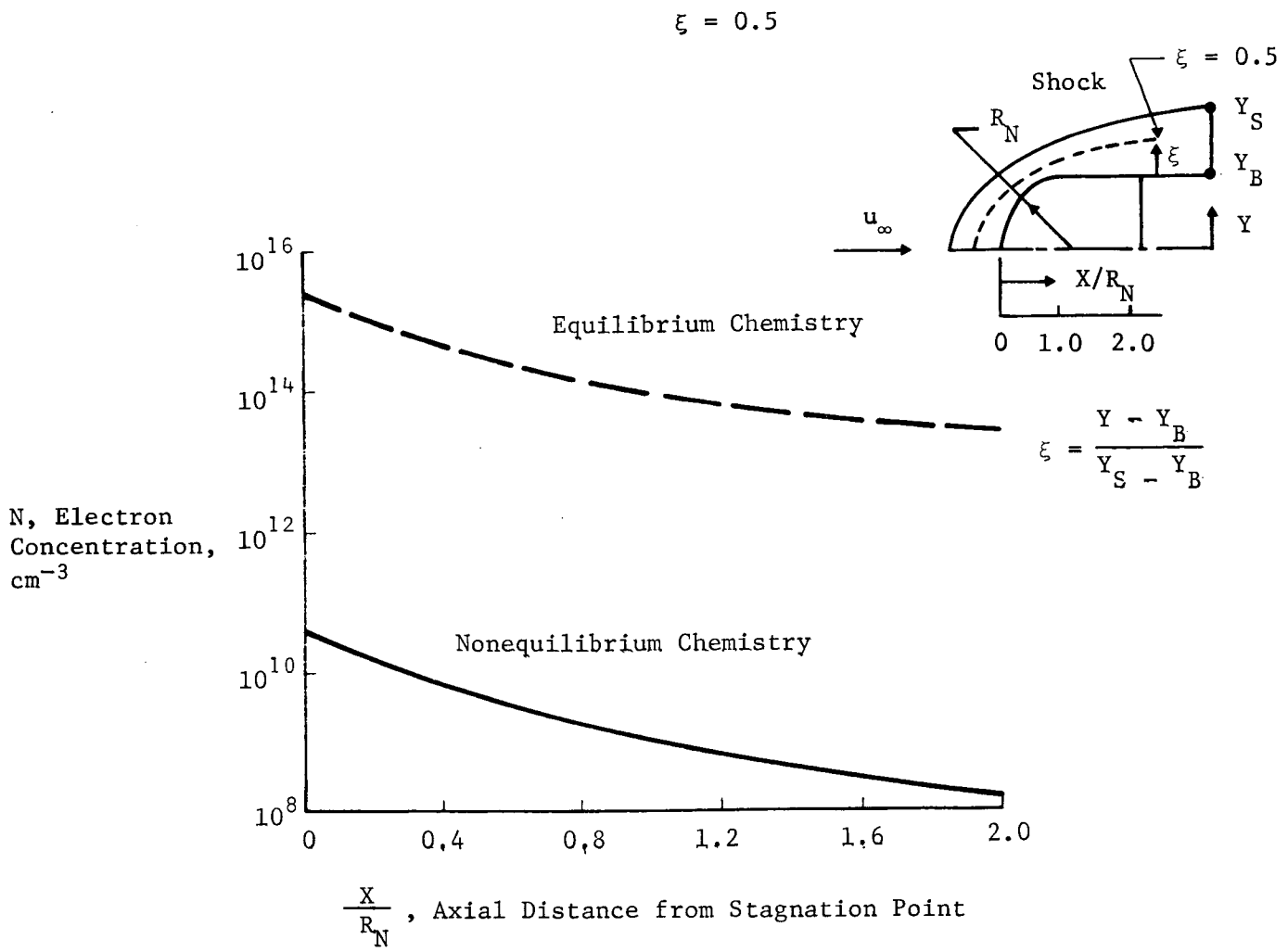

Fig. X-4 Electron Concentrations along Streamline Midway between Shock and Vehicle

c. Conclusions - Two important conclusions from this analysis are:

1) The entry-body flow field at an altitude of 60 km below the turbopause is in a state of thermochemical nonequilibrium.

2) The nonequilibrium of the inviscid forebody flow field results in lower electron concentration than if the flow field were in local thermochemical equilibrium throughout.

Application of these inviscid forebody results to the body boundary layer will be discussed in a later section.

3. Nonequilibrium Viscous Forebody Analysis

At altitudes on the trajectory between the turbopause and anticipated mission termination, calculation of the flow field surrounding the probe requires consideration of finite rate chemistry. Collision frequencies and residence times of the species in the flow field are not large enough to establish chemical equilibrium. In this instance, prediction of the charged particles distribution in the wake of the vehicle becomes extremely difficult, initially requiring validation of the species distributions in the forebody region. At sufficiently low altitudes, the chemical approach of division of the forebody flow field into an inviscid region and a boundary layer can be adopted. At lower free-stream densities, however, this simplification cannot be made and the entire shock layer should be considered viscous. This regime, the nonequilibrium-chemistry viscous shock layer, is one of the most difficult to analyze. In fact, other than in the stagnation region, computer programs for the analysis are not available.

a. Analysis - Present attempts to predict the viscous, finite reaction rate, forebody species distributions are restricted to two areas. First is the laminar boundary layer surrounding the vehicle forebody; second is the stagnation-point viscous shock layer. A single computer program developed by F. G. Blottner (Ref X-7) has been used as the tool for the analyses. Blottner describes the finite-difference solution of the conservation equations for a chemically reacting boundary layer. Solution of the viscous shock layer at the stagnation point requires consideration of the same equations, however, with different boundary conditions (Ref X-8). The program has provisions for up to 30 species and 30 reactions. Thermodynamic and transport properties of the species and mixture are, of course, required. Provision for detailed treatment of a highly ionized gas (electron mole fraction greater than approximately 10^{-2}) like that encountered

in Jovian entry was not originally incorporated in the code. Modifications have been made to properly account for thermodynamic properties, but transport properties are still approximate. However, it was felt that, if possible, solutions would provide valuable information for consideration of the communications problem.

Solution of the appropriate equations is difficult in any case, and the extreme velocities and energies encountered in Jupiter entry further compound the problem. Initial attempts at solution were for a stagnation-point boundary layer at the following conditions:

1) 100 km below the turbopause, where division of the flow field into an inviscid shock layer and a boundary layer may be appropriate;

2) freestream velocity of 50 km/sec;

3) wall temperature of 500°K, with species in equilibrium;

4) a three-reaction chemistry model consisting of H molecule dissociation, and single ionization of both the H and He atoms with the reaction rates described elsewhere;

$$H_2 \underset{}{\overset{K_{f_j}}{\rightleftharpoons}} 2H$$

$$H \rightleftharpoons H^+ + e^-$$

$$He \rightleftharpoons He^+ + e^-$$

where

$$K_{f_j} = A_j T^{B_{j_e}} - C_j/T$$

5) chemical equilibrium boundary-layer edge conditions.

This represents a good approximation at the stagnation points, where velocities are low relative to the body and species residence times are long. These initial solution attempts failed primarily because of high species production and depletion rates encountered in the solution, causing solution divergence and because initial profile estimates were not accurate enough.

To circumvent these problems, two important adjustments were made in the next series of solution attempts. First, He and He ions were dropped from the chemical scheme and pure H plasma substituted, as noted in the figures. Second, velocity was decreased an order of magnitude with the thought of increasing the velocity in steps up to 50 km/sec, using previously converged solutions as initial profile guesses in each step. With these changes, converged solutions were obtained up to 20 km/sec, but further increases were not possible.

Examination of Fig. X-5 reveals a part of the problem. Shown in the figure are the stagnation-point mass fractions of the three species important in the nonequilibrium boundary-layer study (H_2, H, and H^+) as a function of free-stream velocity at 100 km below the turbopause. In the range from 20 to 30 km/sec, there is a rapid drop in the H_2 concentration and an exponential rise in H^+, so that, by 28 km/sec, the electron-mole-fraction (or approximately H^+ mass-fraction) level has passed the limit of program applicability (10^{-2}). This means that, across the boundary layer, there are large species gradients, and numerical problems can be expected.

Convergence problems were associated with species production rates, so rate constants were lowered and further cases attempted. By using this procedure of raising the velocity until no convergence was obtained and then lowering the reaction rate constants, profiles termed "converged" by the program were obtained at 50 km/sec. Because the altitude of primary interest was 60 km below the turbopause, the program was run in 10-km increments to the 60-km location. Because free-stream density at this altitude is more than an order of magnitude lower than at 100 km below the turbopause, leading to lower interparticle collision frequencies, rate constants could again be increased. Despite the fact that the computer program's internal convergence criteria had been met, examination of the output profiles of species and temperature showed unsatisfactory anomalies for many runs. In fact, all runs with entry velocities above 30 km/sec belonged to this group. Although this velocity also approximately corresponds to the arbitrary division between high and low ionization at the boundary-layer edge (electron mole fraction of 10^{-2}), this may be a coincidence, and further analysis at the higher velocities might eliminate the objections. Further discussion is limited to cases in which the converged results are satisfactory.

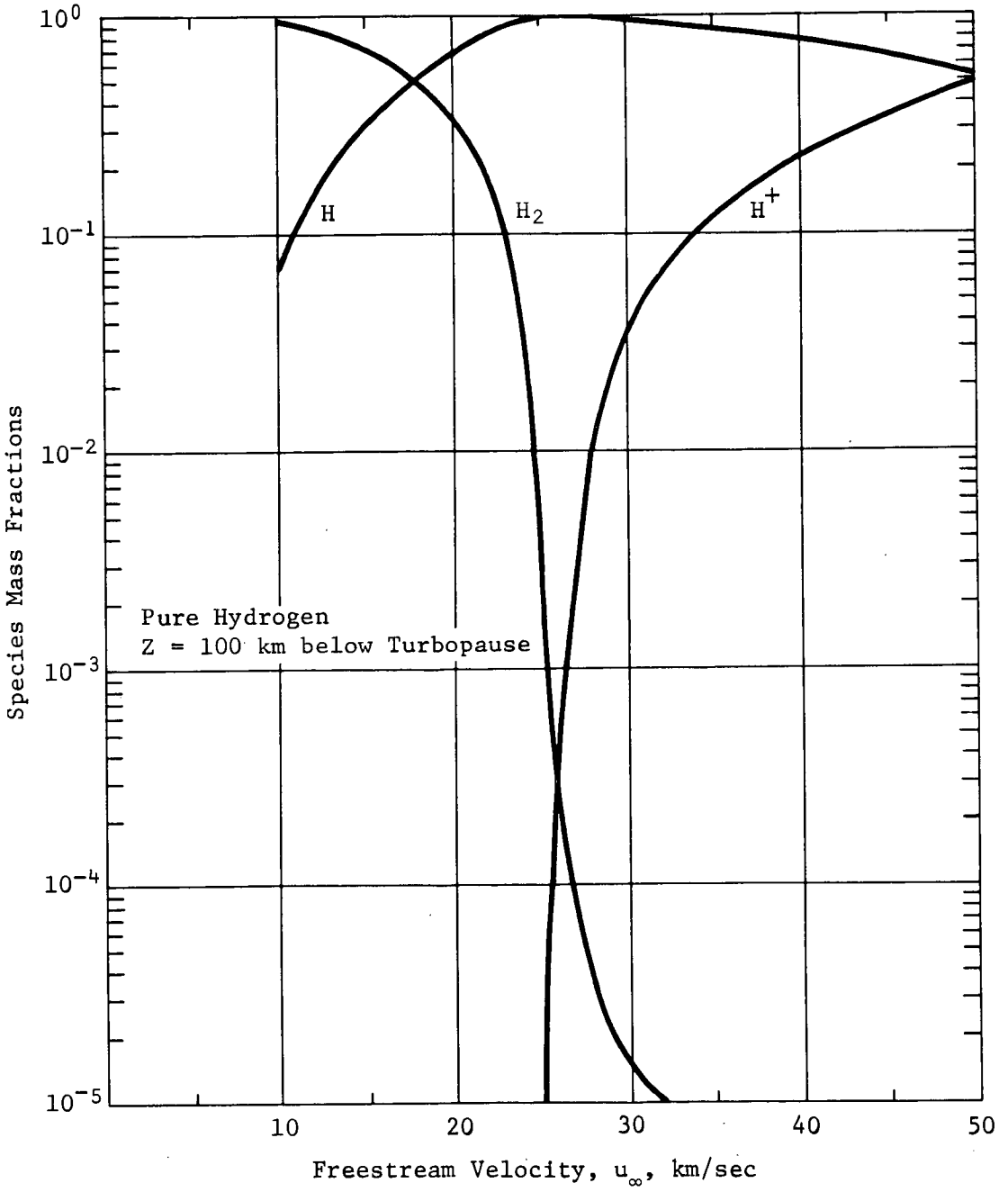

Fig. X-5 Variation of Stagnation-Point Species Mass Fractions with Freestream Velocity

b. Results - Boundary-layer temperature profiles for entry velocities between 20 and 30 km/sec are shown in Fig. X-6. The edge temperatures, equilibrium stagnation-point values, rise rapidly in this velocity range consistent with the species population shown in Fig. X-5. The profiles shown are for values of the rate constants shown in the figure. Only at 30 km/sec was a systematic attempt made to raise these values above those required for the initial converged solutions. The effect on species profiles of changing these constants at 30 km/sec is shown in Fig. X-7. The effect of doubling both constants is to lower the concentration of both H_2 and H^+ over most of the boundary layer. Doubling only the ionization rate, as expected, has only a small effect on the H_2 species, but again lowers the H^+ concentration. It appears that by judicious choice of the increase of each reaction rate, converged solutions for significantly higher rates can be obtained. However, whether the combination of rates expected from experimental or theoretical data can be used is still in question.

An interesting effect of reaction rate on convective heat transfer is also shown in Fig. X-7. The higher the ionization rate, the lower the ion concentration and gradient near the wall with the catalytic wall-boundary condition imposed in the solution, i.e., equilibrium at the wall temperature. The result is to lower the diffusive transport to the wall. Significantly lower heat transfer to the wall is noted as the ionization rate constant is increased.

The purpose of this forebody viscous analysis was to provide initial conditions for calculation of the electron distribution in the wake. A calculation of the boundary layer around the body was attempted for only one case, and the results are shown in Fig. X-8 and X-9. The calculation was for the sphere-cylinder body at 100 km below the turbopause and 24 km/sec. Edge pressure was obtained from an equilibrium inviscid solution (Ref X-6 and X-9) and edge species concentrations determined by an equilibrium isentropic expansion from the stagnation point. More precise determination of edge conditions would include iteration of the boundary layer with a nonquilibrium inviscid solution including boundary-layer swallowing effects. However, the results shown provide some insight into the phenomena. Note that the boundary-layer edge is assumed to be in thermochemical equilibrium because of the lack of a nonequilibrium solution at the conditions shown in Fig. X-8. Figure X-8 shows the variation along the body of the edge and maximum boundary-layer electron density. Little decay of electron density is noted along the cylindrical section.

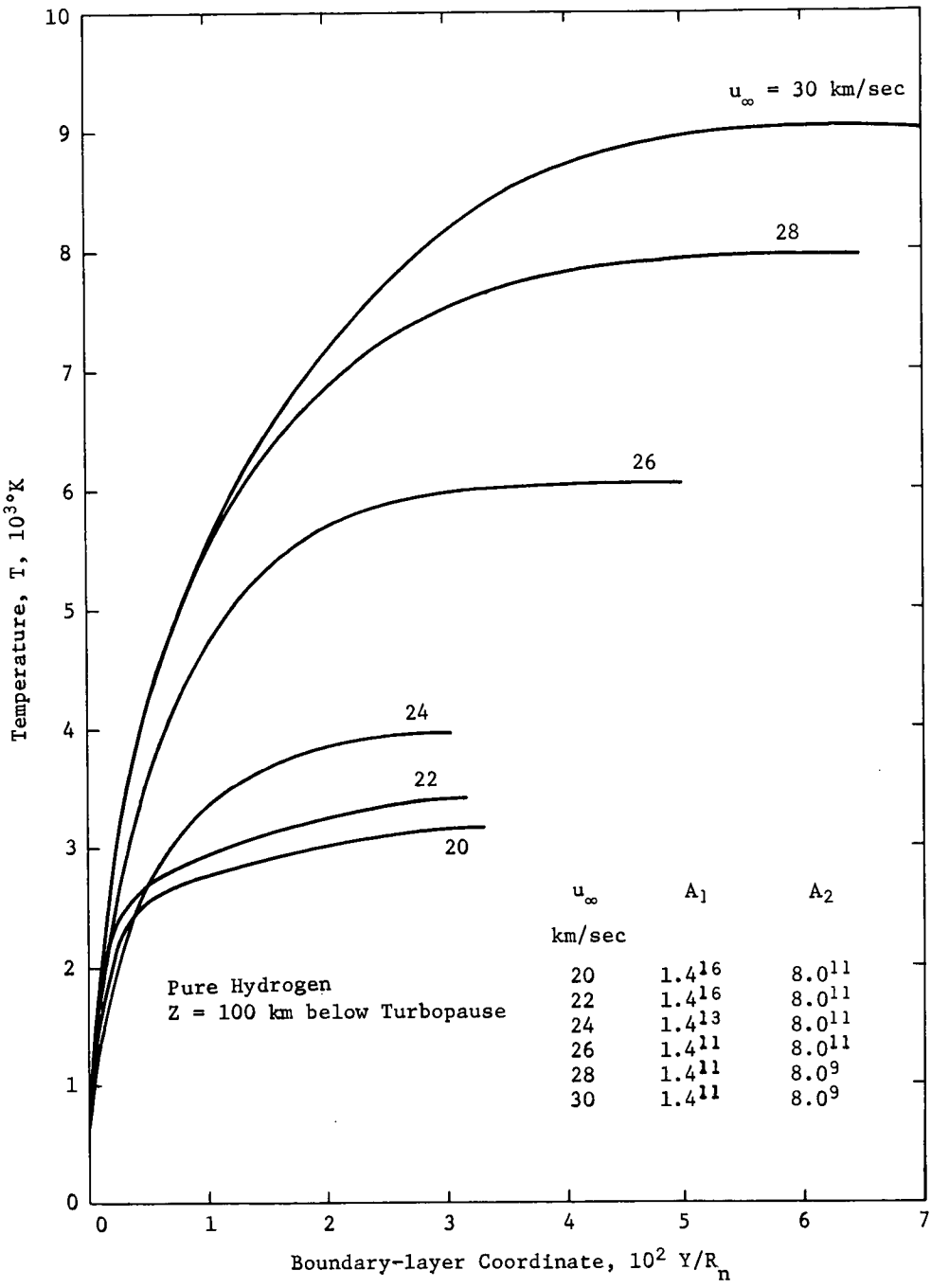

Fig. X-6 Stagnation-Point Nonequilibrium Boundary-Layer Temperature Profiles

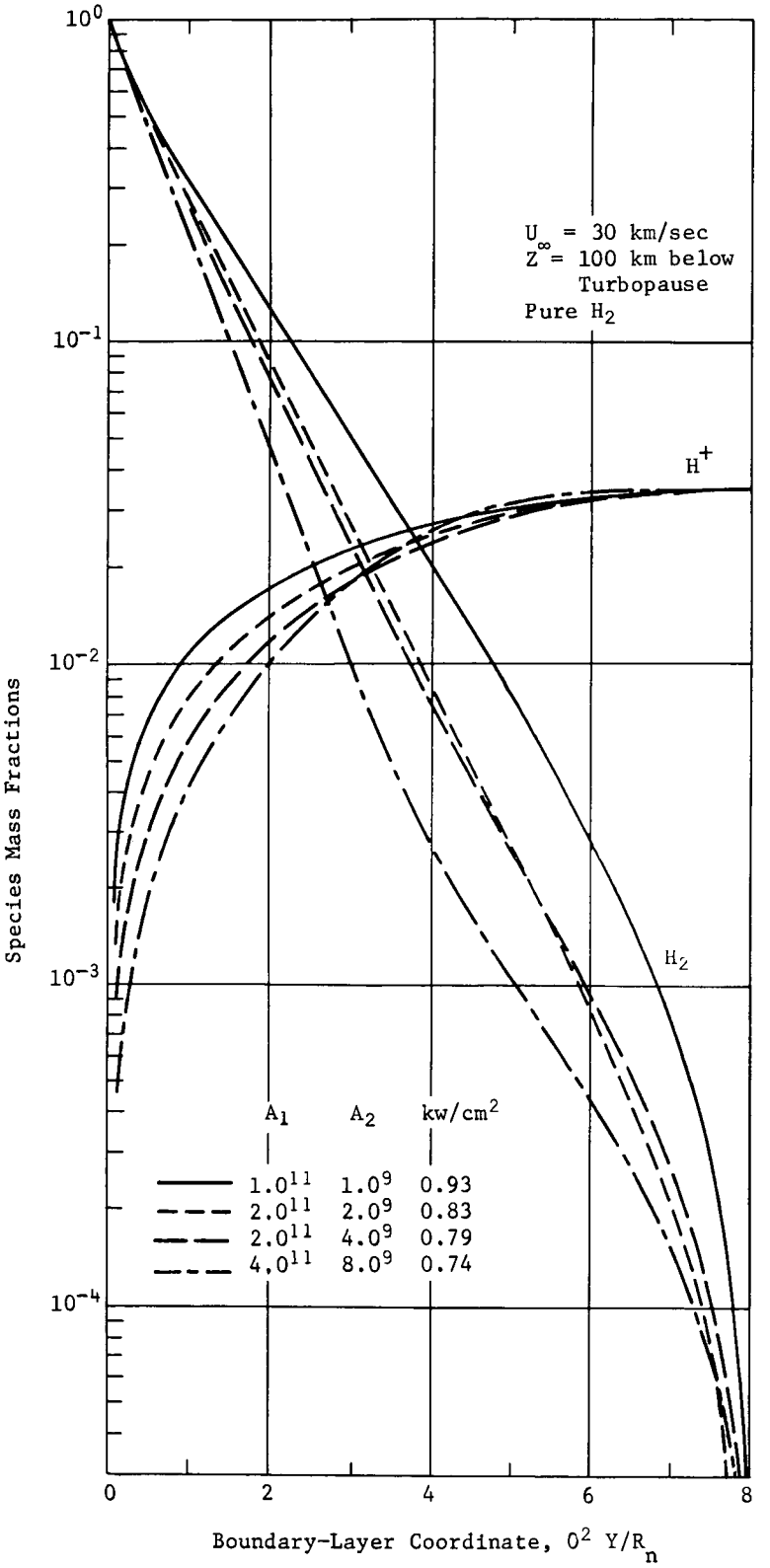

Fig. X-7 Effect of Reaction Rates on Nonequilibrium Stagnation-Point Boundary-Layer Species Profiles

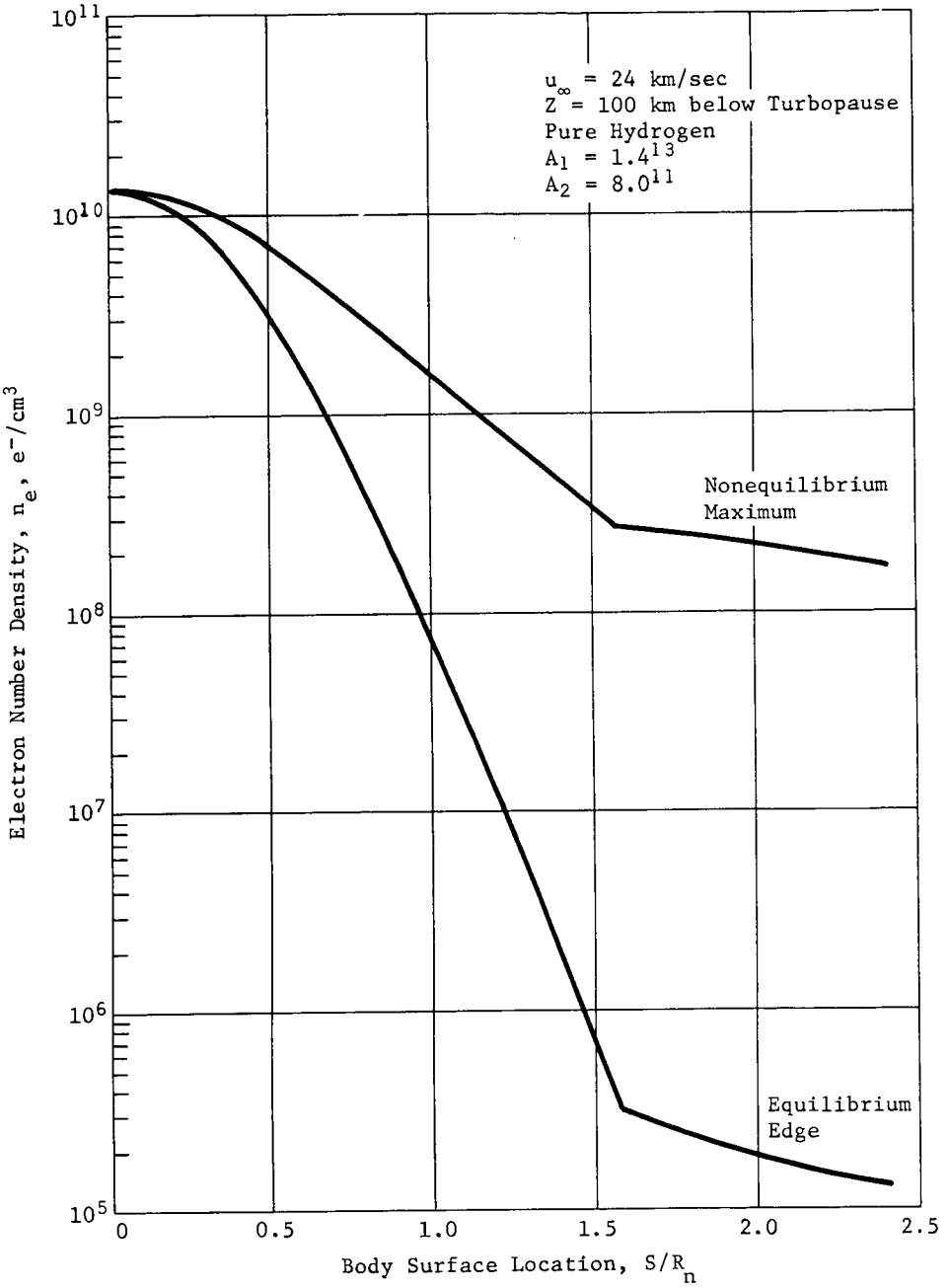

Fig. X-8 Distribution along the Body of Electron Number Density

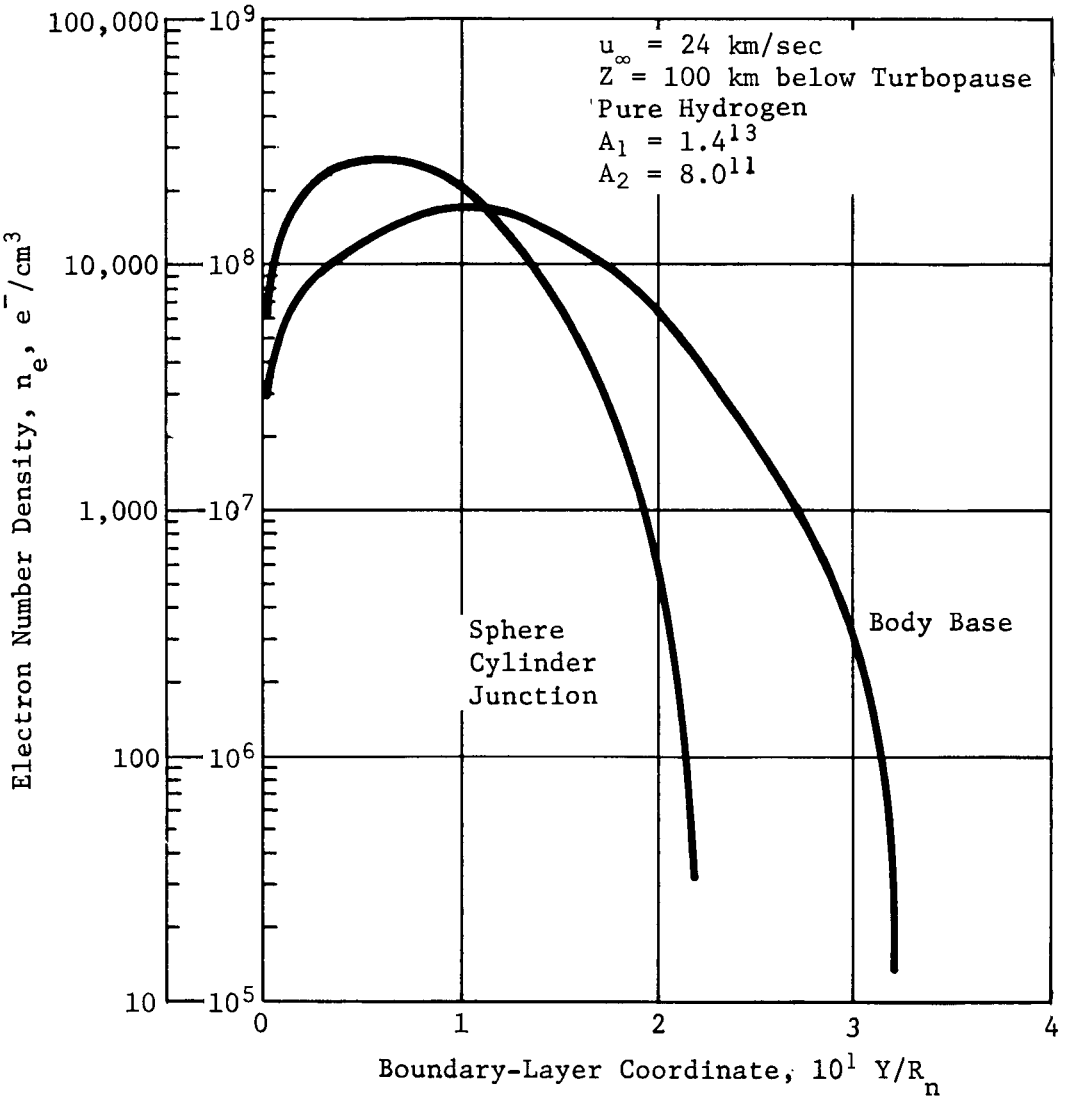

Fig. X-9 Boundary-Layer Profiles of Electron Number Density

Equilibrium edge values drop about five orders to magnitude from the stagnation point to the base. However, recombination rates within the boundary layer are not fast enough to keep pace and a drop of only two orders of magnitude in maximum electron number density is noted from the stagnation point to the base. The edge and maximum values are, of course, coincident at the stagnation point.

Figure X-9 indicates the electron density profiles at the shoulder and base. Considerable boundary-layer growth is shown. The implication for the desired results at a velocity of 50 km/sec would seem to be that not much decay of electron density from the level generated in the stagnation region can be expected in the expected flow around the body. Good definition in the stagnation region is required.

Comparison of boundary-layer thicknesses in the previous figures and calculated adiabatic standoff distances shows that the viscous layer, even at 100 km below the turbopause, is a significant fraction of the shock layer. A more realistic calculation of species profiles would be for a viscous shock layer at higher altitudes; i.e., at lower free-stream densities, boundary-layer calculations become even less appropriate. As mentioned before, the Blottner program can calculate the stagnation-point viscous shock layer. A limited attempt was made to apply this program option at the same trajectory conditions as for the boundary-layer calculations. Any numerical problems encountered in the boundary-layer solution might be expected to be magnified in shock-layer calculations because of the anticipated inflection in the temperature profile and the iteration required for determing shock standoff distance. Temperature profiles for three of the successful solutions in pure H_2 mixture are shown in Fig. X-10. The rate constants, A, required for these solutions are also given. No attempt was made to change these from values necessary to obtain the initial solution. Adiabatic standoff distances are also noted on the figure. It can be seen that the viscous shock-layer solution yields standoff distances somewhat larger than the adiabatic values for each velocity. Serious attempts to obtain shock-layer solutions at higher velocities and reaction rates were not made.

c. Conclusions - Although nonequilibrium boundary-layer and viscous shock-layer solutions were not obtained for the complete set of conditions desired, considerable experience in analyzing these problems was gained, and some insight into their effects on this program was obtained. Addition of He and its first ion to the chemical scheme should be a routine step. In fact, they were eliminated in this analysis only to help clarify more basic physical

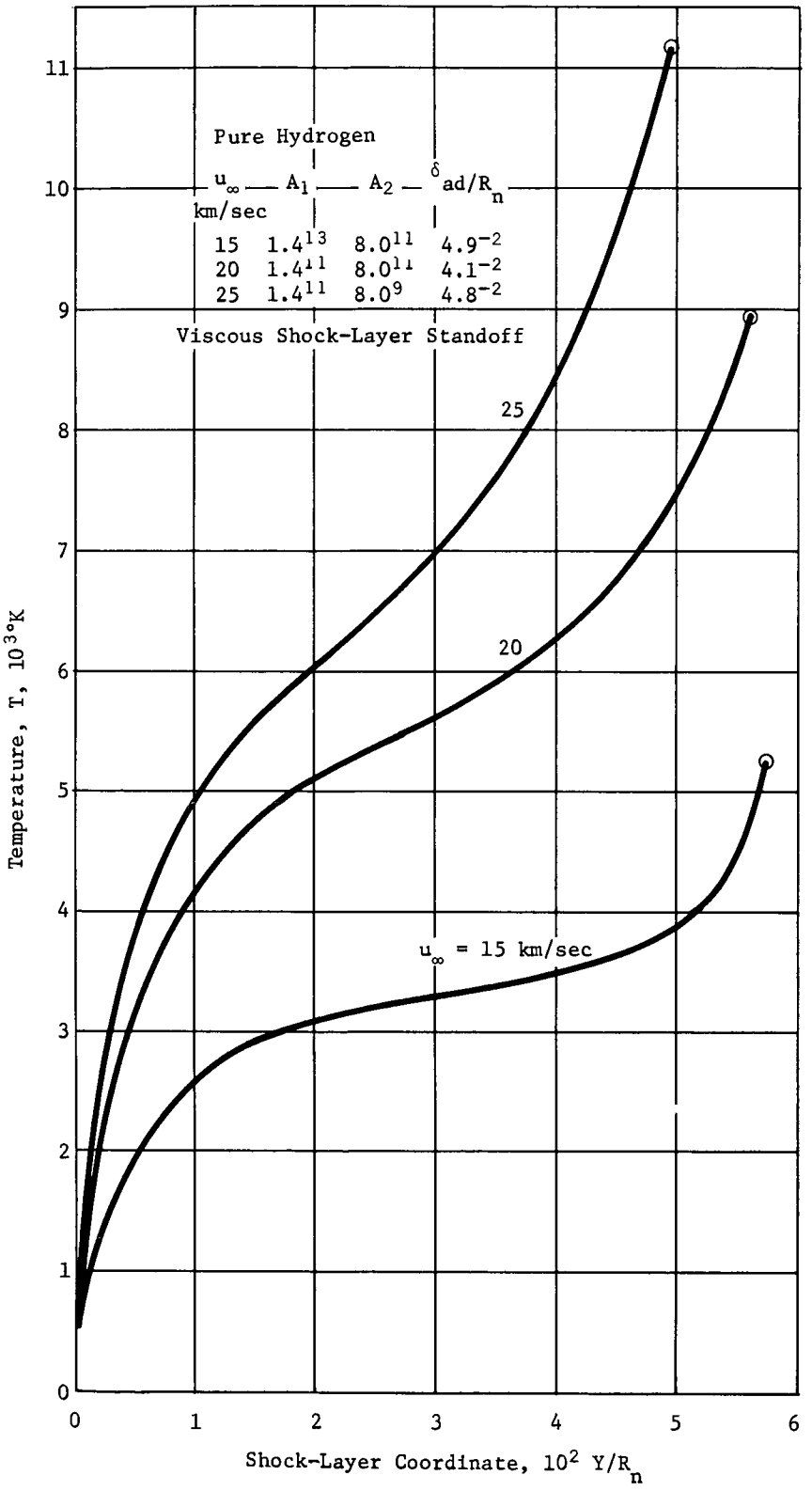

Fig. X-10 Stagnation-Point Shock-Layer Temperature Profiles

and numerical problems. Proper calculation of transport properties for highly ionized gas mixtures is a more difficult problem, but techniques are available and have been reported (Ref X-1). The problems should be primarily programming. Inclusion of the correct transport properties might alleviate some numerical problems encountered in solution attempts at the higher velocities and reaction rates attempted in this study. From the results obtained, however, it seems that a nonequilibrium viscous shock-layer rather than a boundary-layer solution is the only proper procedure at altitudes above 100 km below turbopause. At 100 km and below, both radiative and convective heat rates become so severe that solutions obtained without consideration of heat-shield mass loss are of little value. Of course, for the present vehicle, 100 km is below the altitude of mission termination. Proper analysis then requires development of techniques for analyzing the forebody viscous shock layer at locations away from the stagnation region.

4. Near-Wake Analysis

A reasonable estimate of the probe near-wake flow field (Fig. X-11) is necessary to estimate telemetry-signal attenuation in both the near- and far-wake flow fields. In addition, the near-wake temperature field must be known for heat-load and radiation calculations. More important, a near-wake analysis is required to provide the necessary input to the far-wake analysis.

Because of the lack of a reasonably simple unified computation scheme for the viscous recirculating wake, the near-wake flow field was investigated by analyzing the flow in the four distinct regions (Fig. X-11):

1) Corner expansion of the boundary layer and inviscid flow;

2) Inviscid flow outside of the shear layer;

3) Shear-layer (or mixing-layer) flow;

4) Shear-layer recompression.

Techniques employing isentropic expansion and recompression were used for computation of the corner expansions and shear-layer recompression. An existing mixing program (Ref X-10 and X-11) was modified for use in the shear-layer analysis.

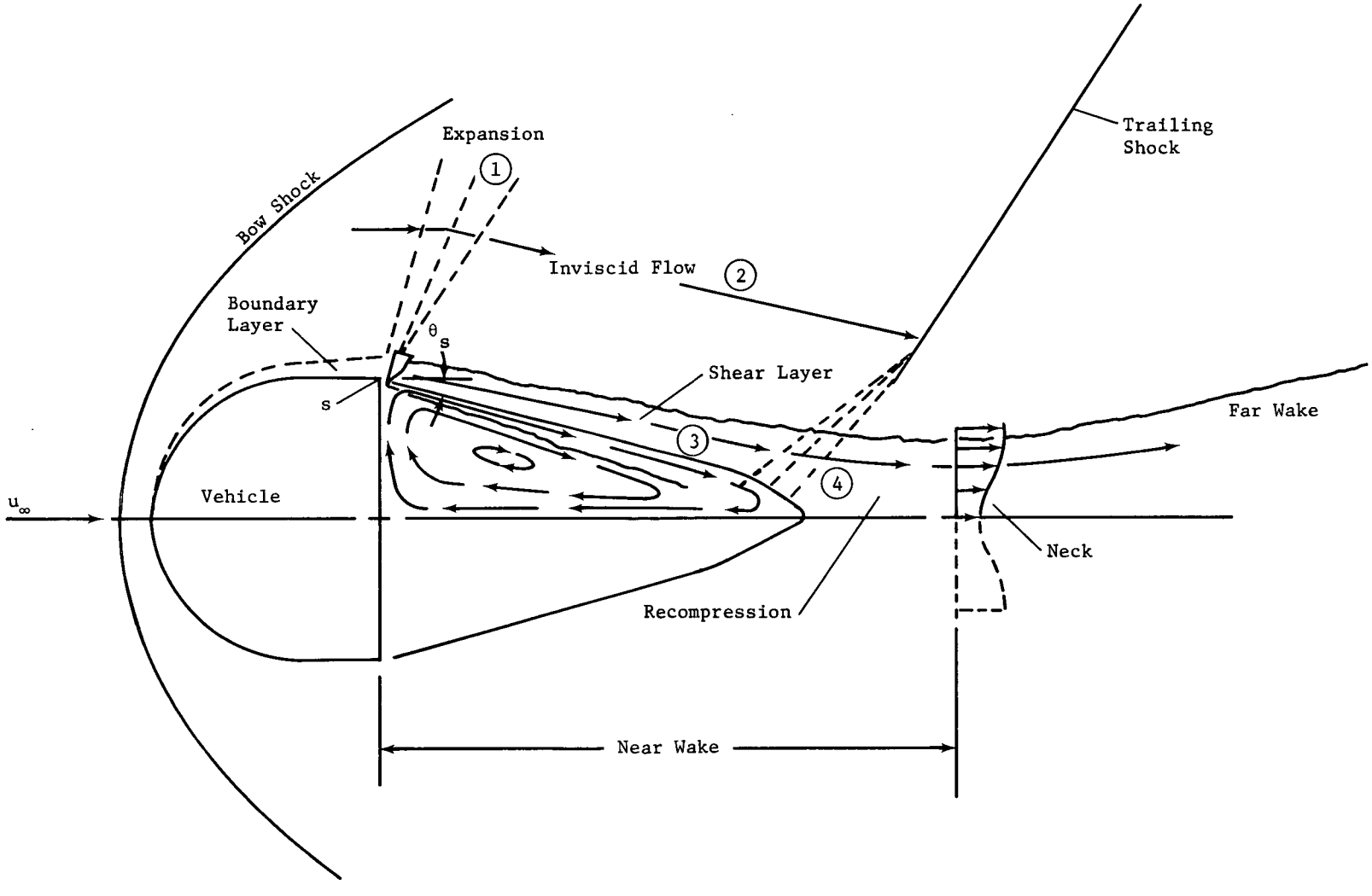

Fig. X-11 Entry-Probe Flow-Field Model Employed in the Near-Wake Analysis

a. Analysis - The following discussion outlines some of the more important aspects of the integrated analysis.

Base Pressure - Both boundary-layer and inviscid flow are assumed to undergo an essentially isentropic expansion at the probe aft corner (Fig. X-11). Flow conditions following this expansion depend on the probe base pressure.

Determination of base pressure is an extremely complicated problem. In fact, base pressure is coupled to the entire near-wake interaction problem in a fundamental way. However, consistent with independent determination of various flow regions in the wake, base pressures were estimated *a priori*.

Because the wake flow is laminar, the classical Chapman laminar mixing analysis result was used (Ref X-12). For two-dimensional flow, the base pressure is given by

$$\frac{p_b}{p_s} = \left\{ \frac{1 + \frac{\gamma - 1}{2} M_s^2}{1 + \frac{\gamma - 1}{1.31} M_s^2} \right\}^{\frac{\gamma}{\gamma - 1}}$$

where

p_b = base pressure

p_s, M_s = pressure and inviscid stream Mach number at s, respectively.

Zumwalt (Ref X-12) has shown that for axisymmetric base flows

$$\left(\frac{p_b}{p_s}\right)_{\text{axisym}} \cong 2.06 \left(\frac{p_b}{p_s}\right)_{\text{2-dims}}$$

Corner Expansion - The inviscid flow was assumed to undergo an ideal Prandtl-Meyer expansion turn to the base pressure, p_b. This process thus defines the inviscid wake region (2 on Fig. X-11) including the mean flow direction, θ_s, in the shear layer.

At the aft corner, the separating boundary layer was divided into a number (typically 15) of individual stream tubes. Properties within each stream tube were assumed to be uniform, with a mean value appropriate to the local flow of that point in the boundary layer. Flow in these stream tubes was then expanded isentropically to the base pressure, thus yielding a starting shear-layer profile.

Shear-Layer Flow - The GASL turbulent mixing program (Ref X-10 and X-11) was implemented for the shear-layer computation. Because the wake flow is laminar, a laminar mixing option was written into the GASL program. The resulting method provides a finite-difference technique for calculation of two-dimensional constant-pressure frozen-chemistry mixing layers.

There are some disadvantages in the use of this program for the Jupiter probe wake, and these will be discussed.

Shear-Layer Recompression - As the shear layer approaches the probe centerline, it begins to turn parallel to the axis and recompress. This usually occurs gradually while the inviscid external stream undergoes a rapid compression through an oblique trailing shock wave. The pressure to which the shear-layer flow recompresses is assumed to correspond to that behind the trailing shock (Fig. X-11). This pressure is calculated by assuming that the shock turns the inviscid stream parallel to the axis. Using the same stream-tube technique adapted for the corner boundary-layer expansion, shear flow is recompressed along stream tubes to the postshock pressure. The resulting profiles are used for the far-wake input.

b. Results - Figures X-12 through X-14 show typical results of the near-wake analysis. They give temperature, mass density, and electron-density profiles at two streamwise locations along the shear layer. Station 1 corresponds to the condition of the separated boundary layer after the corner expansion, while Station 2 corresponds to the point where recompression has occurred and the flow has passed through the trailing oblique shock wave.

The figures show the obvious smoothing of the properties as one proceeds along the shear flow.

Because the shear-layer flow was assumed to be chemically frozen, distributions of thermochemical properties throughout the near wake are dominated by fluid mechanics rather than chemical kinetics. The nature of the temperature and density profiles (increasing temperature in the direction of outer edge and decreasing density radially outward) reflect the structure of these thermodynamic state variables in the boundary layer. This is to be expected because the boundary-layer flow field is the source of the near-wake flow field. The temperature and density profiles at Station 2 of Fig. X-12 and X-13 reflect both flow compression at the rear stagnation point and passage through the trailing oblique shock wave.

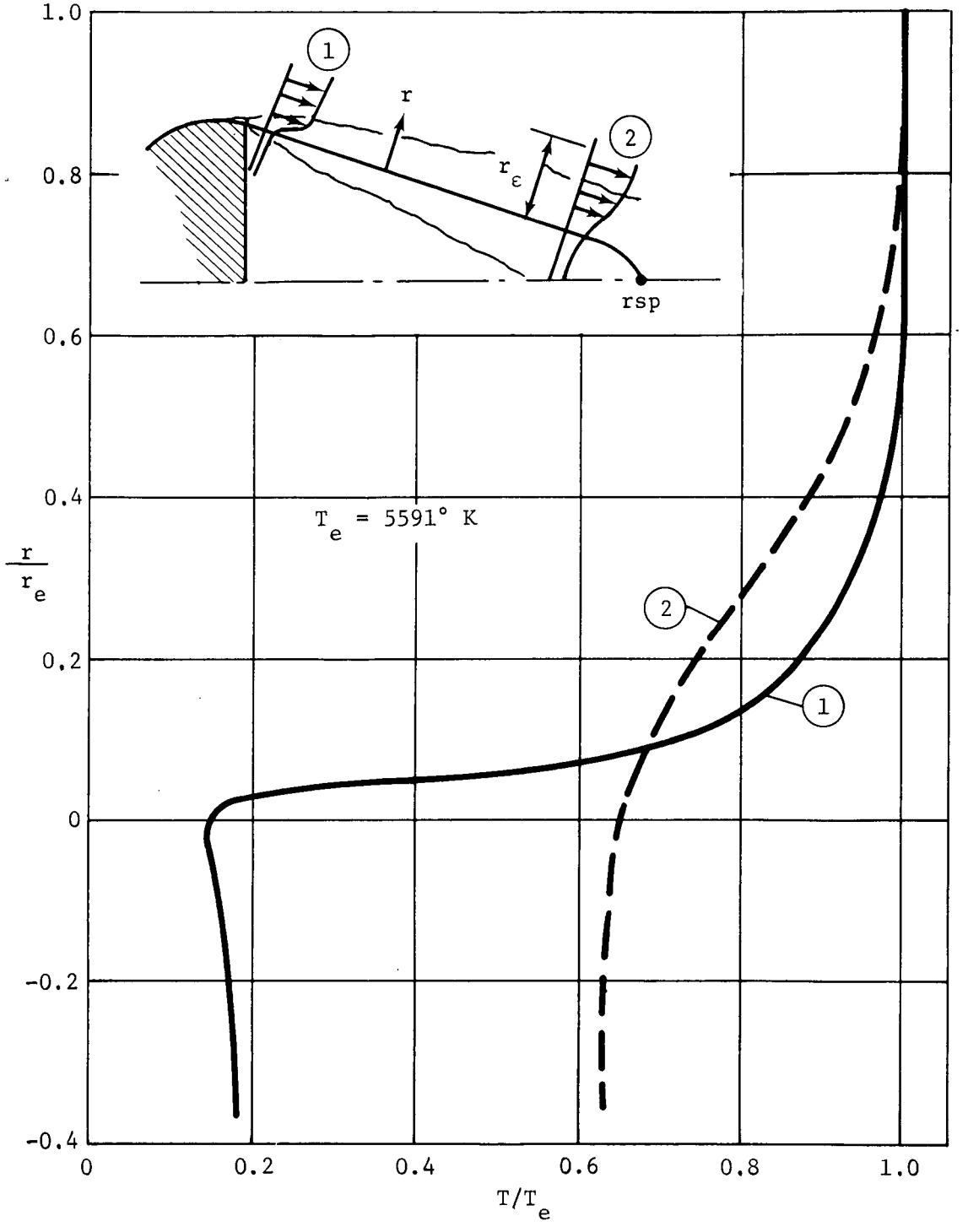

Fig. X-12 Temperature Profiles at Beginning and End of Shear Layer

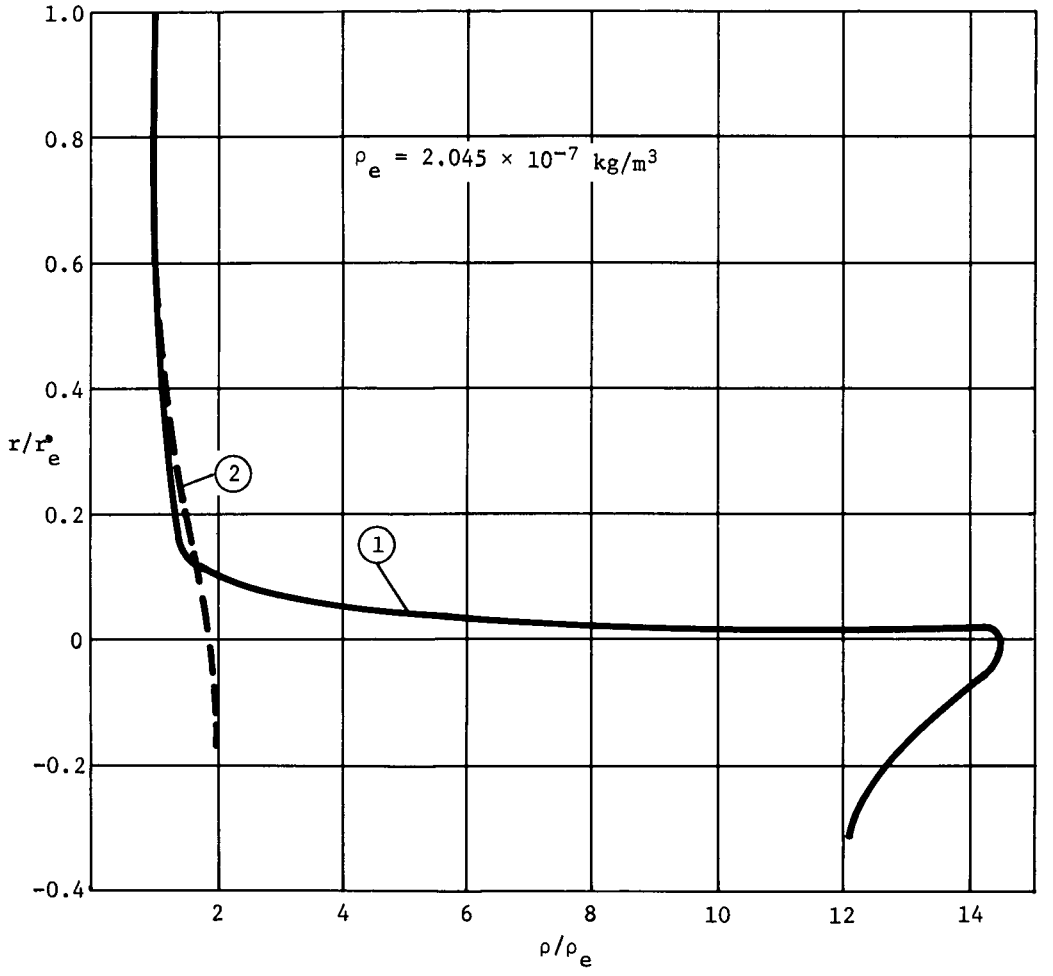

Fig. X-13 Mass Density Profiles at Beginning and End of Shear Layer

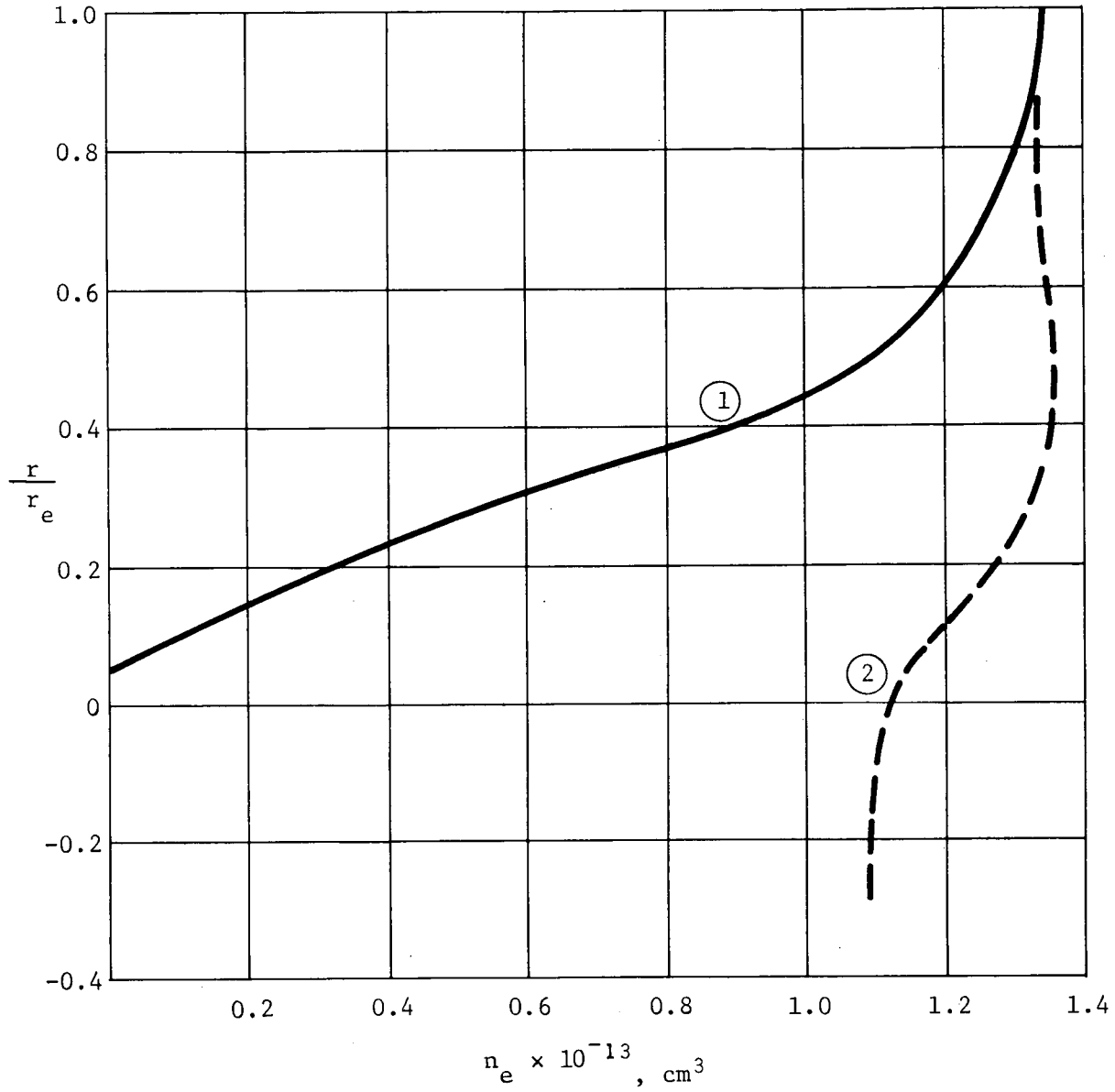

Fig. X-14 Electron Number Density Profiles at Begining and End of Shear Layer

c. Conclusions and Restrictions - The near-wake electron concentration profiles are the results of fluid mechanics; e.g., expansion, mixing, and cooling. This implies that along a typical shear-layer streamline, electron concentration should decrease with increasing distance from the entry probe's baseplate. This is not inconsistent with results at Station 2 of Fig. X-14 when one recalls that Station 2 reflects shock heating by the recompression shock wave.

The two-dimensional nature of the near-wake analysis tends to overpredict electron concentration. Follow-on analyses should include refinement of analytical techniques to include effects of finite pressure decay down the wake and radially. This would tend to lower predicted shear-layer electron-concentration distributions. However, quantitative assessment of the degreee of such relief would require considerably more computer analysis. Nevertheless, such an analysis would be physically more reasonable and would tend to predict lower electron concentrations.

The near-wake analysis provided a means of estimating property profiles at the start of the far wake (neck conditions in Fig. X-11). It is not intended to be a unified accurate treatment of the near wake. The main restrictions are:

1) Corner expansion and shear-layer recompression programs are strictly valid only for two-dimensional flow. This is not the case, especially with regard to the recompression process.

2) The GASL mixing program is also strictly valid only for two-dimensional flow at constant pressure. This is perhaps the most severe restriction in the analysis.

3) As used for this study, the GASL program assumed frozen chemistry throughout the shear layer. It may be that this restric- is not severe. However, this is not obvious, particularly for the high-energy flow encountered by the entering probe. Follow-on analyses should include equilibrium chemistry for comparison.

5. Far-Wake Analysis

The far wake is the region of flow downstream of the recompression shock. This region is important to the success of the mission because the communication path is through its centerline (which is also the probe's axis of symmetry). The results needed for electromagnetic signal-attenuation analysis are electron collision frequency and number density because it is these properties that determine the degree of attenuation.

Downstream of the recompression shock, the far wake consists of two distinguishable regions, as shown in Fig. X-15. The viscous core contains flow originally heated by shearing forces in the probe's boundary layer that has expanded into the free shear layer (i.e., near wake) and later compressed and turned at the wake neck. The inviscid outer portion consists of shock-heated flow, and extends radially outward to the bow shock.

Up to 50 body diameters downstream (Ref X-14 and X-15), the initially laminar viscous core will in some cases develop turbulent disturbances that break through into the inviscid portion and then into the ambient surroundings. McLaughlin (Ref X-16) has shown that the symmetry limitation on axisymmetric wake disturbances forces them to be periodic with some harmonics, and he confirms this experimentally. In other cases, the wake remains laminar. Wilson (Ref X-14 and X-15), Demetriades (Ref X-17), and Moore and Lee (Ref X-18) show that turbulent transition--

1) Is less likely with, and is delayed by, body heating;

2) Occurs earlier for higher Reynolds numbers and will not occur below a critical Re because of viscous damping effects;

3) Is delayed by increasing vehicle bluntness;

4) Occurs earlier with increasing ambient pressure.

When the wake remains laminar, the inviscid portion can develop instabilities 1000 to 8000 body diameters downstream and begin to blur with the viscous core. At this point, the inviscid portion contains significant viscous effects (Ref X-14). Eventually, far downstream, the wake approaches ambient conditions.

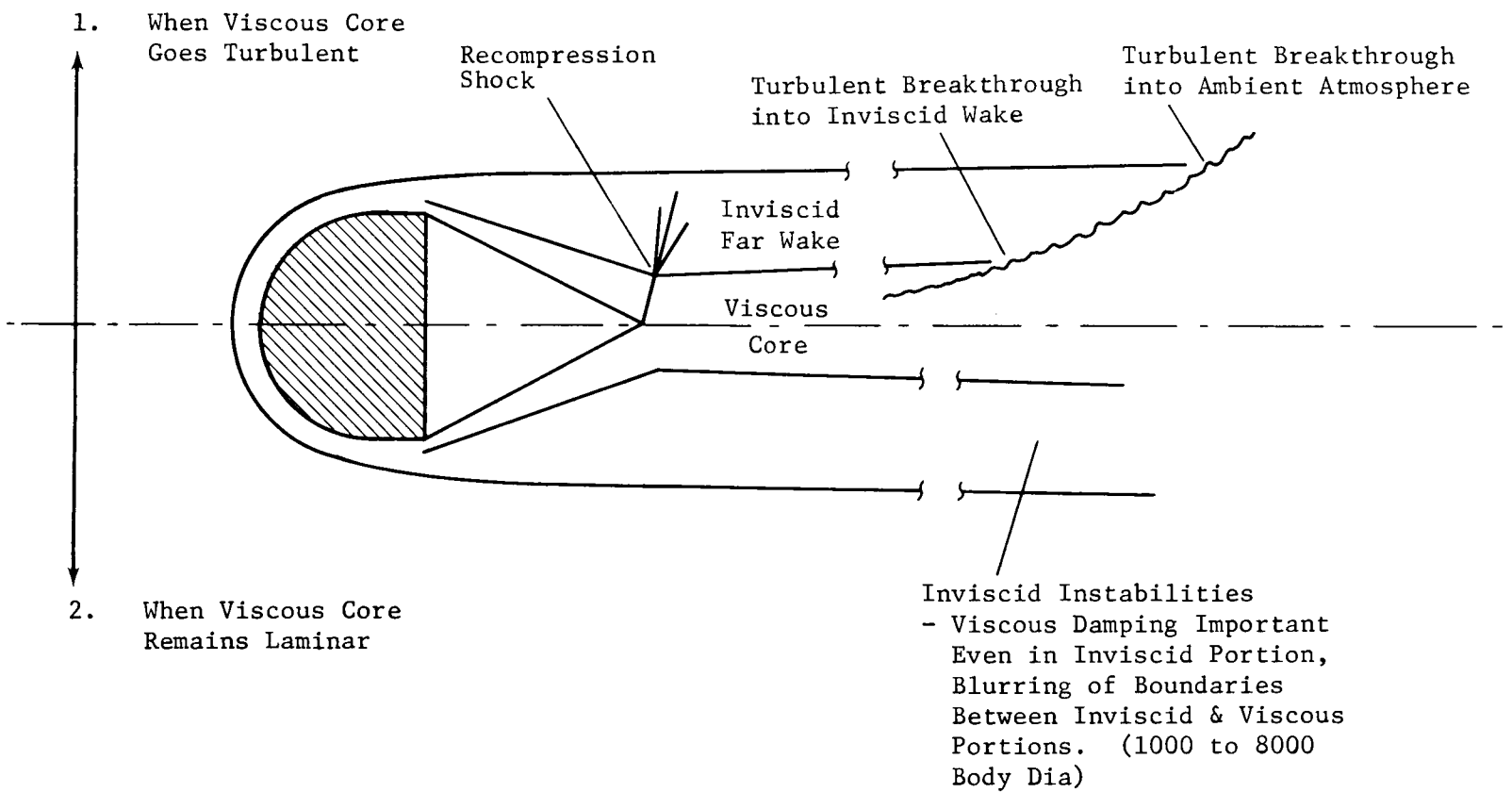

Fig. X-15 Schematic of Far-Wake Region

a. Analysis - For this analysis, only the viscous core was treated in detail. This is consistent with the approach taken by Wen and Chen (Ref X-19) as well as Moore and Lee (Ref X-18) whose analyses were limited to the viscous core of blunted bodies in air mixtures. Although the inviscid flow could be a major portion of the wake's mass flow, the signal path is through the centerline, i.e., the viscous core that was assumed to remain laminar in this study. The inviscid portion was analyzed only to provide edge conditions for the detailed viscous-core analysis. Because the inviscid portion has negligible radial gradients except near the bow shock, it is expected that solutions at the viscous core edge are representative of those throughout the inviscid portion.

The reason for not including turbulent effects is the state of the art in turbulent analysis. Most successful (in the sense of agreement with experiment) turbulent-wake analyses make heavy use of empirical knowledge and correlations of experimental and/or flight-test data (Ref X-16). This knowledge, pertaining to Mach-70 sphere-cylinder shapes in He/H_2 mixtures, is obviously unavailable. Purely theoretical turbulent-wake analysis is in a very incomplete and unsatisfactory state.

Although the inviscid wake for blunted and spherical bodies has strong density gradients near the bow shock, in the vicinity of the viscous core the gradients are negligible in both radial and axial directions (Ref X-14, X-15, and X-18). This makes boundary-layer simplifications valid for the viscous core. It has been shown experimentally that these assumptions (e.g., constant radial pressure) are generally accurate for wakes. The following conservation equations are obtained.

1) Conservation of mass

$$r\left[\frac{\partial(\rho u)}{\partial x} + \frac{\partial(\rho v)}{\partial r}\right] + \rho v = 0$$

2) Conservation of chemical species

$$r\left[\rho u \frac{\partial Y_j}{\partial x} + \rho v \frac{\partial Y_j}{\partial r}\right] = rW_j - \left(1 + r\frac{\partial}{\partial r}\right)\rho Y_j v_j$$

3) Conservation of momentum

$$r\left[\rho u \frac{\partial u}{\partial x} + \rho v \frac{\partial u}{\partial r}\right] = -r \frac{\partial P}{\partial x} + \left(1 + r \frac{\partial}{\partial r}\right) \mu \frac{\partial u}{\partial r}$$

4) Conservation of energy

$$r\left[\rho u \frac{\partial H}{\partial x} + \rho v \frac{\partial H}{\partial r}\right] = ru \frac{\partial P}{\partial x} + ru \left(\frac{\partial u}{\partial r}\right)^2 + \left(1 + r \frac{\partial}{\partial r}\right) \lambda \frac{\partial T}{\partial r}$$

where

H = enthalpy per unit mass

P = pressure

r = distance radially from centerline

x = distance axially aft of wake neck

T = temperature

u = x velocity component

v = r velocity component

W = mass rate of formation of species per unit volume due to chemical reactions

Y = mass fraction of species

ρ = density

μ = coefficient of viscosity

j = species identification subscript

ν = kinematic viscosity

λ = thermal conductivity

in consistent dimensions.

It is obvious that this equation set is incomplete as presented. To complete it, a thermal equation of state and a caloric equation must be added (Ref X-18). Having done so, the system of equations is integrated along coordinates paralleling the streamlines in the far wake. All radial derivatives of a property e.g., $\left(\partial Y_j / \partial r\right)$, are calculated by a curve fitting the property as a function of r and using the resulting derivative.

The viscosity model has been simplified in that viscous parameters are assumed radially constant.

The above equations were integrated numerically from a given set of initial conditions (discussed later) using a first-order accurate integration technique, i.e.

$$g(X + \Delta X) = g(X) + g'(X)\Delta X$$

where

ΔX = distance increment

g = property desired at $X + \Delta X$.

Brooke (Ref X-20) has shown that a first-order integration technique in general is as stable and accurate as a Runge-Kutta technique, and computing-time considerations made the use of this technique desirable.

As the flow-field integration proceeds downstream, it is necessary to provide edge conditions at the boundary of the inviscid and viscous flow fields. Constraints on the form of these conditions are--

1) At infinity, they must equal free-stream values;

2) At the wake neck, they must equal the known inviscid values.

It has been shown experimentally that pressure decays exponentially in a downstream direction in the far-wake region. Using these facts, pressure at any given station becomes

$$P = \left(P_{neck} - P_{\infty}\right) exp(-FX) + P_{\infty}$$

where

X = distance downstream of the neck

F = constant.

The parameter F is related to the downstream distance, X_o, at which $P = 1.01\ P_\infty$. The definition of F is

$$F = \left(-1/X_o\right)\left|\ln\left\{0.01\ P_\infty/\left(P_{neck} - P_\infty\right)\right\}\right|.$$

For 60 km below turbopause, $P_{neck} = 123$ dynes/cm^2 and $P_\infty = 1.821$ dynes/cm^2.

As the downstream distance for which $P = 1.01\ P_\infty$ was unknown, a representative value of X_o was chosen to be 20 body diameters. This turned out to be unsatisfactory because resulting pressure decay was too rapid and diffusion effects, which are expected to dominate laminar far-wake evolution, were overshadowed. An examination of wake profiles with parametric variation of X_o was then made. Figures X-16 and X-17 illustrate some results of this examination.

Profiles of electron momentum-transfer collision frequency were also calculated. Electron collision frequency was calculated as a function of local temperature, species composition, and collision cross-sections for electrons with the various species. Generally, electron collision frequency--

1) Is a strong function of degree of ionization;

2) Increases with increasing density;

3) Increases with increasing temperature.

Nonequilibrium processes of importance in the far-wake region are the recombination of ions into neutrals and neutrals into molecules. Negative ions can be important (Ref X-19), as can three-body recombination reactions. Attachment of electrons to neutral particles in the wake also merits further investigation.

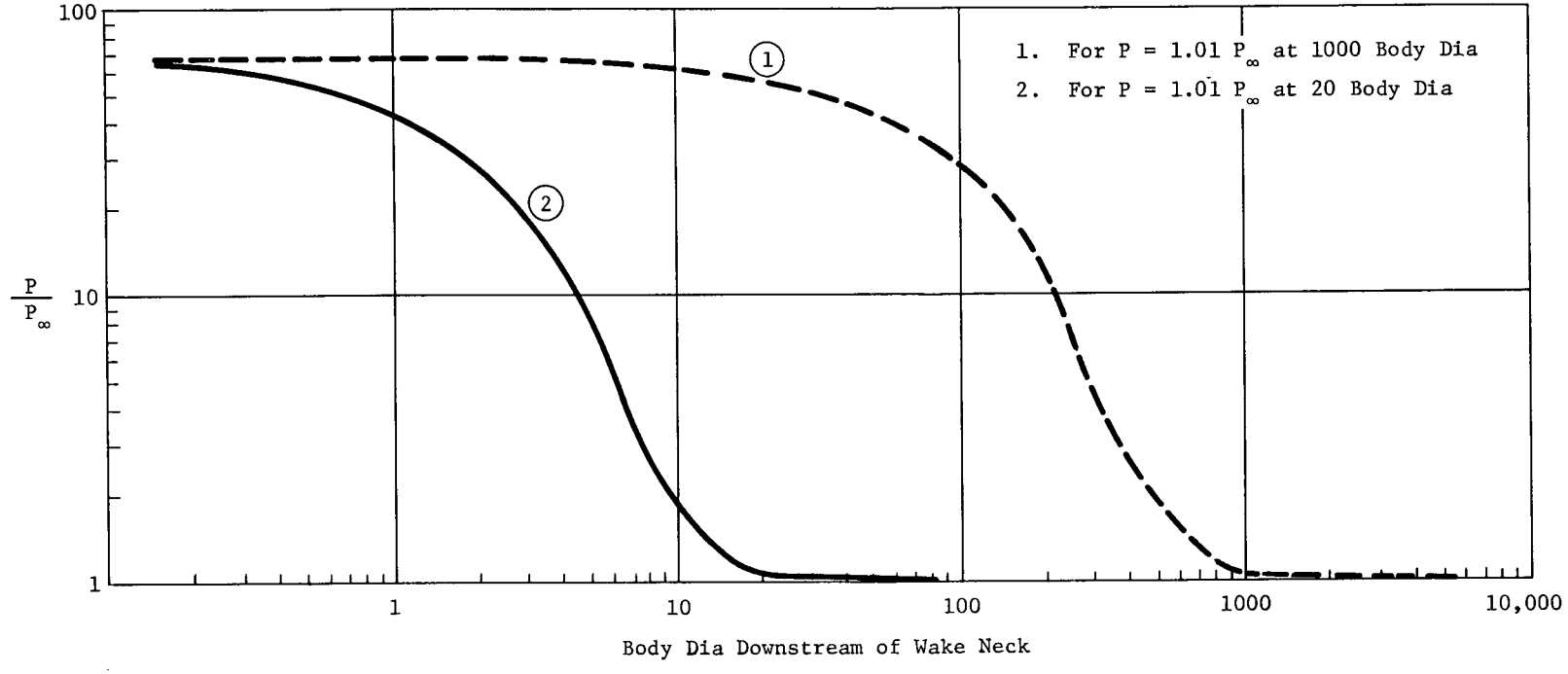

Fig. X-16 Behavior of Pressure Ratio as a Function of Downstream Distance

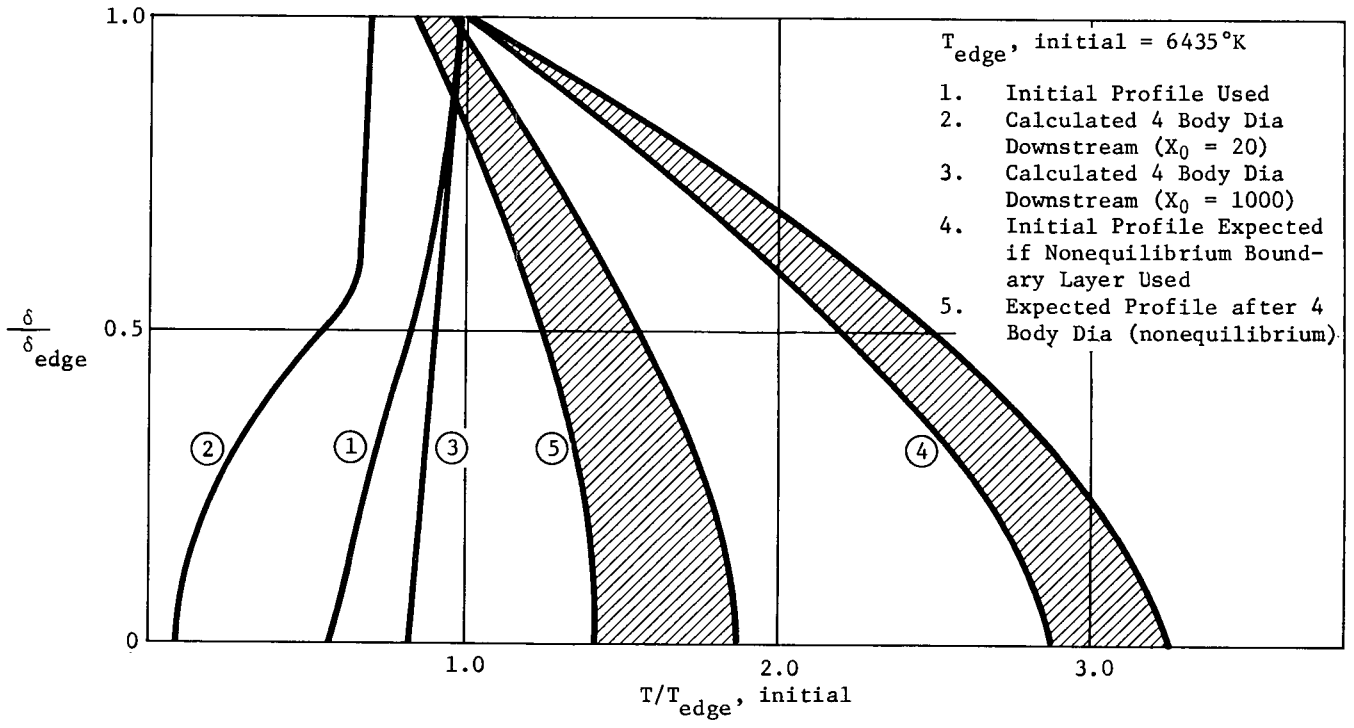

Fig. X-17 Radial Temperature Profiles in the Far Wake

To implement the model, initial conditions for the state variables and composition were needed. These were obtained by isentropically expanding equilibrium boundary-layer results around the vehicle corner, analyzing mixing without chemical reactions in the near wake, and isentropically compressing and turning the flow at the wake neck. As noted in the discussion of boundary-layer analysis, it is predicted that the boundary layer is governed by nonequilibrium processes rather than by the adapted equilibrium formulation. Several serious difficulties occur in the initial near and far wake as a result of--

1) The electron number density being predicted to be two to five orders of magnitude higher than anticipated for the nonequilibrium case.

2) Instead of the temperature excess and velocity defect condition typical of wakes, the reverse being predicted.

Unfortunately, initial conditions have been shown to be critical in the evolution of laminar far wakes (Ref X-18 and X-19). It is felt that defects in the initial conditions used constituted a serious limitation in this analysis.

b. Results - The temperature defect in the calculated initial profile is noted in Fig. X-17. This defect is still influencing the profile four diameters downstream. The types of profiles expected, had a nonequilibrium boundary-layer analysis been used, are also shown. It appears that diffusion effects have removed much of the variation initially present after four diameters, when X_o was chosen as 1000 diameters, but did not influence the profiles noticeably when X_o = 20 diameters. The types of profiles expected for a nonequilibrium boundary-layer analysis are also shown, together with the associated uncertainty bands. The electron density and electron collision frequency along the wake's geometric centerline are shown in Fig. X-18 as a function of distance downstream from the vehicle base. Note that the transition from near-wake to far-wake flow occurs approximately 2.8 body diameters behind the entry vehicle's baseplate. Decay with distance of both the electron number density and collision frequency is due to expansion cooling, ionic recombination, and electron attachment. Electron attachment kinetics were not included in the analysis. This, plus the fact that experimental analytical methods of hypersonic nonequilibrium wake analysis tend to overpredict electron population levels and underpredict decay rates, has led to the consequent uncertainty bands in Fig. X-18.

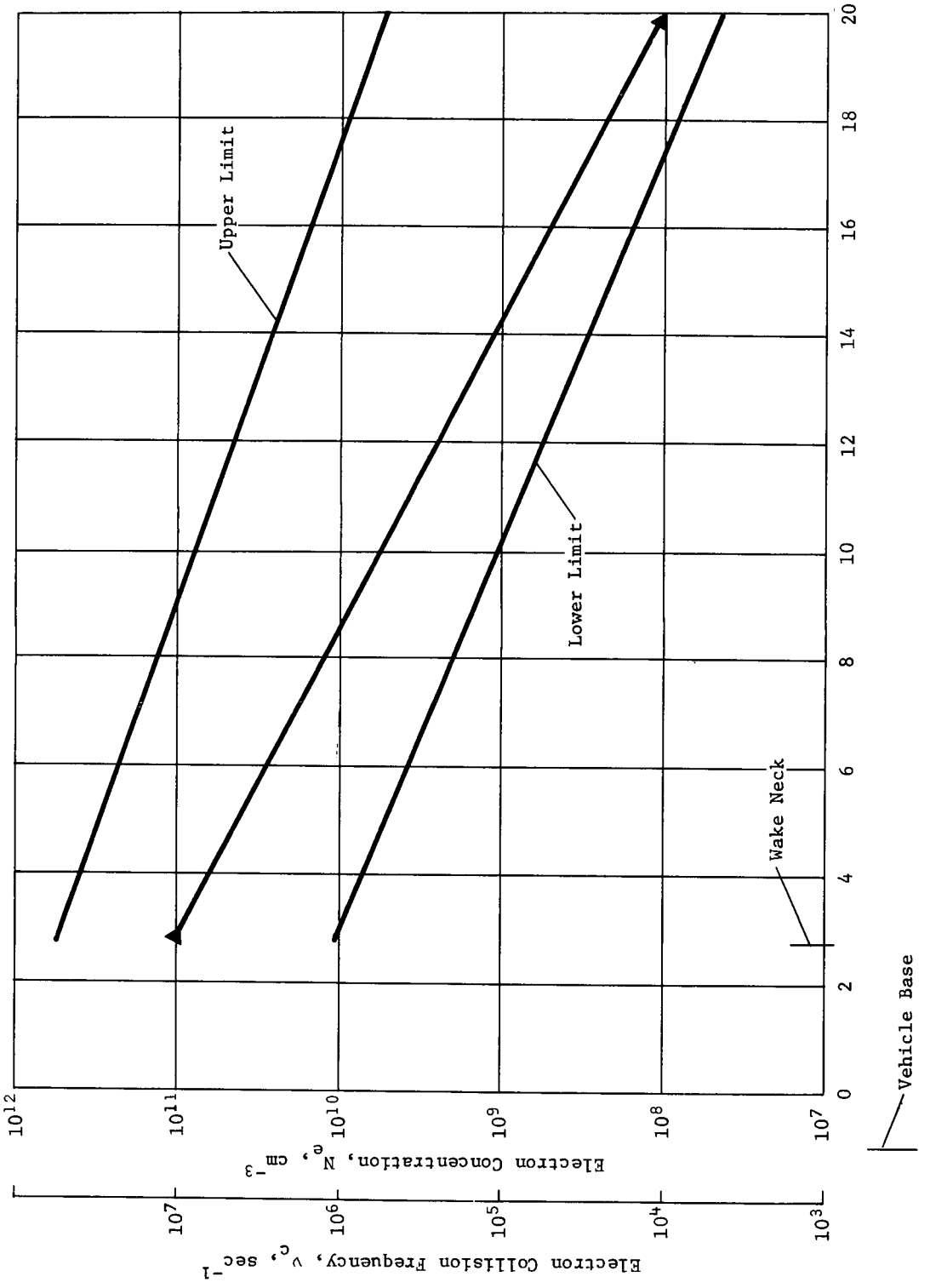

Fig. X-18 Centerline Distribution of Wake Electron Density and Collision Frequency

Attachment of electrons to atomic H might very well provide further relief to the telecommunication problem. Hydrogen-electron attachment mechanisms in the far wake should be further investigated. In addition, the reliability of the chemical reaction rate model should be checked. This can be achieved in part, at least, by examining the effects of rate-constant variation on the resultant calculated electron number density. Also, because wake temperatures are less than 6000°K, experimental determination of reaction rates is feasible. This is not true for the forebody inviscid flow field, for example, where shock-layer temperatures are much higher.

c. Conclusions - Results of the analysis of the far wake at 60 km below turbopause and entry velocity of 50 km/sec indicate that electron concentration and collision frequency in the wake are low enough to assure communication to the orbiter at this altitude. (See Chapter V.) Although the wake is certainly longer than the 20 body diameters shown in Fig. X-18, the fluid mechanics and chemical kinetics governing wake flow indicate that the electron concentration cannot appreciably increase as the flow proceeds further downstream. Detailed thermochemical analysis for greater downstream distances can be obtained, but this requires considerably more computer cost than could be justified. As numerical integration techniques for entry velocities and flow conditions typified by this mission study are improved, computation times should decrease considerably. The effect of implementation of physically more realistic viscosity and electrical conductivity models on entry telecommunication should be investigated. For example, the transport properties model for the H_2/He model used for the body heating analysis (See Section B.) should be incorporated in the wake flow-field analysis.

Because attachment of electrons to atomic H should drive the wake electron concentration even lower than currently predicted, the reaction

$$H + e + M \rightleftharpoons H^- + M$$

should be incorporated in future analyses.

B. ENTRY AEROHEATING

1. Probe Heating Analysis

a. Analysis

Thermodynamic Properties - The continuum heating analysis requires knowledge of the composition and thermodynamic and transport properties of an equilibrium gas mixture. Composition and thermochemical properties of individual species are needed to determine mixture transport properties. Equilibrium species number densities and gas mixture properties were obtained from the Möllier option of the Horton and Menard thermochemical code (Ref X-21), while species properties were computed by the Martin Marietta STP program, using the same basic spectroscopic data as Horton and Menard.

Transport Properties - Transport properties (i.e., viscosity and thermal conductivity) of H_2/He mixtures are needed to solve viscous flow-field and heating problems. A program for computing these properties is available at Martin Marietta, and its theoretical basis is described in Ref X-1. Appendix B. Results obtained from this program are presented in Fig. X-19 and X-20 for viscosity and thermal conductivity, respectively. These transport properties were computed for equilibrium composition of the H_2/He mixture over a temperature range from 250 to 25,000°K and a 10 order-of-magnitude range in density.

Convective Heating - To determine heating in the postshock stagnation region, it is first necessary to define the flow-field properties. Following passage through the transition flow regime, a shock is formed and the postshock region can be analyzed by continuum flow theory. Initially, the shock layer is fully viscous and in chemical nonequilibrium. As the free-stream density increases, the viscous region gradually gives way to a partially viscous, partially inviscid flow field, the viscous portion of which can be treated by boundary-layer theory. Although this theory is strictly applicable only when the viscous layer is thin, its use in situations involving boundary-layer thicknesses that are an appreciable fraction of shock standoff distance can lead to reasonable heating predictions (Ref X-8).

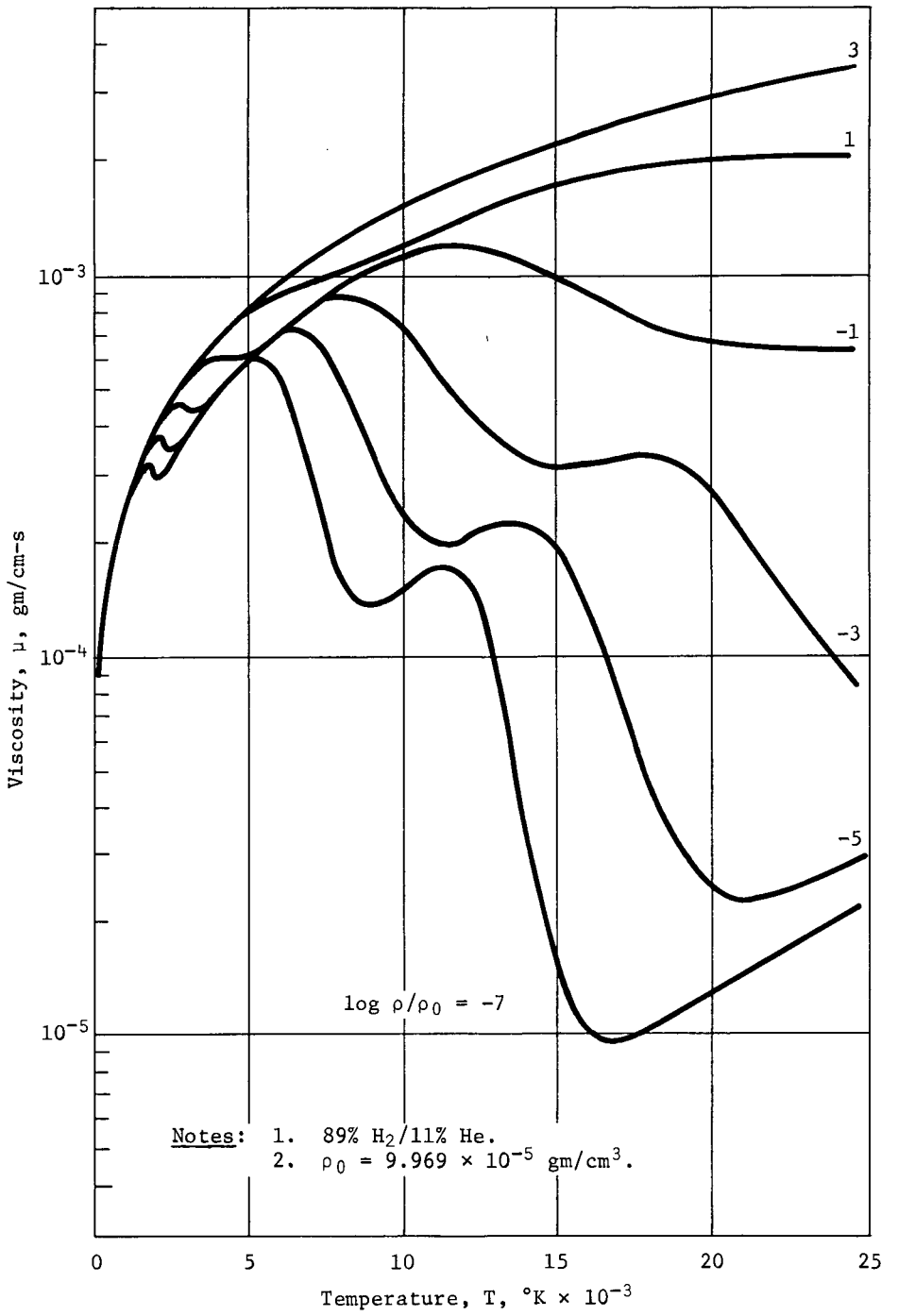

Fig. X-19 Viscosity of a H_2/He Mixture

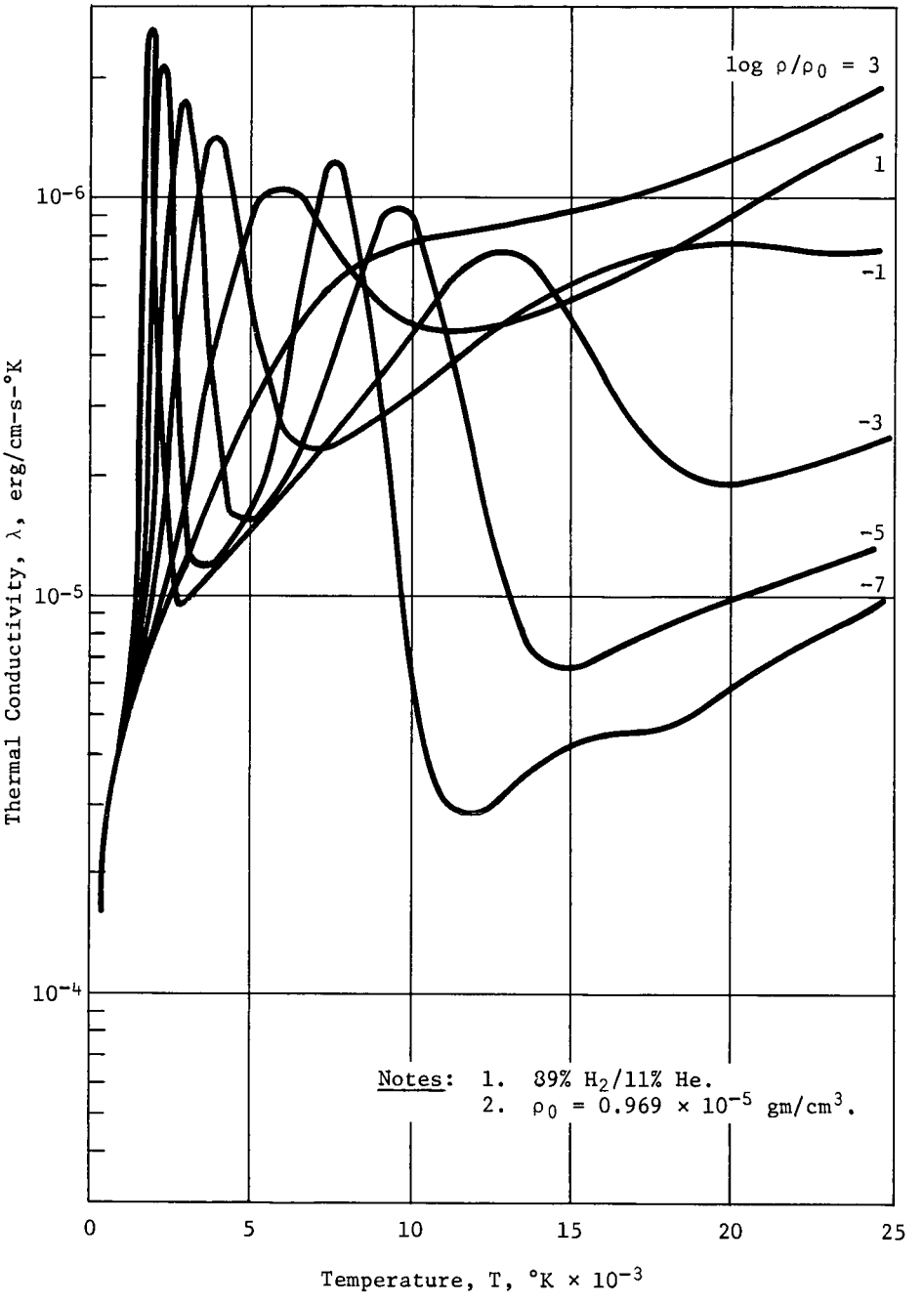

Fig. X-20 Thermal Conductivity of a H_2/He Mixture

The equilibrium boundary layer approach was used for all continuum convective heating calculations. The method employed is an adaption of one developed by Smith and Cebeci (Ref X-22) for numerical solution of boundary-layer equations. An implicit finite-difference technique provides a nonsimilar solution to the compressible laminar or turbulent differential equations. Equilibrium thermodynamic and transport properties of the H_2/He mixture previously discussed were used in these calculations.

b. Results

Hemisphere-Cylinder Heating Results - Cold-wall heating rates for the hemisphere-cylinder body were computed for a range of entry angles and associated trajectories from $\gamma_e = -15°$ to $-85°$. Rates for two of these trajectories, $\gamma_e = -35°$ and $-45°$, are shown in Fig. X-21 and X-22. These are composite rate curves that include free-molecule, transition, and equilibrium continuum heating. Free-molecule heating was computed from the relation $q_{FM} = \frac{\alpha}{2} \rho_\infty U_\infty^3$. The energy accommodation coefficient, α, for the curves of Fig. X-21 and X-22 was set at 0.1, as recommended by Ref X-1. No significant heating occurs above the turbopause altitude of 200 km; below this altitude, the heating rate increases rapidly.

Time-integrated heating-load curves are shown for several entry angles in Fig. X-23, which indicates the much greater total heating that results from shallow-angle entries. The associated long heating times more than compensate for the lower rates that occur for smaller entry angles. This effect of entry angle is seen to be much less important for larger angles, the increase in heating from a nearly vertical entry to $\gamma_e = -35°$ being only about 40%.

To assess the effects of radiative heating from the hot shock-layer gases, a computation was performed using an isothermal-slab radiation model developed by Nelson (Ref X-23), which includes detailed spectral considerations and self-absorption. The radiation cooling-factor technique described by Tauber (Ref X-24) was used to approximately account for the nonisothermal character of the actual shock layer. Results of this computation are given in Fig. X-24. Note that radiative heating is only about 10% of the convective heating rate at 110 km.

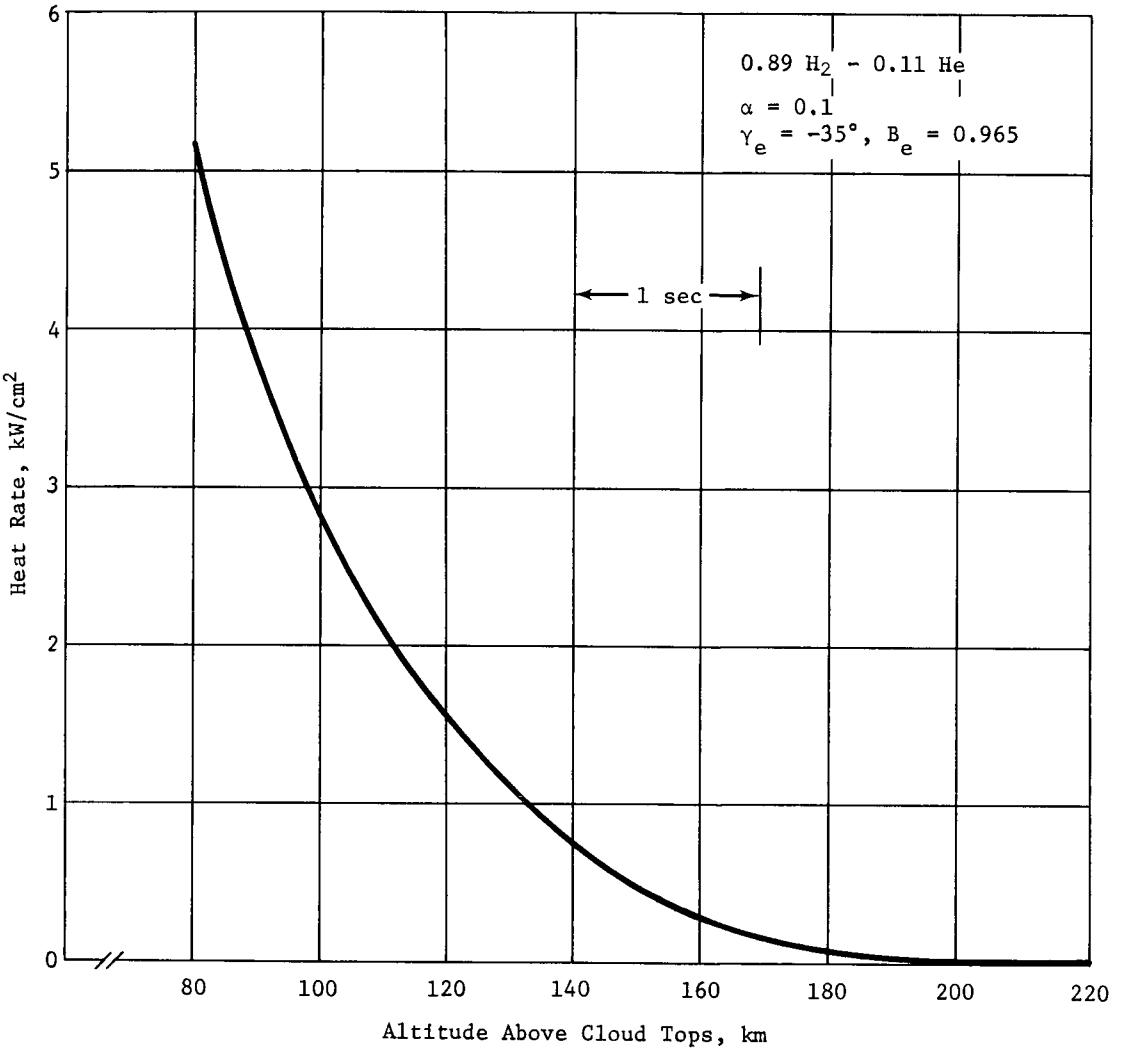

Fig. X-21 Stagnation-Point Convective Heat-Transfer Rate, γ_E = -35°

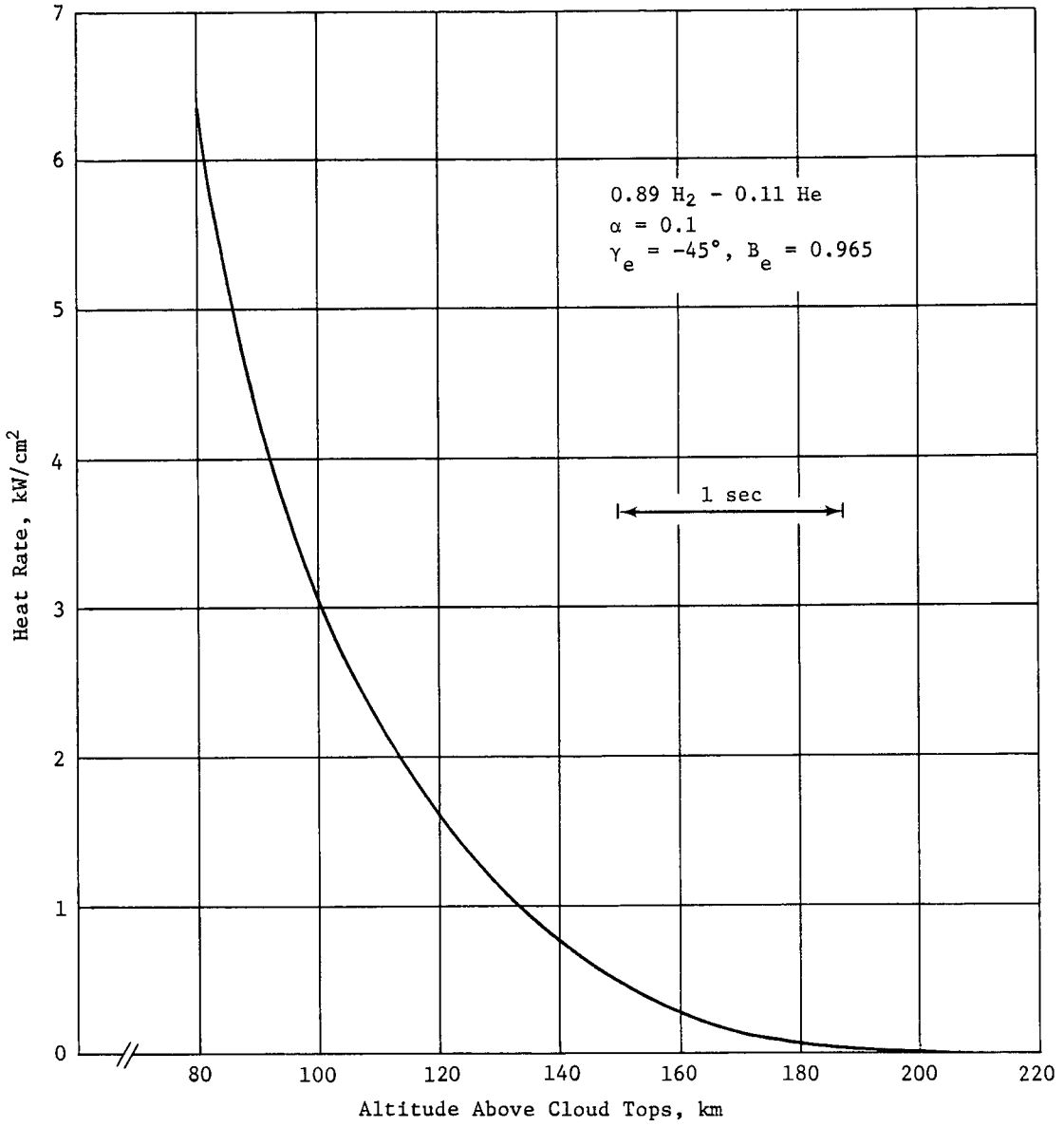

Fig. X-22 Stagnation-Point Convective Heat-Transfer Rate, γ_E = -45°

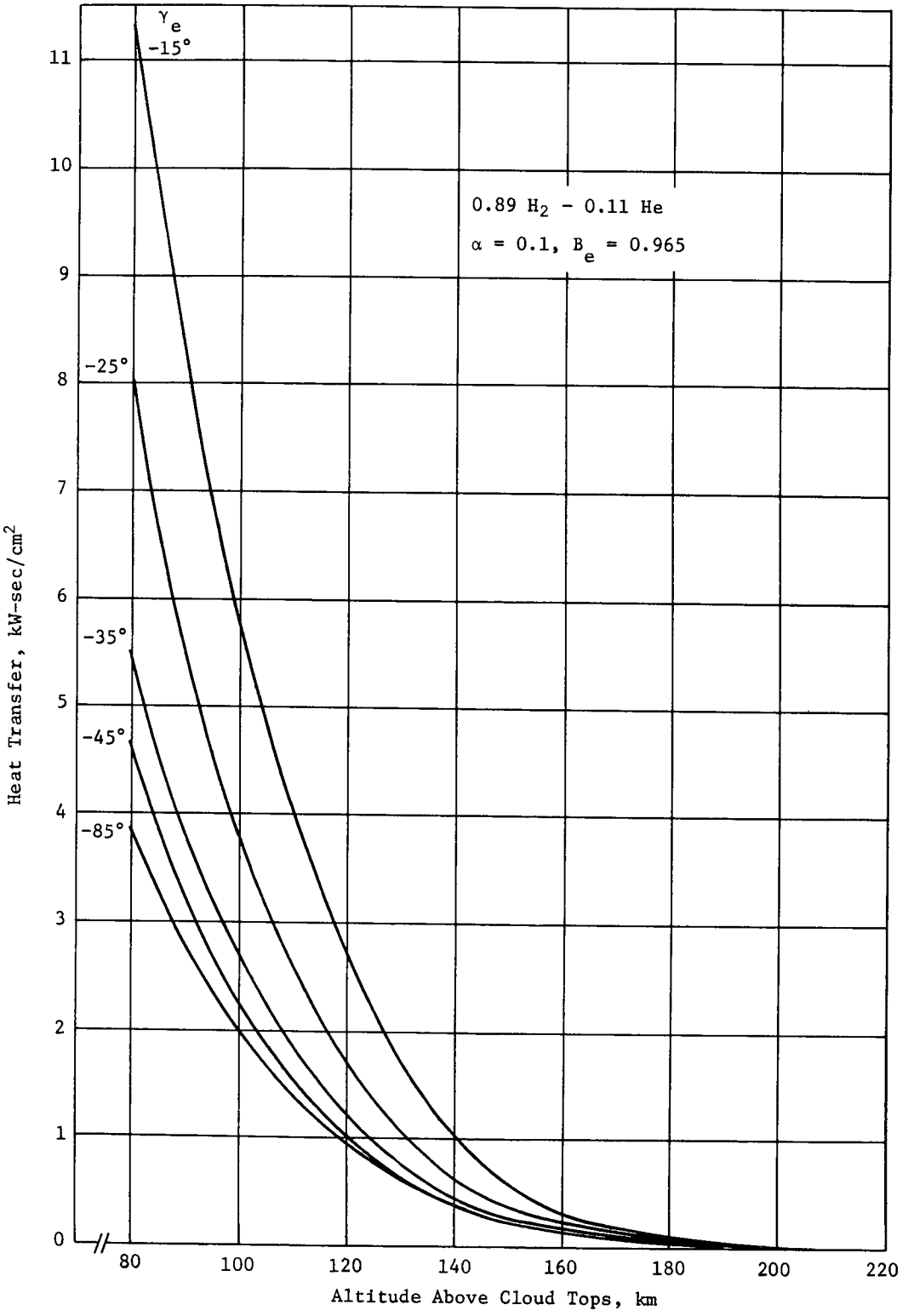

Fig. X-23 Stagnation-Point Convective-Wall Heat Transfer

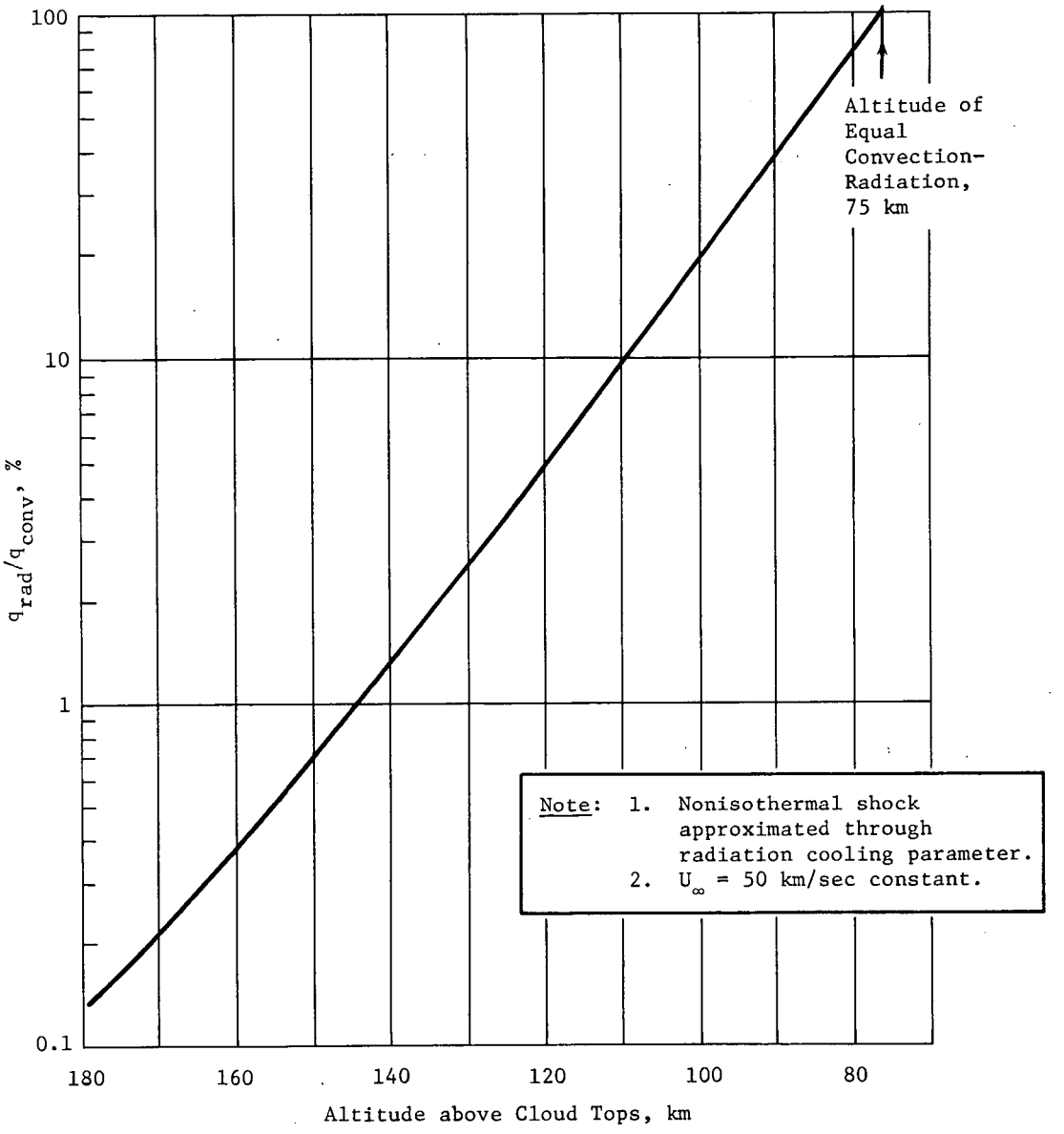

Fig. X-24 Jovian Radiation at Lower Altitudes

Stagnation-point heating represents the most severe thermal environment expected on the blunt body. To assess variations in heating around the body, the boundary-layer program was used to obtain an off-axis distribution up to the hemisphere-cylinder junction. This analysis, of course, includes constraint to flight at zero angle of attack. The results, which are not significantly altitude-dependent, are shown in Fig. X-25, where the off-axis convective heating rate has been normalized by the stagnation-point value. As can be seen from this figure, heating drops off rapidly around the body until, at the hemisphere-cylinder junction, the heating rate is only about 10% of the stagnation rate.

Sphere-Cone Heating Results - Heating calculations similar to those for the hemisphere-cylinder body were performed for a sphere-cone configuration with a nose radius of 10.16 cm, base radius of 40.64 cm, and cone half-angle of 30°. Based on the results for the hemisphere-cylinder shape, only one entry angle $\gamma_e = -35°$ and trajectory were considered. The heating rate curve of Fig. X-26 again is a composite, covering the free-molecule, transition, and continuum flow regimes. Heating still does not become appreciable until below the turbopause, but the smaller probe nose radius results in a faster increase in heating rate than was observed in Fig. X-21 for the hemisphere-cylinder body at the same entry angle. The sphere-cone rate at 80 km is roughly double that for the hemisphere-cylinder at the same altitude.

Total heating load as a function of altitude is presented in Fig. X-27, while the off-axis heating rate distribution is shown in Fig. X-28. The increase in total heating below 200 km is quite rapid, rising to a value of 9.75 kW/cm^2 at 80 km. This can be contrasted with the lower total heating of 5.5 kW/cm^2 predicted at this altitude for the hemisphere-cylinder configuration in Fig. X-23. The off-axis distribution of Fig. X-28 differs in some respects from that for the larger nose-radius body of Fig. X-25. The spherical portion of the curve is similar except for the region near the stagnation point. Here, a locally increased heating rate is caused by vorticity effects, which are of consequence only on bodies with relatively small nose radii. Both distributions show 60% reduction in heating rate at $S/R_N \approx 1$. Beyond this point for the sphere-cone body, a continuing reduction of heating rate is indicated, while the sphere-cone shape heating rate remains at approximately 30% of the stagnation value as far back as the aft shoulder.

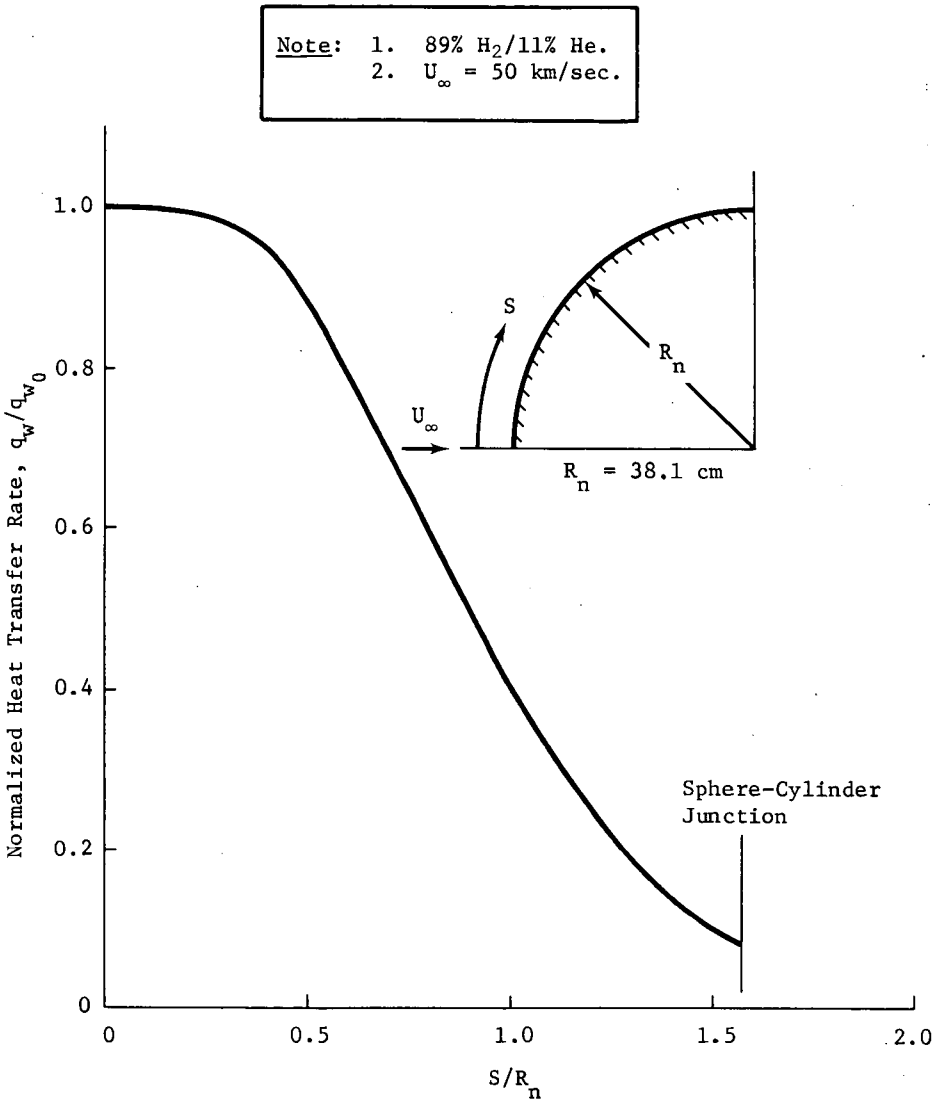

Fig. X-25 Continuum Flow Analysis, Off-Stagnation-Point Heating

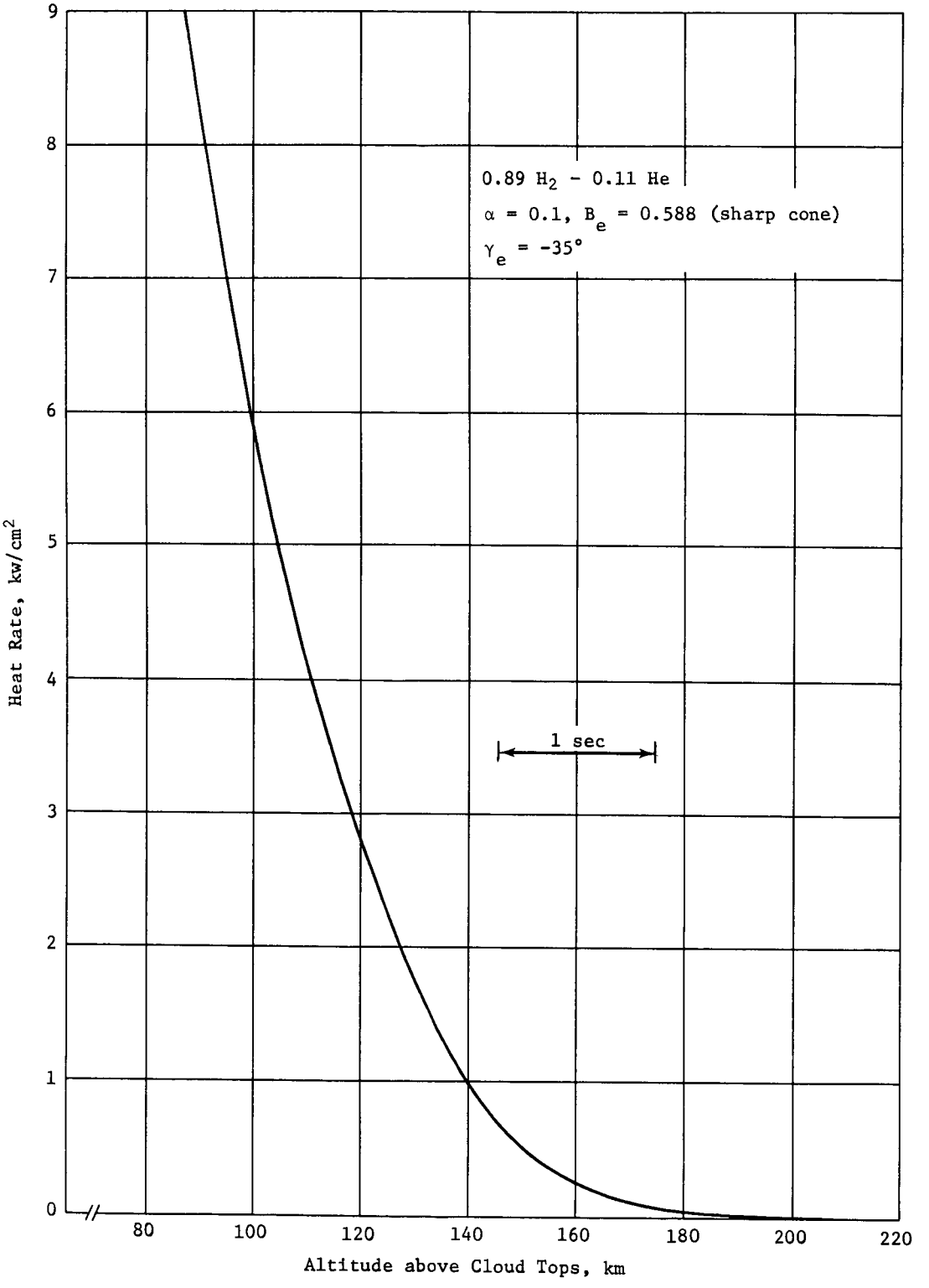

Fig. X-26 Probe Stagnation-Point Convective Heat-Transfer Rate for Sphere-Cone Configuration

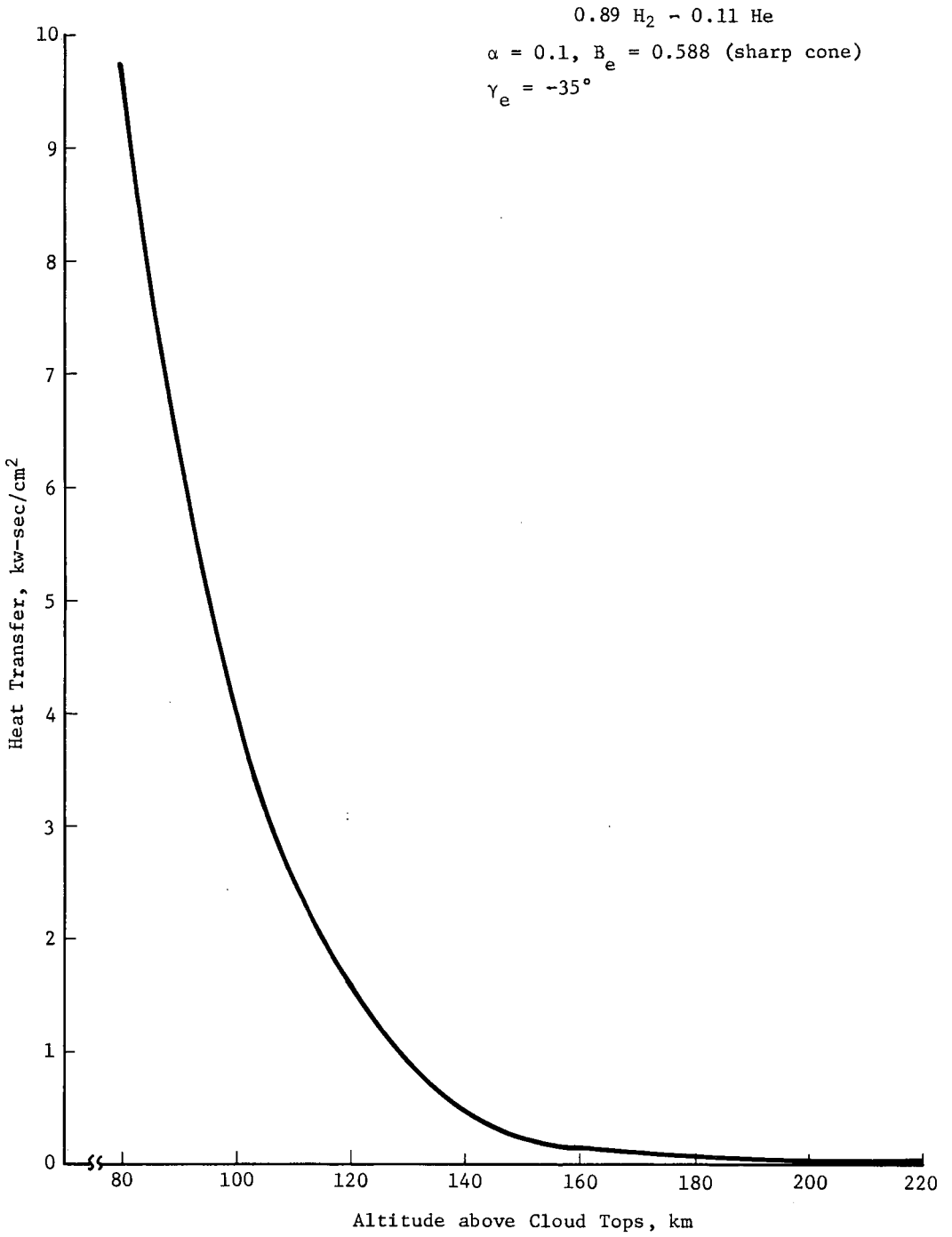

Fig. X-27 Probe Stagnation-Point Convective-Wall Heat Transfer for Sphere-Cone Configuration

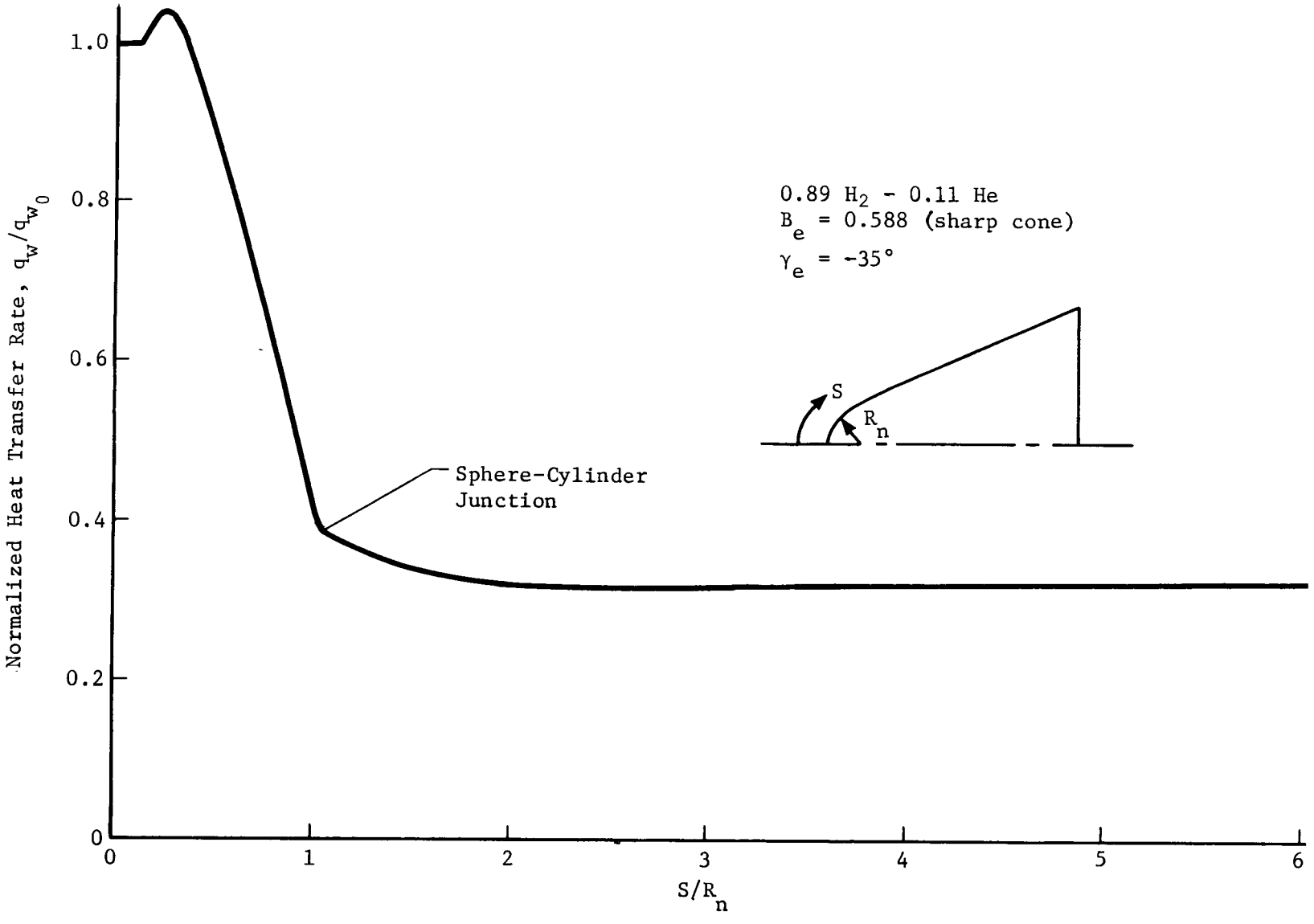

Fig. X-28 Probe Off-Axis Heating Distribution for Sphere-Cone Configuration

Conclusions - The approach adopted to obtain various heat-transfer results is believed to be conservative. Use of equilibrium chemistry leads to higher heat transfer because energy is allowed to be imparted to the body that otherwise would be retained in the gas to maintain the nonequilibrium state. In the vicinity of the stagnation point, the low flow velocity causes the time available for chemical reaction to be long, and equilibrium conditions must be present in this region. Vehicle speed is assumed constant throughout each trajectory for all heating calculations. This leads to higher heat-transfer rates than if vehicle deceleration due to aerodynamic drag were included. Higher heating rates also result from the assumption of a cold-wall condition with wall temperature assumed to equal free-stream temperature. Although its effect on heating is not as readily evaluated, the technique employed in the transition flow regime for bridging between free-molecule and continuum-heating results is also expected to be somewhat conservative.

2. Instrument Heating Analysis

At velocities encountered in Jupiter entry, free-molecule heat-transfer rates are significant and can, in fact, determine the life of critical instrument components. An expression for convective heat transfer is derived in Ref X-1, based on the work of Schaaf (Ref X-25). Bulk temperature rise for a cylindrical body, such as an instrument grid wire, oriented with its axis normal to the flow direction can be written

$$\Delta T_c = \frac{\alpha U_e^2}{\pi \rho_c C_{P_c} R_c \sin \gamma_e} \left[- \int_{z_1}^{z_2} \rho_\infty \, dz \right] .$$

In this expression, reradiation and conduction losses have been neglected and the free-stream speed has been assumed constant at the initial entry value, U_e. Figure X-29 shows a plot of this equation for three values of energy absorption coefficient, α, on a platinum cylinder exposed to an 89% H_2/11% He Jovian atmosphere. Effects of entry angle, entry speed, and cylinder radius are in the parameter on the ordinate. These quantities are readily provided to allow easy computation of temperature rise for specific wire sizes and trajectories.

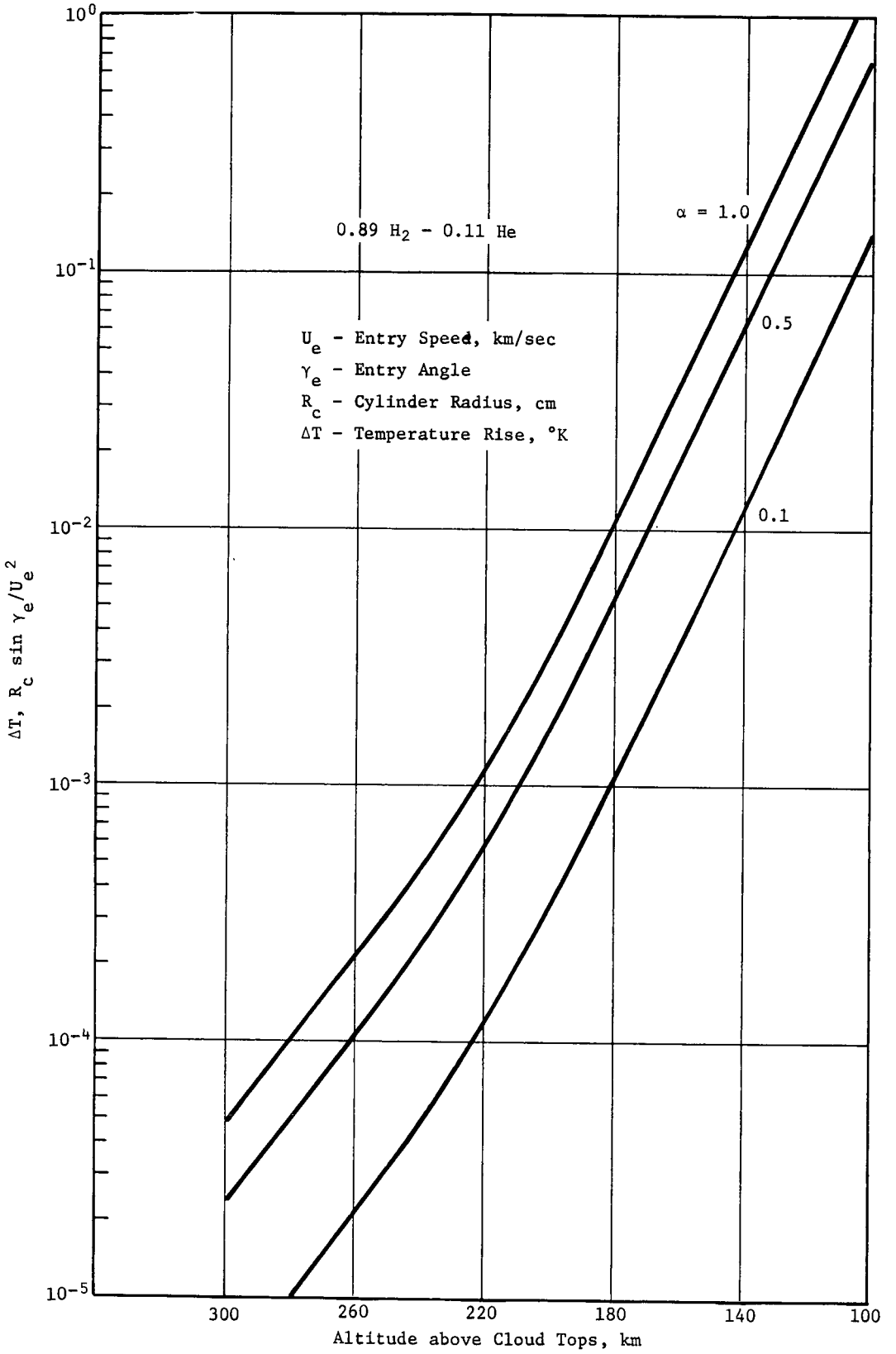

Fig. X-29 Temperature Rise of a Platinum Cylinder in Free-Molecule Regime

In the case of a 1-mil wire and an entry speed of 50 km/sec, this calculation has been performed for two accommodation coefficients and three entry angles. Results are shown in Fig. X-30. This wire size represents a typical critical-instrument grid component exposed to free-molecule heating. For the extreme situation of $\alpha = 1.0$, heating is severe at all entry angles. At $\gamma_e = -20°$, failure would be expected above an altitude of 250 km because structural failure will occur at temperatures below the 2000°K melting point of platinum. The more likely situation, however, is represented by the dashed curves for $\alpha = 0.1$. In this case, the maximum temperature rise, 180°K at 250 km, is associated with the $\gamma_e = -20°$ entry. Thus, considerable confidence can be placed in an assumption of survival to this altitude for all entry angles of interest. If a particular instrument is outside the region of probe bow-shock influence, it may remain in free-molecule flow to much lower altitudes. Free-molecule heating can then be a much more severe problem than it was for the example cited.

The curves in Fig. X-29, while derived for free-molecule flow, can be used to estimate convective heating when a particular instrument or component is experiencing transition or continuum flow. This is because no more than the total flow energy (represented by the $\alpha = 1.0$ curve) can be imparted to any body in the flow field. Such estimates, of course, may be overly conservative, and detailed continuum analyses may be required to ascertain survivability in specific cases.

3. Conclusions

The flow-field analysis presented indicates that electron concentration throughout the near and far wakes is low enough to allow communication to the spacecraft at 60 km below the turbopause. (See Chapter V.) Although entry velocity is extremely high (e.g., Mach 70), the free-stream atmosphere is fairly tenuous. Therefore, the shock-heated flow field has cooled considerably by the time the gas reaches the near and far wakes. Unfortunately, present technology does not allow measurement of chemical reaction rates in gas mixtures shocked up to Mach 70. This is primarily because resultant gas temperature would be too high for confinement. On the other hand, sensitivity analyses can and should be performed to assess the effects of reaction-rate coefficient variation on local electron density. This could either give further confidence to the strictly theoretical chemical reaction-rate model or could indicate where, and in which direction, changes to the rate constants should be considered. For example, activation energy for

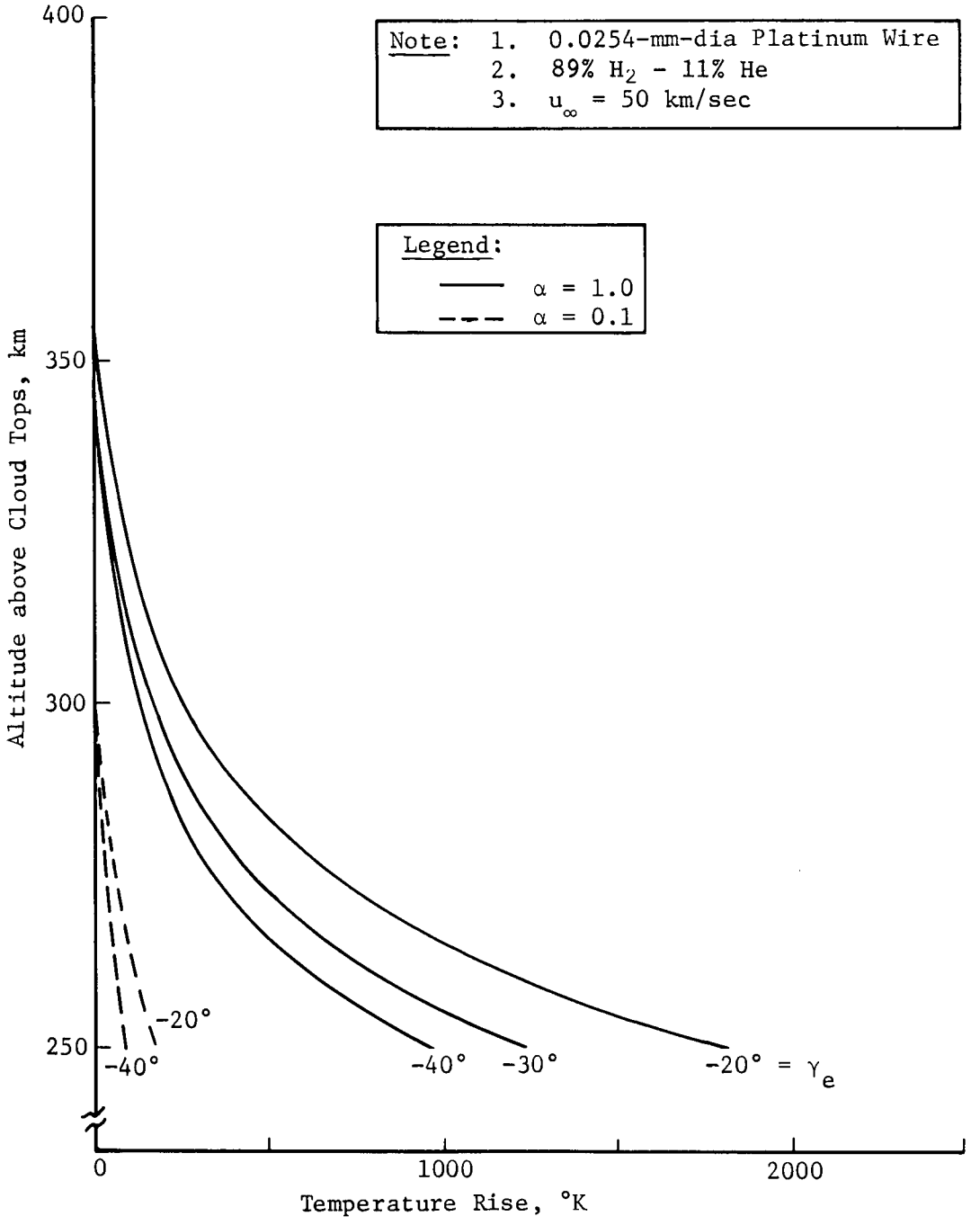

Fig. X-30 Thermal Environment of an Instrument Component in Free-Molecule Regime

ionization of He (in forebody inviscid flow) might be high by 20%. This is suspected because of the similarity between He and argon. Experimental evidence (Ref X-26) indicates that ionization of argon is roughly 80% of its ionization potential. This example is given only to indicate that optimization of the reaction model certainly should be included in follow-on studies.

Questions concerning the relative merits of slender versus blunt bodies are difficult to resolve without further analysis. Therefore, only a few qualitative comments will be presented here. First, the hemisphere-cylinder configuration probably gives a higher inviscid flow-field temperature than would an equivalent sphere-cone. This is primarily because, in the case of the hemisphere-cylinder, forebody bow shock is blunter (e.g., more nearly normal) than corresponding oblique shock created by the sphere-cone configuration. On the other hand, in the cases of the sphere-cone configuration, expansion at the base sees a stronger shock than does the hemisphere-cylinder expansion. This would tend to drive the wake static temperature slightly higher in the case of the sphere-cone. These are competing processes, and quantitative assessment would require detailed flow-field analysis of the sphere-cone configuration.

Based on the unified flow-field analysis performed, it can be concluded that nonequilibrium thermochemical analysis shows a large reduction (factor of $\simeq 10^4$) in the wake electron density over that calculated by equilibrium analysis techniques. This gives further confidence that science requirements of the mission can be fulfilled. Investigation of deeper penetration into the Jovian atmosphere should be given primary consideration in any follow-on studies.

C. REFERENCES

X-1. S. G. Chapin: *Jupiter Turbopause Probe Gas Physics Environment and Instrument Response Study*, Martin Marietta Report MCR-71-142, August 1971.

X-2. R. H. Batten: *Astronautical Guidance*, McGraw-Hill Book Company, New York, N.Y., 1964.

X-3. S. Feldman: "On the Trails of Axisymmetric, Hypersonic Blunt Bodies Flying Through the Atmosphere," *Journal of Aerospace Sciences*, p 433 thru 448, 1961.

X-4. J. T. Curtis and C. R. Strom: *Computations of the Nonequilibrium Flow of a Viscous, Radiating Fluid About a Blunt Axisymmetric Body*, Technical Report AFFDL-TR-67-40, Vol I and II, June 1967.

X-5. S. S. Penner: *Introduction to the Study of Chemical Reactions in Flow Systems*, (Revised Edition), New York, The MacMillan Book Company, 1957.

X-6. H. Lomax and M. Inouye: *Numerical Analysis of the Flow Properties About Blunt Bodies Moving at Supersonic Speeds in an Equilibrium Gas*, NASA Report TR-R-204, July 1964.

X-7. F. G. Blottner: "Finite Difference Methods of Solution of the Boundary Layer Equations," *AIAA Journal*, Vol 8, No. 2, p 193, Feb 1970.

X-8. F. G. Blottner: "Viscous Shock Layer at the Stagnation Point with Nonequilibrium Air Chemistry," *AIAA Journal*, Vol 7, No. 12, p 2281, Dec 1969.

X-9. M. Inouye, J. V. Rakich, and H. Lomax: *A Description of Numerical Methods and Computer Programs for Two-Dimensional and Axisymmetric Supersonic Flow Over Blunt-Nosed and Flared Bodies*, NASA TN D-2970, August 1965.

X-10. R. G. Graham and R. V. S. Yalamanchili: *Mixing and Combustion in Exhaust Plumes*, Nortronics-Huntsville Technical Report 371, March 1968.

X-11. R. Edleman and O. Fortune: *Mixing and Combustion in Exhaust Plumes of Rocket Engines Burning RP1 and Liquid Oxygen*, GASL Technical Report 631, General Applied Sciences Laboratories, Inc., Westbury, Long Island, New York, Nov 1966.

X-12. D. R. Chapman: *Laminar Mixing of Compressible Fluid*, NACA Report 958, 1950.

X-13. G. W. Zumwalt: Unpublished notes on jet mixing theories, Oklahoma State University, June 1963.

X-14. L. N. Wilson: "Far Wake Behavior of Hypersonic Spheres," *AIAA Journal*, July 1967.

X-15. L. N. Wilson: "Far Wake Behavior of Hypersonic Blunted Cones," *AIAA Journal*, Aug 1967.

X-16. D. K. McLaughlin: "Experimental Investigation of the Stability of the Laminar Supersonic Cone Wake," *AIAA Journal*, April 1971.

X-17. A. Demetriades: "Observations on the Transition Process of Two-Dimensional Supersonic Wakes," *AIAA Journal*, Nov 1971.

X-18. J. A. Moore and J. T. Lee: *The Nonequilibrium Laminar and Turbulent Far Wake with Inert Contaminants*, TRW Systems, AF 04(694)-684, 1968.

X-19. Kwan-Sun Wen and Tung Chen: *Axisymmetric Viscous Wake Analysis for a Hypersonic Re-entry Body*, GM Defense Research Laboratories Technical Report TR66-12A, 1966.

X-20. D. Brooke: *The McDonnell Nonequilibrium Normal and Oblique Shock, Computer Program*, McDonnell Douglas Corporation Rept No. E596, Aug 1968.

X-21. T. E. Horton and W. A. Menard: *A Program for Computing Shock-Tube Gasdynamic Properties*. JPL Technical Report 32-1350, 1969.

X-22. A. M. O. Smith and T. Cebeci: "Numerical Solution of the Turbulent Boundary Layer Equations." DAC 33735, May 1967.

X-23. H. F. Nelson: *Equilibrium Radiation from Isothermal Hydrogen-Helium Slabs*. AAES 67-12, Purdue University, July 1967.

X-24. M. E. Tauber and R. M. Wakefield: *Heating Environment and Protection During Jupiter Entry*. AIAA Paper No. 70-1324, 1970.

X-25. S. A. Schaaf: "Mechanics of Rarefied Gases." *Handbuch der Physik*, Vol 8, Part 2, p 591, Springer-Verlag, Berlin, 1963. (S. Flugge, ed.)

X-26. S. I. Sandler: Private communication, Dec 1971.

XI. RADIATION ANALYSIS

The Jupiter turbopause probe missions involve both natural and artificial sources of nuclear radiation that can affect the performance of probe and spacecraft components and materials. Natural sources include solar flares (high-energy protons and other charged particles), the solar wind (low-energy charged particles), cosmic rays originating outside the solar system (very energetic charged particles), and high-energy protons and electrons trapped in Jupiter's magnetic fields. Artificial radiation fields will be generated as a result of radioisotope thermoelectric generators (RTGs) on the spacecraft (S/C) and from radioisotope heaters on board the probe. These nuclear devices emit gamma rays and energetic neutrons throughout the mission.

The radiation environment for the missions will consist of fluxes of four distinct types of particles:

1) Protons
2) Electrons

} from solar, galactic, and Van Allen radiations

3) Neutrons
4) Gamma rays

} from the Pu^{238} RTGs and heaters

These particles differ in charge and mass, which determines the mechanisms by which they interact in matter. Uncharged radiations (neutrons and photons) are attenuated exponentially because they can be absorbed in one or a few atomic collisions. Charged radiations (protons and electrons) exhibit fairly definite ranges in matter because it usually takes thousands of atomic collisions to stop them. Neutrons can produce gamma rays and electrons can produce X-rays as secondary radiations. The attenuation of electrons and protons is relatively insensitive to material composition. Neutrons are best attenuated by hydrogenous material (e.g., H_2O, LiH), while protons are best attenuated by materials of high atomic number (e.g., W, Pb, U).

From Chapter II, it can be seen that the radiation fluences imposed on the probe by artificial sources are significantly serious (i.e., 10^8 n/cm^2); however, estimates of the natural Jupiter radiation environment indicate a significantly greater hazard (i.e., 10^{13} n/cm^2) for the upper-limit model.

In the following paragraphs, the effects of radiation environment and hardware susceptibility to radiation fields on mission trajectories are discussed and approaches recommended.

A. MISSION TRAJECTORIES

Several missions were studied for turbopause probe candidates. The three selected are shown in the tabulation below.

	Mission Type		
	Probe Optimized	(Spacecraft) Radiation Compatible	JS-77
Mission Number	1A	2A	7
Periapsis Radii	1.1 R_J	4.0 R_J	4.85 R_J
Mission Duration	760 days	655 days	557 days
Spacecraft	Pioneer	Pioneer	MOPS
Launch Date	10/21/78	10/13/78	9/5/77
Arrival Date	11/19/80	7/29/80	3/16/79

In mission 1A, the potential radiation damage to the S/C was ignored, the S/C provided the probe deflection energy, and the probe was optimized for science data return. Mission 2A was selected at a 4 R_J flyby radius and nominal radiation environment for Pioneer based on:

1) Radiation Workshop data presented in Chapter II and using 0.5 gm/cm^2 S/C shielding as shown in Table XI-1,

2) cursory review of radiation damage to science carried on the Pioneer, as shown in Fig. XI-1,

3) by a cursory review of the Pioneer component damage threshold as shown in Fig. XI-2.

All these missions are assumed to impose the same natural Jupiter radiation environment on the S/C and probe as that discussed in Chapter II.

C.1.a

Table XI-1 Pioneer S/C Radiation Environment - 0.5 gram/cm^2 Protection (Ref XI-1 & XI-2)

Environment	Fluence, particles/cm^2		Dose, rad		Equivalent Neutrons	
	Nominal	Upper Limit	Nominal	Upper Limit	Nominal	Upper Limit
2 R_J						
Protons (20 MeV)	2.63×10^{10}	1.1×10^{13}	880	377,000	5.26×10^{10}	2.2×10^{13}
Electrons (3 MeV)	2.0×10^{11}	1.12×10^{12}	6800	37,300	6.7×10^{7}	3.7×10^{8}
Totals			7680	414,300	5.26×10^{10}	2.2×10^{13}
3 R_J						
Protons (20 MeV)	1.26×10^{10}	6.45×10^{12}	420	215,000	2.52×10^{10}	1.29×10^{13}
Electrons (3 MeV)	5.0×10^{10}	3.16×10^{11}	180	10,500	1.7×10^{7}	1.1×10^{8}
Totals			600	225,500	2.52×10^{10}	1.29×10^{13}
4 R_J						
Protons (20 MeV)	2.97×10^{9}	2.52×10^{12}	100	84,000	5.94×10^{9}	5.04×10^{12}
Electrons (3 MeV)	8.9×10^{9}	1.05×10^{11}	300	3,500	2.97×10^{6}	3.5×10^{7}
Totals			400	87,500	5.94×10^{9}	5.04×10^{12}
5 R_J						
Protons (20 MeV)	1.87×10^{8}	6.77×10^{11}	10	22,600	3.74×10^{8}	1.35×10^{12}
Electrons (3 MeV)	1.32×10^{9}	3.16×10^{10}	40	1,050	4.4×10^{5}	1.05×10^{7}
Totals			50	23,650	3.74×10^{8}	1.35×10^{12}
Conversion factors:	3×10^{7} protons/rad	1 neutron = 0.5 protons				
	3×10^{7} electrons/rad	1 neutron = 3000 electrons				

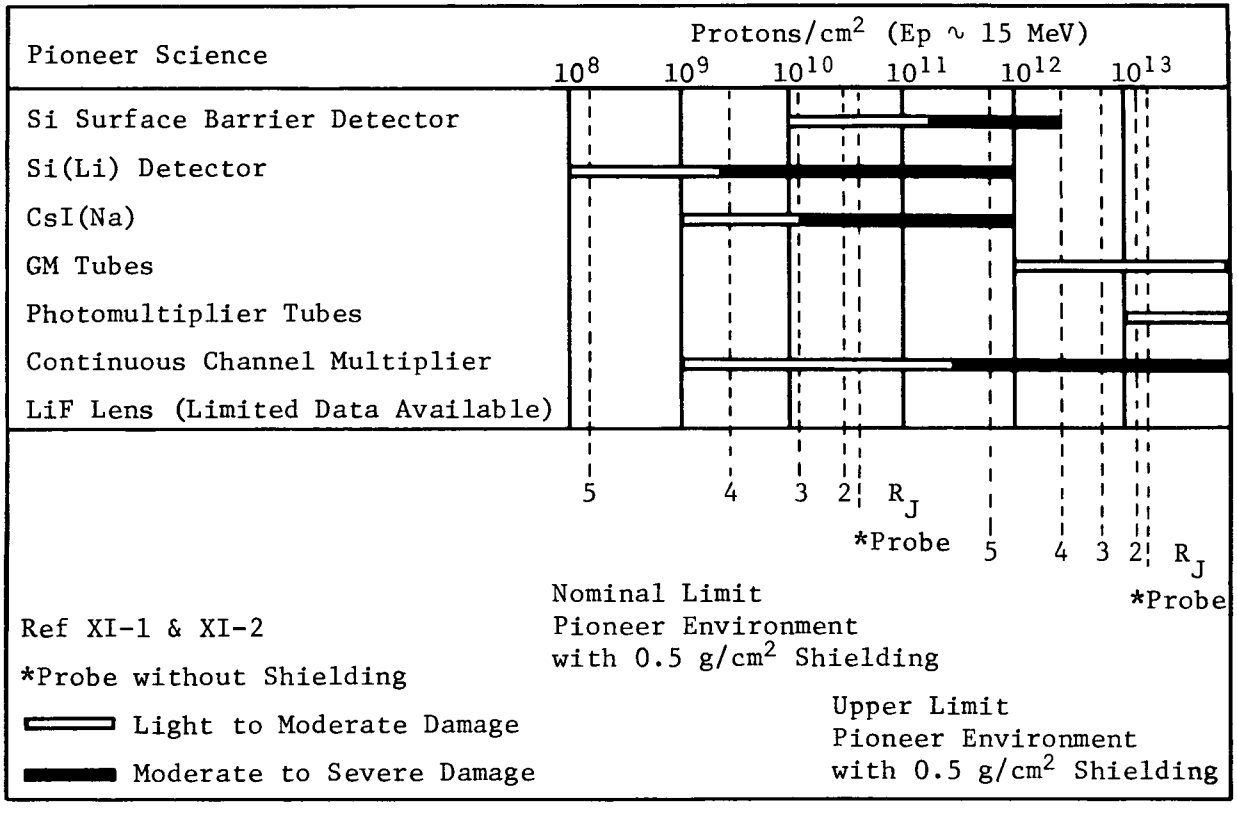

Fig. XI-1 Pioneer Science Typical Radiation Damage for Various Periapsis Radii

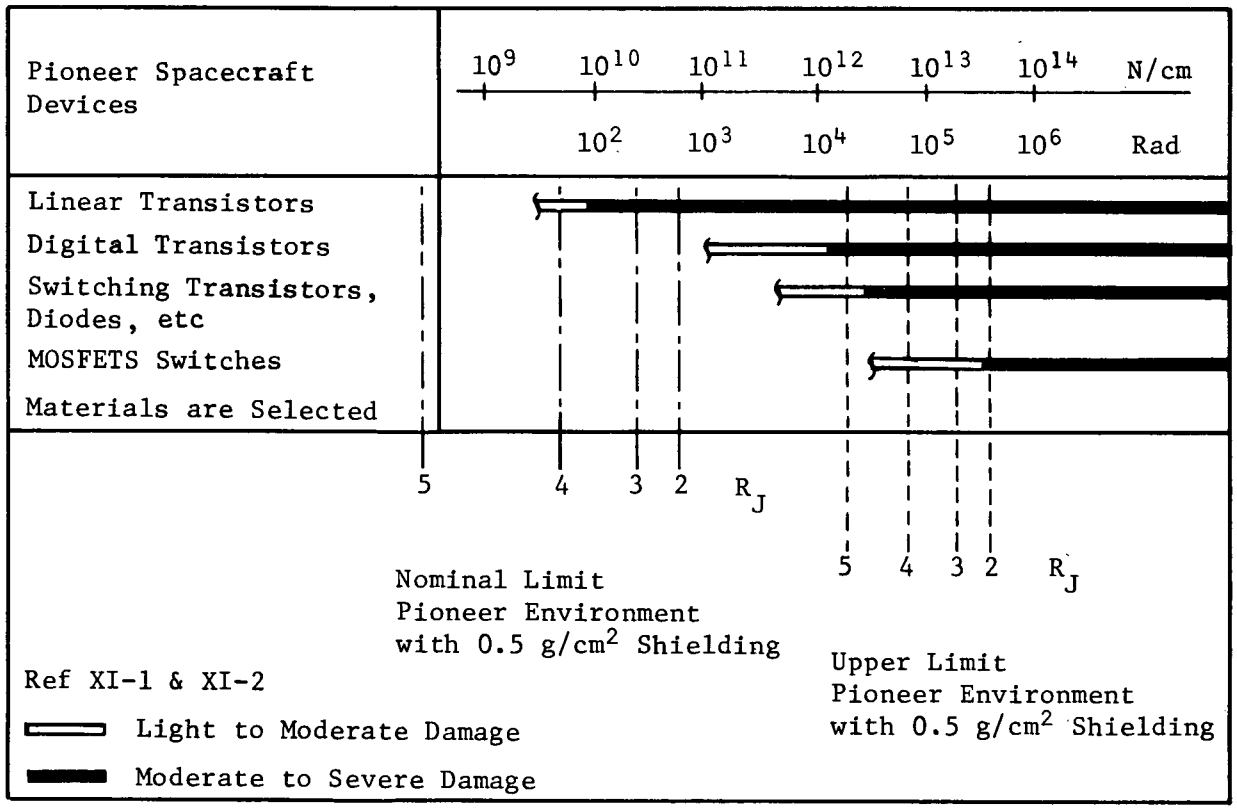

Fig. XI-2 Pioneer S/C Typical Radiation Threshold Levels for Various Periapsis Radii

B. RADIATION ENVIRONMENT

Natural and artificial radiation environments are discussed in Chapter II, Section C. Residual radiation has not been considered. However, it is believed that the probe structure, after passing through the trapped radiation belts, could become so radioactively hot from induced radiation caused by high-energy protons that the residual radiation remaining after the probe emerged from the belts would temporarily incapacitate the science instruments. The problem is not serious in materials of low atomic mass and can be alleviated by careful selection of materials. An in-depth analysis of this subject should be part of any future evaluations of the overall radiation belt hazard to probe and spacecraft.

C. HARDWARE SUSCEPTIBILITY TO RADIATION

1. Science

The Jupiter turbopause probe hardware susceptibility is separated into two areas: science and probe subsystems, including materials. The science complement discussed in Chapter III consists of a neutral mass spectrometer (NMS), neutral retarding potential analyzer (NRPA), ion retarding potential analyzer (IRPA), two electron temperature probes (ETPs) often called Langmuir probes, and either a hydrogen photomultiplier photometer with a helium channeltron photometer or both photometers replaced by a reflection grating optical spectrometer. These instruments include elements such as photomultiplier tubes, electron multiplier tubes, continuous channel multiplier (channeltrons), magnesium fluoride filter, calcium fluoride filter, and reflective surfaces. In Chapter II it was noted that the upper-limit probe radiation field was 1.43×10^{13} protons/cm^2. Reference XI-1 indicates that photomultiplier tubes suffer light to moderate damage at 10^{13} protons/cm^2. More severe damage starts at about 3×10^{11} protons/cm^2. There are limited data for photometer filters and reflective surfaces. Each science instrument is discussed below.

a. NMS - The NMS ion collector consists of an electron multiplier, which is similar to a photomultiplier except it is somewhat less sensitive to radiation. Damage or deterioration of measurements is not expected in the probe environment.

b. NRPA and IRPA - These instruments are not expected to be damaged by probe radiation levels. Stray particles from radiation may cause an erroneous reading.

c. ETP (Langmuir Probe) - The total fluence received by the ETP electronics will not cause a degradation problem. The flux of particles from radiation causes a secondary emission flux of electrons leaving the probe. This is similar to the photoemission caused by the Sun shining on the probe on a vehicle in Earth orbit. Of the projected 15 μA generated by the electrons in the atmosphere, approximately 0.01 μA would be due to photoemission by the Sun at the Earth's distance of 1 AU and only about 0.0001 A at Jupiter's distance of 5.2 AU. A peak radiation fluence of 10^{13} particles/cm^2 would cause a secondary emission current of about 1 μA which is two orders of magnitude greater than the photoemission problem in Earth-orbiting satellites. This is about the limit of correctible current. As long as the radiation field is equal to or less than this strength, the Langmuir probe could function and the data returned would be useful.

d. Hydrogen Photomultiplier Photometer - This photometer consists of two detectors: an 18-stage photomultiplier with a magnesium fluoride filter, and a similar 18-stage photomultiplier with a calcium fluoride filter. The photomultipliers are not expected to be damaged. However, the MgF_2 filter deteriorates approximately 36% at the critical wavelength of 1216 Å, whereas the CaF_2 filter deteriorates very little at the highest wavelength, as shown in Fig. XI-3 and XI-4.

e. Helium Channeltron Photometer - This photometer consists of several channeltrons twisted into a spiral, called a spiraltron. Radiation will cause the spiraltron to have too fast a counting rate or to accept too many photons, which will cause excessive current to be drawn and a breakdown of the gradient. With the high-voltage supply on and operating, the spiraltron will begin to suffer moderate to severe damage at a radiation level of 10^{11} particles/cm^2. However, if the high-voltage supply is left off, and the instrument is not in the operating mode, it does not begin to suffer moderate to severe damage until a level of 10^{14} particles/cm^2 is reached. The upper-limit model environment is about 10^{13} particles/cm^2. Thus, if the instrument was not turned on until after it had passed through Jupiter's radiation belts, it would have survived to make the dayglow measurements. This is acceptable because the strength of the signal caused by the radiation field would completely swamp any signal due to the dayglow. Thus, no measurements could be made inside the belts anyway.

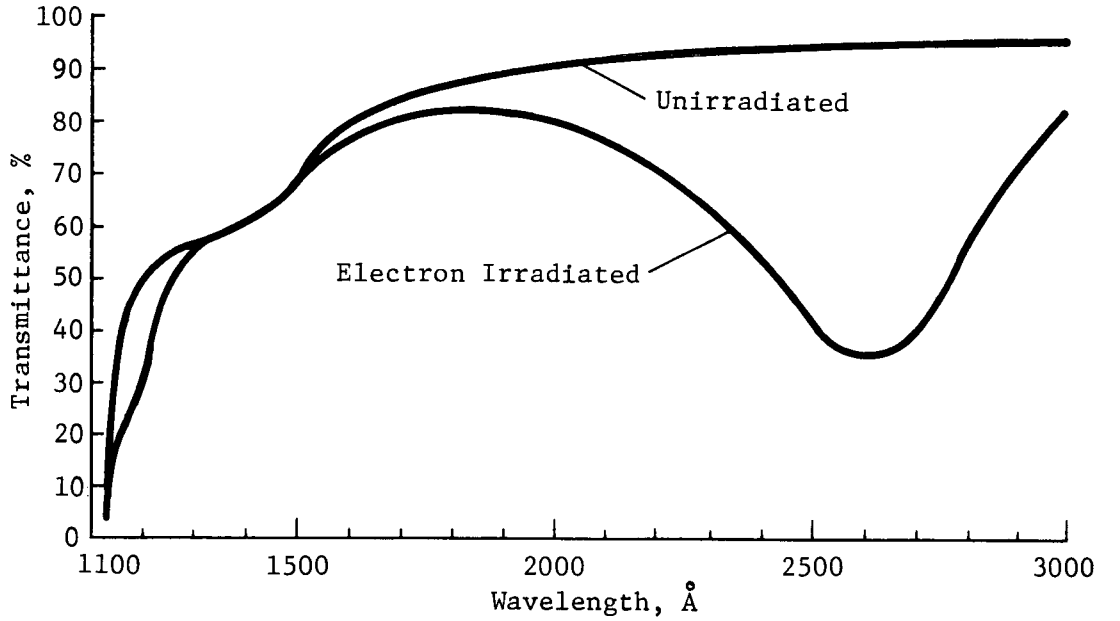

Fig. XI-3 Transmittance of MgF_2 Before and After Irradiation by 10^{14} Electrons/cm^2 at 1 and 2 MeV (Ref XI-3)

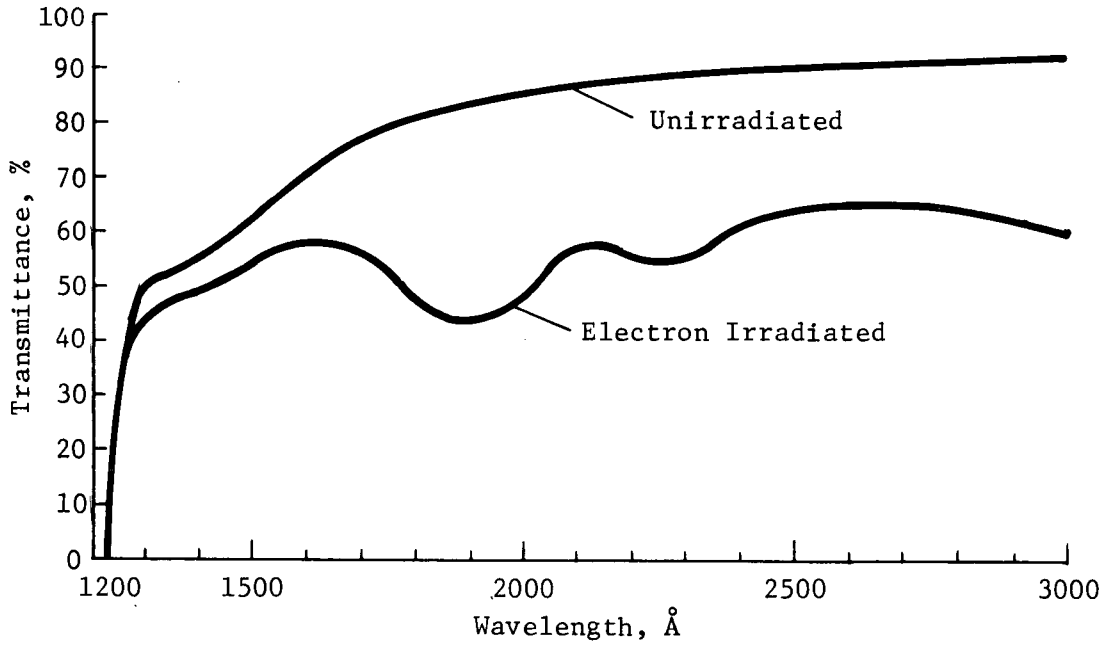

Fig. XI-4 Transmittance of CaF_2 Before and After Irradiation by 10^{14} Electrons/cm^2 at 1 and 2 MeV (Ref XI-3)

Hardening will consist of a radiation detector (e.g., scintillator or semiconductor) to continuously monitor the strength of the radiation field and turn on the optical instrument when the strength drops below some minimum value for a certain length of time.

f. Reflection Grating Optical Spectrometer - This spectrometer uses three channeltrons and a concave grating reflection surface. The channeltron damage is the same as that for the spiraltron discussed above. Few data are available for radiation damage to reflection surfaces.

2. Probe Subsystems and Materials

The sensitivity of probe electronic components is shown in Fig. XI-5 along with the probe upper limit radiation environment. It is seen that the following devices are critical:

Metal-oxide semiconductor field-effects transistors (MOSFETs);

Silicon-controlled rectifiers (SCRs);

Pyrotechnics.

Materials of three general categories were analyzed for their sensitivity to radiation: thermoplastic resins, elastomers, and thermosetting resins. Ionizing radiation produces cross-linking and scission (broken bonds) in all polymeric compounds, resulting in corresponding changes in the mechanical properties of these materials. The most resistant polymeric materials are thermosetting resins because of their three-dimensional molecular structure and high resistance to broken bonds. Among thermoplastic resins, Teflon is the most sensitive to radiation because of a progressive degradation reaction with oxygen. Thermoplastic materials generally decrease in tensile strength and elongation with increased exposure. Polyimide and polymethyl methacrylate are less sensitive than Teflon but still marginal for probe use. The dynamic mechanical properties of elastomers and plastics used in moving seals and other dynamic applications are important. Property changes under dynamic conditions differ from those obtained under static conditions. There are data for radiation damage measured under dynamic conditions.

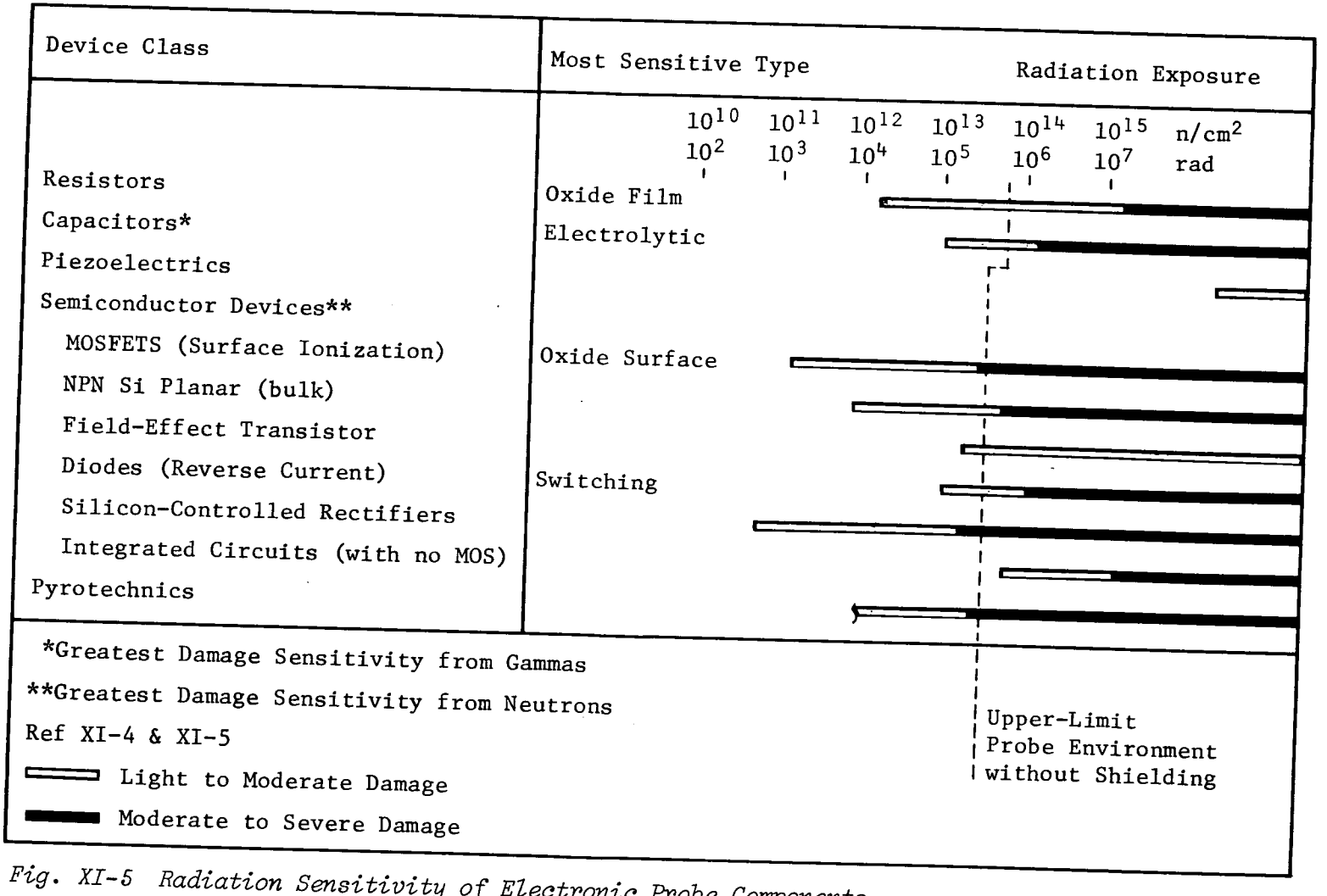

Fig. XI-5 Radiation Sensitivity of Electronic Probe Components

a. MOSFETs - These semiconductor devices include bulk and ionization damage from radiation, which requires a higher voltage for turning on. Radiation hardening will consist of testing such devices in the estimated field including provisions for increased turn-on voltage in the circuit design. Testing is defined in Ref XI-6.

b. SCRs - These devices suffer bulk damage, which affects the transfer ratio across the switch and causes the SCR to fail to switch or to switch inadvertently. The circuit design will avoid SCRs in favor of power transistors and relays. SCRs can be used in circuits required to function only at probe separation, which is before excessive radiation exposure.

c. Pyrotechnics - According to Ref XI-4, after being irradiated, these devices are more sensitive to being ignited, operate at a lower temperature, and contain more energy. Premature operation might be expected because of the radiation environment. Hardening will consist of using pyro devices on the probe for S/C-to-probe separation functions and for probe activation before arrival at Jupiter.

d. Propulsion - Reference XI-4 notes that solid propellants are damaged by radiation at approximately the same levels as pyrotechnics. Their damage consists of quicker ignition and propellant weight loss, which causes faster burning and reduced impulse. For the probe, the solid motors would be used at S/C-to-probe separation before exposure to a high radiation dose.

e. Materials - Hardening consists of selection of the proper materials.

D. RECOMMENDED APPROACH TO MINIMIZE RADIATION HAZARD

The channeltrons used in the helium photometer and optical spectrometer will have the high voltage turned on by some radiation detector at a level that is safe for channeltron operation.

The MOSFETs will be designed for higher turn-on voltage, and SCRs will be used in applications before high radiation exposure, and avoided in favor of power transistors and relays where exposure is severe. Shielding will probably be required.

Materials will be selected that demonstrate high resistance to radiation damage.

Testing of all components and materials at the expected radiation levels must be planned. When the radiation data from Pioneer F and G flights are available, the required design radiation levels must be reevaluated. Residual radiation must be investigated in depth.

E. REFERENCES

XI-1 JPL, Interoffice Memoranda, Richard H. Parker to Distribution, Subject: "Interim Report on Jupiter Radiation Belt Workshop," July, 23, 1971.

XI-2 "Pioneer Jupiter Orbiter, Presentation to the Science Advisory Group," by NASA-ARC, July, 29, 1971.

XI-3 Donald F. Heath and Paul A. Sacher: *Applied Optics*, Volume 5, Number 6, "Effects of a Simulated High-Energy Space Environment on the Ultraviolet Transmittance of Optical Materials between 1050 Å and 3000 Å," June 1966.

XI-4 Giulio Q. Varsi: American Nuclear Society, "Radiation Effects on Pseudostable Material for Long-Term Space Mission," Oct. 17-21, 1971.

XI-5 *Radiation Effects Design Handbook*, NASA CR-1785, July 1971.